

Single photon emission computed tomography : Performance
assessment, development and clinical applications.

Volume One

Gerard J. Gillen

B.Sc. (Honours)

Submitted for the degree of
Doctor of Philosophy

at the University of Glasgow,
Department of Clinical Physics and Bio-Engineering

April 1990

© G.J. Gillen

Summary

This is a general investigation of the SPECT imaging process. The primary aim is to determine the manner in which the SPECT studies should be performed in order to maximise the relevant clinical information, given the characteristics and limitations of the particular gamma camera imaging system used.

Thus the first part of this thesis is concerned with an assessment of the performance characteristics of the SPECT system itself. This involves the measurement of the fundamental planar imaging properties of the camera, their stability with rotation, the ability of the camera to rotate in a perfect circle and the accuracy of the transfer of the information from the camera to the computing system.

Following this the performance of the SPECT system as a whole is optimised. This is achieved by examining the fundamental aspects of the SPECT imaging process and by optimising the selection of the parameters chosen for the acquisition and reconstruction of the data. As an aid to this a novel mathematical construct is introduced. By taking the logarithm of the power spectrum of the normalised projection profile data the relationship between the signal power and the noise power in the detected data can be visualised.

From a theoretical consideration of the available options the Butterworth filter is chosen for use because it provides the best combination of spatial frequency transfer characteristics and flexibility. The flexibility of the Butterworth filter is an important feature because it means that the form of the actual function used in the reconstruction of a transaxial section can be chosen with

regard to the relationship between the signal and the noise in the data.

A novel method is developed to match the filter to the projection data. This consists of the construction of a mean angular power spectrum from the set of projection profiles required for the reconstruction of the particular transaxial section in question. From this the spatial frequency at which the the signal becomes dominated by the noise is identified. ✓ The value which the Butterworth filter should take at this point can then be determined with regard to the requirements of the particular clinical investigation to be performed.

The filter matching procedure can be extended to two dimensions in a practical manner by operating on the projection data after it has been filtered in the y direction.

The efficacy of several methods to correct for the effects of scatter, attenuation and camera non-uniformity are also investigated.

Having developed the optimised methodology for the acquisition and reconstruction of the SPECT data the results which are obtained are applied in the investigation of some specific clinical problems. The assessment of intractable epilepsy using ^{99m}Tc -HMPAO is performed followed by the investigation of ischaemic heart disease using ^{99m}Tc -MIBI and finally, the diagnosis of avascular necrosis of the femoral head using ^{99m}Tc -MDP is studied.

The SPECT studies described in this thesis make a significant contribution to patient management.

Acknowledgements

Thanks are extended to Dr AT Elliott for his careful reading, criticism and general guidance throughout the course of this thesis.

I am also grateful to Mrs M Watson, Mrs A McColl and Mrs C Drew of the Nuclear Medicine Department at the Western Infirmary for their help in the acquisition of the patient data.

The contribution of Professor JH McKillop to the cardiac and skeletal imaging chapters was very helpful and is appreciated. Similarly, the contribution of Dr JK Davidson to the skeletal imaging chapter is acknowledged.

Thanks are also extended to Miss M Finlayson and Mrs M Phillips for their help in the preparation of the figures and to Dr TE Hilditch for his general advice and encouragement.

Finally, I would like to thank my wife, Caroline, for her support throughout a long and difficult period.

CONTENTS

Contents of Volume One	page
Chapter 1 Introduction	1
1.1 Introduction	1
1.2 Development of SPECT	1
1.3 Advantages of SPECT	2
1.4 Thesis aims	3
1.5 System evaluation	5
1.6 Parameter optimisation	6
1.7 Clinical applications	8
Chapter 2 Theoretical Description of SPECT imaging	10
2.1 General Tomographic Reconstruction theory	10
2.1.1 Formation of Projections	10
2.1.2 Reconstruction of projections by filtered back projection	11
2.1.2.1 Reconstruction in frequency space	13
2.1.2.2 Reconstruction in Real space	15
2.1.3. Other reconstruction algorithms	17
2.2 Filtered back projection of real data	19
2.2.1 Finite spatial resolution of the camera	19
2.2.1.1 Combining opposing projections	22
2.2.2 Finite linear sampling rate	23
2.2.2.1 Sampling Theorem	23
2.2.2.2 Data interpolation	26
2.2.3 Finite angular sampling rate	28
2.2.4 Filtering the projection data	30
2.2.5 Conclusions for noise free data	32
2.3 Filtered back projection of noisy data	34
2.3.1 Stochastic noise	34
2.3.2 Noise amplification	35
2.3.3 Noise power spectra	38
2.3.4 Signal and noise power in projection images	41
2.4 Data sampling in the presence of noise	42
2.4.1 Linear sampling in the presence of noise	42
2.4.2 Angular sampling in the presence of noise	44
2.5 Non-stochastic noise	45
2.5.1 Introduction	45
2.5.2 Non-uniform detector response	45
2.5.2.1 Uniformity correction	47
2.5.3 Inconsistent data collection	49
2.6 Attenuation and scattering	50
2.6.1 Introduction	50
2.6.2 Attenuation correction	52
2.6.3 Scatter correction	56
2.6.3.1 Offset energy window	59
Chapter 3 Equipemnt Description	60
3.1 Introduction	60
3.2 The Gamma Camera	60
3.2.1 Camera Gantry	60
3.2.2 Camera Head	60

Contents of Volume One		Page
3.2.2.1	Basic Operation	61
3.2.2.2	Energy and Linearity Correction	62
3.2.2.3	Digitrac Recursive Tuning	64
3.3	Collimators	65
3.4	SPECT operation of the camera	65
3.5	Computing System	66
3.5.1	Hardware	66
3.5.1.1	System Configuration	66
3.5.1.2	Data Storage	67
3.5.1.3	Image Display	68
3.5.1.4	Analogue to Digital Converters	68
3.5.1.5	Hardcopy output	69
3.5.2	System Software	69
3.5.2.1	Operating System	69
3.5.2.2	Applications Software	70
3.5.3	SPECT Software	70
3.5.3.1	Data Acquisition	70
3.5.3.2	Reconstruction Software	71
3.5.3.3	Reconstruction filters	71
3.5.3.4	Attenuation Correction	72
3.5.3.5	Centre of Rotation Correction	73
3.5.3.6	User Generated Software	74
3.6	Phantoms	74
3.6.1	Flood field phantom	74
3.6.2	SPECT phantom	75
Chapter 4	Performance assessment of imaging system	78
4.1	Introduction	78
4.2	Planar imaging performance	79
4.2.1	Introduction	79
4.2.2	Energy resolution	80
4.2.2.1	Theory	80
4.2.2.2	Methods	81
4.2.2.3	Results	81
4.2.3	Intrinsic resolution	82
4.2.3.1	Theory	82
4.2.3.2	Methods	82
4.2.3.3	Results	83
4.2.4	System resolution	83
4.2.4.1	Introduction	83
4.2.4.2	Methods	86
4.2.4.3	Results for non-isotropic PSFs	87
4.2.4.4	Results for isotropic PSFs	87
4.2.4.5	Modulation transfer functions	92
4.2.5	Uniformity	94
4.2.5.1	Introduction	94
4.2.5.2	Methods	95
4.2.5.3	Results	97
4.2.6	Count rate linearity	97
4.2.6.1	Introduction	97
4.2.6.2	Methods	98
4.2.6.3	Results	98
4.2.6.4	Conclusions	99
4.2.7	Sensitivity	100
4.2.7.1.	Introduction	100
4.2.7.2	Methods	100

Contents of Volume One		page
4.2.7.3	Results	101
4.2.7.4	Discusiion	101
4.3	Variation of planar parameters with camera angle.	102
4.3.1	Introduction	102
4.3.2	Variation of energy response with camera angle	103
4.3.2.1	Methods	103
4.3.2.2	Results	104
4.3.3	Variation of point source sensitivity with angle	104
4.3.3.1	Methods	104
4.3.3.2	Results	105
4.3.4	Variation of uniformity with camera angle	105
4.3.4.1	Methods	105
4.3.4.2	Results	105
4.4	Camera-computer interface	106
4.4.1	ADC linearity assessment	106
4.4.1.2	Theory	107
4.4.1.3	Methods	107
4.4.1.4	Results	109
4.4.1.5	Discussion	111
4.4.1.6	Conclusions	111
4.4.2	ADC gain calibration	112
4.4.2.1	Introduction	112
4.4.2.2	Methods	112
4.4.2.3	Results	113
4.4.2.4	Discussion	113
4.4.3	Centre of rotation assessment	114
4.4.3.1	Introduction	114
4.4.3.2	Errors in x-direction	115
4.4.3.3	Errors in y-direction	116
4.4.3.4	Methods	117
4.4.3.5	Results	118
4.5	Quality control of SPECT bed	120
4.5.1	Methods	121
4.5.2	Results	121
4.6	General Conclusions for Chapter 4	122
Chapter 5. SPECT of point and line sources.		125
5.1	Introduction	125
5.2	SPECT Point Spread Function Assessment	125
5.2.1	Introduction	125
5.2.2	Linear sampling rate	126
5.2.3	Angular sampling rate	126
5.2.4	Methods	127
5.2.5	Variation with position in image volume	128
5.2.6	Discussion	129
5.2.7	Variation of SPECT resolution with ROR	130
5.3	SPECT line spread function measurements	131
5.3.1	Introduction	131
5.3.2	Methods	131
5.3.3	Results	132
5.3.4	Effect of lower angular sampling	132
5.3.4.1	Methods	133
5.3.5	Effect of different filters	133
5.4	SLSF variation in amplitude	134
5.4.1	Introduction	134
5.4.2	Methods	134

Contents of Volume One		page
5.4.3	Results	135
5.5	SPECT resolution in scatter	137
5.5.1	Methods	137
5.5.2	Result	138
5.6	General conclusions for Chapter 5	140
Chapter 6 Scatter discrimination and attenuation correction		143
6.1	Introduction	143
6.2	Asymmetric energy windows	143
6.2.1	Introduction	143
6.2.2	Conventional energy window selection	145
6.2.3	Offset energy discrimination windows	146
6.2.3.1	Disadvantages of an offset energy window	146
6.2.4	Literature review	148
6.2.5	Uniformity and window offsets	149
6.2.5.1	Methods	150
6.2.5.2	Results	150
6.2.6	Assessment of sensitivity loss with window offset	152
6.2.6.1	Methods	152
6.2.6.2	Results	152
6.3	Phantom studies	155
6.3.1	Methods	156
6.3.2	Results	156
6.3.3	Conclusions	157
6.4	Scatter subtraction and attenuation correction	158
6.4.1	Introduction	158
6.4.2	Theory	163
6.4.3	Methods	164
6.4.4	Results	165
6.4.4.1	Volume sensitivity	165
6.4.4.2	Scatter correction	166
6.4.4.3	Attenuation correction	167
6.4.4.4	Conclusions	168
6.4.5	Application to structured source distributions	168
6.4.5.1	Methods	168
6.4.5.2	Results	168
6.5	General conclusions for Chapter 6	171

Contents of Volume Two		page
Chapter 7	Parameter optimisation for low noise data	1
7.1	Introduction	1
7.2	Data detection by the camera	1
7.2.1	Assessment of the blurred object spatial frequency content	2
7.2.2	Variation of the power spectra with count density	4
7.2.3	Variation of the power spectra with acquisition angle	7
7.2.4	Variation of the power spectra with collimator	9
7.2.5	Variation of the power spectra with ROR	10
7.3	Data Sampling	11
7.4	Data Interpolation	13
7.5	Filtering	15
7.6	Combined data processing transfer functions	15
7.6.1	Discussion	17
7.7	Angular sampling	18
7.7.1	Methods	18
7.7.2	Results	19
7.7.3	Conclusions	19
7.8	Uniformity correction for high count data	20
7.8.1	Methods	21
7.9	Correction for ADC differential non-linearity	26
7.9.1	Methods	27
7.9.2	Results	28
7.9.3	Conclusions	29
7.10	General conclusions for Chapter 7	31
Chapter 8	Noise control - filter function selection	33
8.1	Local statistical noise	33
8.1.1	Results	35
8.1.2	Conclusions	37
8.2	Noise control - filter function selection	37
8.2.1	Introduction	37
8.2.2	Filter function selection - current status and general considerations	38
8.2.2.1	Conclusions	43
8.3	A suggested filter function selection method	45
8.3.1	Determination of the Butterworth power factor	46
8.3.1.1	Methods	47
8.3.1.2	Results	47
8.3.1.3	Conclusions	48
8.4	The enhanced Butterworth filter	48
8.5	Filter matching	49
8.5.1	Variability of the NPS	51
8.5.2	Determination of the filter cut off value	52
8.5.3	Conclusions	56
8.6	Two dimensional filtering	57
8.6.1	Rotationally symmetric filter	58
8.6.2	The y filter	60
8.6.3	Comparison of the y filter and r filter	60
8.7	Filter matching in two dimensions	61
8.7.1	Effects of y filtering	62
8.8	General conclusions for Chapter 8	64

Contents of Volume Two		page
Chapter 9	Parameter optimisation for high noise data	66
9.1	Introduction	66
9.2	Comparison of collimators	66
9.2.1	Methods	66
9.2.2	Noise considerations	67
9.2.3	Reconstruction	68
9.2.4	Analysis	69
9.2.5	Results	72
9.2.6	Conclusions	72
9.3	Attenuation correction	75
9.3.1	Results	75
9.3.2	Attenuation correction of noisy data	76
9.3.3	Conclusions	77
9.4	Uniformity correction	77
9.4.1	Results	78
9.4.2	Discussion	79
9.5	General conclusions for Chapter 9	80
Chapter 10	^{99m}Tc -HMPAO SPECT ; assessment of intractable epilepsy	82
10.1	Introduction	82
10.2	Methodology	83
10.2.1	Patient positioning - limitation of movement	83
10.2.2	Assessment of patient movement	85
10.2.2.1	Methods	85
10.2.2.2	Results	87
10.2.2.3	Discussion	88
10.2.2.4	Correction for patient movement	89
10.3	Choice of acquisition parameters	89
10.3.1	Choice of pixel size	89
10.3.2	Choice of acquisition time	90
10.3.3	Collimator choice	91
10.3.4	ROR limitations	91
10.4	Choice of reconstruction parameters	91
10.4.1	Choice of reconstruction filter	91
10.4.2	Application of attenuation correction	91
10.4.3	Application of uniformity correction	92
10.4.4	Image display and hardcopy	93
10.5	Activity administration - radiation dosimetry	93
10.6	Assessment of intractable epilepsy	94
10.6.1	Patient group	95
10.6.2	Assessment of patient studies	97
10.6.3	Results	97
10.7	Assessment of reconstruction method	98
10.8	General conclusions for Chapter 10	100
Chapter 11	Cardiac SPECT with ^{99m}Tc -MIBI	102
11.1	Introduction	102
11.2	Choice of SPECT acquisition parameters	104
11.2.1	Pixel size	105
11.2.2	Acquisition time	105
11.2.3	Collimator choice	105
11.2.4	ROR	105
11.2.5	360 degree or 180 degree orbit	106

Contents of Volume Two		page
11.3	Choice of SPECT reconstruction parameters	107
11.3.1	Filter function	107
11.3.2	Attenuation correction	108
11.3.3	Uniformity correction	109
11.3.4	Image display	109
11.4	Assessment of coronary artery disease with ^{99m}Tc -MIBI	110
11.4.1	Methods	110
11.4.2	Results	112
11.4.2.1	Simple detection of CAD	112
11.4.2.2	Identification of abnormal segments	112
11.4.2.3	Identification of diseased arteries	113
11.4.2.4	Differentiation between ischaemic and scarred tissue	114
11.5	General conclusions for Chapter 11	116
Chapter 12	Digital filtering of the bladder in SPECT bone studies of the pelvis.	119
12.1	Introduction	119
12.2	Artefact production	120
12.3	Post-reconstruction processing	122
12.4	Pre-reconstruction processing	123
12.4.1	Bladder identification	124
12.4.2	Interpolative background replacement	125
12.5	Assessment of the processing techniques	127
12.6	Results	127
12.7	Conclusions	132
Chapter 13	General conclusions	134
Appendix 1	Count losses due to high dynamic range data	147
Appendix 2	Publications resulting from this thesis	153

Chapter 1 Introduction

1.1 Introduction

One of the major disadvantages of conventional medical imaging techniques is that the images which are produced represent the superposition of overlapping structures throughout the thickness of the body. Tomography (from the Greek "tomos" - to cut) attempts to overcome this problem by producing an image of a thin section in a transaxial plane which cuts through the subject.

Single photon emission computed tomography (SPECT) uses the photons which are emitted from a radionuclide to produce an image which corresponds to the distribution of the labelled compound. If a rotating gamma camera is used (as opposed to a dedicated single section system) the information required to reconstruct a set of parallel contiguous sections can be acquired simultaneously in a single study. This information effectively defines the three dimensional distribution of radiopharmaceutical concentration within the body. Sections through the distribution can then be taken in coronal and sagittal planes in addition to the transaxial. Indeed, given the appropriate software it is possible to take sections in any plane.

1.2 The development of SPECT

The first SPECT images were produced in the 1960 s which is surprisingly early in the development of nuclear medicine. However, the performance of the imaging hardware and the reconstruction software was such that the quality of the resultant images was very poor.

The development of X-ray transmission tomography in the 1970 s produced improvements in the reconstruction techniques which, allied to the general improvement in gamma camera performance, led several investigators to make further attempts to perform SPECT. Of course with the absence of purpose built SPECT systems, investigators had to attempt to produce their own apparatus to rotate the camera around the patient or, indeed, in some cases, to rotate the patient around the camera!

However, images of reasonable quality were obtained from these prototype systems stimulating the commercial development of gamma cameras able to perform SPECT, the first generation of these becoming available in the late 1970 s.

In the early to mid 1980 s there were significant improvements in the performance of gamma camera systems including the introduction of microprocessor controlled correction circuitry in the camera head. These improvements allied to the introduction of new radiopharmaceuticals which require SPECT for their best use (e.g. HMPAO) have changed the status of SPECT from that of an interesting sideline to an essential requirement for the provision of a modern nuclear medicine service.

1.3 Advantages of SPECT

A considerable degree of care has to be employed over the general operation of the camera and computing system for the production of high quality SPECT images. The advantages of SPECT which justify this extra expenditure of effort are as follows.

The most obvious advantage of SPECT is that the three

dimensional nature of the reconstructed data allows structures which would overlap on an a planar image to be separated by taking an appropriate section through the image volume.

A further advantage is obtained as a consequence of the removal of underlying and overlying activity. By taking a section through the subject the loss of contrast which always occurs in planar images can be restored, figure 1.1. The restoration of the true contrast between structures within the subject can be of importance when the lesion uptake is low. This can occur, for example, in monoclonal antibody imaging where the lesion to background contrast is often just on the boundary of detectability for planar imaging.

Finally, it is in theory possible to use SPECT to quantify tracer uptake in absolute terms of Becquerels per gram of tissue without having to make any assumptions or estimates of the background activity superimposed on the organ or area of interest. There are, however, a number of problems which still have to be solved before this potential advantage is a practical reality. Accurate attenuation correction is required in addition to a method for eliminating scattered photons from the photopeak signal.

1.4 Thesis aims

The second half of the 1980's saw an explosion of interest in the field of SPECT, Coel (1988), Yudd (1988), Tait (1987), Sodee(1987), Chen (1988), Neary (1987), Biersack (1987), De Pasquale (1988), Holman (1988), Murray (1989). There have been two major reasons for this phenomenon. Firstly, technical advances have improved the performance of rotating gamma camera SPECT systems, raising the quality of the images which

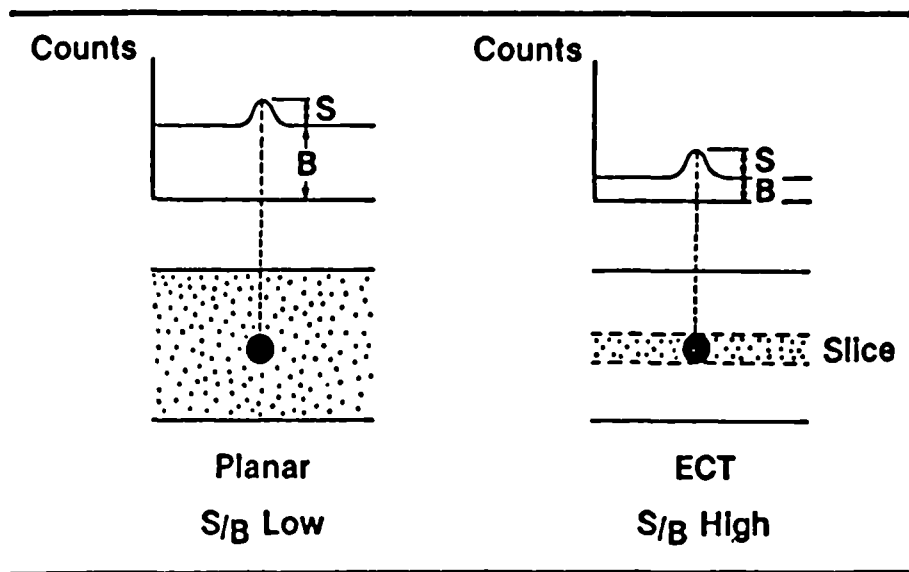


Figure 1.1 The improvement in image contrast with SPECT compared to planar imaging is demonstrated. In conventional planar images, contrast is usually low because the source and background activities are superimposed. SPECT yields slice images with virtually no background activity. The result is an increase in the signal to background ratio which can be particularly important for the detection of small lesions.

are produced to a level which has enabled them to be of routine clinical use.

The second area of improvement, which has occurred in parallel with the technical advances, has been in the field of radiopharmaceutical development where whole new classes of compounds have been produced. The most important examples of these are the radio-labelled monoclonal antibodies, the ^{99m}Tc labelled isonitriles for myocardial perfusion imaging and the lipophilic agents which are deposited in the brain in proportion to blood flow. These factors have greatly increased the areas in which SPECT can be usefully applied.

The aims of this thesis are firstly to explore how the changes in the performance of the constituent parts of the SPECT system affect the manner in which the studies should be performed. Much of the current attitudes to SPECT and how it should be implemented are biased by information provided by workers operating on early generations of SPECT systems, Budinger (1979), Larsson (1980), Jaszczak (1981), Keyes (1982). It is necessary to update these results in the light of advances in gamma camera and computer performance. The emphasis throughout will be on the improvement of image quality as opposed to the production of quantitatively accurate data. This is a consequence of the local clinical requirements. For similar reasons only ^{99m}Tc imaging will be considered.

Thus this thesis will be concerned firstly with a comprehensive assessment of the characteristics and performance of both the planar and SPECT imaging aspects of the gamma camera and computing system at the Western Infirmary, Glasgow.

Having ensured that the system is operating without faults, the results of the information obtained on the fundamental aspects of the system's performance will be used to optimise the way in which the data are acquired and reconstructed.

This optimised methodological procedure will then be implemented to perform some specific clinical imaging tasks. These points will be considered in more detail in the following sections.

1.5 System evaluation

The advantages which arise from the use of SPECT as opposed to planar imaging are not obtained without the requirement for some additional effort in the evaluation and maintenance of the machinery. Rotating gamma camera SPECT essentially uses a general purpose instrument to perform a highly specialised task. This means that the tolerances on the behaviour of the system have to be examined and controlled to virtually an order of magnitude more closely than for conventional planar imaging, Rogers (1982).

Thus, in the first instance, the planar performance of the gamma camera will be thoroughly assessed. The limitations which the characteristics of the constituent parts of the gamma camera impose on the information acquired for reconstruction will be identified.

The extension from planar to SPECT imaging means that the rotational performance of the system has to be assessed. This will include measurements of the stability of planar imaging with camera angle, the mechanical stability of the camera's rotation and, finally, the accuracy with which the projection

images are transferred from the camera to the computing system.

Once the projection images have been acquired the accuracy and reliability of the software used in the reconstruction and display of the data also has to be tested.

Having examined the SPECT system as a whole, a set of quality control procedures have to be implemented to ensure that the constituent parts of the system perform to within well defined limits at all times.

Given that the basic performance of the system has been thoroughly evaluated and is rigorously controlled its SPECT imaging capabilities can then be assessed.

The information obtained from the measurements of the fundamental aspects of the planar and SPECT performance of the system can be used to help in the determination of the best way to perform the SPECT investigations.

1.6 Parameter Optimisation

For the acquisition and reconstruction of a SPECT study there are a large number of parameters for which a range of options are available. The identification of the best set of parameters, for any given imaging task, is one of the most difficult problems in SPECT. Through a systematic evaluation of the effects which different parameter options have on the quality of reconstructed SPECT images it should be possible to produce some practical guidelines for the identification of an optimal parameter set.

Starting with the fundamental detection of photons by the gamma camera a summary of the choices which can be made is given in Table 1.1.

Parameters	Range of Options
Energy window width	10%-25% of photopeak
Energy window position	Centred or offset
Collimator	High sensitivity; General purpose; High resolution.
Acquisition angles	32-240
Acquisition time	5-60 seconds per angle
Image matrix	32*32 - 128*128
Pixel size	2mm-10mm
Orbit shape	Circular; elliptical; contoured
Reconstruction filter	Wide range of functions
Attenuation correction	Variety of methods
Scatter correction	Variety of methods
Image display	Range of colour scales available

Table 1.1 Summary of the available options for the parameters can be varied in the acquisition and reconstruction SPECT study.

During acquisition the width of the energy discrimination window of a gamma camera can with some justification be set anywhere within the range 10% to 25% of the ^{99m}Tc photopeak which occurs at 140.6 keV. The centre of the window can also be offset from the photopeak by a variable amount to reduce the influence of scatter.

A variety of collimators can also be used each having a different combination of resolution and sensitivity characteristics.

For the SPECT acquisition the number of angles at which data can be collected will generally lie somewhere within the range 32 to 240. A continuous acquisition mode is also available on some systems. Each projection image will be acquired for a time period which can vary from 5 to 60 seconds. The dimensions of the digital image matrices can vary from 32*32 to 128*128. The matrices can also be non-square if a higher resolution is required along a projection profile than perpendicular to it. The gain settings of the camera-computer interface can also be adjusted to produce pixels of any required size. The radius of rotation (ROR) of the camera's orbit can also vary as can its shape e.g. it can be circular, semi-circular, elliptical or it can even be made to follow a predefined body contour.

There are also a large number of ways in which the acquired data can be reconstructed. The reconstruction algorithm itself can vary from relatively simple techniques such as filtered back projection to more involved methods such as maximum entropy reconstruction. For this study, however, only filtered back projection will be considered. This means that an appropriate filter function must be chosen from a wide

range of available options. A variety of techniques can also be applied to correct for deviations of the acquired data from the ideal. These processes include the effects of attenuation, the inclusion of scattered photons and the presence of non-uniformities in the response of the gamma camera.

Finally, when the data have been reconstructed there are a variety of ways in which the information can be displayed and hardcopy records produced.

The selection of options for most of the parameters described above cannot be made independently. Their selection depends on the choices made for the remainder of the parameter set. This is one of the major difficulties associated with the identification of an optimal parameter set.

The concept of optimality must also be used with care. The "best" SPECT image will depend on the clinical requirements of the investigation being performed. For example in some situations a high level of specificity for lesion detection may be required at the expense of a reduction in sensitivity. This will alter the way in which the optimal parameter set is chosen.

1.7 Clinical applications

The results obtained in the previous sections will be applied in the investigation of some specific clinical problems, firstly the assessment of focal lesions in an epileptic subject with seizures resistant to medication, secondly the assessment of myocardial perfusion in subjects with suspected coronary artery disease and, finally, the identification of avascular necrosis of the femoral head is considered. The range of problems which are encountered which

are specific to these clinical investigations cover a large proportion of those encountered generally in clinical SPECT imaging.

Chapter 2 Theoretical description of SPECT imaging

An appreciation of the fundamental theory used in the acquisition and reconstruction of SPECT data is required if informed judgements are to be made concerning the factors which contribute to the quality of the resultant images. The theory will be presented for an ideal system and the effects which deviations from the ideal system have will be considered systematically. These deviations include the effects of the gamma camera detection process, of finite linear and angular sampling, the presence of noise and photon scattering.

2.1 General tomographic reconstruction theory

The aim of SPECT is to determine the three dimensional distribution of radionuclide concentration within a volume of tissue. The fundamental problem in this can be reduced to the estimation of the two dimensional distribution within a transaxial section through the volume from a set of measurements made at a number of angles around it. This problem is similar in form to that encountered in several fields. A solution for the general case was given by Radon (1917) and practical implementations have been introduced for radio astronomy by Bracewell (1967), electron microscopy by Crowther (1970), and radiography by Cormack (1973).

2.1.1 Formation of projections

The acquisition of data from a single transaxial section through an object is shown in figure 2.1. The activity concentration within the object is defined in relation to a stationary, orthogonal coordinate system (x,z) and is denoted

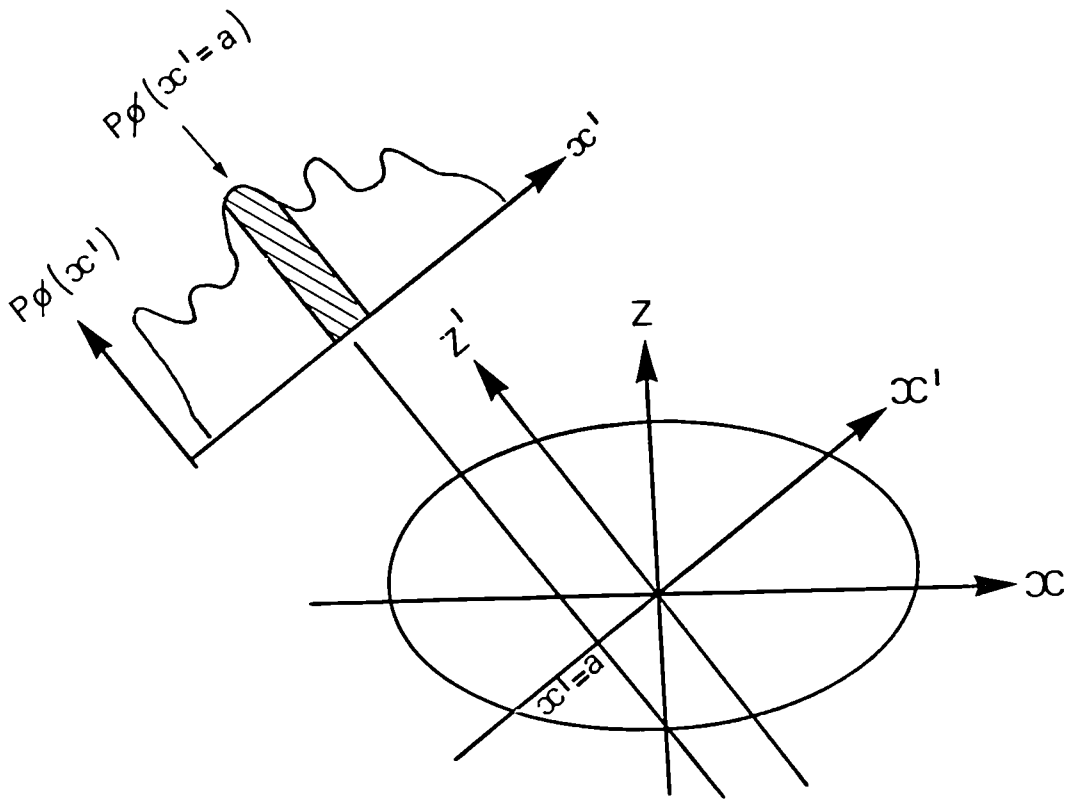


Figure 2.1 Acquisition of a projection profile, $P_\phi(x')$, at an angle ϕ from the object distribution $g(x, z)$.

by $g(x,z)$. The data are acquired and stored in a row of pixels known as projection elements. The row itself is known as a projection profile and is described by the function $p_\phi(x')$. The value of each projection element $p_\phi(x'=a)$, acquired at angle ϕ , is given by the line integral along $x'=a$ of the activity concentration through the object. This is most easily expressed in terms of a coordinate system rotated by ϕ degrees from (x,z) .

$$p_\phi(x') = \int g(x',z') dz' \quad (2.1.1)$$

The relationship between the values of the stationary and rotated coordinate systems is shown in figure 2.2 and is given by

$$x' = x\cos(\phi) + z\sin(\phi) \quad \text{and} \quad z' = z\cos(\phi) - x\sin(\phi)$$

The radionuclide concentration can be completely specified if the data are collected over an angular range equal to or greater than 0 - 180 degrees.

2.1.2 Reconstruction of projections by filtered back projection

The aim of the reconstruction process is to determine the distribution of radionuclide concentration $g(x,z)$, henceforth termed the object distribution, from a sufficient set of projections $p_\phi(x')$.

The most commonly used reconstruction method in SPECT is that of filtered back projection. Simple back projection i.e. back projection without filtering can be thought of as being

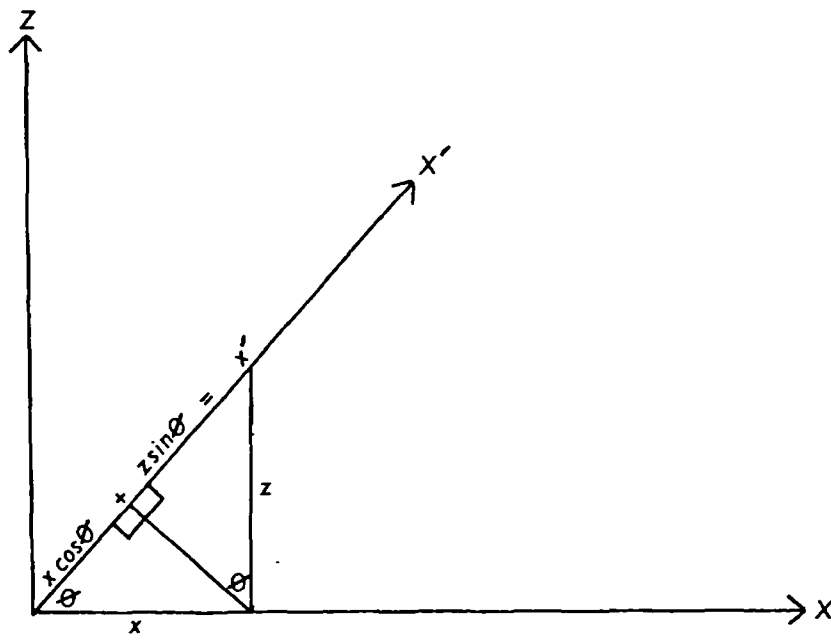


Figure 2.2 Relationship between the values of the stationary and rotated coordinate systems.

analogous to the reverse of the process by which the projection profile data were collected. The value of each projection element is projected onto an initially empty data matrix with the angle of projection set to be equal to the angle at which the original profile was collected. The process of simple back projection is illustrated in figure 2.3. The process can be expressed mathematically as

$$g_{bp}(x, z) = \int p_{\phi}(x') \quad (2.1.2)$$

The final value in any pixel within the reconstruction matrix is an integration of the projection data with the appropriate value of x' for each projection angle ϕ .

If we consider firstly the back projection, without filtering, of the projection data obtained from a section through a line source it can be shown that the resulting function will be of the form $1/r$ where $r^2 = x^2 + z^2$, Bracewell (1967), Brook (1976).

For a distributed source this theoretical impulse input response acts effectively as a blurring function. Thus the function $g_{bp}(x, z)$, resulting from the back projection of data, will be a convolution of the underlying concentration function $g(x, z)$ and the blurring function $1/r$. Thus,

$$g_{bp}(x, z) = g(x, z) * 1/r \quad (2.1.3)$$

It is important to note the assumptions about the nature of the data and the data collection process which have been made in the above ideal analysis. In order to obtain equation (2.1.3) it has been necessary to assume that the the counts

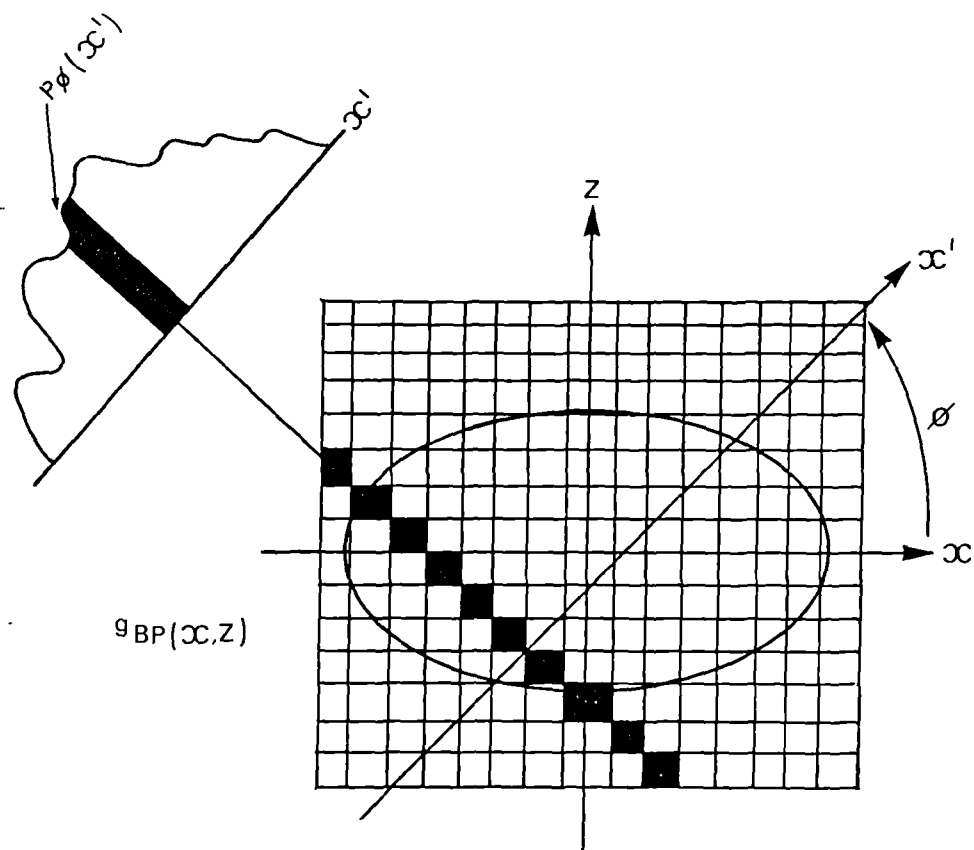


Figure 2.3 Schematic illustration of the back projection process. Each projection element $P_{\phi}(x')$ is back projected at an angle ϕ into an initially empty data matrix.

collected in each projection element $p_\phi(x'=a)$ are proportional to the line integral of the activity $g(x,z)$ along the line $x'=a$. This will only be true if the spatial resolution of the camera is perfect and neither scattering nor attenuation of the detected photons has occurred. Furthermore, it has also been implicitly assumed that the projection data are noise free and have been collected at infinitely high linear and angular sampling rates.

Given these assumptions for the moment, however, the direct methods using back projection are all, in principle, methods of deconvolving $g(x,z)$ from the $1/r$ blurring function.

2.1.2.1 Reconstruction in frequency space

Taking the Fourier Transform (FT) of both sides of equation (2.1.3) gives

$$G_{bp}(u,v) = G(u,v) \cdot (1/R) \quad (2.1.4)$$

where

$$G_{bp}(u,v) = FT[g_{bp}(x,z)]$$

$$G(u,v) = FT[g(x,z)]$$

$$R^2 = u^2 + v^2 \quad \text{and} \quad FT(1/r) = 1/R$$

Thus,

$$G(u,v) = G_{bp}(u,v) \cdot R \quad (2.1.5)$$

The original activity distribution can then be found by taking the inverse Fourier Transform, FT^{-1}

$$g(x,z) = FT^{-1}[G_{bp}(u,v) \cdot R] \quad (2.1.6)$$

Physically, this is equivalent to saying that the back projection process causes the spatial frequency components of the underlying data to be reduced in proportion to their frequency so that to restore the original data it is necessary to correct for this by multiplying by R.

Thus to reconstruct the data using a frequency space approach any algorithm would have to include the following steps,

- 1] Back project the projection data
- 2] Take the Fourier Transform of the back projected data
- 3] Multiply the value at each point (u,v) by R
- 4] Take the inverse Fourier Transform

It is also possible to write equation (2.1.6) in an alternative formulation,

$$g(x,z) = g_{bp}(x,z) * FT^{-1}(R) \quad (2.1.7)$$

This gives a second way of obtaining the original data from the projections without having to calculate Fourier Transforms. To do this any reconstruction algorithm must include the following steps,

- 1] Back project the projection data
- 2] Perform a two dimensional convolution with the function $FT^{-1}(R)$

2.1.2.2 Reconstruction in Real Space

There are practical advantages to be gained by handling the data in Real space during the reconstruction. The way in which this can be achieved uses the 'reconstruction theorem', Deans (1963), Bracewell (1967), which gives the key relation allowing the analysis derived in Fourier space to be transferred to Real space. The reconstruction theorem states that the the one dimensional Fourier Transform $P_\phi(u')$ of the projection data $p_\phi(x')$ taken at angle ϕ equals the profile taken through centre of the two dimensional Fourier Transform of the object data, $G(u,v)$, at an angle ϕ , i.e.

$$G_\phi(u,v) = FT[p_\phi(x')] \quad (2.1.8)$$

As a consequence of this there will be a set of modified projections which back project to give an unblurred reconstruction, Pullan (1980).

To determine the form of the modified projection set consider equation (2.1.4) written for values along a line through the origin of frequency space and at an angle ϕ to the u axis :

$$F_\phi[g_{bp}(x,z)] = F_\phi[g(x,z)] \cdot 1/X \quad (2.1.9)$$

where X is the distance in frequency space in a one dimensional Fourier Transform of the projection and F_ϕ denotes a one dimensional profile through the frequency space representation. Thus,

$$\begin{aligned}
F_{\phi}[g(x, z)] &= F_{\phi}[g_{bp}(x, z)] \cdot X \\
&= F_{\phi}\left[\int p_{\phi}(x')\right] \cdot X \quad \text{from equation (2.1.2)}
\end{aligned}$$

Thus, taking the inverse FT of both sides

$$g(x, z) = \int [p_{\phi}(x')] * FT^{-1}(X)$$

As convolution and summation are linear operators their order can be reversed to give

$$\begin{aligned}
g(x, z) &= \int [p_{\phi}(x') * FT^{-1}(X)] \\
&= \int [N_{\phi}(x')]
\end{aligned}$$

where $N_{\phi}(x')$ represents the amended projection profile set and is given by

$$N_{\phi}(x') = p_{\phi}(x') * FT^{-1}(X)$$

Thus the reconstruction can be performed using an algorithm which contains the following steps :

- 1] Convolve each projection profile with $FT^{-1}(X)$.
- 2] Back project the resultant projection profile set.

As a consequence of this a one dimensional as opposed to a two dimensional convolution is implemented in the data analysis. This means that a large part of the data processing can be performed without the need for the complete projection profile

set to be present allowing much of the data manipulation to be performed while the projections are actually being acquired. The efficient use of time which results makes this form of reconstruction the most frequently employed in SPECT.

2.1.3 Other reconstruction algorithms

In addition to filtered back projection there are a number of alternative approaches which can be used to solve the reconstruction problem. Each method is different in terms of accuracy, noise handling, the ease with which corrections for attenuation and scatter can be implemented and the computing time required.

Iterative reconstruction techniques form an important group and are based on the solution of a set of simultaneous equations relating the projection data to the values of the elements in the reconstruction matrix. An initial, arbitrary, estimate of the solution to the problem is made and the projections which would have resulted from it compared to the observed values. Correction terms are applied to the reconstruction matrix and the whole process repeated. The number of iterations performed is determined by the desired accuracy which is effectively limited by the noise and inconsistencies in the raw data.

The manner in which the amendments are made to the reconstruction matrix can differ giving a variety of iterative reconstruction techniques. The algebraic reconstruction technique (ART), Gordon (1970), calculates a set of ray sums at each projection angle, compares them to the observed projection values, and applies a correction to each pixel. The corrected values are then used for the next angle.

In the simultaneous iterative reconstruction technique (SIRT), Gilbert (1972), each pixel is corrected simultaneously for all rays passing through it and these corrections are incorporated before calculating the next pixel.

Finally, for the iterative least squares technique (ILST), Goiten (1972), all ray sums for all angles are calculated at the beginning of an iteration and then corrections applied to all pixels. Updated values are used only in the next iteration. As the results in each pixel are calculated many times a damping factor must be used. This may be chosen so that a least squares fit to the data is produced at each iteration.

However, no matter which iterative method is used the large number of numerical calculations required for the inversion of large data matrices means that with the computing systems presently employed in typical Nuclear Medicine Departments the reconstruction times are too long for routine clinical applications.

The final group of reconstruction algorithms attempt to assess the probability of the relationship between the cross-sectional image (the solution) and the projection data. This can be done on the basis of the maximum likelihood or maximum entropy , Kemp (1982). Again, however, these methods involve considerably more numerical calculation than the filtered back-projection technique and their use has been largely restricted to research centres or other fields, such as electron microscopy, where the temporal demands are not as stringent as in a routine medical environment.

The use of the more computationally involved reconstruction techniques may become more common if array

processors/parallel processing systems are introduced into routine nuclear medicine computing.

2.2 Filtered back projection of real data

The previous analysis was valid for ideal data which satisfied the assumptions made in Section 2.1.2 . The extent to which the real data acquired in a SPECT study deviates from the ideal, the importance of these deviations and the steps which can be taken to account for them will now be considered. For simplicity this particular section will retain the assumptions that the data are noise free and that the effects of attenuation and scatter are not present. The effects of these processes will be considered separately in sections 2.3 to 2.6.

2.2.1 Finite spatial resolution of the camera

It was assumed in equation (2.1.1) that the value in each projection element, $p_\phi(x')$, was proportional to the line integral of the activity concentration along the line defined by ϕ and x' in figure 1. This assumption is invalid, in the first instance, because of the finite spatial resolution of the camera which means that a contribution will be made to the value of the projection element from activity located outwith the defined line. In fact, the activity at all points (x',z') will contribute to the value of the projection at x' . This will give a new projection profile function $h(x')$. We can postulate that there exists a function related to the detector response and the activity distribution which when convolved with the ideal projection function $p_\phi(x')$ will give the

observed projection function $h(x')$.

$$h(x') = p_{\phi}(x') * r(x') \quad (2.2.1)$$

The form of the function $r(x')$ will depend on $g(x,z)$ and some other function which contains information on the system's impulse response function.

The planar impulse input response function of the camera is usually described in terms of the image which is produced by a very thin line source. This is termed the line spread function (LSF) and its form is determined by the camera's intrinsic resolution and the geometrical properties of the collimator (Section 4.2.4).

If the LSF, $l(x')$, was independent of the source to camera distance then the observed projection element values would be related to the ideal values through the expression

$$h(x') = p_{\phi}(x') * l(x') \quad (2.2.2)$$

This would, in the noise and scatter free situation, allow the ideal projection element values to be calculated from the observed values and the measured LSF. Thus,

$$p_{\phi}(x') = h(x') * FT^{-1}[1/L(u)] \quad (2.2.3)$$

$$\text{where } L(u) = FT[l(x')]$$

However, as a consequence of the geometrical properties of parallel hole collimators the shape and amplitude of the LSF change to a significant extent when the source to camera

distance is varied. This means that the function $r(x)$ in equation (2.2.1) will depend on a set of line spread functions which vary with the source camera distance and, importantly, on the object distribution itself. As a consequence of this the effects of the finite resolution of the camera cannot be separated from the object distribution which makes it impossible, with the filtered back projection approach, to determine the ideal projection element values from the observed values.

Thus the function $h(x')$ which is actually back projected will be a blurred version of the ideal. The blurring function, $r(x')$, is a complex function which depends both on the way in which the system's LSF changes with source camera distance and also on the object distribution itself. Thus, in equation 2.2.1 the term $r(x')$ should be replaced with the function defined by

$$r(x') = f[l_d(x'), g(x', z')]$$

where $l_d(x')$ is the LSF at a distance d from the camera

Although complete image restoration is not possible, even in the noise and scatter free situation, some resolution recovery can be achieved. One approach for example is to assume that the LSF is independent of source camera distance and to apply equation (2.2.3) by selecting a representative function for the LSF. The particular form of the LSF chosen can be determined on a variety of grounds, for example, King (1986) uses the LSF obtained from a source at a depth of 7.5cm in a solid medium as this is the mean free path length of ^{99m}Tc

photons in water.

It is useful to examine these processes in the frequency domain. Thus equation (2.2.1) can be given as

$$H(u) = P(u) \cdot R(u) \quad (2.2.4)$$

where the upper case letters denote the FTs.

$H(u)$ is often termed the blurred object spectrum, the blurring being a consequence of the suppression of the higher spatial frequencies in the data produced by the limited resolution of the camera. This can be demonstrated along with the variation of the blurring with source camera distance by examining the form of the camera's LSFs in frequency space for source collimator distances of 5cm and 10cm, figure 2.4.

2.2.1.1 Combining Opposing Projections

In the ideal data analysis it was shown that the acquisition of data over the range 0-180 degrees was sufficient to determine the underlying activity distribution. In practical SPECT imaging however, it is common to acquire the data over 360 degrees and to combine the data in opposing images before back-projection. This can be achieved by taking either the geometric or the arithmetic mean of opposing projection elements.

This is relevant because the LSF at a source camera distance of d , i.e $l_d(x)$ in equation (2.2.4), will now be given, if the arithmetic mean is used, by

HIGH RESOLUTION COLLIMATOR IN AIR

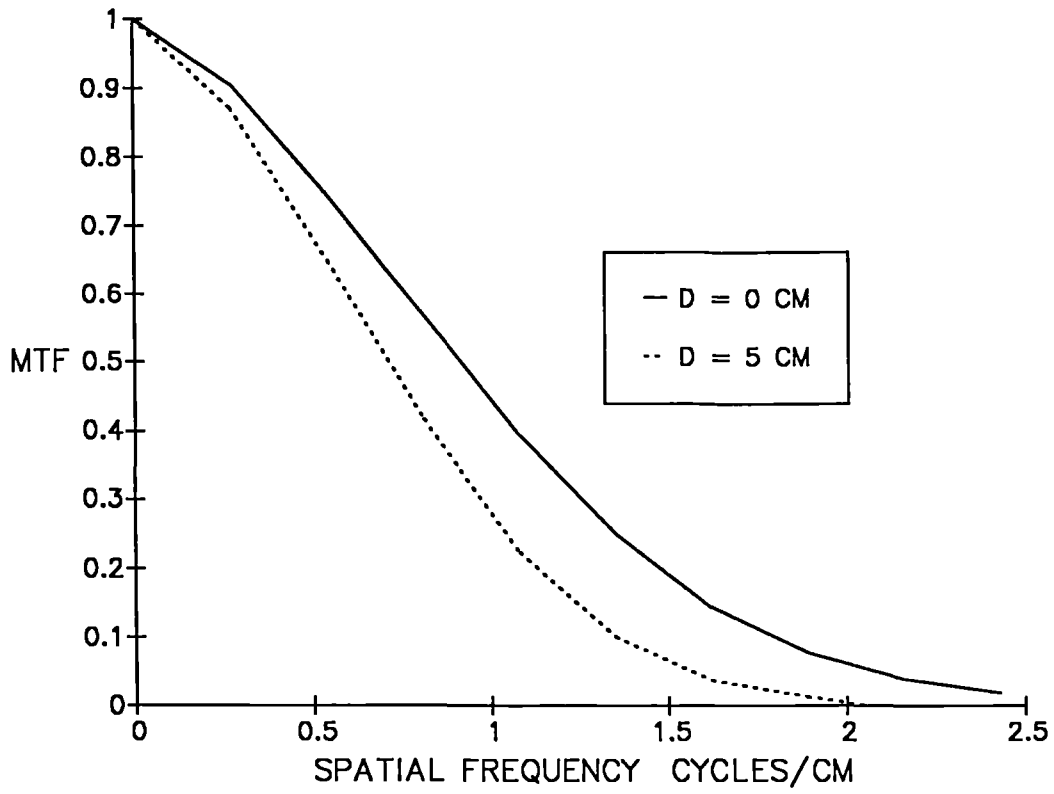


Figure 2.4 Modulation transfer functions for a high resolution collimator and source to camera distances of 0cm and 5cm.

$$l_{r,d}(x) = [l_d(x) + l_{r-d}(x)]/2$$

where $l_{r,d}(x)$ = effective LSF at a source camera

distance of d for a camera ROR equal to r

The function $l_{r,d}(x)$ varies much less with distance from the camera than $l_d(x)$, Chapter 5. Thus, the effect of combining opposing projections is to make the effective LSF of the camera much less dependent on the position of the source within the image volume. This makes the selection of a representative function for the LSF, to be used to deconvolve the effects of the detection process from the projection data prior to back projection, as described in equation (2.2.2), a more reasonable approach.

2.2.2 Finite Linear Sampling Rate

The next assumption which was made in the idealised analysis of the reconstruction problem was that the projection data had been sampled at an infinitely high sampling rate. In practice, however, the reconstruction calculation is performed using a digital computer so that the projection data, which after detection by the gamma camera are in the form of analogue voltage signals, must be sampled at a finite sampling rate. How does this deviation from the idealised situation affect the determination of the underlying activity distribution $g(x,z)$?

2.2.2.1 The sampling theorem

Before considering the specific questions described above the general principles involved in the data sampling process

should be described. The key consideration in all data sampling is the sampling theorem, Shannon (1949). This states that if a sampling distance of $a(\text{cm})$ is chosen, corresponding to a spatial frequency of $(1/a)\text{cm}^{-1}$, then a band limited signal will only be uniquely recovered from its samples if its highest spatial frequency, u_{max} , does not exceed $(1/2a)\text{cm}^{-1}$. The converse is also of relevance. If the signal has been sampled using a sampling distance of $a(\text{cm})$ the the highest spatial frequency present in the sampled data will be given by $(1/2a)\text{cm}^{-1}$. This frequency is known as the Nyquist frequency, u_n .

If there are spatial frequencies present in the signal which are greater than the Nyquist then aliasing artefacts will be produced. These occur because the data in the higher spatial frequencies falsely increase the amplitude of the spatial frequencies below the Nyquist.

The sampling theorem specifies a minimum value for the sampling rate above which aliasing artefacts are avoided. However, it is important to recognise that the selection of sampling rates which correspond to spatial frequencies higher than the Nyquist will have a range of effects on the properties of the sampled data. This can be demonstrated by considering the sampling procedure as a convolution of the continuous projection data as detected by the camera, $h(x)$, and a sampling function, Tsui (1984). Thus,

$$hs(x_i) = h(x) * s(x_i) \quad (2.2.5)$$

where $hs(x_i)$ is the discrete function obtained from sampling $h(x)$

$s(x_i)$ is a rectangular function which equals 1 for $x = a.i \pm a/2$ and equals 0 elsewhere (a is the sampling distance or pixel length)

(A more rigorous definition of the sampling procedure would use a comb of Dirac delta functions to locate the values of x at which the function $h(x)$ is to be sampled. However, when viewed in frequency space the comb of delta functions acts to multiply the value of the FT at each point at which it is defined by unity.)

The effects which the sampling process has on the information content of the detected projection data can be most effectively demonstrated in the frequency domain. Thus we can take the FT of the elements of equation (2.2.5) to give,

$$HS(u) = H(u) \cdot S(u) \quad (2.2.6)$$

where the upper case letters denote the FTs.

Thus the back projection of sampled data will be equivalent to the back projection of the continuous projection data after modulation in frequency space by the function $S(u)$. In fact the FT of the rectangular function $s(x_i)$ is given by the sinc function which is defined to be,

$$\text{sinc}(\pi.u.a) = \sin(\pi.u.a)/\pi.u.a$$

The shapes of the sinc functions for sampling rates chosen to produce Nyquist values which are various multiples of u_{\max} are shown in figure 2.5. It can be seen from the suppression of

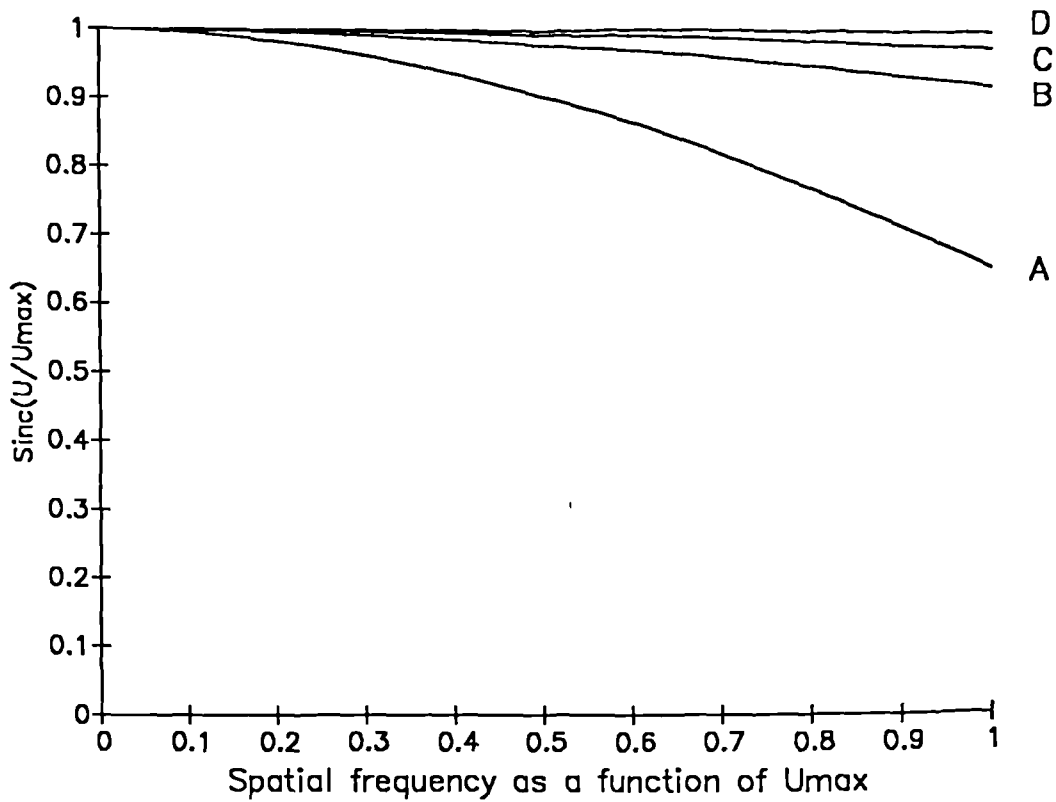


Figure 2.5 Sinc functions which correspond to sampling distances which

- A equal U_{\max}
- B equal twice U_{\max}
- C equal three times U_{\max}
- D equal four times U_{\max}

the amplitude of the higher spatial frequencies, which would result from a multiplication by the sinc function, that the sampling process acts to smooth the projection data. The degree of smoothing increases as the Nyquist frequency, which is dictated from the sampling rate, is decreased to approach u_{\max} . Thus while selecting a sampling rate to give a value for the Nyquist frequency which is just higher than u_{\max} will avoid the production of aliasing artefacts it will not produce the most accurate representation possible of the unsampled data. This topic will be examined in the practical situation in Chapter 8.

2.2.2.2 Data Interpolation

One of the consequences of the data sampling process is that for the back projection procedure the projection line from the reconstruction pixel $g(x,z)$ will not in general intercept the projection axis exactly at a point where the sampled projection data are defined, i.e. at a value of x' equal to $i.a$ where i is an integer. Thus some form of interpolation must be used to assign a value to the projection line from the data in the sampled projection profile. The effect of the interpolation process is equivalent to convolving the projection data with an interpolation function the form of which depends on the details of the interpolation method used. Thus,

$$hsd(x_i) = hs(x_i) * d(x_i) \quad (2.2.7)$$

where $hsd(x_i)$ is the function obtained after interpolation of the detected and sampled projection data, $hs(x_i)$ and $d(x_i)$

is the interpolation function

As before the effect of the interpolation process can be most effectively demonstrated in the frequency domain. Thus,

$$\text{HSD}(u) = \text{HS}(u) \cdot D(u) \quad (2.2.8)$$

where the upper case letters represent the FTs of the function in equation (2.2.7)

Two of the most commonly used interpolation methods are the 'nearest value' method and the linear interpolation method.

The 'nearest value' method assigns a value to be back projected along the projection line equal to that obtained at the nearest sampling point. The form of the interpolation function $d(x_i)$ for this is in fact the same as the rectangular function produced by the sampling process described in section 2.2.2. Thus in the frequency domain the interpolation function will be given by,

$$D(u) = \text{sinc}(\pi \cdot u \cdot a) \quad (2.2.9)$$

The linear interpolation method calculates the value to be back projected from a linear interpolation of the values obtained at the data points positioned on either side of the point where the projection line intercepts the projection profile. This is equivalent to convolving the data with a triangular function,

$$\text{hsd}(x_i) = (c/a) \cdot \text{hs}(x_{i+1}) + (1-c/a) \cdot \text{hs}(x_i) \quad (2.2.10)$$

where a is the pixel length of the projection data
 c is the distance between the projection line and
the projection data point x_i

It can be shown, Shepp (1974), that in frequency space the interpolation function which results from equation (2.2.10) is given by,

$$I(u) = \text{sinc}^2(\pi \cdot u \cdot a) \quad (2.2.11)$$

The frequency space representations of the interpolation functions for the linear and nearest value methods are shown in figure 2.6. The linear interpolation smooths the data to a greater extent than the nearest value approach.

2.2.3 Finite Angular Sampling

A further assumption which was made in the theoretical analysis of the reconstruction problem was that the projection data had been acquired at an infinite number of angles around the object. In practice, however, a finite number of projection profiles must be acquired at a finite number of angles. How does this influence the results obtained from the idealised situation ?

The primary effect is to change the integral in the back projection equation (2.1.2) into a finite summation. This means that the back projection of an impulse input will only give a result which is a good approximation to the $1/r$ function if a large number of angles are used. Thus in equation (2.1.3) the function $g_{bp}(x, z)$ which results from the

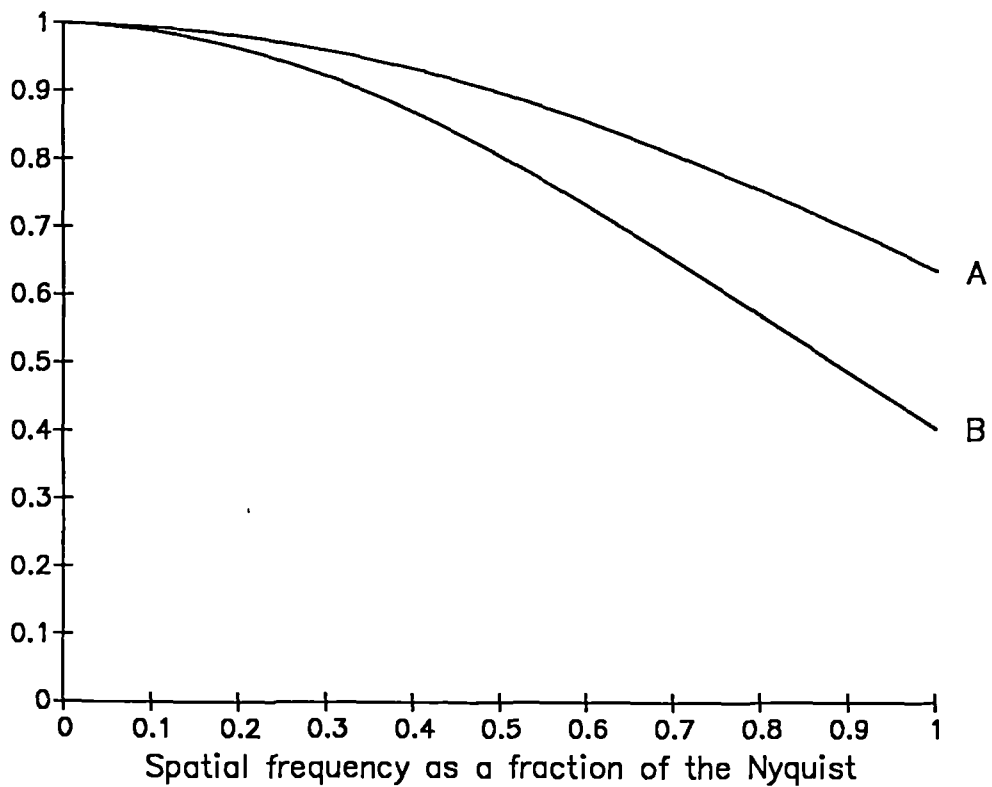


Figure 2.6 Curve A is the interpolation function which results from the nearest value method. Curve B is the interpolation function which results from the linear interpolation method.

back projection of the projection profiles will be given by a convolution of the underlying object function $g(x,z)$ and some function other than the function $1/r$ which is obtained from the idealised theoretical analysis. In fact for a finite number of angles a simple geometrical representation of the back projection process shows that this function is spatially variant. This will lead to the formation of angular sampling artefacts the strength of which will vary inversely with the angular sampling rate.

However, it has been shown that for data which have been sampled at a finite linear sampling rate the angular sampling artefacts can be reduced to zero if the angular sampling rate is above a certain, finite, level. From the work of Bracewell (1967) it can be shown that if $g(x,z)$ is a smoothly varying function with an upper spatial frequency limit, u_{\max} , then the reconstructed data will be free of angular sampling artefacts provided that

$$n_0 > 2 \cdot \pi \cdot D \cdot u_{\max} \quad (2.2.12)$$

where n_0 is the number of sampling angles obtained over 360 degrees and D is the maximum dimension across $g(x,z)$. This relationship has been confirmed using similar analyses by Phelps (1977), Budinger (1977) and Brooks (1978).

The implications can be determined by considering some typical values. A pixel of edge length 0.5cm would give a value for u_{\max} of 1 cm^{-1} which, with a subject diameter of 20cm, would suggest that around 130 projection angles would be required to prevent artefact formation.

In conclusion, the choice of a finite angular sampling

rate should not affect the results obtained by the theoretical analysis, so long as its rate is set above the level determined by the linear sampling. If it is below the level suggested by the theoretical analysis then artefacts will be produced. However, the magnitude of the artefacts and their influence on the image quality of the reconstructed data is not clear. This topic will be investigated in Chapter 7.

2.2.4 Filtering the projection data

In the idealised analysis it was calculated that the form of the filter function used to deconvolve the effects of the back projection was given by $FT^{-1}[X]$ which is equivalent to a ramp function in frequency space. For the sampled data a discrete version of the ramp function must be used.

In practice, however, the ramp is not necessarily the function which gives the best results in terms of the image quality of the reconstructed data. For example, the discontinuous frequency cut off has been shown to produce ringing artefacts in the reconstruction, Chessler (1975). To reduce this effect filter functions which roll off more gradually to zero in frequency space have been used to filter the data prior to back projection.

The effect of filtering the projection data prior to back projection with a filter other than the ramp can be assessed in the same way as the other data processing operations described in the previous sections. A window function can be defined which in frequency space is given by the actual filter function applied to the projection data divided by the ramp. Thus,

$$W(u) = F(u)/u \quad (2.2.12)$$

Where $F(u)$ is the frequency space representation of the function used to filter the projection data

$W(u)$ is the window function

The concept of the window function is useful because it accounts for the effects which the filter has on the spatial frequency content of the projection data over and above the effect of the ramp function. As the ramp function is required to correct for the effects of the back projection process the window defines the effective image processing effects which the application of the filter function $F(u)$ introduces into the projection data. Thus we can write, using equation (2.2.8)

$$HSDW(u) = HSD(u) \cdot W(u) \quad (2.2.13)$$

The form of the window function can be chosen to produce a variety of effects on the projection data and so the reconstructed image. For example $W(u)$ can be selected to correct for the distortions introduced into the ideal projection data by the other data processing operations. Using equations (2.2.6), (2.2.8) and (2.2.13) we can write

$$HSDW(u) = H(u) \cdot D(u) \cdot S(u) \cdot W(u)$$

$HSDW(u)$ is the frequency domain representation of the function which is actually back projected. Its relationship to the ideal projection data, $P(u)$, is given by replacing $H(u)$ with

HSDW(u) in equation (2.2.4).

Now if W(u) is defined to be

$$W(u) = 1/.D(u).S(u)$$

Then,

$$HSDW(u) = H(u)$$

Thus, in the noise free situation, where there is effectively an unconstrained choice of the window function form, it is possible to correct exactly for the effects of data sampling and interpolation. Furthermore, although full image restoration, i.e. the determination of P(u) from H(u), is not possible as discussed in section 2.2.2. the form of W(u) can be further amended to produce any amount of resolution recovery desired.

2.2.5 Conclusions for noise free data

For the analysis of real data, the form of the projection data is altered by the processes of detection by the camera, sampling by the computing system, data interpolation and filtering by a discrete filter function which may be different from the ramp suggested by the theoretical analysis.

The effects which the combination of the individual procedures, required for the reconstruction of real data, has on the ideal projection data can be determined. The total effect on the spatial frequencies present in the projection data can be calculated from the product of the transfer functions of the individual procedures. It allows the relative

effects of the individual procedures to be assessed. This is of particular importance in the determination of the optimal choice of detector, linear sampling rate and filter function for a given imaging situation.

For the noise free situation which has been considered so far there are no real constraints on the selection of the above parameters. The optimal strategy would simply be to choose the options which transferred the spatial frequencies in the ideal projection data as fully as possible. This would imply a choice of the highest resolution collimator available, the highest linear sampling rate the reconstruction algorithm can deal with and a filter with an arbitrary level of resolution recovery.

However, the presence of noise in the data means that a compromise between the resolution in the projection data and the signal to noise ratio must be made. In order to make the choices of the acquisition and reconstruction parameters which give an optimal compromise for a given imaging system the way in which the noise in the projection data is transferred by the reconstruction process has to be considered.

2.3. Filtered back projection of noisy data

2.3.1 Stochastic noise

It was assumed in the idealised analysis that the projection data were noise free. For typical projection data acquired by a rotating gamma camera however, the limited sensitivity of the system and the constraints on total imaging time and the level of activity which can be administered to the patient mean that the data are far from noise free. The noise which is referred to in this section arises from random statistical variations in the radioactive decay and detection process. There are other, systematic effects, which introduce errors into the data and can also be interpreted as noise ; however, these will be considered separately in section 2.5.

The effects which the presence of noise in the projection data has in the calculation of the activity distribution $g(x,z)$ will now be examined.

The statistical variations can be considered to be Poissonian so that the standard deviation (SD), or root mean squared (RMS) error, associated with a projection element containing n counts will be given by $n^{1/2}$ and the fractional standard deviation (FSD), the SD divided by the mean, by $n^{-1/2}$.

It should be noted that the statistical uncertainty per pixel is not a measure of the signal to noise ratio. For this to be the case each photon would have to contribute equally to the signal. This is not true because of the inclusion of scattered photons in the detected counts. Thus increasing the sensitivity of a system to give more counts will improve the statistical uncertainty per pixel but not necessarily the

signal to noise ratio if it involves the detection of a higher proportion of scattered photons.

However, the presence of statistical uncertainty in the data is in itself an important limiting factor in the quality of reconstructed SPECT images. Thus it is appropriate to consider it as a separate issue. The way in which the magnitude of the scatter contribution affects image quality can then be considered for different levels of statistical accuracy. This topic will be addressed in Chapter 6.

2.3.2 Noise amplification

The problems introduced by the limited counts in the projection data are exacerbated by the fact that the reconstruction process acts as a noise amplifier. Given that the statistical uncertainty in a projection element containing n counts is equal to $n^{1/2}$ the uncertainty which results from this in the reconstructed pixels can be determined by considering the way in which errors are propagated by the reconstruction process. As described by Todd-Pokropek (1982) this can be achieved by considering the filtering and back projection processes separately.

The error propagation due to filtering can be determined reasonably simply. The filtering process consists of the convolution of some set of weights $a(i)$ with the input function $f(i)$ to give an output function $g(i)$. If a uniform object is assumed such that $g(i)$ is constant then for the central region $f(i)$ will also be approximately constant. Thus since

$$g(i) = \sum_j a(j-i) \cdot f(j)$$

we can calculate the error in $g(i)$ using the general formula for the variance of a compound function

$$V\langle y(x_1, x_2, \dots) \rangle = \sum_t \left(\frac{dy}{dx_t} \right)^2 \cdot V\langle x_t \rangle$$

Thus, because the projection element values are statistically independent

$$V\langle g \rangle = V\langle f \rangle \cdot \sum_j a(j)^2$$

Thus for any given filter the error amplification is the sum of the squares of the filter weights.

As back projection simply involves summing the values from individual projection elements the RMS error in any reconstruction pixel will, if the inputs are uncorrelated, be given by the square root of the sum of the squares of the errors of the projection elements which are involved in the summation. The errors can also be expressed in terms of the percentage RMS error (RMS%) which is given by the FSD multiplied by 100.

The overall RMS% for a uniform source was determined by Budinger (1977), to be

$$\text{RMS\%} = k \cdot P^{3/4} \cdot N^{-1/2} \quad (2.3.1)$$

$$= k \cdot P^{1/4} \cdot n^{-1/2} \quad (2.3.2)$$

where k = constant which depends on the particular form of the filter and the back projection method

P = number of pixels in the reconstruction matrix

which contain information

N = total number of counts

n = number of counts per reconstruction matrix
pixel

A similar relationship was derived from the error analysis of Huesman (1977) by Todd-Pokropek (1982). For a ramp filter a value for k of around 120 was obtained by the different approaches although the exact value for any particular reconstruction algorithm will depend on the details of the reconstruction procedure used.

It is interesting to note that the $n^{-1/2}$ term is exactly that which would be expected from a conventional image. However, the noise in the reconstruction pixels is amplified by a function which depends on the number of pixels in the image of the reconstructed object.

The strength of this effect can be assessed by considering the example of a pixel with a count value of 400. For a planar image the %RMS error would be 5% however, for a pixel in a reconstruction matrix 62 pixels across the RMS% error is about 44%.

For imaging situations where there is a non-uniform distribution of activity, particularly where most of the activity lies within a small fraction of the reconstruction matrix, the amplification of the stochastic errors in the projection data is considerably less than that which would be expected from an application of equation (2.3.1). This has again been investigated empirically by Budinger (1978) and the following equation determined

$$\text{RMS\%} = 120.M_e^{3/4}.N^{-1/2} \quad (2.3.3)$$

This is similar in form to equation (2.3.1). M_e is the effective number of reconstruction matrix pixels and is related both to the contrast and to the fraction of the image occupied by the object. It is given by N/n_t where n_t is the average number of pixels in the target region. Thus,

$$\text{RMS\%} = 120.N^{1/4}.n_t^{-3/4} \quad (2.3.4)$$

Using this relationship it can be calculated that while the RMS% for a uniform disc with one million events and 2380 pixels in the reconstruction matrix is 50% the corresponding value for an object which covers 20% of the reconstruction pixels and has a target to background ratio of 31 is 15.5%.

Thus the RMS% error is reduced when the activity is concentrated in one portion of the field.

2.3.3 Noise Power Spectra

To this point the noise has been described in terms of the statistical uncertainty per pixel which is a measure of the magnitude of local statistical fluctuations. This measure is appropriate if the noise in an image is uncorrelated (i.e. white). However, if the random variation at one point depends on the random variations at other points then the use of the RMS% will give an incomplete, and possibly misleading, description of the influence of the noise. Although the noise in the projection data is uncorrelated (to a reasonable approximation) the reconstruction process itself introduces a high degree of correlation into the noise of a reconstructed

section. The spatial correlations can be described either by the autocorrelation function or by its FT, the noise power spectrum (NPS).

The effects of the filtering process in the spatial frequency domain can be examined in a similar manner to that of Section 2.3.2. Let $F(u)$ be the frequency space representation of the input function $f(x)$, $G(u)$ of the output function $g(x)$ and $A(u)$ of the filter function. Then if $E_f(u)$ is the noise power spectrum of the input function and $E_g(u)$ the noise power spectrum of the output function then since,

$$G(u) = F(u) \cdot A(u)$$

therefore,

$$E_g(u) = E_f(u) \cdot A(u)^2$$

Note that $E_f(u)$ is in principle independent of u as the input noise is assumed to be Poissonian. Also the filters used in the reconstruction are based on the ramp function so that $A(u) = k \cdot u$. Thus the filtered projection has a noise power spectrum which is approximately a function of u^2 .

The effect of the backprojection process is to modify the spatial frequency content of the projection data by $1/u$, Todd-Pokropek (1982). Thus, to a first approximation the noise power spectrum of a SPECT image is proportional to u , i.e. it is ramp shaped.

This simple analysis illustrates one of the most important characteristics of SPECT, that the reconstruction process preferentially amplifies the noise at high spatial

frequencies. For this reason care must be taken to ensure that the projection data do not contain high spatial frequencies with a low signal to noise ratio otherwise the high frequency noise will be amplified to dominate the reconstructed image. This can be achieved by smoothing the projection data, which is equivalent to multiplying the ramp function used to filter the data by a window function as described in Section 2.2.4. The effect of the window function on the tomographic noise power spectrum is to modulate the ramp shape by $W(u)^2$ where $W(u)$ is the frequency space representation of the window function. Thus,

$$\text{NPS} = k \cdot u \cdot [W(u)]^2$$

The use of a window function can have a strong effect on the total noise power (given by the FSD which is equal to the integral of the NPS) because it is involved as a second order term.

The above analysis suggests that the NPS is rotationally symmetrical with a value of zero at a spatial frequency of zero. (i.e. it has a zero DC value). However, it has recently been shown by Kijewski (1987) that the discrete nature of the reconstruction and the requirement for data interpolation mean that the actual NPS is rotationally asymmetric and has a non-zero DC value. Furthermore, the effect of the nonstationary nature of the noise encountered in projection data has also been shown to produce a relatively large DC component to the NPS, Moore (1988). The effect of a rotationally asymmetric NPS will be to make the detectability of an object, or the precision with which the mean value of a region can be

estimated, dependent on the orientation of the reconstruction matrix. The effect of the non-zero DC component will be to reduce the detectability of large, low contrast structures.

2.3.4 Signal and noise power in projection images

Given that the reconstruction process acts as a high frequency noise amplifier, an appreciation of the relationship between the signal and noise in the projection data as a function of spatial frequency is important.

This can be achieved using the work of Goodman (1976) who modelled image dependent Poisson noise. With images degraded by Poisson noise the power spectrum of the image (the square of the FT of the image) was found to be equal to that of the blurred object (the blurring being a consequence of the detection process) plus the power spectrum of the noise. They also predicted that the power spectrum of the noise would have a constant mean value (i.e. white noise) given by the mean total object count. Thus,

$$PI(u,v) = N + MTF^2(u,v) \cdot PO(u,v)$$

where $PO(u,v)$ = object power spectrum

$MTF(u,v)$ = system modulation transfer function

N = mean value of the NPS

This can also be stated for the one dimensional case and used to describe the relationship between the noise power and the signal power as a function of spatial frequency for the projection profile data. This topic will be investigated in

greater detail for specific imaging situations in Chapters 7, 8 and 9.

2.4. Data Sampling in the Presence of Noise

2.4.1 Linear Sampling in the Presence of Noise

As described in Section 2.2.2 the selection of the linear sampling rate in the noise free situation was straightforward. If the sampling rate was chosen to give a Nyquist frequency which was higher than the maximum spatial frequency present in the blurred object spectrum, $H(u)$, then aliasing artefacts will be avoided. Furthermore, for any given sampling rate above the Nyquist a correction could be performed to restore the blurred object spectrum to its original form.

In the presence of noise, however, the choice of very small pixels can produce SPECT images of poor quality because of the low signal to noise ratio. This effect can be explained both in terms of the RMS% error and the noise spectrum of the reconstructed image.

For a given count level a reduction in the size of the pixels used not only reduces the number of counts per pixel in the reconstructed image but also increase the number of pixels within a target organ. From equation (2.3.4) the error amplification produced by a reduction in pixel size can be calculated.

In the frequency domain whereas the blurred object power spectrum, $H(u)$, is bandlimited, with a maximum spatial frequency, u_{\max} , the NPS is not, having a constant value for all spatial frequencies which extends up to the Nyquist . Thus the choice of a sampling rate which gives a Nyquist frequency

which is higher than u_{\max} will mean that the power spectrum in the frequencies between u_{\max} and the Nyquist will consist purely of noise. Thus the greater the gap between u_{\max} and the Nyquist the lower the overall signal to noise ratio in the projection data. The high spatial frequencies are then amplified by the reconstruction process, Section 2.3.2, to further reduce the signal to noise ratio in the reconstructed image.

However, as long as the sampling rate is chosen to give a Nyquist frequency greater than u_{\max} the projection data can be filtered with a function which rolls off to zero to control the noise. The problem then is to attempt identify u_{\max} or alternatively the frequency at which the noise power begins to dominate the signal. This topic will be investigated more fully in Chapters 7 and 8.

There are also some independent variables which are under operator control which can influence the selection of a suitable linear sampling rate. These include

- 1] The resolution and sensitivity combination of the collimator
- 2] The choice of the energy discrimination window
- 3] The angular sampling rate
- 4] The filter function

In practice the choice of a linear sampling rate has to be made in parallel with the choice of the other variables. The collimator and energy window selection effectively determine the signal to noise ratio and resolution content of the unsampled data. The choice of a suitable angular sampling rate is a similar problem to the choice of the linear sampling rate. Finally, the filter function is used during the

reconstruction to alter the balance between the resolution and the noise in the acquired data.

The relationship between these variables and a strategy for choosing an optimal set for a given imaging situation will be investigated as part of the work of this thesis.

2.4.2 Angular Sampling Rate in the Presence of Noise

The choice of an optimal angular sampling rate for noise free data can be calculated from the linear sampling rate using simple geometrical considerations, 2.2.3. However, the analysis in the presence of noise is more complex.

The results from Heusman (1975) show that for a finite angular sampling rate, n_0 , above a certain threshold level the stochastic error in a reconstruction pixel is in fact independent of the angular sampling rate. For this case the RMS% error in the value of a reconstruction pixel can be expressed in the form

$$\text{RMS\%} \sim [S/n_0]^{1/2}$$

where S is the variance of the value in a projection element which is given by Poisson statistics to be equal to the number of counts. Thus, for a constant imaging time, any increase in n_0 will produce a proportional decrease in S so that RMS% will not depend on n_0 .

The threshold angular sampling rate level above which this independence holds has been shown by Heusman to be equal to 1.5 times the number of projection elements acquired at each acquisition angle. Thus, if there are 64 pixels in a projection profile the threshold level is 96 angles per 180

degrees. This is similar to the value obtained in the noise free analysis, section 2.2.3, as the threshold below which angular undersampling artefacts can be expected. It would appear therefore that the increase in the value of the RMS% which occurs if the angular sampling rate is reduced below the threshold level is a consequence not of stochastic noise but of errors due to angular undersampling.

2.5 Non-Stochastic Noise

2.5.1 Introduction

In Sections 2.3 and 2.4 the effects and consequences of the presence of stochastic noise in the data were considered. However, there are also several other important sources of noise. The presence of scattered radiation in the detected photopeak for example and the effects of the attenuation of primary photons can both be considered to be noise processes. These will be treated separately in Section 2.6.

This leaves two other major sources of noise in SPECT imaging which are non-stochastic in nature. The first is due to the non-uniformity of the response of the detector and the second is due to incomplete or inconsistent data collection.

2.5.2. Non-Uniform Detector Response

When a gamma camera is irradiated by a uniform photon flux the detected image exhibits a significant level of non-uniformity. The reasons for this will be fully discussed in Chapters 3 and 4.

The consequences of the non-uniform response of the gamma camera are important. The filtered back projection process

will amplify the effects which the non-uniform detector response has on the projection image data. The nature of the amplification process has been studied by several authors, Shepp (1982), Todd-Pokropek (1980).

A non-uniform region on the camera face will appear as a hot or cold ring on the reconstructed transaxial section. The amplitude of the circular artefact can be related to the amplitude of the non-uniformity, Todd-Pokropek (1983).

$$A_t \propto A. [(R.Np)/(2\pi^4r)]^{1/2}$$

where A_t is the amplitude of the ring artefact.
 A is the amplitude of the original non-uniformity.
 Np is the ratio of the length of the projection divided by the size of the non-uniformity.
 R is the radius of the reconstructed object.
 r is the distance of the non-uniformity from the axis of rotation.

Thus the amplification will depend inversely on the square root of the defect's distance from the axis of rotation. This makes the uniformity of the detector close to the y-axis particularly critical. The amplification is also dependent on the relationship between the size of the uniformity and the size of the reconstructed object. The bigger the object or the smaller the area of non-uniformity the larger the amplification. It should also be noted that the amplification will also depend on the relationship between the spatial frequency components of the defect and the reconstruction filter.

2.5.2.1 Uniformity Correction

Although sophisticated uniformity correction methods are employed in modern gamma camera systems, Chapter 3, the residual level of non-uniformity is still greater than desirable for SPECT imaging. Most systems have non-uniform responses with coefficients of variation in general higher than 2%, Elliott (1980,1982,1985,1986). Rogers (1982), has performed simulation studies which suggest that camera uniformity must be corrected to about 0.5% in order to keep image distortion under 5% for objects between 20 and 30cm in diameter. Thus some form of uniformity correction would appear to be desirable.

The most commonly employed approach is to assume that the non-uniform response is due to non-uniform point source sensitivity and that the contribution due to spatial distortion is small. This can then be corrected for by measuring the camera's response when irradiated by a uniform photon flux and performing a multiplicative correction of the data:

$$f_i = c_{\text{mean}}/c_i$$

where f_i = correction factor for the i th pixel.

c_i = no of counts in i th pixel.

c_{mean} = mean counts per pixel.

Unfortunately, there are several theoretical and practical difficulties arising from the application of a simple multiplicative flood field correction method. The assumption that the non-uniformity is due solely to point source

sensitivity variations is incorrect. Furthermore, the pattern of detector non-uniformity will vary with the scatter fraction of the detected radiation. Thus it will be dependent on the source distribution itself. The use of a flood field correction is therefore only valid if it is used to correct another flood image acquired under identical imaging conditions.

The major practical difficulty involves the level of non-uniformity in the flood source itself. Commercial flood sources are only uniform to within 5% which is totally unsuitable for SPECT. In fact even for precision made liquid filled flood phantoms it is difficult to ensure uniformity levels of better than 0.5%, Rogers (1982). This does not compare favourably with the suggested limits for corrected camera uniformity responses of between 0.5% and 1%.

Similar difficulties exist with the collection of flood images with sufficiently low stochastic noise levels. For a 64 x 64 image, 120×10^6 counts are required to give pixel count variations of less than 0.5% which again is too high for the suggested accuracy levels. For 128 x 128 image data nearly 500×10^6 counts are required to keep pixel count variations below 0.5%. This is probably beyond what is practically achievable if count rates are to be kept to levels below 10,000 cps since it is known that the uniformity of the camera's response changes at high count rates, Sharp (1985). Furthermore, the presence of high activity flood sources would have difficult radiation protection considerations.

The problem of statistical reliability can be ameliorated if the flood data are smoothed. Rogers (1982) suggests that

this is a reasonable approach if the same smoothing function is used on both the projection data and the flood image.

It should be noted that the correction of a particular subset of the system non-uniformity is not constrained by the above considerations. The non-linearity of the ADCs can add to the non-uniform response of the camera itself. It is however possible to measure this accurately, Gillen (1989), and to perform a correction which is free from variations in the flood phantom, from significant statistical error and which is independent of the source distribution.

The issues discussed above will be examined practically in Chapters 7 and 9.

2.5.3 Inconsistent data collection

One of the fundamental assumptions made in the idealised analysis of the reconstruction process was that the source distribution and the response of the camera to it remained constant during the period of acquisition. Alterations in the detected distribution will make the projection data set inconsistent leading to the production of artefacts, Bok (1987).

The main source of inconsistency artefacts encountered in the routine clinical situation is patient movement. Particularly for patients who feel unwell, it can be difficult to lie completely still for the 40 minutes or so required to acquire the SPECT data. The problem in the authors experience is most severe for brain imaging. This topic will be addressed in Chapter 10.

Another common source of inconsistency artefacts occurs when performing skeletal studies of the pelvis. The imaging

agent is excreted into the bladder causing the activity level within it to change during the period of acquisition. This problem will be addressed in detail in Chapter 12

2.6 Attenuation and scattering

2.6.1 Introduction

The previous analysis has, for simplicity, ignored the effect which the attenuation and scattering of photons has on the relationship between the detected data and the source distribution. It has been implicitly assumed that the photons which are emitted by the source distribution do not undergo any interactions with the attenuating media containing the source distribution before they are detected by the gamma camera. In fact when the emitted photons travel through attenuating media of the form encountered clinically (tissue, bone etc.) there is a highly significant level of interaction.

The two processes which are involved are Photoelectric absorption and Compton scattering. The level of interaction can be described by the linear attenuation coefficient (LAC) , μ . This is observed by measuring the decrease in the intensity of a very narrow beam of photons after travelling through a set thickness of the attenuating medium. If the initial intensity is I_0 then the intensity observed at a length l through the attenuator is given by a single exponential

$$I = I_0 \exp(-\mu l)$$

As an example the linear attenuation coefficient for a 141keV photon from Tc^{99m} travelling through water is 0.152cm^{-1} .

As the LAC refers to the reduction in intensity of a very narrow beam of photons it is not directly applicable to the general case of an extended source distribution. This is because photons which are Compton scattered are physically removed from the narrow beam and so are not included in the detected signal. For the case of an extended source distribution the scattered photons can only be removed from the detected signal if an infinitely high degree of collimation is used or if the detector has infinitely high energy resolution. For a gamma camera however the degree of collimation is limited by sensitivity constraints and the energy resolution has a finite value of around 10%. Thus, the photons within the photopeak will consist of a combination of scattered and unscattered data.

The addition of the extra, scattered photons to the photopeak means that the amplitude of the signal detected from a known source distribution within a known attenuation distribution will be greater than that expected from the application of the simple LAC. One approach to this problem has been to define an effective LAC which attempts to account for the inclusion of scattered photons in the detected signal. For example a value of 0.12cm^{-1} is often used for 141keV photons in water. This is an approximate approach however because the magnitude of the scatter component at any point is both source and attenuation distribution dependent. The magnitude of the source distribution dependence even for a uniform attenuating medium can be assessed by considering an example given by Todd-Pokropek (1983). A point source placed in the centre of a uniform object 19cm in diameter has an amplitude of 24% that of a point source at the edge of the

object. This is approximately what would be expected for a LAC value of 0.15cm^{-1} . However, the value at the centre of a uniform distribution was measured to be 57% which is 240% greater than expected.

Thus, any attenuation correction algorithm which aims to produce accurate quantitative information must include some way of estimating the scatter contribution. It should be noted that this is a difficult task. The scatter contribution has to be known to calculate the source distribution but the scatter contribution depends upon the source distribution so that the source distribution must be known before the scatter contribution can be calculated ! Indeed, this is even before the problem of a variable attenuating medium is introduced.

It should be noted that a correction for the detector response function, of the form described in Section 2.2.1, would also be required before applying any attenuation correction algorithm if quantitatively accurate information is required. The quantitative errors which are produced by the variation of the detector response with distance are of the same order of magnitude as those produced by a failure to account for scattered radiation.

2.6.2 Attenuation correction

As described above the correction for attenuation and scatter required to produce accurate quantitative data is extremely complex. However if accurate quantification is not essential then simpler attenuation correction routines can be employed to improve the qualitative aspects of the reconstructed images.

The most obvious approach to this is simply to ignore the

problem of the inclusion of scattered photons within the detected signal and to assume that the photons are attenuated in a simple single exponential manner. Using this assumption an approximate compensation for attenuation can be made by applying simple multiplicative corrections to the data either before or after reconstruction.

Of the prereconstruction methods the most commonly applied is that of Sorenson (1974) and Budinger (1977). The fundamental assumption used (in addition to that of scatter free data) is that there is a region of uniform activity within a larger medium of constant attenuation. An approximate value for each projection element in the absence of attenuation can be obtained by taking the geometric mean of opposing elements and dividing by a factor which corrects for the attenuation along the projection rays between the edge of the source distribution and the body contour. This factor is a hyperbolic sine function. The method requires the definition of a body contour and an estimate of the size and location of the source region. Both can be obtained from a reconstructed image without correction. This method uses a crude assessment of the source distribution and is unlikely to be accurate for highly non-uniform distributions.

Simple multiplicative corrections can also be applied to the data after the reconstruction has been performed.

For example the method developed by Chang (1978) considers the reconstruction of a point source within an attenuating medium. The expected point source detection efficiency for each pixel in a transaxial section is calculated from a knowledge of the body outline and a suitable value for the LAC. After a transaxial section has been reconstructed each

pixel within it can be corrected according to its calculated detection efficiency.

This approach is commonly known as the 'first order Chang' and gives reasonable results for source distributions which do not strongly contradict the initial assumptions which were made. It is possible to vary the value of the attenuation coefficient with position with this method.

The major problem with a pointwise multiplicative operator, such as this, is that no account whatsoever is taken of the non-uniform nature of the source distribution.

To attempt to overcome this a group of methods which use iterative techniques have been developed. The projection data for a convex region of uniform attenuation are given by the attenuated Radon transform, Radon (1917). The solution of the attenuated Radon transform can, in principle, be obtained using iterative methods.

There are several different approaches which can be made all of which, however, account for the effects of attenuation by estimating the projection data which would be obtained by imaging a hypothetical activity distribution contained within a measured or assumed distribution of attenuating material.

The initial estimate is usually made using the data obtained from a straightforward filtered backprojection of the acquired information perhaps with one of the first order, multiplicative corrections applied. The estimated projections are obtained by taking into account the attenuation along each projection ray. The difference between the estimated projections and the real data is used to correct the starting image. The way in which the differences are used to correct the original data in each iteration provides a variety of

different iterative correction methods.

In principle, iterative reconstruction techniques may provide accurate compensation even for non-uniform tissue attenuation, if the distribution of the attenuation coefficient in the patient is obtained by transmission tomography in the same position as the emission scan, Soussaline (1982). However, this procedure is time consuming and is not suitable for many clinical applications.

In addition to attenuation it is also possible to incorporate the effects of the camera line spread function when estimating the hypothetical projection data from any iteration.

Thus, using iterative approaches it is in principle possible to account for the effects of the attenuation of a non-uniform activity distribution within non-uniform attenuation media and also to correct for some of the systematic errors introduced by the detection process.

There are two major problems with the iterative methods however. Firstly, the percentage root mean squared image noise is two to three times higher than for the first order pointwise multiplicative correction Moore (1982). Secondly, they require a great deal of computer time.

A more computationally rapid group of correction methods which also account for non-uniform source distributions attempts to provide an analytical solution to the attenuated Radon transform (this is significantly more difficult than the inversion of the non-attenuated Radon transform).

Trietak (1978) proposed a reconstruction method which involves convolving the projection data with a suitably chosen function before back projecting with an exponential weighting

factor.

This work was extended by Bellini (1979) who proposed an exact analytical solution by performing the inversion in Fourier space. This has the advantage that information from all projections is used to evaluate the function. This is the method which is used in this thesis, Chapters 7 and 9.

It is difficult to incorporate the effects of non-uniform attenuation with the analytical methods. Furthermore, neither of the previously described methods uses frequency components in the data which are less than the frequency divided by 2π . The reconstructions may therefore be inaccurate in this 'D.C.' region which could affect absolute quantitative capabilities.

In all of the previously described approaches a value for the attenuation coefficient which is lower than the LAC can be used to give a rough correction for scatter. This is approximate because no account is taken of the structure inherent in the scattered radiation which is a consequence of its dependence on the source distribution.

It should be noted that a correction for the detector response function, the form of which was described previously, would improve the quantitative accuracy of any of these attenuation correction methods (in fact this correction is as important as the correction for scatter). However, it is not clear whether this would result in an improvement in image quality.

2.6.3 Scatter correction

As described previously an approximate correction for the qualitative effects of scatter can be made with first order attenuation correction methods by using an attenuation

coefficient value lower than the LAC. The quantitative inaccuracy which remains however, because the scattered photons have not been removed from the data, has been illustrated by an example given by Jaszczak (1985). When a value of 0.12cm^{-1} is used as the effective attenuation coefficient the count density measured from a SPECT image of a photon deficient sphere, 6cm in diameter and placed near the centre of a cylinder, 22cm in diameter by 25cm long and containing a uniform distribution of Tc99m, erroneously indicates that the sphere is "emitting" photons at a rate that is approximately 30% of the cylinder's background activity.

These quantitative errors are to be expected since a pointwise multiplicative operator cannot correct for scatter since the scatter count rate at one position depends upon the photon sources at all other positions (and in addition to the distribution of attenuating structures).

An approach which should, in theory, give a more accurate quantitative correction for scatter uses an estimation of the average value for the scatter fraction, Jaszczak (1981). The use of an average value is based on the assumption that the parameters which are usually measured are not sensitive to small errors in the value of the scatter fraction. This assumption is reasonable for the measurement of uptake and concentration ratios but not for absolute concentration levels. Again this is a consequence of the failure to account for the structure inherent in the scattered data.

To account for the structure a second energy window can be used below the photopeak and the assumption made that the ratio of this to the photopeak counts is proportional to the scatter fraction. Thus an arbitrary fraction of the counts in

the lower window can be subtracted from the photopeak data either before or after reconstruction. The arbitrary factor will depend on the source geometry but can be estimated empirically or by using Monte Carlo techniques. It is claimed, however, that the application of this is simple and improves the SPECT data both quantitatively and qualitatively.

A final group of correction methods estimates the form of the scattered data by assuming that it can be obtained from a convolution of the unscattered data with an exponential function. As the measured projection data are then considered to depend on the unscattered data and an arbitrary exponential function the parameters of the exponential function can be varied to produce an estimate of the unscattered data. In a similar manner to the use of the constant of proportionality for the dual window technique the values for the exponential function can be estimated from Monte Carlo simulations or empirical measurements

The use of Monte Carlo modelling is particularly useful in providing guidance in the development of scatter compensation procedures since it is possible to perform a detailed analysis of the scatter process which cannot be performed experimentally. For example, Jaszczak (1985), has calculated the profiles of the scatter component of the photopeak of projection data for an off axis Tc99m line source positioned within a 22cm diameter water filled cylinder. It would not be possible to do this experimentally because the scattered and unscattered photons within the photopeak are not separable. Another example of the use of Monte Carlo modeling is to assess the scatter fraction for any particular source and attenuation distribution.

2.6.3.1 Offset Energy Windows

If the aim is not to produce accurate quantitative information but simply to improve the images qualitatively through an increase in contrast then the most direct approach is simply to exclude a fraction of the scattered data by increasing the value of the lower level of the energy discrimination window. Of course the disadvantage of this is that some of the unscattered photons will also be excluded from the signal.

As was demonstrated from a Monte Carlo simulation by Jaszczac (1985), there is a diminishing return to be obtained from increasing the lower level of the energy discrimination window. The ratio of scattered to unscattered photons rejected will depend on the scatter fraction and so on the source and attenuation distribution. Experimentally, the reduction in sensitivity can be measured for any given source and scatter distribution but this gives no information, apart from an upper boundary, on the number of scattered photons rejected. Furthermore, the effects of an offset energy window for SPECT imaging has not been examined for modern camera designs. This is investigated in Chapter 6.

Chapter 3 Equipment Description

3.1 Introduction

The results obtained in any study of SPECT imaging are particularly dependent on the characteristics of the particular equipment used. Thus a detailed description of the equipment is required if the results which are presented are to be interpreted in their correct context.

3.2 The Gamma Camera

The gamma camera used was a Siemens ZLC DIGTRAC Orbiter. It was installed in July 1986.

3.2.1 Camera gantry

The head is supported by a C-arm and a counterbalance. This particular configuration means that the camera has a fixed axis of rotation. As a consequence of this the orbit of the camera must be circular i.e. elliptical or body contour orbits are not possible unless the bed supporting the patient is moved. The radius of rotation (ROR) can vary from a maximum of 40cm to a minimum which will be dictated by the width of the patient or of the SPECT bed.

The gantry angle and head tilt are continuously output on two digital displays.

The whole gantry can be rotated if required.

3.2.2 Camera head

The camera head contains 75 photomultiplier tubes. The crystal thickness is 9.5mm and the field of view (FOV) is circular with a diameter of 39cm.

There are two major electronic features within the camera head, energy-linearity correction known as ZLC, and a recursive tuning capability, DIGITRAC. These features will be described in Section 3.2.2.2 and 3.2.2.3. A selection of collimator inserts are provided details of which will be given in Section 3.3.

3.2.2.1 Basic operation

There are three energy analysers which can be adjusted independently to give multiple photopeak imaging. Each analyser should be peaked using a scatter free source prior to each study. The analysers can be peaked automatically by selecting the camera's preset energy levels for the selected isotope. The window of each analyser is then set to 20% of the photopeak energy and an up-down counter is used to balance the counts in two narrow energy windows placed on either side of the photopeak. By this method the centre of the energy window is positioned over the centre of the photopeak. After an analyser has been peaked the original window width is restored. A message is output after peaking which gives the amount of correction which has had to be applied to each analyser in order to shift the analyser energy from the nominal preset value to the actual value at which the photopeak was detected. From this the numerical value of the photopeak position can be determined.

The analysers can also be peaked manually by directly selecting the photopeak energy as opposed to using the cameras preset values. The peaking process is exactly the same as for the preset isotope selections.

The analysers can be adjusted for off peak imaging simply

by entering the desired shift of the analyser window from the photopeak as a percentage of the selected energy level.

3.2.2.2 Energy and linearity correction

A useful feature of the camera system is the electronic correction of the energy and spatial location of the detected photons. This has been trademarked under the name ZLC.

The purpose of the ZLC system is to correct for intrinsic energy variations and for systematic errors in the calculation of the position of detected events. The major effect of this is to improve camera uniformity which is of prime importance for the production of high quality SPECT images, Todd-Pokropek (1980).

Energy correction of detected photons is necessary because the light output which is detected from the crystal is not uniform across the field of view. The regional variations in light intensity are due to intrinsic variations in the crystal itself and to the transfer of the light photons from the crystal to the PMTs. Events which occur in areas of the crystal with low light output can be incorrectly interpreted by the pulse height analyser as lower energy events which would be disproportionately discriminated against. These variations are then added to by unmatched PMT response characteristics. By assessing the energy response of the crystal (called the Z map) in the factory a 64*64 correction matrix is determined which is stored on an EPROM and used to multiply the energy signals of the detected photons depending on their position. This process produces near uniform energy response over the camera face. It should be noted that if a PMT fails and has to be replaced the values for the correction

matrix have to be remeasured and the EPROM "re-burned". A similar situation exists if the PMT gains drift substantially, although it is claimed by the manufacturer that the camera's stability is such that the factory calibration data will be valid for the life of the camera so that periodic recalibrations are not necessary.

There is a separate source of non-uniformity in the response of a gamma camera, however, which is due to systematic errors in the positioning of detected photons. This phenomenon is known as spatial distortion and is produced because the position of a detected photon is calculated so that it is displaced towards the centre of the nearest PMT. This is an inevitable consequence of the geometry of the light transfer from the crystal to the PMT assembly which is a function of the finite size and circular shape of the PMTs. This will mean that there are gaps between PMTs which the positioning arithmetic is not designed to handle.

To correct for this, images of carefully calibrated slit phantoms are acquired in the factory and used to measure the linearity distortions. The information from this is then used to create a 64*64 correction matrix. The elements of the matrix consist of vectors which are used to reposition each detected event back to its true position. The four vectors nearest to the position of the detected photon are bilinearly interpolated to give the final correction vector. In addition to the improvements in uniformity due to the correction of spatial non-linearity an improvement in intrinsic spatial resolution is also observed.

It should be noted that the ZLC corrections require samples of the voltage signals firstly to be transferred into

digital form using an analogue to digital converter (ADC) and then back to analogue form again using a digital to analogue converter. Thus the correction circuitry has added extra components to the system the linearity of which are crucial to the production of artefact free images.

3.2.2.3 DIGITRAC recursive tuning

The camera is kept in a state of optimal tuning at all times by the DIGITRAC recursive tuning facility which essentially uses the unscattered photons on the high energy side of the detected photopeak as a reference standard against which the gains of the individual PMTs can be assessed. As a change in the energy response of any individual PMT affects the detected response of every other PMT a deconvolution has to be performed to separate the PMT responses from each other. The PMT responses are continuously analysed and adjusted to ensure that the variation in energy response across the crystal face is within 0.7%.

Every PMT exhibits a minor semi-random gain drift that varies with many factors including time, electron current and temperature. When the gain of any individual PMT changes it affects the observed energy response (Z-map) over the whole crystal. The Z-map is measured by DIGITRAC by analysing the unscattered photons which occur on the high side of the photopeak. This is performed using a special tune analyser which has a relatively narrow window which is placed on the high side of the photopeak. The difference between the observed Z-map and the original factory measured Z-map will be due to the gain changes of the PMTs.

By making measurements of the PMT response to source

position, the Z-map error pattern for any PMT gain error pattern can be accurately predicted. Inverting the matrix of coefficients produced by this process results in a reverse matrix of coefficients which is a Z-map deconvolution pattern. It is this derived pattern which compensates for surrounding PMT gain error effects and allows the gain error for each specific PMT to be obtained. One matrix table of reverse coefficients is required for each PMT the elements of which are dependent on the PMT position within the assembly. These tables make it possible to directly derive the underlying PMT gain errors from the observed Z-map errors. The individual PMT gains can then be adjusted in parallel to eliminate the Z-map errors.

3.3 Collimators

A range of collimators can be used for imaging with ^{99m}Tc which offer different combinations of sensitivity and resolution. The collimators are manufactured by affixing lead foil strips to produce hexagonal shaped holes. The specifications of the collimators which were available are shown in Table 3.1. In addition a variety of collimators are also available for imaging higher energy isotopes.

3.4 SPECT operation of camera

The camera acquires SPECT data in a step and shoot mode. The collection time per angle is specified from the computing system which controls the camera rotation. 360 and 180 degree rotations are both possible. The number of angles is also selected from the computing system the possible options being 32, 64, 120 and 128.

Collimator type	LEAP	High resolution
Number of holes	51,600	85,400
Hole length	2.36cm	2.36cm
Septal thickness	0.20mm	0.16mm
Relative sensitivity	100%	64%
Effective hole diameter	1.43mm	1.11mm
Geometric collimator resolution (FWHM) at distances of 0 at 10cm	0cm - 1.9mm 10cm - 8.2mm	0cm - 1.5mm 10cm - 6.4mm
System Resolution (FWHM) at distances of 0 and 10cm	0cm - 4.4mm 10cm - 9.1mm	0cm - 4.2mm 10cm - 7.5mm
5% Penetration energy	160keV	160keV
Field of view	39cm	39cm

Table 3.1 Collimator specifications provided by the manufacturer. These measurements were made with a 20% window

The camera design imposes some practical limitations on the acquisition of SPECT data. A fixed centre of rotation and a camera FOV of 39cm means that it is not possible to image objects which are more than 19.5cm from the centre of rotation. Thus it is important to note that increasing the ROR over the value of 19.5cm will not increase the size of the image volume. When the torso is imaged, for example, it is important that the central axis of the patient is positioned close to the axis of rotation if superficial structures are to be included in the image volume.

It should also be noted that the circular shape of the camera face means that the usable transaxial image diameter decreases with displacement from the centre of the FOV.

3.5 Computing system

During the course of this investigation two computing systems were used within the Nuclear Medicine Department. The original system, the Nodecrest MICAS3, was replaced with the more powerful Nodecrest MICASV. As most of the data processing aspects of this thesis were performed on the MICASV the following description will concentrate on it.

The Nuclear Medicine applications software for both systems was virtually identical.

3.5.1 Hardware

3.5.1.1 System Configuration

The MICASV system was based on two SUN, 32 bit, microcomputers which were networked through an Ethernet connection. The system acquires data, independently, from two gamma cameras including the one set up for SPECT as described

in Section 3.3. Associated with each camera is a video display unit (VDU) on which acquisition and analysis programs can be run. There is also a colour display monitor on which acquired data can be displayed. A separate VDU and display system is present which can be used to analyse data when the camera terminals are being used for acquisition. Most of the specific Nuclear Medicine facilities e.g. the display drivers and the analogue to digital converters (ADCs) have been designed by Nodecrest .

The original computing system, the MICAS3, was considerably less powerful than the MICASV being built around a Univac V76 central processing unit. This is a 16 bit processor which imposes some limitations on the data handling e.g. the highest pixel count possible is 32,768.

3.5.1.2 Data Storage

Each SUN microcomputer has three megabytes of random access memory available for data storage and processing. For short to medium term storage each system has a 300 megabyte hard disk. There is a 60 megabyte streamer for long term data storage.

For the MICAS3 system there were 192 kilobytes of random access memory available for data storage. This was partitioned into three 64 kilobyte segments each of which was associated with one of the terminals. The memory size imposed a limitation on the matrix handling capabilities of the system, the largest matrix which could be held in memory at any one time being 128*128. For short to medium term data storage a 200 megabyte fixed Winchester disk was used. There was a 9 track magnetic tape unit for long term data storage.

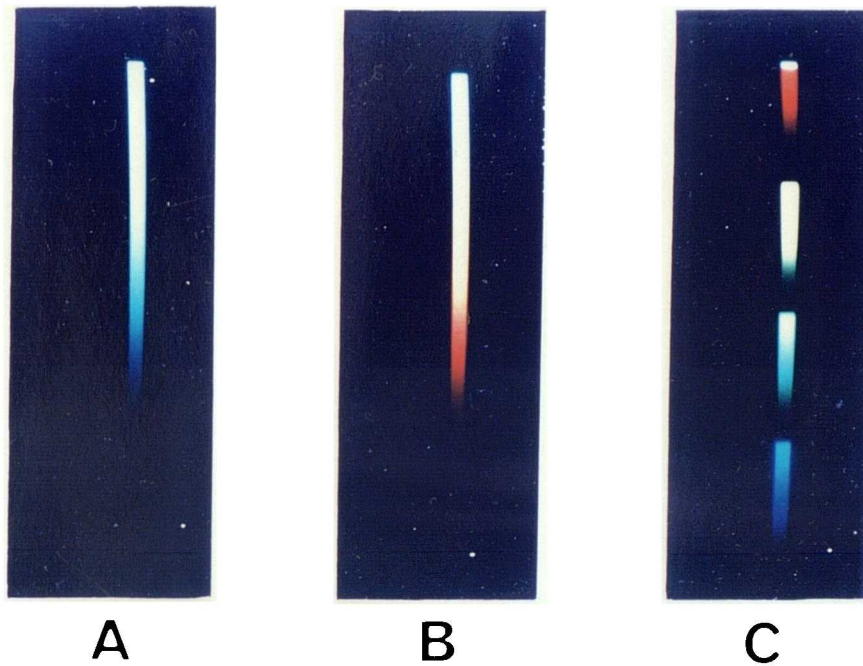


Figure 3.1 The colour scales available for image display are shown. The grey scale, A, and the "hot metal" scale, B, are similar in that the pixel count values are proportional to screen brightness. This has the disadvantage that the full display range cannot be reproduced on polaroid film. The false colour scale, C, is not affected in this way.

3.5.1.3 Image display

The colour display monitors are of a resolution such that four 256*256 images can be displayed simultaneously. There is a special memory provision for data display which allows the manipulation of images without having to use the central memory.

For the display of clinical images a variety of colour scales were provided by the manufacturer. The three scales most commonly used are shown in figure 3.1. The grey scale and the "hot metal" scale are similar in that the pixel count values are proportional to screen brightness. They have the advantage that they are continuous, easy to understand and are commonly used in a wide range of imaging modalities.

The false colour scale is different in that pixel count values are associated with particular colours. The use of this colour scale allows quantitative comparisons to be made more rapidly. It is easier to identify the colour of a group of pixels and compare it with the colour of another region than it is to compare different levels of brightness.

It was also easier to take a hard copy of the colour mapped images using the polaroid camera. The full range of contrast on the screen brightness scales could not be reproduced on polaroid film.

3.5.1.4 Analogue to Digital Converters

The analogue position and energy signals from the gamma camera are converted into digital form by the analogue to digital conversion circuitry. The ADCs themselves are of the successive approximation type. There are 12 bits which should

allow the collection of images of size 256*256 without having to utilise the four least significant bits.

The gains and offsets of the ADCs can be altered easily and accurately through the adjustment of ten turn potentiometers.

3.5.1.5 Hardcopy output

For the MICASV, text and a rough grey scale image could be output onto a laser printer. The images from the laser printer were not of sufficient quality to be of use clinically.

Polaroid photographs of images taken directly from the colour monitor screen are the only available form of hardcopy output.

For the MICAS3 system images could be output onto X-ray film via the Siemens microdot system.

3.5.2 System Software

3.5.2.1 Operating system

For the MICASV, the operating system used was UNIX. There is a sophisticated text editor and FORTRAN and C compilers which permit the user to produce customised software.

For the MICAS3, the systems software was written by Nodecrest specifically for use in a nuclear medicine environment. The operating system, known as SIS, was written to provide a real time multitasking capability. There was a text editor and a Fortran compiler available.

3.5.2.2 Applications Software

There is a suite of programs written to perform the data and image manipulation tasks commonly required in nuclear medicine. These will not be described in detail.

3.5.3 SPECT Software

A detailed description of the SPECT software is relevant. A definition of the coordinate system used in this thesis is required for the description of the software and is given in figure 3.2.

3.5.3.1 Data acquisition

The gamma camera rotation is controlled by the computer which determines the data acquisition parameters. The available options are 32, 64 or 128 projection angles ; 32, 64 or 128 transaxial sections ; 64 or 128 points per projection profile ; 180 degree or 360 degree rotation.

Centre of rotation correction is possible during acquisition. The x-coordinates of the signals can be shifted by a specified value. The value is input in terms of the highest resolution pixel which means that a correction to within a $1/4$ or a $1/2$ a pixel for 64 or 128 point projection profiles is possible. A more precise correction is possible by manually adjusting the x-ADC offset potentiometer.

Some sorting of the data takes place during acquisition. The acquisition matrices are stored in the form of sinograms in addition to or as an alternative to the projection images.

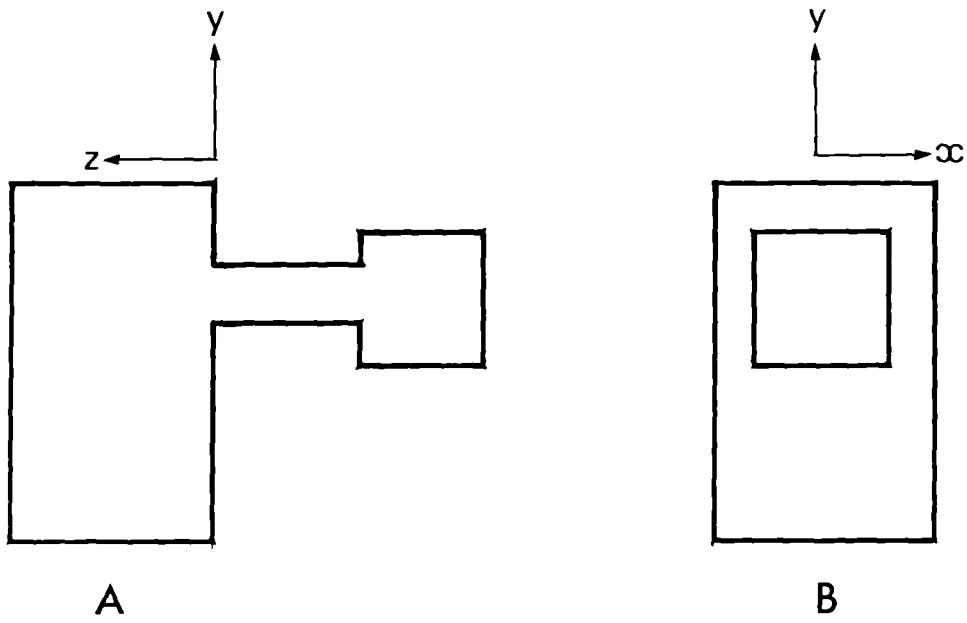


Figure 3.2 Definition of coordinate system relative to the gamma camera. The gantry is side on in A and the camera head is towards the observer in B.

3.5.3.2 Reconstruction Software

The reconstruction of the axial images from the sinograms is performed by filtered back projection. For 360 degree rotations the arithmetic mean of opposing views is taken prior to back projection.

Data collected with 64 points across each sinogram may only be reconstructed as 64*64 axial slices ; data collected with 128 points across each sinogram may be reconstructed as 64 or 128 square axial slices, or a 64*64 zoom into any part of a 128 square image. Before back projection the data in the projection profile are interpolated to 1024 points. Thus if the data are acquired at 128 points and reconstructed as 64 the image quality should increase because the interpolation is more accurate but will decrease because of the increased noise.

3.5.3.3 Reconstruction filters

There are a number of filter functions which can be applied to the projection profile data prior to back projection. The filtering process occurs in real space so that a convolution of the filter function with the projection data is performed. Each filter has a kernel of 33 points but to save time in the reconstruction only 24 are generally used. The three filters recommended for use by the manufacturer are

Filter 1	Shepp-Logan
Filter 2	Shepp-Logan (soft)
Filter 3	Ramp

The frequency space representations of the three filters are

shown in figure 3.3 and are defined to be :

$$\text{Filter 1 } F_1(u) = \sin(\pi ua)/\pi a$$

$$\text{Filter 2 } F_2(u) = [\sin(\pi ua)/\pi a] \cdot [0.4 + 0.6\cos(2\pi ua)]$$

$$\text{Filter 3 } F_3(u) = u$$

where u is the spatial frequency

a is the sampling distance

It can be seen from the frequency space representations that filters 1 and 3 are similar, the major difference being the smoother roll off of filter 1 at the Nyquist frequency. Filter 2 produces a significantly higher suppression of the higher spatial frequencies and so is more likely to be of use in high noise imaging situations.

The real space representations of the three filters and are defined to be :

$$\text{Filter 1 } R_1(ia) = -2/[\pi^2 a^2 (4i^2 - 1)]$$

$$\text{Filter 2 } R_2(ia) = 0.4[R_1(ia) + 0.3R_1((i-1)a) + 0.3R_1((i+1)a)]$$

$$\text{Filter 3 } R_3(ia) = \sin(\pi ia)/\pi a$$

where $i = 0, +/- 1, +/- 2, \dots$

3.5.3.4 Attenuation correction

This is performed using the method of Bellini (1979). This is an analytical method (assuming the body to be a uniform attenuating medium) consisting of two stages ;

(1) A correction for the varying air gap between the patient and the camera. For this the patient's body outline is

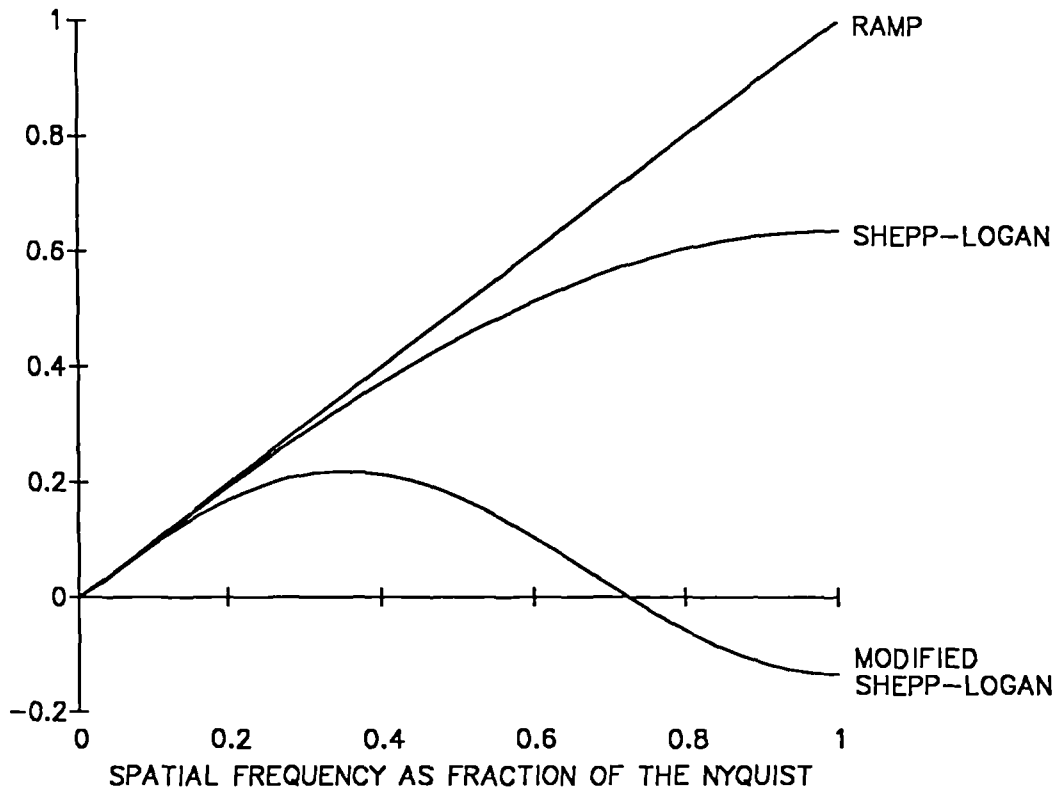


Figure 3.3 Frequency space representations of the filter functions recommended for use by the manufacturer.

approximated by an ellipse.

(2) A correction for the differing attenuation of sources at different depths within the body. This is done by performing frequency substitution on each line of the sinogram according to the formula :

$$p(k,t)=p(\sqrt{k^2 + c^2}, t + i*\sinh^{-1}(c/k))$$

where $p()$ = the Fourier transform of the sinogram line

k = the spatial frequency

t = the angle of projection

c = the attenuation coefficient

3.5.3.5 Centre of rotation correction

It is essential for the production of good quality SPECT images that the x-ADC offset is adjusted so that the mechanical y-axis of the camera corresponds to the centre of the image matrix. This will be discussed fully in Section 4.4.6 .

A routine, called ALIGNT, is provided by Nodecrest to enable a quick assessment of the x-ADC offset to be performed. The program uses four images of a point source collected 90 degrees apart using matrix sizes of 256*256. The x coordinate of the centroid of the source is calculated for each view and the mean value calculated. The difference between this figure and the expected value of 128.5 is output.

If a non-zero value is obtained from ALIGNT the reconstruction software can correct for it. Alternatively the x-ADC offset potentiometer setting can be adjusted until an

offset error of zero is obtained.

In either case if a SPECT study is acquired using a matrix size of 64*64 then the error in the X-ADC offset setting will not be greater than 0.125 pixels. This is probably within acceptable limits for the noise levels encountered in clinical studies, Saw (1986), but greater accuracy may be required if high count density phantom studies are to be performed.

If the matrix size for the SPECT study is 128*128 then then the error in the x-ADC offset setting will not be greater than 0.25 pixels. This is probably not sufficiently accurate for clinical studies, Saw (1986), and will certainly limit the image quality of high count density phantom studies.

Thus, ALIGNT serves as a rapid but approximate assessment of x-ADC offset setting. More accurate techniques will be described in Section 4.4.6

3.5.3.6 User generated software.

The applications software provided by the manufacturer was sufficient for the performance of most of the common image manipulation and analysis tasks required for routine nuclear medicine use. However, in the course of this investigation many non-standard and more sophisticated analytical procedures were required for which software was generated by the author.

3.6 Phantoms

3.6.1 Flood field phantom

The assessment of the uniformity of the response of a gamma camera over its field of view is one of the most important measurements of its performance. This was

accomplished in this thesis by irradiating the camera with a uniform flux of photons which was produced by the activity in a liquid filled flood field phantom. The phantom was designed and manufactured at the Western Infirmary to provide the high level of accuracy and stability required for SPECT imaging. It was constructed from square plates of perspex of edge length 61cm and thickness 3cm. The cavity for the liquid was obtained by accurately drilling circular spaces of diameter 50cm to a depth of 1cm in two of the plates. The plates were then glued together to form the enclosed volume for the liquid. The thickness of the cavity was measured to be uniform to a tolerance of better than 0.1%. Two holes were drilled in the side of the phantom to allow activity to be introduced.

To counteract the tendency of the perspex to distort under its own weight the phantom was encapsulated in a steel frame which ran around its perimeter. The whole assembly was then attached to a support stand which consisted of a steel cradle mounted on four wheels. The wheels allow the stand to be moved and positioned with ease. The phantom itself was attached to the cradle so that it could be pivoted around its centre line allowing it to be positioned against the collimator. This design was based on that described by Hall (1986).

3.6.2 SPECT phantom

An object with a known distribution of activity and attenuating structures can be used to assess the overall performance of the SPECT system and to measure the effects of the variation of a range of parameters involved in the production of the SPECT images. To achieve this a phantom manufactured by SIEL Ltd. was used.

The phantom consists of an acrylic cylindrical tank of outside diameter 8.5 inches, inside diameter 8 inches and length 12 inches. It is resealable with fill and drain ports and provides the background activity with the desired ^{99m}Tc -water solution.

A set of acrylic inserts, figure 3.4, are provided which can be used to assess various aspects of system performance. All inserts are of outside diameter 7.875 inches and thickness 3 inches. The hot lesion (HL) insert contains 9 pairs of holes drilled through a solid acrylic block. The hole diameters are 19mm, 11.5mm, 9mm, 7mm, 4.5mm, 3.5mm, 3mm and 2mm. The distance between hole centres is five times the hole radius.

The linearity/uniformity insert has a crossed grid of cut-out channels in an acrylic block. The channels are 6mm wide and leave square sections of edge length 22mm.

The cold lesion (CL) insert contains seven plastic rods of diameter 6mm, 7mm, 9mm, 11mm, 14mm, 17.5mm and 22mm. The rods displace the radioactive solution in the source tank thereby creating the effect of cold lesions.

The pie insert consists of a block of acrylic with different sizes of holes drilled in each of six segments. The hole diameters are 6mm, 9mm, 12mm, 15mm, 18mm and 21mm. The distance between the edges of the holes in any particular segment is equal to the hole diameter.

The SPECT phantom is held in position using a specially designed jig. This consists of a cylindrical base plate into which the phantom tank is inserted. The phantom is fastened to the base plate by an aluminium strip which is placed against its free end. The phantom is clamped between the base plate and the metal strip via two acrylic rods of diameter 5mm. The

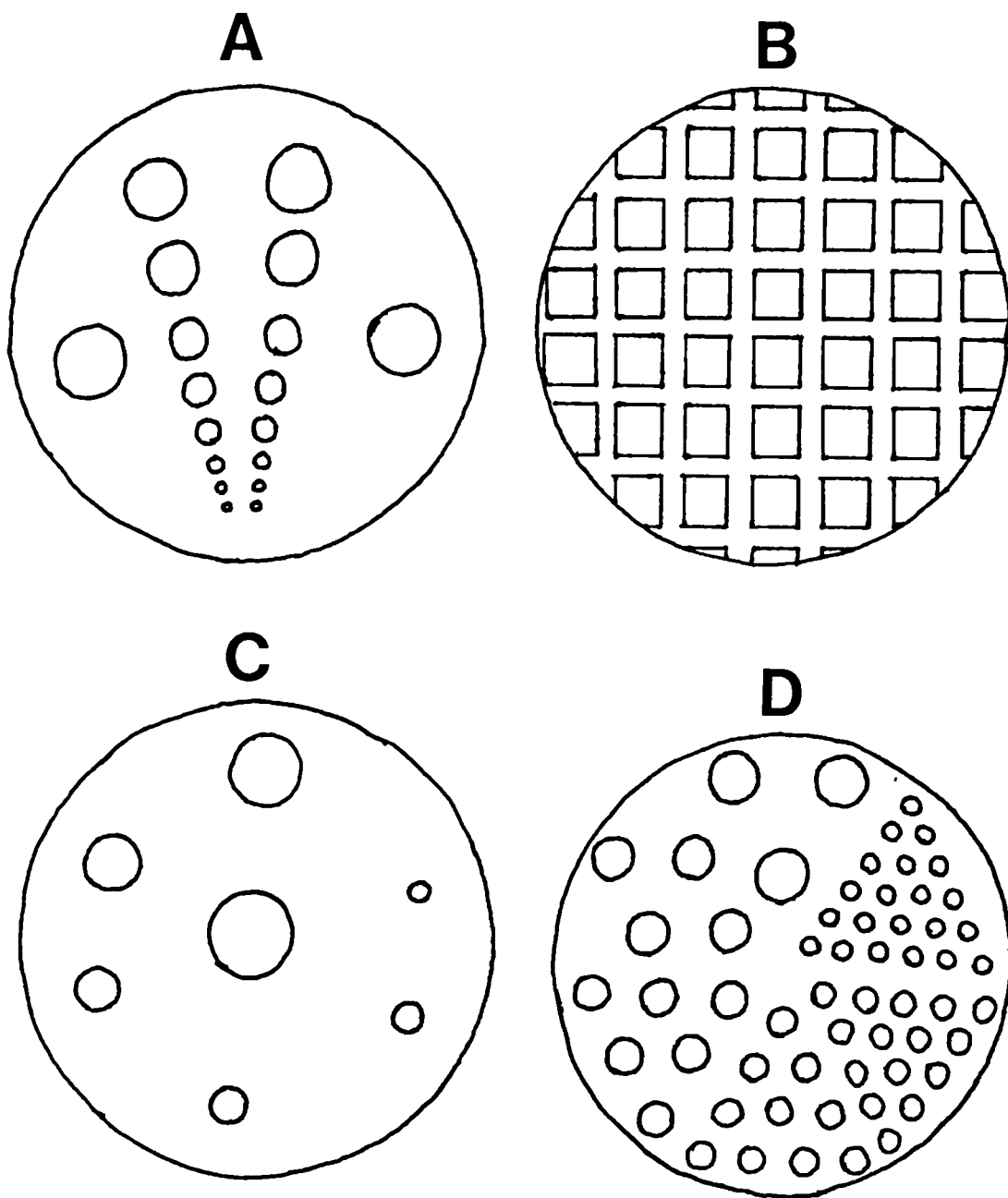


Figure 3.4 Schematic illustration of the inserts used with the SPECT phantom :

- A - Hot lesion insert
- B - Uniformity/linearity insert
- C - Cold lesion insert
- D - Pie insert

base plate is held by a cast iron assembly which is clamped onto the end of the SPECT bed. In this way the phantom can be held so that the camera can rotate around it with a minimum of attenuating structures being interposed between the two (in fact only the thin acrylic rods come between the camera and the phantom). The clamping screws of the cast iron assembly can be adjusted to alter the angle at which the phantom is held. This allows the central axis of the phantom to be aligned with the axis of rotation of the camera so that the transaxial sections through the inserts are perpendicular to the insert structures.

Chapter 4 Performance assessment of imaging system

4.1 Introduction

The implementation and routine application of SPECT places stringent demands on the performance of the imaging system. Conventional planar imaging is a relatively robust modality in that clinically useful images can be produced using systems performing well below specification. The same, however, does not apply to SPECT. Small deficiencies in the performance of any of the component parts of the system can have a large effect on final image quality. For this reason accurate assessment and rigorous quality control are of much greater importance than for planar imaging.

Thus, it was necessary to make a detailed assessment of the imaging system in order to ensure that the performance of the system had been optimised before any other measurements were made. An example of this would be in the detection of component parts of the system which were either faulty or performing at a substandard level. Having optimised the performance of the system continuous measurements were also required to ensure that no deterioration with time occurred.

An additional consideration in this was that a detailed description of performance should enable comparisons to be made with other systems so that results obtained in the remainder of the thesis can be interpreted with respect to any differences found.

The parameters which are of importance are firstly the planar imaging performance in terms of field uniformity, spatial resolution, energy resolution, sensitivity and countrate linearity.

It is also essential that the planar imaging performance

remains stable as the head is rotated around the subject. Variations in the energy response of the camera with angle, for example, can lead to losses of uniformity and the creation of artefacts in the reconstructed sections, Jarrit (1984).

Next, the mechanical performance of the gantry has to be sound. The camera head has to rotate in a perfect circle so that the centre of rotation (COR), corresponding to each axial section, has to be as close to a point as possible.

The accurate transfer of the image data from the camera to the computing system is a critical link in the imaging chain. The ADCs have to be linear because any non-linearities appear as non-uniformities which are correlated spatially leading to the creation of ring artefacts in the reconstructed axial sections. In addition the x-ADC offset has to be accurately adjusted so that the electronic y-axis of the camera is positioned exactly in the centre of the image matrix.

Finally, the software used to reconstruct the acquired data is an integral part of the imaging system as a whole. Its characteristics and limitations should be assessed with the same rigour as the data acquisition components of the system.

4.2 Planar Imaging Performance

4.2.1 Introduction

Standard tests for the measurement of planar Anger camera performance have been produced by several international bodies; the National Electrical Manufacturers Association (NEMA) in the United States (Meuhllehner 1981) and the International Electrotechnical Commission (IEC) in Europe (Sano 1980).

The IEC protocol, unlike NEMA, uses tests which examine

camera performance in the presence of scattered photons and thus are of more relevance to the clinical situation. For this reason they were used as a basis for the assessment of cameras in routine use in the United Kingdom by the Department of Health and Social Security (DHSS), Elliott (1980), (1982), (1985), (1986).

A further set of tests has been proposed by the Hospital Physicists' Association (HPA), Horton (1978), which are more suitable for the routine quality control assessment of cameras in a hospital environment.

The tests for planar camera performance employed in this thesis are substantially the same as in the protocol developed by the DHSS group. The main reason for this was the fact that the inclusion of scattered photons makes these tests more relevant to the situation encountered in SPECT imaging. An additional consideration was that much of the equipment used by the DHSS group was available for use.

4.2.2 Energy Resolution

4.2.2.1 Introduction and Theory

The energy resolution of a system is determined by its ability to accurately identify the energy of detected events. The finite energy resolution of an Anger camera means that photopeak events cannot be completely separated from scattered photons. As a consequence of this the contrast present in the images produced by the camera will always be limited.

The limited energy resolution of the camera arises because of the small number of light photons which are produced for each photoelectric event in the crystal. An example of the

	Efficiency	No. of Particles
1. Conversion of 140keV photon into 3eV light photons	10%	4,200 photons
2. Light photons reach photocathode	30%	1,250 photons
3. Photo-electrons ejected	20%	255 electrons
4. Electrons reach first dynode	75%	185 electrons

Table 4.1 Example of the conversion of a 141keV photon. The above conversion assumes that the photon has interacted with the crystal by the photoelectric effect. The photopeak efficiency (i.e. the fraction of photons which interact by the photoelectric effect) of NAI(Tl) crystals is high for 140keV photons ; it is equal to 98%, 95% and 90% for crystals of thicknesses 2.54, 1.27 and 0.64 cm.

conversion of a 140keV photon into an electrical pulse in a PMT is shown in Table 4.1. As is illustrated only a few hundred electrons are produced in the conversion of the photon into a current pulse. Thus statistical fluctuations will result in variations in the heights of the voltage pulses produced by photons of the same energy.

The energy resolution can be quantified by expressing the FWHM of the photopeak distribution as a percentage of the photopeak energy.

4.2.2.2. Methods

In order to measure the energy resolution, special equipment in the form of a multi-channel analyser is required. In addition, for this particular camera design, the energy signal has to be taken from a specific point in the circuitry inside the camera head which requires the presence of a service engineer. Thus it was not possible to make direct measurements of the energy resolution on our system. However, measurements were made on a similar system at a different site by the DHSS evaluation team Elliott (1986). The value obtained from this was checked on our system by directly examining the spectrum of detected photons which can be displayed on the camera's persistence monitor.

4.2.2.3 Results

The value obtained for the energy resolution of the same model of camera was 10.1%. The value obtained on our camera by directly examining the displayed spectrum was consistent with this value.

4.2.3 Intrinsic resolution

4.2.3.1 Introduction and theory

The intrinsic resolution is a measure of the accuracy with which the position of a photon incident on the crystal face can be determined. It is limited by random statistical errors inherent in the detection process, by systematic errors in the positioning of events (spatial distortion) which are due mainly to the finite size of the PMTs, and by the finite thickness of the crystal and lightguide assembly.

The intrinsic resolution can be specified by the FWHM of the camera's LSF obtained without a collimator.

4.2.3.2 Methods

The intrinsic resolution was measured using the methods and equipment (including the computing system) described in the DHSS gamma camera performance assessment report, Elliott (1980). A slit transmission phantom was placed centrally on the camera face (collimator removed) and the area of the field of view outside the edge of the phantom was masked with lead sheeting. An uncollimated source containing approximately 500MBq of ^{99m}Tc was positioned vertically above the centre of the phantom at a distance of 2m. The orientation of the phantom was adjusted until its slit axis was aligned parallel to the electronic axis of the camera.

The choice between 1024*16 and 2048*16 matrices was made by a preliminary examination of the number of pixels within the full width at half maximum (FWHM) of the line spread function. Data were acquired until the counts in each pixel were greater than 10,000. By taking profiles across the lines

produced by the slits the FWHM and full width at tenth maximum (FWTM) were calculated.

4.2.3.3 Results

The intrinsic resolution of the camera was measured to be 4.05mm .

4.2.4 System Resolution

4.2.4.1 Introduction and Theory

The intrinsic resolution of the camera is measured using photons which have been collimated by slits in a lead shield. In the clinical situation this function is performed by a collimator which, for most applications, consists of a lead block containing many parallel holes. The resolution, in air, of the system as a whole will thus depend both on the intrinsic resolution and the influence of the structure of the collimator.

The effect which the collimator structure has on the transfer of photons through the complete imaging system can be determined from simple geometrical considerations, Anger (1964). If the resolution R_p is measured by the FWHM of the image of a point source a distance d from the collimator surface then from Sharp (1985 p23)

$$R_p = 2r (t_e + d + c) / t_e$$

where r = hole radius

c = distance of crystal from collimator

t_e = effective thickness of collimator after penetration has been accounted for, Maher (1957)

$t_e = t - (2/u)$ where t = hole thickness

u = linear attenuation coefficient for collimator

Thus, as a result of the geometrical properties of the collimator the resolution of the system will deteriorate with increasing source-camera distance.

The resolution of the system as a whole when measured in air can be determined, to a good approximation, from the intrinsic resolution and collimator geometry by assuming the PSFs are Gaussian

$$R_s = (R_p^2 + R_i^2)^{1/2}$$

To calculate the system resolution if there is a solid medium between the source and camera the presence of scattered photons must be taken into account. The inclusion of scattered photons within the energy discrimination window degrades the resolution of the system by incorporating falsely positioned events into the acquired data. Ehrhardt (1974) has shown that the effect of scatter can be denoted by an extra resolution component, R_{sc}

$$R_s = (R_p^2 + R_i^2 + R_{sc}^2)^{1/2}$$

The "resolution" of an imaging system is, in fact, a property which has no single, unique and rigorous definition. As a result of this there are several ways in which it can be assessed and described. In general terms resolution is usually

taken to represent a measure of an imaging systems ability to detect two closely spaced objects as separate entities. This leads to the simplest index of resolution, equivalent to the Rayleigh criterion in optics, which states that an imaging system will be able to resolve two objects if they are separated by more than the FWHM of the system's point spread function (PSF) or line spread function (LSF).

The FWHM provides information on the transfer of fine detail or high spatial frquencies by the imaging system. However, it is possible to assess the transfer of all spatial frequencies by using the modulation transfer function (MTF). The MTF is defined to be the normalised modulus of the Fourier transform of the system's line spread function and is a measure of the contrast transfer from object to image as a function of spatial frequency i.e. object size.

Both measurement methods have their advantages and disadvantages. The FWHM, because it is a single parameter serves as a succint index of the sizes of objects which it is reasonable to expect to discern. The MTF provides more general information on the behaviour of the imaging system over the whole range of spatial frequencies but it is difficult to analyse statistically or make quantitative measurements which utilise all of the information.

Thus, measurements of system resolution were made using both approaches. The FWHM was used to provide a summary of the variation of resolution with distance from the collimator in air and in scatter for the available collimators. The MTF was used to provide a detailed comparison of the performance of the different collimators over the full range of spatial frequencies. This is of particular importance when scatter is

present as this tends to have a larger effect on the transfer of lower spatial frequencies which will not be described by FWHM measurements.

4.2.4.2 Methods

A point source of linear dimensions $0.2 * 0.2 * 0.2$ cm was created by injecting a small volume of ^{99m}Tc into the tip of a 1ml syringe. The source was taken from a high specific activity solution of 800MBq in 1ml. The source was placed approximately in the centre of the camera's field of view and digital acquisitions were performed using the Nodecrest computer at a variety of collimator-source distances.

To create a large number of pixels within the PSF the gains of the ADCs were increased to their maximum values before the images were acquired. This produced pixels of edge length 0.0578cm.

To ensure good statistical accuracy high count images were obtained. The acquisition time was increased with source-collimator distance to ensure that the maximum count value in the peak of each study was at least 10,000 counts. This maintained the statistical accuracy as the PSF spread out.

In theory, the PSF should be a radially symmetric function so that it can be represented by a one dimensional profile taken through its centre. The data were analysed in this manner with the FWHM being calculated from the counts in a single row of pixels taken through the maximum point in the PSF. As a check on the radial symmetry of the PSF the analysis was performed along both the x and y axes. It is actually more common to use the FWHM of the LSF as an index of the resolution of an imaging system. The LSF data has the

advantage that it is slightly easier to analyse. However, it does not provide the two dimensional information obtained by measuring the PSF. Having measured the PSF, the LSF can in fact be obtained from it simply by integrating over one dimension :

$$\text{LSF}(x) = \int \text{PSF}(x,y) dy \quad (4.1)$$

The transfer in the other direction is more complex, Dainty (1980).

Using the same data the MTFs were also obtained for both collimators. To calculate the MTF's a Fast Fourier Transform (FFT) program was written using the Cooley-Tukey radix 2 algorithm, Dainty (1980).

4.2.4.3 Results for non-isotropic PSFs

The variation of the FWHM of the PSF with source-collimator distance for the LEAP collimator is shown in figure 4.1. A systematic difference between the FWHM values when measured along the electronic x and y axes of the camera was observed. The FWHM when measured in the y-direction was consistently greater than when measured in the x-direction. A similar phenomenon was observed with the HR collimator, figure 4.2, although in this case the FWHM values measured in the x-direction were consistently larger.

The non-isotropic nature of the PSF can be clearly observed in figure 4.3A and 4.3B where the images of a point source of ^{99m}Tc at a distance of 20cm from the camera face are shown. The most significant feature is the presence of a line of detected events which runs through the PSF's of the two

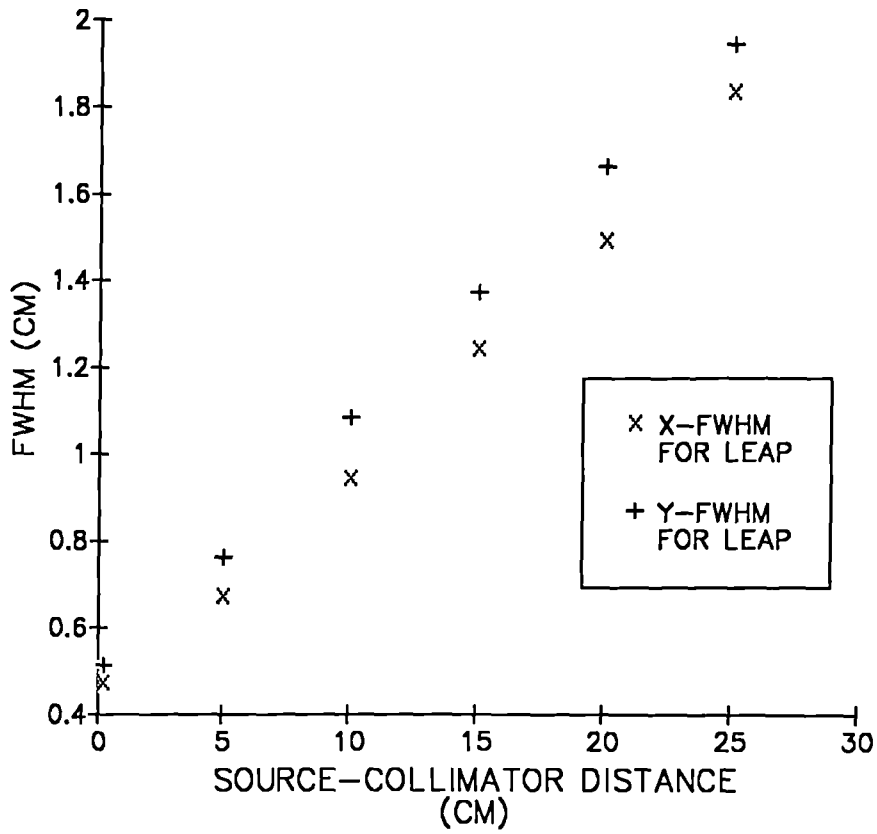


Figure 4.1 Variation of the FWHM of the PSF in the x and y directions with distance from the LEAP collimator.

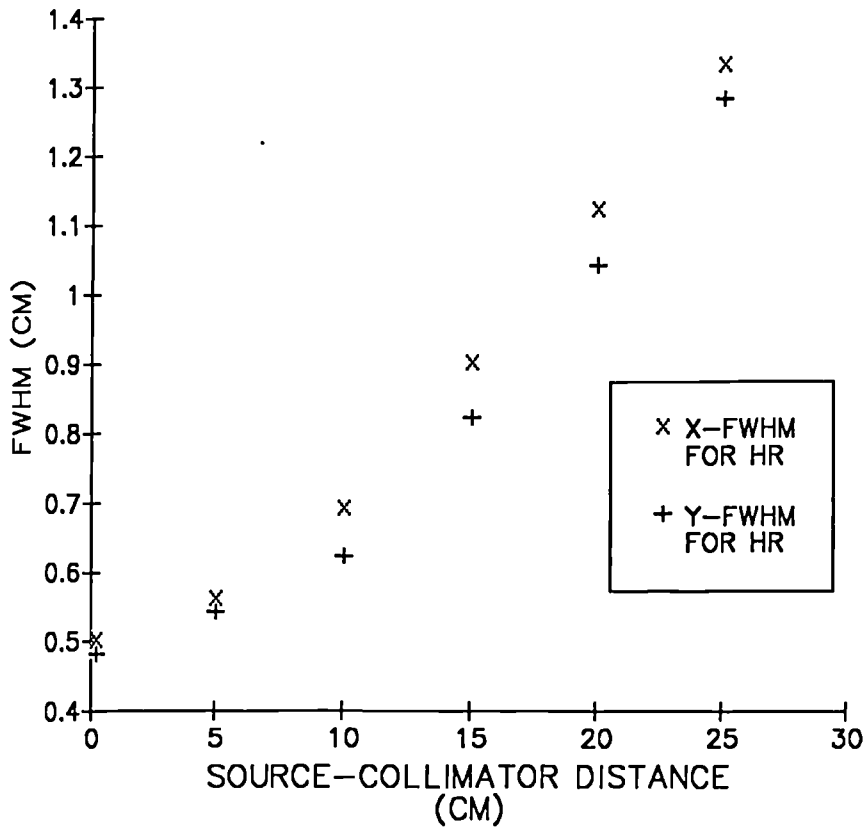


Figure 4.2 Variation of the FWHM of the PSF in the x and y directions with distance from the HR collimator.

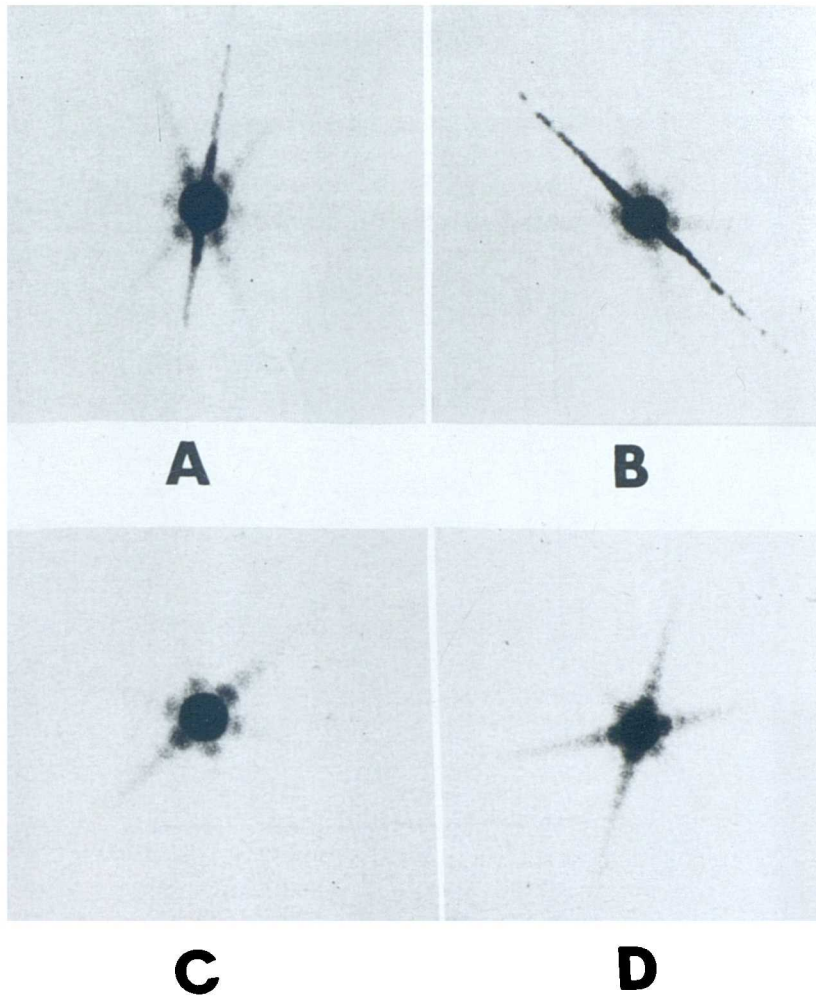


Figure 4.3 PSFs from : A - original LEAP collimator
B - original HR collimator
C - replacement LEAP collimator
D - replacement HR collimator

collimators. For the LEAP collimator this occurs at a small angle to the y-axis producing the observed increase in the FWHM along this direction. For the HR collimator the line is at an angle of 38 degrees to the x-axis which produces the observed increase in the FWHM along the x-axis and also explains why the differences between the results obtained along the two axes are not as large as for the LEAP collimator.

With the cooperation of the camera manufacturer it was identified that the above phenomena were produced by a combination of defects in both the design and manufacture of the collimators.

The collimators are constructed by affixing lead foil strips with glue to produce hexagonal holes (this explains the six point radial symmetry in the detected PSFs which can be observed if the previously described lines are ignored). If the construction process is less than perfect then gaps in the junction between the lead strips will allow photons to pass through the collimator preferentially in the direction of the strips. This produces the lines through the PSFs.

Redesign of the collimators and correction of errors in the manufacturing process have increased the homogeneity of the camera's response. Replacements for the substandard collimators were obtained and the FWHM values are shown in figures 4.4 and 4.5. A very close agreement is obtained for the HR collimator. However, there is still a difference in the FWHM values when measured along the x and y axes for the LEAP collimator. The two-dimensional structure of the PSFs for these collimators are shown in figure 4.3C and 4.3D. As can be seen the intense lines of detected events when ran through the

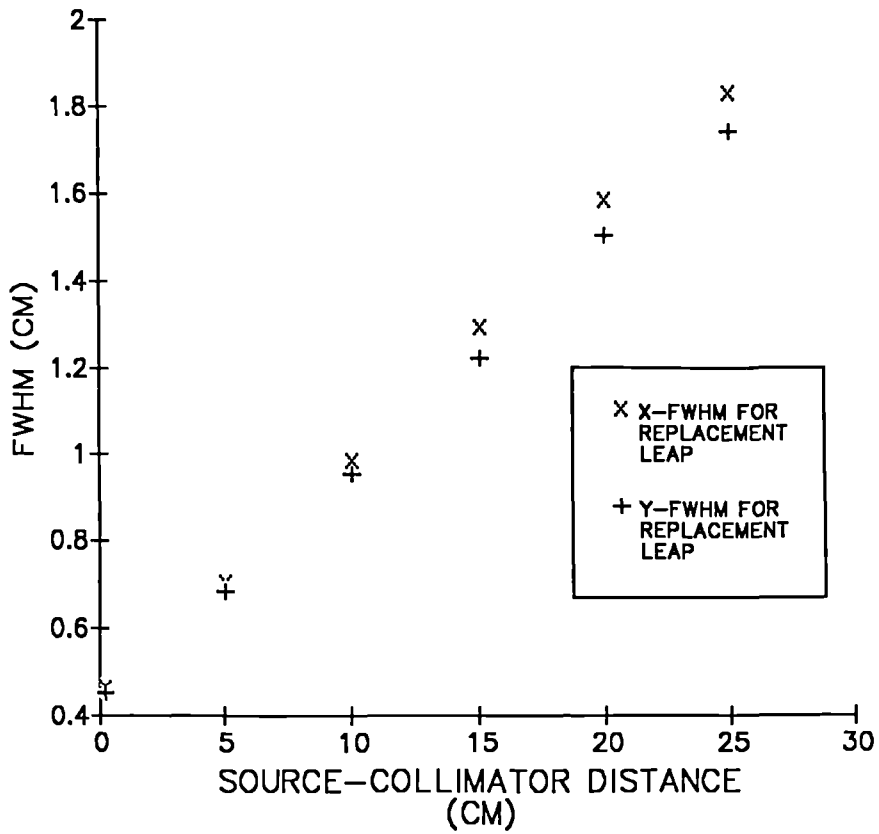


Figure 4.4 Variation of the FWHM of the PSF in the x and y directions with distance from the replacement LEAP collimator.

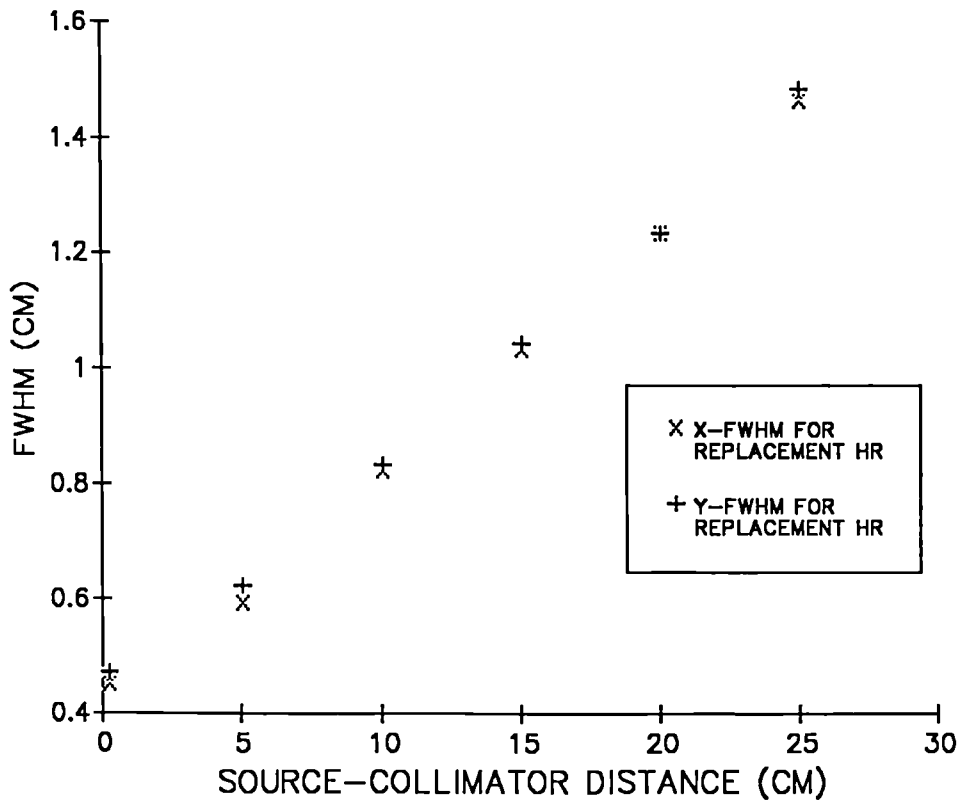


Figure 4.5 Variation of the FWHM of the PSF in the x and y directions with distance from the replacement HR collimator.

centres of the PSFs of the faulty collimators are now no longer observed. However, the hexagonal structure of the PSFs, which is a consequence of the hole shape is still observed. For the LEAP the orientation of the longer axis of the hexagon along the x-axis is the most likely explanation for the increase in the FWHM of the PSF when measured in this direction.

In general, the two-dimensional structure of the PSF is not usually examined as part of gamma camera quality control investigations. The most common method for the assessment of system resolution is through the measurement of the FWHM or the MTF of a line source. By using a point source important information on the directional nature of the camera's response is gained.

A full examination of the above results has been published separately, Gillen (1988).

4.2.4.4 Results for isotropic PSFs

The results in the remainder of this thesis refer to measurements made with the collimators used to replace those in which faults were identified.

The variation in resolution with source-collimator distance for the different collimators was examined. The FWHM of the LSF was chosen as the parameter to describe this variation as this is the parameter which is most commonly quoted. The LSFs were obtained from the PSFs by integrating the data along one axis as described by equation 4.1. For the HR collimator the FWHM values were independent of the axis used for integration. For the LEAP collimator the mean of the FWHM values obtained from the LSFs produced after integration

along the x and y axes was used. The results are shown in figure 4.6. The expected gain in resolution obtained through the use of the HR collimator can be assessed. For the HR collimator a linear regression produced a fit described by

$$\text{FWHM} = D \cdot (0.044 \pm 0.002) + (0.389 \pm 0.031)$$

where D is the source-collimator distance and all measurements are in units of cm. The correlation coefficient was 0.996.

Similarly, for the LEAP collimator we get

$$\text{FWHM} = D \cdot (0.0596 \pm 0.001) + (0.418 \pm 0.021)$$

with a correlation coefficient of 0.999.

The price which has to be paid for the increased resolution obtained with the HR collimator is a loss of sensitivity, the magnitude of which will be examined in section 4.2.7.

Information on the width of the tails of the LSFs can be obtained by calculating the full width at tenth maximum (FWTM) values. This parameter is more descriptive of the loss of image contrast produced by the spreading out of the LSF than as an index of resolution. The results are shown in figure 4.7.

A linear regression of the results for the HR collimator gave

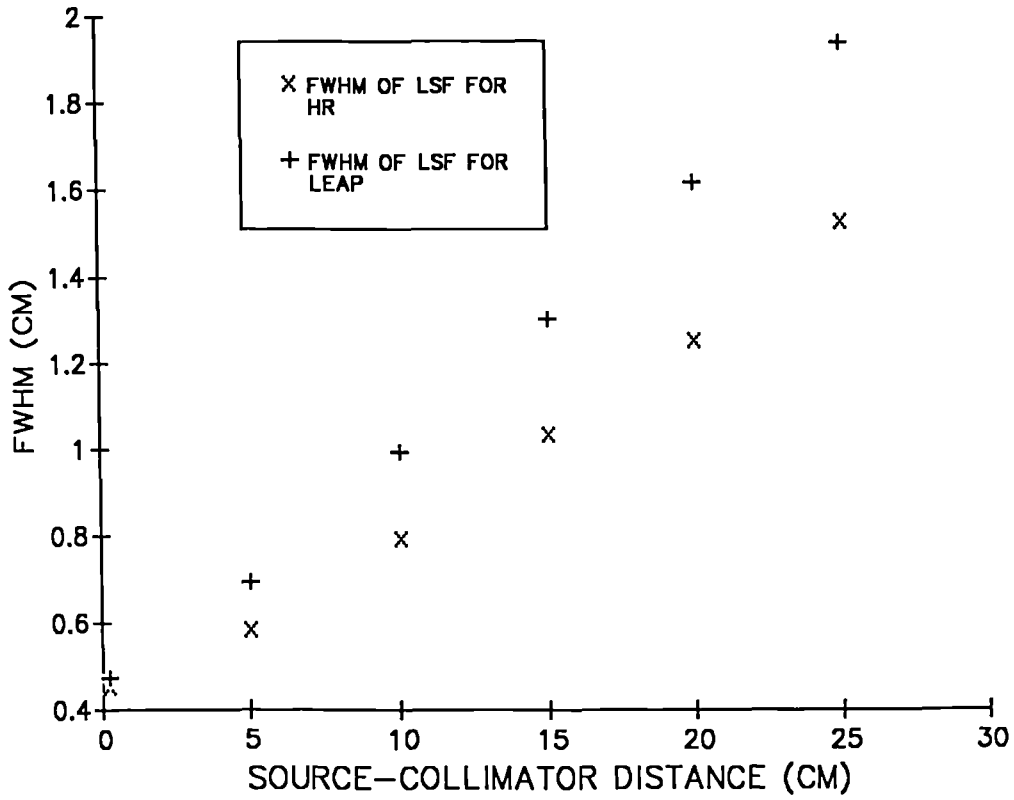


Figure 4.6 Variation of the FWHM of the LSF with distance from the LEAP and HR collimators.

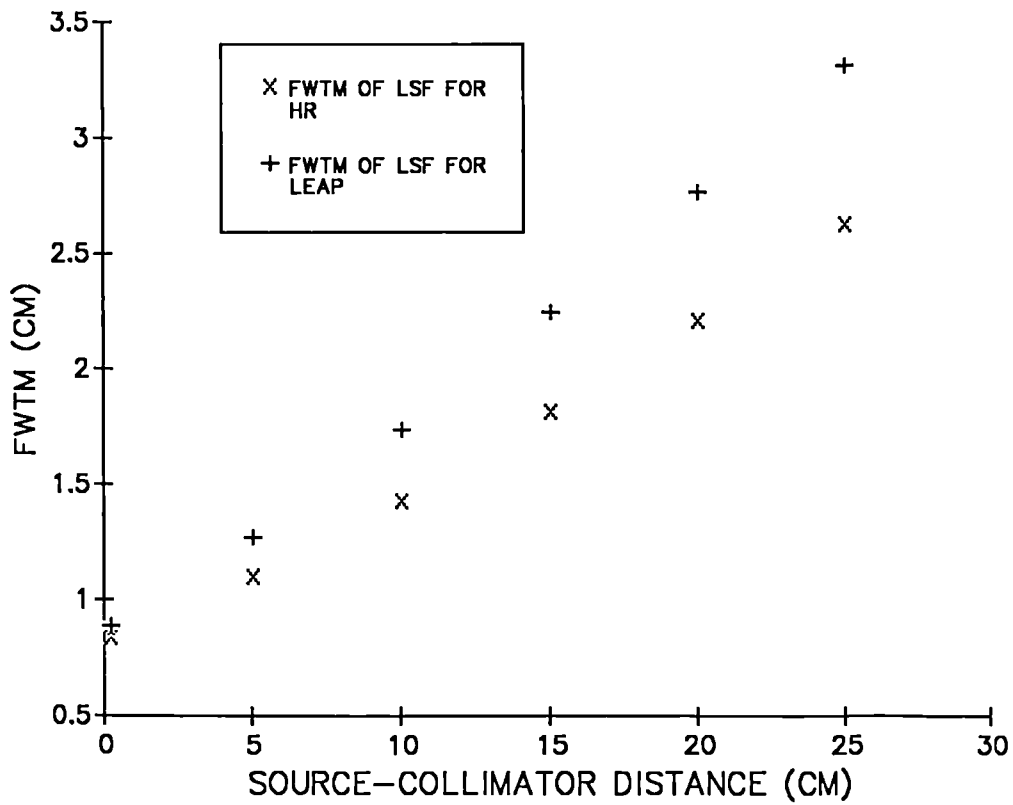


Figure 4.7 Variation of the FWTM of the LSF with distance from the LEAP and HR collimators.

$$\text{FWTM} = D. (0.0728 \pm 0.003) + (0.749 \pm 0.0395)$$

with a correlation coefficient of 0.997.

Similarly, for the LEAP collimator

$$\text{FWTM} = D. (0.099 \pm 0.002) + (0.793 \pm 0.038)$$

with a correlation coefficient of 0.999.

All of the previous results were obtained in air, i.e. without a scattering medium between the source and camera. Thus, to gain information of more direct relevance to the clinical situation the PSFs were measured with perspex sheets interposed between the camera and the source. A comparison of the FWHM values of the LSFs when measured in air and at different depths of perspex for the HR collimator is shown in figure 4.8. In scatter the linear regression gives

$$\text{FWHM} = D . (0.053 \pm 0.002) + (0.43 \pm 0.02)$$

with a correlation coefficient of 0.999.

A comparison of the FWHM of the LSFs when measured in air and at different depths of perspex for the LEAP collimator is shown in figure 4.9. For the scatter values a linear regression gives

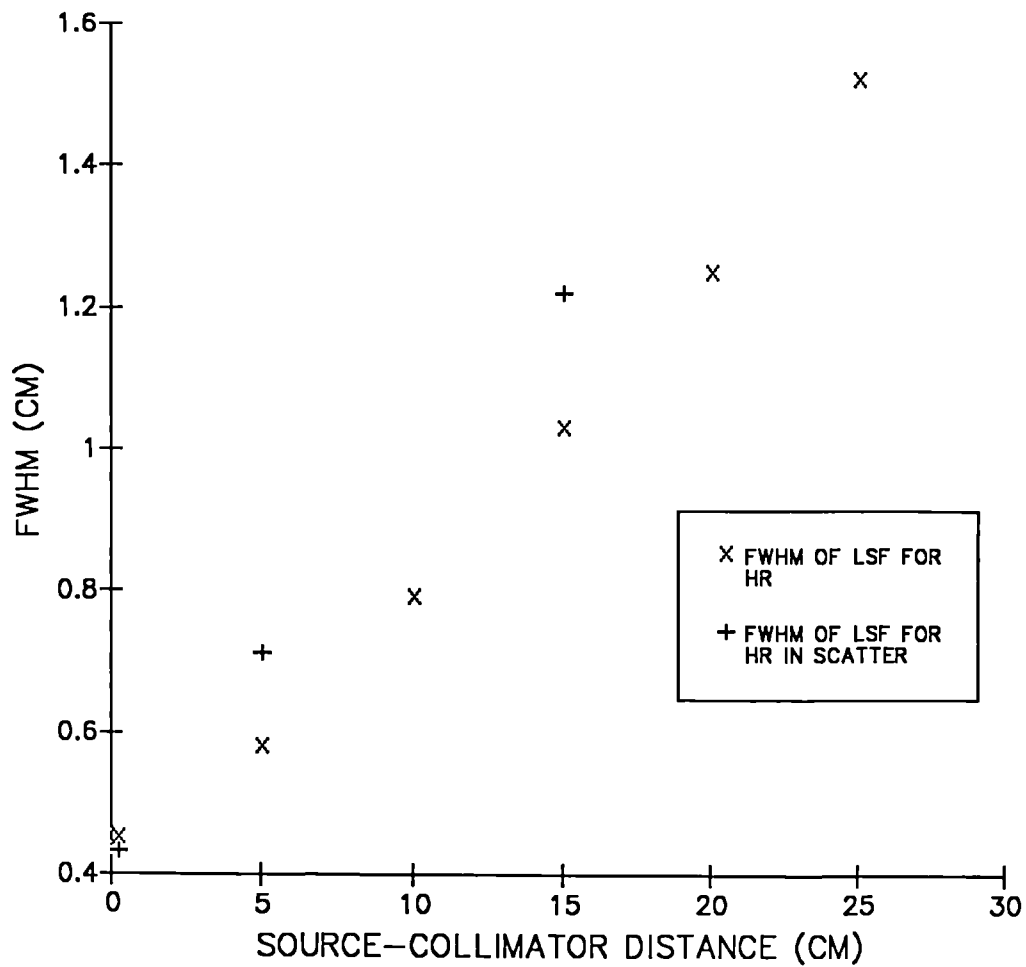


Figure 4.8 Variation of the FWHM of the LSF with distance in air and in perspex from the HR collimator.

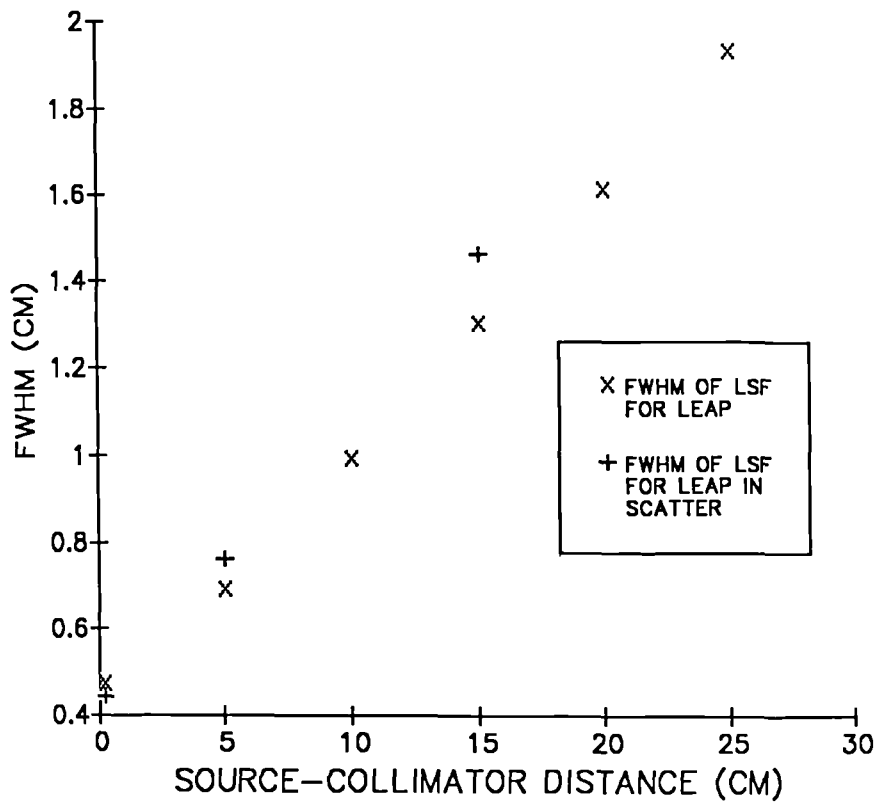


Figure 4.9 Variation of the FWHM of the LSF with distance in air and in perspex from the LEAP collimator.

$$\text{FWHM} = D \cdot (0.069 \pm 0.001) + (0.42 \pm 0.01)$$

with a correlation coefficient of 0.999.

The introduction of the scattering material increases the gradient of the linear regression line for the HR collimator by 21%. For the LEAP collimator this figure is 16% indicating that the resolution difference between the two collimators is not as great as in air because of the finite energy resolution of the camera and the increased flux of scattered photons produced by the solid medium. A direct comparison of the FWHM values of the LSFs in scatter for both collimators is given in figure 4.10.

As was discussed previously the FWHM does not give a full description of the image transfer characteristics of the system. To do this we have to use the MTFs.

4.2.4.5 Modulation Transfer Functions

The MTFs have been calculated using the methods described in Section 4.2.4.2 using the same PSF data as in Section 4.2.4.3. The LSFs were obtained from the PSFs by summing the data in the PSFs along one axis.

The results for the HR collimator are shown in figure 4.11 for source collimator distances, D , of 0cm, 5cm, 10cm, 15cm, 20cm and 25cm. The measurements were made in air. As expected from the FWHM results the ability of the imaging system to transfer high spatial frequencies is reduced as the source-camera distance increases. The MTF data however shows that there is also a reduction in the amplitude with which all spatial frequencies are transferred. Similar results are shown

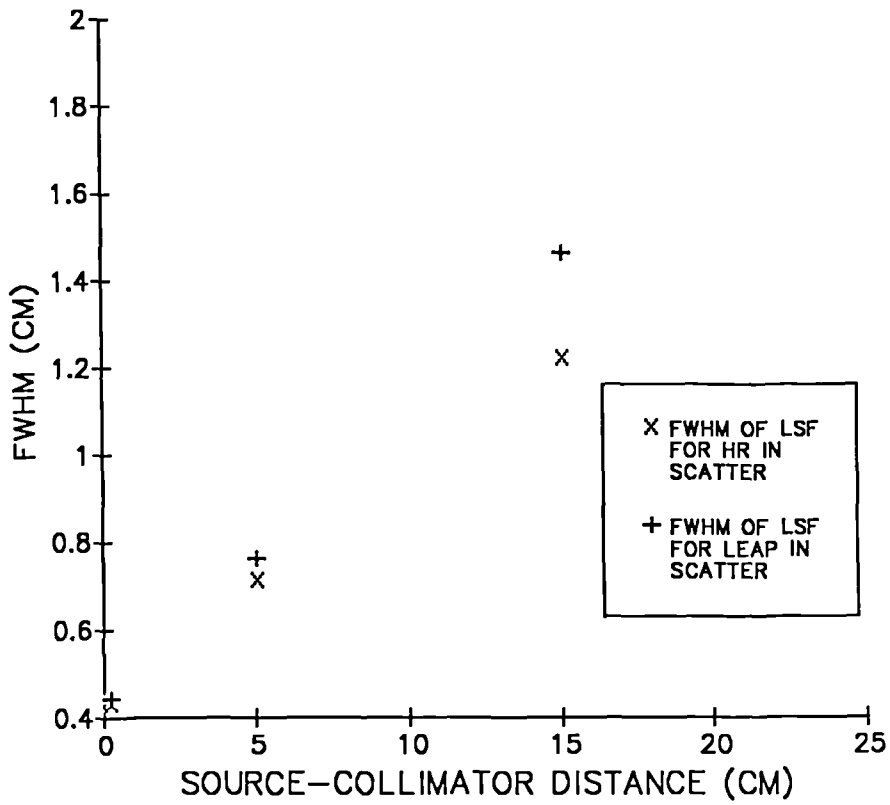


Figure 4.10 Variation of the FWHM of the LSF with distance in perspex from the HR and LEAP collimators.

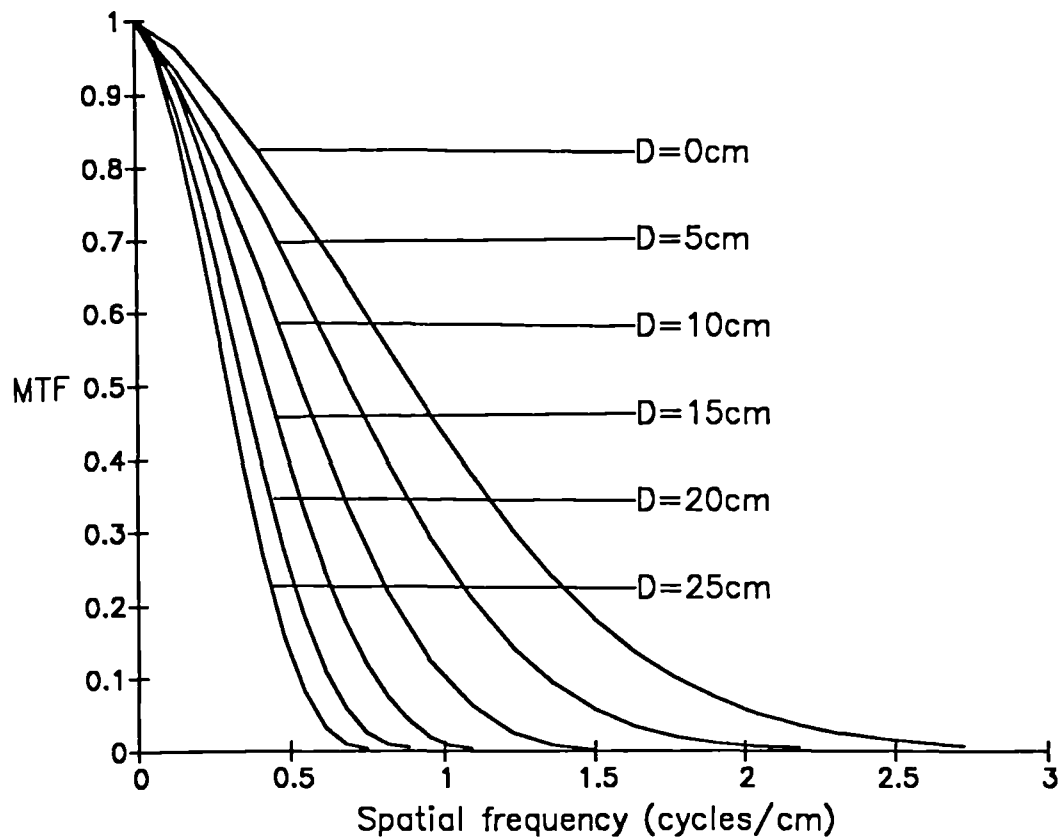


Figure 4.11 MTFs for the HR collimator obtained at distances, in air, of 0cm, 5cm, 10cm, 15cm, 20cm and 25cm.

for the LEAP collimator in figure 4.12.

A comparison of the MTFs for the LEAP and HR collimators for a selection of source-collimator distances is shown in figure 4.13. The enhanced transfer of all spatial frequencies obtained from the use of the HR collimator is clearly demonstrated. In addition, for any particular spatial frequency, the proportional increase in the MTF value obtained from the use of the HR collimator increases with the source-collimator distance.

The MTFs were also calculated for the PSF data obtained with a scattering medium interposed between the source and the collimator as described in Section 4.2.4.2.

In figure 4.14 the results are shown for the HR collimator for values of D equal to 0cm, 5cm and 15cm. As with the results in air the amplitude with which all spatial frequencies were transferred was reduced with increasing values of D .

A comparison of the MTFs obtained with the HR collimator in air and with scatter is shown in figure 4.15. The most obvious effect is the disproportionate reduction in the amplitude of the lower spatial frequencies produced by the inclusion of scatter.

Similarly, the MTFs for the LEAP collimator in scatter for values of D equal to 0cm, 5cm and 15cm are shown in figure 4.16. Again when a comparison was made with the MTFs obtained in air there was a disproportionate reduction in the amplitude of the lower spatial frequencies, figure 4.17.

The reason for this effect can be determined by examining the form of the LSFs. Figure 4.18 shows the LSF for the HR collimator at D equal to 15cm in air. This can be compared

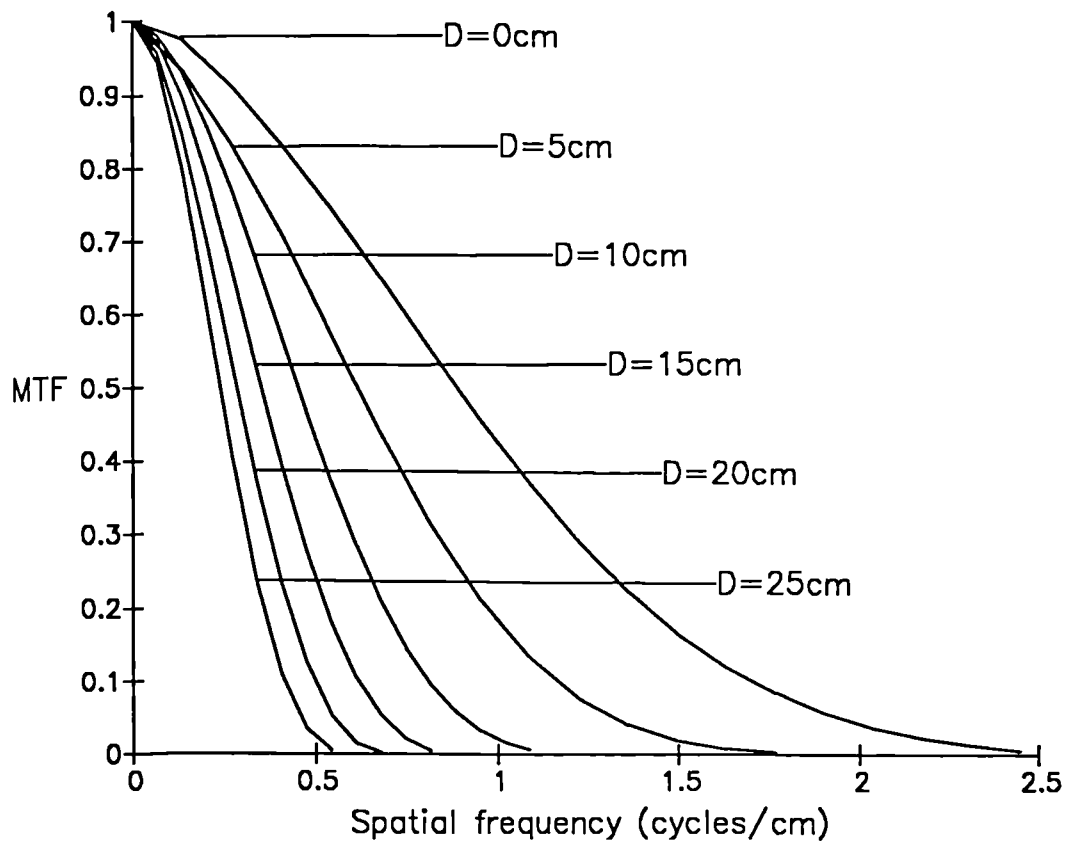


Figure 4.12 MTFs for the LEAP collimator obtained at distances, in air, of 0cm, 5cm, 10cm, 15cm, 20cm and 25cm.

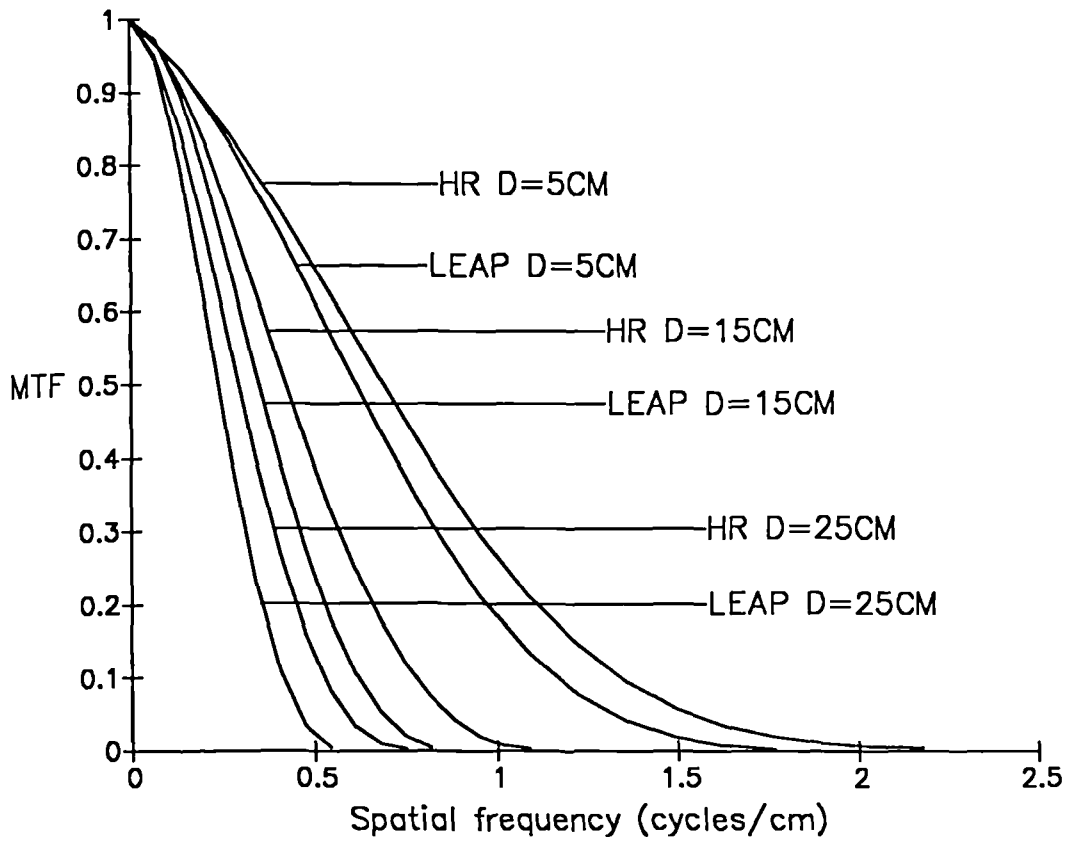


Figure 4.13 Comparison of MTFs for HR and LEAP collimators obtained at distances, in air, of 5cm, 15cm and 25cm.

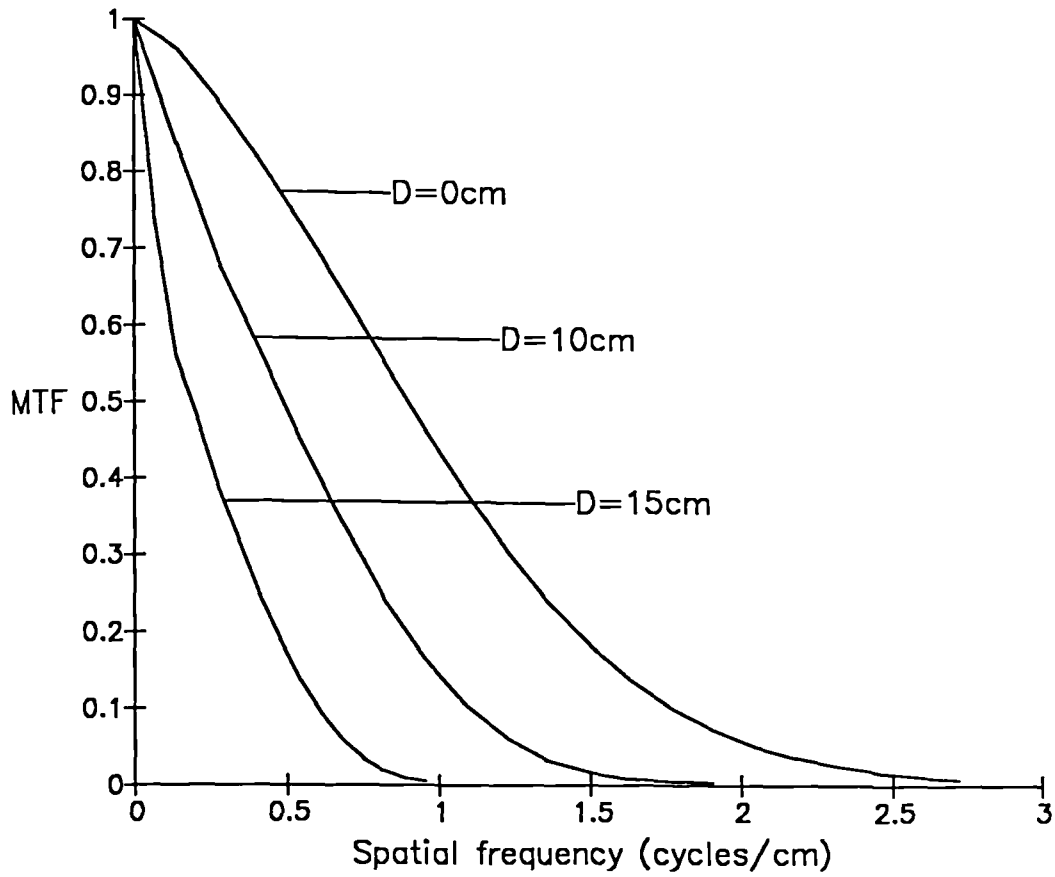


Figure 4.14 MTFs for the HR collimator obtained at distances, in perspex, of 0cm, 5cm and 15cm.

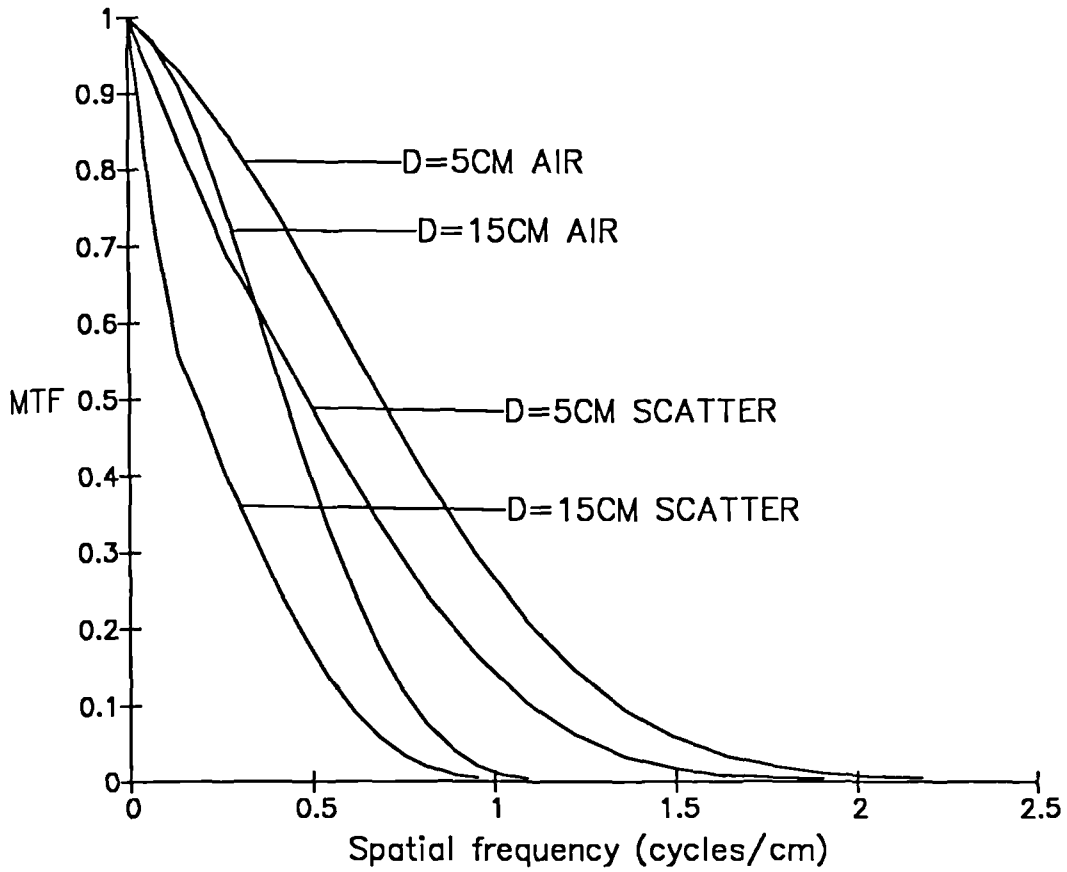


Figure 4.15 Comparison of MTFs for HR collimator obtained at distances, in air and perspex, of 5cm and 15cm.

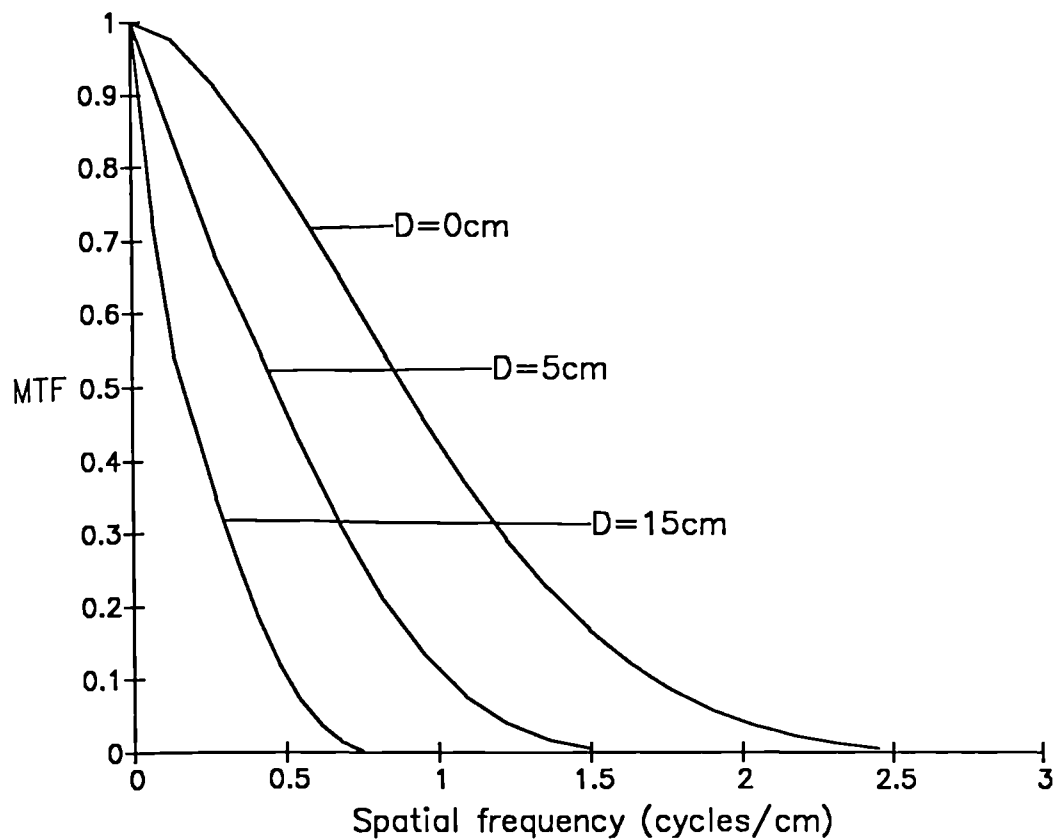


Figure 4.16 MTFs for the LEAP collimator obtained at distances, in perspex, of 0cm, 5cm and 15cm.

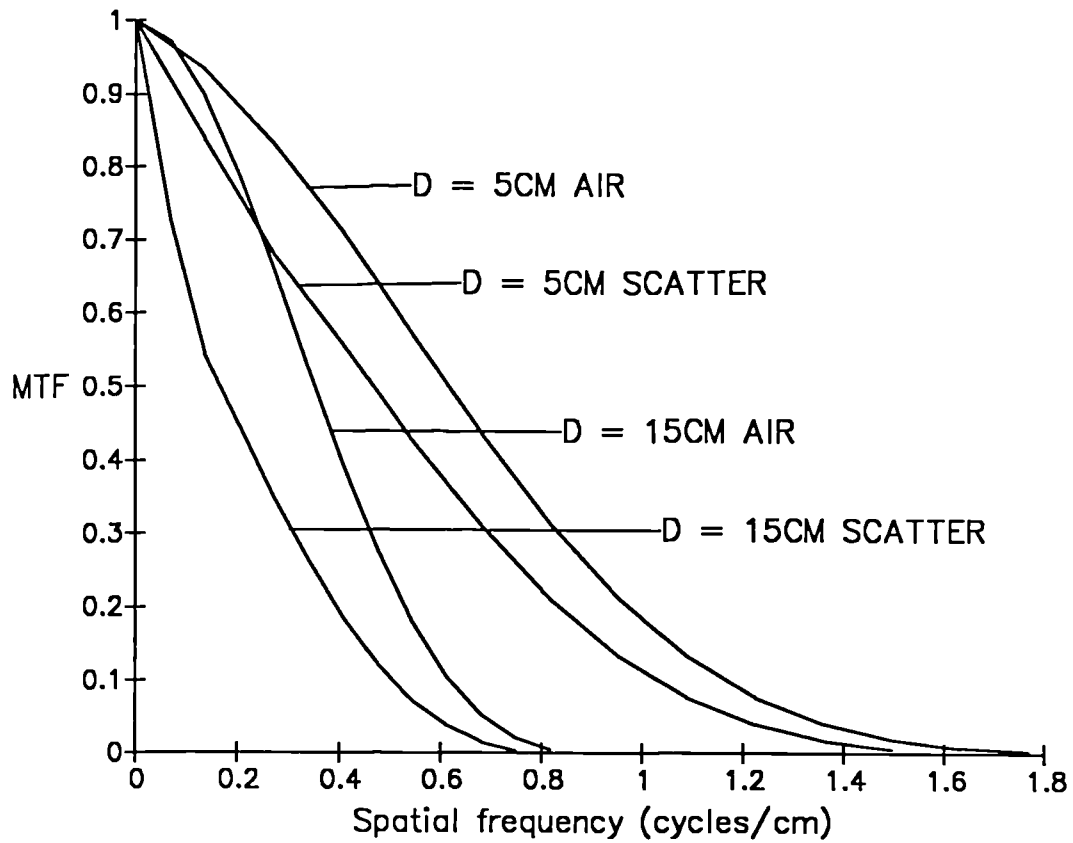


Figure 4.17 Comparison of MTFs for LEAP collimator obtained at distances, in air and perspex, of 5cm and 15cm.

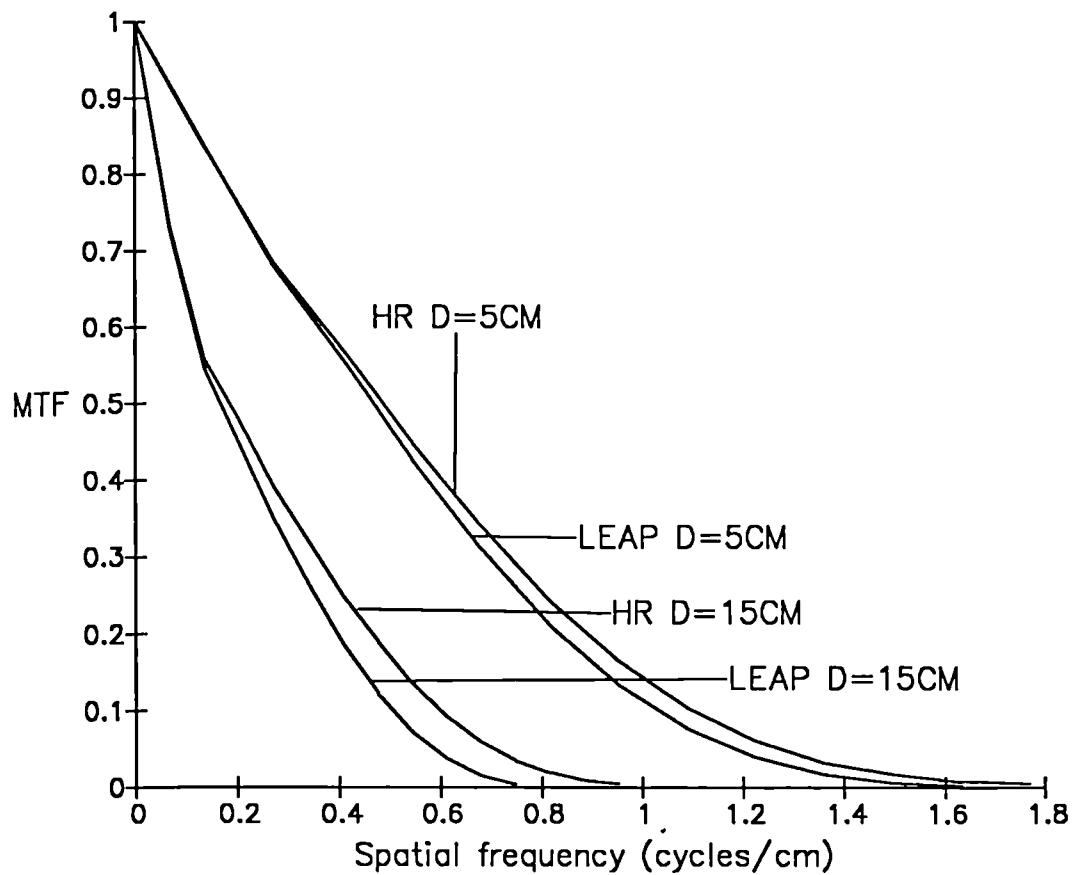


Figure 4.10 Comparison of MTFs for HR and LEAP collimators obtained at distances, in perspex, of 5cm and 15cm.

with the LSF at D equal to 15cm in scatter, figure 4.19. The 'tail' present in the scatter LSF is responsible for the reduced amplitude with which lower spatial frequencies, in particular, are transferred by the imaging system (Note also the slight asymmetry in the LSF shown in figure 4.19 which results from some residual non-isotropism in the PSF which was described previously).

Finally, figure 4.20 shows a comparison of the MTFs in scatter for the LEAP and HR collimators. It is notable that the differences in the responses of the two collimators are less marked than in air. This is particularly true for the lower spatial frequencies where there would appear to be no advantage to be gained by using the HR over the LEAP collimator. This would suggest that the imaging performance of the system at low spatial frequencies is limited by the energy resolution of the detection process.

4.2.5 Uniformity

4.2.5.1 Introduction and theory

The origin of and correction for the inherently non-uniform response of an Anger camera to a uniform flux of photons is described in detail in Chapter 3.

The uniformity of response of the gamma camera over its FOV is one of the most critical parameters for the production of high quality SPECT images. Any non-uniformity is amplified by the reconstruction process to produce artefacts in the axial sections. The artefacts can appear as hot or cold spots in the centre of the sections or as concentric hot and cold rings.

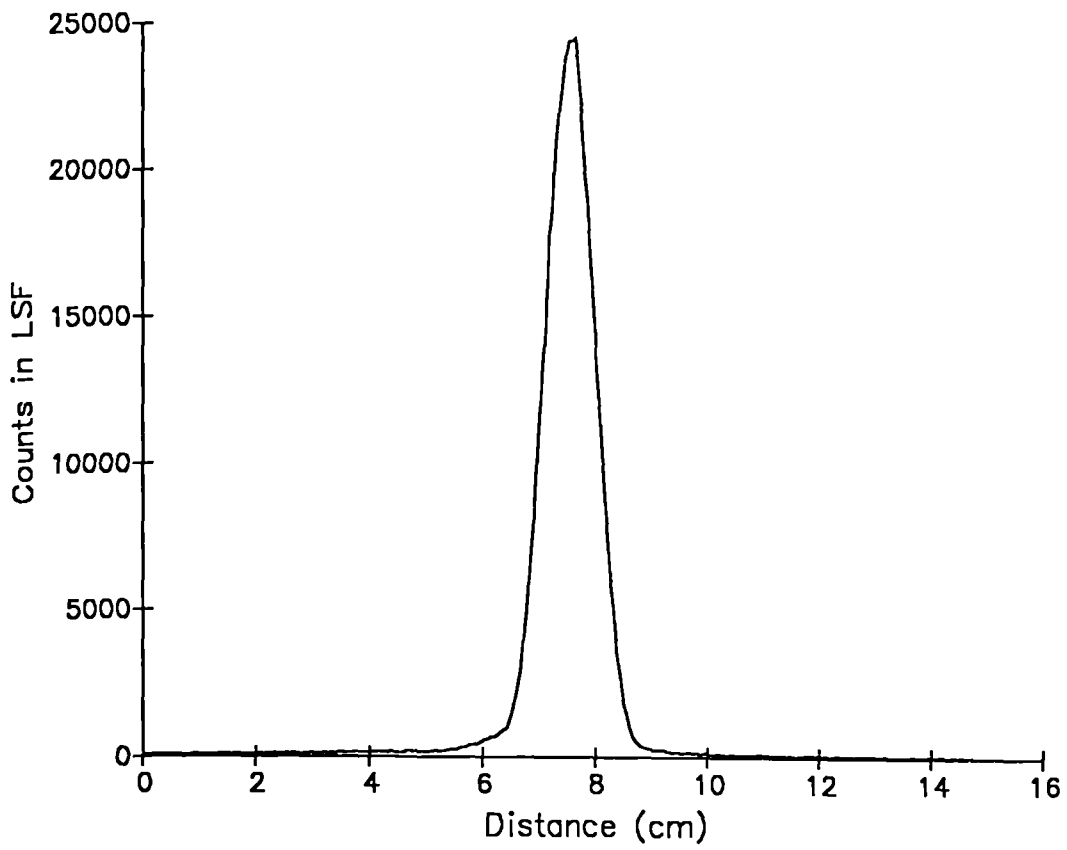


Figure 4.18 LSF for HR collimator obtained at a distance, in air, of 15cm.

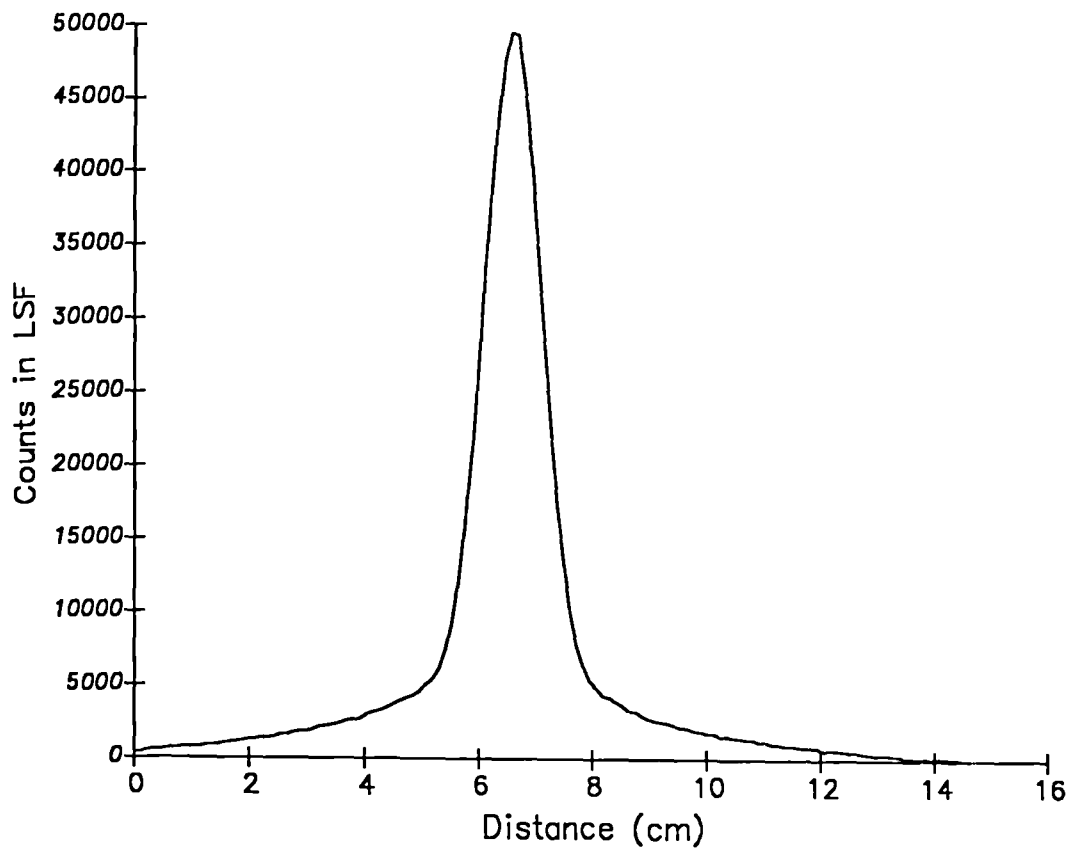


Figure 4.19 LSF for HR collimator obtained at a distance, in scatter, of 15cm.

The severity of the problem was illustrated by Rogers (1982) who showed that a 2% non-uniformity in planar imaging was amplified by the reconstruction process to produce a 15% non-uniformity in the SPECT image.

The amplification depends inversely on the square root of the defect's distance from the centre of rotation and directly on the diameter of the source distribution being imaged Shepp (1977). Thus non-uniformities close to the centre of the camera's field of view are particularly important .

4.2.5.2 Methods

The uniformity of the camera was assessed using the flood source described in Chapter 3. As a general quality control procedure measurements were made on a weekly basis. Any deterioration in uniformity was detected at an early stage and the camera serviced to resolve the problem. Thus the camera was kept in a state of near optimal performance at all times.

Before any uniformity measurement was made the camera was peaked with the collimator off using a scatter free point source of ^{99m}Tc to ensure accurate and reproducible energy window selection. A 15% energy window placed symmetrically over the photopeak was used and thirty million counts collected into a 256*256 matrix. For analysis the matrix was binned to size 64*64 to give a statistical error in each pixel of less than 1%. The collection of the data in the larger matrix size was found to be of use for the assessment of the linearity of the low significance bits of the ADC's. Care was taken to position the camera face in the centre of the flood source. The source was generally filled early in the morning and rotated at various intervals throughout the day to ensure

adequate mixing of the isotope throughout the source volume. When the data acquisition was performed in the evening no problems with poor mixing were encountered.

The countrate during acquisition was always less than 5000 counts per second.

The images were analysed by defining a region of interest in a similar manner to that used for the HPA's useful field of view (UFOV). This is taken to be equal to 90% of the geometrical field of view (GFOV) as defined by NEMA.

The data were analysed to produce values for ;

N = mean pixel counts

SD = standard deviation of pixel counts

CV = coefficient of variation of pixel counts

U+,U- = integral non-uniformity

UD = differential uniformity

5%,10%,15% = values of the percentage of pixels whose counts are within 5,10 and 15% of the mean.

These parameters were calculated as follows ;

$$CV = SD/N$$

$$U+ = (C_{max}-N)/N \quad \text{where } C_{max} = \text{maximum pixel count}$$

$$U- = (C_{min}-N)/N \quad \text{where } C_{min} = \text{minimum pixel count}$$

$UD = (C1 - C2) / C1$ where C1, C2 are the counts in adjacent pixels.

4.2.5.3 Results

The values obtained for the above parameters over a typical four month period are shown in Table 4.2.

Allowing for slight differences in the definition of the portion of the field of view to be analysed a comparison of these results with those obtained on other modern gamma camera systems by Elliott (1986) using similar measurement techniques would indicate that the uniformity of this camera was excellent .

4.2.6 Countrate linearity response

4.2.6.1 Introduction

The countrate response of a gamma camera is linear over a limited range of incident photon fluxes. Data loss and distortion are caused both by the response of the scintillation crystal and by the camera electronics. A scintillation in a NaI(Tl) crystal has a decay time constant of about 0.2 microseconds and about 0.8 microseconds is required for maximum light collection, Anger (1958). At high countrates there is an increasing probability that two events will occur within this time and consequently signals will overlap. If these pile up pulses result from low energy events the recorded energy may occur within the energy discrimination window causing spatial distortion. Thus it is important for SPECT imaging that the linear part of the count rate response be assessed and the camera only operated within this range.

In addition to crystal response the electronic signal

WEEK	N	SD	15%	10%	5%	CV	U+	U-	UD
1	12995	213.4	100	99.9	99.2	1.6	5.7	6.1	7.3
2	13145	210.1	100	100	99.2%	1.6	8.0	5.6	6.3
3	13075	228.4	100	99.9	98.5	1.7	9.0	11.6	14.8
4	13157	240.1	100	100	98.8	1.8	6.3	5.2	8.8
5	13152	206.4	100	100	99.4	1.6	8.4	6.1	6.1
6	12928	198.4	100	100	99.5	1.5	6.6	5.7	6.8
7	12941	201.1	100	100	99.5	1.6	6.2	14.9	17.7
8	13140	213.5	100	100	98.7	1.6	6.7	7.1	9.1
9	13143	187.0	100	100	99.7	1.4	5.5	6.1	6.7
10	12992	238.0	100	100	98.0	1.8	7.0	6.5	6.8
11	13101	231.5	100	100	99.0	1.8	6.3	8.2	11.9
12	13107	220.3	100	100	99.3	1.7	6.8	6.6	6.9
13	11142	191.0	100	100	98.8	1.7	7.5	6.0	7.4
14	11154	188.6	100	100	99.1	1.7	6.8	12.6	13.6
15	11175	201.6	100	100	98.6	1.8	7.6	7.7	8.2
16	11177	222.3	100	100	97.9	2.0	8.3	8.1	8.2

Table 4.2 Results of the flood field uniformity measurements made over a sixteen week period. A definition of the parameters and a description of the way in which they were calculated is given in the text.

processing time also limits performance. This is particularly so for cameras which employ electronic energy and spatial linearity correction techniques ; the greater the processing the poorer the countrate response, Sharp (1985 pp74-77). In fact a high countrate option is available with the camera which disables some of the correction circuitry to speed signal processing. This may be useful for first pass studies but the distortion of both positional and energy information makes it inappropriate for SPECT.

4.2.6.2 Methods

To measure the countrate performance known increments of activity were placed into the active volume of the cylindrical phantom shown in figure 4.21 which was placed directly on the LEAP collimator surface.

The observed countrate and the time elapsed from the beginning of the test were recorded for each increment in source activity until the countrate reached around 30,000 counts per second. This is well above the maximum count rate encountered in SPECT imaging.

The background counts were assessed with the phantom on the camera face prior to the addition of any activity and the time required to acquire 100,000 counts was noted on both the camera scalar and the Nodecrest computer using a 64*64 image matrix.

4.2.6.3 Results

A plot of net countrate recorded by the computer against activity volume is shown in figure 4.22. There was no significant difference between the results recorded on the

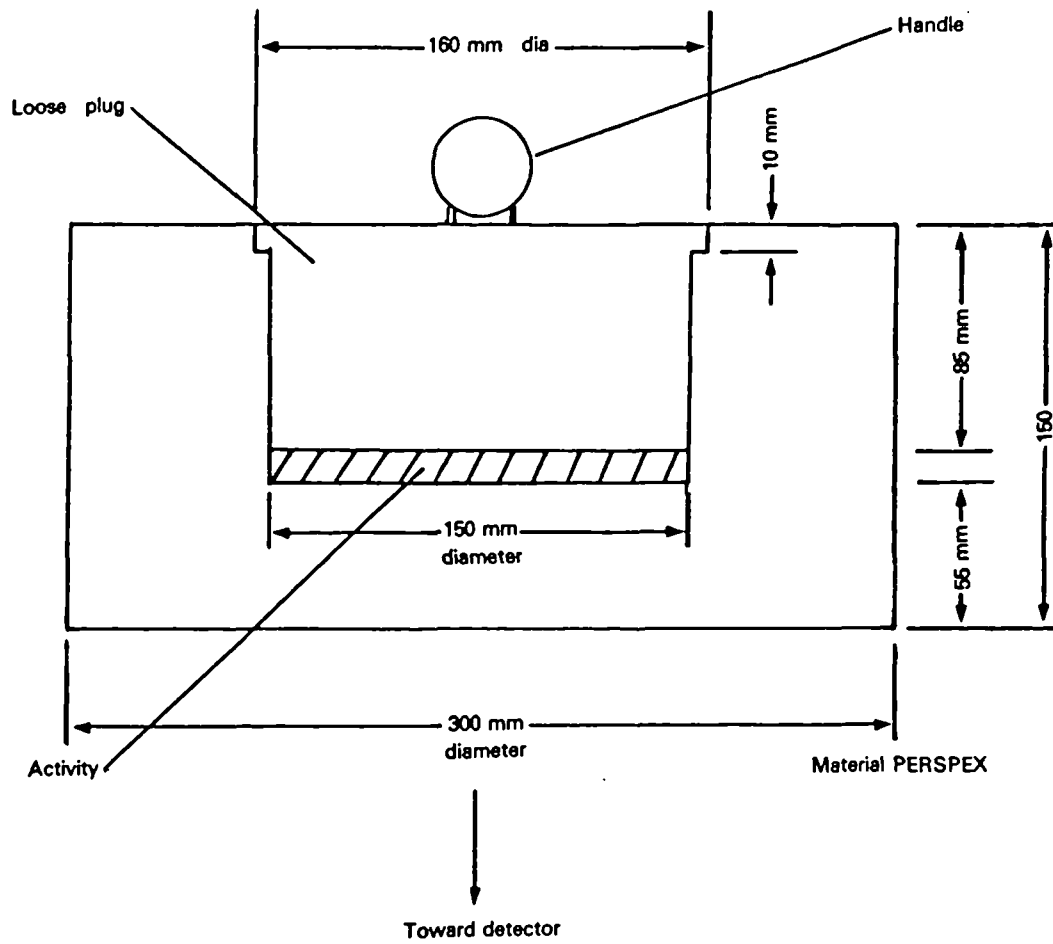


Figure 4.21 Source for measurement of count-rate capability.

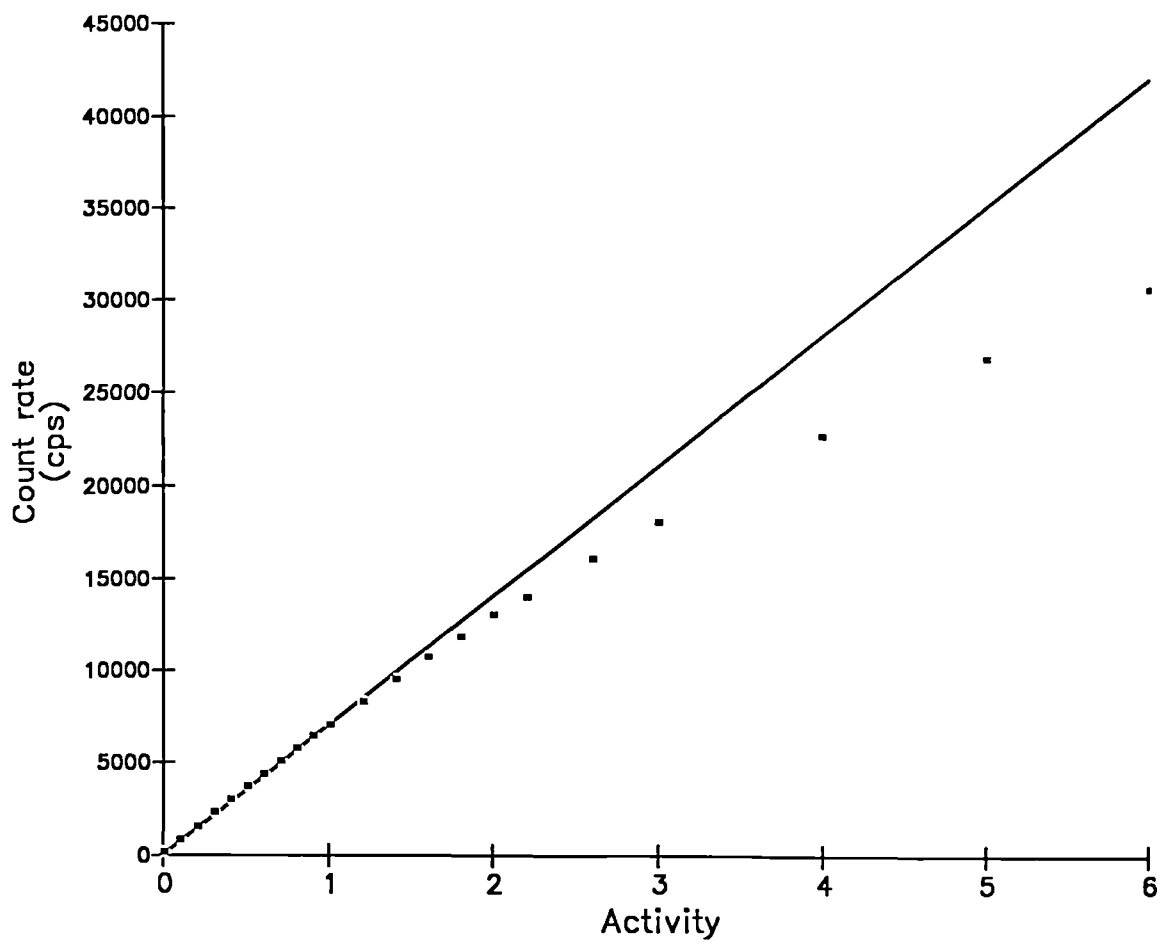


Figure 4.22 Comparison of the observed count-rate (dots) with that predicted from a linear extrapolation from the low count rate values (solid line).

camera and the computer. A linear regression was performed using the first eight points which were assumed to be in the linear portion of the countrate response, the observed countrate being less than 5,500 counts per second. This gave a good straight line fit with a correlation coefficient of 0.9999. The expected countrates were predicted from the linear regression and compared with the observed values to determine the count rate losses. The differences between the observed countrates and the countrates expected from the linear regression are shown in figure 4.23.

5%, 10% and 20% countrate losses occurred with observed countrates of around 9000, 14000 and 22000 counts per second respectively.

4.2.6.4 Conclusions

Due to the limited sensitivity of the camera and the restrictions on the amount of activity which can be injected into the patient, countrates above 7,000 counts per second are unusual in clinical studies. Thus countrate non-linearities are unlikely to affect clinical studies.

For phantom experiments, however, high count density studies are often required and there are no limitations on the activity concentration. In practice an upper limit of 9,000 counts per second corresponding to a countrate loss of 5% is suggested. Above this value significant quantitative errors will occur in addition to the production of artefacts due to inconsistent projection data.

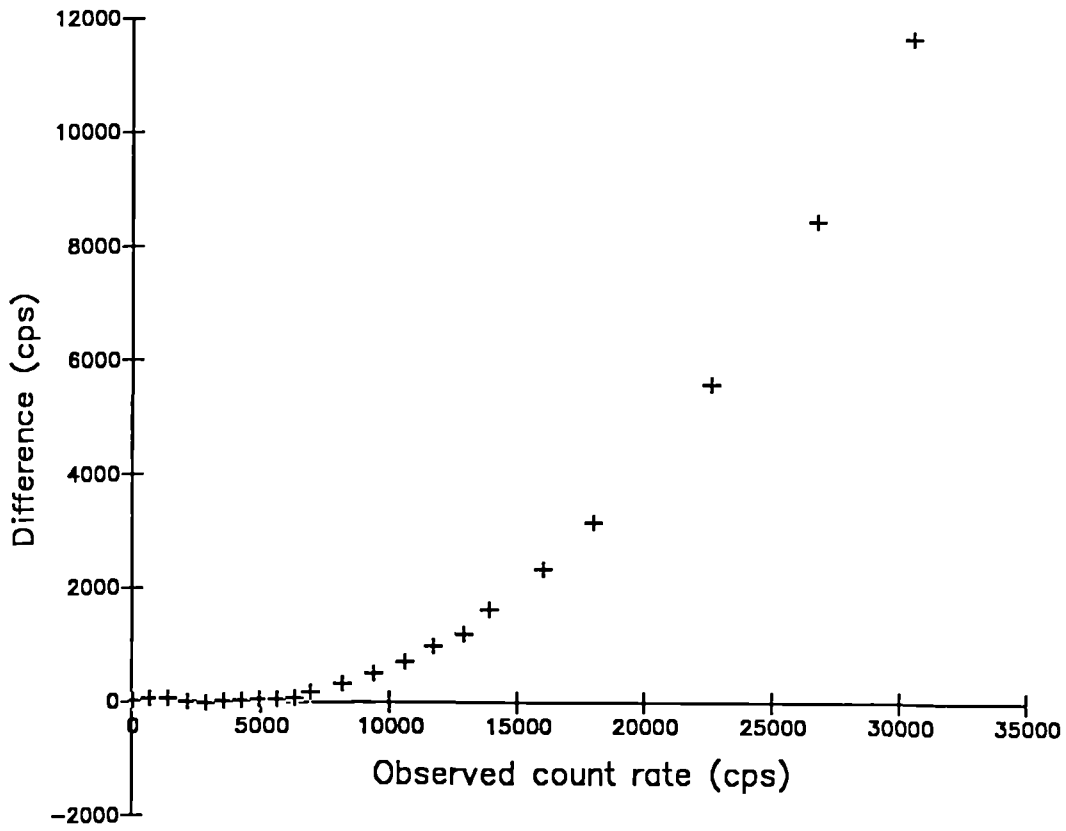


Figure 4.23 Difference between the observed count-rate and that predicted from a linear extrapolation from the low count-rate values.

4.2.7 Sensitivity

4.2.7.1 Introduction

The sensitivity of a gamma camera is a measure of the fraction of incident photons used to form the image. This will depend not only on the geometrical efficiency of the collimators and the sensitivity of the crystal-PMT assembly but also on the shape of the spectrum of the incident photons and the position and width of the energy discrimination window. Thus the sensitivity of any individual camera will depend both on the collimator used and the scatter fraction of the radiation emitted from the source.

The plane sensitivity of the system can be measured by uniformly irradiating the camera FOV. In practice this is performed by measuring the countrate obtained from a plane source of activity larger than the FOV.

An alternative measurement is the point source sensitivity which has the advantage that because the source can be small the scatter fraction can be strictly limited. A disadvantage of this measurement is that the response of the camera is not completely uniform so that a number of measurements have to be made at different positions across the FOV to provide a mean value. (For this measurement NEMA uses a 10cm plane source positioned at the centre of the FOV while HPA recommends a square source of side length 10cm. IEC measurements attempt to include scatter by using a 10cm diameter cylinder surrounded by several cm of perspex.)

4.2.7.2 Methods

The plane sensitivity was measured routinely as part of an

ongoing quality assurance program. The source used was the same as that used to make the camera uniformity measurements, Section 4.2.5. In fact the plane sensitivity measurements were made alongside the uniformity measurements and so were performed at frequent intervals. As described previously the use of an extended source distribution will mean the inclusion of scattered photons within the detected signal. Thus before each measurement the camera was accurately peaked using a scatter free source and the DIGITRAC tune calibration function enabled ensuring that the system was optimally tuned. The liquid filled phantom was injected with an activity chosen to be approximately equal to 150MBq at the time of counting. The exact dose used for any given measurement was determined by measuring the activity in the syringe used to deliver the dose to the phantom before and after injection. The phantom was mixed for a period of 8 hours before any measurements were made.

To assess the sensitivity in the scatter free situation a point source was placed 15cm from the camera face at 5 different positions. The time taken to acquire 100,000 counts was measured on the camera console for each collimator.

4.2.7.3 Results

For the plane source sensitivity a representative set of results was taken over a four month period to give values of 108.4 ± 4.5 counts per second per MBq for the LEAP collimator and 69.8 ± 2.6 counts per second per MBq for the HR. The inter-measurement variability of around 5% was produced by variations in the sensitivity of the dose calibrator.

For the point source measurements the sensitivity of the

LEAP collimator was 139 ± 1 counts per second per MBq and for the HR 87 ± 1 counts per second per MBq.

4.2.7.4. Discussion

For the scatter free situation the sensitivity of the LEAP collimator was 1.6 times that of the HR (the manufacturer's value was 1.56). With a 15% energy window this was also the case when there was some scatter included in the detected signal through the use of the extended source distribution.

The plane source sensitivity was lower than the point source sensitivity because of the effects of attenuation within the plane source itself.

4.3 Variation of planar performance with camera angle

4.3.1 Introduction

For the production of good quality SPECT images the planar imaging performance of the camera must remain stable as it is rotated. The parameter which is most likely to show a deviation with camera angle is the energy response. This was a problem which was particularly serious for early models of gamma camera because of the interaction between the earth's magnetic field and the PMTs, Jarritt (1984 pp 48-49). For cameras of modern design mu metal shielding has reduced the severity of these effects ; however it is still important that they are quantified.

Alterations in the energy response of the camera will introduce non-uniformities into the projection data which will be amplified by the reconstruction process to produce artefacts in the final images.

4.3.2 Energy response with camera angle

4.3.2.1 Methods

The selected energy discrimination window can be centred over the photopeak of the selected isotope using the automatic peak tracking facility described in Chapter 3. The difference between the actual photopeak position and the nominal energy value selected as an initial position for the peak tracking to begin is displayed on the control screen. Thus the exact location of the photopeak position can be determined.

This facility was used to determine the variation of detected photopeak position as a function of camera angle. A small source of ^{99m}Tc was attached to the end of a plastic rule which was fixed to the end of the SPECT bed leaving the source essentially suspended in air to avoid scattered radiation. The collimator was taken off the camera so that the camera face was as uniformly irradiated as possible. The activity in the source was selected to give a countrate less than 5,000 cps.

With the source positioned at the centre of rotation the camera was rotated around it with a radius of rotation of 40cm. At selected angles the automatic peak tracking facility was used to determine the exact position of the photopeak. These measurements were performed on a Sunday to avoid complications arising from the presence of external sources of activity e.g from patients waiting to be scanned etc. Care was taken to ensure that the only source of radiation in the vicinity of the camera at the time of measurement was the measurement source itself. This was essential as the measurements were performed without a collimator making the

camera susceptible to the detection of small, extraneous, levels of activity.

4.3.2.2 Results

For the initial run the camera angle was set to 0 degrees and measurements made at successive 20 degree angular increments over 360 degrees. It was noted that the 0 degree and 360 degree measurements were not in agreement so that a second set of measurements were made. There was still some unexplained variability so that a final set of measurements were made whereby the camera was peaked five times for each angle before being rotated by 180 degrees so that measurements were made alternately at opposing camera angles. These results are shown in figure 4.24.

For the final set of measurements the variation of photopeak position with camera angle was small. The maximum difference between any two values was 0.4% or 0.56 keV..

It is likely that the variability encountered in the early measurements was due to thermal effects arising from the removal of the collimator. By the time the third set of measurements had been performed over two hours had passed by which time the camera head had probably reached thermal equilibrium at an altered temperature.

4.3.3 Variation of Sensitivity With Gantry Angle

4.3.3.1 Methods

The effect which the small variation in the position of the photopeak with gantry angle had on the sensitivity of the system was investigated. A SPECT acquisition was performed of a point source positioned on the centre of rotation and the

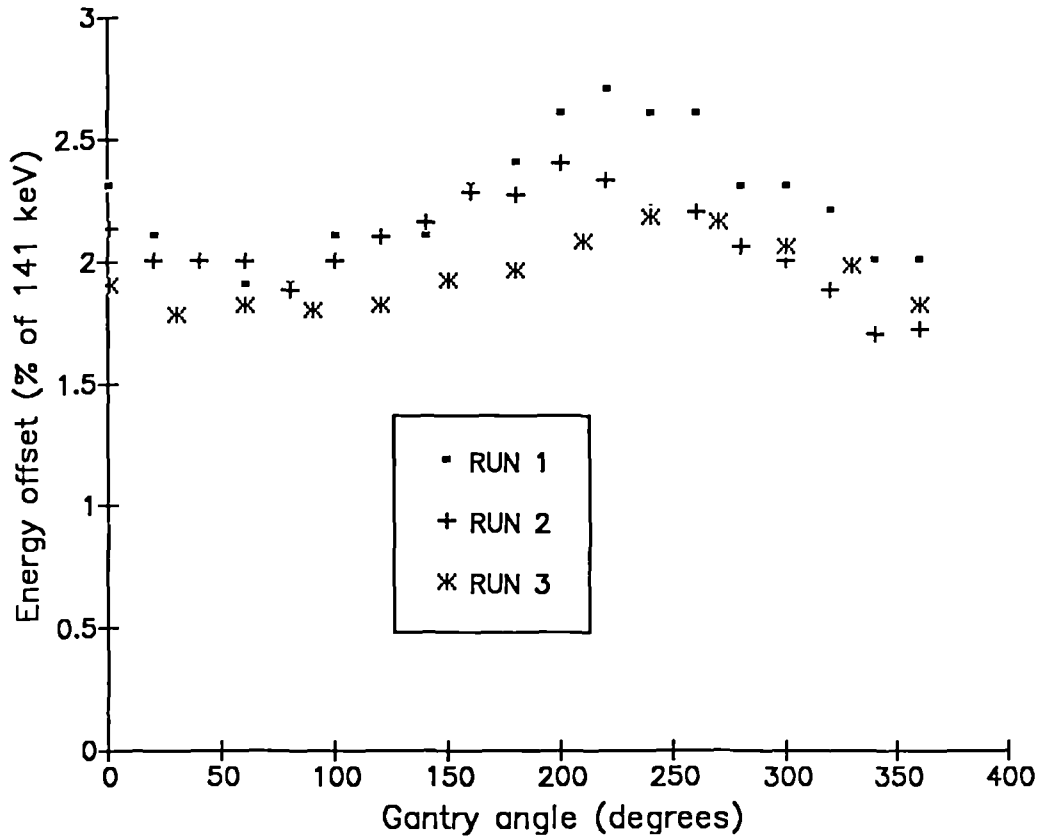


Figure 4.24 Variation of photopeak position with gantry angle in terms of the percentage difference from the expected value of 141keV.

counts acquired in each projection image determined. These were corrected for the decay of $^{99\text{m}}\text{Tc}$ during the acquisition and plotted against camera angle to give figure 4.25.

4.3.3.2 Results

Although a cyclic variation was noted in the energy response a similar variation was not observed with the sensitivity. The standard deviation of the counts detected over the 360 degrees was 0.7% of the mean value. Thus any variations in sensitivity with gantry angle will be significantly lower than the variations encountered over the face of the camera due to the limitations in the uniformity of its response, Section 4.2.5.

4.3.4 Variation of Uniformity with Gantry Angle

4.3.4.1 Methods

The flood field source described in Chapter 3 was used to perform the measurements of the variation in camera uniformity with angle. Before the measurements were made the camera was peaked using a scatter free source of $^{99\text{m}}\text{Tc}$. The source had been filled 8 hours prior to the measurements and had been rotated at various intervals to ensure proper mixing of the isotope. Acquisitions were made using the LEAP collimator at four camera angles 0, 90, 180 and 270 degrees. Eight million counts were acquired into 64*64 data matrices which were analysed in the same way as described in section 4.2.5.2.

4.3.4.2 Results

The results of the uniformity measurements at the four camera angles are shown in Table 4.3. The figures for the

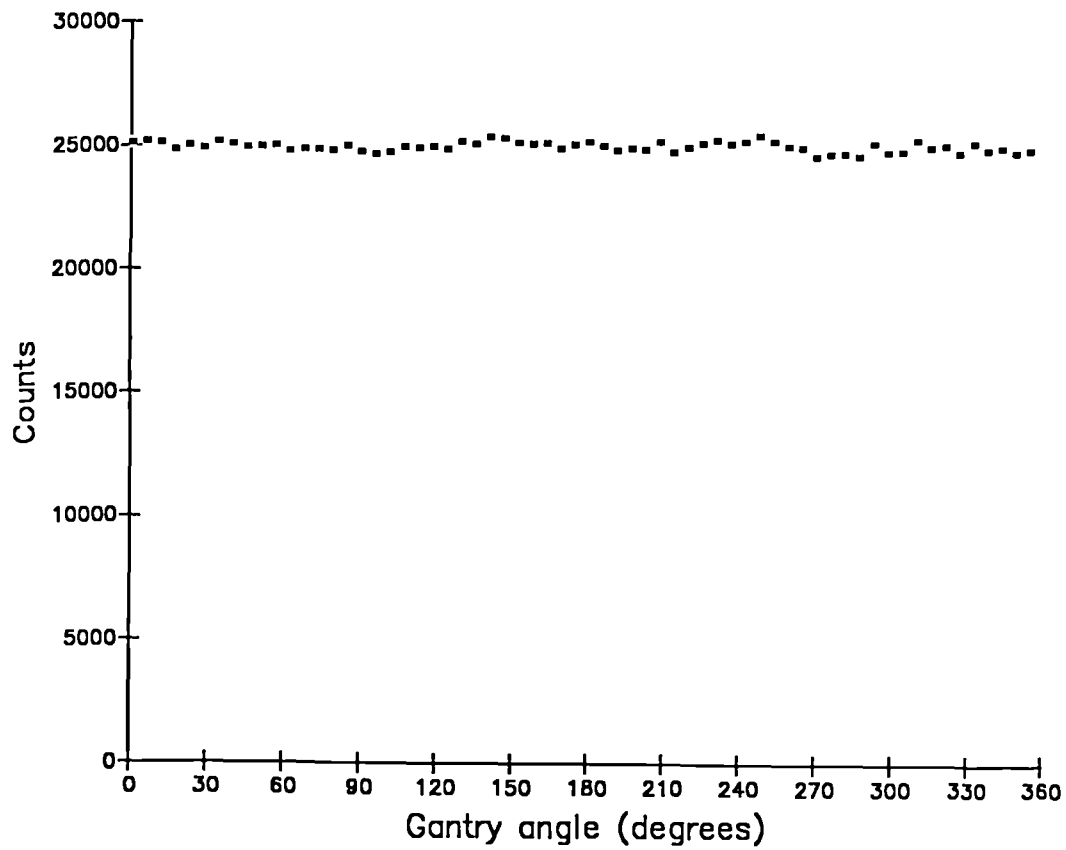


Figure 4.25 Variation of sensitivity with gantry angle.

Gantry angle	CV(%)	U+(%)	U-(%)	10%	5%
0	2.2+/- .2	9.5+/-1	9.1+/-1	100%	95.5+/- .5
90	2.1+/- .2	9.3%+/-1	7.6+/-1	100%	96.9+/- .5
180	2.4+/- .2	8.7%+/-1	9.4+/-1	100%	94.9+/- .5
270	2.3+/- .2	8.8%+/-1	10.8+/-1	100%	94.9+/- .5

Table 4.3 Variation of camera uniformity with gantry angle.

CV = coefficient of variation

U+/- = integral non-uniformity

5%,10% = the percentage of pixels within 5% and 10% of the mean

errors which are quoted in the table were obtained by examining the reproducibility of the measurement parameters used to produce Table 4.2. There was no significant variation with camera angle for any of the parameters used to assess uniformity except for the 5% pixel figure. This is probably due to the smaller number of counts which were acquired for these uniformity acquisitions producing a greater variability in the measurement parameter. Similarly, the values for the coefficient of variation are higher than those obtained in section 4.2.5 because only eight million as opposed to thirty million counts were acquired. The increase is due to additional variations introduced by statistical fluctuations into the counts obtained in each pixel.

4.4 Camera computer interface

Having tested the planar performance of the camera the next link in the imaging chain is the interface between the camera and the computer. It is essential that the information collected by the camera is transferred accurately to the computing system. This function is performed by the analogue to digital conversion circuitry described in Chapter 3.

4.4.1 ADC linearity assessment

The linearity of the analogue to digital conversion process is of particular importance for SPECT imaging. Non-linearities in the ADCs will produce non-uniformities in the projection data which are amplified by the reconstruction process to produce circular artefacts, figure 4.26.

To date the most commonly used approach to the assessment of ADC linearity has consisted of a subjective visual

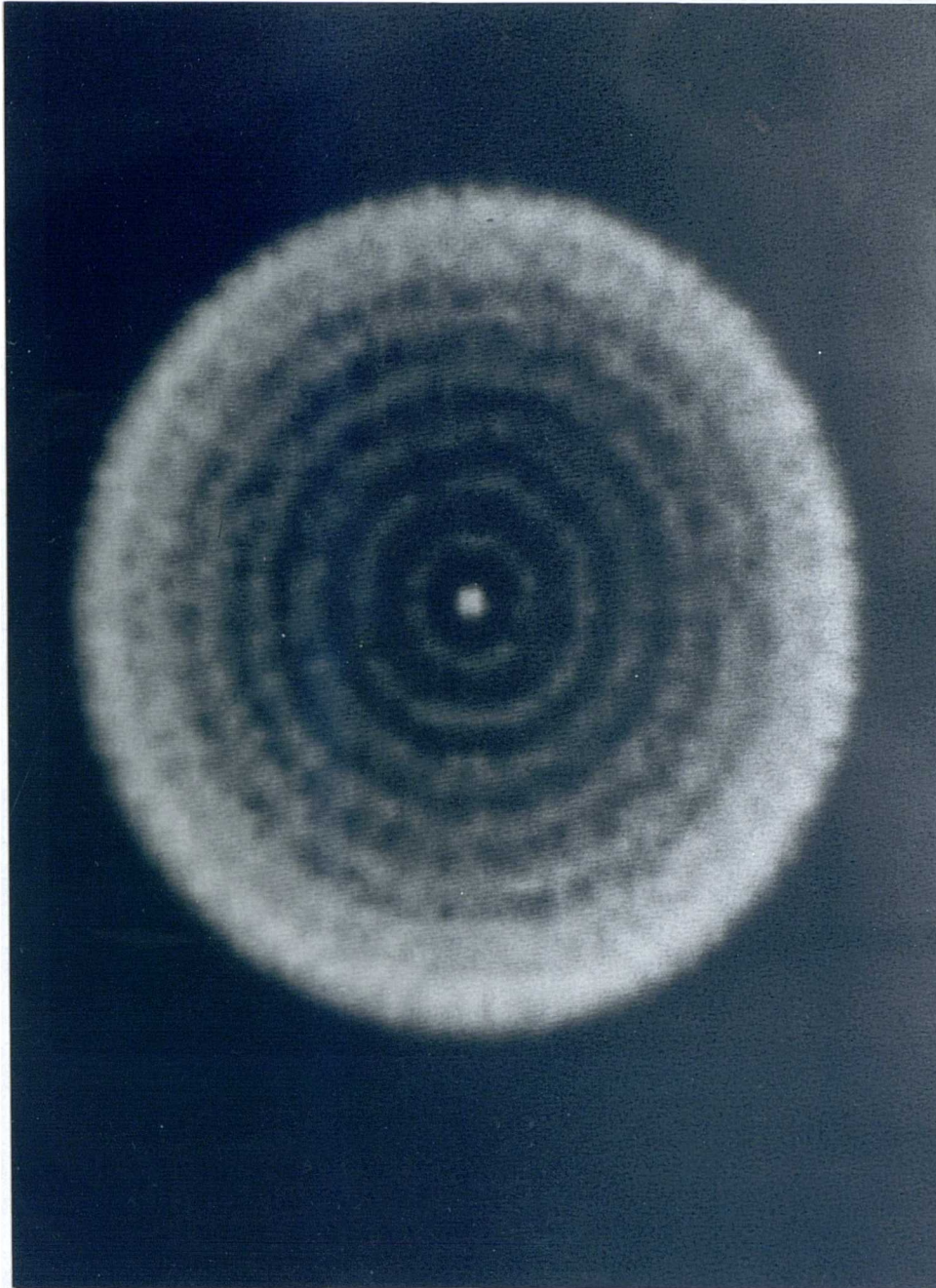


Figure 4.26 Transaxial section through a uniform, cylindrical distribution of activity showing circular artefacts as a result of an ADC non-linearity. The section has not been corrected for attenuation.

inspection of the digital images. An attempt has been made to improve on this through the development of an objective method for the quantitative assessment of the accuracy of the analogue to digital conversion process, Gillen (1989).

4.4.1.2 Theory

For accurate conversion the relationship between the input voltage levels and the output positional information must be linear. For this to occur two criteria must be satisfied :

1. The input voltage levels between which bit changes occur must be of uniform size. If this is not true then stripes will be produced in the digital images as counts are misplaced into pixels corresponding to the larger voltage "bins". This is commonly termed differential non-linearity.

2. The relationship between the input voltage and output position signal should be linear over the whole voltage range i.e. the distance on the digital image corresponding to a one volt change in input voltage should be independent of the input voltage level. If this is not so then the sizes of objects on the digital image will vary with their position. This is commonly termed integral non-linearity.

4.4.1.3 Methods

An objective, quantitative assessment of ADC performance can be made by analysing the data obtained when the camera is irradiated by a uniform photon flux. This was achieved by acquiring a thirty million count flood field image using a ^{99m}Tc liquid sheet source. The data were acquired into a

matrix of dimensions 256*256. For analysis the central quadrant of the flood field image was used. From this profiles in horizontal and vertical directions were taken, the width of each profile being equal to the width of the central quadrant. This is equivalent to summing all pixels with the same x-coordinate (to form the horizontal profile) and also those with the same y-coordinate (to form the vertical profile).

Integral Non-Linearity Measurement

If the relationship between input voltage and output position is linear then the gradient of the profiles obtained from the flood field image should equal zero. The level of ADC integral non-linearity can be quantified from the magnitude of the deviation of the gradient from zero. The gradient can be measured by performing a linear regression on the profile data.

Differential Non-Linearity Measurement

If the input voltage levels between which bit changes occur are of uniform size then there should be no periodic variations in pixel counts with position. This can be examined most clearly in frequency space by taking the Fourier Transform of the profile data. For error free performance there should be no spatial frequency (SF) components with values which are greater than zero. If there are then the identity of the bit which is non linear can be calculated from the frequency of the non zero component. The magnitude of the differential non-linearity can be made independent of the number of counts acquired in the flood image by assessing the normalised modulus of the Fourier Transform (MFT).

Thus by calculating the MFT both the magnitude and the frequency of cyclic variations in the profile data can be determined.

4.4.1.4 Results

The results of the previously described analysis will be shown for two sets of ADCs. The first set (set 1) consisted of the ADCs which were originally present in the camera computer interface. After an initial set of measurements had been made it was found that the performance of these ADCs was unacceptable so that they were replaced by another set (set2).

The flood field images obtained from the original set of ADCs (i.e. set 1) are shown in figure 4.27. Note the obvious striping pattern caused by a differential non-linearity in one of the low significance ADC bits. The profile in the x-direction through the central quadrant of the flood field image is shown in figure 4.28.

The flood field images obtained from the replacement set of ADCs (i.e. set 2) are shown in figure 4.29. The profile in the x-direction through the central quadrant of the flood field image is shown in figure 4.30.

Integral Non-Linearity

Linear regressions were performed on the curves shown in figures 4.28 and 4.30 to give the following results :

	Curve Gradient	x-Axis Intercept
Set 1 :	3.5 (+/-128)	171310 (+/-4735)
Set 2 :	3.7 (+/-12)	186707 (+/-443)

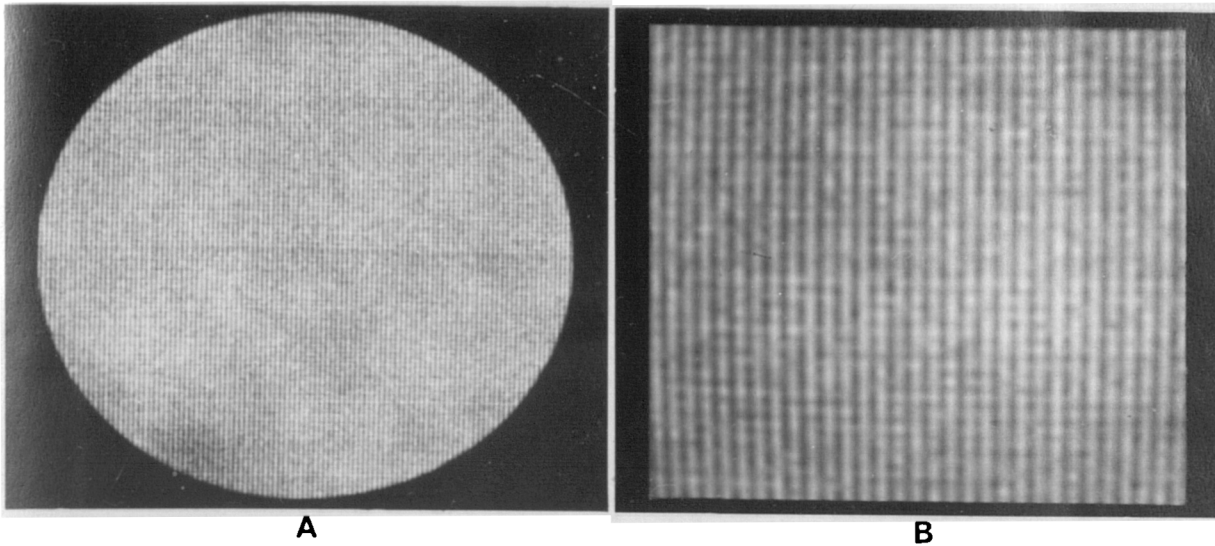


Figure 4.27 The flood field image, A, and its central quadrant, B, are shown for an interface with a non-linear x-ADC.

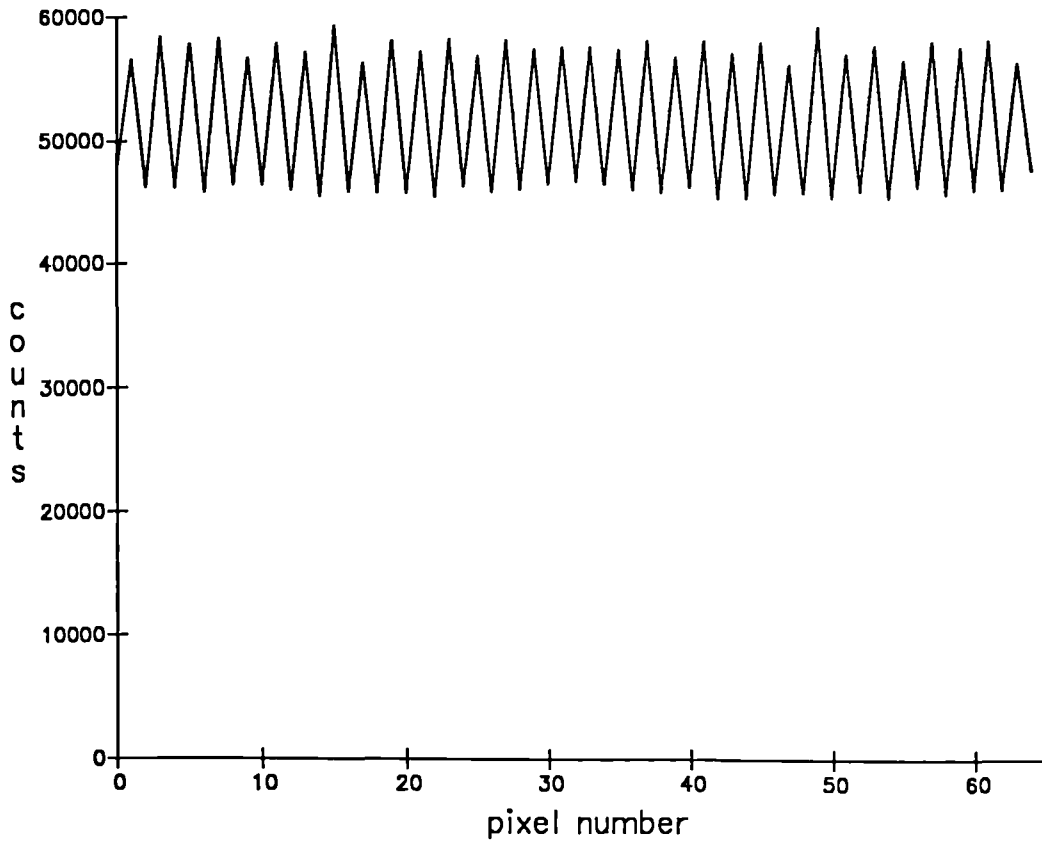


Figure 4.28 Profile taken through the central quadrant of the flood field image obtained with the non-linear x-ADC.

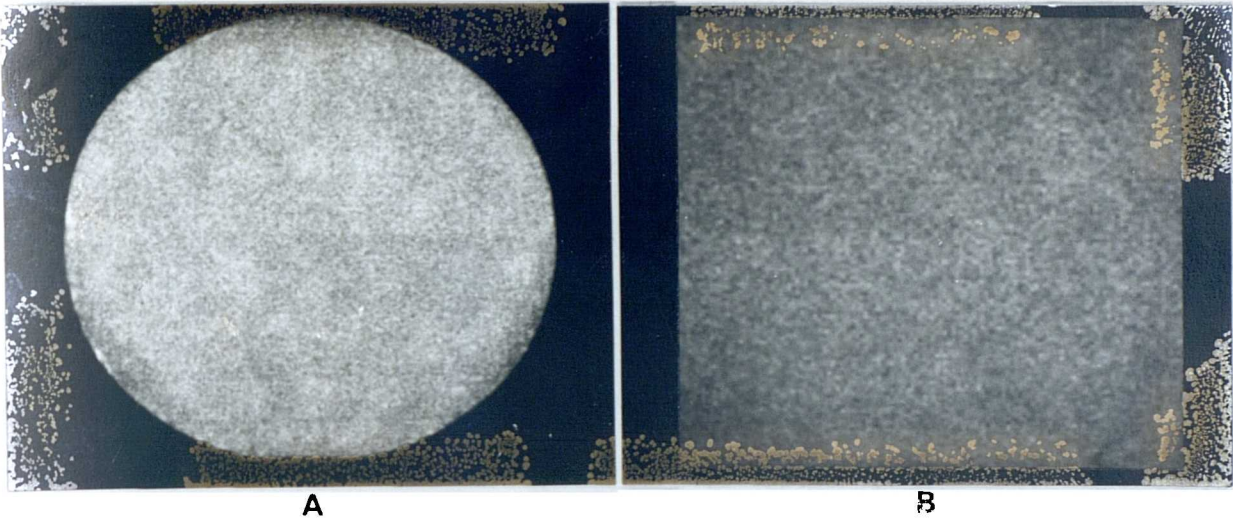


Figure 4.29 The flood field image, A, and its central quadrant, B, are shown for an interface with ADCs exhibiting good linearity.

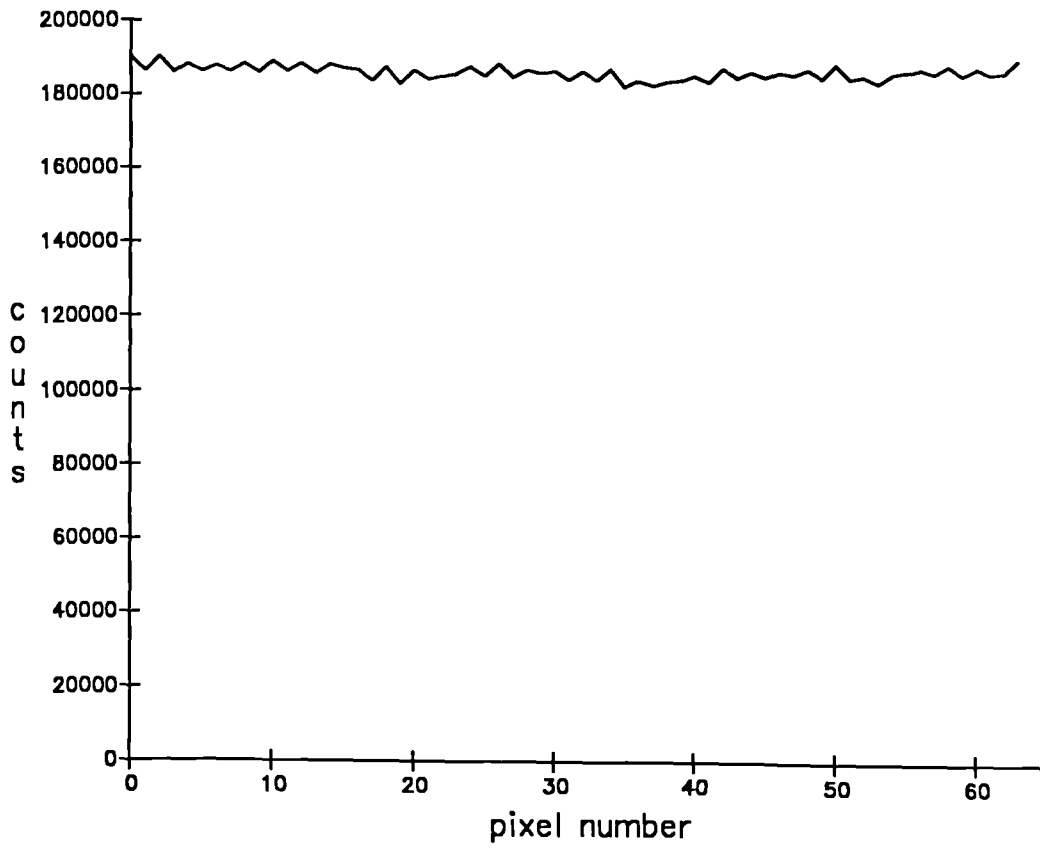


Figure 4.30 Profile taken through the central quadrant of the flood field image obtained with the linear ADCs.

The figures in brackets represent the standard deviations of the measurements. For both systems the curve gradient was not significantly different from zero ($p < 0.005$) indicating a satisfactory level of integral linearity.

Differential Non-Linearity

The level of differential non-linearity for the two systems can be assessed by examining the MFTs of the curves shown in figures 4.28 and 4.30. The MFT curves are shown in figures 4.31 and 4.32. For a perfectly adjusted system the amplitude of the zero SF component would equal one while the amplitudes at all other SFs would equal zero. This is almost achieved with set 2, figure 4.32, where the only component which has an amplitude significantly greater than zero is that with SF equal to 0.5 cycles/pixel. The significance is measured using a MFT value of greater than 0.003 which is two standard deviations greater than the mean of the non-zero SF components.

The most obvious feature from figure 4.31 is the highly significant MTF value of 0.12 at the SF equal to 0.5 cycles/pixel. This is a quantitative measure of the differential non-linearity of the least significant ADC bit (i.e. bit number 8) which is responsible for the striping effect seen in figure 4.27. There are also SF components with amplitudes significantly greater than zero at 0.25 and 0.375 cycles/pixel (corresponding to non-linearities in bits 4 and 6). These are not obvious from a visual inspection of the images or of the curve in figure 4.28.

The amplitude of the SF components greater than zero can be more clearly demonstrated by multiplying the MTF by 10^4

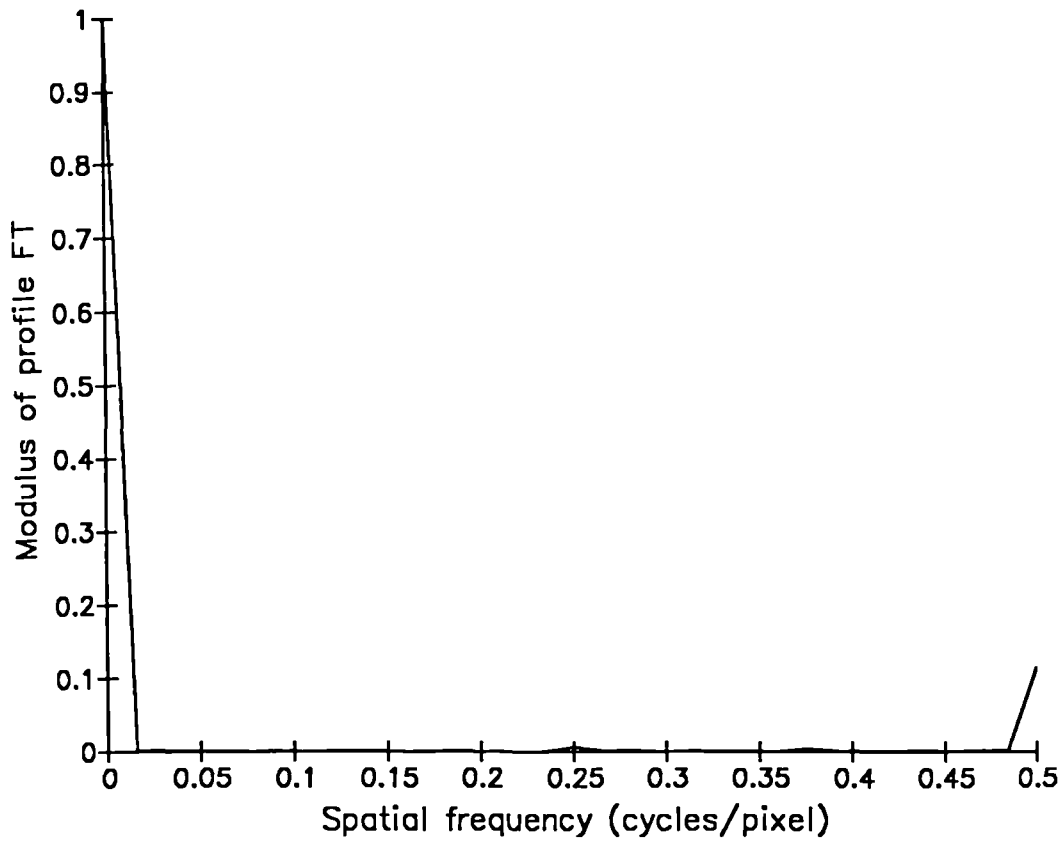


Figure 4.31 The modulus of the FT of the profile obtained from the non-linear x-ADC is shown.

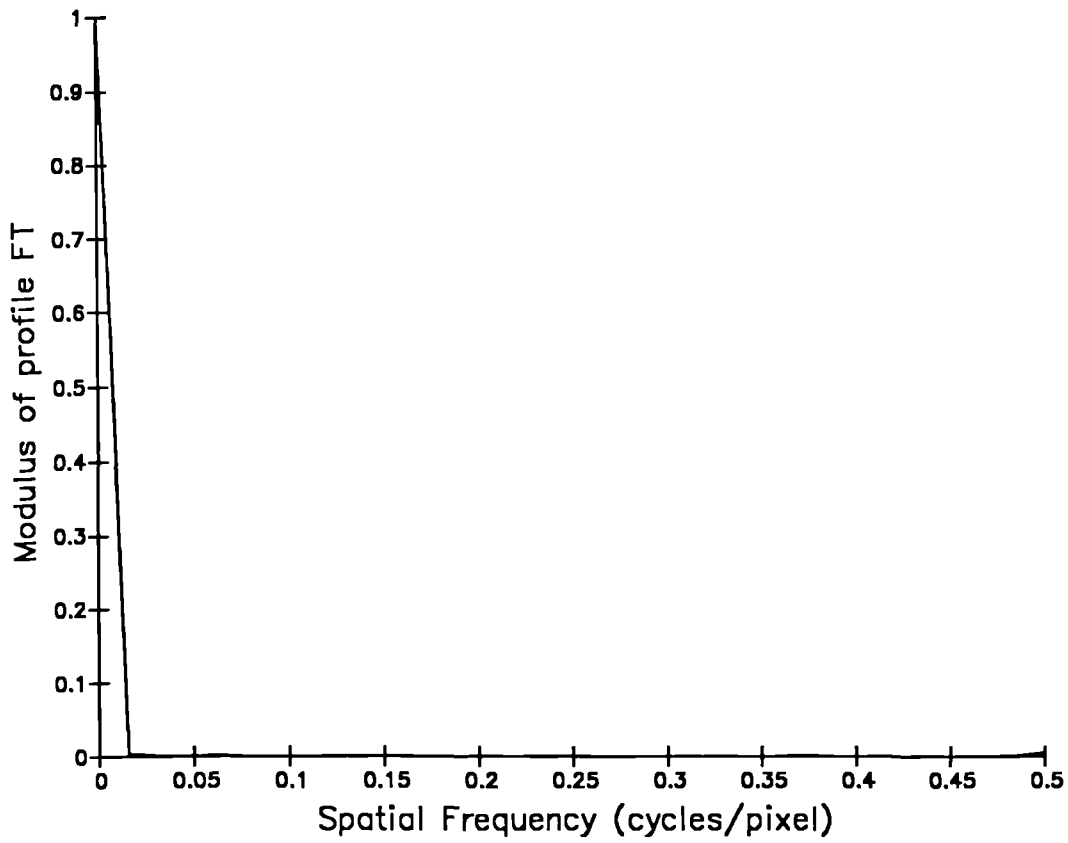


Figure 4.32 The modulus of the FT of the profile obtained from the set of ADCs which operate satisfactorily.

then taking the Log. This is shown in figures 4.33 and 4.44 where the relationship between the SFs and the bits in the ADC can also be seen.

4.4.1.5 Discussion

While high levels of integral non-linearity are obviously undesirable the gradual nature of the changes across the digital matrix mean that the effects on SPECT image quality are unlikely to be significant.

Of more importance are the variations in the uniformity of the digital image matrix produced by the differential non-linearities. A differential non-linearity which produces a non-uniformity in the projection data of 0.5% can produce circular distortions of 5% in the reconstructed images. It is suggested that this value should be the maximum level acceptable before corrective action is taken. This is based on the magnitude of camera non-uniformities (at least 1%) which exist after flood field correction and also on the noise levels which are commonly encountered in clinical SPECT images (percentage root mean squared errors above 10% per pixel, Chapter8).

4.4.1.6 Conclusions

A method for the objective, quantitative assessment of ADC performance has been developed. The accuracy of the method permits deteriorations in the performance of ADCs to be detected well before significant reductions in SPECT image quality are produced. This approach should be useful in the specification and acceptance testing of SPECT systems providing a set of parameters which can be specified and

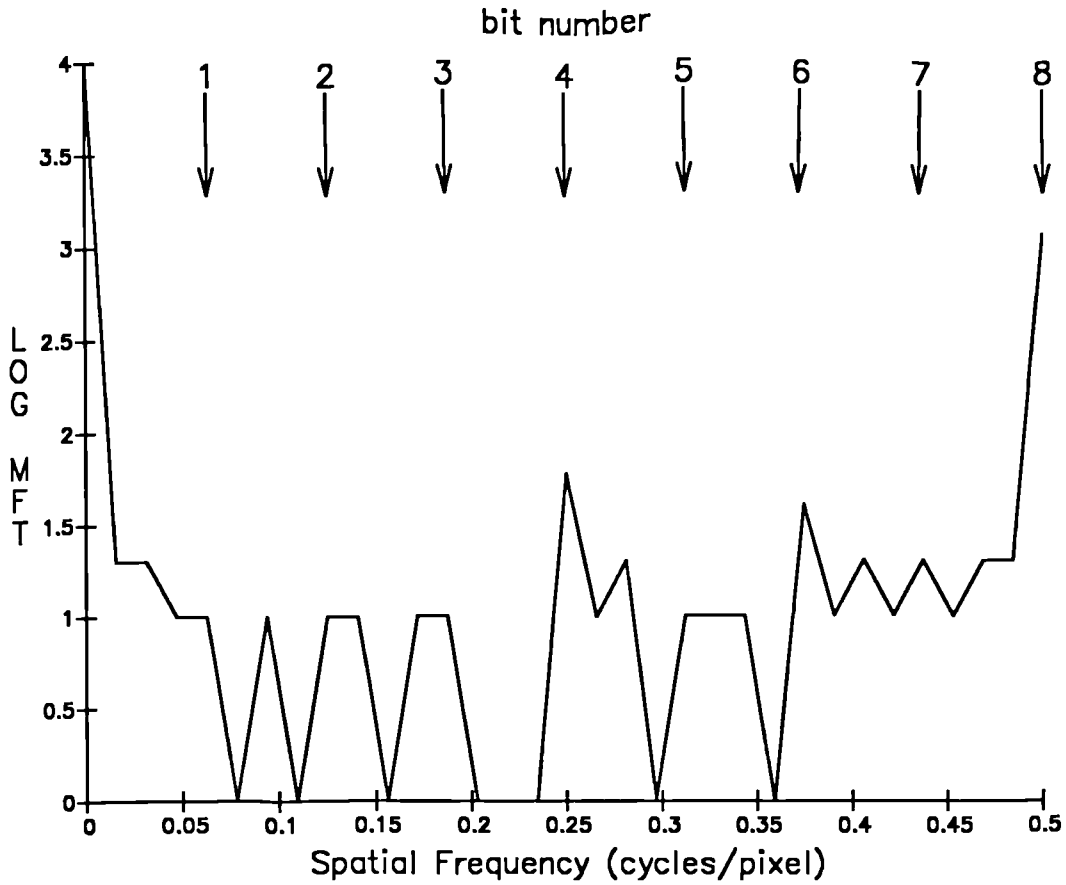


Figure 4.33 The large amplitude of the zero spatial frequency component makes the amplitudes of the other components difficult to visualise on the MFT curves. To overcome this, the values were multiplied by 10^4 and the Log taken. The result of this procedure for the profile from the non-linear x-ADC is shown. The spatial frequencies which correspond to specific ADC bits are highlighted.

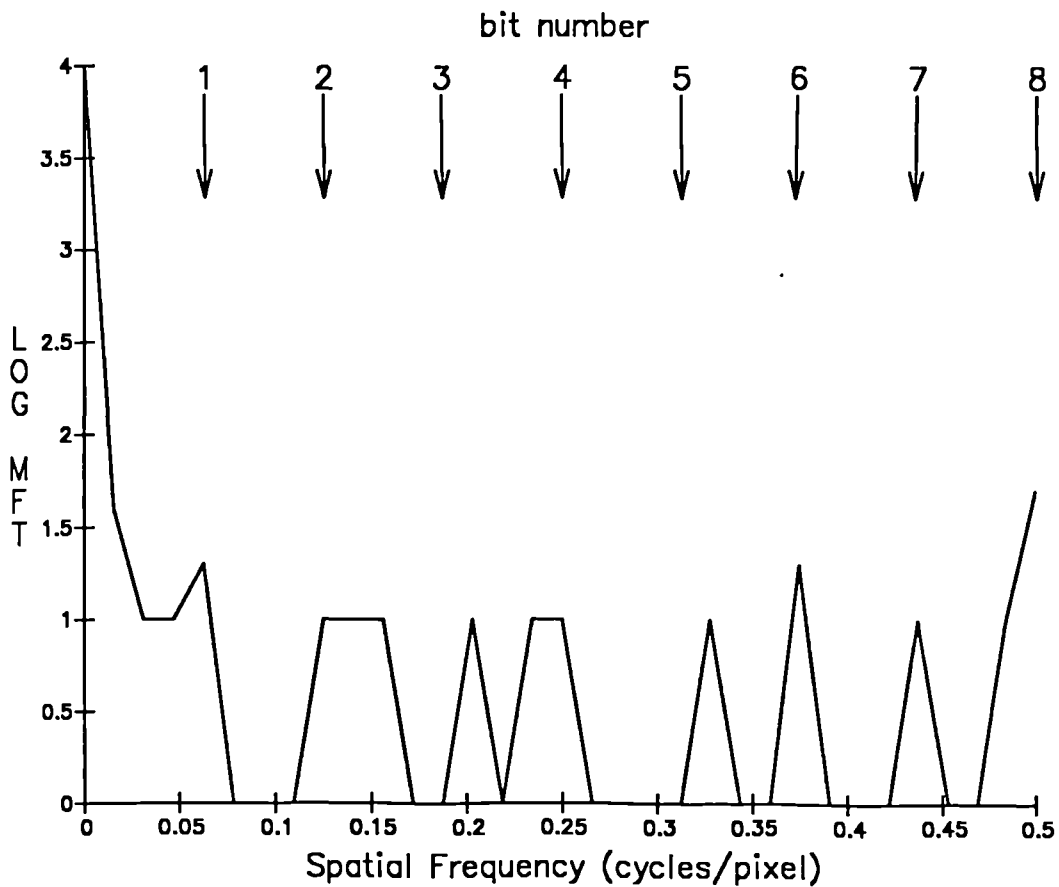


Figure 4.34 The large amplitude of the zero spatial frequency component makes the amplitudes of the other components difficult to visualise on the MFT curves. To overcome this, the values were multiplied by 10^4 and the Log taken. The result of this procedure for the profile from the x-ADC which performs satisfactorily is shown. The spatial frequencies which correspond to specific ADC bits are highlighted.

measured.

The use of this method allowed the substandard performance of the ADCs which were originally present in the camera computer interface to be accurately assessed. This evidence when presented to the manufacturer expedited their replacement.

4.4.2 ADC gain calibration

4.4.2.1 Introduction

As described in Chapter 3 the ADC gains can be adjusted by altering the settings on ten turn potentiometers. Using this a plot of ADC gain (or the reciprocal of pixel size) can be plotted against potentiometer setting. This information is required if the effects on image quality of the choice of different pixel sizes is to be examined.

4.4.2. Methods

A point source of size 0.2*0.2*0.2cm was created by injecting a small volume of ^{99m}Tc into the tip of a 1ml syringe. All measurements were made with a source to collimator distance of 15cm (it has been suggested that placing the source directly onto the collimator face can produce an interaction between the source and the collimator septa).

Acquisitions were made of the point source when placed at a variety of positions along the x and y electronic axes. The location of the axes was determined by a preliminary set of measurements and marked on a card which was used to position the source for the actual measurements. An image with 100,000 counts was acquired for each measurement into a 64*64 matrix.

This was performed for a range of x and y gain potentiometer settings.

The coordinates of the source position were calculated from the centroid of the count distribution using

$$Y_{CEN} = \frac{\sum_{x=1}^{64} \sum_{y=1}^{64} C(x,y) * y}{\sum_{x=1}^{64} \sum_{y=1}^{64} C(x,y)}$$

$$X_{CEN} = \frac{\sum_{x=1}^{64} \sum_{y=1}^{64} C(x,y) * x}{\sum_{x=1}^{64} \sum_{y=1}^{64} C(x,y)}$$

where C(x,y) is the number of counts in the pixel with coordinates (x,y) and (XCEN,YCEN) is the centroid.

4.4.2.3 Results

A good linear relationship between the gains and potentiometer settings for the two ADC s was obtained, figure 4.35. A linear regression of gain against potentiometer setting gave ;

x-ADC

$$\text{Gain} = 0.366 \pm 0.002 * \text{setting} + 0.69 \pm 0.01 \quad r = 0.99998$$

y-ADC

$$\text{Gain} = 0.373 \pm 0.002 * \text{setting} + 0.69 \pm 0.024 \quad r = 0.99995$$

4.4.2.4 Discussion

The gain setting for routine use is selected to give a data matrix size which is slightly larger than the camera FOV. Thus a gain setting of 2.0 is used for routine imaging to give a pixel size of 0.7cm and a matrix of edge length 45cm.

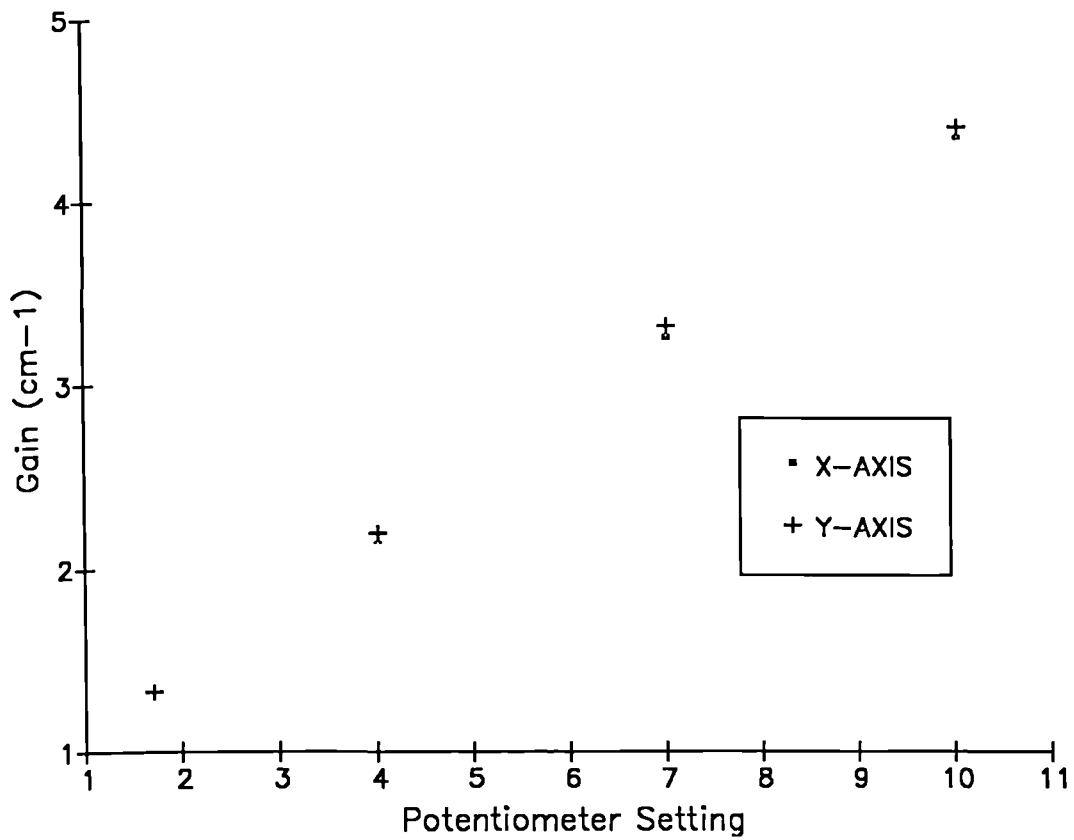


Figure 4.35 Variation of ADC gain (i.e. the reciprocal of pixel size) with the ADC potentiometer setting.

Smaller pixel sizes can be obtained by using larger matrices e.g. 128*128 or 256*256. Alternatively, to avoid the extra data handling consequent on the use of the larger matrices the potentiometer setting can be increased. This however will limit the area covered by the data matrix. For example the smallest pixel size obtainable will be achieved by using a 256*256 matrix size and a potentiometer gain setting of ten. This will give pixels of edge length 0.0575cm but will mean that the edge length of the area covered by the image matrix is only 14.7cm.

4.4.3 Centre of Rotation Assessment

4.4.3.1 Introduction

For the production of high quality SPECT images it is essential that the centre of rotation (COR) of the camera/computing system is as close to a point as possible for any individual axial section. For this to occur, three criteria have to be met ;

- (a) The camera head has to rotate in a perfect circle
- (b) The camera face has to remain perpendicular to the rotation plane
- (c) The mechanical axes of the camera have to be correctly aligned with respect to the digital matrix on the computing system. Specifically, the mechanical y-axis, taken to be parallel to the axis of rotation, has to be positioned exactly along the central vertical axis of the digital matrix.

Thus deviations of the SPECT imaging system's COR from a mathematical point can arise from several possible sources ; poor mechanical performance of the gantry leading to a failure of the camera face to be directed at a single point (the COR)

during rotation; incorrect adjustment of the camera head tilt; rotation or translation of the axes of the image matrix with respect to the mechanical axes of the camera.

It is possible to quantify these aspects of the rotational performance of the system by acquiring planar images of a point source and by examining the coordinates of the point in the projection images as a function of camera angle. The coordinates of the centroid of the source can be calculated in the manner described previously, Section 4.4.2. For a system performing in an ideal manner the y coordinate of the source centroid (YCEN) should remain constant with respect to camera angle while the x coordinate (XCEN) should be given by a function of the form

$$XCEN(\theta_i) = A1 + A2 \sin(\theta_i + \phi) \quad (4.2)$$

where θ_i = camera angle

A2 is equivalent to the maximum displacement of the source from the COR and ϕ is a function of the initial x coordinate. A1 is the x coordinate of the centre of the image matrix and should for example equal 32.5 for a 64*64 matrix.

4.4.3.2 Errors in the y-direction

A variation in YCEN can arise either because the camera head is not perpendicular to the plane of rotation or because the electronic axes of the camera are rotated with respect to the mechanical axes.

The errors can be calculated simply from the deviation of the value of YCEN at each angle from the mean value.

4.4.3.3 Errors in the x-direction

A displacement in the x direction of the image axes relative to the mechanical axes of the camera will be seen as a deviation of the average value of XCEN with camera angle from the expected value which corresponds to the centre of the image matrix.

A rapid assessment of the translational error in the origin of the image axes can be made by acquiring two static acquisitions of a point source at opposing camera angles. The average x coordinate should lie at the centre of the data matrix and any deviation from this is an estimate of the value by which the x-ADC offset setting should be altered. The Nodecrest routine ALIGNT uses this principle.

While errors in the x-ADC offset setting will add a constant value to every point in the curve of XCEN against gantry angle, gantry rotation faults (slippage, wobble, distortion etc.) will tend to produce local variations which only affect a small number of points.

The errors in the XCEN values at each angle due to gantry instability and x-ADC offset error can be assessed independently by fitting a function of the form of equation (4.2) to a curve of XCEN against gantry angle. This allows the angle at which the maximum gantry instability occurs to be picked out.

The function was fitted to the data using a simple Fourier analysis in which the first order Fourier harmonics were calculated from the XCEN values obtained at a set of gantry angles during a SPECT acquisition. A simple expansion of equation (4.2) will give a function of the form

$$XCEN(\theta_i) = C1 + C2 \cos(\pi*\theta_i/32) + C3 \sin(\pi*\theta_i/32) \quad (4.3)$$

This corresponds to a 64 projection image study where θ_i varies from zero to 63 corresponding to camera angles zero to $63*\pi/32$ radians.

The coefficients are given by

$$\begin{aligned} C1 &= (1/64) * \sum_{i=1}^{64} XCEN(\theta_i) \\ C2 &= (1/32) * \sum_{i=1}^{64} XCEN(\theta_i) \cos(\pi*\theta_i/32) \\ C3 &= (1/32) * \sum_{i=1}^{64} XCEN(\theta_i) \sin(\pi*\theta_i/32) \end{aligned}$$

The value of C1 is equal to the mean XCEN value.

If the function $XCEN(\theta_i)$ is subtracted from the original data then the residual values will represent the amount by which the camera head deviates from a circular path for each particular gantry angle.

This is the major advantage of this more sophisticated analytical approach ; the constant error due to incorrect x-ADC adjustment is separated from the variable error caused by imperfect gantry rotation. It also permits the precise location at which aberrant gantry behaviour occurs to be identified.

4.4.3.4 Methods

To acquire the data for the application of these analytical techniques a SPECT study of a point source is performed and the projection views stored.

The point source was created using 0.1ml of Tc^{99m} in the bottom of the barrel of a 1ml syringe. This gives a source size of approximately 4mm*4mm*4mm which is small enough to

constitute a point source given the source to camera face distances involved (15cm-20cm). If a high specific activity source, e.g. 800MBq/ml, is used then a countrate of around 8,000 cps can be obtained allowing a short imaging time.

The SPECT acquisition was performed using 64 projection angles with an acquisition time of ten seconds per angle. The radius of rotation was 20cm and the source was positioned about 5cm from the centre of rotation.

The data were analysed by creating two curves of XCEN and YCEN as a function of camera angle. The mean value of YCEN is calculated and a new curve created from the differences between it and the individual values. The mean and maximum values of the moduli of the residual data are output.

For the x-coordinate values the mean value of the data set was calculated and the difference between it and the coordinate of the centre of the data matrix output as the x-ADC offset error. The function described in equation (4.3) was also fitted to the data set and a new curve consisting of the differences between the fitted function and the data calculated. The mean and maximum values of the moduli of the residuals were calculated and output as a measure of gantry instability.

4.4.3.5 Results

The data obtained from a single representative analysis of the alignment and rotational performance of the camera-computer system will be given. The x-ADC offset error as measured by ALIGNT was 0.

The values for the x-coordinate of the point source as a function of gantry angle are shown in figure 4.36. Also shown

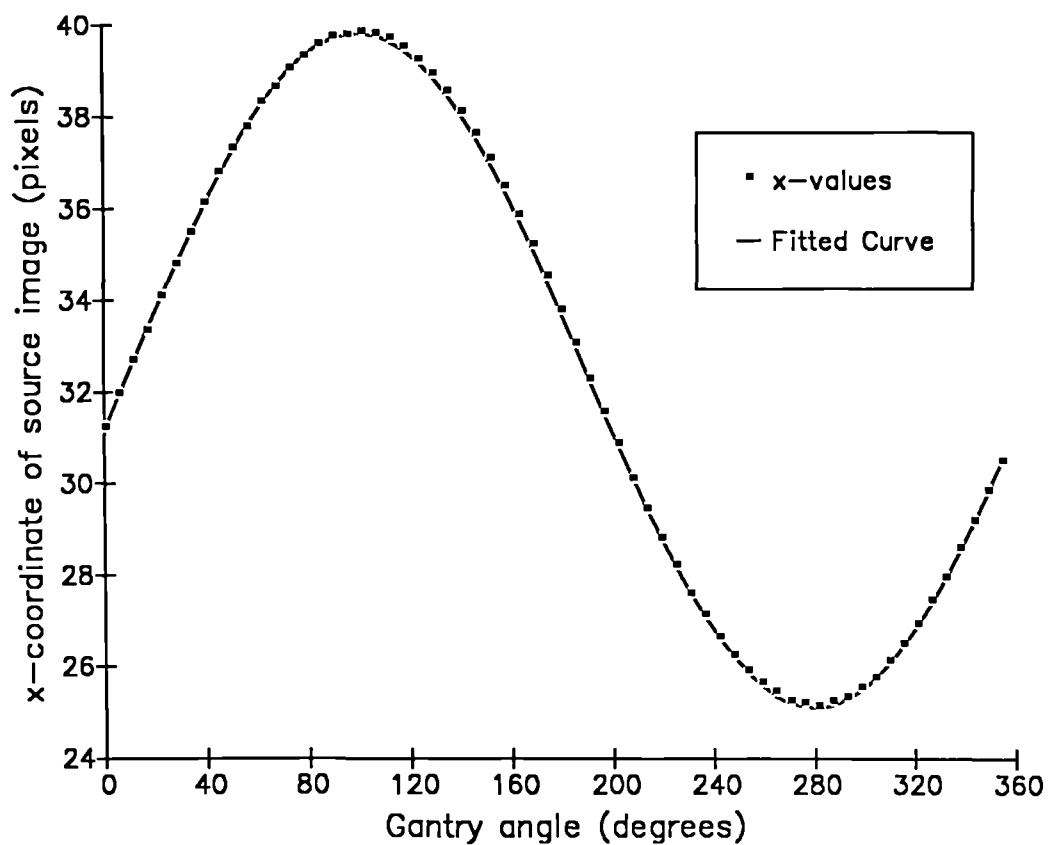


Figure 4.36 Variation of the x-coordinate of the centroid of a point source image with gantry angle (dots). The best fit sine function to the observed data is also shown.

is the function described by equation (4.3) which has been fitted to the measured data. The differences between the fitted function and the measured data are shown in figure 4.37. For this particular case the x-ADC offset error was measured to be 0.03 pixels and the maximum gantry error (obtained from the maximum difference between the measured and the fitted data) was 0.09 pixels. As described in Section 3.5.3.5 these are well within the limit of 0.125 pixels suggested by Saw (1986).

The data for the y-coordinate values after the subtraction of the mean are shown in figure 4.38. The maximum deviation of any value from the mean was found to be 0.15 pixels with a mean value for the residual data of 0.007 pixels. Errors in the y-coordinate values indicate that the camera head is not perpendicular to the plane of rotation at all times. To minimise this error, measurements were made with the camera head tilted from the horizontal prior to the acquisition. It was found that an initial tilt of +1.5 degrees was required to minimise the y-coordinate errors. This is a likely source of error in many systems because the rotation plane does not necessarily have to be vertical. Furthermore, the effects which errors in the y-coordinate have on image quality have never been fully evaluated.

A summary of the quantitative results obtained from the measurements made over a six month period is shown in Table 4.4. From this it can be seen that any time the x-ADC offset error was greater than 0.1 pixels readjustment of the potentiometer setting reduced the error back to an acceptable level. Similarly, by altering the initial head tilt, errors in the y-coordinate values could also be corrected although this

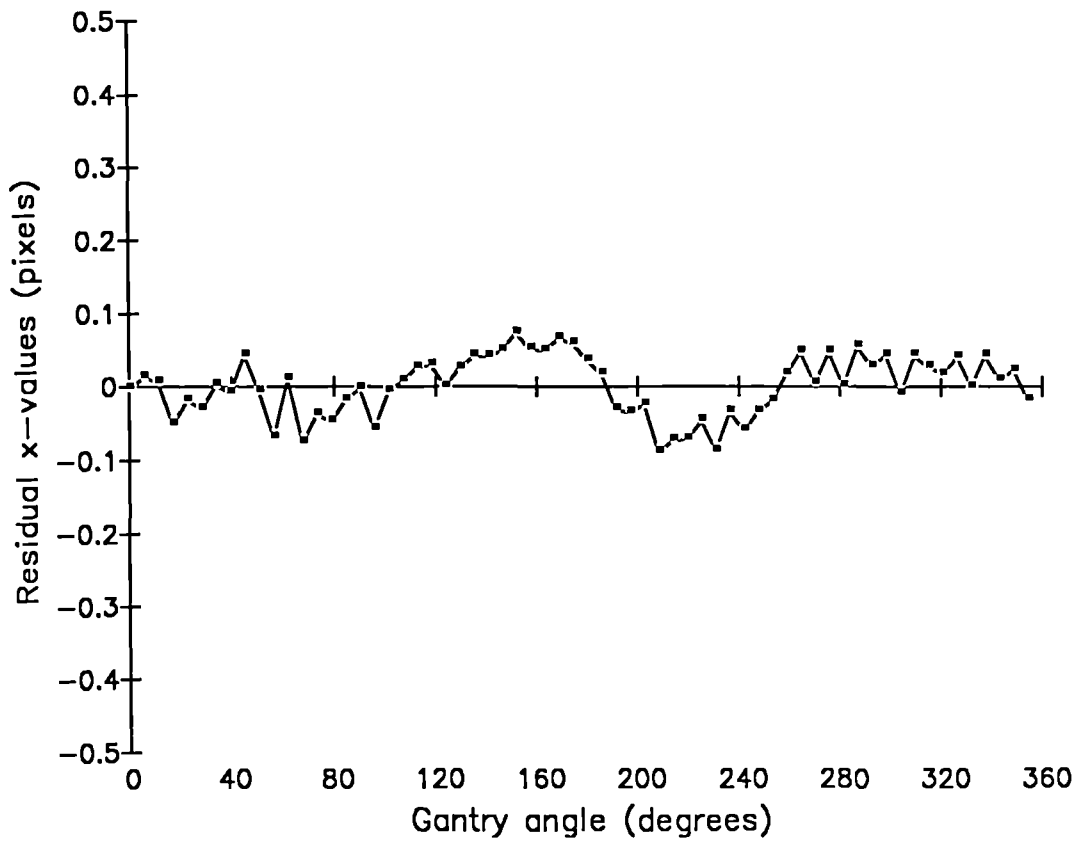


Figure 4.37 Variation of the difference between the fitted and observed x-coordinate values with gantry angle.

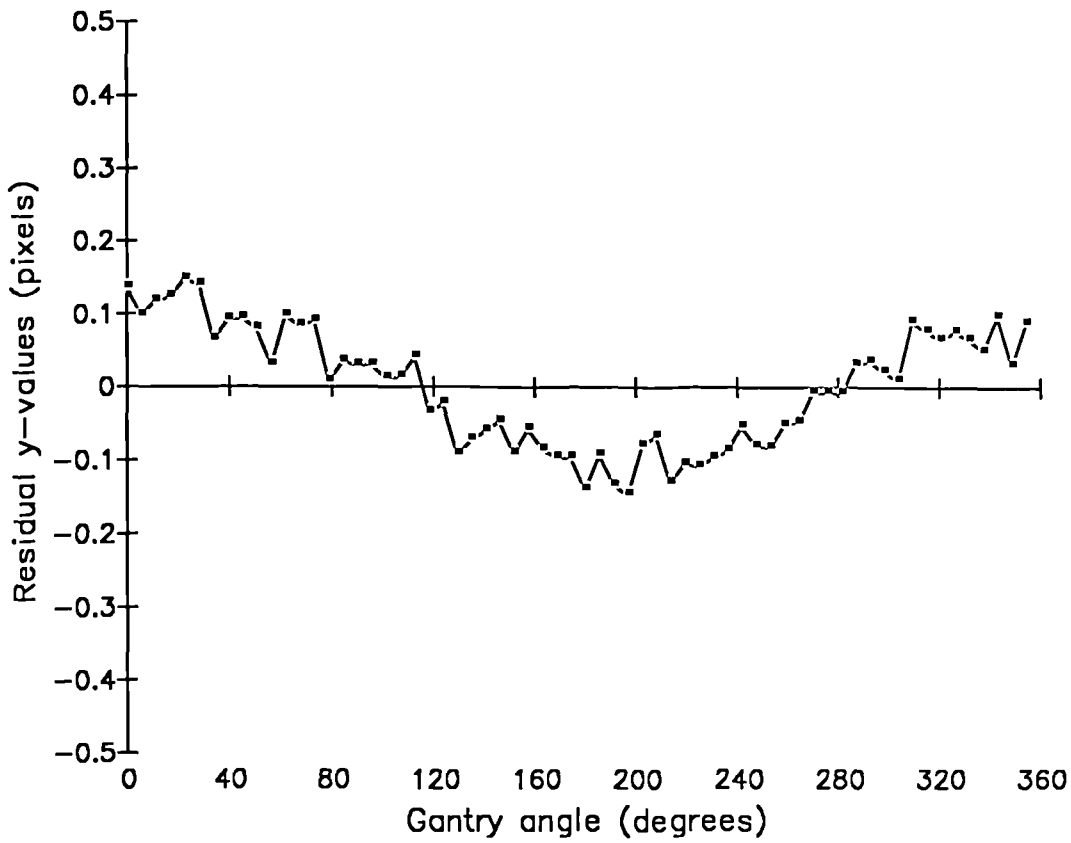


Figure 4.38 Variation of the difference between the fitted and observed y-coordinate values with gantry angle.

	ADC Offset	DX (mean)	DX (max)	DY (mean)	DY (max)
1	.0163	.0465	.1132	.0794	.1635
2	.1063	.0603	.1631	.1218	.2607
3	.086	.0366	.355	.0791	.152
4	.0926	.0309	.07	.07	.1243
5	.0942	.0316	.0795	.1148	.2424
6	.0394	.0453	.0977	.1151	.2087
7	-.0345	.034	.0899	.0715	.1468
8	-.1506	.0524	.1579	.0946	.2413
9	.0302	.0457	.1066	.0852	.1530
10	-.0486	.0538	.1079	.061	.1257
11	-.0214	.0522	.1177	.073	.1431
12	.0422	.0564	.1203	.0675	.1552
13	.0262	.1132	.2818	.0955	.1799
14	.0866	.1408	.3433	.068	.1647
15	-.0047	.1437	.3578	.069	.1525

Table 4.4 Centre of rotation measurements made over a six month period.

ADC offset is the difference between the mean value of the x coordinates of the centroids of the projection images and the centre of the data matrix.

DX (mean) is the average of the modulus of the difference between the x coordinates of the centroid of the projection images and the fitted sinusoidal curve.

DX (max) is the maximum of the modulus of the difference between the x coordinates of the centroid of the projection images and the fitted sinusoidal curve.

DY (mean) is the average of the modulus of the difference between the y coordinates of the centroid of the projection images and the mean value.

DY (max) is the maximum of the modulus of the difference between the y coordinates of the centroid of the projection images and the mean value.

is not as accurate a method as the potentiometer adjustment is for the x-ADC.

It can be seen from measurement numbers 13, 14 and 15 that an error in the mechanical performance of the gantry was detected. It is interesting to note that this did not affect the x-ADC offset error illustrating the usefulness of the curve fitting analysis procedure. The separation of the gantry rotation fault from an ADC error allowed the service engineer to locate and correct a fault in the optical encoder which determines gantry angle position.

In general the rotational performance of the system was good and also relatively stable. The application of the previously described measurement and analytical methods allowed any faults which developed to be precisely identified and accurately corrected. Thus the performance of the camera-computer interface and the mechanical performance of the gantry were always optimally adjusted throughout the period of operation of the SPECT system.

4.5 Quality control of SPECT bed

The system for supporting the patient while the camera rotates consists of a solid base upon which a mobile pallet is attached. The patient lies on the pallet and is manoeuvred into position beneath the camera. The pallet can be extended beyond the edge of the base to allow the camera to orbit around it.

The pallet is constructed from a lightweight plastic material to limit the attenuation of photons from the patient. The level of attenuation which was actually present was measured as part of the SPECT quality control procedure.

4.5.1 Methods

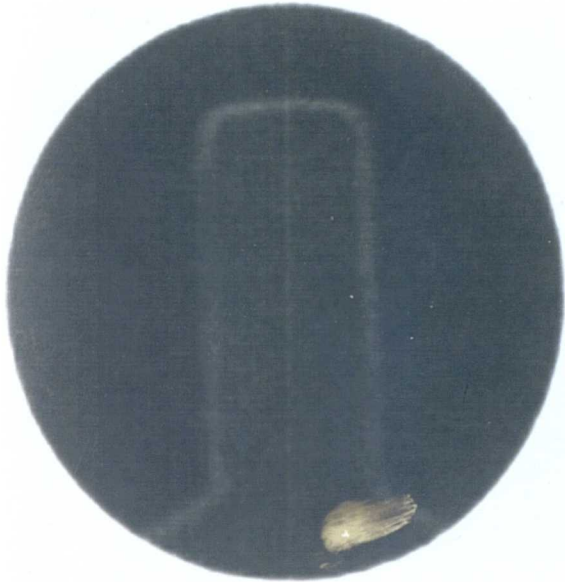
The SPECT pallet was positioned beneath the camera and irradiated with a uniform flux of photons which was produced by the flood field phantom described in Chapter 3. Eight million count images were obtained from this set up. A baseline image without the pallet was also acquired for comparison.

4.5.2 Results

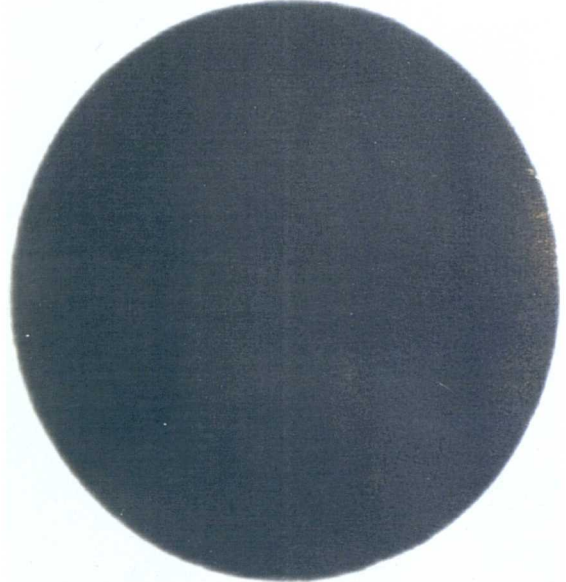
The transmission image of the pallet which was obtained is shown in figure 4.39A. The most striking feature is the band of reduced counts which runs around the edge of the pallet image. Inspection of the pallet showed the presence of a metal strip which was attached to the edge, presumably to increase its mechanical strength.

The level of attenuation produced by the bed and the metal strip was assessed quantitatively from a profile taken across it on an image stored on the computer. This profile is shown in figure 4.40. At the centre of the bed the counts were reduced by 6%. At the edge of the bed the counts were reduced by 24%.

The presence and effects of the metal strip were agreed by the manufacturer to be unacceptable and another pallet was provided. The transmission image of this pallet is shown in figure 4.39B. The profile which was taken through this image is shown in figure 4.41. The attenuation at the centre of the bed was 6% and at the edge 10%. For clinical count density SPECT studies no artefacts were observed which could be related to the effects of attenuation by this SPECT pallet.



view number 3



view number 4

Figure 4.39 The transmission image of the original SPECT pallet is shown in A. An area of increased attenuation can be seen around the perimeter. This pallet was replaced by another, the transmission image of which is shown in B. The vertical line through the centre of the images is due to a faulty ADC.

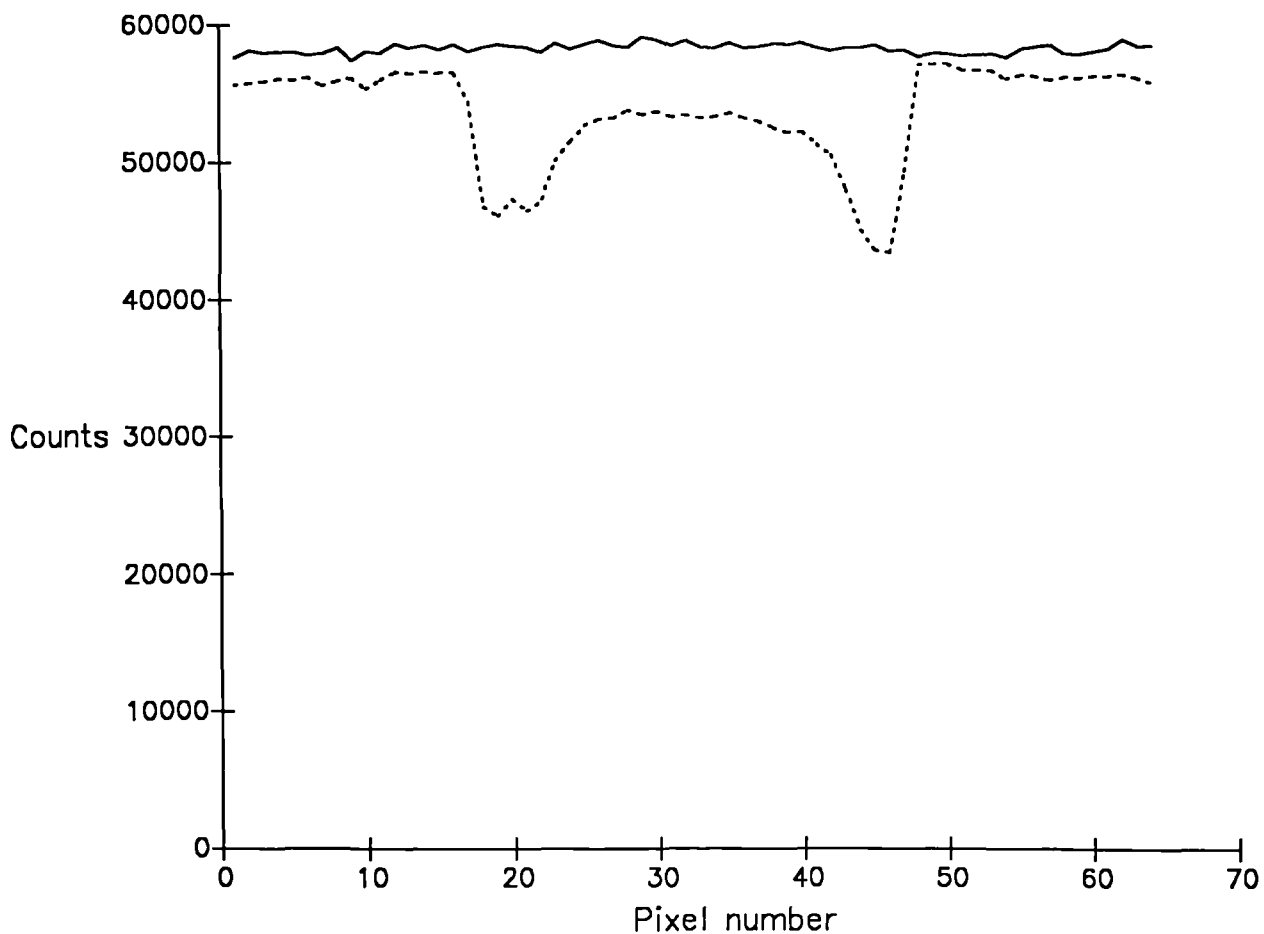


Figure 4.40 A profile across the transmission image of the original pallet was taken (dotted line). This can be compared to with the profile taken through the flood field image without the presence of the pallet (solid line).

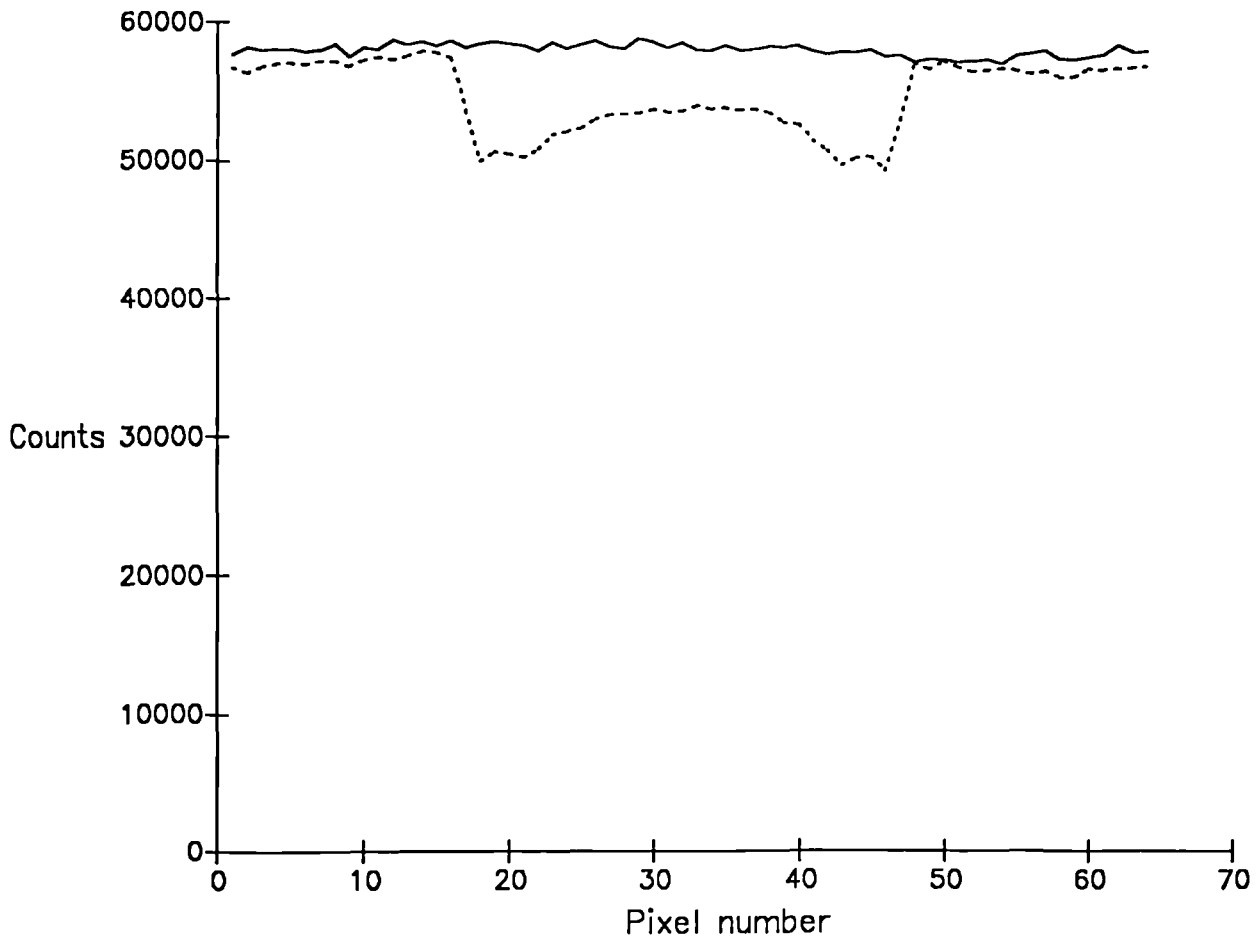


Figure 4.41 A profile across the transmission image of the replacement pallet was taken (dotted line). This can be compared to with the profile taken through the flood field image without the presence of the pallet (solid line).

4.6 Conclusions for Chapter 4

1. The energy resolution of the camera was 10.1%. This can be compared with the average energy resolution of 16.7% which was obtained from measurements made on 13 different gamma camera systems in 1979 by Elliott (1980). The improvement in energy resolution makes the use of a 20% energy window for ^{99m}Tc unnecessary. A consequence of this is a reduction in the influence which scattered radiation has on image quality.

2. The intrinsic resolution was 4.05mm. This can be compared to the average value of 5.3mm which was obtained from measurements made on 15 different gamma camera systems in 1979 by Elliott (1980).

3. A non-isotropic PSF was identified and related to faults in the design and manufacture of the collimators. The faulty collimators were replaced.

4. The FWHM of the HR collimator was smaller than that of the LEAP. This difference increased as the source to camera distance increased.

When measurements were made with a scattering material, as opposed to air, between the source and camera the differences between the FWHM values of the LSFs of the HR and LEAP collimators were reduced.

Similar conclusions were drawn from the collimator MTFs. The differences between the two collimators was less marked in scatter than in air. This was particularly true for the lower spatial frequencies where the MTFs of the LEAP and HR

collimators were very similar.

5. When the uniformity of the camera was measured over a four month period the average coefficient of variance for the counts per pixel in a flood field image was found to be 1.7%. This can be compared to a mean value of 4.3% which was obtained from measurements made on 8 different cameras by Elliott (1982).

The uniformity of the camera was also found to remain stable with time.

6. When the countrate linearity was measured 5%, 10% and 20% countrate losses occurred with observed countrates of around 9000, 14000 and 20000 cps respectively. The countrates encountered clinically are generally less than 5000 cps and thus are well within the linear range.

7. The point source sensitivity of the HR collimator was 63% that of the LEAP.

8. The planar imaging performance was stable to within acceptable limits as the camera head was rotated.

9. The ADCs which were originally present in the camera computer interface were found to exhibit an unacceptable level of differential non-linearity. These were replaced, after several attempts, by a set which performed satisfactorily.

The analysis of ADC performance was improved by the development of a novel quantitative measurement method.

10. The mechanical performance of the gamma camera was such that deviations from the path of a circular orbit were very small. However, the digital readout of the camera head tilt was found to be erroneous. When the head tilt was set to zero the camera face was not parallel to the axis of rotation. The nominal head tilt which had to be introduced to correct for this was determined using software developed by the author.

11. The attenuation of the SPECT bed was assessed and the presence of a metallic strip beneath the plastic coating identified. The attenuation produced by this strip was unacceptably high and the SPECT bed was replaced.

12. In general, significant improvements in camera performance over previous generations of systems have been identified. The improvements in energy resolution, field uniformity and mechanical stability are of particular importance for SPECT imaging.

13 From conclusions 3, 9, 10 and 11 it is apparent that, even when obtained from a major manufacturer, it is unlikely that rotating gamma camera SPECT systems can be operated in a "turnkey" manner. A thorough performance assessment and quality control program is required.

Chapter 5. SPECT of point and line sources.

5.1 Introduction

Having assessed and optimised the performance of the SPECT system the fundamental properties of the data which are produced by the SPECT process can be examined. By investigating the basic aspects of SPECT imaging a greater understanding can be gained of the properties of the inherently more complex clinical images. This is important because it permits some of the factors which limit the quality of the final clinical data to be identified.

The most fundamental element of SPECT is the SPECT point spread function (SPSF). This is dependent on a large variety of factors and will be examined in detail.

5.2 SPECT Point Spread Function Assessment

5.2.1 Introduction

In a similar manner to planar imaging the response of the SPECT system to a point source provides fundamental information on the behaviour and limitations of the system. The number of factors which influence the SPSF are much greater than those which influence the planar PSF. Thus in addition to linear sampling rate, source -collimator distance, collimator characteristics and the presence of scatter, the variation of the SPSF with angular sampling rate, radius of rotation, position in the image volume and reconstruction filter have to be examined.

Obviously, an exhaustive examination of the effects of all of these parameters would be a very large task. However, by approaching the problem in a systematic manner and by

utilising the data obtained in the assessment of the planar imaging performance the total number of independent variables can be reduced.

5.2.2 Linear sampling rate

The first step is to identify an appropriate maximum linear sampling rate. Having identified this the effect of lower sampling rates on the SPSF can be examined. The maximum should be high enough to ensure that the rate is appropriate even for the smallest radius of rotation and source to camera distance which are encountered in the clinical situation. These are approximately 13cm and 5cm respectively.

In fact the maximum achievable sampling rate is limited by practical considerations. The largest data matrix which the computer software can handle in the reconstruction process has dimensions of 128*128 pixels. If the digital FOV is to be large enough to investigate the behaviour of the SPSF out to clinically relevant distances from the COR then an effective limit is imposed on the size of pixels which can be used. Thus for a digital FOV of diameter 36cm the smallest pixel size which could be used for SPECT imaging is 0.28cm in length.

From Section 4.2.4.5 it can be shown that, for source to collimator distances of 5cm, spatial frequencies above 1.7cm^{-1} are not transferred. This is comparable to the Nyquist frequency of 1.8cm^{-1} for a pixel length of 0.28cm. Thus aliasing artefacts should not be produced in the projection data for pixels of this size and collimators of the resolution studied.

5.2.3 Angular sampling rate

A strict application of the simple analysis described in Section 2.2.3 for the previously described linear sampling rate and a subject of diameter 20cm would imply a required angular sampling rate of 220 per 360 degrees. This analysis however is based on matching the effective linear sampling at the edge of the object, which is produced by the finite angular sampling rate, to the actual linear sampling rate. Closer to the centre of the object the effective linear sampling rate is much greater for a given angular sampling rate so that the use of the maximum available rate of 128 per 360 degrees should be sufficient to avoid the introduction of severe angular sampling artefacts into the SPSF.

For larger subject diameters and radii of rotation the reduction in the required linear sampling offsets the increase in the calculated angular sampling rate so that . 128 angles, the maximum available, should be used throughout.

As lower angular sampling rates are often used in the clinical situation their effect on the size and shape of the SPSF is of interest.

5.2.4 Methods

A source of dimension 2mm*2mm*2mm was created by injecting a high specific activity solution into the tip of a 1ml syringe. The countrate which was achieved with the LEAP collimator was approximately 5,000cps. Care was taken to assess and optimise the rotational performance, including the x-ADC offset adjustment, before each set of measurements as described in Section 4.4.3. The linear and angular sampling rates described above were used.

The source was attached to the end of a plastic rule so

that it was effectively suspended in air free from any scattering media. It was accurately positioned at the centre of the image volume by calculating its coordinates in planar images taken at 0 and 90 degrees. This allowed the source position to be located to within 1mm. A SPECT study was then acquired into 128 projection matrices of dimension 128*128 using an acquisition time of 10s per angle. This was repeated after the source had been moved vertically downwards by 5cm, 10cm and then 15cm. In the coordinate system described in Chapter 3 this corresponds to a negative displacement along the z axis. The whole process was performed for ROR values of 13cm, 20cm and 25cm.

The data were reconstructed using a ramp filter with a cut off at the Nyquist frequency (Nodecrest filter number 3). Profiles one pixel wide were taken through the pixel with the maximum count value along the x, y and z directions. The FWHM and FWTM of the three profiles were then calculated.

5.2.5 Variation of SPSF with position in image volume

The FWHM values of the SPSF along the three coordinate axes for ROR values of 13cm, 20cm and 25cm are shown in figures 5.1, 5.2 and 5.3.

One of the most obvious features of the results is the independence of the FWHM of the SPSF in the z direction with displacement in the z direction. This can be contrasted with the marked reduction in the FWHM values along the other axes with displacement in the z direction. This was observed for all three ROR values.

The FWHM values in the x and y directions are not exactly the same. However, one would not expect this to be the case as

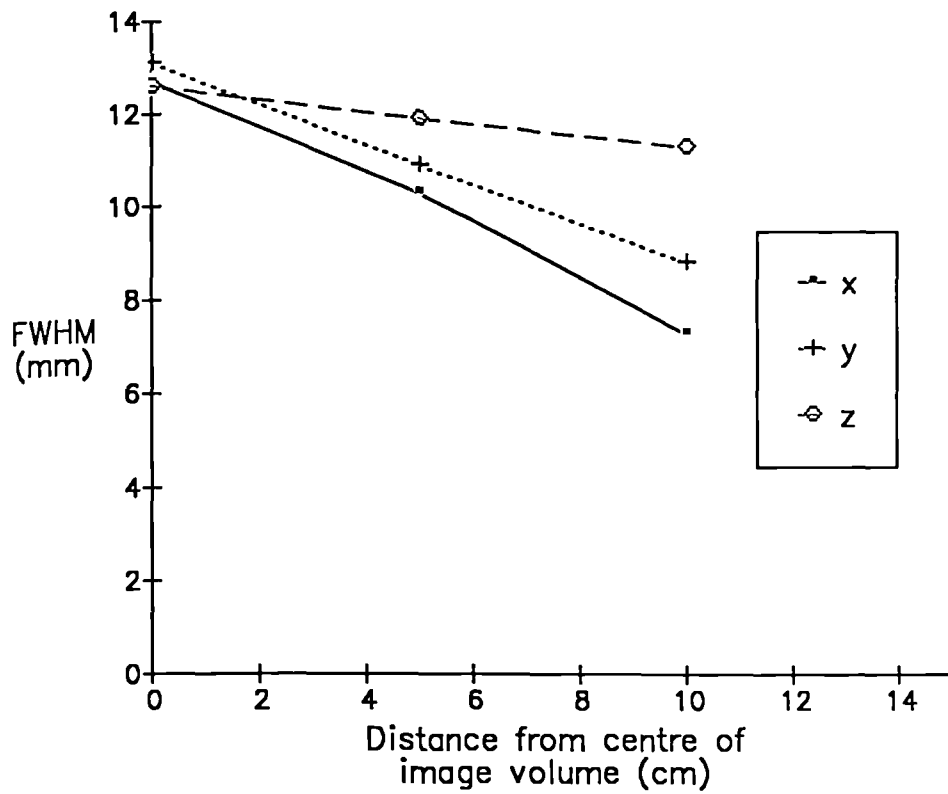


Figure 5.1 Variation of the FWHM of the SPSF, measured along the three coordinate axes, with distance from the centre of the image volume. The ROR was 13cm.

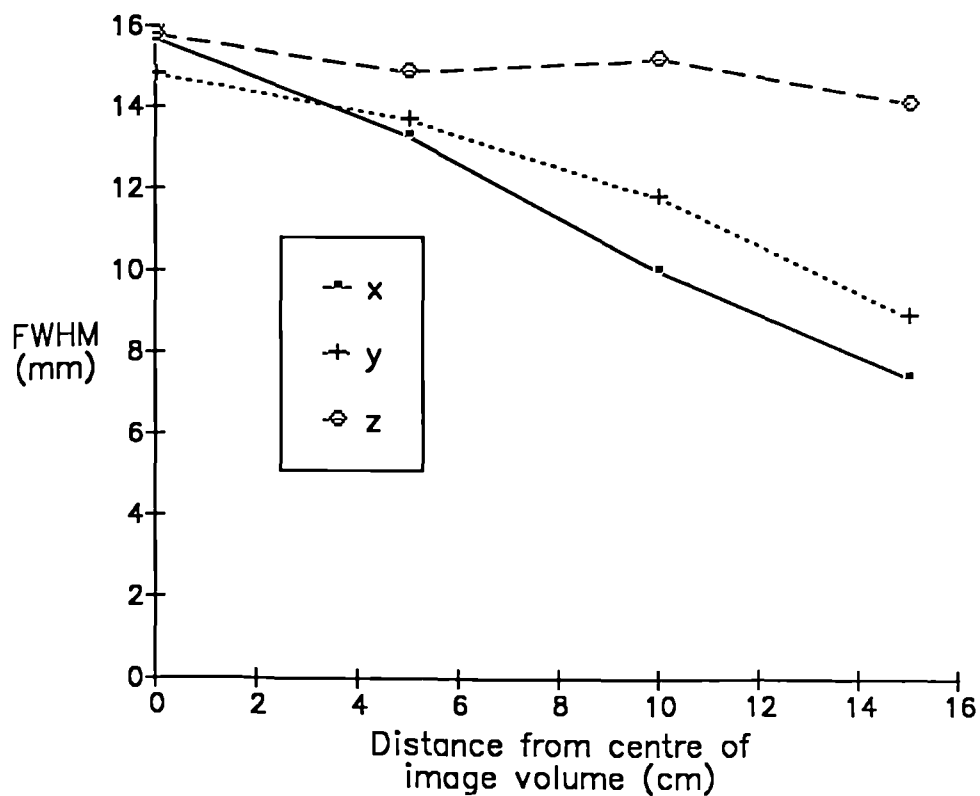


Figure 5.2 Variation of the FWHM of the SPSF, measured along the three coordinate axes, with distance from the centre of the image volume. The ROR was 20cm.

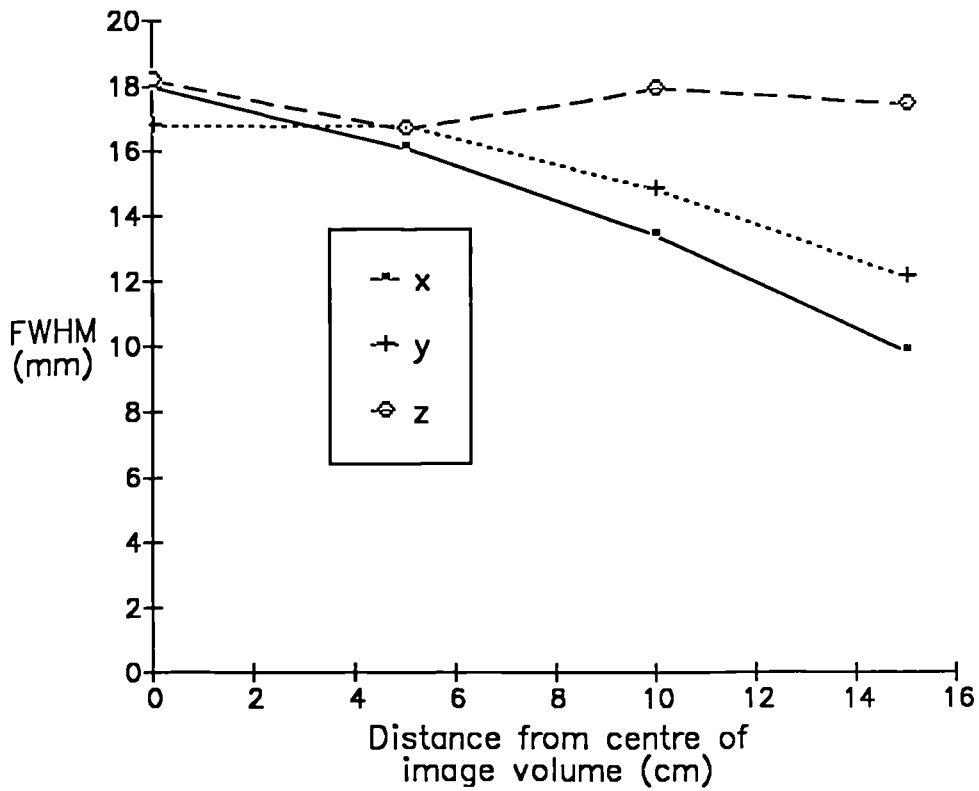


Figure 5.3 Variation of the FWHM of the SPSF, measured along the three coordinate axes, with distance from the centre of the image volume. The ROR was 25cm.

they are dependent on different aspects of the SPECT process. As the y axis is perpendicular to the reconstruction plane the resolution in this direction is more a measure of the effective section thickness for the SPECT study. The resolution in the x direction however is more directly dependent on the reconstruction process because it is within the reconstruction plane.

5.2.6 Discussion

Effectively, this set of measurements has determined the variation in the three-dimensional shape of the SPSF with position within the image volume for a range of ROR values.

Using the circular symmetry inherent in the imaging process we can determine the shape of a two dimensional cross-section through the SPSF in an axial plane for a source position anywhere within the image plane. This is shown schematically in figure 5.4 where the lines represent the locus of FWHM values for a particular source position. This illustrates the observation that the SPECT resolution improves in a direction tangential to the surface of the image volume when the source position is displaced from the centre of the image plane. However, the resolution when measured along a radial axis (i.e. perpendicular to the tangential direction) remains relatively independent of source position. Thus the SPSF is circular in shape at the centre of the image plane but becomes elliptical (or more accurately pear shaped) as it is displaced radially. Also, for coronal and sagittal sections the resolution in the y direction will improve if the source position is closer to the surface of the image volume.

All of the above effects can be explained by the fact that

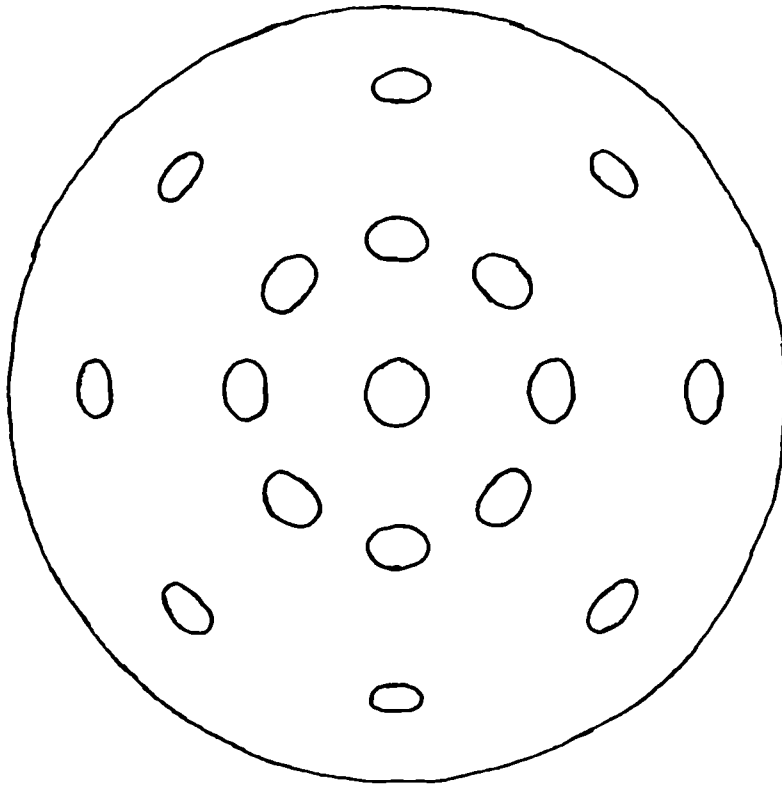


Figure 5.4 A schematic illustration of the variation in the shape of the SPSF with position in the image volume. The perimeter of the image volume is represented by the large circle. The shapes within this represent the locus of FWHM values of the SPSF at that particular position.

when the source position is close to the surface of the image volume the source-camera distance will be small for a large fraction of the camera's orbit. The improvement in resolution which occurs with a reduced source-camera distance is responsible for the lower FWHM values which were observed.

The difference in resolution between the radial and tangential directions is of relevance clinically and should be accounted for particularly in the interpretation of brain images.

5.2.7 Variation of SPECT resolution with ROR

A further relevant aspect of these results is the way in which the FWHM values vary as the ROR is increased. For example, it would be useful to know in the clinical situation what magnitude and pattern of resolution degradation to expect for any given increase in ROR.

The variation of the FWHM values of the SPSF with the ROR along the three coordinate axes are shown in figures 5.5, 5.6 and 5.7. The variation is shown for each position of the point source within the image volume which described in terms of its displacement from the COR.

In general it can be seen that the FWHM values for all three coordinates increase with the ROR and that the rate of increase appears to be roughly independent of source position and the direction in which it is measured. Thus, an increase in the ROR of 5cm will increase the FWHM in the x direction by 2.4 ± 0.5 mm, in the y direction by 2.4 ± 0.7 mm and in the z direction by 2.5 ± 0.5 mm (these figures being obtained from an average of all the differences between the measured values).

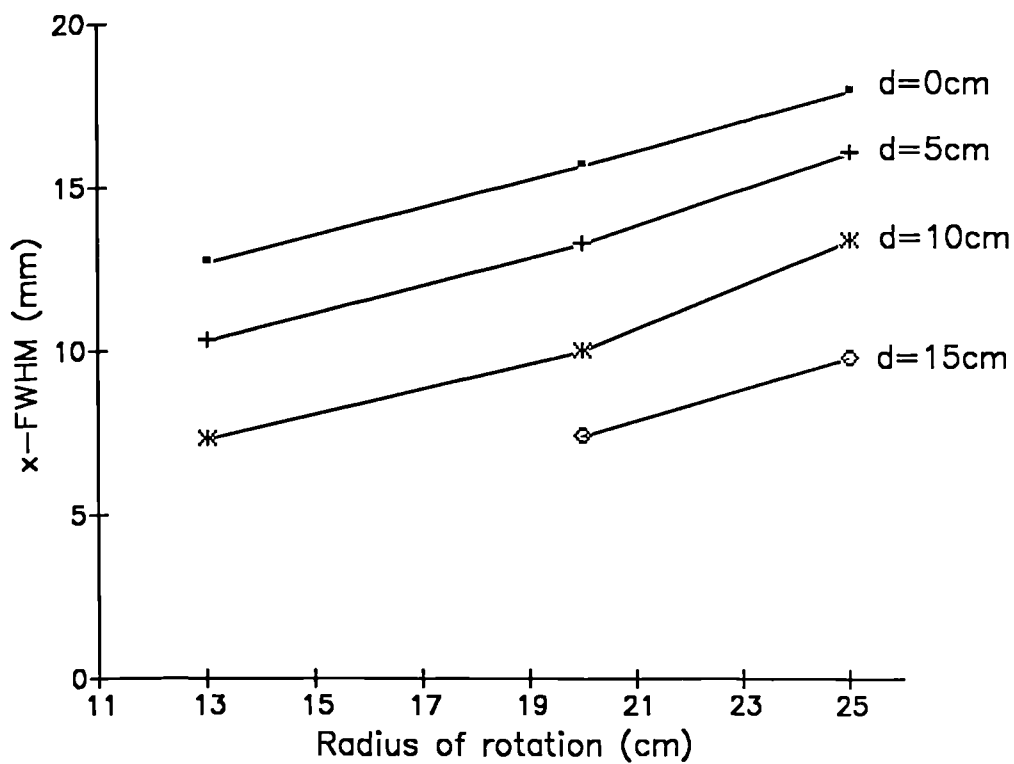


Figure 5.5 Variation of the FWHM of the SPSF when measured in the x-direction with ROR and distance, d, from the COR.

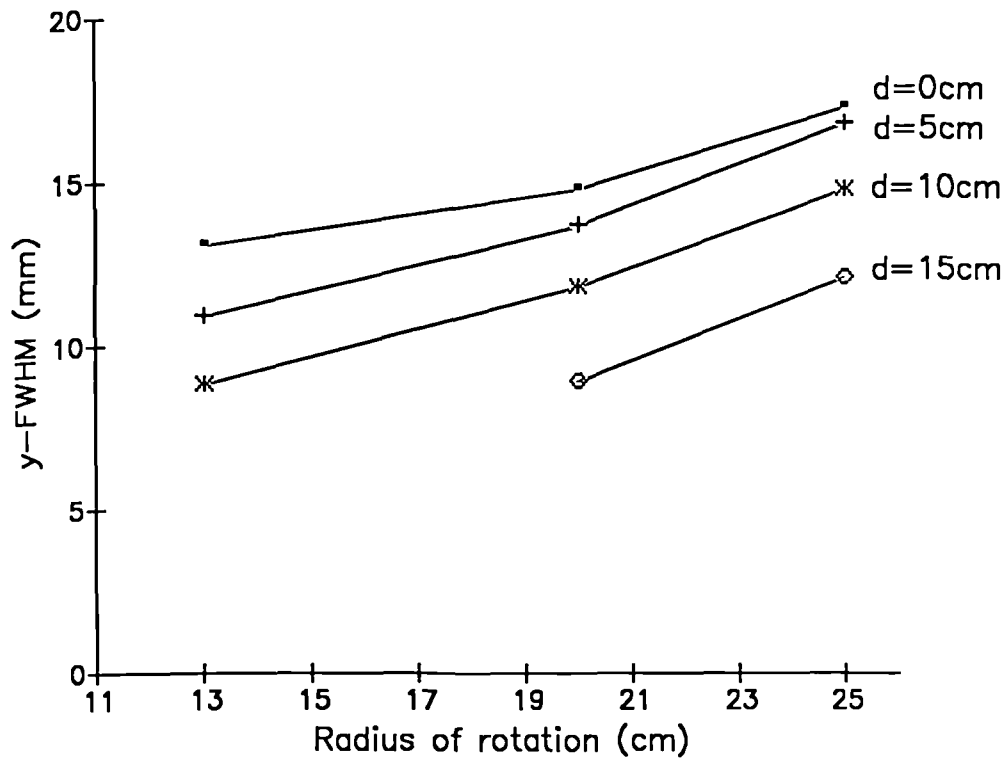


Figure 5.6 Variation of the FWHM of the SPSF when measured in the y-direction with ROR and distance, d , from the COR.

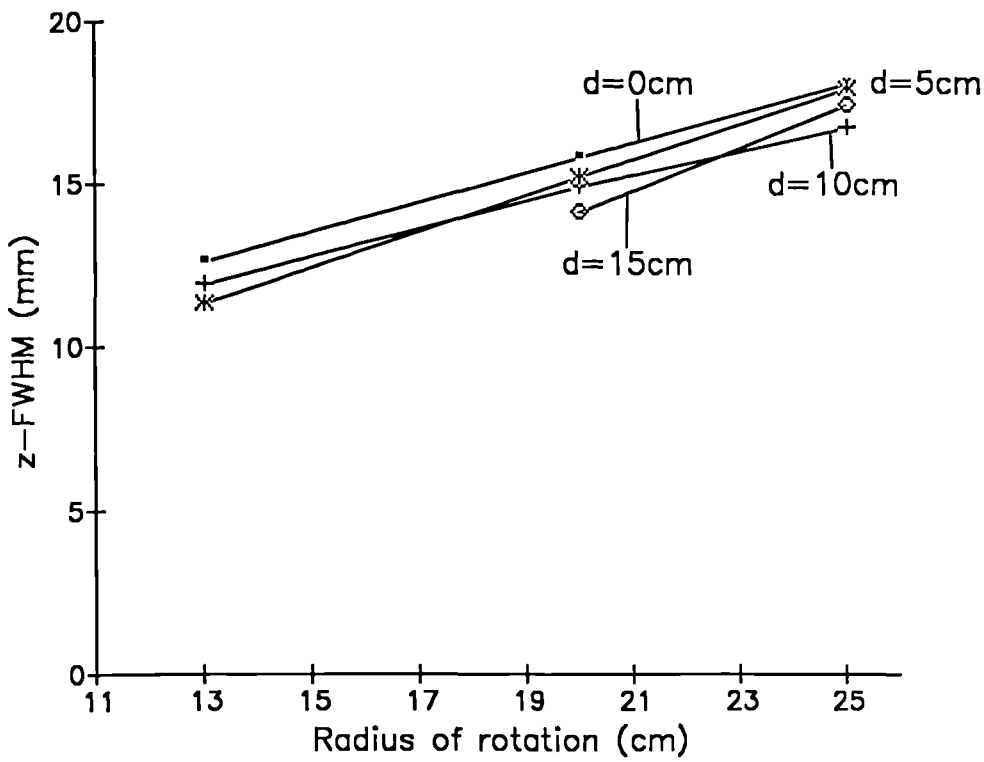


Figure 5.7 Variation of the FWHM of the SPSF when measured in the z-direction with ROR and distance, d, from the COR.

5.3 SPECT Line Spread Function Measurements

5.3.1 Introduction

The behaviour of the SPECT LSF (SLSF) was also investigated. This is defined to be the function which is obtained when a thin transaxial section is taken through a line source. It is useful to derive this function in order to enable direct comparisons to be made between measurements made in air and in a scattering medium (it is difficult to produce a point source in a scattering medium but a line source can be produced easily).

5.3.2 Methods

A line source was created using a glass capillary tube with an inside diameter of 1mm and an active volume 10cm long. This was fixed to the end of the SPECT bed so that the active volume was effectively suspended in air. A solution of ^{99m}Tc of specific activity 600MBq per ml was used giving a countrate of around 6000 cps for the LEAP collimator.

SPECT acquisitions of the line source were performed using 128 angles and 128*128 projection image data. The LEAP collimator was used. The position of the source within the image volume and the ROR were varied.

The data were reconstructed in the first instance using the ramp filter. Six transaxial sections two pixels wide were taken through the central segment of the line source. Profiles one pixel thick were taken through each of the six sections in the x and z directions. The FWHM values of the profiles were calculated. The mean value and the standard error were determined from the six values.

5.3.3 Results

A very similar pattern to that observed for the SPSF data is observed for the SLSF measurements. The results are shown in figures 5.8 and 5.9. The SLSF FWHM values tend to be slightly larger (the average difference is less than 1mm and the maximum difference is less than 2mm).

In fact the increase in statistical accuracy obtained with the SLSF data produced information which was better behaved than the SPSF data. For example a small but consistent fall in the FWHM of the z coordinate can be observed with increasing values of the displacement of the source from the centre of rotation, figure 5.9. This cannot be clearly observed with the SPSF data, figure 5.7.

The FWHM values obtained when the source was positioned at the centre of the phantom were very close to those obtained for the planar LSFs for source-camera distances equal to the radii of rotation. The maximum difference between any two values was less than ten percent indicating that when the SPECT system is properly adjusted the resolution in the reconstructed images should be approximately equal to that obtained in planar images at equivalent source-camera distances.

5.3.4 Effect of lower angular sampling rates

The effect on the SLSF of using a lower angular sampling rate was investigated. The main effect of angular undersampling should be the introduction of artefacts which will be most evident for large values of the ROR and for source positions close to the surface of the image volume.

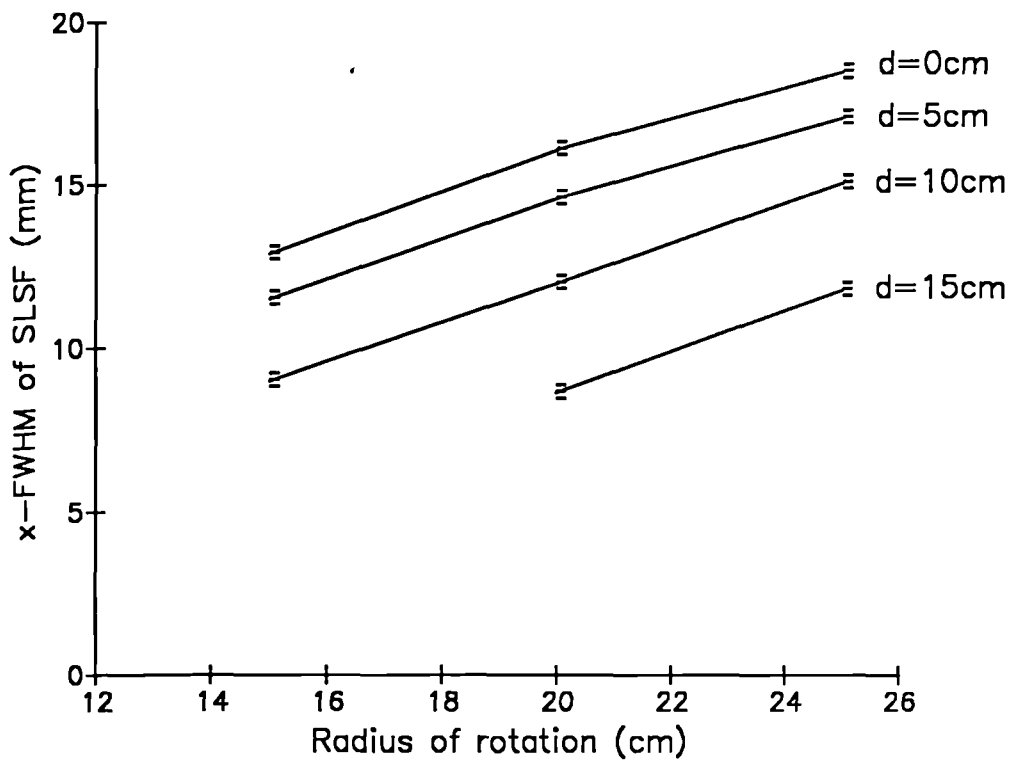


Figure 5.8 Variation of the FWHM of the SLSF when measured in the x-direction with ROR and distance, d, from the COR.

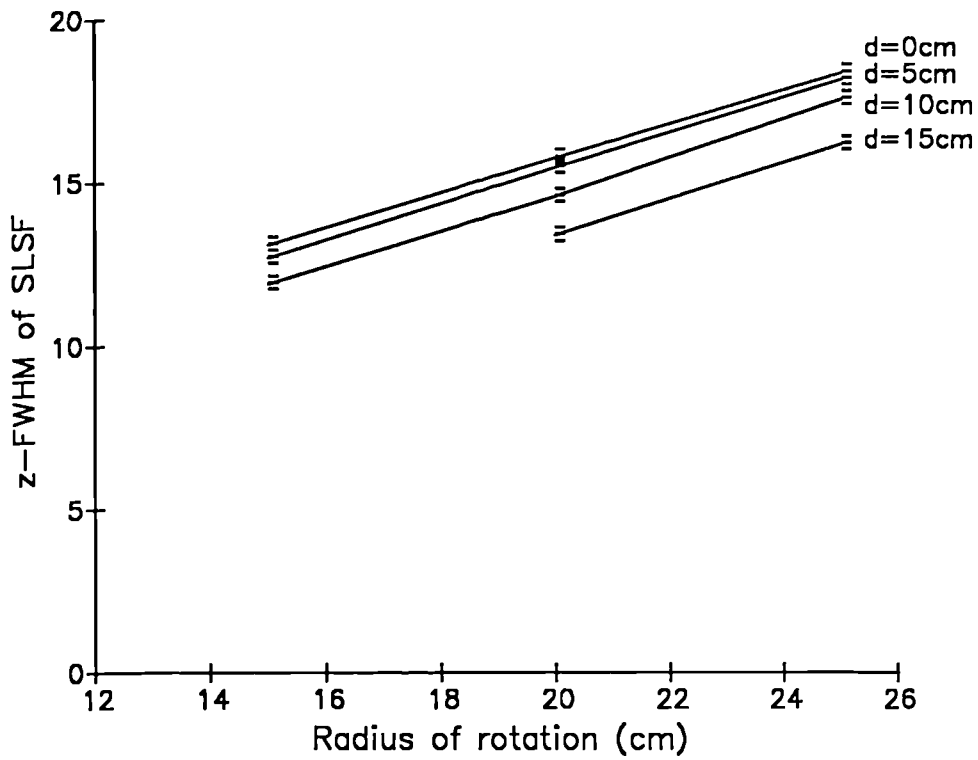


Figure 5.9 Variation of the FWHM of the SLSF when measured in the z-direction with ROR and distance, d, from the COR.

5.3.4.1 Methods

The data used in the previous analysis were altered by selecting every alternate projection image to give a study which consisted of 64 angular samples over 360 degrees (compared to the original 128). This was performed for the studies with a ROR of 25cm and source displacements from the COR of 0 and 15cm.

5.3.4.2 Results

A visual examination of the SLSFs showed no obvious differences between the studies with 64 and 128 angular samples. The quantitative analysis demonstrated no significant differences in the FWHM values. The mean difference was 0.1mm (0.4%) and the maximum 0.2mm (0.8%). The FWTM measurements might be expected to be a more sensitive measure of the presence of artefacts, however, there were still no detectable differences between the two studies the mean value being 0.1 (0.3%) and the maximum 0.2mm (0.8%).

5.3.5 Comparison of different reconstruction filters

The use of a filter other than the ramp will affect the transfer of high spatial frequencies in the reconstructed data. To quantify this effect the FWHM and FWTM values of the SLSF when reconstructed with the ramp and the soft Shepp-Logan filter were compared. The data acquired at the smallest ROR, 15cm, was used as this should contain the highest spatial frequency data.

5.3.5.1 Results

When the source was positioned at the COR the FWHM and

FWTM values in the x and z directions increased by 10% \pm 1% when the soft Shepp-Logan as opposed to the ramp filter was used.

When the source was displaced by 10cm in the z direction from the COR the FWHM and FWTM values in the z-direction both increased by 13% \pm 1%. The increase in the x direction was significantly greater at 21% \pm 2% and 25% \pm 2% for the FWHM and FWTM values.

Thus, significant reductions in the resolution of the reconstructed data were produced, as expected, from the application of the softer filter. The largest loss of resolution occurred in the tangential direction when the source was displaced radially from the COR. This is not surprising as this contained the highest spatial frequency information to begin with.

5.4 SLSF variation in amplitude

5.4.1 Introduction

In addition to the changes in shape the variation in the amplitude of the SLSF data also has an important effect on the nature of the SPECT images. A correction for the behaviour of the amplitude of the SLSF is necessary if attempts at quantification are contemplated, (Section 2.5.2). It may also be possible to improve the qualitative aspects of the images by applying a suitable correction.

5.4.2 Methods

The methods of acquisition and analysis were the same as those used in Section 5.3.2. The maximum pixel count value in

the SLSF was determined and a correction for the decay of the ^{99m}Tc between measurements was applied.

5.4.3 Results

Taking the value at the centre of the image volume as 100% the variation in the amplitude of the SLSF with position within the image volume is shown in figure 5.10.

Differences in the amplitudes of the SLSFs of the order of 50% are observed. This agrees with the data of Todd-Pokropek (1983).

The fundamental reason for the drop in the amplitude of the SLSF towards the centre of the image volume lies in the decrease in the amplitude of the planar LSF with distance from the camera. Using data from Section 4.2.4 the maximum values of the planar LSFs were determined and are shown in figure 5.11.

The use of the arithmetic mean of opposing views ameliorates the effect of the decrease in the amplitude of the planar LSF with distance. An example of this is also shown in figure 5.11 where the amplitude of a line source after combining opposing projection has been calculated from the planar data for a variety of source positions within the image volume. For a displacement from the centre of rotation of 10cm the planar data would predict that the amplitude should increase by 29%. This agrees with the measured value from the actual SPECT acquisition of $28\% \pm 1\%$.

As can be seen the use of the arithmetic mean of opposing views does not fully compensate for the drop in the value of the amplitude of the LSF with distance from the camera. This is because the drop in the amplitude of the LSF with distance

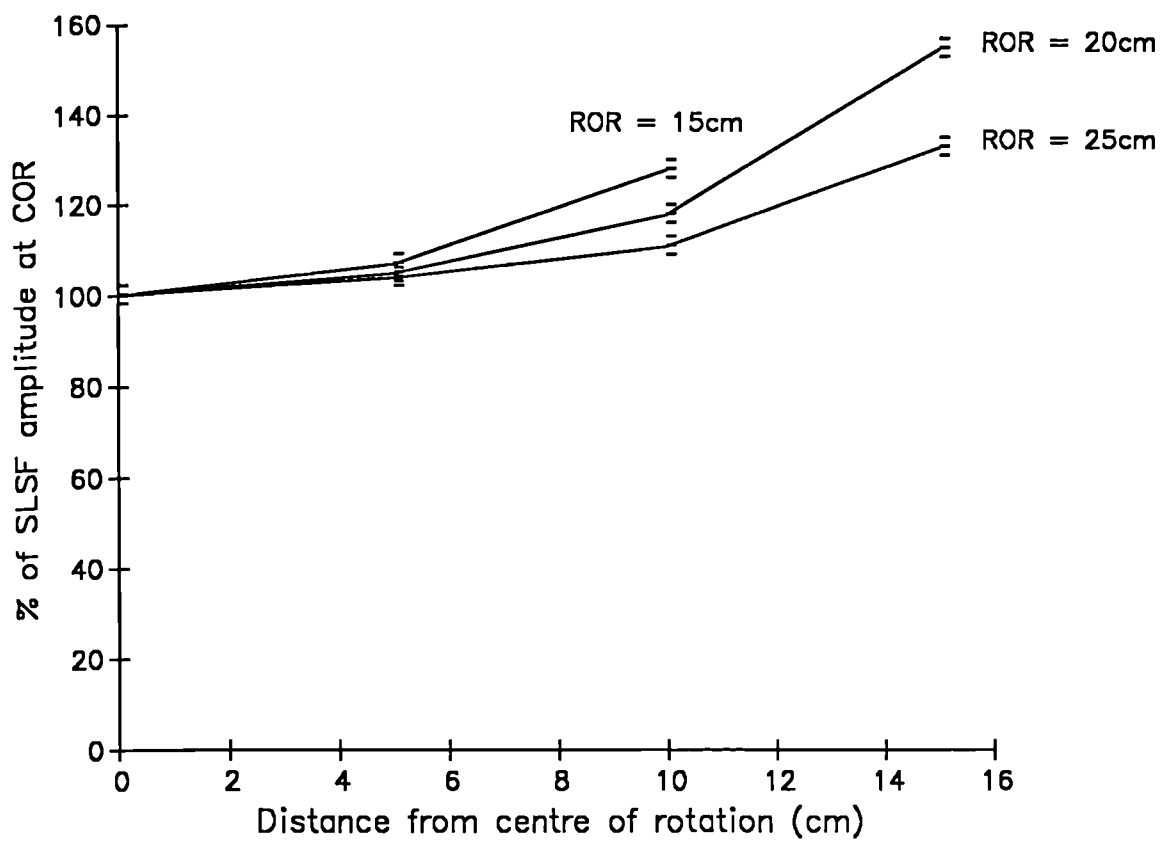


Figure 5.10 Variation of the amplitude of the SLSF with distance from the COR.

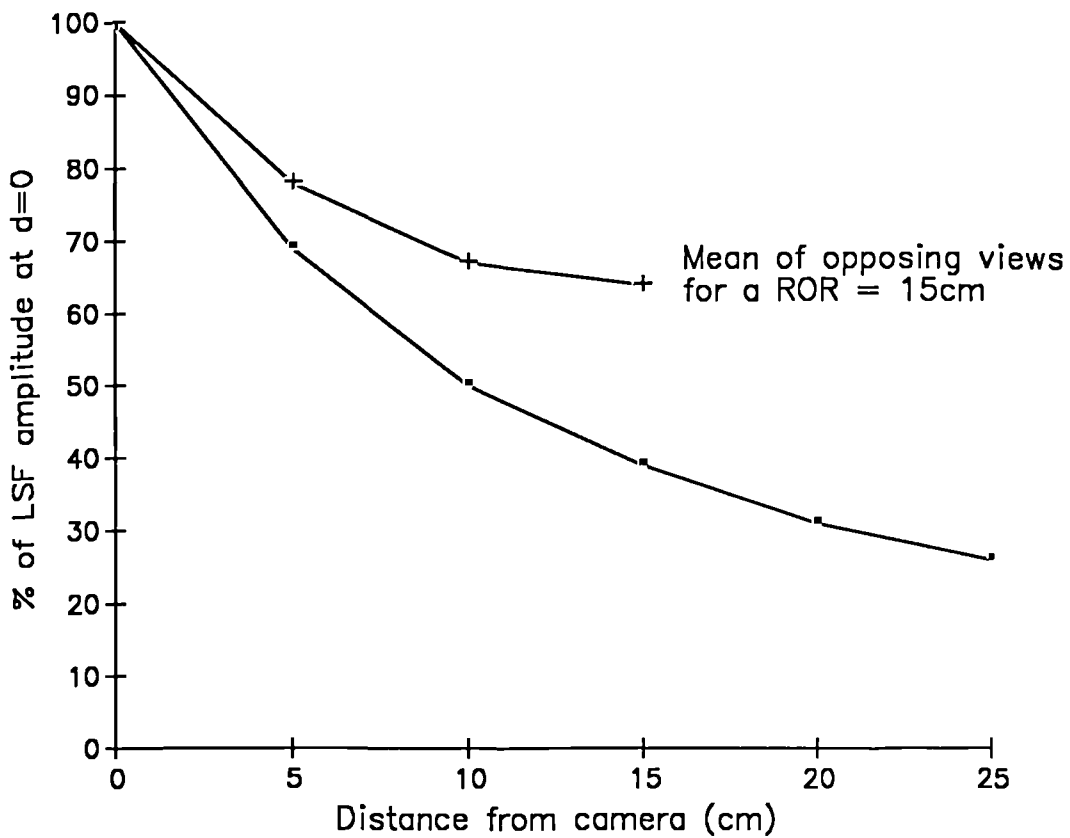


Figure 5.11 Variation of the amplitude of the planar LSF with source to camera distance. Also shown is the amplitude of the LSF which results when the arithmetic mean of opposing views in a SPECT study is taken.

is too rapid. These results do not agree with the widely stated belief that averaging opposing images produces a distance independent camera response, Ying-Lie (1983), Larsson (1982). This is because the distance effect will be particularly dependent on the characteristics of the particular collimator used.

The magnitude of the effects of the collimator response function can be estimated from this data. For the hypothetical example of a 30cm diameter object of zero attenuation (e.g. a gas) positioned at the centre of a 20cm ROR SPECT acquisition the counts from a point source at the centre of the object will be 65% of those from a point source at the edge. This is due solely to the collimator response and shows the potential additive effect to that of tissue attenuation.

It is important to recognise however that these results cannot be directly transferred to extended source data. For a uniform source distribution for example the drop in the amplitude of the SLSF with increasing source-collimator distance will be compensated for by the additional contribution which will be made from neighbouring points due to the increased spread of the planar LSF. In fact for a uniform source the response function of the camera arising from the activity at a set distance will be given by a convolution of the LSF and a step function of length equal to the source width. Thus as the area beneath the LSF is independent of distance (because it is a parallel hole collimator) the response of the camera due to the activity at different distances will only be different at the edges of the source.

For source distributions varying in type between that of a

point and a uniform distribution the effect of the collimator response will vary in importance. For example for a monoclonal antibody study a single localised region of uptake may be obtained. In this case if accurate quantification is required a correction for the collimator response will be necessary. However for a liver study there is a fairly uniform uptake over a large volume so that the effect of the collimator response will be negligible.

5.5 SPECT resolution in scatter

The previous measurements give an indication of the variation of the resolution of the SPECT system with ROR and position within the image volume. The results however, as for the planar PSF in air, are not directly relevant to the clinical situation because they do not include the effects of scatter and attenuation which will occur if the space between the source and the camera is filled with a solid medium.

5.5.1 Methods

A line source 10cm long and 1mm in diameter was used. This was filled with a high specific activity solution of Tc^{99m} (1600MBq per ml) and supported inside the SPECT phantom cylinder described in Chapter 3. The phantom cylinder was filled with water and positioned with its central axis coincident with the axis of rotation of the camera. The phantom itself was supported in the jig, also described in Chapter 3, so that it was held clear of the SPECT bed. Thus the only scattering material present was that in the phantom. The position of the line source within the phantom was determined by the location of the support holes in the two

circular perspex plates which were used to hold the source. The ADC gains were set to give pixels of side length 2.8mm for a 128*128 matrix size.

SPECT acquisitions were made of the line source using 128 projection angles with 128*128 projection image data. The position of the source within the phantom was varied as was the ROR. The minimum ROR achievable was 16cm, this being determined by the jig size.

The data were reconstructed using a ramp filter. The resolution measurements were made by taking profiles, one pixel thick through the maximum value in the SLSF. The FWHM and FWTM values of the profiles were determined as described previously.

5.5.2 Results in scatter

The FWHM values of the profiles taken through the SLSFs in the x-direction are shown for the LEAP and HR collimators in figure 5.12. The values for the profiles in the z-direction are shown in figure 5.13. The FWHM values obtained when the source was positioned at the centre of the phantom were very close to those obtained for the planar LSFs for source-camera distances equal to the radii of rotation. The maximum difference between any two values was less than ten percent, again indicating that when the SPECT system is properly adjusted the resolution in the reconstructed images should be approximately equal to that obtained in planar images at equivalent source-camera distances.

From figures 5.12 and 5.13 it can be seen that a similar pattern to that observed for the SLSF measurements made in air is obtained. The resolution in the tangential direction

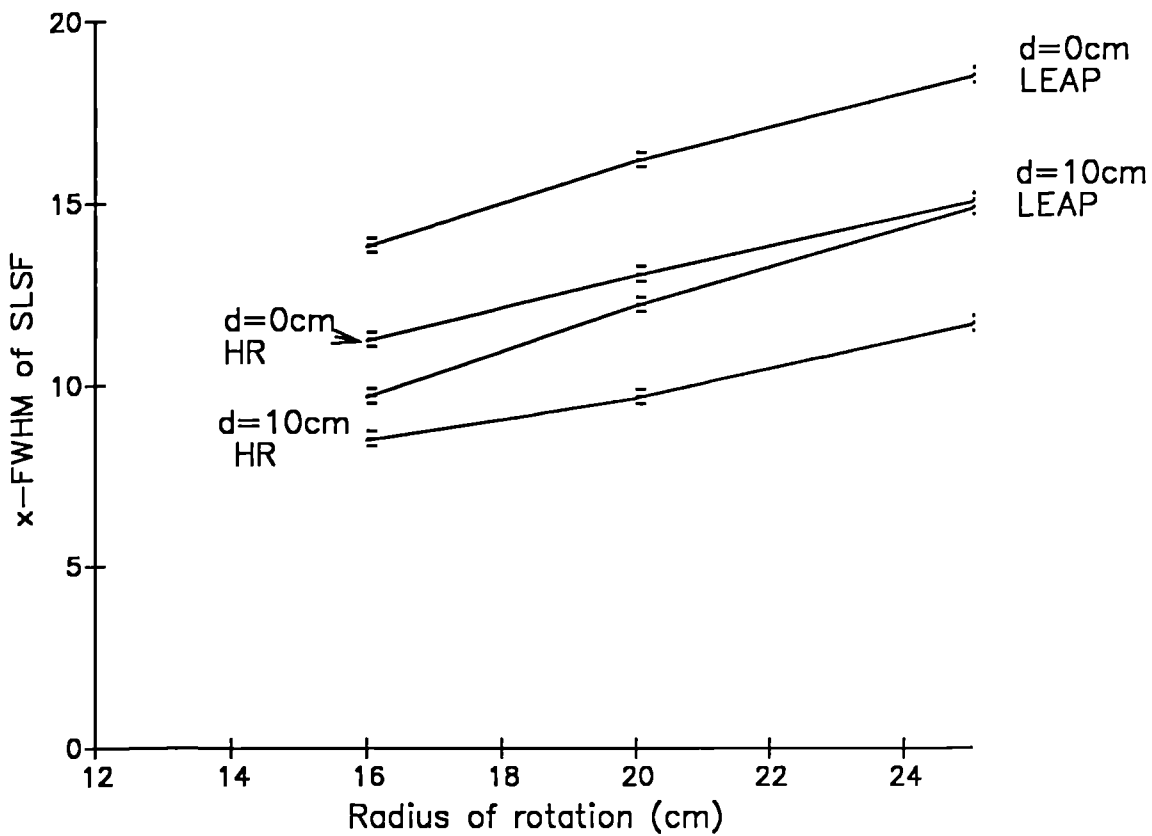


Figure 5.12 Comparison of the FWHM values of the SLSF when measured in the x-direction for the LEAP and HR collimators. The variation of the values with the ROR is shown.

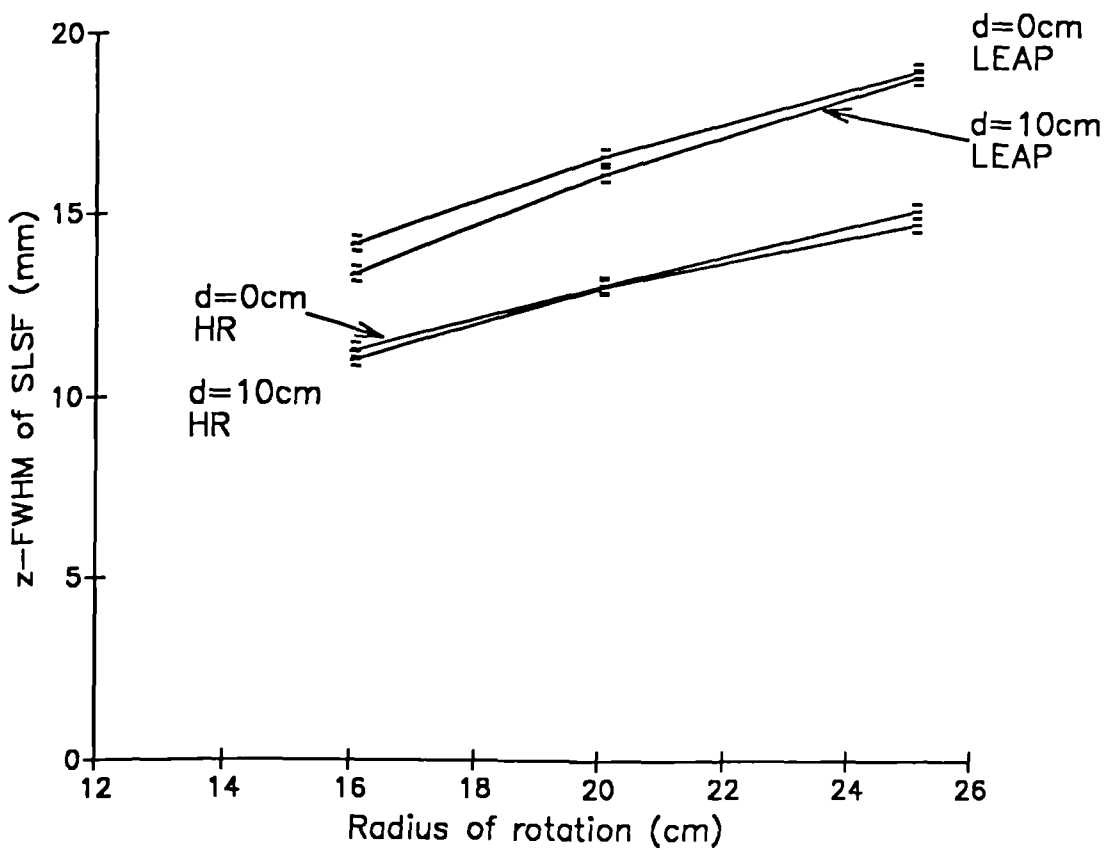


Figure 5.13 Comparison of the FWHM values of the SLSF when measured in the z-direction for the LEAP and HR collimators. The variation of the values with the ROR is shown.

improves while that in the radial direction changes only slightly as the position of the source is moved towards the edge of the object. In fact the differences in the FWHM values of the individual SLSFs when measured in air and scatter are very small. The mean difference between the air and scatter measurements of the FWHM values for the LEAP collimator is 0.7mm (4%) with the largest difference being 1.5mm. As the main effect of the presence of scatter is to add "tails" to the planar LSFs (figure 4.20) it may be expected that differences between the air and scatter SLSFs may be seen in the FWTM values. However, the differences between the measured FWTM values were still small with a mean value of 1.7mm (5%) and a maximum value of 3.2mm (10%).

A close examination of the shape of the SLSFs showed that there were tails to the SLSFs when measured in scatter but that their amplitude and extent were much lower than those found for the planar LSFs. This can be seen in figures 5.14 and 5.15 where the profiles in the x-direction through the SLSFs obtained with the source at the COR in air and scatter respectively are shown. A ROR of 16cm was used. This effect was also observed by Mueller (1986) and King (1986).

The reasons for the relative absence of the tails to the SLSFs are not clear. One factor will certainly be that because the minimum ROR achievable was 16cm there was an air gap of 6cm between the edge of the phantom and the camera. Thus the resultant planar LSFs in the projection images will be given by a convolution of the LSF in air at 6cm with the LSF in scatter at 10cm. The use of a larger phantom may make the importance of the scatter component to the SLSF more evident.

From figures 5.12 and 5.13 the effect of using the HR

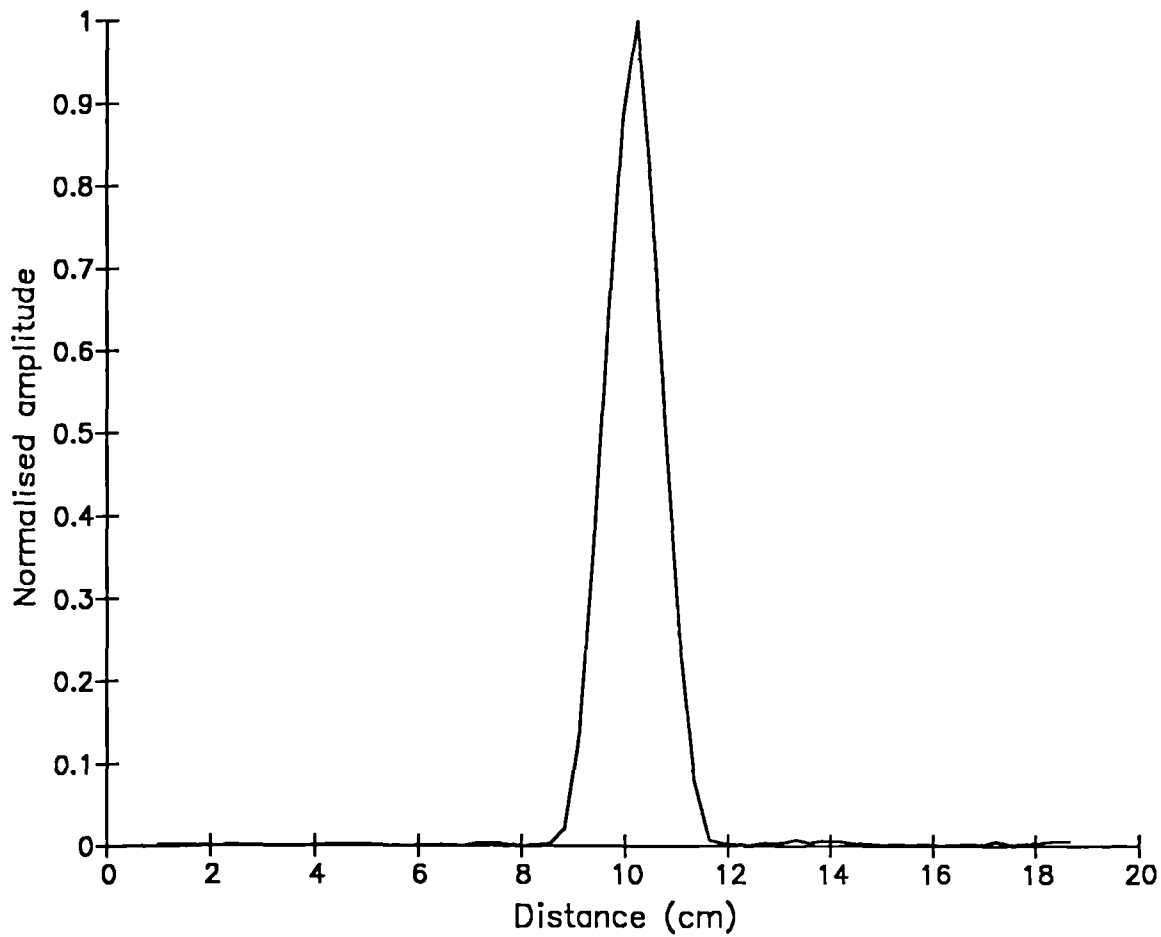


Figure 5.14 Profile through the SLSF in the x-direction at the COR. The measurement was made in air.

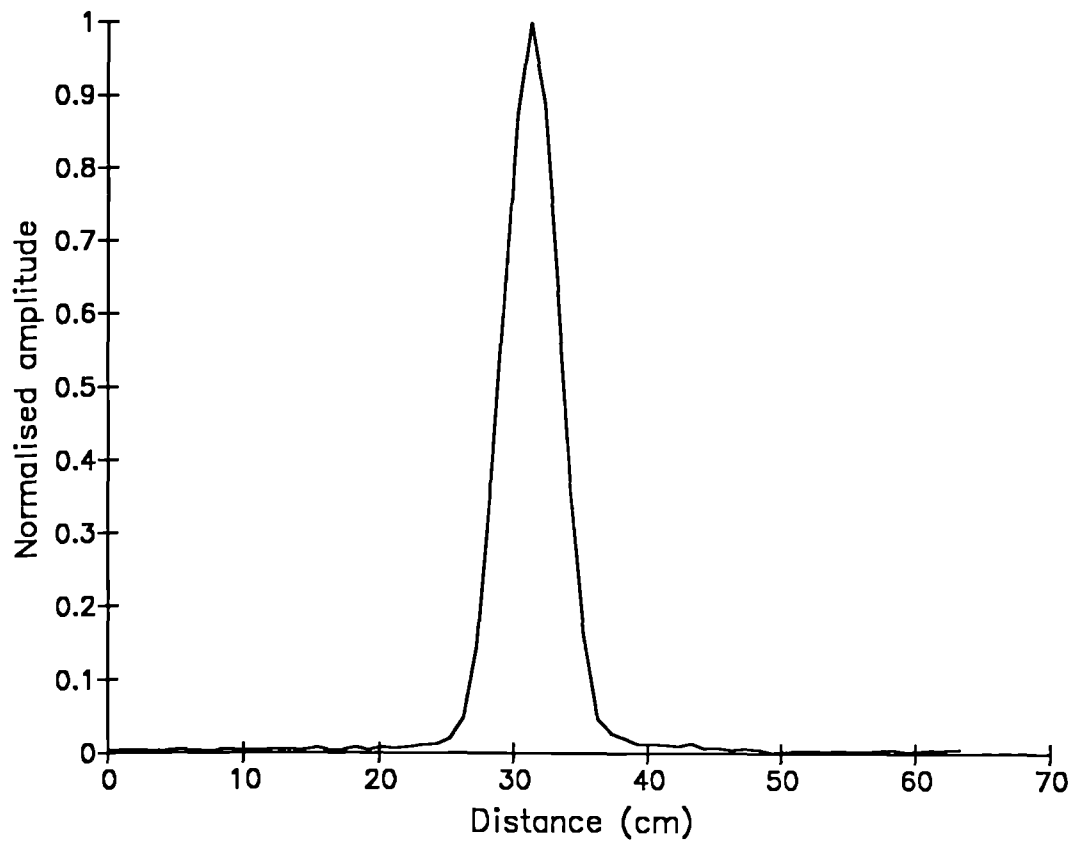


Figure 5.15 Profile through the SLSF in the x-direction at the COR. The measurement was made in scatter.

collimator can be assessed. A significant difference from the FWHM values obtained with the LEAP collimator was observed, the mean difference being 2.9mm (20%) and the maximum 6.2mm (27%). This is similar to the situation which was observed with the planar data, figure 4.10.

5.6 Conclusions for Chapter 5

1. The resolution within a SPECT image varies with the direction in which it is measured and with distance from the COR. The resolution measured in a direction tangential to the surface of the image volume improves with distance from the COR. However, the resolution measured along a radial axis is relatively independent of source position. Thus, the SPSF is circular in shape at the centre of the image plane but becomes elliptical as it is displaced radially.

2. The FWHM of the SPSF increases as the ROR is increased. The rate of increase of the FWHM with the ROR is roughly independent of the source position and the direction in which it is measured. Thus, for the LEAP collimator, an increase of 5cm in the ROR will increase the FWHM of the SPSF throughout the image volume by approximately 2.5mm.

3. When the source was positioned at the COR the FWHM values of the SPSF were very similar to those obtained for the planar LSF at a source to camera distance equal to the radius of rotation. This indicates that when the SPECT system is properly adjusted the resolution in the reconstructed images should be approximately equal to that obtained in planar

images at equivalent source camera distances.

4. No significant differences between the SLSFs obtained with 64 as opposed to 128 projection angles were observed.

5. The FWHM of the SLSF, for a source at the COR, increased by 10% when the soft Shepp-Logan as opposed to the ramp filter was used. The effect of the softer filter was more apparent when the source was close to the surface of the image volume. At a distance of 10cm from the COR the FWHM of the SLSF increased by 21% when the soft Shepp-Logan filter was used.

6. A decrease in the amplitude of the SLSF was observed as the source was positioned close to the COR. This is caused by the reduction in the amplitude of the planar LSF with increased source to collimator distances. This fall in amplitude was only partly compensated for by taking the arithmetic mean of opposing projection images.

The effect of the variation of the amplitude of the planar LSF on a SPECT study of an extended source will depend on the form of the source distribution. For distributions which are uniform in nature the above effects will be of less importance than for distributions which are highly localised.

7. When the SLSF was measured in a scattering medium the variation with position in the image volume was similar to that obtained in air. In fact the differences between the individual SLSFs when measured in air and scatter were small.

8. From a comparison of the behaviour of the collimators in

8. From a comparison of the behaviour of the collimators in the presence of scatter it was concluded that the resolution differences were small for low ROR values and object positions distant from the COR but increased with larger ROR values and object positions close to the COR. Thus it would appear that there may be advantages to be gained from using the HR collimator for clinical situations where a large ROR is required and the organ of interest is centrally located. Whether the loss of sensitivity which would result from this is justified by the gain in resolution is a separate question. This will be investigated in Chapter 9.

Chapter 6 Scatter discrimination and attenuation correction

6.1 Introduction

While the examination of the behaviour of point and line sources provides useful information about some of the fundamental aspects of the SPECT imaging process, not all of the factors which are of importance can be investigated. A full examination of SPECT can only be performed using extended source distributions. In this chapter extended source distributions will be used to examine the effects of scatter and attenuation and to investigate methods for their correction. In effect this is an approach to the first step in the parameter optimisation chain, described in Chapter 1, i.e. to determine the best way to select photons of the appropriate energy.

Thus, this chapter will include a full description of the effects of scatter, the use of an asymmetric energy window and the use of a scatter correction method which uses a low energy window to subtract counts from the photopeak. The Bellini attenuation correction algorithm will also be investigated.

6.2 Asymmetric energy windows

6.2.1 Introduction

It is the aim of this work to determine the best approach to counter the reduction in image quality which is caused by the inclusion of scattered photons within the the acquired image data. The problem of accurate quantification of regional radionuclide concentration is a separate and difficult one which is outwith the scope of this investigation .

In addition to the primary radiation, emitted gamma rays comprise photons which have undergone Compton scattering within the object. Although the energy of the scattered photons is lower than the energy of the primary radiation, the finite energy resolution of the detector means that a portion of the scattered radiation will be included within the photopeak energy window. The scattered photons can produce large numbers of falsely positioned events introducing a low frequency blurring the main effect of which is to reduce image contrast and hence lesion detectability in qualitative imaging.

The inclusion of photons which have been scattered through relatively large angles might also be expected to reduce the resolution of the system. However the resolution of the system is dominated by the intrinsic resolution and the geometrical characteristics of the collimator. The inclusion of scattered photons changes the shape of the system's PSF mainly by broadening its tails : the FWHM for example changes only slightly, Section 4.2.4.4. In frequency space the MTF shows little difference at high spatial frequencies but significant differences at low spatial frequencies 4.2.4.5. Thus the inclusion of scatter does not affect the transfer of high spatial frequencies per se, however, lesion detectability as a whole is reduced because of the loss of contrast due to the broadened tail of the PSF .

In general, the blurring function due to scatter, the scatter point spread function (SPSF), is spatially variant, depending on the distribution of attenuating structures and the activity concentration within the object. Thus a rigorous solution to the scatter problem, applicable to the general

case, is extremely difficult. However, there are a variety of reasonable approaches which go some way towards avoiding or correcting for the effects of scatter and which are simple enough to be appropriate for routine application.

The most direct approach is to offset the energy discrimination window towards the high side of the photopeak, which is considered here.

6.2.2 Conventional energy window selection.

The energy of the photopeak of ^{99m}Tc occurs at 140.6 keV. The energy resolution of modern gamma camera ranges from 10% to 15% as measured by the FWHM of the photopeak spectrum, Elliott (1986). Typically, the energy discrimination window is centred on the photopeak energy and varies in width between 15% and 20% . This means that the lower edge of the window is typically positioned between 126.5 and 130 keV which can result in scattered radiation comprising a substantial proportion of the total counts. It should also be noted that a photon which has been Compton scattered through an angle of 45 degrees will only have lost 10keV of its original energy . Thus photons scattered through relatively large angles will not be discriminated against by the conventional window selection .

In this work an energy window width of 15% has been selected. Wider energy discrimination windows were often used with older designs of gamma camera, Jaszczak (1985). However, as the energy resolution of the Orbiter is 10.1%, Section 4.2.2, a window width of more than 15% would be inappropriate.

6.2.3 Offset energy discrimination windows.

The most direct way to reduce the influence of scatter is to shift the lower threshold of the energy discrimination window to the upper part of the total absorption peak, Atkins(1977), Sanders(1971). This topic was extensively investigated in the early 1970's, Lange (1972), Bloch (1973), however, there is very little data on the behaviour of gamma cameras of modern design. The development of energy and linearity correction techniques may permit the use of offset energy windows without the loss of uniformity which occurred with the older systems

6.2.3.1 Disadvantages of offset energy window

There are several disadvantages associated with the use of an offset energy window. For example, some non-scattered photons will be excluded in addition to scattered photons. This will increase the statistical variations in the acquired data.

Also, the elimination of photons may not occur uniformly over the camera face. Events which occur between photomultiplier tubes (PMTs) may be disproportionately discriminated against because they will tend to produce a lower light output and so produce a lower energy signal than events which occur directly beneath a PMT.

However, in modern gamma cameras this effect may be reduced because the energy correction circuitry has been designed to ensure that the energy signal is independent of the location of the original photon event, Section 3.2. Thus if an event is detected at a particular position the energy is altered by a predefined value to compensate for variations in

the collection and conversion of the scintillation photons over the crystal face .

Even with energy correction circuitry, however, substantial local sensitivity variations can occur if individual PMT gains drift differentially with respect to the average gain drift of the set. These variations are mild for on peak imaging and produce about a 1% loss in sensitivity per keV for the ^{99m}Tc photopeak. Substantially greater sensitivity variations are present for off peak imaging; these effects were found to be greater than 8% per keV when there was a shift of the energy discrimination window of 7keV, Stoub (1986). Thus for most cameras the magnitude of the non-uniformity introduced by the use of an offset energy window will depend on the state of tune of the camera at that particular moment. However the presence of the DIGITRAC tune control facility on the Siemens Orbiter, described in Chapter 3, maintains the camera in a state of near optimal tuning at all times. Thus with this particular design of camera there would appear, in theory, to be an opportunity to perform studies with an offset energy window without the previously debilitating effects on uniformity.

Finally, with an offset energy window some scattered photons will still be included in the signal. Thus if quantitative accuracy is required a method for correcting for scatter will have to be employed in any case. It is arguable therefore that if quantitative accuracy is necessary then it may be as well to use a symmetric window, avoiding the previously described problems, and to attempt to develop a suitable correction technique.

6.2.4 Literature review

The use of asymmetric energy windows was investigated at an early stage in the development of nuclear medicine, Beck, (1969). Because the use of an asymmetric window reduces the number of counts in the image, if the total time is held constant, considerable effort was employed in the determination of optimal window settings, Rollo (1971). There is a compromise, for any given imaging situation, between the improvement in spatial resolution and contrast, and the increase in image noise. No single window setting can be optimal for all imaging situations because of the variation in the amount of scatter which is present. It is worth noting, however, that the optimal baseline setting, as measured by statistical criteria, is a slowly varying function of the scatter fraction and it has been suggested by Atkins (1977) that a single window setting may be close to the optimal value for all patients undergoing a specific type of scan (e.g. a liver scan or a brain scan).

Although asymmetric windows were used for early models of cameras, subsequent improvements in spatial resolution and uniformity meant that their selection produced images of unacceptably high field non-uniformity. Subsequent developments however, in particular the introduction of special electronic circuits to correct for variations in the location of the photopeak across the face of the crystal, brought about renewed interest in the reduction of scatter by this technique. Lewellen (1982) used a series of disks to study improvements in edge sharpness and contrast. More recently Collier (1984) reported improved qualitative and quantitative results with the use of asymmetric windows in a

series of bone imaging studies. The effect of different levels of asymmetry on spatial resolution and uniformity was investigated by Graham (1986) who found that most of the improvements in resolution occurred with small degrees of asymmetry which did not introduce unacceptable levels of non-uniformity.

Surprisingly, very little has been published on the use of asymmetric energy windows for SPECT imaging. One reason for this may have been the concentration on absolute quantification which requires a correction for scatter to be made in any case. If one is not interested in absolute quantification it would appear that the use of asymmetrical energy windows could improve image quality in SPECT.

6.2.5 Uniformity loss with window offset

As discussed previously one of the major reasons for the lack of use of asymmetric energy windows imaging is the loss of uniformity which occurs. Good uniformity is fairly important for planar imaging but it is an extremely critical component of camera performance when SPECT studies are performed, Section 2.5. A camera non-uniformity as small as 1% relative standard deviation can produce disturbing and misleading artefacts in SPECT images. An artefact of this type generally appears as a central hot spot or cold spot in the image although it may also take the form of a concentric hot or cold ring, Rogers (1982). The amplitude of the artefact is related to the amplitude of the camera non uniformity, but it also depends strongly on the distance, r , from the non-uniform region to the axis of rotation as detected by the camera, being maximum if the non uniform region overlies the detected

axis, and decreasing in proportion to the inverse of the square root of r , for regions at a distance from the axis, Shepp (1982). The on axis non-uniformities produce the hot or cold spots, while the off axis defects produce the rings, which are much less disturbing because of their lower amplitudes, Shepp (1982), Rogers (1982).

6.2.5.1 Measurement of uniformity loss with window offset

The flood source described in Section 3.6 was used to make the measurements of camera uniformity. Before each measurement a small point source of ^{99m}Tc was placed centrally beneath the camera face. It was supported about 15 cm from the floor to avoid back scatter and the camera was moved to its maximum height. Thus the camera-source distance was about 2.5m. The collimator was taken off of the camera and the camera peaked using the scatter free source. The DIGITRAC tune status check was run so that the central field of view was tuned to within 0.7%. Thus the camera was in a state of optimal tuning for each measurement.

The flood source was placed in front of the camera and a thirty million count image acquired. To test the variation of uniformity with window offset the centre of the photopeak was moved by a certain percentage and a further thirty million count acquisition performed. This was repeated with 10cm of perspex interposed between the flood source and the camera.

The data were analysed as described in Section 4.2.5.

6.2.5.2 Results

The results of the effects on camera uniformity of off-

peak energy window selection are shown in Tables 6.1 and 6.2. The patterns shown by the coefficient of variance values and the percentage of pixels within 5% of the mean value are very similar. There is a deterioration in uniformity with increasing values of energy window offset both in the presence of scatter and in the scatter free situation. For higher values of offset the uniformity in the presence of scatter is superior to that measured in the scatter free situation. This is because the blurring effect of the scattered photons effectively smooths the resultant image.

In general terms the uniformity of the camera when a symmetric energy window was used was superior to a range of other cameras of modern design, Elliott (1985,1986). The results obtained from the 3% window offset were still comparable to values obtained using symmetric windows in the best of the cameras tested in the previous references. Even at an offset value of 6% the uniformity was comparable to most of the cameras tested.

Thus, it can be concluded that there is a significant deterioration in the uniformity of the camera's response when an offset energy window is used. This is despite the ameliorating effects of the DIGITRAC facility. The level of non-uniformity introduced would be expected to compromise SPECT image quality to a significant degree, particularly for the 6% offset value.

However, the levels of non-uniformity for this camera, even for the worst case of a 6% window offset, still compare favourably with the values obtained with symmetric windows using many of the models of camera in common use for SPECT imaging.

	Energy window offset		
	0%	3%	6%
CoV (air)	1.6%	2%	2.7%
CoV (10cm perspex)	1.5%	1.7%	2%

Table 6.1 The uniformity of the camera was measured at energy window offset values of 0%, 3% and 6%. The measurements were performed in air and with 10cm of perspex interposed between the camera and the source. The parameter used to quantify the uniformity is the CoV.

	Energy window offset		
	0%	3%	6%
Pixels within 5% (air)	99.7%	98.1%	93.4%
Pixels within 5% (10cm perspex)	99.4%	99.3%	98.9%

Table 6.2 The uniformity of the camera was measured at energy window offset values of 0%, 3% and 6%. The measurements were performed in air and with 10cm of perspex interposed between the camera and the source. The parameter used to quantify the uniformity is the percentage of pixels with count values within 5% of the mean.

6.2.6 Assessment of sensitivity loss with window offset.

The use of an offset window means that photons which would otherwise have been included in a study are rejected. Some of these photons will have been scattered and some will not. Before a sensible choice of window offset can be made some measurements have to be made of the magnitudes of these losses.

6.2.6.1 Methods

The camera was peaked with the collimator off using a scatter free source with a 15% energy window. The background countrate was assessed for a range of energy offset values.

A small source of ^{99m}Tc was placed 40cm from the camera face, again with the collimator off, and the time taken to acquire 200,000 counts noted from the camera console. This was performed for a range of energy window offsets which can be specified by defining a shift of the discriminator from its original position in terms of a percentage of the central value, Section 3.2. This process was repeated with increased scatter fractions by placing 5cm and then 10cm of perspex between the source and the camera. At all times the countrate was below 5,000 counts per second.

This procedure was repeated with the LEAP collimator in place and also for a series of symmetrical energy windows with a variety of widths.

6.2.6.2 Results

The loss of sensitivity with energy window offset is shown in figure 6.1 for the different levels of scatter in the detected radiation. The sensitivities for the different

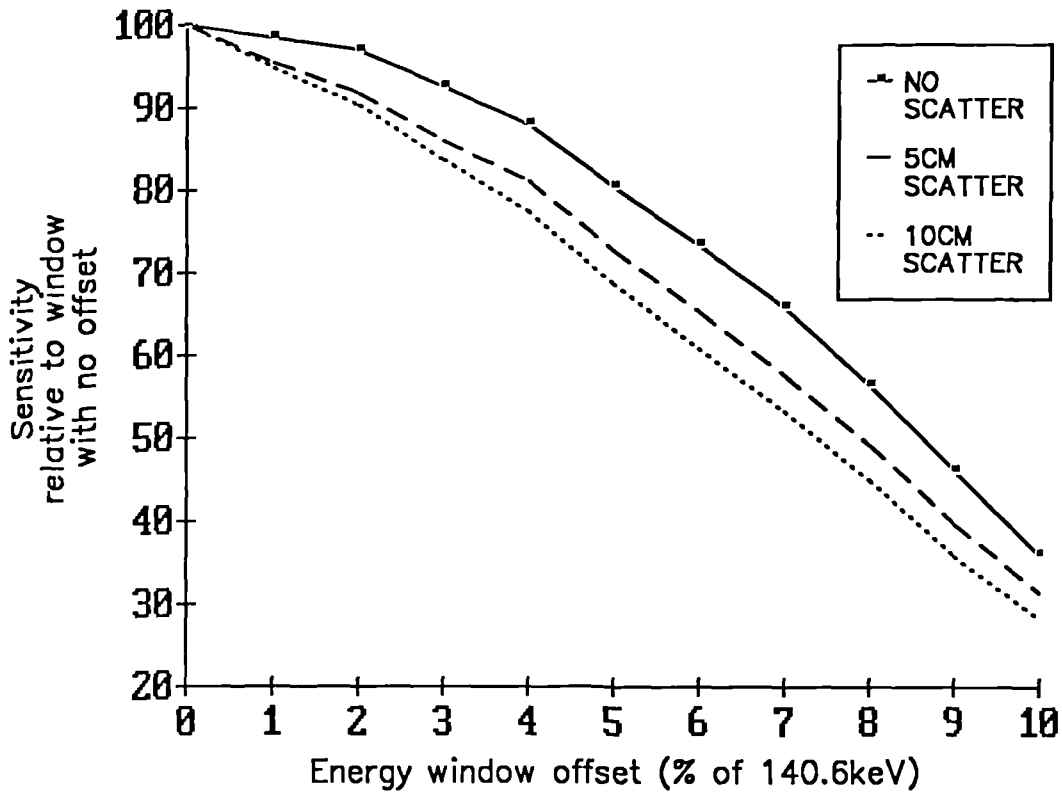


Figure 6.1 Variation of sensitivity with energy window offset for different scatter fractions produced by interposing 5cm and 10cm of perspex between the source and camera.

scatter fractions are expressed as a percentage of the sensitivity when no offset was used. It should be noted that the data in figure 6.1 have to be interpreted with care; the absolute values of the count losses, for a specific offset value and different scatter fractions, are not directly comparable because the 100% values refer to differently shaped spectra.

However, it should also be noted that it is possible to apply the results of the no scatter case to the situation in which scatter is present i.e. the percentage of unscattered photons rejected by applying an offset to the energy window will be independent of the scatter fraction of the incident radiation. What is not known is the percentage which this comprises of the total counts in the original symmetric window. This would require a knowledge of the scatter fraction which is impossible to measure in the general case and can only be estimated by Monte Carlo simulations.

The independence of the unscattered photon rejection fraction from the scatter fraction is a consequence of the fact that the camera is always peaked using only unscattered photons.

The data shown in figure 6.1 are for the measurements made with the collimator off. The results of the measurement with the LEAP collimator were almost identical to those shown. The maximum difference between any two data points was less than 1%.

For the scatter free case there is a shoulder in the curve at about a 3% offset value. Thus the rate of sensitivity loss is initially low but starts to increase rapidly after this point. For the cases where scatter is present the curves in

figure 6.1 are more linear in shape, implying a higher rate of sensitivity loss at the lower offset values. This is simply what one would expect from an examination of the shape of spectra which have been produced from Monte Carlo simulations in which scattered and unscattered photons can be followed separately, Jaszczak (1984). From this it is evident that the rate of rejection of unscattered photons will be lower than the rate of rejection of scattered photons for a baseline window positioned at a low energy setting. As the value of the baseline is increased the ratio of scattered to unscattered photons rejected will increase in a manner dependent upon the scatter fraction of the detected radiation .

Choosing an offset value on the shoulder of the sensitivity curve, e.g. 3%, will produce a decrease in sensitivity, when compared to the symmetric window, which ranges from 7% to 17% depending on the scatter fraction used. 7% of the unscattered photons in the symmetric window will be rejected by applying a 3% offset. These values would not be expected to produce an increase in the SPECT image noise which would seriously impare image quality. Whether enough scattered photons have been rejected to make a signifiacnt improvement in the contrast of the SPECT images, however, will have to be tested using phantom studies.

The use of a larger offset, e.g. 6%, will cause a reduction in sensitivity which ranges from 28% to 40% depending on the scatter fraction. 28% of the unscattered photons in the symmetric window will be rejected by applying a 6% offset. Count losses of this magnitude would be expected to have a noticeable effect on image quality. However, the level of scatter rejection would also be expected to produce a

significant improvement in image contrast. Whether the increased statistical noise in the SPECT images, particularly in the count limited clinical situation, is justified by this increase in contrast is the critical question.

There is also the question of whether the improvement in image contrast will be offset by the loss of uniformity which was discussed previously.

We can go some way to answering these questions by performing phantom studies.

6.3 Phantom studies

In order to assess how the effects of an offset energy window on planar images, as studied in the previous sections, are transferred to a SPECT study a series of phantom studies were performed. The phantom used was the SIEL phantom described in Section 3.6. This is 20cm diameter phantom so that the scatter fraction produced by it will be closer to that of a brain study than a study of the trunk, and the results have to be interpreted with this in mind.

To ensure that the effects of the offset window were not obscured by noise it was important that the data be as statistically accurate as possible. To this end the SPECT studies were acquired over a period of time around twenty times that which would be used in clinical practice. As an important parameter in this investigation is the contrast in the final images it was also necessary to make the linear sampling as fine as possible to avoid partial volume effects. Also, to preserve the high spatial frequencies in the acquired data the filter used in the reconstruction of the data had to be as sharp as possible.

6.3.1 Methods

The SIEL phantom, with inserts, was filled with water containing 250MBq of ^{99m}Tc seven hours before the start of the SPECT acquisition to ensure adequate mixing. Before any measurements were made the DIGITRAC daily quality control procedure, described in 3.2.2.3, was employed to ensure that the camera was peaked properly and that the camera response was as uniform as possible. The x-ADC offset setting was also tested and adjusted to within 0.1 pixels of its correct value using the procedure described in Section 4.4.1.

The phantom was positioned in the jig described in Section 3.6 with care being taken to ensure that its central axis was parallel to the camera face at camera rotation values of 0 and 90 degrees. This was achieved to an accuracy of less than 0.25cm.

The camera gains were set to give pixels of edge length 0.28cm for a 128*128 matrix which is the smallest pixel size which will completely image a cylinder of length 30cm and radius 10cm. The SPECT acquisitions were performed using 64 projection angles with an acquisition time of 600s per angle. The LEAP collimator and a ROR value of 17cm were used. Separate acquisitions were made using energy window offsets of 0%, 3% and 6%.

The data were reconstructed using the ramp filter.

6.3.2 Results

The application of the 3% window offset reduced the countrate to 88% of the value obtained with the symmetric window. The 6% offset reduced the countrate to 68% its

original value. These figures and an examination of the curves in figure 6.1 would suggest that the spectrum produced by the phantom must be similar in shape to that produced by a point source behind 5-10cm of perspex.

The images of the phantom inserts which resulted from the symmetric and offset energy window SPECT acquisitions are shown in figures 6.2 to 6.5.

A qualitative assessment of the images suggests that using a 3% energy window offset does not have a large effect on image quality. This was confirmed by a quantitative analysis which was performed by taking profiles at a variety of angles through the insert images. It should be noted that quantitative measurements were made whenever possible to confirm the findings of the subjective, qualitative assessments of the SPECT images.

A qualitative examination of the images produced by the 6% window offset would suggest that some increase in the image contrast is achieved. The quantitative analysis shows that the difference produced in the hot lesion, pie and linearity inserts is small. An example for the linearity image is given in figure 6.6 . The main change produced by the 6% window offset is an increase in the contrast of the smaller cold lesions, figure 6.2 and figure 6.7. However, there were some circular artefacts observed on the cold lesion insert image which introduced some distortion into the quantitative results. For example the contrast of the largest cold lesion was actually reduced.

6.3.3 Conclusions

These findings can be explained using the results of the

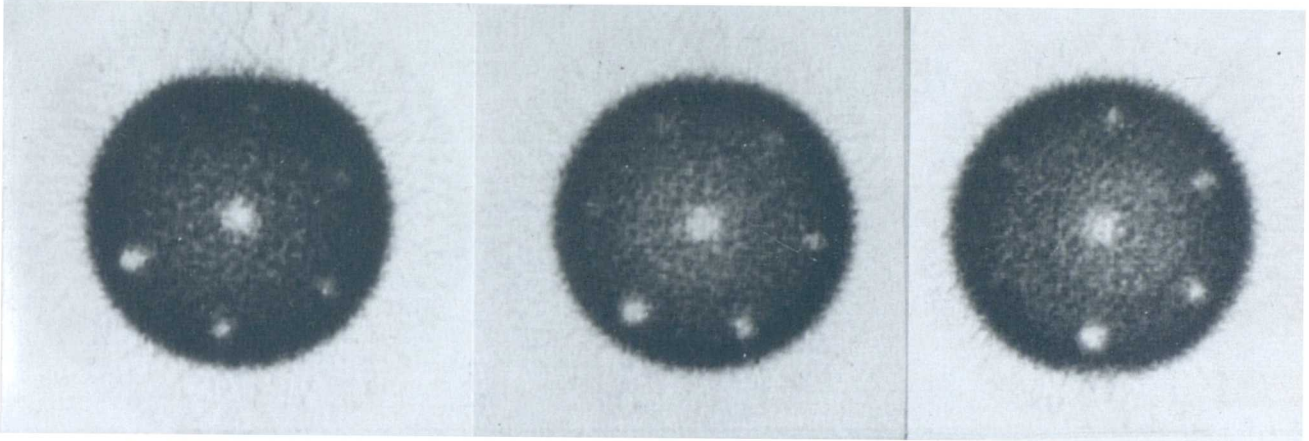
A**B****C**

Figure 6.2 Sections through the CL insert with energy window offsets of 0%, 3% and 6% in A, B and C respectively.

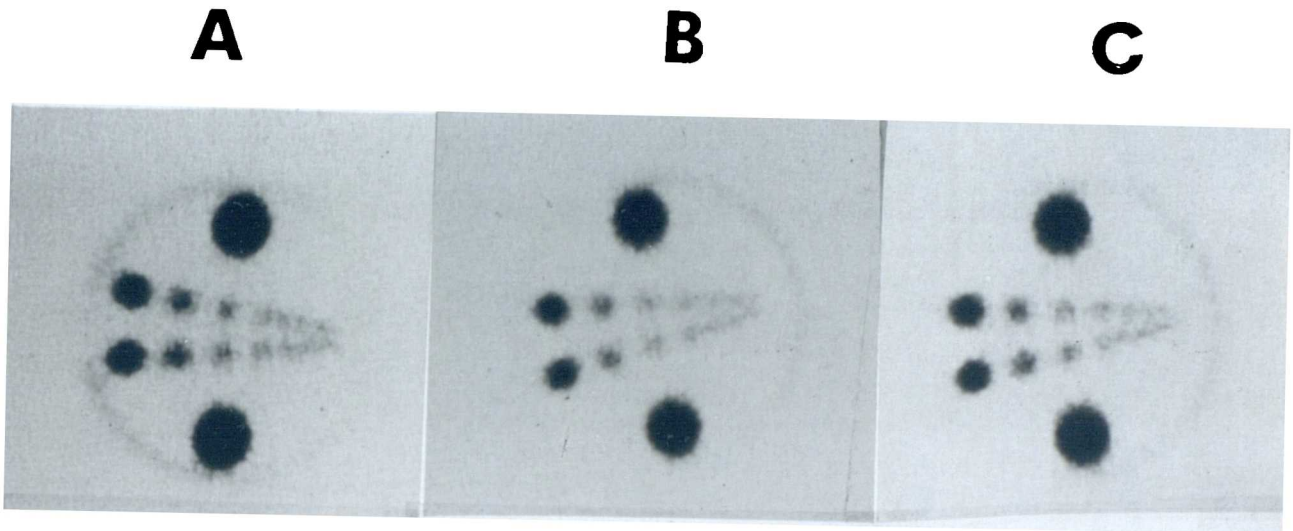


Figure 6.3 Sections through the HL insert with energy window offsets of 0%, 3% and 6% in A, B and C respectively.

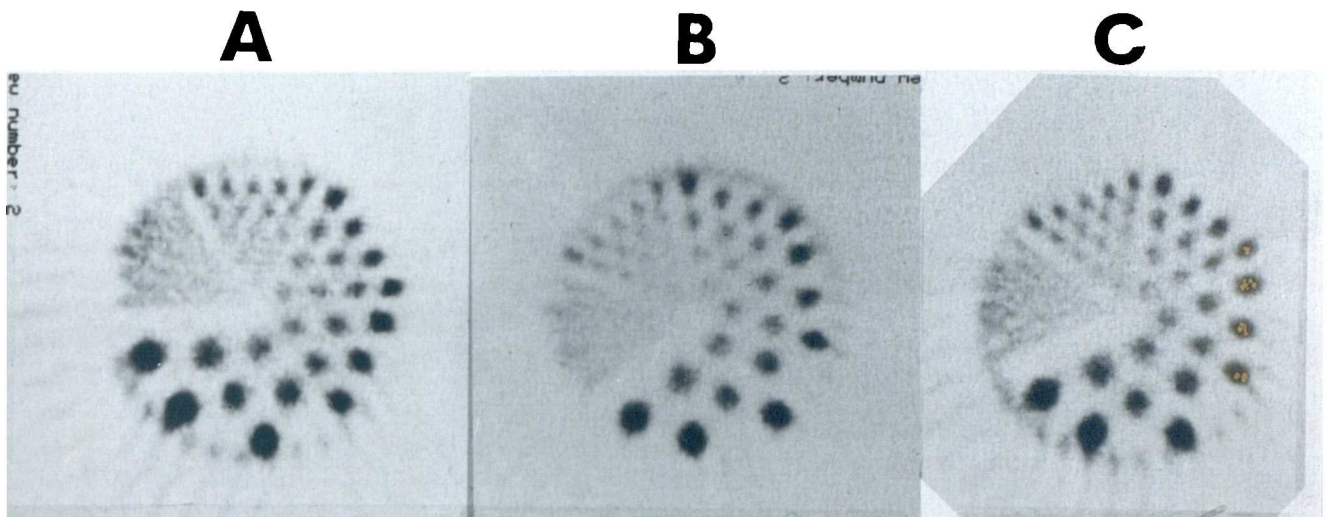


Figure 6.4 Sections through the pie insert with energy window offsets of 0%, 3% and 6% in A, B and C respectively.

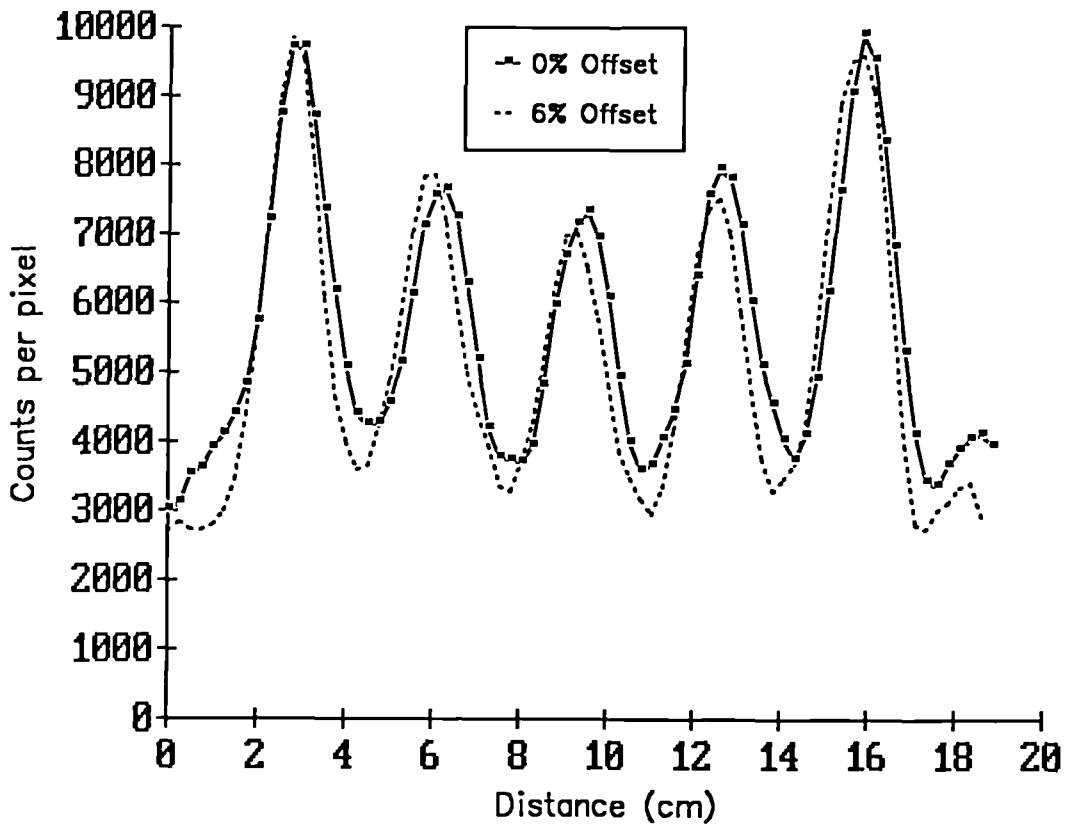


Figure 6.6 Profiles taken through the linearity insert images from the 0% and 6% energy window offset acquisitions.

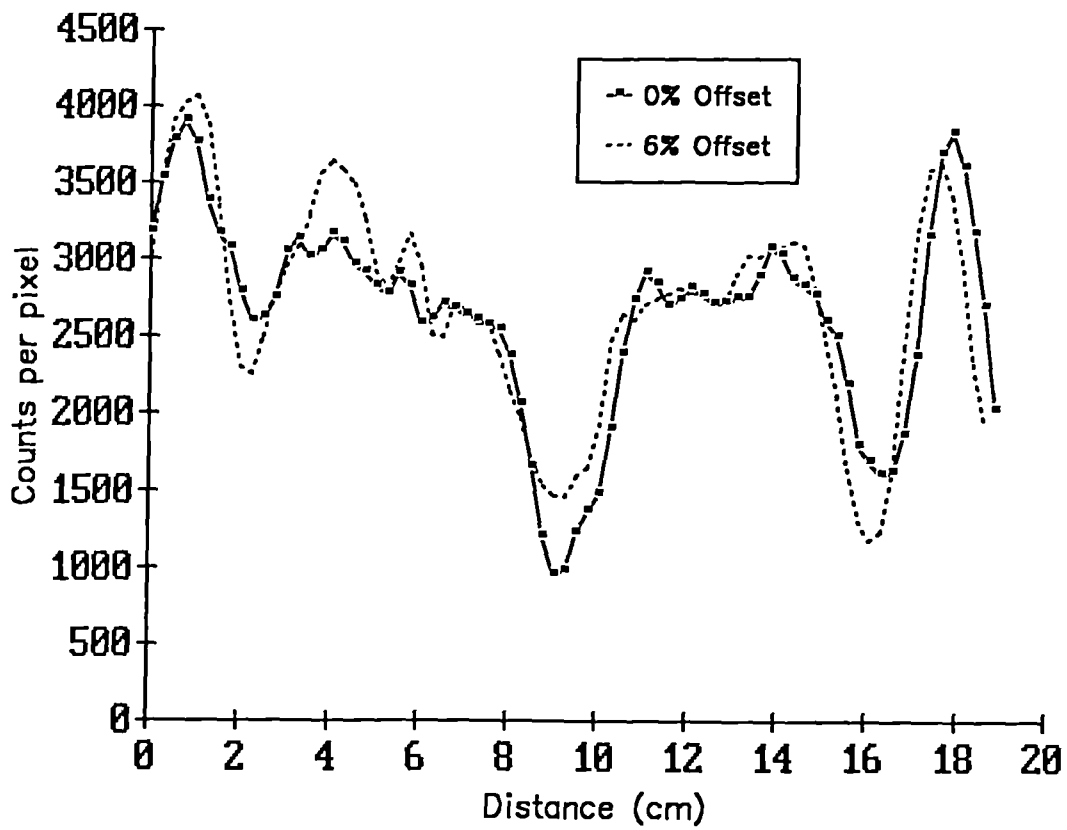


Figure 6.7 Profiles taken through the CL insert images from the 0% and 6% energy window offset acquisitions.

previous Sections and of Section 6.4.4.2. The use of a 3% offset value produces a small level of scatter rejection reducing the percentage of unscattered photons by 7%, figure 6.1. The results of Section 6.4.4.2 give a calculated value for the scatter fraction of around 20% for a uniform source distribution of the same dimensions as the SIEL phantom. It can be calculated from these values, given the total reduction in counts of 12%, that 6% consists of unscattered photons and 6% is from scattered photons. Thus the images show no obvious changes when a 3% offset is applied because small numbers of scattered and unscattered photons are excluded in roughly equal amounts.

For the 6% offset setting the total reduction in counts is 32%. 21% of this comes from unscattered photons and 11% is from scattered photons. Thus approximately half of the scattered photons in the original spectrum are excluded so that some improvement in image contrast is expected. The level of improvement however, is not as clear as might have been expected given this level of scatter rejection. The explanation for this lies in the fact that around 20% of the unscattered photons have also been excluded. Thus, the scatter fraction of the resultant spectrum has in fact only been reduced from 20% to 16% even though half the scatter photons have been excluded. This is the factor which limits the usefulness of the offset window approach. Reducing the number of scattered photons by a level which has a significant effect on image contrast involves a greater reduction in the number of unscattered photons which means that the net effect on image quality is small.

6.4 Scatter subtraction and attenuation correction

6.4.1 Introduction

Given the failure of a direct exclusion of scattered photons from the projection data to produce a significant improvement in SPECT image quality, the use of an alternative approach to the scatter problem was investigated. In particular a correction method which subtracts an estimate of the distribution of scattered photons from the photopeak image was assessed. The first step in this process is the determination of the scatter fraction. This can be achieved for the specific case of a uniform cylindrical source distribution.

While the examinations of the behaviour of point and line sources performed in Chapter 5 provided useful information about some of the fundamental aspects of the SPECT imaging process, not all of the factors which are of importance can be investigated. A full examination of SPECT can only be performed using extended source distributions. The simplest form of extended source is a cylinder with a uniform concentration of activity and a uniform attenuation throughout its volume. Using this, measurements can be made of volume sensitivity, SPECT uniformity, noise and the effects of attenuation and scatter. The symmetry and the known geometry of the source distribution and the distribution of attenuating structures also allows an assessment to be made of the performance of the Bellini attenuation correction algorithm, Section 3.5.3.4.

6.4.2 Theory

The Bellini attenuation correction algorithm assumes that the data collected consists of unscattered photons only so that in order to test the behaviour of the method some way of correcting for the scatter is required. Having performed the scatter correction the Bellini method can be checked against an exact analytical correction which can be derived because of the uniform nature of the source distribution.

The scatter correction method used is based on the relatively common approach of using a second energy window positioned below the photopeak to provide an estimate of the structure of the image produced by the scattered data. An arbitrary fraction of the scattered image is then subtracted from the the photopeak image to give an estimate of the scatter free image. However, using the fact that the source distribution is known for the case of a uniform cylinder a method has been developed which calculates exactly the factor which should be used to multiply the scatter image before subtraction from the photopeak image. The manner in which this is achieved uses a development of an approach originally described by Jaszczac (1985), the major difference being the use of the actual scatter image as opposed to the sum of the image counts to perform the subtraction.

The principal idea is that the counts which would be expected from a uniform cylinder if scattered photons were not detected can be calculated from the point source sensitivity and the linear attenuation coefficient for any given isotope concentration. This value can then be compared with the actual countrate observed from the cylinder ; the extra counts which are observed must be due to scattered photons allowing the

scatter fraction to be calculated. Having determined the absolute value of the scatter fraction an estimate of the distribution of the scattered photons can be made using the data collected from an energy discrimination window set below the photopeak. The image from the scatter window, after being corrected by a factor determined by the scatter fraction, can then be subtracted from the photopeak image to produce an estimate of the form of a scatter free image.

Having obtained the scatter free projection data the reconstructions can be performed after correction for attenuation using the Bellini algorithm. The data can be checked against the theoretical values because, again, due to the uniformity of the source it is possible to calculate the exact values of the correction factors which should be applied to each projection element to compensate for attenuation. A further check can also be made by deriving the values of the projection data which would be obtained, in the absence of both scatter and attenuation, from a cylinder containing a uniform source distribution with a concentration equal to that of the real cylinder.

In summary we wish to perform the following procedure :

1. Acquire the projection data for a uniform cylinder using both a photopeak and a scatter window.
2. Combine adjacent sections to produce projection element values as free from statistical variations as possible.
3. Compare the counts acquired in the photopeak window with that predicted from a uniform source without the presence of scatter. The predicted values being calculated from the activity concentration in the real cylinder, the measured point source sensitivity and the linear attenuation coefficient

of ^{99m}Tc in water (0.152cm^{-1}).

4. The difference between the predicted and observed values must be due to the presence of scattered photons. The projection element values in the lower energy window can be used to estimate the structure of the scatter. The correct fraction of the scattered data, obtained from the difference between the observed and predicted values, can then be subtracted from the photopeak projection element values.

5. Having obtained the form which the projection data should take in the absence of scatter the Bellini attenuation correction algorithm can be tested. As the attenuation of the projection data from a uniform cylinder can be calculated analytically the resultant corrected data can be used to check the more general algorithm.

The key to the above analysis lies in the analytical derivation of the values of the projection data obtained from both an attenuated and an unattenuated uniform cylinder of activity. The theoretical calculation will now be described.

Consider, firstly, the projection element values which would be obtained from a uniform disc of activity, as shown in figure 6.8, in the absence of both scatter and attenuation. The projection element values are given simply by the length of the line integral through the circle multiplied by the activity concentration per unit area and the pixel size.

Thus,

$$\begin{aligned} P(x) &= \int_0^{2L} \text{S.C.W.} dy \\ &= \text{S.C.W.} \int_0^{2L} dy \\ &= \text{S.C.W.} \cdot 2L \\ &= \text{S.C.W.} \cdot 2 \cdot (R^2 - x^2)^{1/2} \end{aligned} \quad (6.1)$$

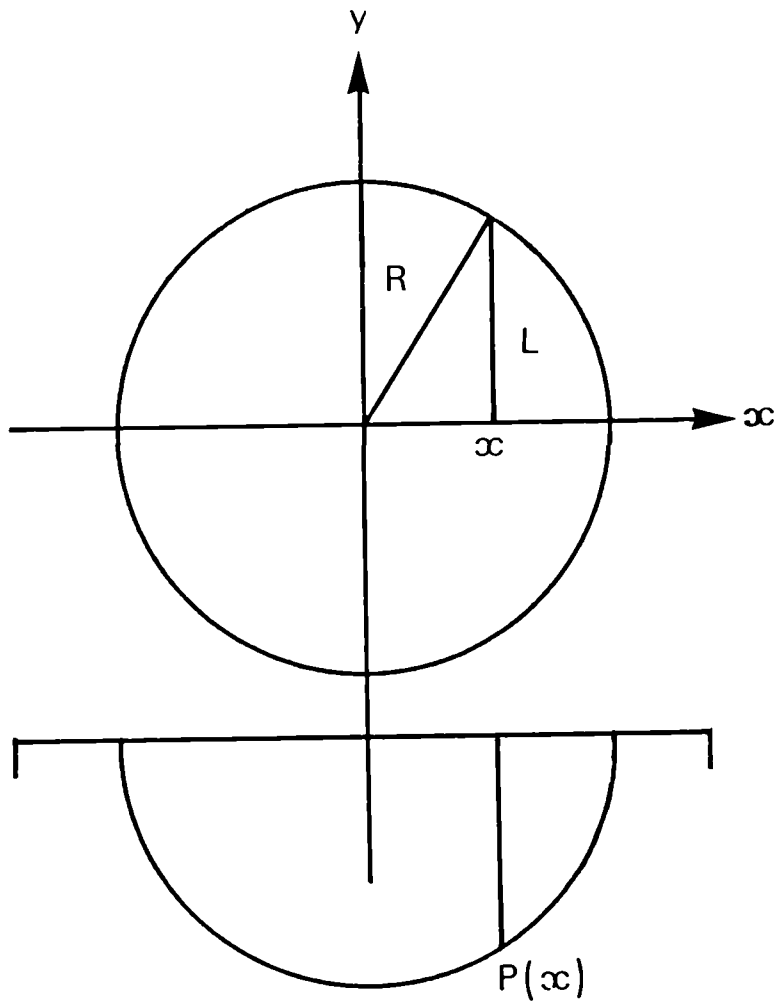


Figure 6.8 The projection element values, $P(x)$, for a uniform cylindrical distribution can be obtained by calculating the line integral along the chord of length $2L$.

where $P(x)$ = value of the projection element with centre
a distance x from the source centre.

S = point source sensitivity

C = activity per unit area of the disc

W = projection element length

L = half the chord length = $(R^2 - x^2)^{1/2}$

If the photons are attenuated with an attenuation coefficient,
 u , then the projection element values are given by

$$\begin{aligned}
 PA(x) &= \int_0^{2L} S.C.W.\exp(-uy)dy \\
 &= S.C.W. \int_0^{2L} \exp(-uy) dy \\
 &= (S.C.W/u) \cdot (1 - \exp(-2uL)) \\
 &= (S.C.W/u) \cdot \{1 - \exp[-2u(R^2 - x^2)^{1/2}]\} \quad (6.2)
 \end{aligned}$$

The ratio of the values $PA(x)/P(x)$ gives a set of attenuation
correction factors which can be used to multiply acquired
values after the scatter component has been removed. The mean
value of $PA(x)/P(x)$ for the uniform source distribution of
diameter 20.32cm provided by the SIEL phantom was calculated
to be 2.73.

It should be noted at this point that a similar
calculation of the attenuated projection element values made
by Jasczsac (1985) is in error. This suggested that the value
of $PA(x)/P(x)$ was a constant, i.e independent of x , equal to
3.165. This has the effect, for a cylinder of diameter 20cm,
of overestimating the scatter fraction by 16%.

Correction for perspex shell

A final correction has to be made for the attenuation

produced by the acrylic shell of the phantom cylinder which is 0.635cm thick. The path length of a projection ray through the shell will depend on its distance, d , from the centre of the phantom and can be calculated from simple geometrical considerations. The attenuation of each projection ray produced by the shell can be calculated using a linear attenuation coefficient of 0.152cm^{-1} . Although this effect is small for projection rays close to the phantom centre it is highly significant for projection rays close to the edge of the phantom.

The total counts from the cylinder are reduced by 4.2% due to the cylinder shell attenuation.

6.4.3 Methods

The SIEL phantom cylinder, without inserts, was filled with water containing 252MBq of $^{99\text{m}}\text{Tc}$ seven hours before the start of the SPECT acquisition to ensure adequate mixing. Before any measurements were made the DIGTRAC daily quality control procedure, described in Section 3.2.3.3, was employed to ensure that the camera was peaked properly and that the camera response was as uniform as possible. The x-ADC offset setting was also tested and adjusted to within 0.1 pixels of its correct value using the procedure described in Section 4.4.3.

The point source sensitivity was then measured in the same way as described in 4.2.7.

The phantom was positioned in the jig described in Section 3.6 with care being taken to ensure that its central axis was parallel to the camera face at camera rotation values of 0 and 90 degrees. This was achieved to an accuracy of better than

0.25cm. The ROR was 16.8cm and the LEAP collimator was used. To acquire data on the structure of the scatter component a second energy window was used from 85keV to 115keV. The countrates in both windows were measured before the start of the SPECT acquisition.

The camera gains were set to give pixels of edge length 0.28cm for a 128*128 matrix which is the smallest pixel size which will completely image a cylinder of length 30cm and radius 10cm. The SPECT acquisitions were performed using 64 projection angles with an acquisition time of 600s per angle.

6.4.4 Results

6.4.4.1 Volume sensitivity

The volume sensitivity is a parameter which is often used in the assessment of SPECT systems. It can be expressed in terms of the sensitivity per axial centimetre (i.e. total counts per 1cm thick section) and calculated from the quantity of activity in the cylinder and the observed countrate. This is not a fundamental parameter because the scattering of photons makes the value dependent on the source distribution. However, given that the cylinder dimensions used are those of a phantom in common usage, the volume sensitivity can be useful for comparing different SPECT systems.

For the LEAP collimator with a 15% energy window the volume sensitivity per axial centimetre for a 20.3cm diameter cylinder was 54.6cps/MBq/phantom which equals 1.8cps/MBq/axial cm.

6.4.4.2 Scatter Correction

The count values which would be expected from the uniform cylinder if no scattered photons were included was calculated using equation 6.2. The value of the attenuation coefficient was set equal to 0.152cm^{-1} , the linear attenuation coefficient for $^{99\text{m}}\text{Tc}$ photons in water. The point source sensitivity which was measured immediately before starting the SPECT acquisition was found to be 140.2cps/MBq. For the calculations only the central 17cm length of the cylinder was used. This avoids the problem of a variable scatter distribution at the cylinder ends which are 6.5cm from the outermost section considered (the amplitude of the LSF in scatter is less than 1% of its central value at a distance of 6.5cm, Section 4.2.4).

The total value of the counts which resulted from the theoretical calculation were compared with those obtained from the real acquisition and found to be 14.3% less. The extra counts in the real data are due to the inclusion of scattered photons within the photopeak window. The extra counts when expressed as a fraction of the unscattered photons gives a scatter fraction of 16.7%. The projection profiles obtained at a camera angle of 0 degrees for both the real and the simulated data are shown in figure 6.9.

Also shown in figure 6.9 is the projection profile obtained from the lower energy window which represents the distribution of scattered photons. The data obtained from the scatter window was multiplied by a fraction which was determined so that when the resulting images were subtracted from the photopeak images the total counts in the photopeak images were reduced by 14.3%. This gives the estimate of the

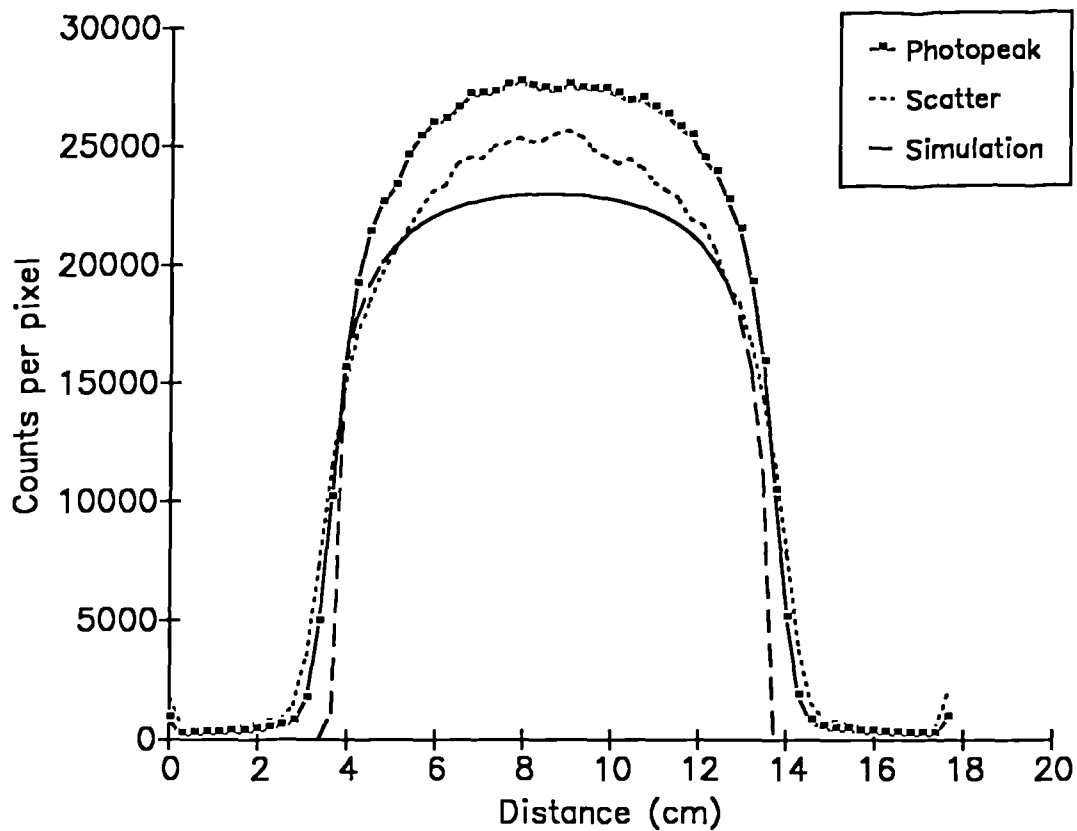


Figure 6.9 Profiles through a projection image of the uniform cylinder for the photopeak and scatter acquisitions. Also shown is the analytically determined profile which would be obtained if no scattered radiation was detected.

magnitude and the distribution of unscattered photons. The projection profile corresponding to a camera angle of 0 degrees was taken from the scatter corrected data and compared to the corresponding projection profile from the simulated data; this is shown in figure 6.10. There is a good agreement between the corrected data and the theoretical prediction. It can be concluded from this that the distribution of counts within the lower energy window must be a reasonable approximation to the distribution of scattered photons within the photopeak window.

The largest errors occur close to the edges of the source where no account has been made in the theoretical calculation of the finite size of the PSF.

6.4.4.3 Attenuation Correction

Having obtained data which has been corrected for scatter the Bellini attenuation correction algorithm can be checked. This was achieved by applying the algorithm to the scatter corrected phantom studies using attenuation coefficient values of 0.071, 0.11, 0.152 and 0.18cm^{-1} .

Profiles through the centre of these images were taken and compared with the result which was obtained without attenuation correction, figure 6.11. From these profiles it can be determined that the Bellini method behaves correctly in a number of respects. Firstly it should be noted that the amplitude of the pixels at the perimeter of the reconstructed images have their count values increased i.e. the method does not simply alter the values of the central pixels. This is an essential requirement for quantitatively accurate attenuation correction.

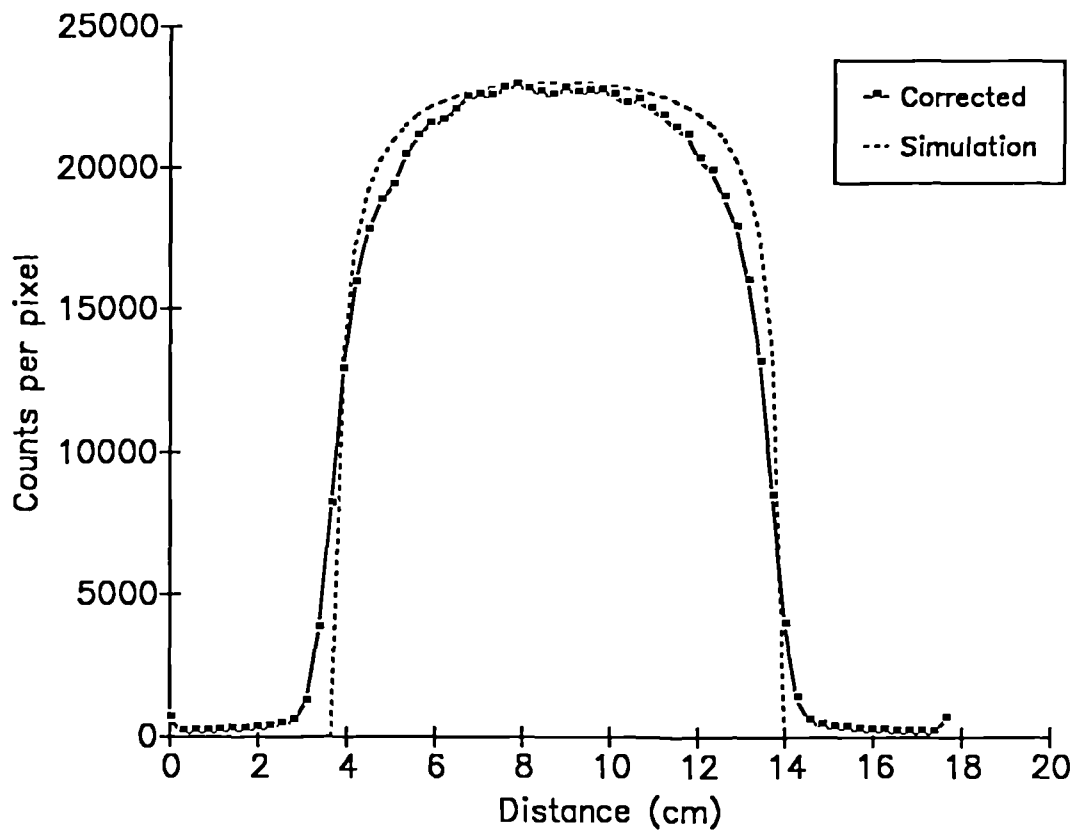


Figure 6.10 Comparison of a profile through a projection image of the uniform cylinder after correction for the scatter contribution with the analytically calculated profile.

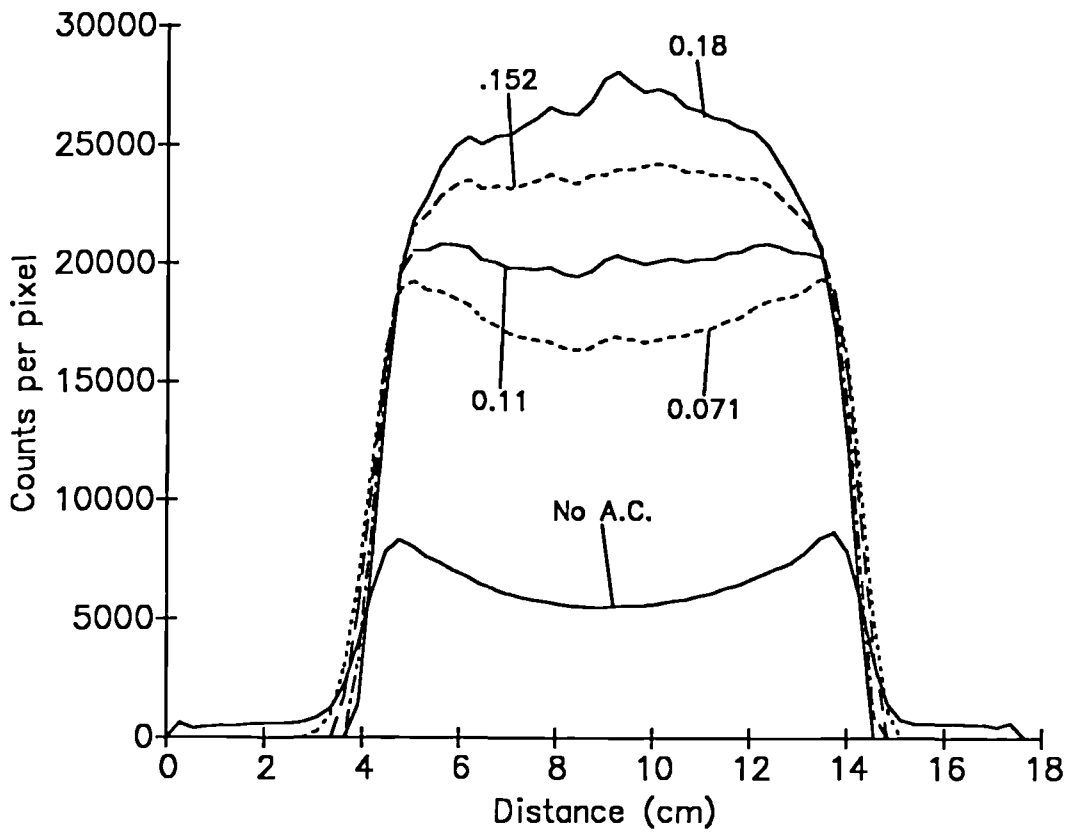


Figure 6.11 Profiles through the centre of the section through the uniform cylinder after the Bellini algorithm has been applied with correction coefficient values of 0, 0.071, 0.11, 0.152 and 0.18cm^{-1} .

Next, the use of the correct value for the LAC gives, qualitatively, the best results in that the flattest profile is produced (this is what would be expected from a profile through a section of a uniform source distribution).

The quantitative accuracy of the Bellini method can be assessed by comparing the profiles through the images from the reconstruction of the scatter corrected phantom data with that obtained from the image which results from the reconstruction of the simulated data calculated without the effects of attenuation (i.e. from equation 6.2). This is shown in figure 6.12. It can be seen from this that the use of the correct value for the LAC, i.e. 0.152cm^{-1} , produces the best quantitative accuracy. This is an important point because the accuracy of the Bellini attenuation correction method has been questioned, Moore (1982). It has been suggested that there may be a DC error in the calculated values. This can be refuted on the basis of the results shown in figure 6.12. Although the accuracy of the Bellini method has not been demonstrated for a structured source distribution, any DC error would have been evident with the uniform source.

Figure 6.13 shows the images from the reconstruction of the simulated scatter free projection data, with and without the effects of attenuation (i.e. using equations 6.1 and 6.2 respectively). Also shown are the images from the reconstruction of the scatter corrected phantom data both before and after attenuation correction using a value of 0.152cm^{-1} for the coefficient.

6.4.4.4 Conclusions

The Bellini attenuation correction method has been shown

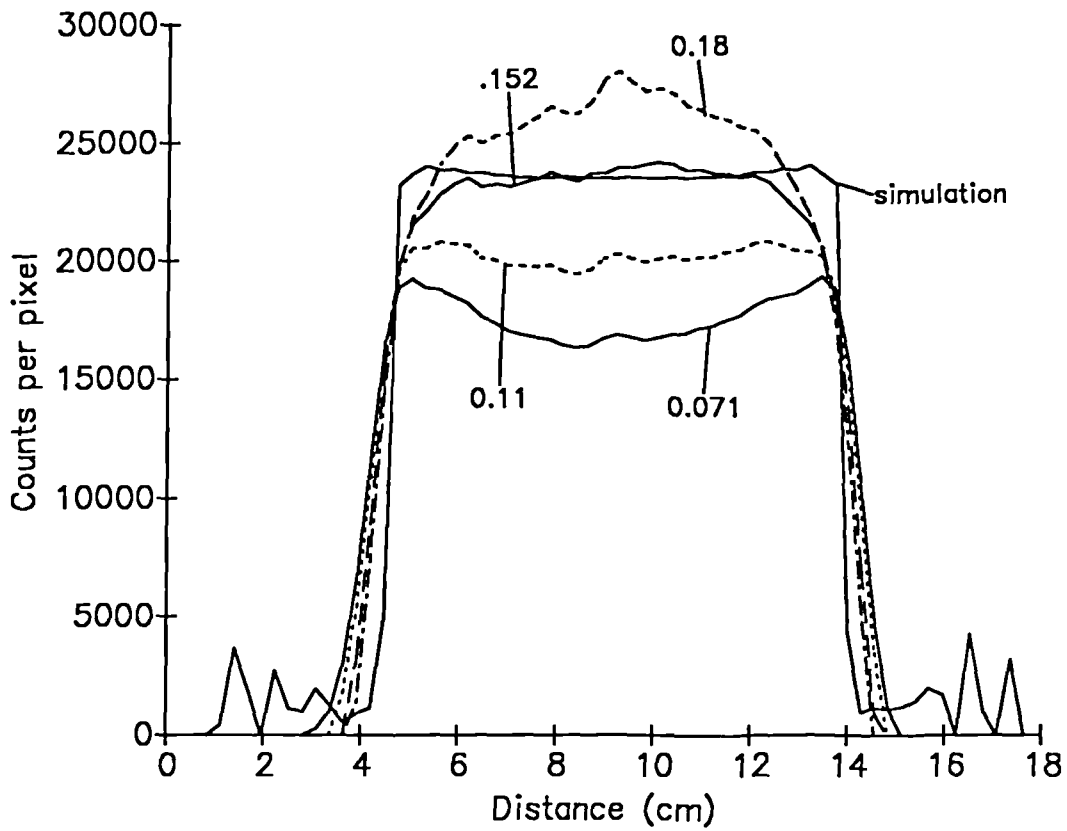


Figure 6.12 Comparison of a profile through the centre of the image obtained after reconstruction of the analytically calculated projection data with the scatter and attenuation corrected phantom data.

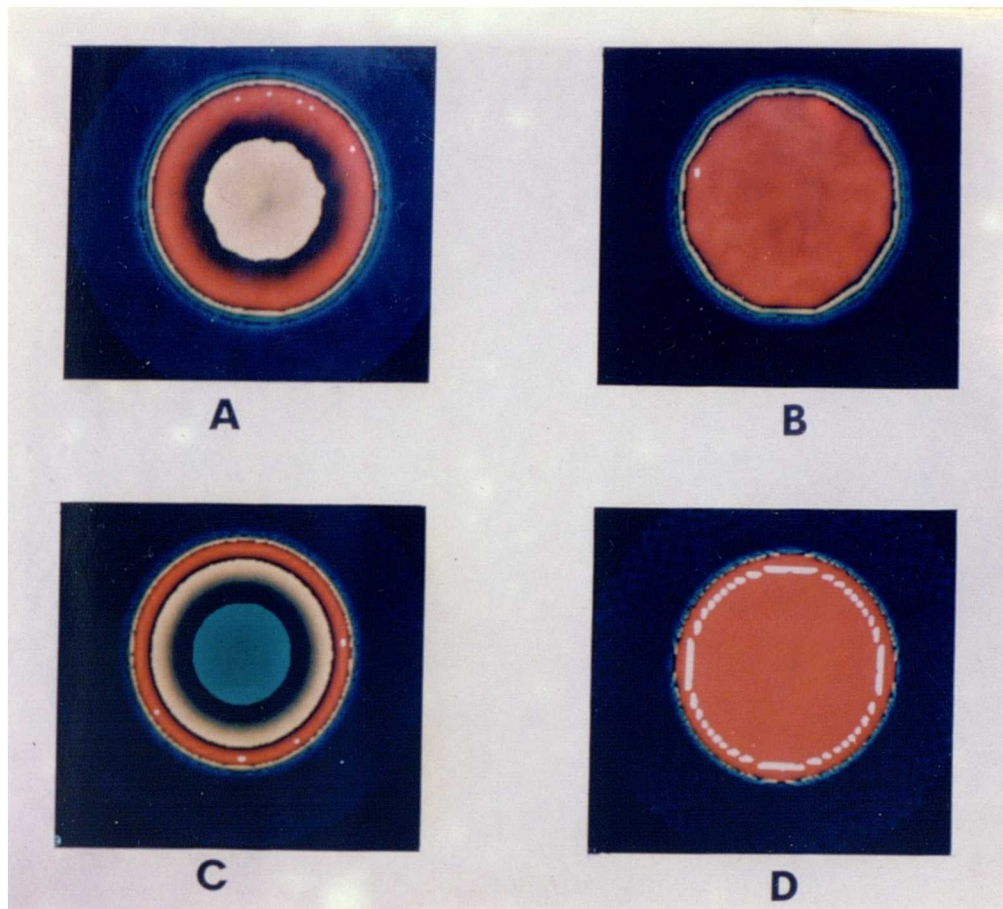


Figure 6.13 The reconstructed transaxial sections through the uniform cylinder are shown both before and after attenuation correction, A and B. These can be compared to the images reconstructed from the simulated projection profiles obtained from equations 6.1 and 6.2, i.e. with attenuation correction, C, and without, D.

to produce results which compare well, both qualitatively and quantitatively, with results obtained from analytical calculations which can be performed for the special case of a uniform source distribution.

Also, a predetermined fraction of the image obtained from an energy window placed below the photopeak can be subtracted from the photopeak image to produce data which when, reconstructed with an appropriate attenuation correction, produces images which are consistent with those predicted analytically. The extension of this scatter correction approach to a structured source distribution will be considered in the following section.

6.4.5 Applications to structured source distributions

The efficacy of the the scatter correction method for structured source distributions was assessed by performing SPECT acquisitions of the SIEL phantom with inserts.

6.4.5.1 Methods

SPECT acquisitions were performed of the SIEL phantom with inserts using the same procedure as described in 6.4.3

6.4.5.2 Results

The images of the phantom inserts for the photopeak window, the scatter window, the corrected data and the photopeak window data after a simple background subtraction are shown in figures 6.14, 6.15, 6.16 and 6.17.

The presence of structure in the scatter images can be seen indicating that subtraction of scatter data is different

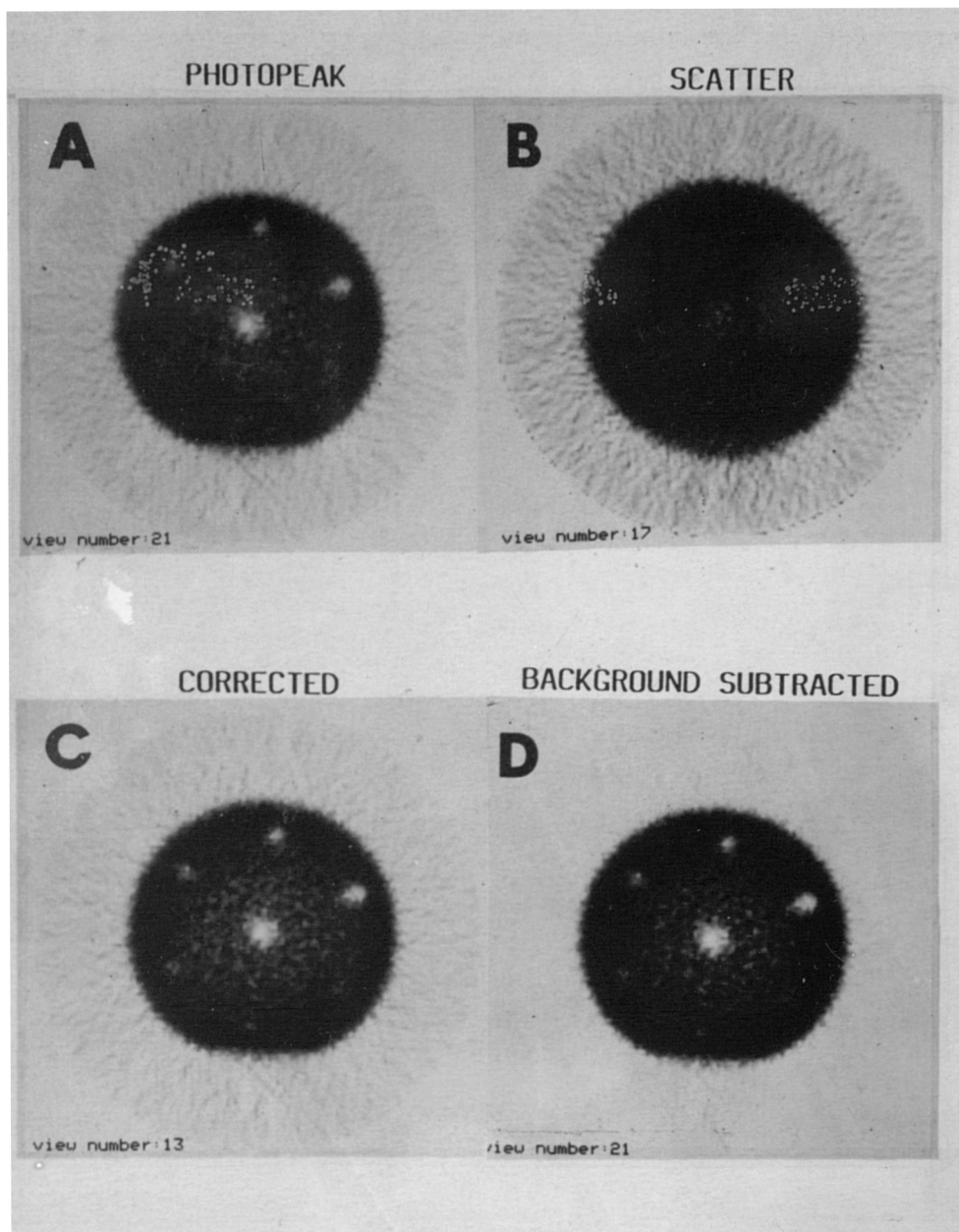


Figure 6.14 Sections through the CL insert from ;

- A - the photopeak window
- B - the scatter window
- C - the scatter corrected data
- D - the photopeak data after a simple background subtraction

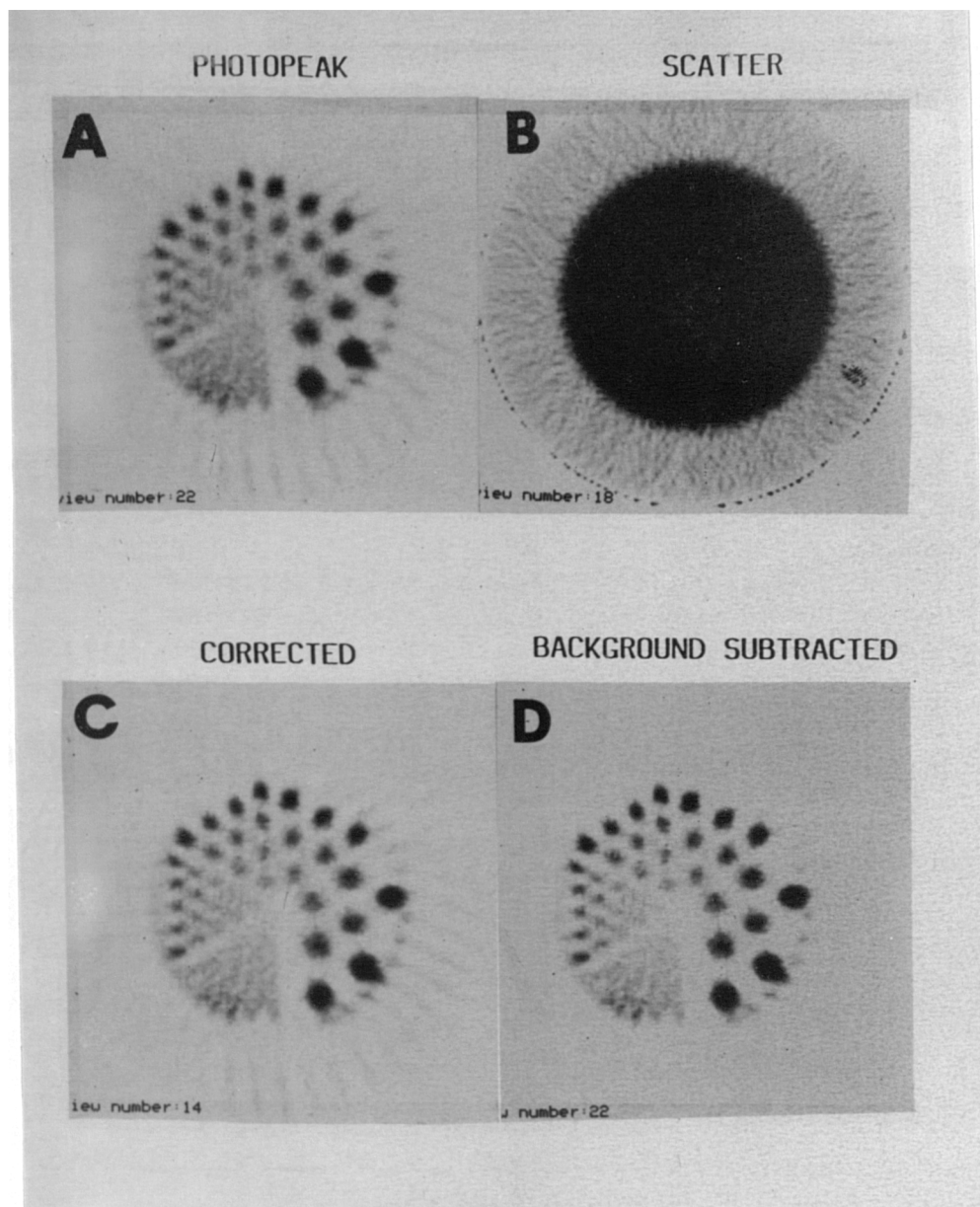


Figure 6.15 Sections through the pie insert from ;

- A - the photopeak window
- B - the scatter window
- C - the scatter corrected data
- D - the photopeak data after a simple background subtraction

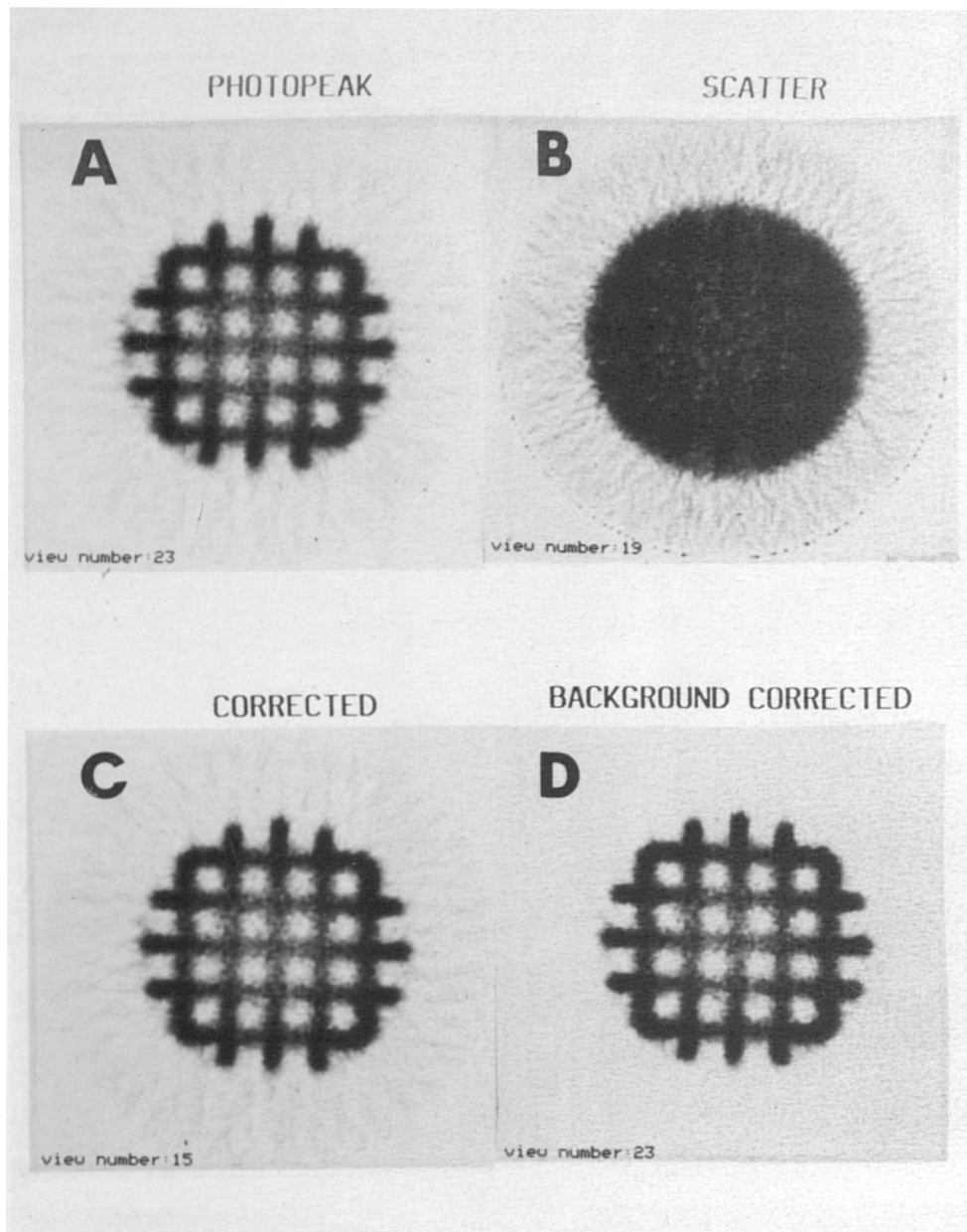


Figure 6.16 Sections through the linearity insert from ;

- A - the photopeak window
- B - the scatter window
- C - the scatter corrected data
- D - the photopeak data after a simple background subtraction

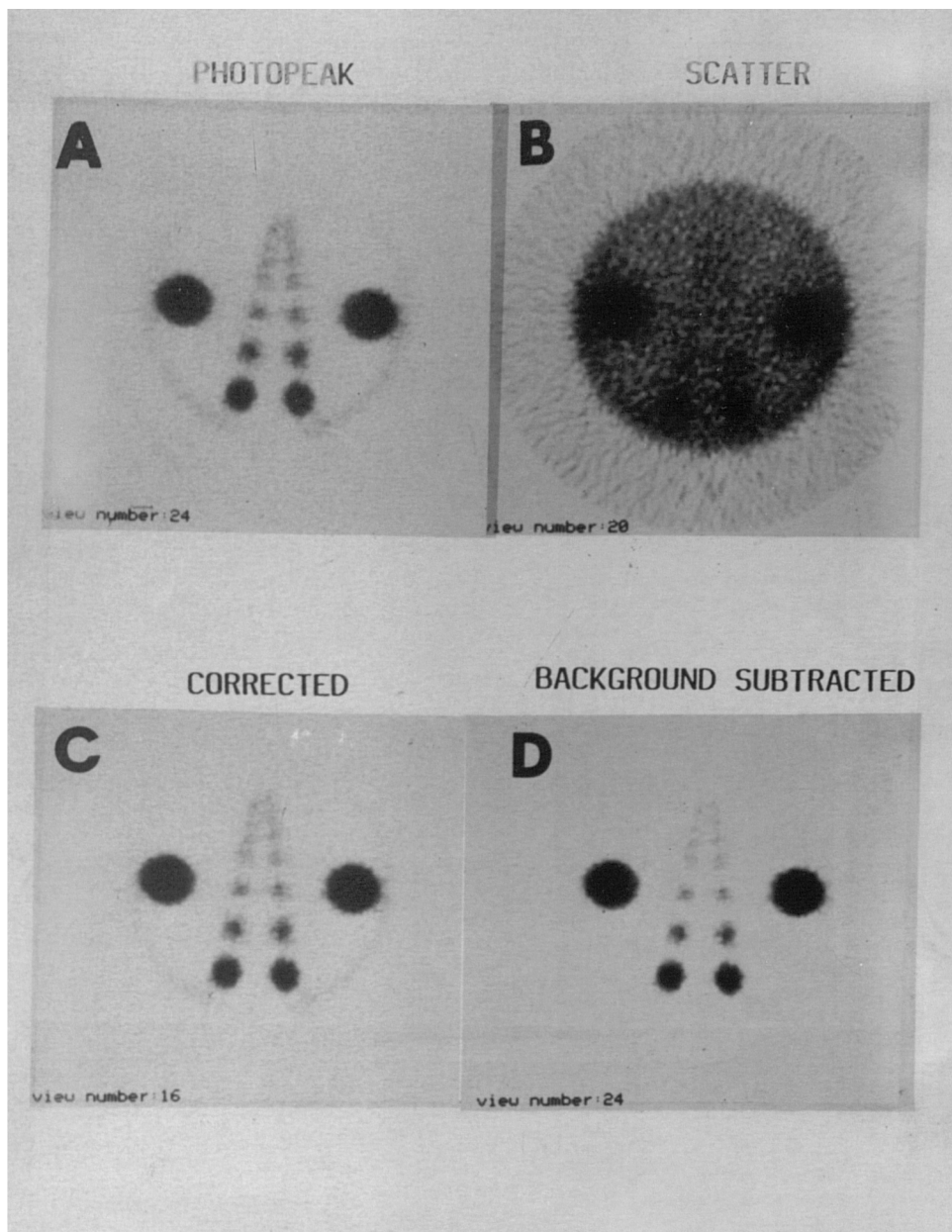


Figure 6.17 Sections through the HL insert from ;

- A - the photopeak window
- B - the scatter window
- C - the scatter corrected data
- D - the photopeak data after a simple background subtraction

from a simple background subtraction where a constant value is subtracted from each pixel.

Nevertheless, it would appear that, as far as a subjective assessment of image quality is concerned, there is little to be gained from performing the preprocessing scatter correction. Any desired improvement in contrast can be achieved simply by altering the image background subtraction level.

The subjective impressions were confirmed by a quantitative analysis of the data. Figure 6.18 shows the counts obtained in a profile through the cold lesion insert. The profile was angled to cut through the central lesion and the lesions of diameter 17.9 and 9.2mm. The failure, in the photopeak window images, of the cold lesion pixels to give the correct values of zero counts is caused by three processes : the inclusion of scattered photons, the limited resolution of the detector and the smoothing effects of the reconstruction process. After the correction has been made for scattered photons the cold lesion pixels still do not give zero count values. In fact the magnitude of the discrepancy would suggest that scatter is not the dominant factor in the loss of contrast produced by the detection and reconstruction of SPECT images. A similar pattern and similar conclusions can be drawn from the quantitative analysis of the linearity insert image, figure 6.19.

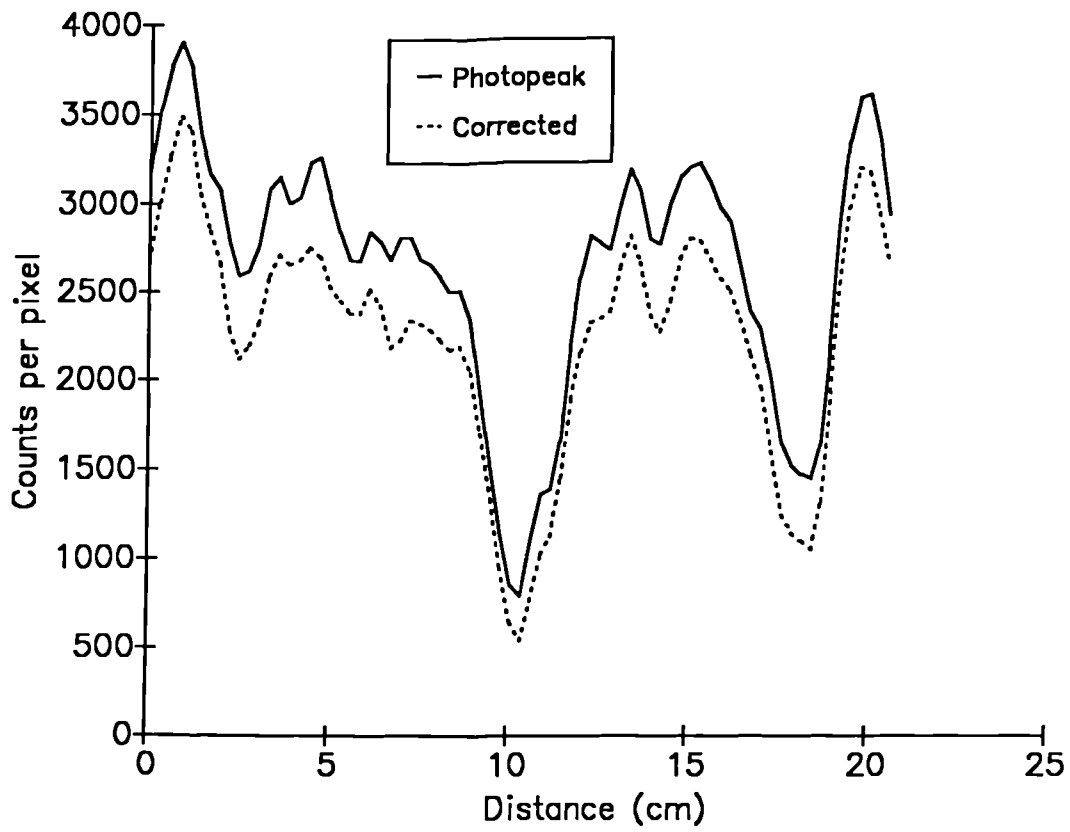


Figure 6.18 Profiles through the CL insert before and after scatter correction.

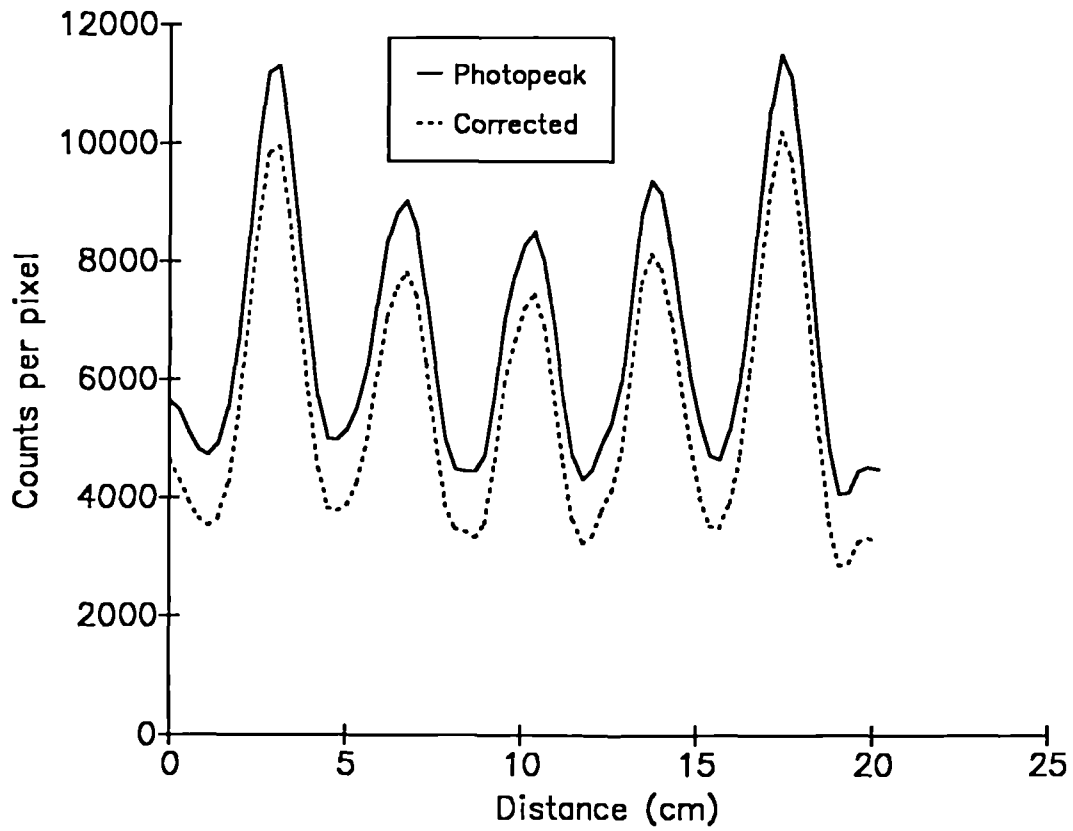


Figure 6.19 Profiles through the linearity insert before and after scatter correction.

6.5 General conclusions for Chapter 6

1. Two main attempts have been made to correct for the effects of scatter. The use of an asymmetric energy window, offset from the photopeak by 3%, produced no clear improvement in the quality of sections taken through the inserts of a high count phantom study. When a 6% offset was used some increase in image contrast was observed but at a cost of a reduction in sensitivity of around 30% and an increase in the level of artefacts caused by a decrease in uniformity. It was concluded that, although simple to perform, there were no significant improvements in image quality obtainable from the application of an energy window offset from the photopeak.

2. The second approach consisted of estimating the magnitude of the scatter component from a knowledge of the systems point source sensitivity and an analytical calculation of the projection profiles which would be obtained from a uniform source distribution. The structure of the scatter component was estimated from an image taken using a window positioned below the photopeak. Reconstruction of the scatter corrected data with the application of the Bellini attenuation correction algorithm produced images which were consistent with the predicted data.

This approach was also used to confirm the accuracy of the Bellini attenuation correction algorithm. Although the results obtained from a uniform source distribution cannot be fully extended to a structured source distribution they can be used to exclude the introduction of DC errors in the corrected data.

3. The application of the low energy image scatter correction method to a structured source distribution again did not produce significant improvements in the quality of the resultant images (despite its previously demonstrated quantitative accuracy).

4. The main conclusion to be drawn from these results is that, for a modern gamma camera with good energy resolution which permits the use of a 15% energy window, the reduction in image quality caused by the inclusion of scattered radiation is small. In fact the dominant processes which limit the contrast in the reconstructed images are the limited resolution of the camera and the smoothing effects inherent in the reconstruction procedure. Thus there is little to be gained in improvements in image quality through the application of scatter correction methods.

It is recognised that the above results were obtained using a phantom with a diameter of 20cm. Thus while they are applicable to head imaging their extension to imaging of the trunk which will have a higher scatter fraction should be made with care. A repeat of this work with a larger phantom would be of value.

Single photon emission computed tomography : Performance
assessment, development and clinical applications.

Volume Two

Gerard J. Gillen

B.Sc. (Honours)

Submitted for the degree of

Doctor of Philosophy

at the University of Glasgow,

Department of Clinical Physics and Bio-Engineering

April 1990

© G.J. Gillen

CONTENTS

Contents of Volume Two		page
Chapter 7	Parameter optimisation for low noise data	1
7.1	Introduction	1
7.2	Data detection by the camera	1
7.2.1	Assessment of the blurred object spatial frequency content	2
7.2.2	Variation of the power spectra with count density	4
7.2.3	Variation of the power spectra with acquisition angle	7
7.2.4	Variation of the power spectra with collimator	9
7.2.5	Variation of the power spectra with ROR	10
7.3	Data Sampling	11
7.4	Data Interpolation	13
7.5	Filtering	15
7.6	Combined data processing transfer functions	15
7.6.1	Discussion	17
7.7	Angular sampling	18
7.7.1	Methods	18
7.7.2	Results	19
7.7.3	Conclusions	19
7.8	Uniformity correction for high count data	20
7.8.1	Methods	21
7.9	Correction for ADC differential non-linearity	26
7.9.1	Methods	27
7.9.2	Results	28
7.9.3	Conclusions	29
7.10	General conclusions for Chapter 7	31
Chapter 8	Noise control - filter function selection	33
8.1	Local statistical noise	33
8.1.1	Results	35
8.1.2	Conclusions	37
8.2	Noise control - filter function selection	37
8.2.1	Introduction	37
8.2.2	Filter function selection - current status and general considerations	38
8.2.2.1	Conclusions	43
8.3	A suggested filter function selection method	45
8.3.1	Determination of the Butterworth power factor	46
8.3.1.1	Methods	47
8.3.1.2	Results	47
8.3.1.3	Conclusions	48
8.4	The enhanced Butterworth filter	48
8.5	Filter matching	49
8.5.1	Variability of the NPS	51
8.5.2	Determination of the filter cut off value	52
8.5.3	Conclusions	56
8.6	Two dimensional filtering	57
8.6.1	Rotationally symmetric filter	58
8.6.2	The y filter	60
8.6.3	Comparison of the y filter and r filter	60
8.7	Filter matching in two dimensions	61
8.7.1	Effects of y filtering	62

Contents of Volume Two		page
8.8	General conclusions for Chapter 8	64
Chapter 9	Parameter optimisation for high noise data	66
9.1	Introduction	66
9.2	Comparison of collimators	66
9.2.1	Methods	66
9.2.2	Noise considerations	67
9.2.3	Reconstruction	68
9.2.4	Analysis	69
9.2.5	Results	72
9.2.6	Conclusions	72
9.3	Attenuation correction	75
9.3.1	Results	75
9.3.2	Attenuation correction of noisy data	76
9.3.3	Conclusions	77
9.4	Uniformity correction	77
9.4.1	Results	78
9.4.2	Discussion	79
9.5	General conclusions for Chapter 9	80
Chapter 10	^{99m}Tc -HMPAO SPECT ; assessment of intractable epilepsy	82
10.1	Introduction	82
10.2	Methodology	83
10.2.1	Patient positioning - limitation of movement	83
10.2.2	Assessment of patient movement	85
10.2.2.1	Methods	85
10.2.2.2	Results	87
10.2.2.3	Discussion	88
10.2.2.4	Correction for patient movement	89
10.3	Choice of acquisition parameters	89
10.3.1	Choice of pixel size	89
10.3.2	Choice of acquisition time	90
10.3.3	Collimator choice	91
10.3.4	ROR limitations	91
10.4	Choice of reconstruction parameters	91
10.4.1	Choice of reconstruction filter	91
10.4.2	Application of attenuation correction	91
10.4.3	Application of uniformity correction	92
10.4.4	Image display and hardcopy	93
10.5	Activity administration - radiation dosimetry	93
10.6	Assessment of intractable epilepsy	94
10.6.1	Patient group	95
10.6.2	Assessment of patient studies	97
10.6.3	Results	97
10.7	Assessment of reconstruction method	98
10.8	General conclusions for Chapter 10	100
Chapter 11	Cardiac SPECT with ^{99m}Tc -MIBI	102
11.1	Introduction	102
11.2	Choice of SPECT acquisition parameters	104
11.2.1	Pixel size	105
11.2.2	Acquisition time	105

Contents of Volume Two	page
11.2.3 Collimator choice	105
11.2.4 ROR	105
11.2.5 360 degree or 180 degree orbit	106
11.3 Choice of SPECT reconstruction parameters	107
11.3.1 Filter function	107
11.3.2 Attenuation correction	108
11.3.3 Uniformity correction	109
11.3.4 Image display	109
11.4 Assessment of coronary artery disease with ^{99m}Tc -MIBI	110
11.4.1 Methods	110
11.4.2 Results	112
11.4.2.1 Simple detection of CAD	112
11.4.2.2 Identification of abnormal segments	112
11.4.2.3 Identification of diseased arteries	113
11.4.2.4 Differentiation between ischaemic and scarred tissue	114
11.5 General conclusions for Chapter 11	116
Chapter 12 Digital filtering of the bladder in SPECT bone studies of the pelvis.	119
12.1 Introduction	119
12.2 Artefact production	120
12.3 Post-reconstruction processing	122
12.4 Pre-reconstruction processing	123
12.4.1 Bladder identification	124
12.4.2 Interpolative background replacement	125
12.5 Assessment of the processing techniques	127
12.6 Results	127
12.7 Conclusions	132
Chapter 13 General conclusions	134
Appendix 1 Count losses due to high dynamic range data	147
Appendix 2 Publications resulting from this thesis	153
Bibliography	

CONTENTS

Contents of Volume Two		page
Chapter 7	Parameter optimisation for low noise data	1
7.1	Introduction	1
7.2	Data detection by the camera	1
7.2.1	Assessment of the blurred object spatial frequency content	2
7.2.2	Variation of the power spectra with count density	4
7.2.3	Variation of the power spectra with acquisition angle	7
7.2.4	Variation of the power spectra with collimator	9
7.2.5	Variation of the power spectra with ROR	10
7.3	Data Sampling	11
7.4	Data Interpolation	13
7.5	Filtering	15
7.6	Combined data processing transfer functions	15
7.6.1	Discussion	17
7.7	Angular sampling	18
7.7.1	Methods	18
7.7.2	Results	19
7.7.3	Conclusions	19
7.8	Uniformity correction for high count data	20
7.8.1	Methods	21
7.9	Correction for ADC differential non-linearity	26
7.9.1	Methods	27
7.9.2	Results	28
7.9.3	Conclusions	29
7.10	General conclusions for Chapter 7	31
Chapter 8	Noise control - filter function selection	33
8.1	Local statistical noise	33
8.1.1	Results	35
8.1.2	Conclusions	37
8.2	Noise control - filter function selection	37
8.2.1	Introduction	37
8.2.2	Filter function selection - current status and general considerations	38
8.2.2.1	Conclusions	43
8.3	A suggested filter function selection method	45
8.3.1	Determination of the Butterworth power factor	46
8.3.1.1	Methods	47
8.3.1.2	Results	47
8.3.1.3	Conclusions	48
8.4	The enhanced Butterworth filter	48
8.5	Filter matching	49
8.5.1	Variability of the NPS	51
8.5.2	Determination of the filter cut off value	52
8.5.3	Conclusions	56
8.6	Two dimensional filtering	57
8.6.1	Rotationally symmetric filter	58
8.6.2	The y filter	60
8.6.3	Comparison of the y filter and r filter	60
8.7	Filter matching in two dimensions	61
8.7.1	Effects of y filtering	62

8.8	General conclusions for Chapter 8	64
-----	-----------------------------------	----

Contents of Volume Two		page
Chapter 9	Parameter optimisation for high noise data	66
9.1	Introduction	66
9.2	Comparison of collimators	66
9.2.1	Methods	66
9.2.2	Noise considerations	67
9.2.3	Reconstruction	68
9.2.4	Analysis	69
9.2.5	Results	72
9.2.6	Conclusions	72
9.3	Attenuation correction	75
9.3.1	Results	75
9.3.2	Attenuation correction of noisy data	76
9.3.3	Conclusions	77
9.4	Uniformity correction	77
9.4.1	Results	78
9.4.2	Discussion	79
9.5	General conclusions for Chapter 9	80
Chapter 10	^{99m}Tc -HMPAO SPECT ; assessment of intractable epilepsy	82
10.1	Introduction	82
10.2	Methodology	83
10.2.1	Patient positioning - limitation of movement	83
10.2.2	Assessment of patient movement	85
10.2.2.1	Methods	85
10.2.2.2	Results	87
10.2.2.3	Discussion	88
10.2.2.4	Correction for patient movement	89
10.3	Choice of acquisition parameters	89
10.3.1	Choice of pixel size	89
10.3.2	Choice of acquisition time	90
10.3.3	Collimator choice	91
10.3.4	ROR limitations	91
10.4	Choice of reconstruction parameters	91
10.4.1	Choice of reconstruction filter	91
10.4.2	Application of attenuation correction	91
10.4.3	Application of uniformity correction	92
10.4.4	Image display and hardcopy	93
10.5	Activity administration - radiation dosimetry	93
10.6	Assessment of intractable epilepsy	94
10.6.1	Patient group	95
10.6.2	Assessment of patient studies	97
10.6.3	Results	97
10.7	Assessment of reconstruction method	98
10.8	General conclusions for Chapter 10	100
Chapter 11	Cardiac SPECT with ^{99m}Tc -MIBI	102
11.1	Introduction	102
11.2	Choice of SPECT acquisition parameters	104
11.2.1	Pixel size	105
11.2.2	Acquisition time	105

11.2.3	Collimator choice	105
11.2.4	ROR	105
11.2.5	360 degree or 180 degree orbit	106
Contents of Volume Two		page
11.3	Choice of SPECT reconstruction parameters	107
11.3.1	Filter function	107
11.3.2	Attenuation correction	108
11.3.3	Uniformity correction	109
11.3.4	Image display	109
11.4	Assessment of coronary artery disease with ^{99m}Tc -MIBI	110
11.4.1	Methods	110
11.4.2	Results	112
11.4.2.1	Simple detection of CAD	112
11.4.2.2	Identification of abnormal segments	112
11.4.2.3	Identification of diseased arteries	113
11.4.2.4	Differentiation between ischaemic and scarred tissue	114
11.5	General conclusions for Chapter 11	116
Chapter 12	Digital filtering of the bladder in SPECT bone studies of the pelvis.	119
12.1	Introduction	119
12.2	Artefact production	120
12.3	Post-reconstruction processing	122
12.4	Pre-reconstruction processing	123
12.4.1	Bladder identification	124
12.4.2	Interpolative background replacement	125
12.5	Assessment of the processing techniques	127
12.6	Results	127
12.7	Conclusions	132
Chapter 13	General conclusions	134
Appendix 1	Count losses due to high dynamic range data	147
Appendix 2	Publications resulting from this thesis	153

7.1 Introduction

As the first stage in the identification of an optimal imaging set, Chapter 1, the relationships between the various parameter choices can be examined for structured source distributions in the low noise situation. This has the advantage that the effects of the processes being investigated are not obscured by uncertainties in the data produced by stochastic variations.

The relationships between the different processes involved in the production of a SPECT image, for noise free data, were discussed in general terms in Section 2.2. The major considerations were the effects which the detection of data by the camera, its digitisation, filtering and back projection had on the spatial frequency content of the source distribution with particular attention being paid to the relationships between the strengths of the effects of the different processes.

These considerations will now be investigated for the specific SPECT system described in Chapter 3.

7.2. Data detection by the camera

As described in Section 2.2.1 the first stage of the SPECT imaging system is the detection of data by the camera. This has been studied for point and line sources in air and scatter using the two available collimators, Section 4.2.4. A direct extension of the information obtained from these measurements to the case of an extended, structured source distribution is difficult because of the variation of the the camera's MTF

with distance from the source. Thus the effects of the gamma camera detection process on the spatial frequency content of the signal emitted from an extended, structured object have to be examined directly. If this is performed for noise free (or very low noise) data acquisitions then the effects which the use of different collimators, acquisition angles and source-camera distances have on the signal can be assessed.

7.2.1 Assessment of the blurred object spatial frequency content

Images which have a low noise content (relative to a typical projection image) can be obtained by performing acquisitions of the phantom with inserts described in Section 3.6 over an extended period of time. It is difficult to use patient data because of the extended time periods involved and the lack of reproducibility. It is assumed that the spatial frequencies in the phantom inserts are representative of those obtained in clinical studies.

The images of the phantom were acquired and stored on the computing system using a 128*128 matrix with a pixel edge length of 0.28cm.

One dimensional profiles were taken through the insert images and the spatial frequency content of the data analysed (the cylindrical form of the phantom inserts allows the analysis to be performed in one dimension). The method of analysis followed the approach described in Section 2.3.4. Using this, the power spectrum can be written in its one dimensional form

$$PI(u) = NPS + MTF^2(u) \cdot PO(u) \quad 7.1$$

where $PI(u)$ is the power spectrum of the image profile
 NPS is the noise power spectrum
 $MTF(u)$ is the modulation transfer function
 $PO(u)$ is the object power spectrum

The power spectrum of the image profile is obtained by taking the square of the FT of the profile. Note that because the noise is "white" the noise power spectrum has a constant value, i.e. independent of u .

From equation 7.1 the blurred object power spectrum can be defined to be

$$BO(u) = MTF^2(u) \cdot PO(u) \quad 7.2$$

which allows equation 7.1 to be written in the form

$$PI(u) = NPS + BO(u) \quad 7.3$$

As the count density in the image is increased the relative magnitude of the NPS decreases and $PI(u)$ tends to $BO(u)$. Thus, the spatial frequency content of the object after blurring by the detection process can be investigated if low noise data are used.

To examine the spatial frequency content of the low noise data the most obvious approach would be simply to examine $PI(u)$ directly. This does not work in practice however because the value of the zero spatial frequency component is generally at least two orders of magnitude greater than the other values. The consequence of this is that the detailed shape of

the frequency spectrum is difficult to assess ; all frequency spectra appear to have the same shape.

To overcome this the following approach was developed. The first step normalises the data in the FT of the profile so that the first point (i.e. the zero frequency component) has a value of unity. This permits the data from images with different count levels to be compared. The power spectrum of the normalised profile is then obtained by taking the square of the data values. Finally the LOG (base 10) of the data is taken to produce the LOG power spectrum of the normalised profile, LNP(u). By using the LOG of the data the detail contained in the higher spatial frequencies can be visualised.

The usefulness of this novel construct, particularly in the investigation of the relationship between the signal and the noise in the image data, will be demonstrated in this chapter.

7.2.2 Variation of the power spectra with count density

Given that the power spectrum of the image, $PI(u)$, can be described in terms of equation 7.3, what effect will variations in the signal to noise ratio have on the appearance of LNP(u)? Figure 7.2 shows the LNP(u) curves obtained from profiles taken through the images of the HL insert which were obtained from acquisitions taken at an angle of 0 degrees using the LEAP collimator (a schematic representation of the orientations of the various inserts used in this chapter is shown in figure 7.1). The acquisition times were 100s, 1200s and 15000s giving a spread of noise values of an order of magnitude. These acquisition times should be compared with the 30s per projection angle used clinically. The camera was

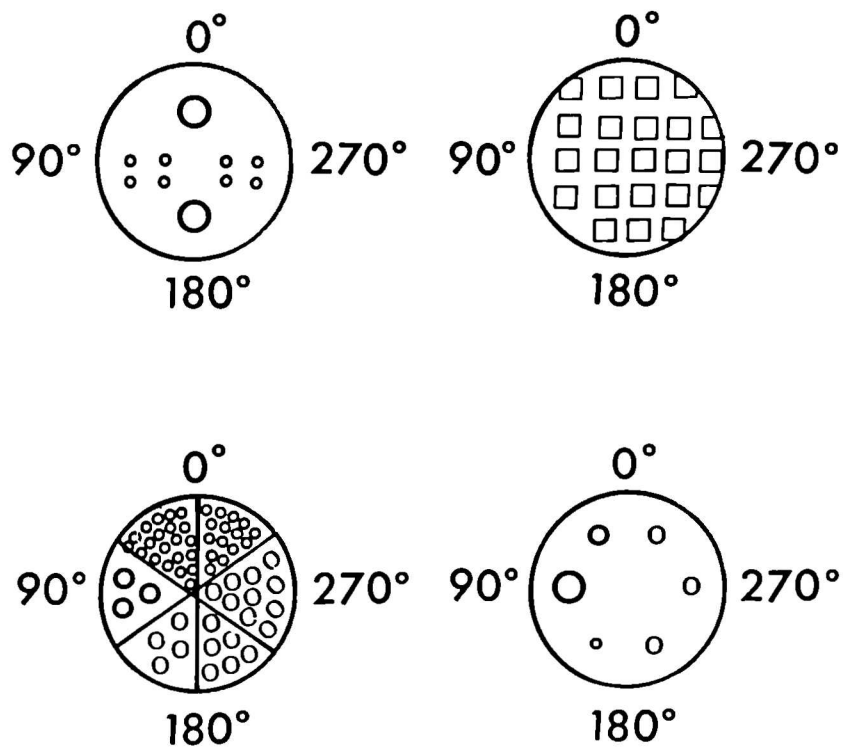


Figure 7.1 Schematic illustration of the orientations of the phantom inserts used for the SPECT acquisitions in Chapter 7.

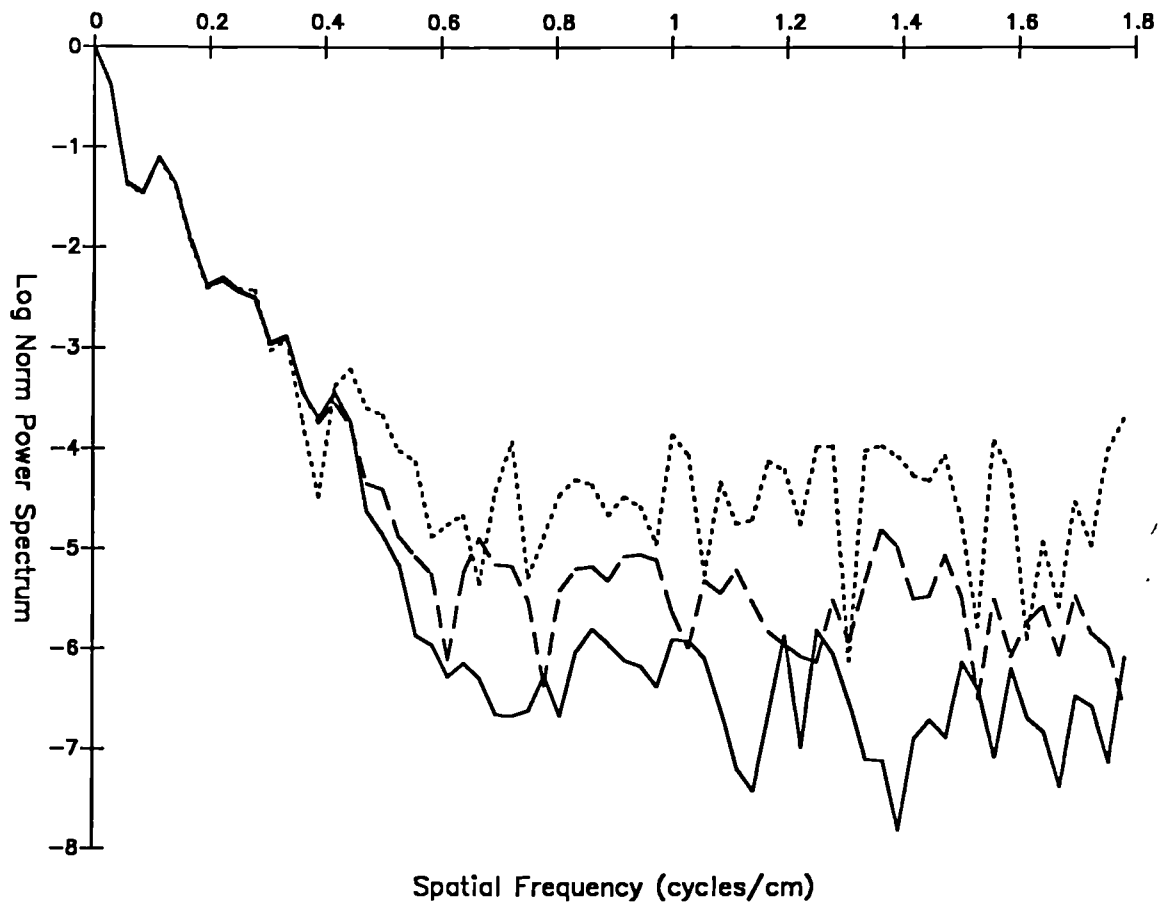


Figure 7.2 LNP(u) curves obtained from profiles taken through an image of the HL insert acquired at an angle of zero degrees. The LEAP collimator was used and the acquisition times were 100s (dotted line), 200s (dashed line) and 15000s (solid line).

placed 15cm from the phantom surface which is equivalent to a ROR value of 25cm.

The shape of the LNP(u) curves is of the same general form for all adequately sampled nuclear medicine data. The spatial frequencies from the blurred object dominate the curve at low spatial frequencies before becoming obscured by the NPS which at high spatial frequencies varies around a constant mean value.

The effect which the presence of different noise levels in the data has on the LNP(u) curves can be seen from figure 7.2. The amplitude of the NPS relative to the blurred object power spectrum is higher for the higher count image data. Furthermore, the spatial frequency at which the signal merges with the noise is lower for the lower count image data. It is these properties which make the LNP(u) construct useful in the examination of the effects of the data detection process.

It has been postulated that the amplitude of the NPS is given simply by the total number of counts in the profile, Section 2.3.4. This can be tested by examining the portion of LNP(u) with spatial frequency values above a threshold over which the blurred object spectrum has no power. This value can be determined by examining the transfer characteristics of the LEAP collimator, Section 4.2.4.5. From figure 4.13, for a source-camera distance of 15cm, no spatial frequencies greater than 1cm^{-1} are transferred. As 15cm is the smallest source-camera distance for the acquisitions used to produce the data this value will serve as a suitable threshold.

For the 100s image the predicted value for the NPS on the LNP(u) curve, using the total number of counts in the profile, was -4.38. The mean of the LNP(u) values corresponding to

spatial frequencies greater than 1cm^{-1} was -4.24 with a 95% confidence interval which ranged from -4.11 to -4.52 . Thus the predicted value was consistent with the measured data to a significance level of $p < 0.05$. The 95% confidence interval values were determined by calculating the LOG of the mean plus and minus two standard errors. Note that the statistical calculations were performed on the data before the LOG was taken.

For the 1200s image the predicted value for the NPS on the LNP(u) curve was -5.38 . The LNP(u) values with spatial frequencies greater than 1cm^{-1} had a mean value of -5.48 with a 95% confidence interval which ranged from -5.32 to -5.72 . Thus the predicted value was again consistent with the measured data.

Similarly for the 15000s image the predicted value for the NPS on the LNP(u) curve was -6.37 . As the LNP(u) values greater than 1cm^{-1} had a mean value of -6.44 and a 95% confidence interval which ranged from -6.28 to -6.72 the predicted value was again consistent with the measured data.

A similar approach to the data can be used to determine the spatial frequency value at which the amplitude of the LNP(u) curve becomes significantly greater than the noise. Again using the values with spatial frequencies which are higher than 1cm^{-1} the mean and standard deviation, SD, of the NPS can be measured. The LNP(u) curve values can be taken to be greater than the noise at a significance level of $p < 0.05$ when they are greater than the mean NPS value plus two SDs. For the 100s image the LOG of the mean plus two SDs of the curve values above 1cm^{-1} was -3.8 . From figure 7.2 it can be seen that the LNP(u) curve values were higher than the noise

threshold of -3.8 for spatial frequencies below 0.39cm^{-1} .

For the 1200s image the threshold noise amplitude was -4.8 giving a cut off frequency for the noise of 0.52cm^{-1} .

For the 15000s image the threshold noise amplitude was -5.7 giving a cut off frequency for the noise of 0.57cm^{-1} .

7.2.2.1 Discussion

The construct of the LNP(u) curve will be used throughout the remainder of this work. It provides a useful format for the assessment of the relationship between the signal and the noise power in the detected data.

The predicted value for the amplitude of the NPS, i.e. equal to the total number of counts in the profile data, was found to be consistent with the measured values and the analytical approach chosen. This indicates that the model used to describe the noise in the data was correct, Section 2.3.4.

7.2.3 Variation of the power spectra with acquisition angle

Images of the phantom inserts were acquired using the HR collimator at three different acquisition angles. The relationship between the angles and the objects within the phantom inserts is shown in figure 7.1.

Profiles were taken through each of the phantom inserts at the different acquisition angles and the LNP(u) curves produced.

Figure 7.3 shows the variation in the spatial frequency content of the profiles taken through the HL insert at angles of 0 degrees, 90 degrees and 180 degrees. The curves obtained from the 0 and 180 degree data are similar, particularly at the lower spatial frequency values where the influence of the

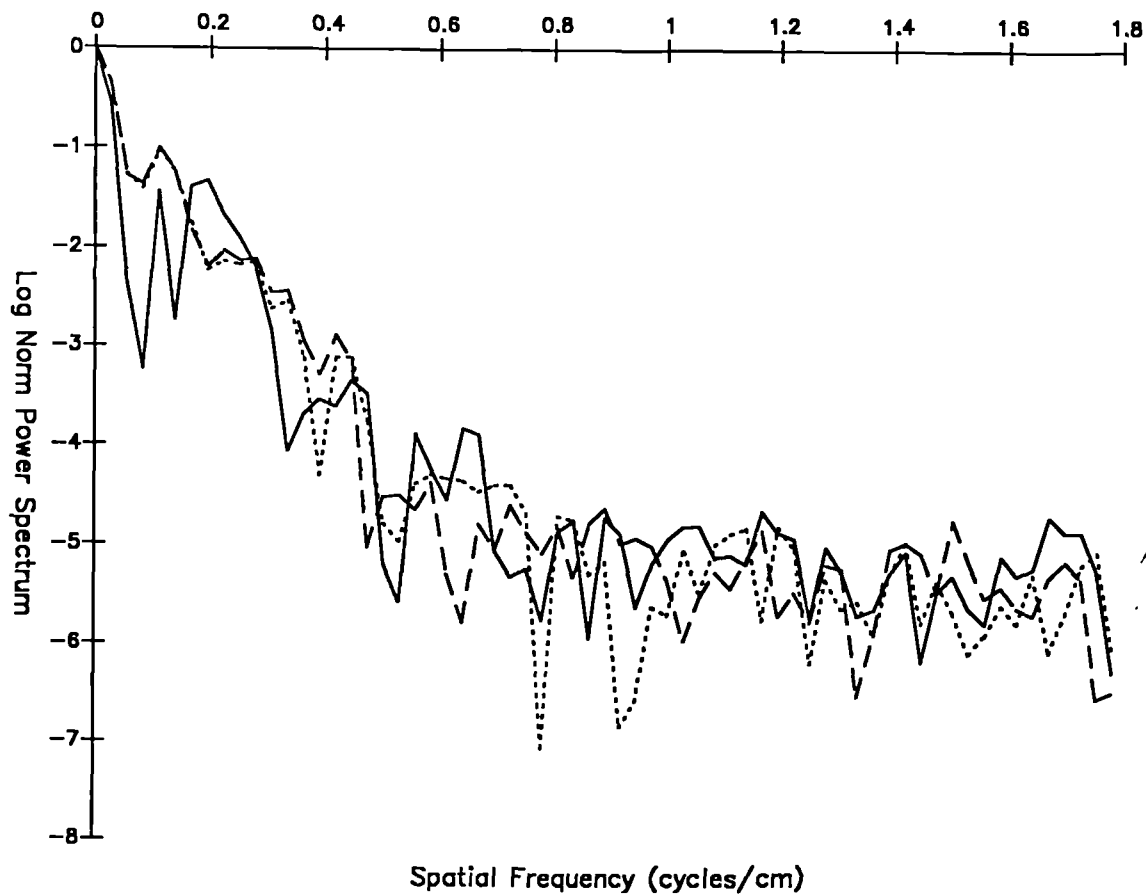


Figure 7.3 LNP(u) curves obtained from profiles taken through images of the HL insert acquired at angles of zero degrees (dotted line), 90 degrees (dashed line) and 180 degrees (solid line).

noise is low. This is to be expected from the symmetry of the insert structure. The curve obtained from the 90 degree image however shows large differences from the other two.

Figure 7.4 shows the same data for the linearity insert. All three curves are very similar in shape which is again to be expected from the symmetry of the insert. This serves as a good illustration of the reproducibility of this approach.

Figure 7.5 shows the results for the pie insert. There are large differences between all three curves without any overall pattern being apparent.

Figure 7.6 shows the results for the CL insert. The low level of structure in the insert produces smoother curves below 1cm^{-1} than observed previously - no spatial frequencies stand out above the rest. In addition the level of angular variation is low particularly when compared to the HL insert.

7.2.3.1 Discussion

Several authors, King (1983), Madsen (1985), have based their approaches to the production of an optimal filter for SPECT reconstruction on analyses of the spatial frequency content of the data in a "representative" projection image.

It is clear from these results however that there may be circumstances where there is a large variation in the spatial frequency content of projection images acquired at different angles around the subject. Thus the existence of a "representative" image requires further investigation. This will be performed in Chapter 8 using data with noise levels closer to those encountered in the clinical situation.

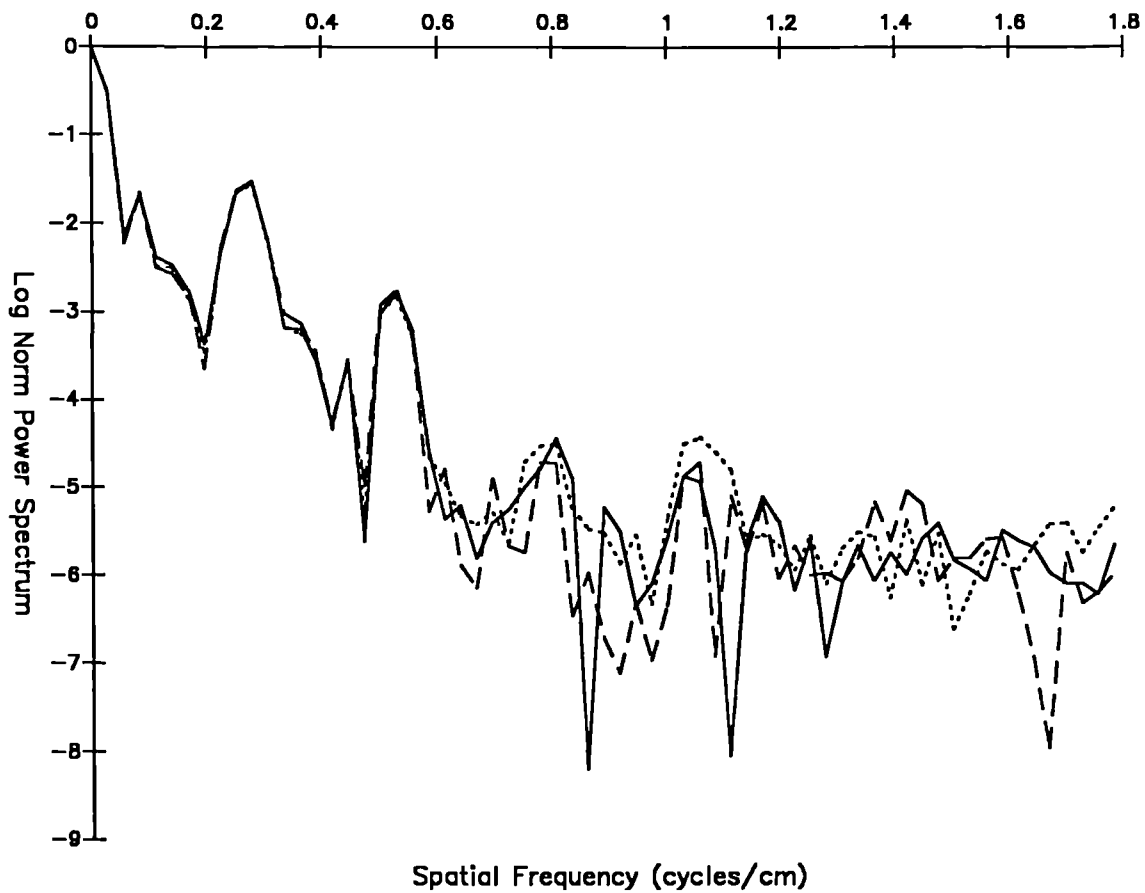


Figure 7.4 LNP(u) curves obtained from profiles taken through images of the linearity insert acquired at angles of zero degrees (dotted line), 90 degrees (dashed line) and 180 degrees (solid line).

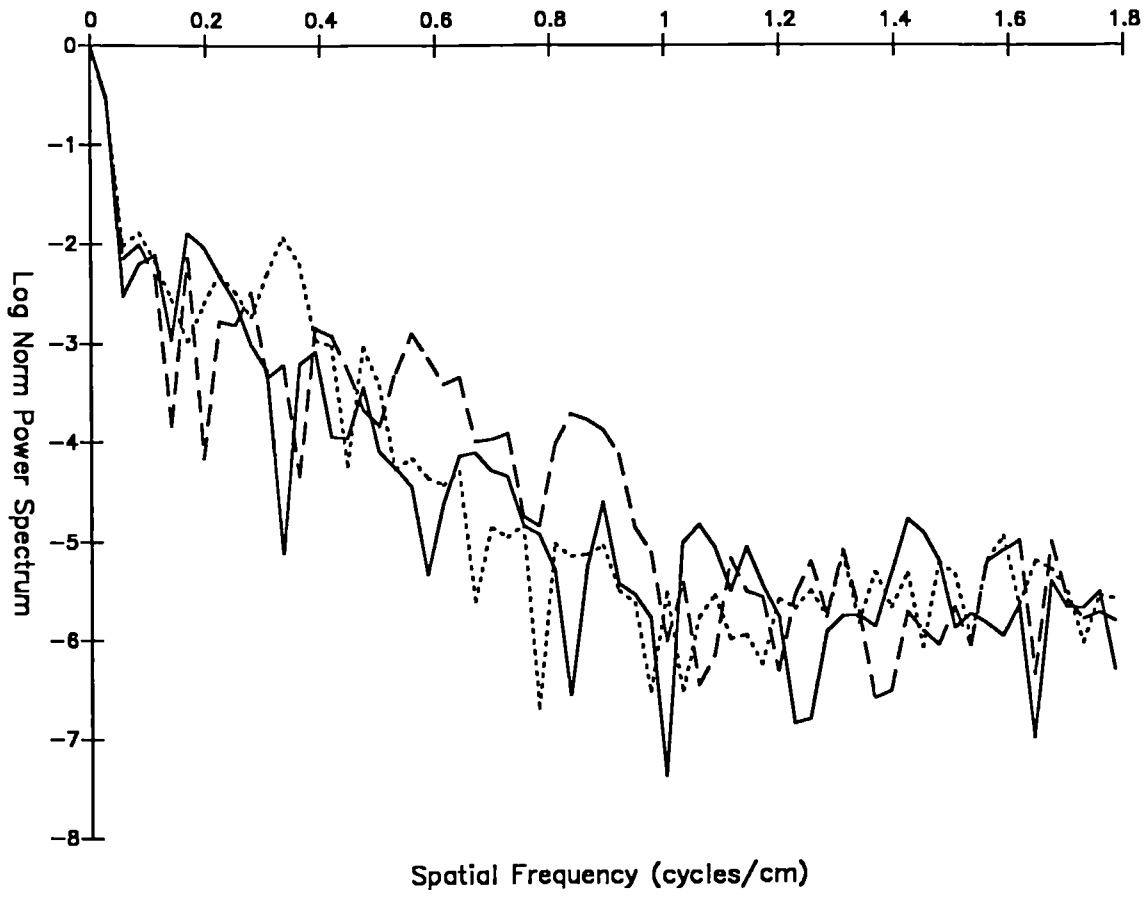


Figure 7.5 LNP(u) curves obtained from profiles taken through images of the pie insert acquired at angles of zero degrees (dotted line), 90 degrees (dashed line) and 180 degrees (solid line).

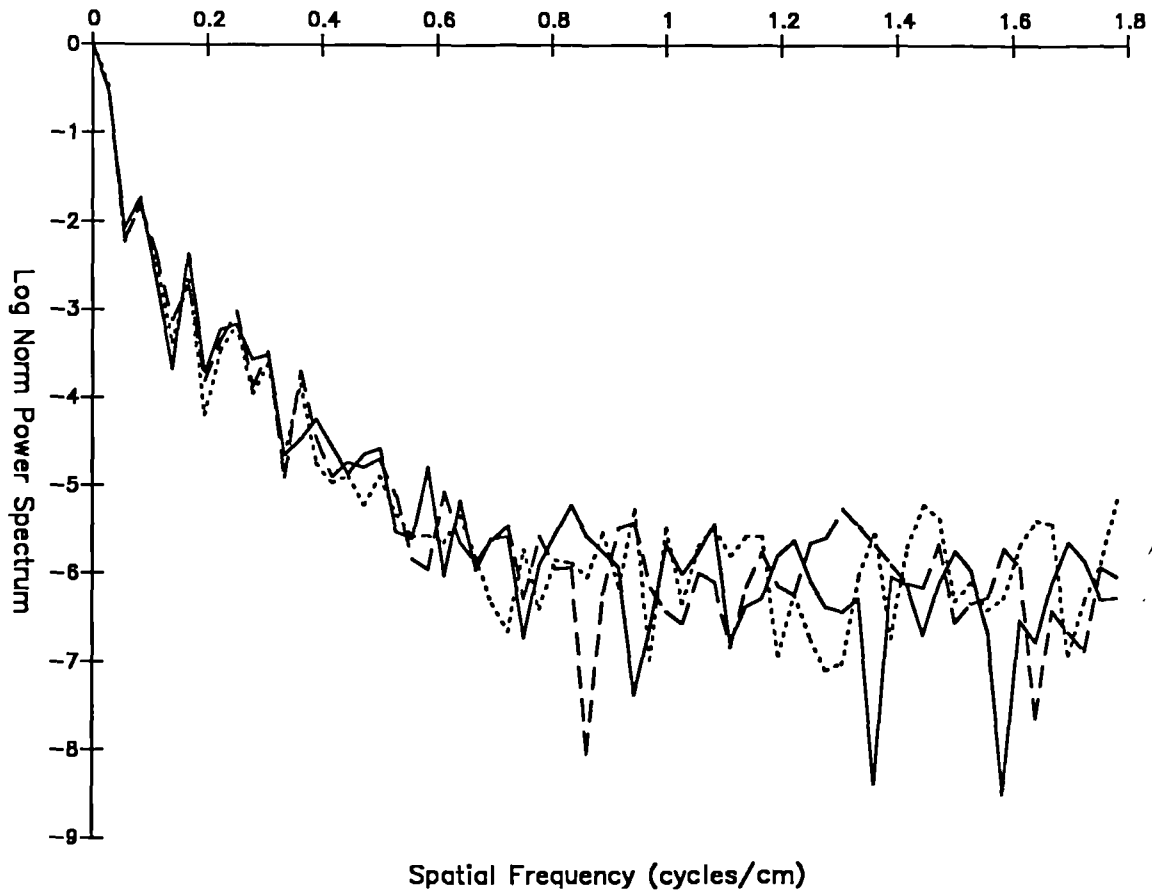


Figure 7.6 LNP(u) curves obtained from profiles taken through images of the CL insert acquired at angles of zero degrees (dotted line), 90 degrees (dashed line) and 180 degrees (solid line).

7.2.4 Variation of the power spectra with collimator choice.

In Chapter 4 the effects of the use of different collimators on the transfer characteristics of the detector system were investigated by examining the spatial frequency content of the images obtained from point and line sources. We can use the LNP(u) construct to extend this information to extended source distributions.

Figure 7.7 shows the results obtained from the HL insert at an acquisition angle of 0 degrees and a ROR of 15cm for both the LEAP and the HR collimators. The HR collimator does show a superior transfer of spatial frequencies when compared to the LEAP however the difference appears to be small. For example the difference between the curves was much less than that obtained when the camera angle was varied.

When the ROR was increased to 25cm the difference in the responses obtained from the LEAP and HR collimators increased, figure 7.8. This reflects the observations of Chapter 4 where the differences between the transfer characteristics of the collimators was magnified with increasing source-camera distances. Even at a ROR of 25cm the differences in the spatial frequency content of the projection data did not appear to be strongly dependent on the collimator used.

Similar results were obtained with the other inserts.

7.2.4.1 Discussion

For the high count density images which were studied to produce the results of the previous section the choice of collimator appeared to have a marginal effect on the spatial frequency content of the projection data. The dominant feature appeared to be the spatial frequency content of the object

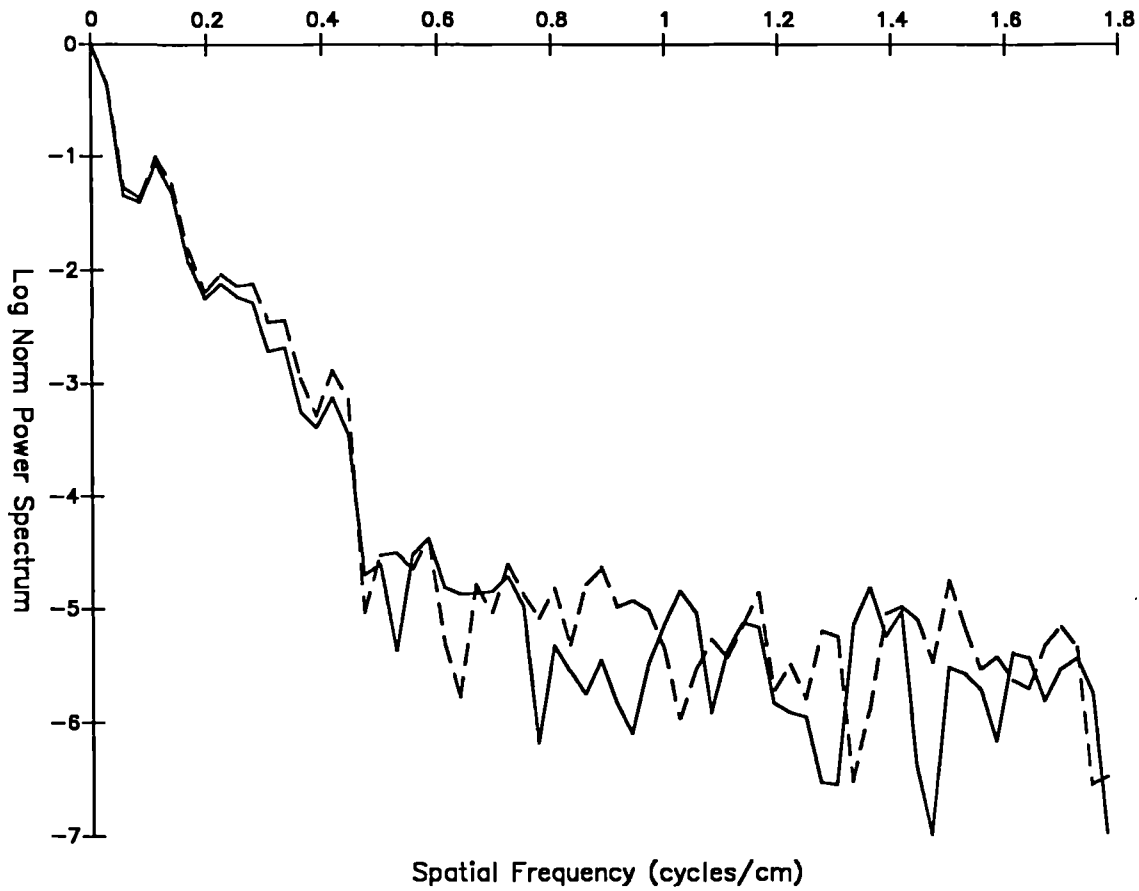


Figure 7.7 LNP(u) curves obtained from profiles taken through the HL insert image for the LEAP (solid line) and the HR collimator (dashed line). The source to camera distance was 15cm.

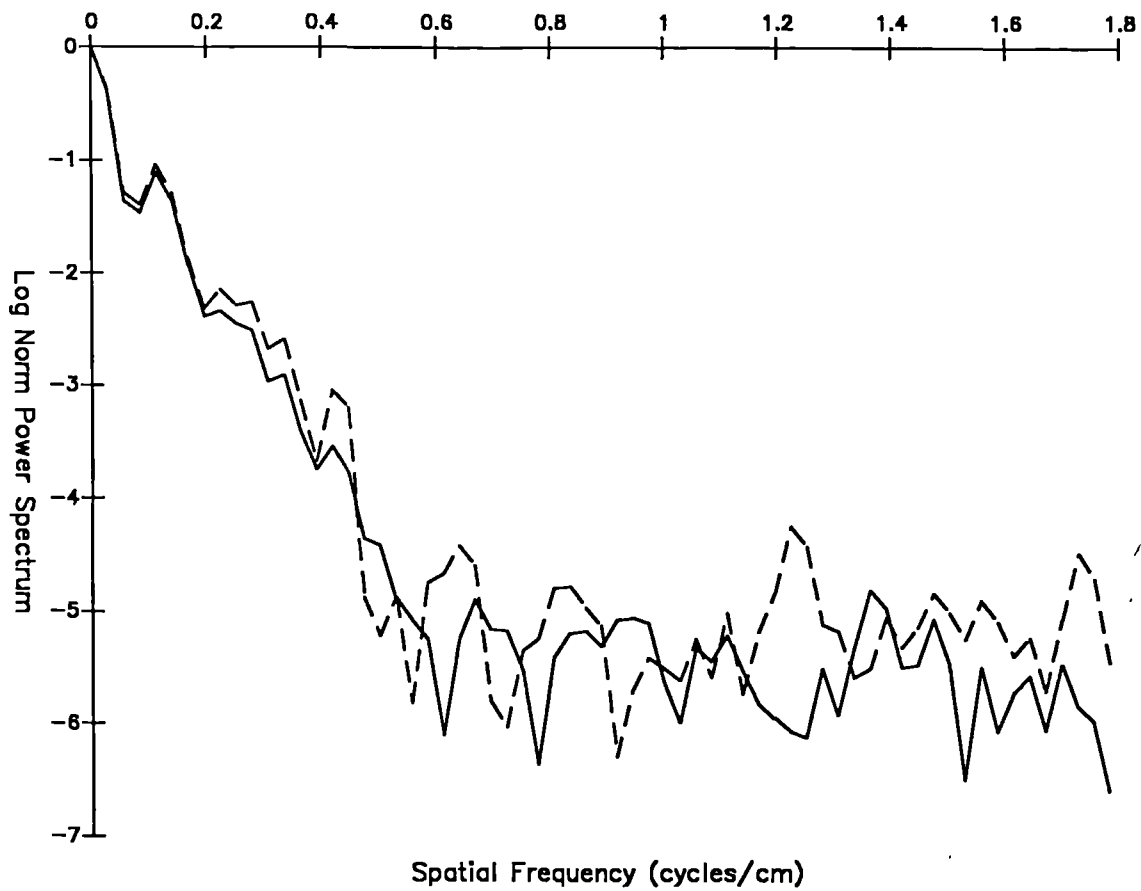


Figure 7.8 LNP(u) curves obtained from profiles taken through the HL insert image for the LEAP (solid line) and the HR collimator (dashed line). The source to camera distance was 25cm.

function itself.

For low count density images the increased sensitivity of the LEAP collimator may offset the superior transfer characteristics of the HR collimator. This will be investigated in Chapter 8.

7.2.5 Variation of the power spectra with ROR

The final parameter which can be investigated using the insert images is the variation of the power spectra with source to camera distance. This was examined for point and line sources in Chapter 4 but the extension of these results to that of an extended, structured source distribution is difficult because of the variation of the transfer characteristics themselves.

Figure 7.9 shows the LNP(u) curves for the HL insert imaged for 1200s at an acquisition angle of 0 degrees using the HR collimator with source to camera distances equivalent to ROR values of 15cm and 25cm. There was a reduction in the power of the mid-range spatial frequencies with the larger ROR value. The magnitude of this reduction, however, was small when compared, for example, to the level of variation in the LNP(u) curves observed with acquisition angle.

Figure 7.10 shows the same data for the LEAP collimator. The difference between the curves was greater than that observed with the HR collimator. This is to be expected from the results of Chapter 4.

Similar findings were observed for the LNP(u) curves of the other inserts.

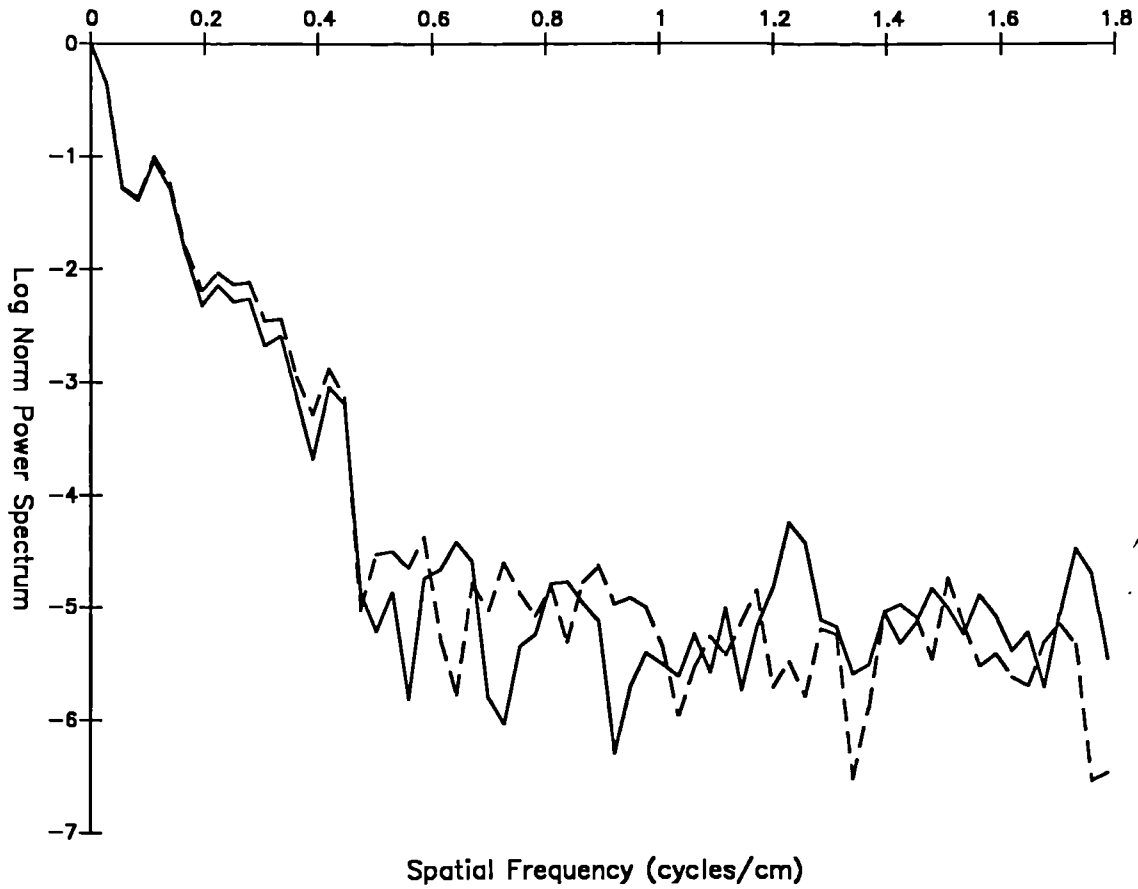


Figure 7.9 LNP(u) curves for the HL insert with source to camera distances equivalent to ROR values of 15cm (solid line) and 25cm (dashed line). The acquisition angle was zero degrees, the acquisition time was 1200s and the HR collimator was used.

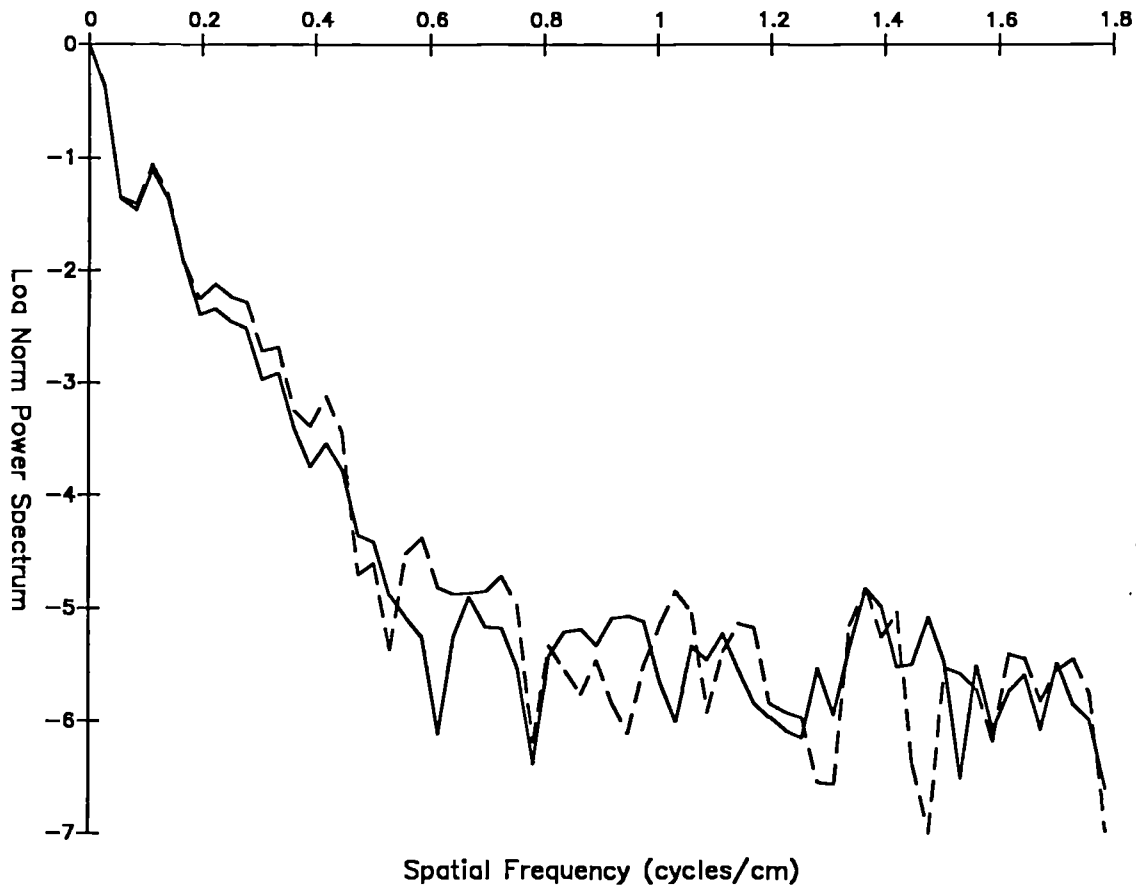


Figure 7.10 LNP(u) curves for the HL insert with source to camera distances equivalent to ROR values of 15cm (solid line) and 25cm (dashed line). The acquisition angle was zero degrees, the acquisition time was 1200s and the LEAP collimator was used.

7.2.6 Conclusions

Using the LNP(u) construct various aspects of the data detection process were investigated in a low noise situation. This permitted the effects of the data detection process to be differentiated from the effects of stochastic noise.

From these results the dominant effects on the spatial frequency content of any individual projection image were produced by the structure of the object itself, the angle at which it is viewed and the noise level of the data. The choice of collimator and the ROR were less important.

This does not necessarily mean that the small but systematic effects produced by the collimator choice and the ROR value do not combine over a whole projection image set to have a strong influence on image quality.

7.3 Data Sampling

As described in Chapter 2, once the data have been detected by the camera the next stage of the imaging system is concerned with its conversion into digital form for computer storage and manipulation.

As described in Section 2.2.2 the conversion of the continuous position signals into digital form is equivalent to convolving the data with a "comb" of rectangular functions of width equal to the sampling distance (i.e. pixel length). The frequency space representation of this gives the data processing transfer function , $S(u)$,

$$S(u) = \text{sinc}(\pi \cdot u \cdot a) \quad 7.4$$

where u = spatial frequency

a = sampling distance

The form of this function for four different sampling distances is shown in figure 7.11. The functions are only shown up to the Nyquist frequency for each sampling distance because above this value no spatial frequencies will be transferred. For example for the 0.7cm pixels the form of the function is defined up to spatial frequencies 0.71cm^{-1} . The sampling distance values of 0.35cm and 0.7cm correspond to the pixel lengths which are obtained for the gain settings used routinely with 128×128 and 64×64 matrix sizes respectively.

The other sampling distances shown in figure 7.11 are obtained from a higher gain setting than that used routinely with 64×64 and 128×128 matrix dimensions. These are useful for phantom studies and also perhaps for imaging organs which do not cover the whole camera FOV.

It is interesting to note from the transfer functions shown in figure 7.11 how the choice of smaller pixels improves the transfer of low spatial frequencies as well as high.

A comparison of the spatial frequency content of the blurred object functions from the phantom inserts, figures 7.2 to 7.10, and the sinc functions for the different pixel sizes shows several features. Firstly, the highest spatial frequencies present in the blurred object spectra were below 1cm^{-1} , Section 7.2.2. Thus, to avoid aliasing artefacts the Nyquist frequency produced by the sampling must be above this value imposing an upper limit on the pixel size of 0.5cm. However, the choice of a pixel size well below this value, 0.35cm for example, would still not be an optimal choice for noise free data. This is because the amplitude of the data sampling transfer function, $S(u)$, has a value less than unity

Transfer functions due to data sampling

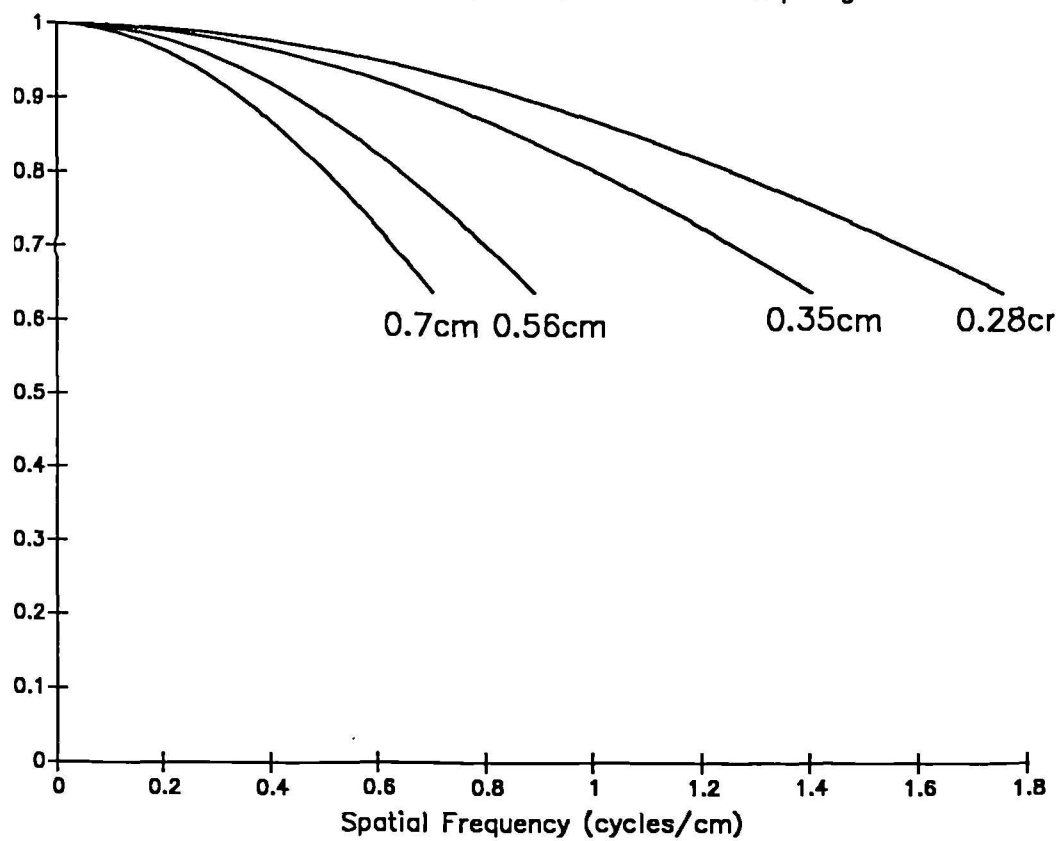


Figure 7.11 Transfer functions associated with the data sampling process for pixels of edge length 0.75cm, 0.56cm, 0.35cm and 0.28cm.

(0.75 in fact) at a frequency of 1cm^{-1} . This implies that some suppression of the information in the signal is produced.

This illustrates the point made in Section 2.2.2 that for noise free data an infinitely high sampling rate is required in order to avoid a loss of information caused by the sampling process. If very low noise data were available the pixel size should be chosen to be as small as possible, given the limitations imposed by the size of the digital FOV and the size of the data matrix which the software can handle.

The real problem in SPECT imaging, however, is the sampling of data which has a finite, and usually large, noise level. This topic will be investigated in Chapter 8.

Finally, it should be noted that the true blurred object spectrum can be recovered from the sampled blurred object spectrum by multiplying its FT by the reciprocal of $S(u)$ for the pixel size used.

7.4 Data Interpolation.

As described in Section 2.2.2.2 some method of registering the projection element values onto the transaxial image matrix is required for the back projection process. On the Nodecrest system this is performed by linearly interpolating the data to give a projection profile of length 256 elements and then using the nearest neighbour method of interpolation during back projection. The effect of the linear interpolation of the profile is given, as described in Section 2.2.2.2, by the function

$$IA(u) = [\text{sinc}(\pi \cdot u \cdot a/4)]^2 \quad 7.5$$

The factor of four arises because it is not a continuous interpolation which is performed but an interpolation from a 64 to a 256 element function.

Also, as described in Section 2.2.2.2 the nearest neighbour

interpolation gives a transfer function of

$$IN(u) = \text{MOD}[\text{sinc}(\pi \cdot u \cdot a)] \quad 7.6$$

The product of these two functions gives the combined effect of the interpolation procedure used by the Nodecrest algorithm

$$I(u) = IA(U) \cdot IN(U) \quad 7.7$$

This function is shown in figure 7.12 for a pixel length of 0.7cm. It is compared with the transfer functions which would be produced if a simple nearest neighbour or a full linear interpolation procedure had been applied. The simple nearest neighbour approach is inaccurate and would be expected to introduce artefacts into the data. The full linear interpolation is more accurate but suppresses the higher spatial frequencies to a greater extent. It is also time consuming to perform. As can be seen from figure 7.12 the chosen procedure lies somewhere between the two previously described methods in terms of spatial frequency transfer behaviour.

For projection profiles of length 128 pixels the interpolation to a length of 256 is less so the factor of 4 in equation 7.5 should be changed to 2.

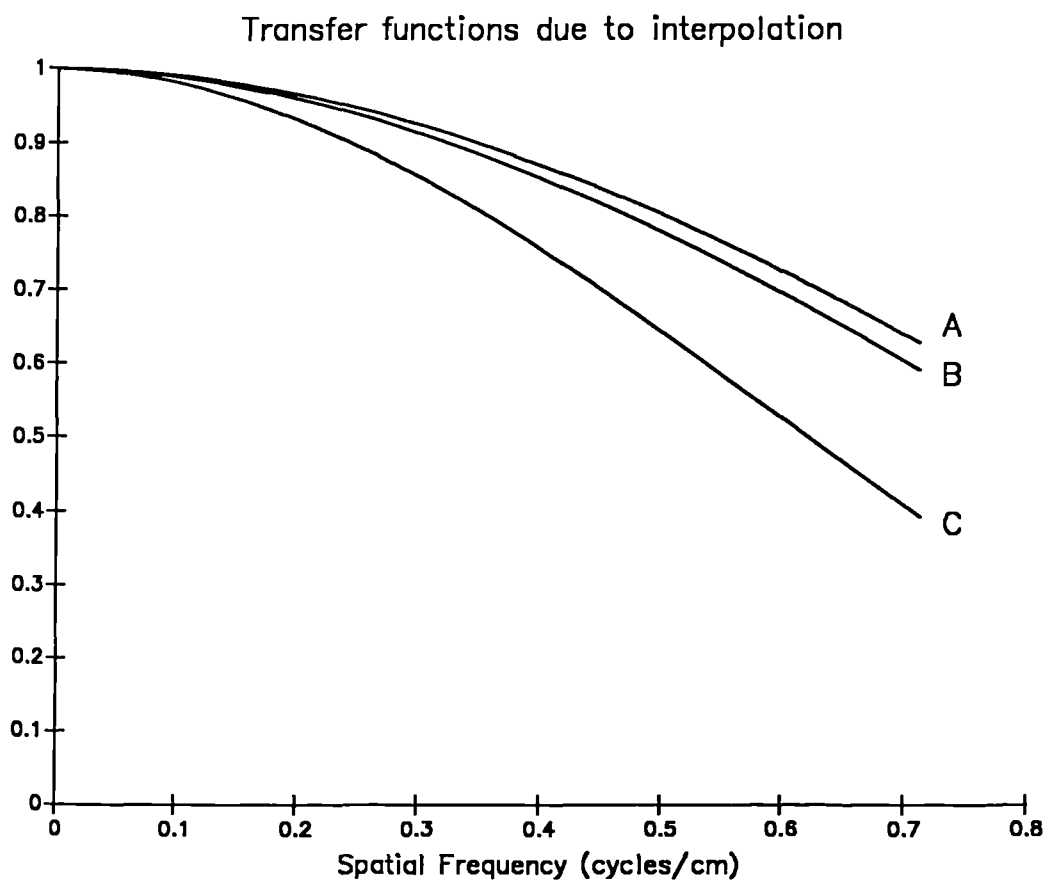


Figure 7.12 Interpolation transfer function for ;

- A - the nearest neighbour method
- B - the Nodecrest method
- C - the linear interpolation method

7.5 Filtering

Having obtained the digital image information the data have to be filtered prior to back projection. As described in Section 2.1 convolving the projection data with the inverse F.T. of a ramp function is necessary to remove the blurring effects of the back projection process. In addition a window function is usually used to multiply the ramp in order to produce a less discrete cut off at the Nyquist frequency and more importantly to reduce the effects of noise in the reconstructed data by reducing the relative amplitude of the higher spatial frequencies.

The effect of different window functions can be best illustrated, as described in Section 2.2.4 and, by examining the form of their spatial frequency transfer functions. As described in Section 3.5.3.3, on the Nodecrest system, the Shepp-Logan filter is recommended for use with 64*64 data and the soft Shepp-Logan for 128*128 data. The frequency space representations of these functions are shown in figure 7.13 for pixel lengths of 0.28cm and 0.56cm and their transfer functions are shown in figure 7.14.

It is important to recognise that the effects of the filter transfer functions cannot be interpreted by comparing them directly with the blurred object spatial frequency data, an error frequently made in the literature, King (1986), Madsen(1985). The effects of the filters have to be assessed as a part of a combined process which includes the effects of data sampling.

7.6 Combined data processing transfer functions

When considering the application of different window

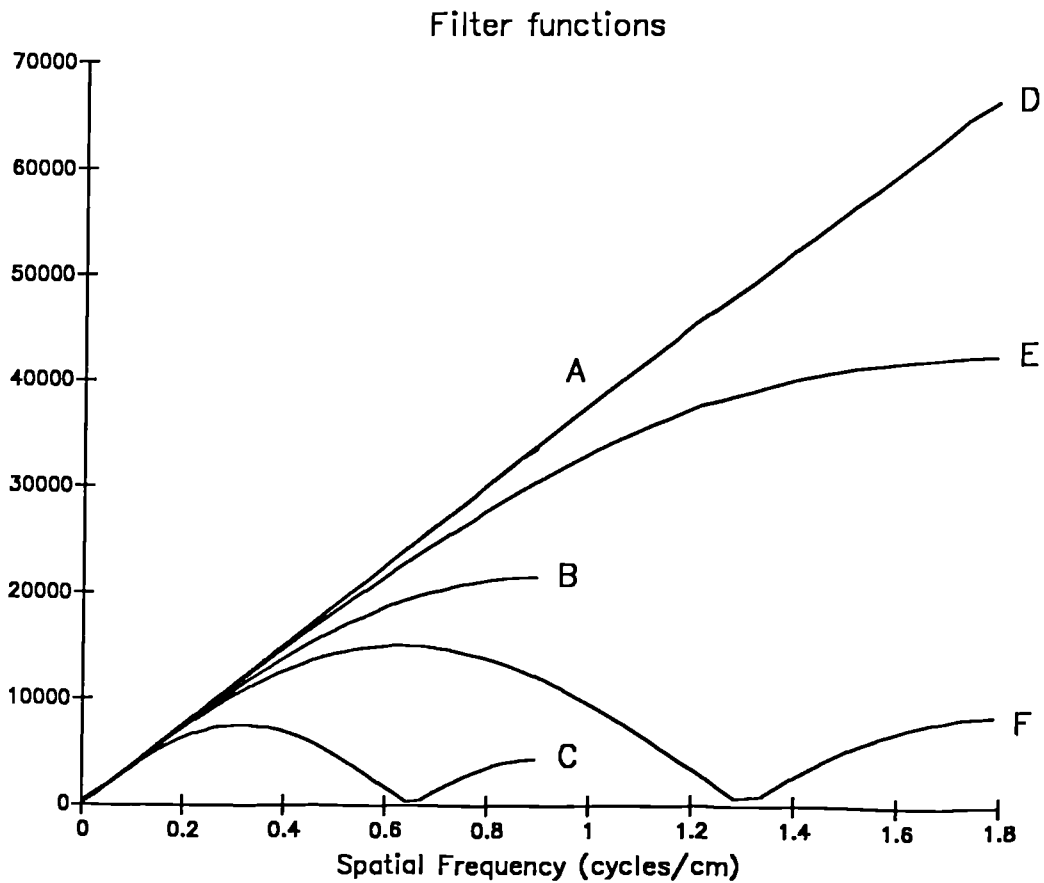


Figure 7.13 Frequency space representations of the Nodecrest filter functions for ;

- A - ramp with 0.28cm pixels
- B - Shepp-Logan with 0.28cm pixels
- C - soft Shepp-Logan with 0.28cm pixels
- D - ramp with 0.56cm pixels
- E - Shepp-Logan with 0.56cm pixels
- F - soft Shepp-Logan with 0.56cm pixels

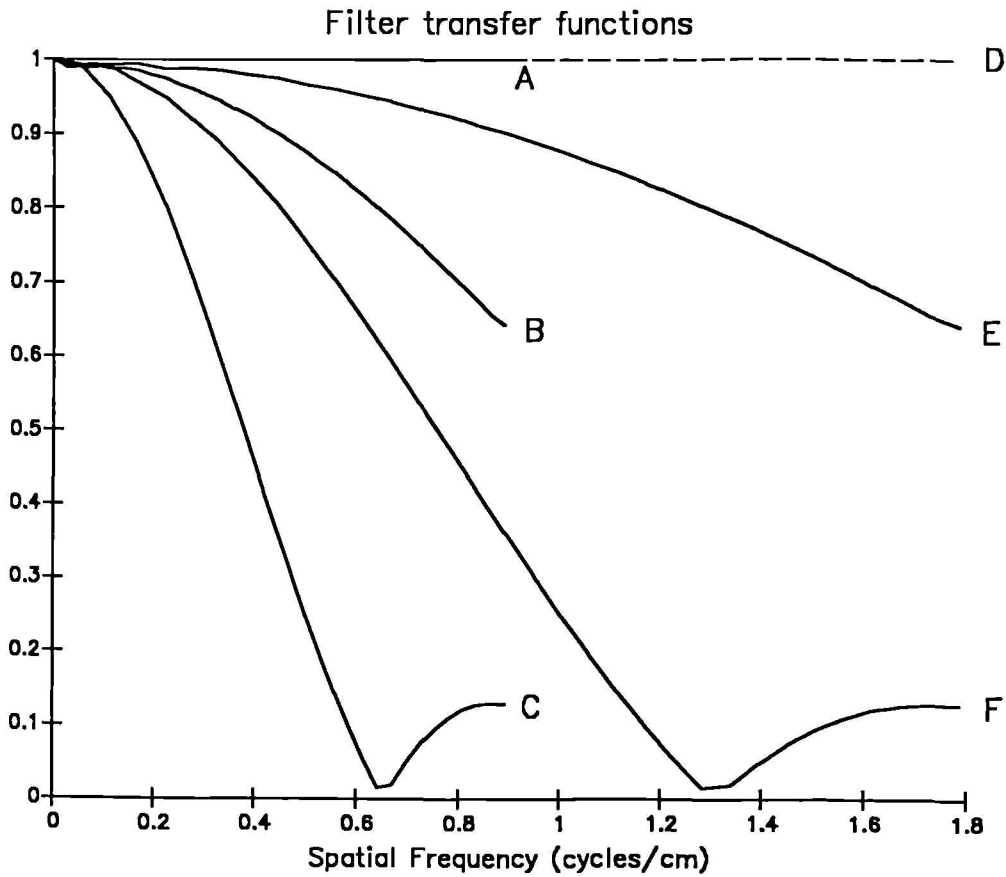


Figure 7.14 Transfer functions of the Nodecrest filter functions for ;

- A - ramp with 0.28cm pixels
- B - Shepp-Logan with 0.28cm pixels
- C - soft Shepp-Logan with 0.28cm pixels
- D - ramp with 0.56cm pixels
- E - Shepp-Logan with 0.56cm pixels
- F - soft Shepp-Logan with 0.56cm pixels

functions it is important that the frequency transfer properties of the other data processing operations, described previously, are also accounted for.

For this reason a unified data processing transfer function can be defined. It is given by the product, in frequency space, of the filter transfer function, $W(u)$, the interpolation transfer function $I(u)$ and the data sampling transfer function $S(u)$. Thus,

$$T(u) = S(u) \cdot W(u) \cdot I(u) \quad 7.8$$

The form of this function for any combination of the data processing parameter choices can be calculated. For example the use of the Shepp-Logan filter with a pixel size of 0.56cm and a 64 pixel projection profile gives

$$S(u) = \text{sinc}(0.56 \cdot \pi \cdot u) \quad 7.9$$

$$W(u) = \text{sinc}(0.56 \cdot \pi \cdot u) \quad 7.10$$

$$I(u) = \text{sinc}(0.56 \cdot \pi \cdot u) \cdot [\text{sinc}(0.14 \cdot \pi \cdot u)]^2 \quad 7.11$$

Thus,

$$T(u) = [\text{sinc}(0.56 \cdot \pi \cdot u)]^3 \cdot [\text{sinc}(0.14 \cdot \pi \cdot u)]^2 \quad 7.12$$

A comparison of $T(u)$ with the filter transfer functions, $W(u)$, alone for the three filters recommended by Nodecrest is shown in figure 7.15 for pixels of edge length 0.56cm.

Points to note from this are the differences in the filter transfer functions, particularly for the sharper filters, which are produced when all of the data processing effects are accounted for. Thus a naive assumption, for example, that the application of the ramp filter will preserve the spatial

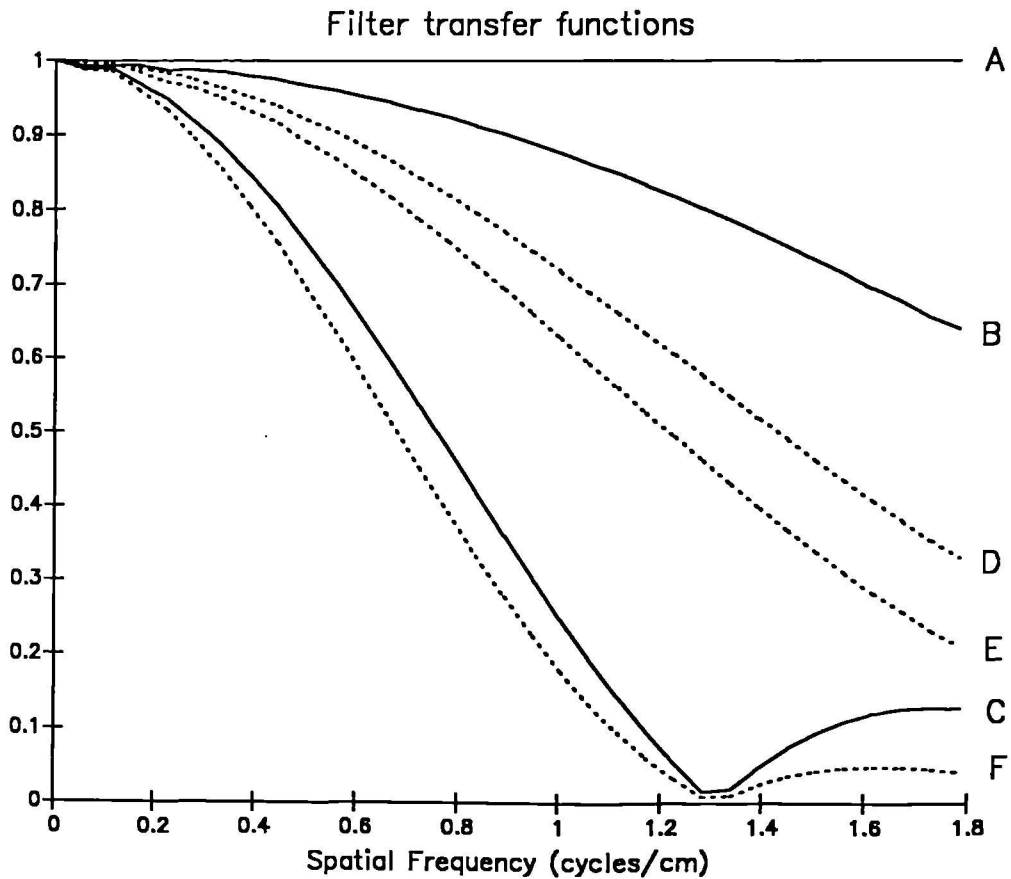


Figure 7.15 Comparison of the filter transfer functions with the unified data processing transfer functions ;

- A - Filter transfer function for the ramp
- B - Filter transfer function for the Shepp-Logan
- C - Filter transfer function for the soft Shepp-Logan
- D - Unified transfer function for the ramp
- E - Unified transfer function for the Shepp-Logan
- F - Unified transfer function for the soft Shepp-Logan

frequency content of the blurred object function would be significantly in error.

7.6.1 Discussion

An important point to note from the previous analysis is the critical role which the choice of pixel size has on the form of the reconstructed SPECT image if the system is used in a "turnkey" manner. This can be seen from figure 7.15 where the unified transfer functions for the three filters recommended by the manufacturer are shown for pixel sizes of 0.56cm and 0.28cm. The magnitude of the difference in the transfer functions for any given filter can be compared with that observed when, for example, different collimators are used, figure 4.17.

The reason for this is that the pixel size, a , affects not only the inherent filtering due to digitisation, $S(u)$, but also the form of the interpolation transfer function, $I(u)$, and the form of the filter transfer function $W(u)$. While the pixel size is an integral part of $S(u)$ and $I(u)$ it is only involved in the form of $W(u)$ because the cut off frequency of the filter function is tied to the Nyquist frequency, i.e. $1/2a$.

Thus the critical role which the selection of pixel size has can be removed by making the cut off frequency of the filter function independent of the Nyquist frequency. This allows the operator to control the form of $T(u)$, the combined data processing transfer function, more conveniently, allowing it to be matched to the requirements of the imaging task to be performed.

The use of filter functions designed specifically to

achieve this purpose will be investigated in Chapter 8.

7.7 Angular sampling

Another aspect of the data detection process which can be usefully investigated using low noise data is the choice of the angular sampling rate. This is a suitable subject for investigation in the noise free situation because, as discussed in 2.2.3, splitting a constant total acquisition time into different numbers of projection angles does not affect the stochastic noise in the reconstructed data. Thus the results obtained from the low noise studies will be directly transferable to the clinical situation.

Also, as discussed in Section 2.2.3, a theoretical value can be calculated for the angular sampling rate above which angular undersampling artefacts do not occur. For typical imaging situations this suggests that the collection of a large number (around 200) of projection images is required. However, the data from the SPECT line and point spread function measurements in Section 5.3.4 suggested that, even for high linear sampling rates, the use of 64 projection angles did not introduce significant artefacts. Thus, the significance of these results for extended source distributions should be investigated.

7.7.1 Methods

High gain, low noise SPECT acquisitions of the SIEL phantom with inserts were performed using the the standard approach and set up described in Section 6.3.1. The HR collimator was used so that any angular undersampling artefacts which resulted from the use of lower angular

sampling rates were not masked by the lower spatial frequency cut off of the LEAP collimator. The first acquisition used 128 projection with an acquisition time of 300s per angle. The second acquisition used 64 projection angles with an acquisition time of 600s per angle. A third study was obtained from this by using every alternate projection image to form a new study with 32 projection images.

The studies were reconstructed using the ramp filter.

7.7.2 Results

The images of the phantom inserts produced by the 128, 64 and 32 angle SPECT studies are shown in figures 7.16, 7.17, 7.18 and 7.19. There is a large difference in quality between the 32 and 64 angle studies which is most evident on the pie and linearity inserts. However, it is difficult to detect any significant differences between the 128 and 64 angle studies. Quantitative assessments of the data were made by taking profiles through the insert images. Again, however, the results obtained from the 128 and 64 angle studies were very similar. An example of this is shown in figure 7.20 where profiles have been taken through the HL insert images.

7.7.3 Conclusions

Simulated data of Biesk (1987) suggested that the use of 64 angles would compromise SPECT image quality. However, this result does not seem to hold for real data. The effects of the spread of the LSF with source to camera distance and of attenuation and scatter produce additional degradations in image quality not taken into account by the simulation. This also holds for the theoretical analysis of angular sampling

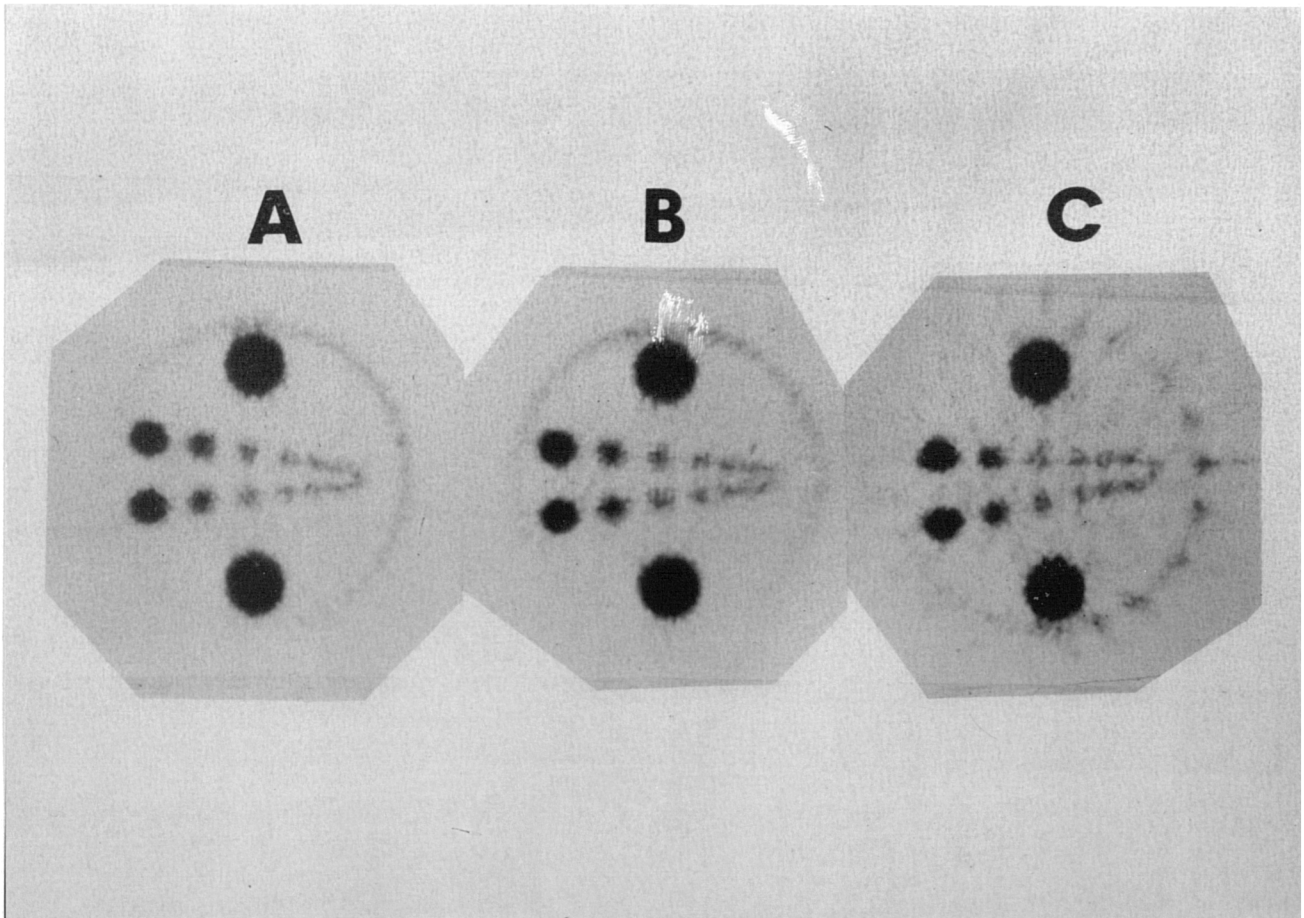


Figure 7.16 Section through the HL insert from acquisitions using ;

- A - 128 projection angles
- B - 64 projection angles
- C - 32 projection angles

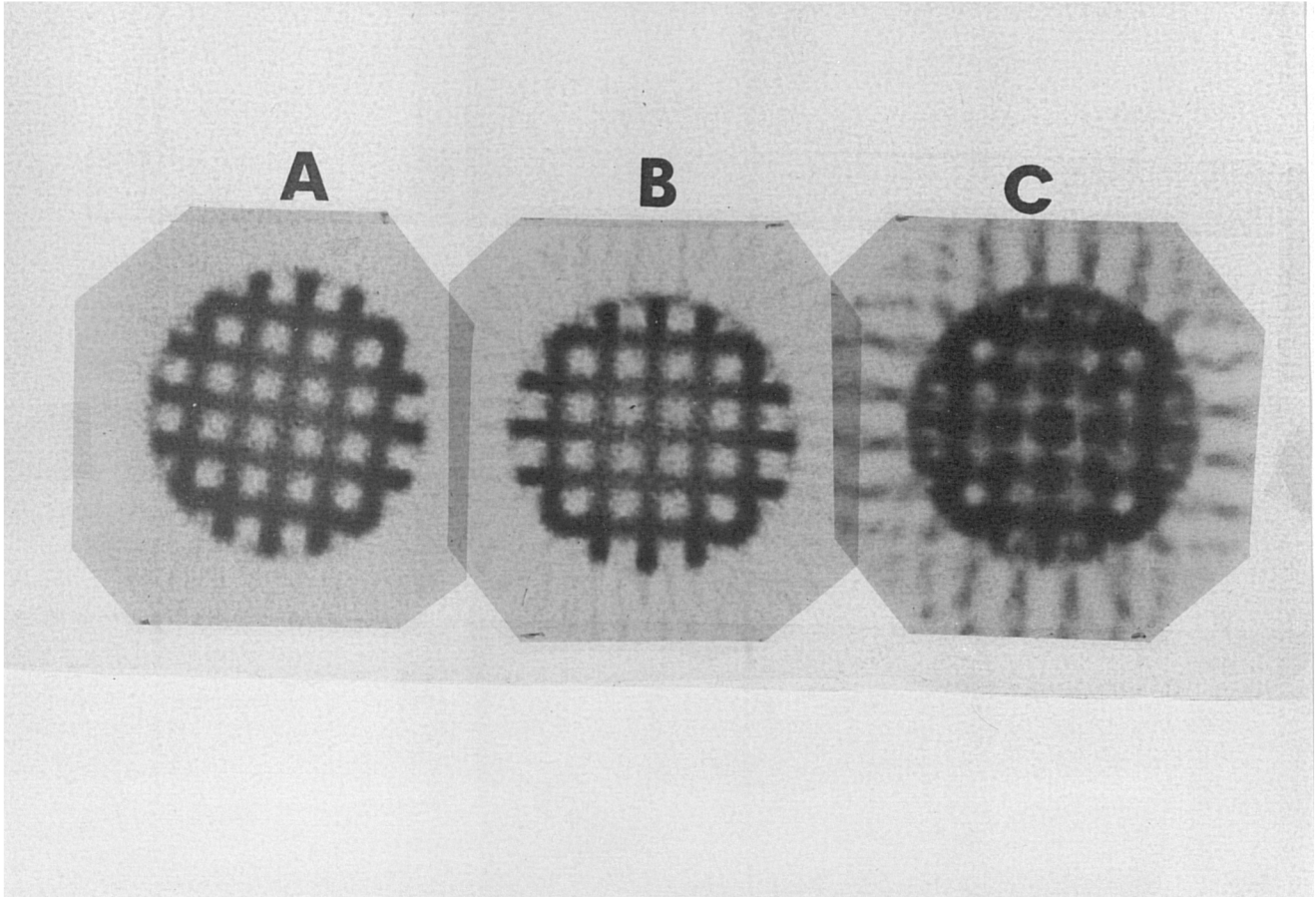


Figure 7.17 Section through the linearity insert from acquisitions using ;

- A - 128 projection angles
- B - 64 projection angles
- C - 32 projection angles

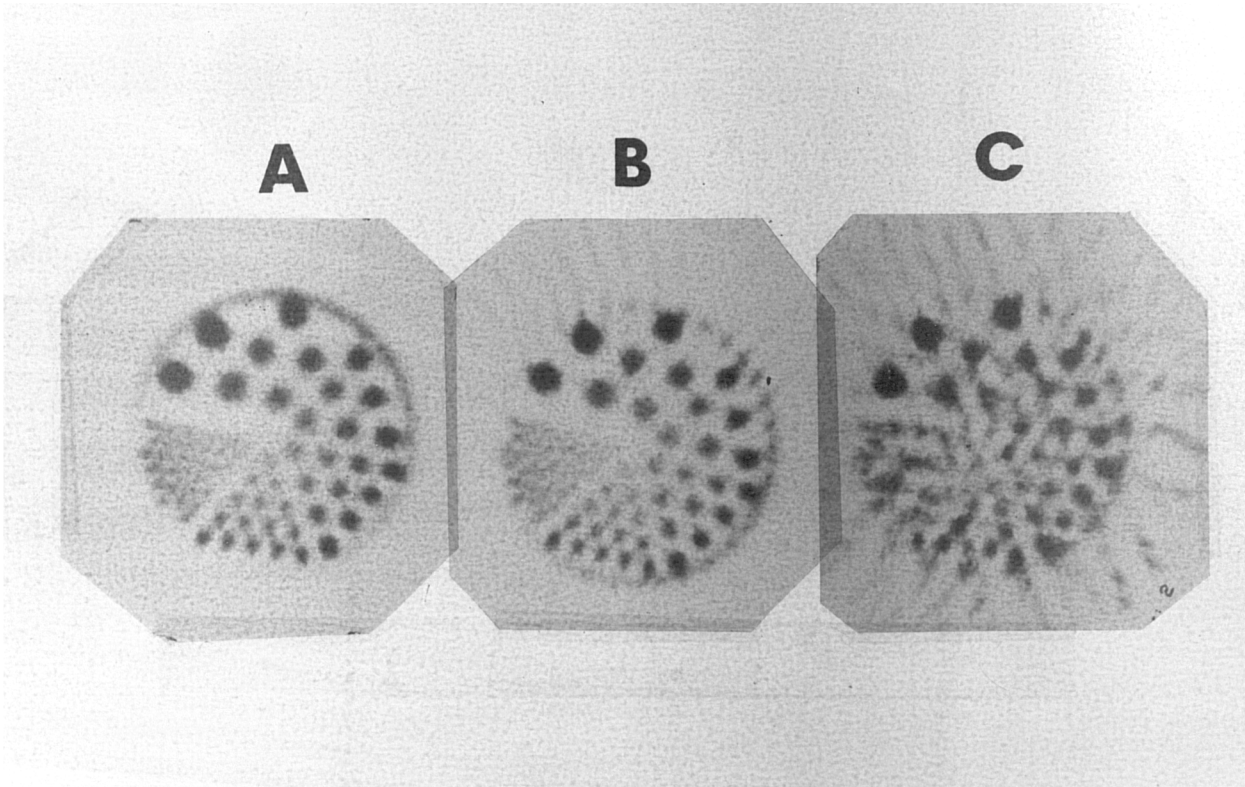


Figure 7.18 Section through the pie insert from acquisitions using ;

- A - 128 projection angles
- B - 64 projection angles
- C - 32 projection angles

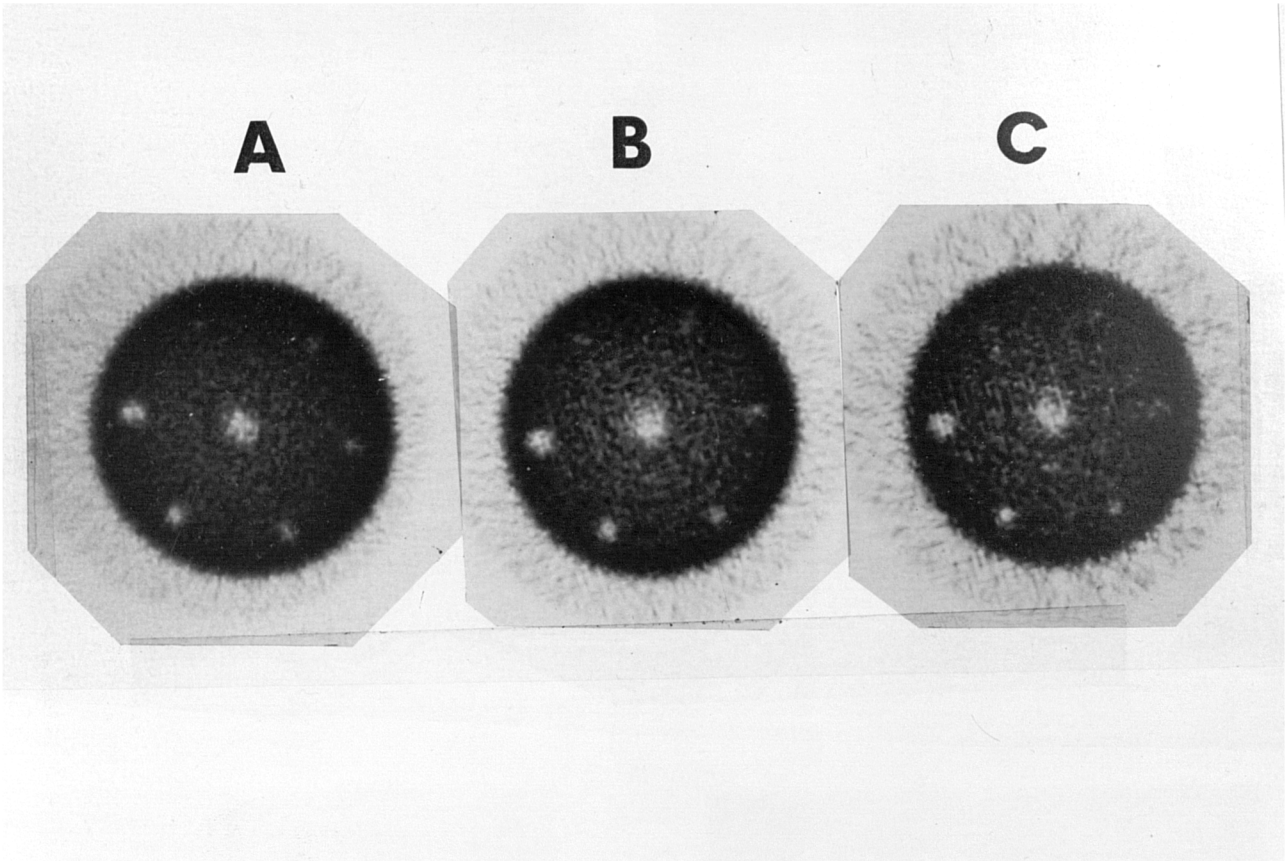


Figure 7.19 Section through the CL insert from acquisitions using ;

- A - 128 projection angles
- B - 64 projection angles
- C - 32 projection angles

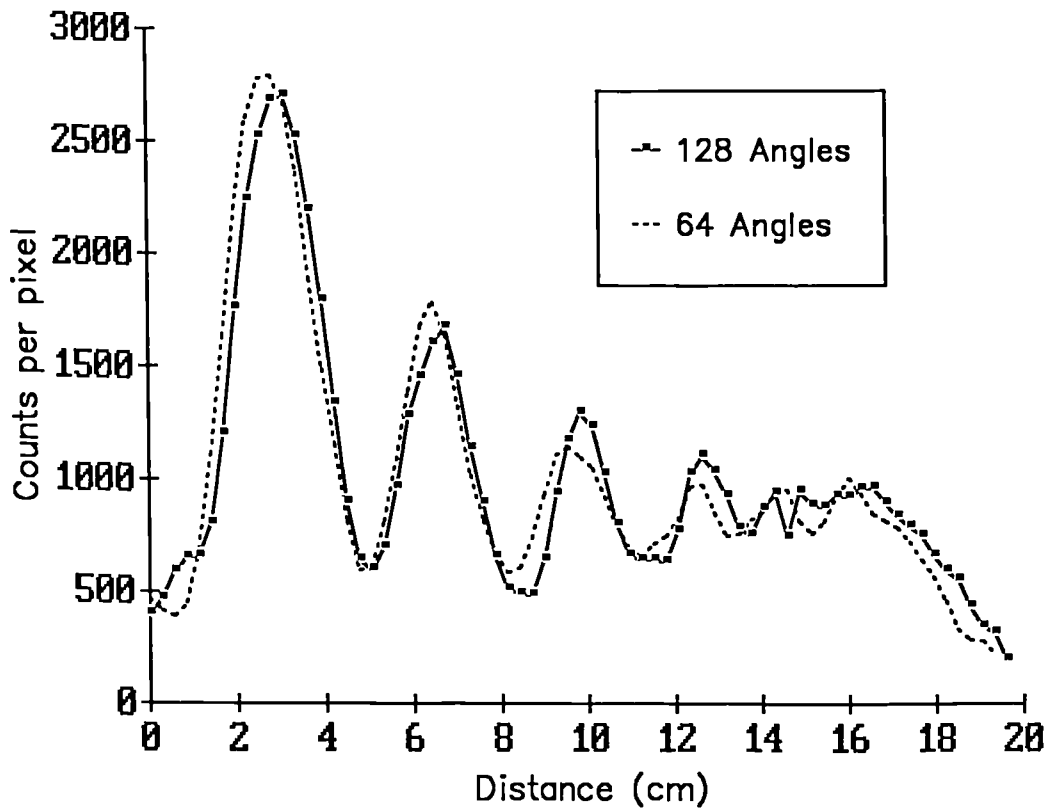


Figure 7.20 Profiles taken through the HL insert images obtained from acquisitions using 64 and 128 projection angles.

rates, Bracewell (1967), Snyder (1977), Budinger (1977), all of which used the idealised line integral.

For the collimators available no significant improvement in image quality was observed by using 128 as opposed to 64 projection angles. This is consistent with the quantitative measurements made using point and line sources. The use of 32 angles introduced significant artefacts. These results are consistent with the general findings of Todd-Pokropek (1983).

Perhaps if an ultra-high resolution collimator were available the use of more than 64 angles could be justified for very high count phantom studies. For clinical data however it is unlikely that the spatial frequencies unmasked by the higher angular sampling rate would be detectable in the presence of typical levels of noise which are encountered.

The use of 64 as opposed to 128 projection angles has several practical advantages. The amount of data to be stored is halved as is the reconstruction time. The use of a smaller number of angles also increases the effective sensitivity of the system. This is because a waiting period is introduced before the acquisition of data from any angle to allow camera vibrations to subside. This period is set to 2s for the Nodecrest system but can actually be longer (up to 10s) if "on the fly" sorting of larger data matrices is performed. Thus significant time savings can be made through the choice of 64 projection angles.

7.8 Uniformity correction for high count data

As described in Section 2.5 the presence of non-uniformities in the detector can produce artefacts which significantly degrade the image quality of SPECT studies. In

the gamma camera system used in this work microprocessor controlled correction circuitry in the camera head is used to minimise the level of non-uniformity by correcting for spatial distortion and sensitivity variations across the camera face, Section 3.2. The consequence of this is that the residual level of non-uniformity is low compared to other systems, Section 4.2.5. Nevertheless, it is still possible that a further correction for the remaining non-uniformity could reduce the level of artefact production.

The most common approach to this problem uses a simple multiplicative correction of acquired images using a high count flood field image. As described in Section 2.5 the application of this method has a number of problems associated with it. These include variations in the detector response with the scatter fraction of the incident radiation, non-uniformities in the flood phantom itself and random statistical variations due to the limited number of counts acquired in the flood field image. Whether the effects of these problems introduce more artefacts into the reconstructed SPECT images than they remove is not clear, particularly for modern camera systems with high initial uniformity levels.

Information about these concerns can be obtained, again, through the investigation of low noise phantom studies where the artefacts are not hidden by the noise.

7.8.1 Methods

A high count density SPECT acquisition of the SIEL phantom filled with a uniform concentration of ^{99m}Tc was made. The initial countrate was around 5000cps and 64 projection images were acquired for 600s each. The projection images were of dimension 128*128 with pixel edge lengths of 0.35cm. The LEAP

collimator was used and the ROR was 20cm.

A 120 million count flood image was collected using the liquid filled sheet source described in Section 3.6.

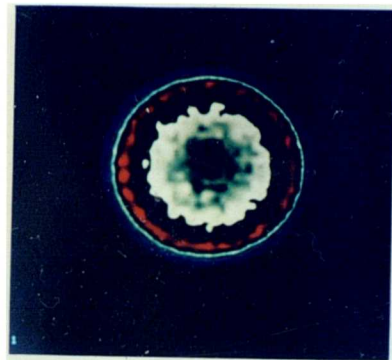
7.8.2 Results

To minimise statistical errors the projection images were binned to 64*64 before reconstruction giving pixel sizes of 0.7cm. The total counts in the SPECT study was 203 million and the counts in a 0.7cm transaxial section through the centre of the phantom was around 5 million.

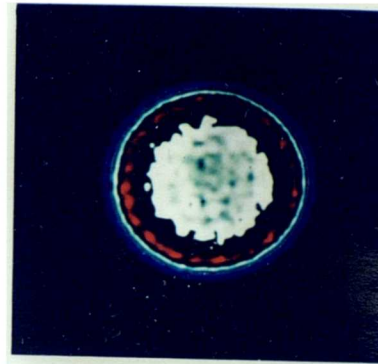
The data were reconstructed using the ramp filter. Using the results of Section 8.1 this will produce RMS% errors in the count values of the individual pixels in a single transaxial section of around 10%. Thus even acquiring as high a count density uniform acquisition as possible, with the available equipment, the statistical error in the SPECT images when reconstructed with a ramp filter is still significant.

To reduce the noise level to around 6%, three adjacent sections in the centre of the phantom were summed after reconstruction. This 2.1cm thick section is shown in figure 7.21A. The use of a section of this thickness will tend to smooth out some of the non-uniformity artefacts but as sections of this thickness are often used in clinical practice, Podreka (1987), it is still of relevance. The presence of circular artefacts, particularly in the centre of the image, are clearly visible above the noise.

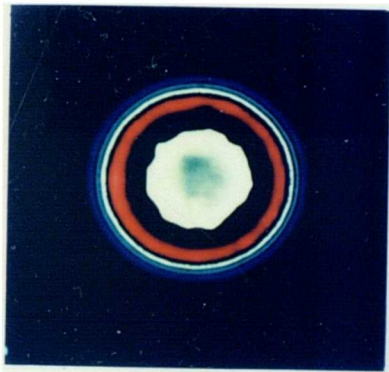
The projection images were then corrected using the flood image and reconstructed using the ramp filter. Figure 7.21B shows the resultant image of the section at the same position and thickness as that of 7.21A. There has been a clear



A



B



C



D

Figure 7.21 Sections through the uniform source distribution using 0.7cm pixels and ;

- A - the ramp filter without uniformity correction
- B - the ramp filter with uniformity correction
- C - the soft Shepp-Logan filter without uniformity correction
- D - the soft Shepp-Logan filter with uniformity correction

improvement in the quality of the SPECT image after the application of the uniformity correction.

The application of the ramp filter in clinical studies is unusual due to the high noise levels encountered. Thus the effects of a smoother filter on the presence and correction of uniformity artefacts was also investigated. The data were reconstructed using the soft Shepp-Logan filter which should give RMS% variations of around 4% per pixel in the transaxial sections, Section 8.1. Figure 7.21C shows the 2.1cm thick section which was obtained. A comparison with figure 7.21A shows that the magnitude of the uniformity artefacts has been significantly reduced through the use of the smoother filter.

Before the application of the uniformity correction the flood field image was smoothed by convolving it with the spatial representation of the Shepp-Logan filter. This is necessary because, as pointed out by Rogers (1987), smoothing the projection data without smoothing the flood field image introduces systematic errors into the data. The results of this process are shown in figure 7.21D. Comparison with figure 7.21C shows that the uniformity artefacts have been clearly reduced in amplitude - they are in fact difficult to see at all.

It would appear from this, despite the reservations about the application of the simple multiplicative flood correction method, that significant reductions in the level of artefacts in the reconstructed data can be achieved. From the high count density studies it can be concluded that the flood phantom must be of sufficiently high uniformity and that the use of a 120 million count flood field image is of sufficient statistical accuracy for the correction of 64*64 projection

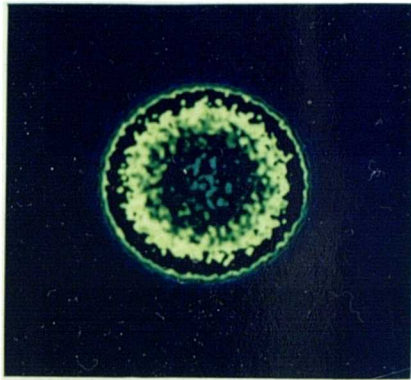
data matrices.

The use of the multiplicative correction method was also investigated for projection images of dimension 128*128. The same 2.1cm section used in figure 7.21 is shown in figure 7.22A after reconstruction with the ramp filter using 128*128 projection images. The level of noise in the data is high, from the work of Section 8.1 the RMS% error per pixel was expected to be around 30% for a single section 0.35cm thick and around 10% for the 2.1cm thick section. Despite this high noise level some circular artefacts can still be seen.

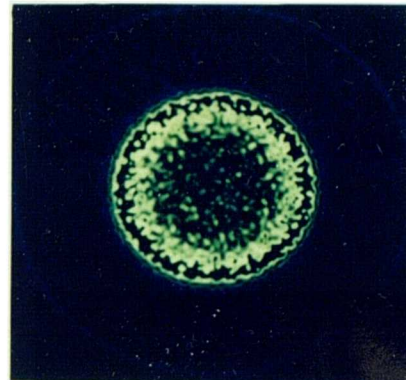
Figure 7.22B shows the same section after correction of the projection data with the smoothed flood field image. The level of artefact production has been reduced.

To investigate the effectiveness of the flood field correction for less noisy data the section was reconstructed using the soft Shepp-Logan filter, figure 7.22C. From Section 8.1 this would be expected to give RMS% values of around 10% per pixel for a single 0.35cm thick section and around 4% for the 2.1cm thick section. This is approximately equal to that obtained with the ramp filter when using the 64*64 projection image data. A comparison of figures 7.21A and 7.22C confirms this.

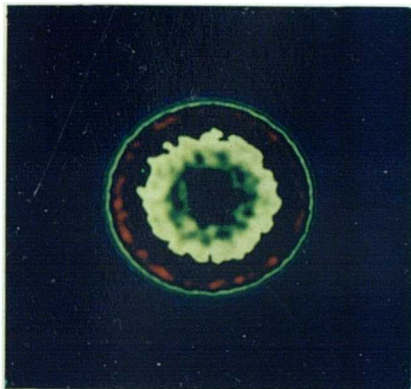
The circular artefacts due to detector non-uniformity are more evident when the smoother filter is used with the 128*128 data, figures 7.22A and 7.22C. This is due to the reduction of the noise in the image. Note that for the 64*64 data the use of the smoother filter had the opposite effect - the artefacts became less apparent. The explanation for this lies in the relationships between the noise in the data, the spatial frequencies of the uniformity artefacts and the transfer



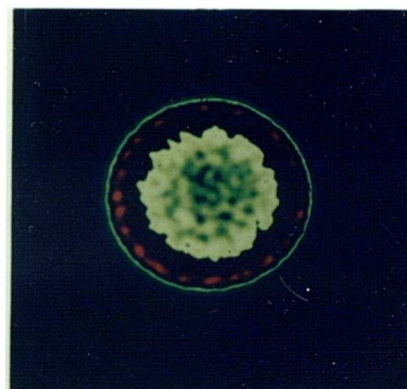
A



B



C



D

Figure 7.22 Sections through the uniform source distribution using 0.35cm pixels and ;

- A - the ramp filter without uniformity correction
- B - the ramp filter with uniformity correction
- C - the soft Shepp-Logan filter without uniformity correction
- D - the soft Shepp-Logan filter with uniformity correction

characteristics of the filter functions. In figure 7.22A the noise in the data is of roughly the same amplitude as the circular artefacts which tend to be obscured. Thus the reduction of the noise through the use of the soft Shepp-Logan filter makes the artefacts more apparent. As the noise in the section in figure 7.21A has approximately the same amplitude as that in figure 7.22C the artefacts are obscured by the noise to the same extent. The lower value of the Nyquist frequency of the filter for the 64*64 data in fact means that some of the higher frequency circular artefacts have been smoothed out. This explains the lower amplitude of the artefacts in figure 7.21A compared to figure 7.22C. When the soft Shepp-Logan filter is applied to the 64*64 data both noise and artefacts are smoothed. The smoothing of the artefacts makes them less evident than they were in 7.22A.

When the projection data were corrected using the smoothed flood field images and reconstructed with the soft Shepp-Logan filter the image shown in figure 7.22D was obtained. Again a clear reduction in the level of artefact production is apparent.

This would indicate that for 128*128 data the collection of a 120 million count flood image is sufficient to obtain a level of statistical accuracy which permits good results to be obtained with the flood field correction.

7.8.3 Conclusions

From the use of the high count density phantom data the application of the simple multiplicative flood field correction method produced significant improvements in the image quality of the object studied. This is despite the

reservations about the validity of the method outlined previously and the good initial levels of uniformity which the camera system exhibited.

The extension of these results to the clinical situation where the count densities in the projection data are a factor of twenty or so lower than those used for the previous work will be made in Chapter 9. As has already been demonstrated the visibility of the circular artefacts depends not only on their amplitude but also on their relationship to the noise in the data and the transfer characteristics of the filter function used. Thus the use of the high count data serves as an initial validation of the method. Its clinical utility will have to be tested using data with the same levels of noise as those encountered clinically and the same filter functions as are used for the reconstruction of clinical data.

7.9 Correction for ADC Non-Linearity

It should be noted that a theoretically exact correction for an important source of non-uniformity in the projection data can be made. The presence of a differential non-linearity in the x-ADC produces vertical stripes which are spaced regularly across the digital projection images. This process was described fully in Section 4.4.1.

The high level of correlation in the pattern of non-uniformity produced by a differential non-linearity amplifies its effect. For example, for other sources of non-uniformity, where there tends to be little correlation in the response along the y-axis, summing adjacent sections will smooth the artefacts. However, the non-uniformities produced by differential non-linearity will add together increasing their

amplitude relative to other structures in the summed section.

However, the effects of the differential non-linearity can be measured to a high degree of accuracy and a high precision correction applied to the projection data.

7.9.1 Methods

A 120 million count flood field image was acquired using a high ADC gain setting, Section 4.4.2. The ADC gains were selected so that the image from the gamma camera completely filled the digital image matrix. As the image from the camera is circular and the digital image matrix square this means that the camera image will extend beyond the matrix edges causing a pile up of counts in the perimeter. The count pile up was removed by setting the value of each pixel in the perimeter of the image matrix equal to the value of the pixel nearest to it and one element closer to the centre.

High levels of differential non-linearity will be visible as a regular banding structure running across the image. Lower levels may not be visible but can be measured using the approach described in Section 4.4.1.

A profile was obtained from the flood image by integrating the counts along the y-axis for each x-coordinate value. This completely specifies the pattern of non-uniformity produced by the ADC non-linearity. The statistical accuracy of the profile data is extremely high; for 128*128 data the mean count value is around one million counts giving an RMS% value of 0.1%.

This profile can be used to correct the projection data using a simple multiplicative correction method;

$$f_i = c_{\text{mean}}/c_i$$

where f_i = correction factor for the i th pixel in each row of the image matrix.

c_{mean} = mean value of the profile.

c_i = value of the i th point in the profile.

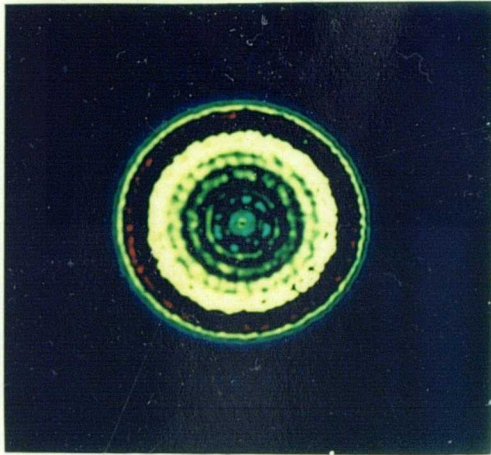
To test this method high count density acquisitions of the SIEL phantom filled with a uniform concentration of $^{99\text{m}}\text{Tc}$ were made.

7.9.2 Results

Figure 7.23A shows the image of a section taken through a uniform phantom cylinder after acquisition by a system with poorly functioning ADCs, Section 4.4.1. The regularly spaced circular artefacts can be clearly seen. The amplitudes of the artefacts vary inversely with their distance from the image centre.

Figure 7.23B shows the same section after the projection data had been corrected using the profile shown in figure 4.28. It is clear that the level of artefact production has been greatly reduced.

The level of ADC non-linearity responsible for the image in figure 7.23A is obviously unsatisfactory and the faulty ADCs would have to be replaced or repaired. However, it is not uncommon for ADCs to be performing reasonably well, e.g. to an acceptable level for the non-SPECT imaging requirements of the department, but not well enough to prevent circular artefacts from being produced in SPECT images. It may be difficult to



A



B

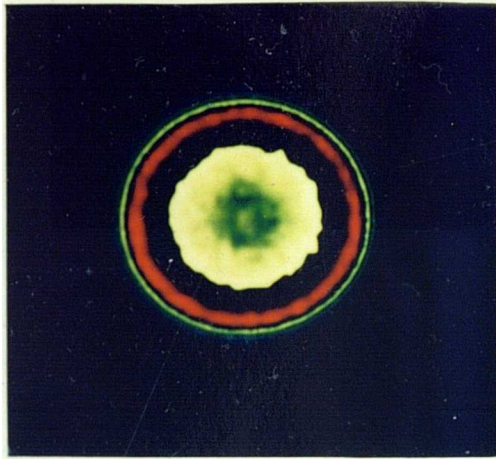
Figure 7.23 Section through a uniform source distribution obtained from a system with poorly functioning ADCs both before, A, and after, B, correction for the x-ADC differential non-linearity.

have the ADCs replaced with a better set on this basis so that an accurate correction method is in this case of particular importance. Figure 7.24A shows the image obtained using a system with ADCs which fit the above description. Circular artefacts are present with, in particular, a hot spot in the centre surrounded by a cold ring. By taking a profile through the image the amplitude of these artefacts was estimated to be around 15%. The projection data were corrected using a profile obtained from a recently acquired high gain flood field acquisition and reconstructed to produce the image shown in figure 7.24B. The circular artefacts are no longer visible, the amplitudes of the central values being consistent with those in the surrounding pixels.

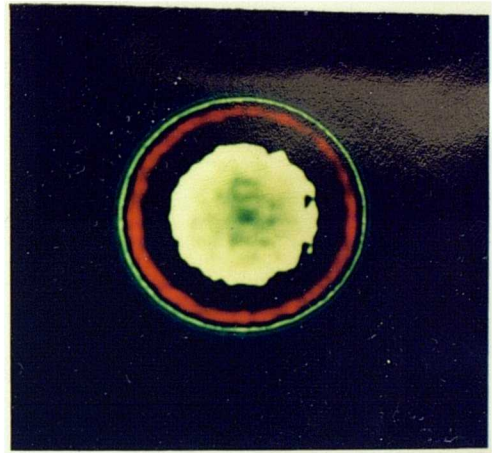
7.9.3 Conclusions

The correction for the non-uniformities in the digital projection data produced by ADC non-linearity can be made to a high degree of accuracy. The theoretical objections to the general uniformity correction method described in Section 7.8 do not apply to the ADC correction method. This is because the cause of the non-uniformity is independent of the source distribution and also because its effects can be measured with a very low level of statistical noise.

An alternative method for the correction of ADC non-linearity has been described by Todd-Pokropek (1980). This involved filtering the projection data in frequency space taking advantage of the unusual frequency distribution which the linear artefacts have in two dimensional frequency space. This has the advantage that it does not require the acquisition of a separate flood field image to correct the



A



B

Figure 7.24 Section through a uniform source distribution obtained from a system with a set of ADCs which are acceptable for planar imaging but which produce artefacts with SPECT. The sections are shown both before, A, and after, B, correction for the x-ADC differential non-linearity.

data. However, the time consuming nature of the process, where two dimensional FTs have to be taken of each projection image, is a serious disadvantage.

The ADC correction method can be applied to the data in combination with the standard uniformity correction method. Non-uniformities in the projection data due to ADC non-linearities can be corrected first by applying the previously described correction method. The remainder of the non-uniformities can then be corrected by applying a standard multiplicative flood field correction. The only difference is that the flood field image used to correct the data must itself be corrected for ADC non-linearity.

While the ADC correction method produces measurable improvements in image quality for high count density studies its usefulness in clinical practice can only be fully assessed by examining data with noise levels similar to those encountered in patient studies.

7.10 General conclusions for Chapter 7

By using low noise data the theoretical considerations described in the first part of Chapter 2 (i.e Sections 2.1 to 2.3) can be examined for the specific SPECT system described in Chapter 3. The low noise allows information to be obtained on various aspects of the SPECT imaging process as implemented using this system without the complications produced by the presence of stochastic noise.

The main conclusions which resulted were ;

1. By using the LOG of the power spectrum of the normalised profile data the relationship between the signal power and the noise power in the detected data can be visualised.

2. Using the LNP(u) curves for the phantom inserts showed that the NPS was "white" in form. Furthermore, it was shown that the NPS varied around a constant mean value which is given by the number of counts in the detected data.

Also, by assessing the variability of the NPS a value for the LNP(u) curve can be calculated above which the data will be dominated by the signal. The spatial frequency at which this occurred was shown to increase with increasing counts.

3. The level of variation of the LNP(u) curves with acquisition angle can be large.

4. The variation of the LNP(u) curve with collimator and ROR was less than that observed with acquisition angle indicating that the spatial frequency content of the data is dominated by

that of the object spectrum and the NPS.

5. The effects of data sampling and interpolation significantly alter the shape of the effective filter function. More flexible control over the discrimination between the signal and noise in the data can be obtained by removing the tie between the Nyquist frequency and the filter function cut off frequency.

6. For high count density studies the differences in image quality obtained by using 128 acquisition angles as opposed to 64 were small. The use of 64 angles for acquisition should be sufficient for clinical count density studies.

7. For high count data the application of a simple multiplicative uniformity correction using a 120 million count image of a liquid filled sheet source of ^{99m}Tc produced a significant improvement in image quality.

8. A theoretically exact correction for ADC differential non-linearity can be made which reduces the occurrence of circular artefacts in high count SPECT images.

Chapter 8 Noise control - filter function selection

8.1 Local Statistical Noise

In Chapter 7 some of the options available for the acquisition and processing of SPECT data were examined for the situation in which the noise levels in the data were low. However, in order to be relevant to the real clinical situation the issues of parameter optimisation have to be examined for noise levels which are similar to those encountered clinically.

As a first step the magnitude of the noise levels can be examined for various imaging situations. The theory of this was discussed fully in Chapter 2 where the key relationship describing the magnitude of local statistical noise in a reconstructed SPECT section was given, equation (2.3.1).

$$\text{RMS\%} = k \times P^{3/4} \times N^{-1/2}$$

where k = constant which depends on the particular form
of the filter and back projection method used

P = number of pixels in the reconstruction matrix
which contain information

N = total number of counts

The relationship was derived from a theoretical analysis by Heusman (1975) and tested using simulation studies by Budinger (1978). In the real imaging situation this relationship has only been tested approximately. This is because of the difficulties involved in separating the effects of statistical variations from the other processes involved. The main problem

is the drop in counts towards the centre of a reconstructed section due to attenuation which prevents the assessment of RMS% levels within the section. The variation in counts within a section through a uniform cylindrical source distribution, for example, due to noise cannot be separated from the variation caused by attenuation. Some workers have chosen to include this approximation in their assessment of noise levels by simply calculating RMS% values for, say, 5 x 5 pixel ROIs placed at the centre and periphery of phantom studies, King (1984). This, however, will produce an overestimate of the noise levels.

To overcome some of these difficulties the following method was developed. SPECT acquisitions of a uniform cylindrical phantom were made and reconstructed using the Nodecrest filters described in Section 3.5.3. For each reconstructed study the sections within 7.5cm of the phantom ends were excluded from the analysis because the scatter contribution will be different from the sections in the middle of the phantom.

The remaining sections should be almost identical having been acquired under identical imaging circumstances and so can be used to represent an ensemble of estimates of the section which would be produced in the absence of noise. The variation of count levels for any individual pixel located at a specific position within the section can then be calculated from the values of that pixel within the ensemble. A quantitative measure of this variability, e.g. the RMS%, can be associated with each pixel and used to produce a "noise image".

Using the circular symmetry of the study the mean noise level in a set of annuli can be calculated to produce a curve

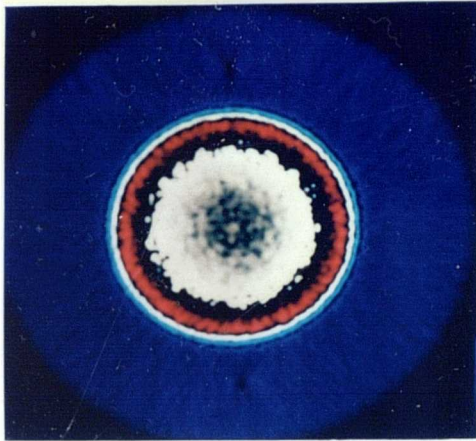
of RMS% noise against radial distance from the centre of the phantom.

8.1.1 Results

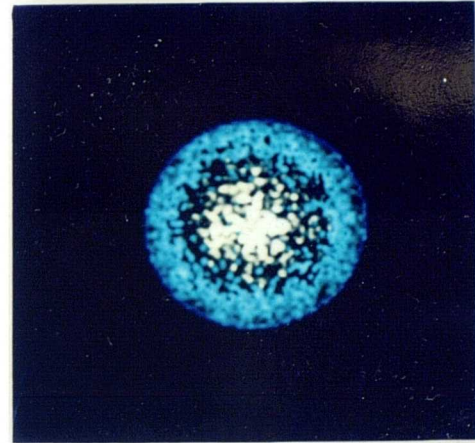
A typical noise image obtained from a SPECT study with 1,707,000 counts per section, 0.35cm pixels and after reconstruction with the ramp filter is shown in figure 8.1. The noise levels are highest at the centre of the phantom and fall off towards the edge. The curve which results from this when the values within 20 annuli are averaged is shown in figure 8.2.

The average values of the curves obtained from a variety of SPECT studies which have been acquired and reconstructed using a range of count densities, pixel sizes and filter functions are shown in Table 8.1. All the studies were acquired using the LEAP collimator and a ROR of 20cm. The initial countrates were approximately equal and the acquisition times were varied from 30s to 600s. This produced a range of count densities starting with that typically obtained in a clinical study and increasing to give as low a statistical noise level as achievable. A 64 angle SPECT study with an acquisition time of 600s per angle gives a total acquisition time of over 10 hours. If the initial countrate has been chosen to be within the linear range then the decay of ^{99m}Tc means that there is little to be gained from imaging for a longer period than this. The use of a high initial countrate would lead to the creation of artefacts, Bok 1987.

From Table 8.1 it can be seen, for studies G and H which have acquisition times and count densities which correspond most closely to the clinical situation, that the measured



A



B

Figure 8.1 A - The reconstruction, with the ramp filter, of a 15cm thick section through a uniform cylindrical phantom. the pixel edge length was 0.35cm and there were 4,877,142 counts per axial cm.

B - The RMS% values for the ensemble of 0.35cm thick sections which were summed to produce the image shown in A.

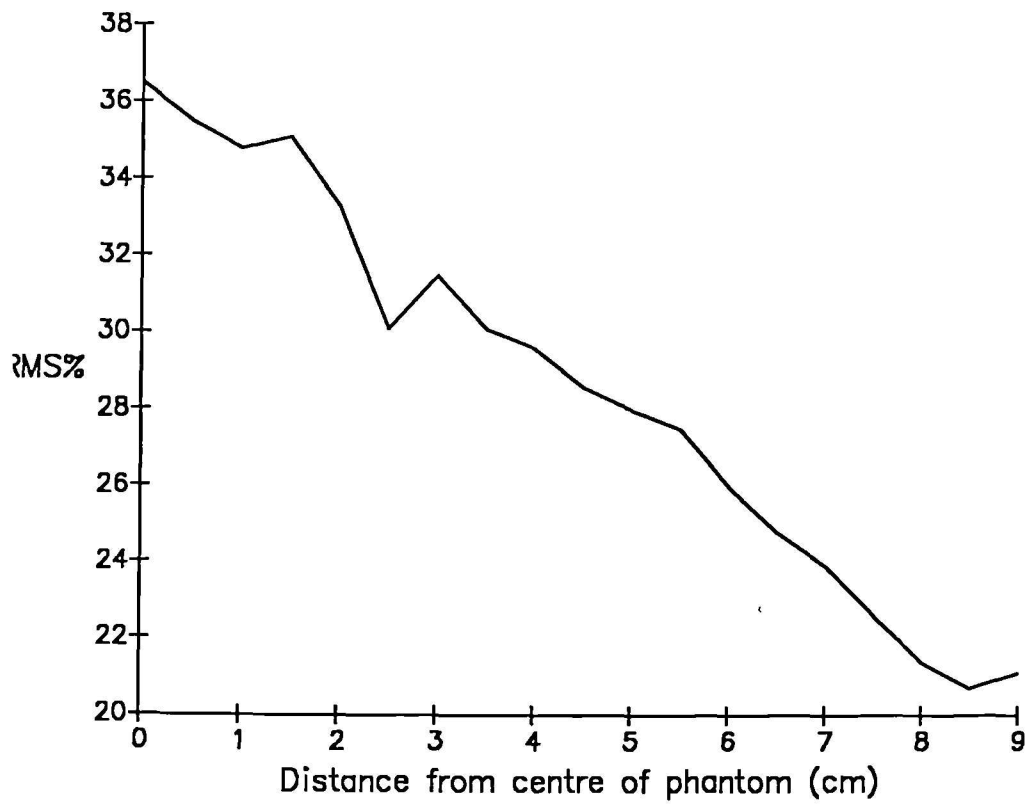


Figure 8.2 Variation of RMS% values with distance from the centre of the section through the uniform cylindrical distribution.

Study	N	P	RMS% values			t
			F3	F1	F2	
A	3414	0.7cm	8.7%	7.2%	3.4%	600s
B	3416	0.56cm	11.7%	9.6%	4.3%	600s
C	1707	0.35cm	28.8%	23.3%	9.2%	600s
D	1708	0.28cm	34.8%	28.3	11.2%	600s
E	900	0.7cm	12%	9.8%	4.2%	100s
F	450	0.35cm	41.6%	34%	13.1%	100s
G	186	0.7cm	25.7%	20.8%	8%	30s
H	93	0.35cm	78.3%	68.9%	31.3%	30s

Table 8.1 RMS% values from sections through a uniform cylindrical source distribution.

N = number of counts per section in thousands

P = edge length of pixels in projection and reconstruction matrices. This also equals the section thickness.

F3 = ramp filter

F1 = Shepp-Logan filter

noise levels are high. For a clinical study these values would be reduced because the activity is not uniformly distributed throughout the object. The level of reduction can be up to a factor of five depending on the particular distribution, Budinger (1978). Nevertheless, for studies in which the distribution is fairly uniform, e.g. the liver or brain, the figures in Table 8.1 will be close to the noise levels found in practice.

Even for the highest count densities achievable, studies A,B,C and D, the noise levels are still significant. For example, the use of the ramp filter for the smaller pixels sizes would appear to be precluded by the magnitude of the noise levels unless very thick sections are taken. This is relevant to the high count phantom studies which are used to test system performance.

The average values for the RMS% curve which are shown in Table 8.1 can be substituted into equation 2.3.1 to determine the value of k for the particular filter used. The results of this are shown in Table 8.2. From this it can be seen that the k values depend strongly on the counts and filter and weakly on the pixel size.

The variation with counts is a consequence of the fact that the RMS% values are a measure of all sources of variation, which, in addition to statistical noise, include the effects of gamma camera non-uniformity and ADC non-linearity. Thus for high count density studies the contribution to the total RMS% arising from the non-stochastic sources is proportionately high - this produces a higher k value than that which would have been predicted from simulation studies which contain only stochastic noise. For low count density

Study	N	P	k values		
			F3	F1	F2
A	3414	0.7cm	127	105	50
B	3416	0.56cm	121	99	44
C	1707	0.35cm	104	84	33
D	1708	0.28cm	90	73	29
E	900	0.7cm	90	73	31
F	450	0.35cm	77	63	24
G	186	0.7cm	87	71	27
H	93	0.35cm	66	58	26

Table 8.2 k values from equation 2.3.1 calculated for a variety of SPECT acquisitions and reconstructions.

N = number of counts per section in thousands

P = edge length of pixels in projection and reconstruction matrices. This also equals the section thickness.

F3 = ramp filter

F1 = Shepp-Logan filter

F2 = soft Shepp-Logan filter

studies the stochastic component of the noise dominates the RMS% and the k value tends towards that which would be obtained from simulation studies. For count densities arising from less than 1×10^6 counts per section the variation in k values is low eg compare E with G and F with H.

The variation of k with pixel size is a consequence of the fact that although the same nominal filter is used the shape in frequency space will vary because of the change in the Nyquist value. This phenomenon was discussed in Chapter 7.

8.1.2 Conclusions

This method can be used to produce useful information on the noise levels which can be expected from real SPECT acquisitions (i.e. not just simulations) obtained from a specific imaging system. This can be used to guide the user in the choice of, for example, the most appropriate filter function. The information provided is more accurate than that obtained by using a ROI within a single transaxial section which will be affected by attenuation and will be dependent on ROI position. The results of the ROI measurements will also vary with the particular section chosen for analysis.

8.2 Noise control - filter function selection

8.2.1 Introduction

The previous section described a method for estimating the magnitude of noise levels in SPECT images. As described in Chapter 2 a more complete description of the influence of noise can be obtained by considering its form in frequency space through the NPS. Also, as described in Chapter 2 the

noise in a SPECT image is not white but has a distribution in frequency space which depends on the filter function used in the reconstruction process.

For this reason more attention will be paid to the NPS of the projection data and to the form of the filter function than to their consequence, the NPS of the SPECT image.

Assuming that the data have been acquired at a sufficiently high sampling rate then the effects of the sampling and interpolation processes can be determined exactly, Sections 2.2.5 and 7.6. This means that if the effects of these processes are incorporated into the filter function form then the filter alone can be used to discriminate between the noise and the signal in the acquired data. In practice this means that the data should be acquired at a sampling rate much higher than that dictated by the sampling theorem with the noise in the data being controlled by the filter function.

8.2.2 Filter function selection - current status and general considerations.

An examination of the form of the low noise image power spectra in Chapter 7 illustrates the fact that most of the useful information is contained in spatial frequencies below about 0.6cm^{-1} . It is therefore desirable that these spatial frequencies are transferred by the filtering process as fully as possible. This immediately raises problems with the filter functions most commonly used until relatively recently in SPECT, the soft and sharp Shepp-Logan filters and the Hanning windowed ramp filter, Larsson (1980), Gustafson (1986), Jarrit

(1984) and Chessler (1975). The window functions associated with these filters, Section 2.2.4, all have values which fall from unity at spatial frequencies greater than zero, figure 8.3.

There are several filter functions which are available, however, which do not suffer from this disadvantage. Of these the most commonly used is probably the Butterworth filter. This is defined in the frequency domain as

$$B(u) = \{1+(u/u_c)^n\}^{-1/2}$$

- where - u is the spatial frequency
- u_c is the cut off frequency
- n is the power factor

The form of the Butterworth filter for a number of combinations of u_c and n is shown in figure 8.4. The Butterworth filter maintains a value close to unity up to a point determined by the cut off frequency, u_c . At u_c the gain of the filter is reduced to 0.707. The filter can be made to roll off sharply to zero, the steepness of the roll off being determined by the parameter n which is known as the power factor.

The superiority of the Butterworth filter over the Hanning windowed ramp, which would be expected from the theoretical considerations, has been clearly demonstrated in practice by Gilland (1988) and Penney (1988).

Although the general shape of the Butterworth filter is better suited to the control of noise in the data than the other filters there still remains the problem of the choice of

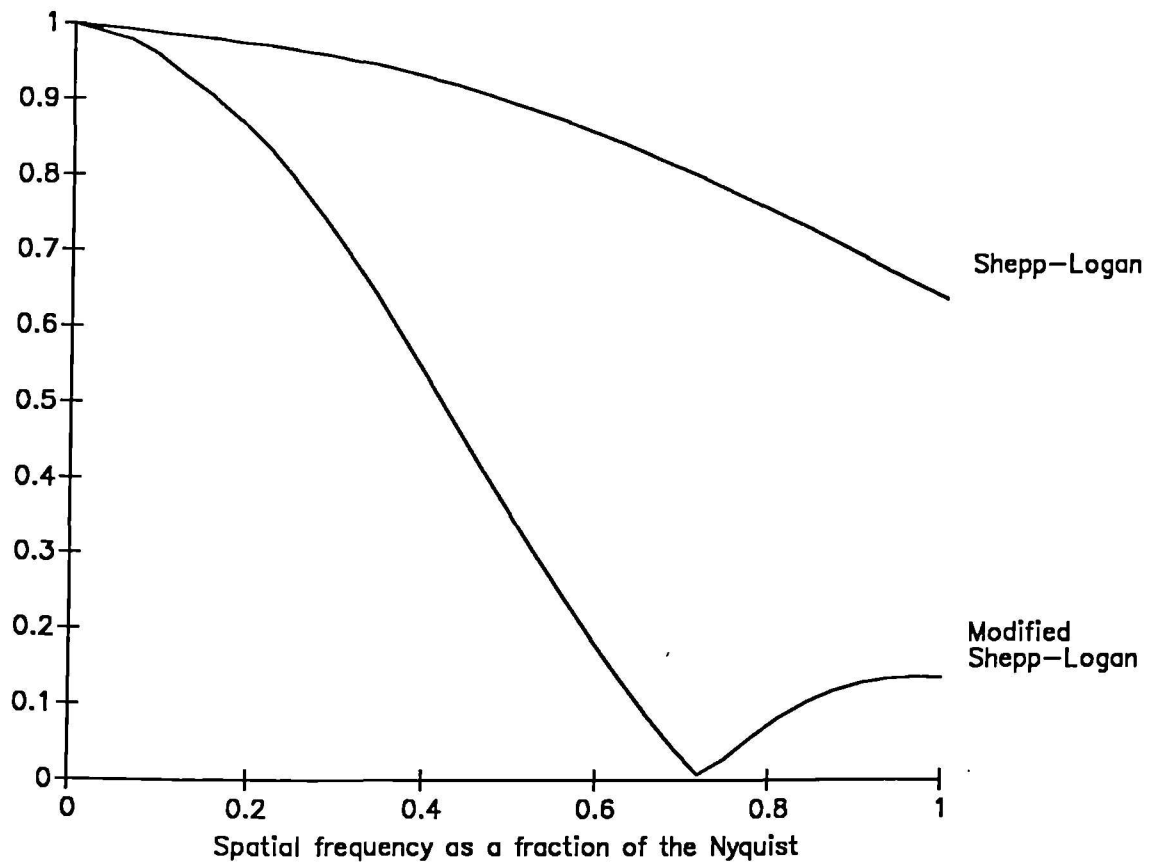


Figure 8.3 The window functions associated with the Shepp-Logan and modified Shepp-Logan filters.

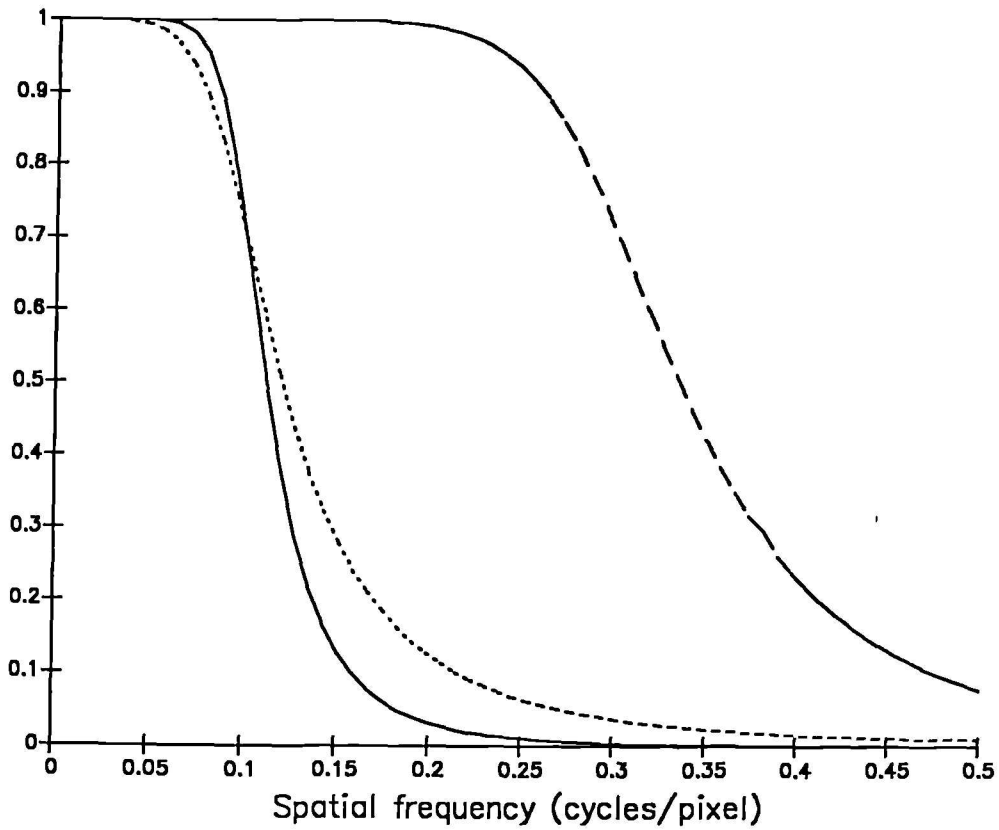


Figure 8.4 Butterworth filters with different values for the cut off frequency and power factor.

Solid line - Power = 10, Cut off = 0.1 cycles/pixel
 Dotted line - Power = 6, Cut off = 0.2 cycles/pixel
 Dashed line - Power = 10, Cut off = 0.3 cycles/pixel

the values for the cut off frequency and the power factor for any particular imaging situation. This problem is related to the general problem of the determination of an optimal filter shape for a given set of data.

The power spectrum of a projection profile can be written

$$I(u) = MTF(u)^2 \cdot O(u) + NPS(u)$$

where $O(u)$ is the object power spectrum.

As described in Chapter 7 the NPS is white with a mean value given by the total number of counts in the data. The task of an optimal filter is to recover $O(u)$ as accurately as possible from $I(u)$. This can be achieved by reducing the noise and by correcting for the blurring introduced by the detection process. Unfortunately, for nuclear medicine data no mathematical models are available to predict exactly how this should be done. Nevertheless, some approximate solutions have been implemented.

An attempt to correct for the blurring introduced by the detection process can be made by applying the Metz filter. This is defined to be

$$M(u) = MTF(u)^{-1} \{1 - [1 - MTF(u)^2]^X\}$$

This filter can be considered to consist of two parts. At low spatial frequencies the filter is dominated by the term $MTF(u)^{-1}$ which deconvolves the blurring produced by the detection process i.e. an inverse filter. At higher spatial frequencies the low pass filter term dominates and the filter

function is made to roll off to zero. The point at which the low pass filter begins to dominate is determined by the parameter X. The major problem with the Metz filter is that for nuclear medicine data there is no single value for the MTF. Some attempts have been made to overcome this difficulty by using a representative function for the MTF e.g the MTF obtained from a source in 7.5cm of scattering material, King (1983), Miller (1982). The absence of a unique MTF however effectively negates any attempt at image restoration. The Metz filter is in fact a resolution recovery filter with an inverse filter term which bears only the loosest relationship to the effective MTF of the data.

Despite these criticisms considerable interest has still been shown in the application of this type of filter, King (1984), Gilland (1988), Penney (1987). For example, it can be made to adapt to the noise level in the data by making the factor X depend on the total counts. This can be achieved by determining the values of X which minimise the mean squared error (MSE) for a set of object/image pairs, King (1983).

There are some dangers inherent in the use of resolution recovery filters based on essentially arbitrary inverse filter components. The overcorrection of specific spatial frequency components, for example, can introduce artefacts into the data. A comparison of the Metz and the Butterworth filters by Gilland (1988) showed that no clear advantage was obtained from the resolution recovery properties of the Metz. Penney (1988) showed that the Metz and Butterworth filters gave very similar results over a range of count densities which one would expect to find in a clinical study. Only at higher count densities did the resolution recovery properties of the Metz

filter produce an improvement in the measures of image quality used. Even here, however, the question of the production of false positive results as a consequence of artefacts from the application of an arbitrary resolution recovery filter were not addressed.

One of the disadvantages of the count dependent Metz filter is that no account is taken of the object power spectrum. Thus the values of X determined for one set of object/image pairs will not be applicable for a different type of object. Attempts to overcome this difficulty have been made by producing a filter function which adapts both to the noise in the data and to the image itself. A function with these properties is the Weiner filter

$$W(u) = \text{MTF}(u)^{-1} \cdot \text{MTF}(u)^2 / [\text{MTF}(u)^2 + N/O(u)]$$

where N is the total counts

O(u) is the object power spectrum

As with the Metz filter, the Weiner filter consists of the product of an inverse filter and a low pass filter. The roll off of the low pass filter is dependent on the magnitude of the ratio of the noise to object spectra compared to the square of the MTF.

Again however the absence of a unique MTF negates the theoretical basis of the Weiner filter's image restoration properties. In effect, for nuclear medicine, implementations of the Weiner filter are simply implementations of a resolution recovery filter with some arbitrary correction being made to the data on the basis of an estimate of the

signal to noise ratio as a function of frequency.

Given the absence of a theoretically rigorous method for image optimisation several attempts have been made to use the observer as part of the optimisation process. For example, instead of using a mathematical criterion for assessing optimal performance, observer preference can be used, King (1987). . . . Allowing the operator to adjust the filter interactively until the "best" image was obtained permitted the identification of a heuristic criterion which could be used for subsequent studies. This criterion depended upon the identification of the spatial frequency at which the blurred object power spectrum became dominated by the noise. This analysis was performed on the power spectrum of a "representative" projection image which was compressed into a one dimensional form by averaging over annuli in frequency space. The Metz filter was then adjusted to have a value of one at the point where the one dimensional compression of the power spectrum had a value greater than the 90% confidence limit for the noise. This process resulted in the selection of filter functions which were close to those chosen in the observer preference study.

A major advantage of this approach is that the human viewer and his visual system are introduced into the optimisation process.

8.2.2.1 Conclusions

From the previous review of the current status of filter function selection the following conclusions were drawn.

In the absence of any clearly beneficial effects the group of filters with arbitrary resolution recovery components

should be used with caution. Until clear advantages are shown the Butterworth filter would appear to have the most desirable general form. This can be applied without the danger of the creation of artefacts in the data.

The use of mathematical models to produce optimality criteria are based on uncertain fundamental principles. There is probably no "optimal" image which can be created from the data because the aspects of the image which are important depend on the clinical considerations of the task to be accomplished. Because of this, there are no measures of image fidelity which correlate well with observer performance for a specified task for images which contain both normal anatomical detail and information about pathologies, Penney (1987). Measures such as the NMSE, for example, can be applied to phantom studies or to simulation studies where the object distribution is known. These measures can be used to guide filter function selection but in the final analysis either observer preference or, if a "gold standard" test is available, an ROC analysis must be used.

For this reason the approach to filter function selection which the author would favour uses a direct involvement of the observer in the assessment of the quality of the images produced by different filters.

The most familiar example of this type of approach is in fact the standard "trial and error" method adopted by most workers in the field of SPECT imaging. The problems with this are that it is time consuming, laborious and in the hands of an inexperienced observer can produce highly sub-optimal results. The task is therefore to identify a set of heuristic criteria which, in a way similar to that described by King

(1987), can reproduce the filter selections made by an experienced observer.

The application of an objective set of criteria will increase the speed of the filter selection process and reduce the reliance on the level of expertise of the observer.

8.3 A suggested filter function selection method.

A consideration of the shape of the image power spectrum in figures 7.2 to 7.10 shows that it consists of a blurred object power spectrum which generally decreases in amplitude with spatial frequency until it reaches a point where it becomes insignificant compared to the NPS which fluctuates around a constant mean value. The spatial frequency at which this point is reached will depend upon the total number of counts in the image, the form of the object and the effective MTF of the imaging system (which will be spatially variant because it will depend on the object itself).

The aim of this work is to identify the point at which the blurred object spectrum merges with the NPS and to use this information to determine the shape of the filter curve. The relationship between this transition point and the filter curve can be determined so that the filter function selections which result are similar to those made by an experienced observer using a visual assessment of the quality of the reconstructed images produced from a series of trials using a range of filters.

In accordance with the discussion in Section 8.2 the Butterworth filter was identified as having the most suitable general form for optimisation. The optimisation problem can thus be simplified to the establishment of a method for

determining the parameters u_c and n from a consideration of the image power spectrum.

8.3.1 Determination of the Butterworth Power Factor

As described previously the Butterworth filter has a gain of unity or close to unity at low spatial frequencies and can be made to roll off sharply to zero by choosing a high value for the parameter n . This makes it well suited to the image processing task to be performed ; the useful information in the low spatial frequencies should be preserved up to a point at which the noise level becomes significant whereupon the transfer of information should be attenuated.

Although as sharp a roll off of the filter as possible would appear to be desirable there is a practical limit to which the Butterworth power can be raised. This is a consequence of the fact that if a function with a sharp transition, or discontinuity, is to be specified digitally then a very large number of points are required if aliasing artefacts are to avoided.

This is a similar problem to that originally described for the ramp filter by Chessler (1975). The digital underspecification of a function with a sharp transition will lead to ringing artefacts being introduced into the reconstructed images.

The Butterworth filters used in practice were created in the frequency domain from a 512 point definition of the analytical function after multiplication by the ramp. The inverse FFT was taken to produce the spatial representation of the filter. From this the central 65 points were used as the filter kernel. The truncation of the filter in the spatial

domain also contributes to the ringing artefacts.

Given these limitations on the accuracy with which the Butterworth filter could be defined the maximum power factor which could be applied was determined from a simulation study.

8.3.1.1 Methods

The projection profiles which would be obtained from the acquisition of data from a cylindrical object containing a uniform concentration of activity were calculated as described in Section 6.4.2. As the sharp discontinuity at the edge of the object distribution produces an unrealistic test of the reconstruction process the projection data were convolved with the LSF obtained from a source in 5cm of scattering material. The resultant projection data were then reconstructed using Butterworth filters with different power and cut off factors.

8.3.1.2 Results

It was found for a cut off value of 0.1 cycles per pixel that the amplitude of the ripple artefacts were below 2% if the power factor was less than or equal to 10.

The results of the reconstruction of the simulated data for the power factor values of 10, 12 and 14 and a cut off value of 0.1 cycles per pixel are shown in figure 8.5. The ripple artefacts are most obvious in the image obtained using the filter with a power factor equal to 14 where their magnitude was measured to be 4%.

The results for power factor values of 10, 12 and 14 and a cut off value of 0.15 cycles per pixel are shown in figure 8.6. The magnitudes of the ripple artefacts were less than

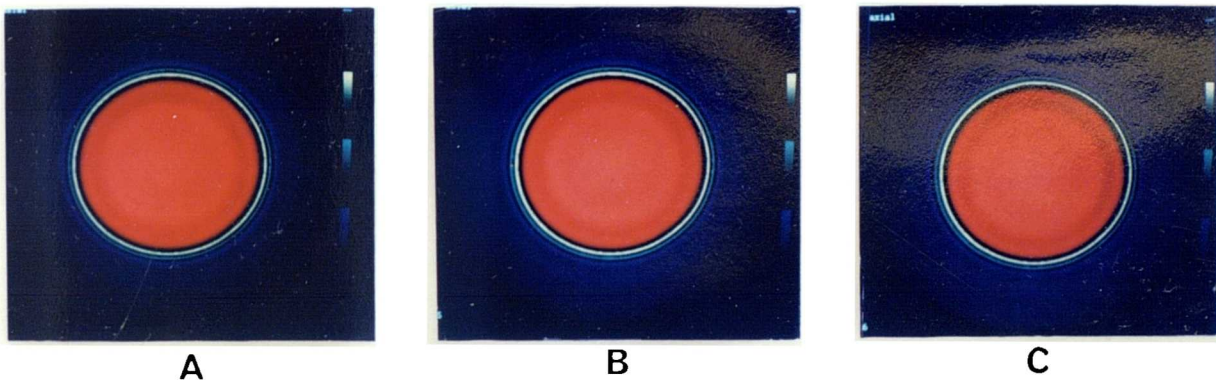


Figure 8.5 Reconstruction of simulated uniform cylindrical distribution. A Butterworth filter with a cut off frequency of 0.1 cycles per pixel has been used in all cases. In A, B and C power factors of 10, 12 and 14 respectively were used.

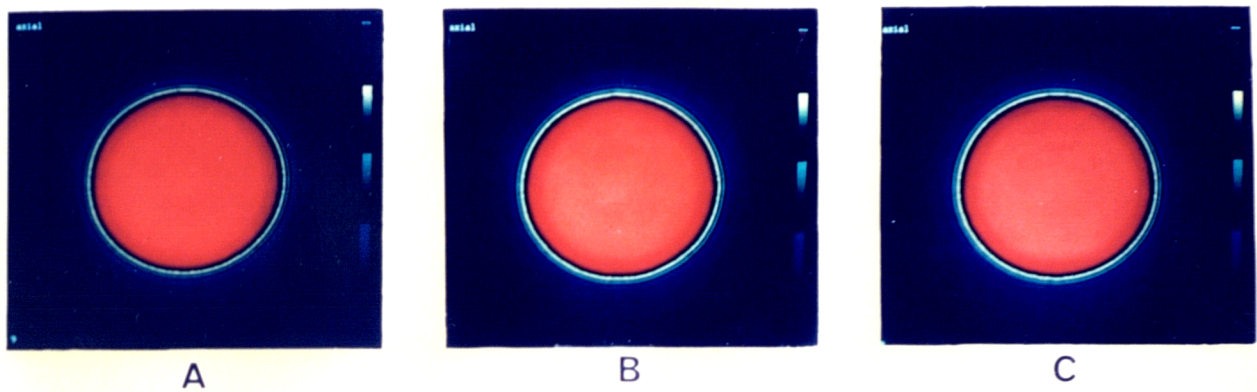


Figure 8.6 Reconstruction of simulated uniform cylindrical distribution. A Butterworth filter with a cut off frequency of 0.15 cycles per pixel has been used in all cases. In A, B and C power factors of 10, 12 and 14 respectively were used.

those obtained when a cut off value of 0.1 was used. Thus the value of the power factor is limited by the use of filters with low cut off values.

8.3.1.3 Conclusions

As it is unlikely that Butterworth filters with cut off values significantly below 0.1 cycles per pixel would be used in practice an upper limit of 10 for the power factor was decided upon. A consideration of the magnitude of the RMS noise levels obtained in SPECT images with clinical count rates, section 8.1, would suggest that the introduction of artefacts with amplitudes below 2% would not significantly compromise the quality of the reconstructed data. This choice for the power factor is consistent with the results obtained by other investigators, Gilland (1988).

8.4 The enhanced Butterworth filter

As described in Sections 2.2 and 7.6 the effects of sampling and interpolation can be defined exactly and corrected for by amending the form of the filter function. For example when the data have been acquired using matrices of dimension 128 * 128 and pixels of edge length 0.35cm the effects of interpolation are given, from equation 7.7, by

$$I(u) = \text{sinc}(0.35 \pi u) \cdot \{\text{sinc}(0.175 \pi u)\}^2$$

and the effects of sampling are given, from equation 2.2.6, by

$$S(u) = \text{sinc}(0.35 \pi u)$$

Thus the combined effects of the data processing operations are

$$I(u).S(u) = \{\text{sinc}(0.35 \pi u)\}^2 \cdot \{\text{sinc}(0.175 \pi u)\}^2$$

Thus the effects of data processing can be corrected for by dividing the filter which is to applied to the data by the above function.

The effects of this on the Butterworth filter with a cut off frequency equal to 0.12 cycles per pixel and a power factor of 10 is shown in figure 8.7. The effect of the correction is to enhance the higher spatial frequency components.

The effects which the enhancement of the Butterworth filter has on the reconstruction of a section from a $^{99\text{m}}\text{Tc}$ -HMPAO brain study are shown in figure 8.8. A small but significant improvement in image contrast is observed. The differences between the standard and enhanced Butterworth filters were observed to increase with increasing cut off values.

8.5 Filter matching

As described in section 8.2 the Butterworth filter can be matched to the projection data by identifying the spatial frequency at which the blurred object power spectrum merges with the noise. An approach of this nature has previously been used by King (1987). In this case a "representative" projection image was selected for analysis, the two dimensional power spectrum obtained and a one dimensional power spectrum curve produced by averaging over annuli in

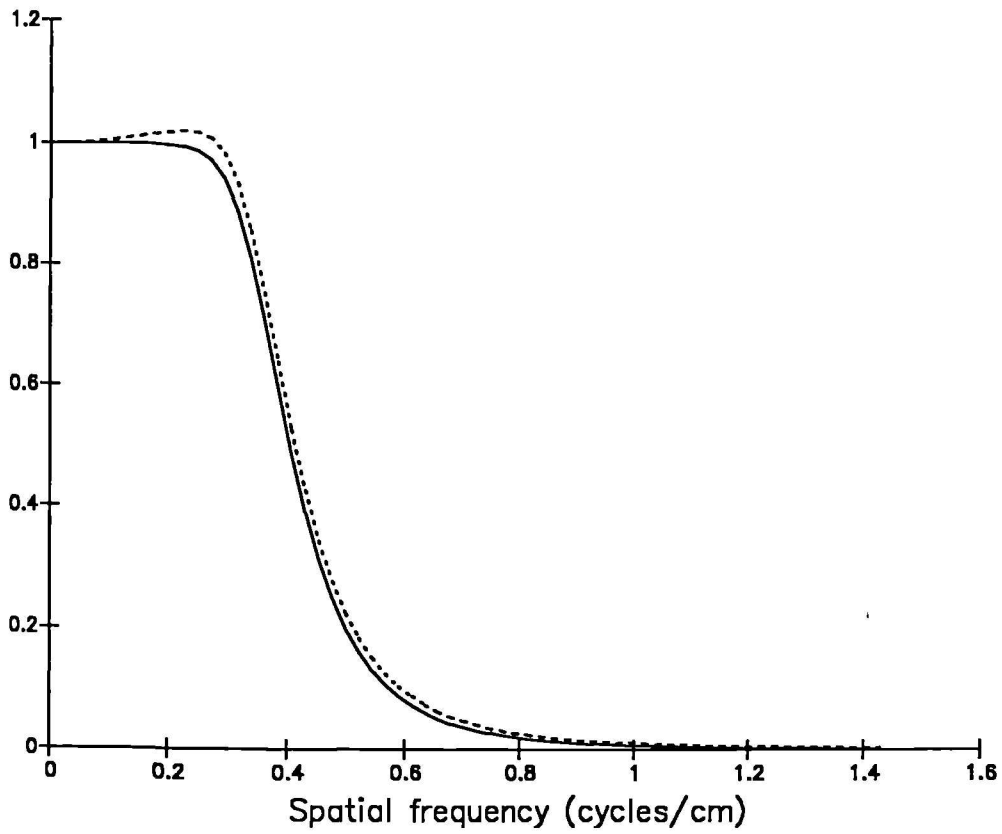
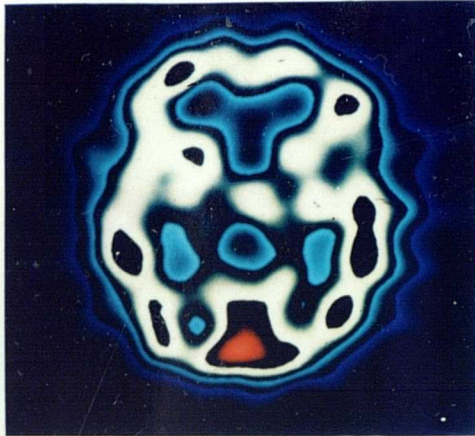


Figure 8.7 Solid line shows Butterworth filter with power 10 and cut off 0.34cm^{-1} . Dotted line shows the same filter after correction for the effects of sampling and interpolation.



A



B

Figure 8.8 A - Section through HMPAO study using a Butterworth filter with power 10 and cut off 0.343cm^{-1} .
B - The same section as A but reconstructed using the enhanced Butterworth filter with the same power and cut off frequency values as used to produce the image in A.

frequency space. There are several disadvantages associated with this approach. As described in Section 7.2.3 the variation in the shape of the power spectrum with projection angle throws into question the existence of a projection image which can be considered to be representative of the projection image set. Furthermore, the use of the information contained in a whole projection image to provide data to optimise the filter for the reconstruction of a single transaxial section can also produce difficulties. If there is a wide range of structures within the "representative" projection image then the filter may be optimised for parts of the image distant from the projection profile corresponding to the section to be reconstructed.

To overcome these problems it was decided to optimise the filter function for the reconstruction of a particular section on the basis of the information contained within the projection profile set for that section, i.e the sinogram. This was done by calculating the power spectrum of each projection profile in the sinogram and determining the mean value for each spatial frequency component. A measure of the level of variation with acquisition angle can be obtained by calculating the standard deviation of the values obtained for each spatial frequency component. For a visual examination of the resultant information the techniques described in Section 7.2 were applied i.e. the LNP(u) curve was created from the mean power spectrum.

The results of these processes are illustrated in figure 8.9 which shows the LNP(u) curve of the mean angular power spectrum (MAPS) obtained from the sinogram corresponding to a 0.28cm thick section through the pie insert of the SPECT

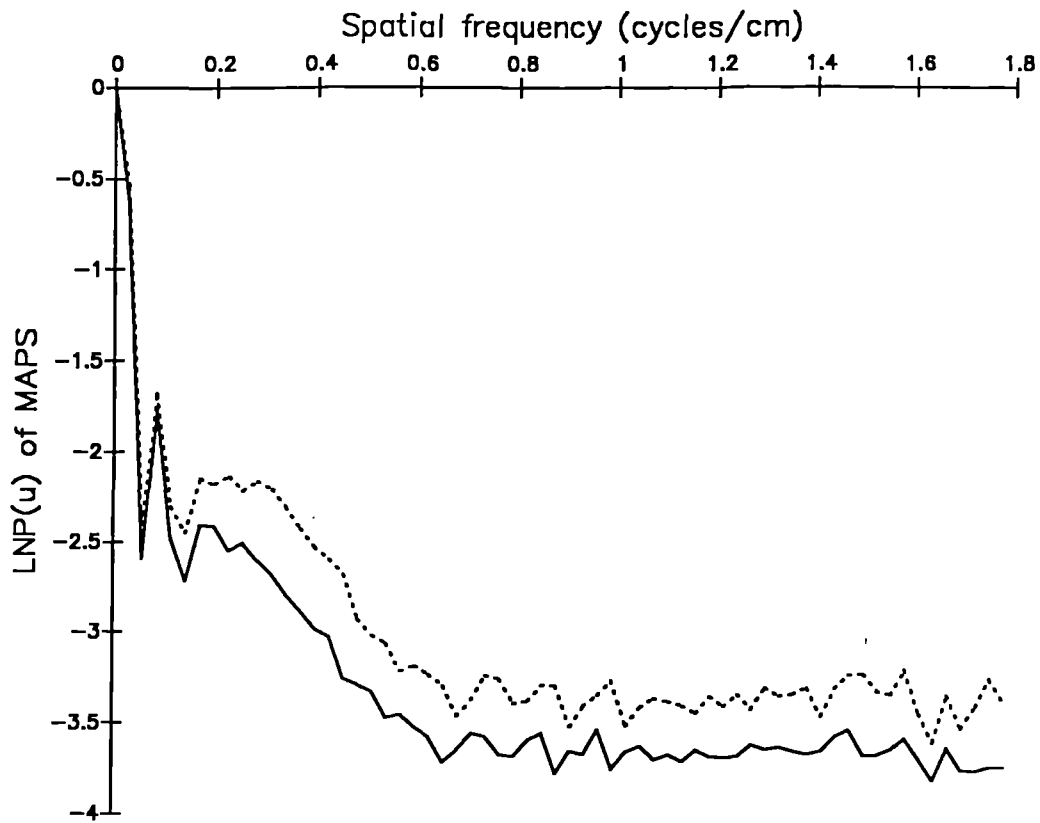


Figure 8.9 LNP(u) curve of the MAPS from the sinogram corresponding to a 0.28cm thick section through the pie insert of the SPECT phantom. Also shown, dotted line, is the LNP(u) curve of the MAPS plus one SD.

phantom. Also shown is the LNP(u) curve of the MAPS plus one standard deviation which was obtained from the variation in the values of each SF component.

A comparison with the data in figure 7.5 which shows the LNP(u) curves for single projection profiles for the pie insert shows that the LNP(u) curve from the MAPS is much smoother and so more suitable for analysis.

Figure 8.9 also shows that the MAPS has the same general form as the image power spectrum i.e. it consists of a blurred object power spectrum which decreases in amplitude with spatial frequency until it merges with the NPS which varies around a constant mean value. The mean value of the NPS is given by the total number of counts in the sinogram divided by the number of acquisition angles i.e. the average number of counts per projection profile.

8.5.1 Variability of the NPS

The identification of the point at which the blurred object power spectrum merges with the NPS requires an assessment of the confidence with which the amplitude of the NPS at any particular spatial frequency can be estimated. To examine this the distribution of NPS values in the projection profile power spectra were assessed. For the sinogram used to produce figure 8.9 the values of the power spectra of each of the projection profiles with spatial frequencies greater than 1cm^{-1} were taken to represent the noise. This gave 1984 estimates of the noise power which were used to produce the distribution shown in figure 8.10. It has been previously reported, Jenkins (1986), that the individual terms of a two dimensional NPS follow a Chi squared distribution with two

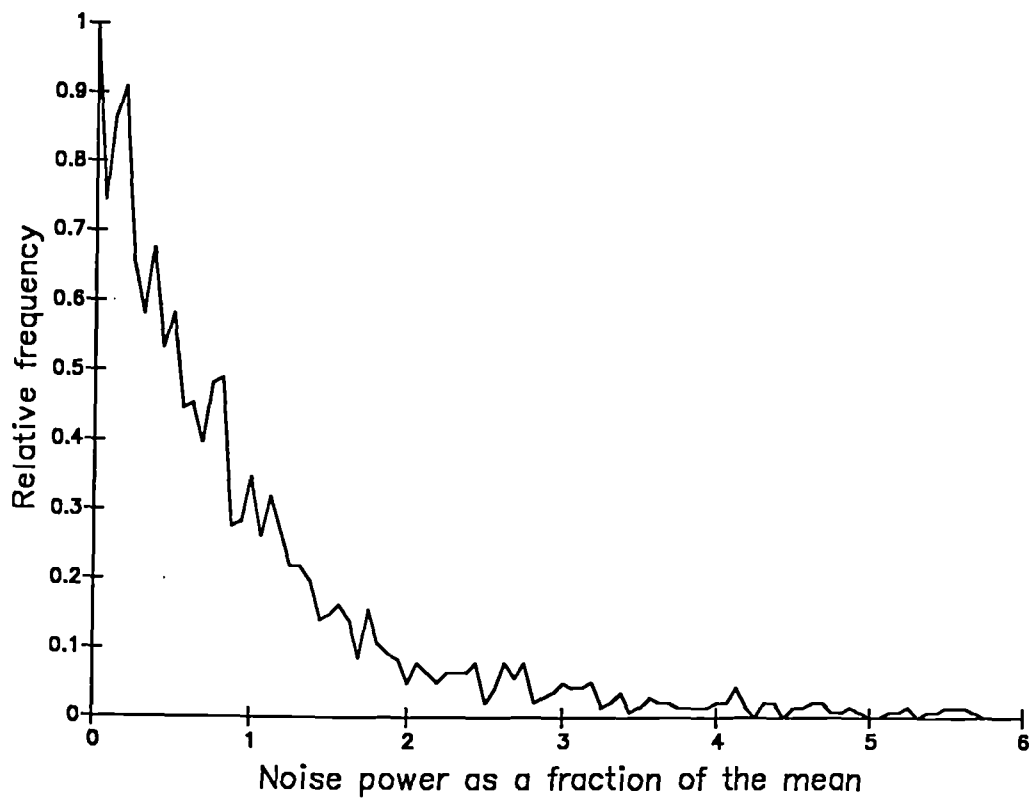


Figure 8.10 Distribution of noise power values.

degrees of freedom. The power spectra from the projection profiles are not related in any simple manner to the components of the two dimensional power spectra produced from the projection images, Dainty and Shaw (1974,pp224). Nevertheless, their distribution is very close to that of a Chi squared distribution with two degrees of freedom. For example the 90% confidence limit for this distribution is predicted to be given by 2.3 times the mean value; for the measured distribution 90.02% of the values were found to be below 2.3N where N is the mean NPS value (given by the mean counts per projection profile). Similarly it would be predicted that 63.4% of the values would be less than N ; the measured value was 63.2%.

The close correlation between the measured distribution of the noise power values from the projection profile set and the Chi squared distribution with two degrees of freedom was found for a wide range of study types and count levels.

8.5.2 Determination of Filter Cut Off Value

One of the consequences of the way in which the noise power values are distributed is that it provides a simple way to calculate the spatial frequency at which the blurred object power spectrum merges with the noise. A reasonable definition of this transition frequency would be that at which the amplitude of the image power spectrum falls below the 90% confidence limit for the noise power values. This is given by 2.3 times the mean counts per projection profile.

Alternative definitions of the location of this transition frequency are possible. Inspection of the LNP(u) curves from the MAPS of a variety of study types and count levels shows

that the 90% confidence limit tends to be located on a reasonably smooth and well behaved portion of the curve making it suitable for analysis.

Having determined the transition frequency the Butterworth filter can be matched to the data by specifying its amplitude at this point. In this way the filter should adapt to both the noise and the spatial frequency content of the projection data. The amplitude of the Butterworth filter at the transition frequency can be determined to optimise the information in the reconstructed images to suit a given clinical investigation. For example, if a high level of specificity is required a low value for the Butterworth filter at the transition frequency can be specified which will tend to produce soft filters which will limit the number of false positive findings.

The most computationally convenient way to define the amplitude of the Butterworth filter at the transition frequency is to set the cut off frequency of the filter equal to the transition frequency multiplied by a constant. Depending on the value of the multiplicative constant the cut off frequency of the Butterworth filter can be shifted by variable amounts to be higher or lower than the transition frequency.

For any particular clinical investigation the value of the filter shift factor can be determined on the basis of a preliminary trial which uses observer preference to determine the best images. This factor can then be applied automatically to determine the optimal filter for the remainder of the studies in the investigation.

This approach is best illustrated by a practical example ;

the selection of an optimal filter for the reconstruction of ^{99m}Tc -HMPAO studies in patients with intractable epilepsy. Full details of the investigation as a whole are given in Chapter 10, however the aims of the study can be summarised as the determination of an area of either increased or decreased cerebral blood flow which identifies the epileptic focus. Identification of a focal lesion makes the patient a candidate for surgery so that a high level of specificity is required.

For the preliminary trial, to determine the filter shift factor which optimises the information in the data, three representative sections at different levels in the brains of eight subjects were used. One section was taken from the base of the brain another from the mid-brain and the third at a level close to the superior surface of the cortex. The brain structures tend to decrease in complexity as one moves superiorly so that the sections chosen should cover the range of image power spectra which are encountered in practice.

For each section the transition frequency was determined from the 90% confidence limit for the noise fluctuations. From this a range of filter shift factors with values 0.9, 1, 1.1, 1.2, 1.3 and 1.4 were used to specify the cut off frequencies of the Butterworth filters which were used to reconstruct the data. From the set of images produced for each section the best image was selected by an experienced observer taking into account the requirements of the clinical task to be performed. The filter shift factor which produced the optimal filter for each image was noted. A particular example of this is illustrated in figure 8.11 which shows the LNP(u) curve from the MAPS of a basal brain section. The 90% confidence limit of the noise is also shown and the transition frequency marked.

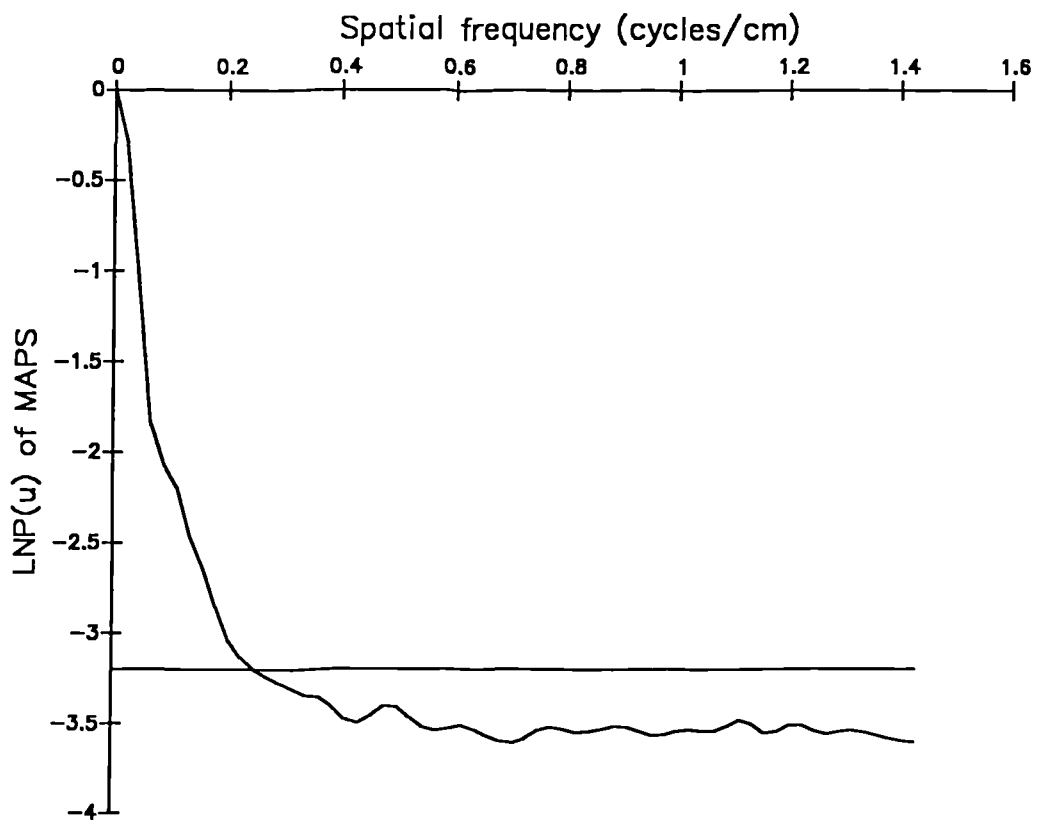


Figure 8.11 LNP(u) curve of the MAPS for the sinogram corresponding to a section through an HMPAO study. The 90% confidence limit for the noise is also shown. The intersection of the two curves defines the transition frequency.

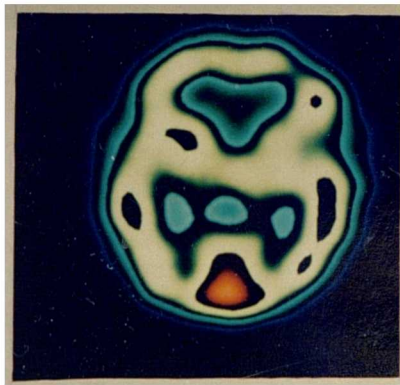
Figure 8.12 shows the images obtained when the reconstruction was performed using filters obtained from filter shift factors of 1, 1.1, 1.2 and 1.3. In this case the image obtained when the factor was equal to 1.1 was judged to be the best for the clinical requirements of the investigation. The image corresponding to a factor value of 1 was too smooth and those from values of 1.2 and 1.3 were too noisy (although the difference in this case between the images from factors 1.1 and 1.2 was small).

The results of this preliminary trial are summarised in figure 8.13. There is a well defined peak in the distribution of filter shift values with the majority of images being selected from the reconstruction which used a filter shift factor of 1.1. However, in a significant proportion of the cases a filter shift factor of 1.2 was chosen so that the optimal value probably lies somewhere between these two points.

For the sections taken through the base of the brain the transition frequency varied from 0.232cm^{-1} to 0.272cm^{-1} over the patient group. Similar levels of variation were observed from the other sections.

Larger variations were observed between the sections taken at different levels within the same brain. For example in one subject the transition frequency was 0.272cm^{-1} for the basal brain section and 0.19cm^{-1} for the superior brain section even though the 90% confidence limits for the noise fluctuations were almost identical (because there were approximately the same number of counts in each sinogram).

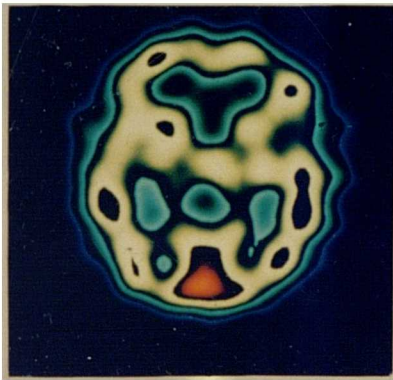
Nevertheless, the filter shift factor chosen to produce the best images was close to the same value in all cases. This



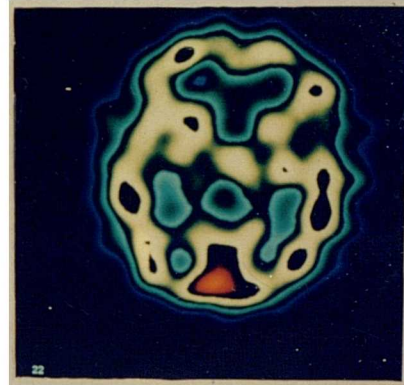
A



B



C



D

Figure 8.12 Section through an HMPAO study reconstructed using filter shift values of 1, 1.1, 1.2 and 1.3 (A, B, C and D respectively). These correspond to Butterworth filters with cut off frequencies of 0.095, 0.1, 0.114 and 0.124 cycles per pixel.

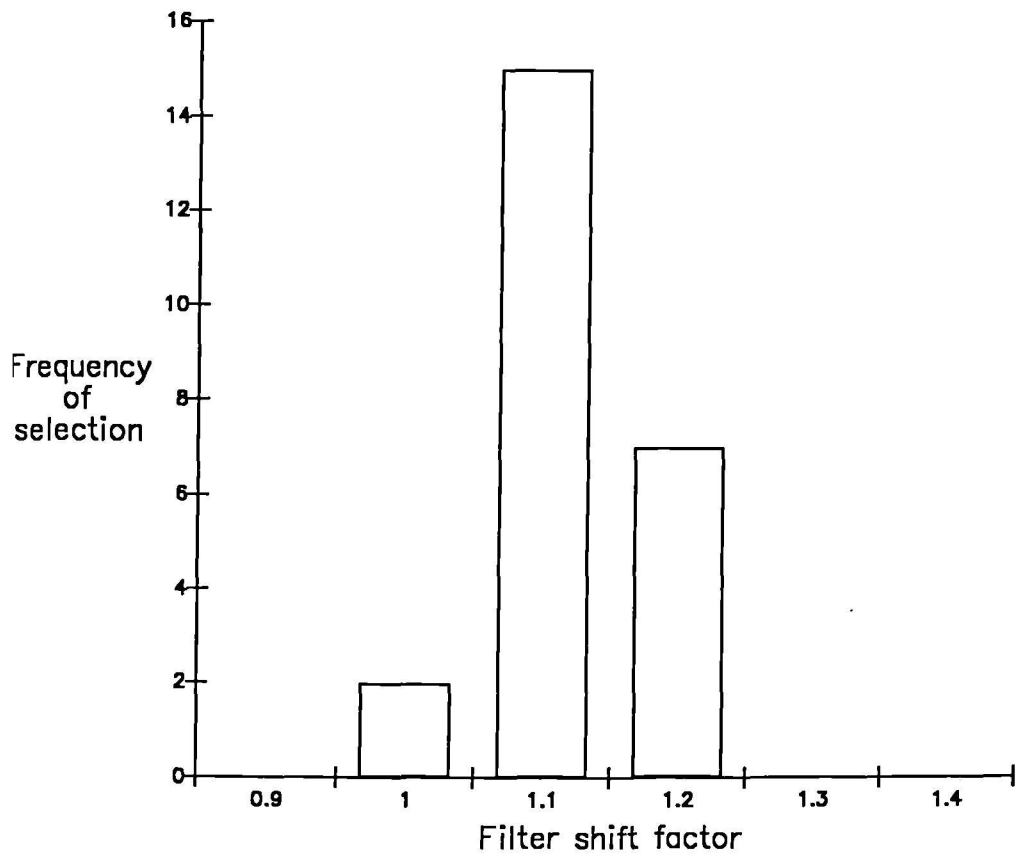


Figure 8.13 Frequency of selection of filter shift factors from preliminary trial of HMPAO studies.

is a consequence of the fact that it is the relationship between the signal and the noise in the data which is being optimised. This relationship is in effect defined by the transition frequency which identifies the point at which the signal becomes dominated by the noise. The filter shift factor which is chosen then dictates the signal to noise ratio in the filtered data. If consistent optimality criteria are applied to all the reconstructed images then it is not surprising that those with similar signal to noise ratios are identified as the "best". Thus, even though filters with different cut off frequencies can be applied in the reconstruction of different sections within the same patient, the signal to noise ratios of the reconstructed data will be approximately the same. The signal to noise ratio/filter shift factor having to be chosen to suit the clinical requirements of the investigation being performed.

8.5.3 Conclusions

The previously described methodology permits the identification of a well defined heuristic guide which accurately reproduces the choice of Butterworth filter made by an experienced observer. This is achieved because the criterion adopted means that the filter which is produced depends both on the noise level and the spatial frequency content of the projection data.

The use of the projection data alone to determine the relationship between the noise and the object power spectrum distinguishes this method from other approaches. The reconstruction of a section within a SPECT study depends only

on the information in the projection data which pertain to that section and not on extraneous structures distant from the section which exist in "representative" projection images.

By using observer preference as the optimality criterion the choice of filter function can be matched to the requirements of the clinical investigation to be performed.

The existence of a well behaved heuristic criterion means that the judgements made by an experienced observer can be reproduced rapidly and automatically by any operator.

8.6 Two Dimensional Filtering

Many of the data processing techniques used in the reconstruction of SPECT images have been adapted from the field of X-ray transmission computed tomography (CT) . This factor, in addition to the limited computing power available to early workers in SPECT, has meant that much of the initial work on SPECT was performed using one-dimensional filter functions. While this is appropriate for CT where the width of the X-ray beam can be confined to a thin transaxial plane it is not the best approach for radionuclide images. This is because of the intrinsically two dimensional nature of the detection process and the fact that the two dimensional PSF can extend over a large area compared to the thickness of a transaxial section.

Improvements in the quality of the reconstructed data would be expected if two dimensional filtering of the projection images was performed prior to back projection. For any particular projection profile there will be information about the projection element values contained in the count data of adjacent profiles. Thus filtering in two dimensions

should allow this information to be utilised effectively increasing the signal to noise ratio of the data.

8.6.1 The rotationally symmetric filter

Extending the filtering from one dimension to two dimensions can be achieved in a rigorous manner. Having determined the optimal filter from the power spectra of the projection data set a two dimensional version can be created by rotating the filter in frequency space to produce a rotationally symmetric function (r filter). The filtering process can then take place in frequency space by determining the two dimensional FT of the projection image set. After multiplication by the filter function the inverse FT is performed and the back projection with the ramp filter applied to the result.

Care has to be taken, however, during the practical application of the frequency domain implementation of any filter. Before the FT of the projection images is taken the data have to be amended because of the properties of the digital FT. A 128*128 image has to be extended to a 256*256 matrix by adding zeroes at the edges. This "zero packing" technique is required because the digital FT effectively treats the data as a periodic function so that differences in count values between pixels at opposing edges of the image appear as discrete jumps ; this will produce aliasing artefacts in the transformed data. Further manipulation may also be required, for similar reasons, to avoid discrete jumps between the edges of the image and the zero packed region. This can often be achieved by adding reflections of the original image to the raw data within a larger data matrix. As

a consequence of these considerations the FT has to be taken of matrices considerably larger than those used to acquire the data. Without an array processor this tends to make the implementation of the r filter in frequency space impractical because of the computing time required. For 128×128 data, two-dimensional filtering of 64 projection images in the frequency domain takes over thirty minutes on the Micas V system.

The implementation of the r filter can also take place in the spatial domain by taking the inverse FT of the filter and performing a two dimensional convolution with the projection images. Again however there are problems associated with the practical implementation of this method. In the spatial domain a large convolution matrix is required because too severe a truncation of the ideal matrix will result in the application of filter with a frequency response which differs greatly from the original definition. Furthermore a straightforward application of the convolution process takes considerably longer than the frequency domain implementation because of the efficiency of the FFT algorithm. An increase in the speed of the two dimensional convolution operation can be obtained through the use of a new Chebyshev algorithm, Miller (1983). However, this requires that the filter function be reducible to two orthogonal one dimensional functions. As this cannot be done exactly with a rotationally symmetric function the fast algorithm can only be applied to the data if some form of approximation is used, McLellan (1982).

Thus the application of the r filter in a theoretically correct form would be too time consuming for routine use particularly if different filter functions are required to reconstruct different sections within the study. To overcome

this problem a compromise between practicality and rigour was developed.

8.6.2 The y filter

The simplest approach to two dimensional filtering is to apply a one dimensional filter firstly in the y-direction and then in the x-direction as part of the standard reconstruction procedure, Jarritt (1984). The application is most conveniently performed by a convolution in the real domain.

A potential criticism of the y-filtering approach is that because there are two preferred directions the composite filter will not be rotationally symmetrical in frequency space so that the filtering procedure will not be completely isotropic.

8.6.3 Comparison of the y-filter and the r-filter

Although the r-filter is theoretically more accurate than the y-filter it is, as described previously, not as convenient to use in practice. This is particularly true for the two-dimensional implementation of the filter matching process which will be described in section 8.7. The differences between the y-filter and the r-filter are illustrated in the example shown in figure 8.14. It can be shown that the y-filter and r-filter are identical along the horizontal and vertical axes through the origin in the frequency domain. The differences between the filters are greatest along the diagonal axes which pass through the origin. This can be seen in figure 8.15 where diagonal profiles through the y-filter and x-filter are compared. From this it can be seen that the main influence of the application of the y-filter as opposed

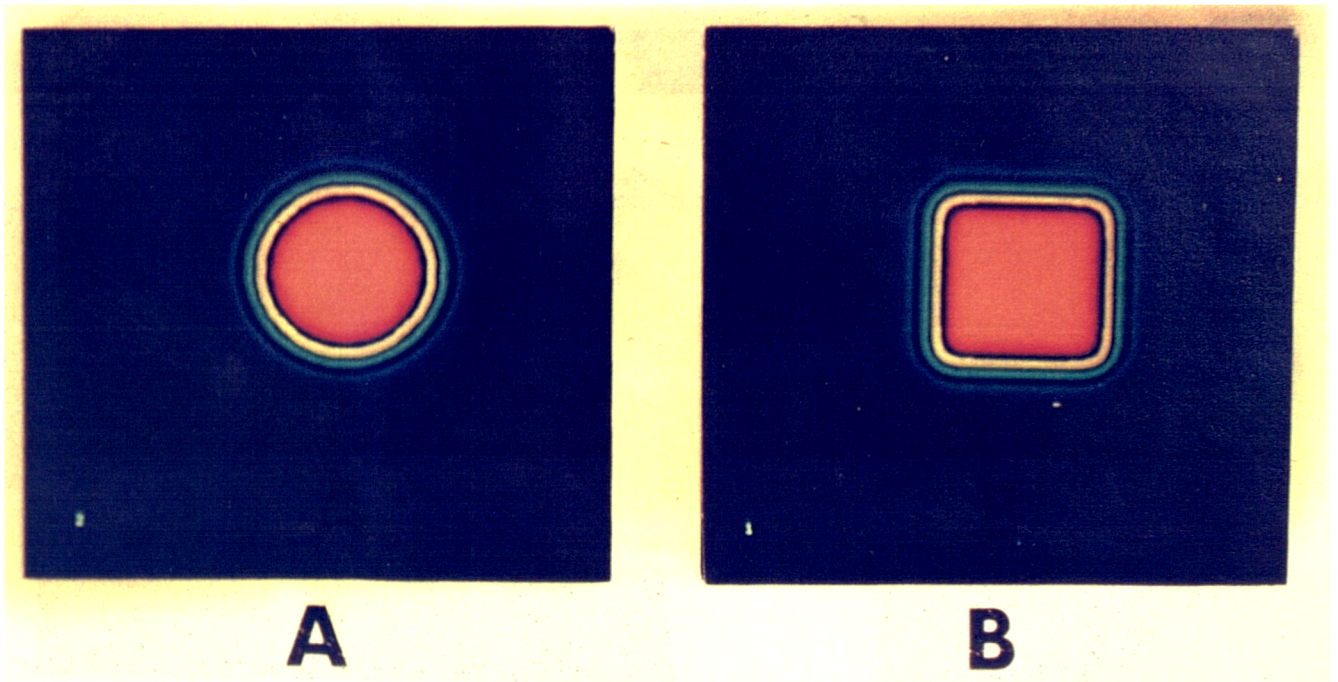


Figure 8.14 A - Frequency domain representation of the two dimensional Butterworth r-filter with power 10 and cut off frequency 0.11 cycles per pixel.
 B - Frequency domain representation of the two dimensional Butterworth y-filter with power 10 and cut off frequency 0.11 cycles per pixel.

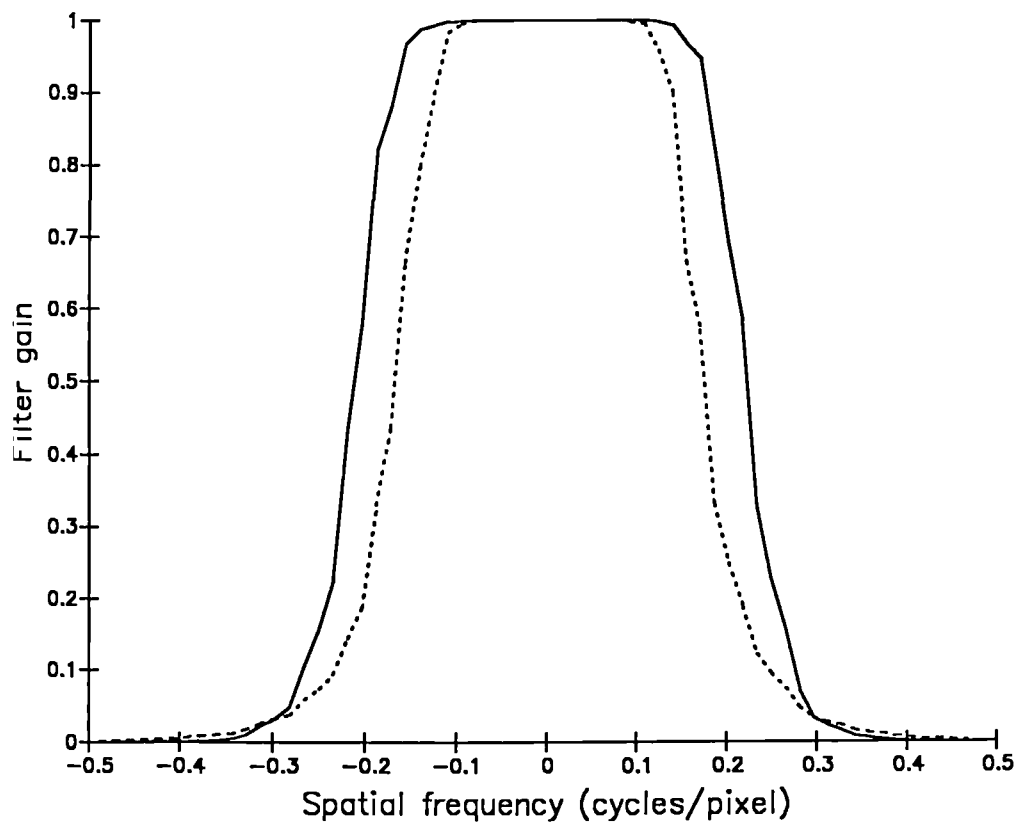


Figure 8.15 Diagonal profiles through the r-filter of figure 8.14A, dotted line, and the y-filter of figure 8.14B, solid line.

to the r-filter will be an increased transfer of the higher spatial frequencies along the diagonal directions in real space, i.e. along the directions given by the lines $x=y$ and $x=-y$.

The effects of these differences can be seen in figure 8.16 which shows the effects of the two-dimensional filtering of a ^{99m}Tc -Methylene diphosphonate (MDP) image acquired twenty minutes after administration. The filtering was performed in the frequency domain. The differences between the y-filter and the r-filter are small.

To assess how the small differences which are introduced into planar images affect a SPECT study the projection data for a ^{99m}Tc -HMPAO investigation were filtered in the frequency domain using a Butterworth filter with power 10 and a cut off frequency of 0.314cm^{-1} . A comparison of the results obtained with the y-filter and the r-filter for a section 0.7cm thick through the base of the brain are shown in figure 8.17. The image produced by the r-filter is smoother than the y-filtered image but no obvious deterioration in image quality has occurred. Similar findings were obtained for a variety of study types and Butterworth filters.

8.7 Filter matching in two dimensions

The methods described in section 8.5 for matching the form of a one dimensional Butterworth filter to the projection data in a transaxial section can be extended to two dimensions by utilising the result that the y filter can be used in place of the r filter without introducing a deterioration in image quality.

A straightforward extension of the filter matching process

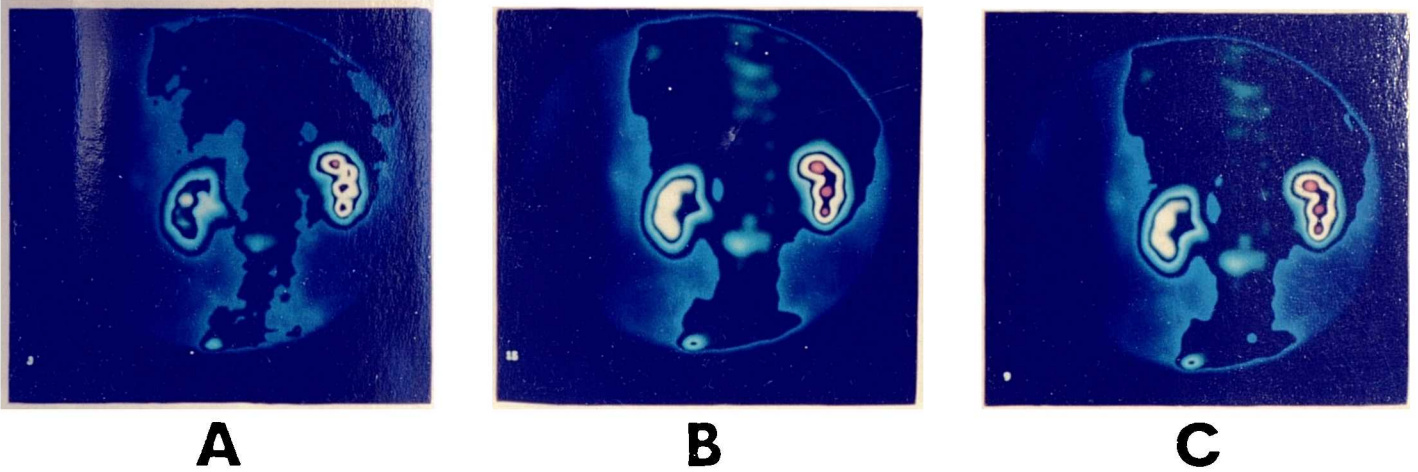


Figure 8.16 A - Posterior image of the abdomen taken twenty minutes after the administration of ^{99m}Tc -MDP.
B - The image shown in A after application of the Butterworth r-filter with power ten and a cut off frequency of 0.11 cycles per pixel.
C - The image shown in A after application of the Butterworth y-filter with power ten and a cut off frequency of 0.11 cycles per pixel.

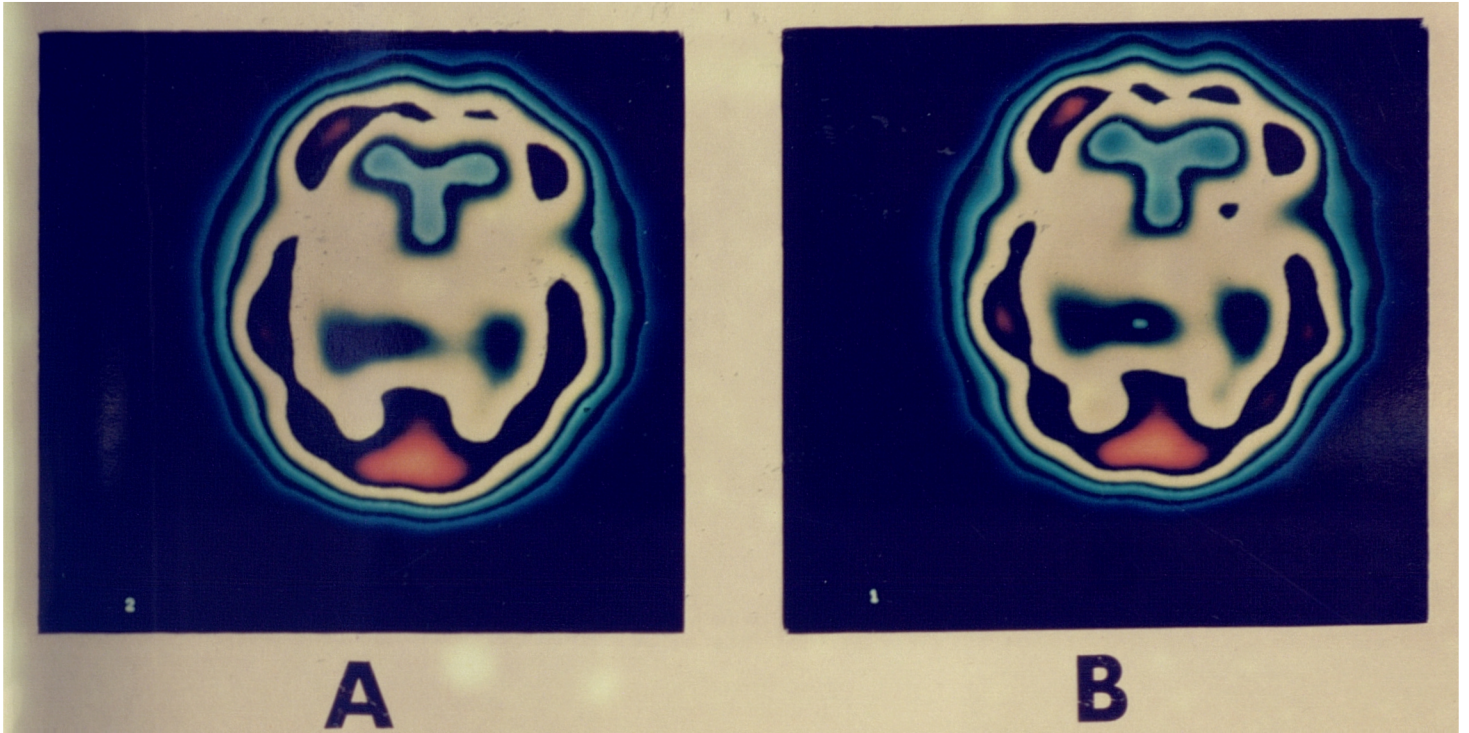


Figure 8.17 A - Section through a ^{99m}Tc -HMPAO study which was reconstructed after filtering with the Butterworth r-filter of power 10 and a cut off frequency of 0.314cm^{-1} .

B - The same section as shown in A but reconstructed after filtering with the Butterworth y-filter of power 10 and a cut off frequency of 0.314cm^{-1} .

described in section 8.5 would be impractical because of the time taken to filter the data in the y-direction i.e around ten minutes for 64 projection images of size 128*128. Because a different y-filter would be required for each transaxial section this makes both the initial trial to determine the optimal filter shift factor and the subsequent routine application of the optimised filters too time consuming to be practical.

This problem can be overcome by using the observation that the quality of a reconstructed section is not particularly sensitive to the exact form of the filter used in the y direction. It is dominated by the form of the filter in the x direction. This means that the same y filter can be used for the reconstruction of all of the transaxial sections in a study. Thus a preliminary estimate of the optimal filter can be made and the y filtering of the data in the study performed. The optimisation process described in section 8.5 can then be applied to the y filtered data. If for any individual study in the preliminary optimisation trial or the complete investigation, the y filter originally used was significantly different from the functions obtained by the optimisation process then the optimisation procedure for that study can be repeated using the improved estimate for the y filter function.

8.7.1 Effects of y filtering

The effects of the y filter on the projection data can be seen from figure 8.18 which shows the LNP(u) curves of the MAPS obtained from the projection data used to produce the image shown in figure 8.17. The curves shown correspond to the

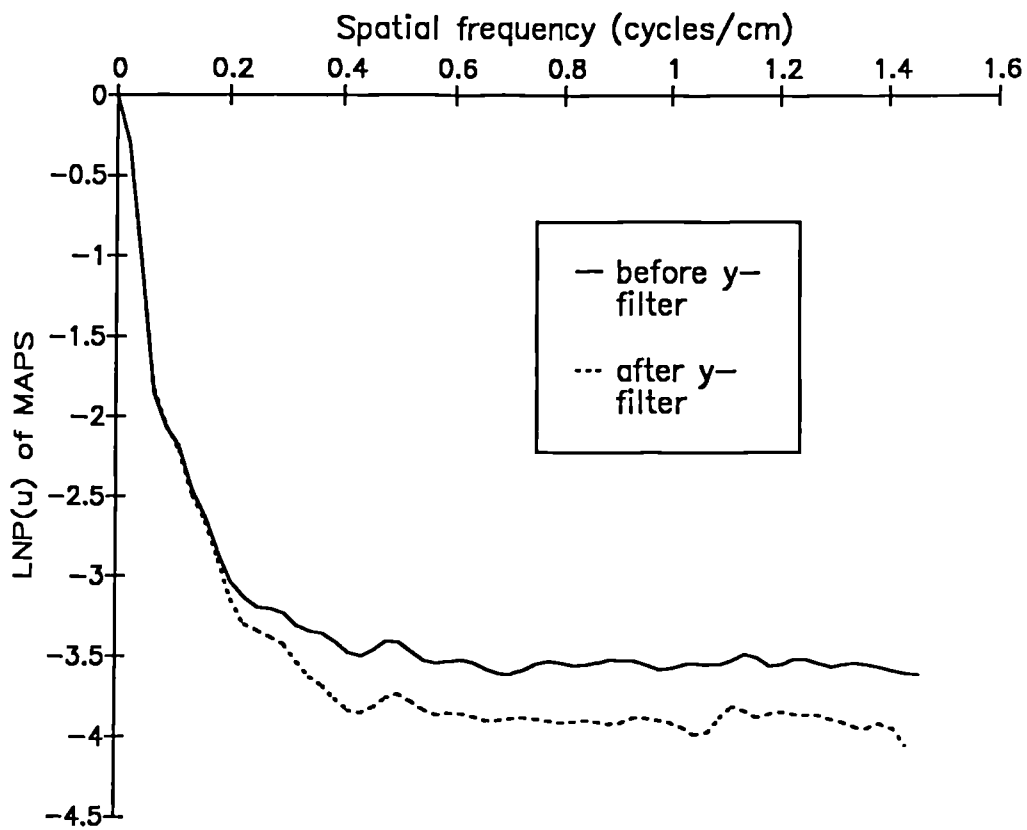


Figure 8.18 LNP(u) curves of the MAPS for a section through an HMPAO study both before, solid line, and after, dotted line, y-filtering.

data before and after y filtering. The higher signal to noise ratio in the y filtered data is demonstrated by the lower amplitude of the mean noise level. This is reflected in the change in the 90% confidence limit for the noise which causes the transition frequency to increase from 0.27cm^{-1} to 0.32cm^{-1} .

The consequences which this change in the form of the projection data have on the reconstructed sections are shown in figure 8.19. The y filtered image is considerably smoother even though the same filter function was used in the x direction.

The use of the y filter changes the results of the filter matching trial. The application of the y filter increased the value of the transition frequency by, on average, 21%. Figure 8.20 shows the values of the filter shift factors identified as being those which optimised the quality of the reconstructed data. A comparison with the values of figure 8.13 shows that the optimal filter shift factor has been reduced by around 10%. The combined effect of these two results is to increase the cut off frequency of the Butterworth filter by approximately 10%.

A separate consequence of the y filtering procedure is an increase in the quality of the coronal and sagittal sections. This is shown in figure 8.21. The reason for this improvement lies in the fact that the two dimensional nature of the imaging process is being taken into account to produce a consistent degree of smoothing in the x and y directions.

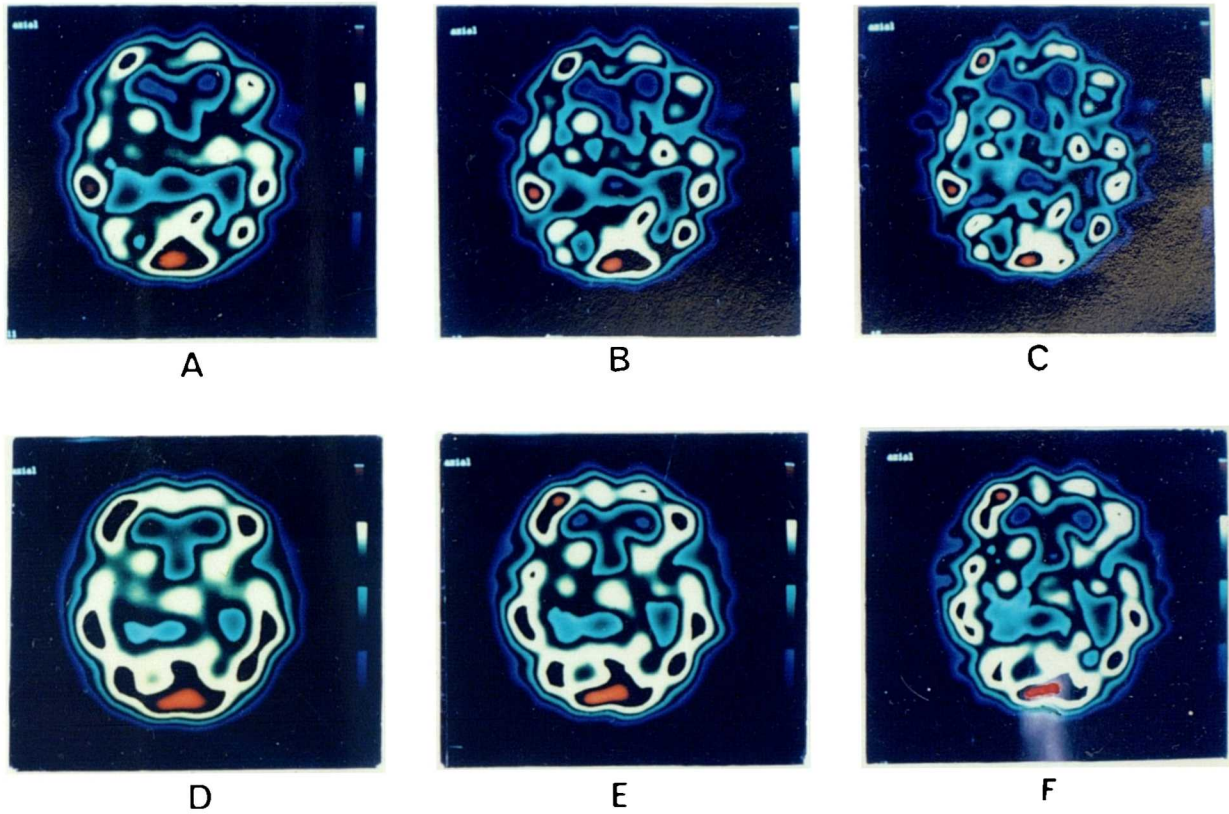


Figure 8.19 Comparison of sections through an HMPAO study with (D, E and F) and without (A, B and C) y filtering. The Butterworth power was 10 and the cut off frequency was 0.1 (A,D), 0.13 (B,E) and 0.15 (C,F) cycles per pixel

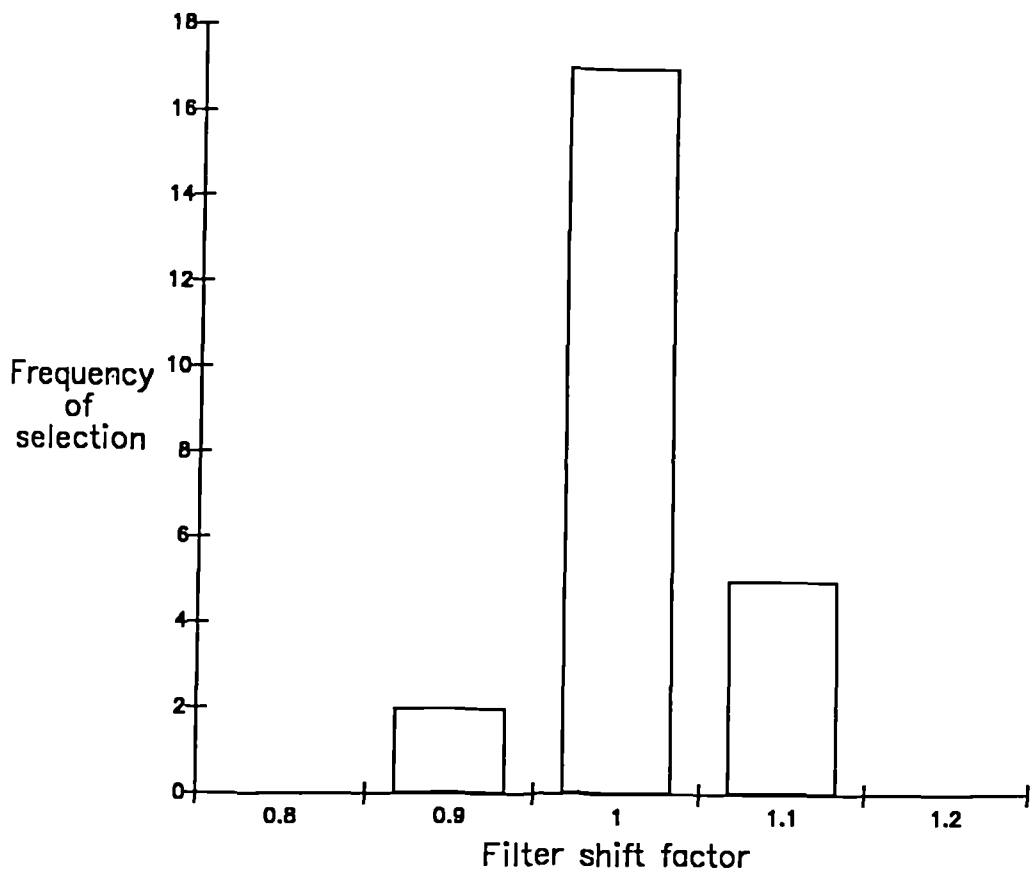
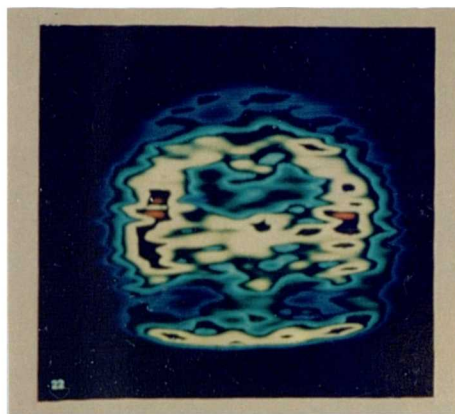
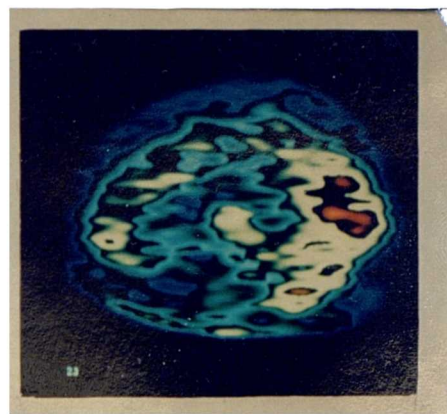


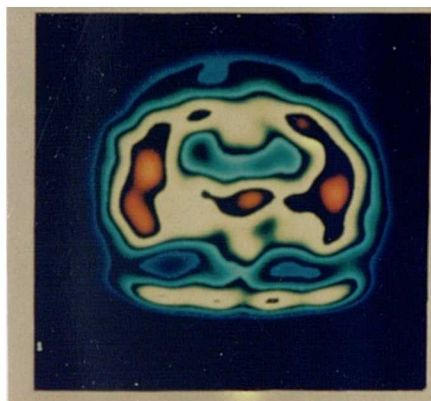
Figure 8.20 Frequency of selection of filter shift factors from preliminary trial of y-filtered HMPAO studies.



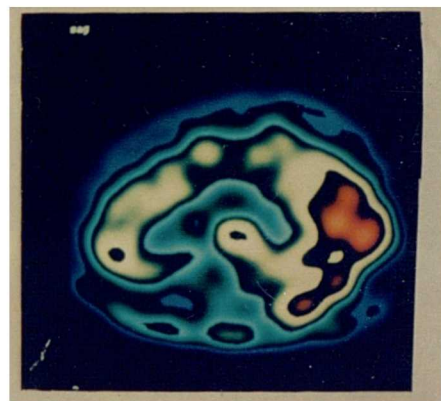
A



B



C



D

Figure 8.21 Comparison of coronal and sagittal sections through an HMPAO study with (C,D) and without (A,B) y-filtering. A Butterworth filter with power 10 and a cut off frequency of 0.13 cycles per pixel was used.

8.8 General conclusions for Chapter 8

1. A method has been developed for the measurement of local statistical noise levels in sections through a uniform cylindrical distribution. This method permits the variation of RMS% values across a transaxial section to be accurately assessed. It can be used to compare the noise levels produced by different filter functions.
2. From a consideration of the properties of the filter functions available for use in filtered back projection the Butterworth filter was judged to have the most desirable characteristics.
3. The power of the Butterworth filter should not be greater than 10 if ripple artefacts of a magnitude greater than 2% are to be avoided.
4. A small but significant improvement in image contrast can be obtained by correcting for the effects of sampling and interpolation.
5. The Butterworth filter can be matched to the data by identifying the spatial frequency at which the signal becomes dominated by the noise. For the reconstruction of a particular section in a study the projection data for that section is used in the filter matching process. This is achieved by creating a MAPS from the set of projection profiles. The properties of the MAPS can be visualised by taking the LOG of the normalised data to produce a LNP(u) curve.

6. For any particular clinical investigation the value which the Butterworth filter should take at the transition frequency is determined by the filter shift factor. The value of the filter shift factor is obtained from a preliminary trial using a small number of patients in which the best images are identified by an experienced observer. The filter shift factor which produces the best images most frequently is chosen for use in the remainder of the study.

7. The filter matching procedure can be extended to two dimensions in a practical manner by operating on the projection data after it has been filtered in the y-direction. The differences between the two dimensional y-filter and the rotationally symmetrical filter were found to be small. The LNP(u) curve of the MAPS from the y-filtered data shows that the signal to noise ratio for each transaxial section has been increased. The two dimensional filtering also produced significant improvements in the quality of the coronal and sagittal sections.

9.1 Introduction

The results of Chapter 8 can be used to extend the parameter optimisation investigations of Chapter 7 to SPECT data with noise levels similar to those encountered clinically.

The use of low count data means that smoother filter functions than the ramp have to be used for the reconstruction which adds an additional layer of complexity to the analysis. To help with this the information obtained in Chapter 8 can be utilised.

9.2 Comparison of collimators

Various fundamental aspects of collimator performance have been investigated during the course of this thesis, Sections 4.2.4, 5.2 and 7.2.4. However, the only way in which this information can be collated to produce practical guidelines is to examine the effects of the use of different collimators on SPECT studies of a known object. To achieve this a number of acquisitions were made of the SPECT phantom with the inserts described in Section 3.6.

9.2.1 Methods

The SPECT phantom, with inserts, was filled with a solution of ^{99m}Tc and left to mix for a period of at least eight hours. The phantom was then mounted on the jig described in Section 3.6 for the SPECT acquisitions to be performed. Care was taken to ensure that the central axis of the phantom was parallel to the camera face at camera rotation angles of zero

and ninety degrees. This was achieved to an accuracy of less than 0.25cm. The same amount of activity, 90MBq, was used for each study. In the first instance a set of low noise SPECT acquisitions were performed using both collimators at ROR values of 16cm and 25cm. The gain of the system was set to give pixels of edge length 0.28cm and the projection data were acquired into matrices of dimension 128*128. There were 128 projection angles and the acquisition time per angle was 300s. Before each acquisition the DIGITRAC daily quality control procedure was implemented to ensure that the camera was in a state of optimal tuning and was properly peaked. The centre of rotation offset value was also checked before each acquisition.

A further set of SPECT studies was performed to produce data with count densities similar to those found clinically. The methodology was the same as above apart from a shorter acquisition time of 30s per projection angle and the use of 64 as opposed to 128 projection angles.

9.2.2 Noise considerations

As described in Section 8.1 the sensitivity and count rate linearity of the gamma camera limit the total number of counts which can be acquired in a SPECT study. Thus, even for phantom studies where very long acquisition times are possible the noise levels which are encountered can still be significant. For example, the results in Table 8.1 show that for pixels of edge length 0.28cm a reconstruction of a uniform cylindrical source distribution with the ramp filter produces a mean RMS% level of 34.8% per pixel. As the phantom inserts are uniform along their length 10 adjacent sections can be summed together

to reduce the noise level to around 11%. From Section 2.3.2 it was calculated that the RMS% noise levels in a source distribution in which the activity was concentrated in a small portion of the object could be up to a factor of 5 lower than that for the uniform cylinder case. Thus, for example, the HL insert could be expected to exhibit noise levels of the order of 2%-4% whereas the CL insert, which has an activity distribution closer to that of the uniform cylinder, would still have RMS% values of around 10%. The values for the pie and the linearity inserts would be expected to lie somewhere between these two extremes.

It should also be noted that the figures quoted are averaged over the whole source distribution. The noise levels at the edge of the distribution can be double those at the centre, Section 8.1.

Thus, even for very high count density phantom studies the noise levels encountered with the ramp filter may limit the quality of the reconstructed images, particularly for the CL insert. For this reason the use of filters other than the ramp must be considered when comparing the results of the studies obtained from the different collimators.

9.2.3 Reconstruction

For each study a number of Butterworth filters with a range of cut off frequencies were used to reconstruct the transaxial sections through the phantom inserts. Because adjacent sections were summed together over a thickness of 2.8cm there was no point in using the two dimensional form of the filter functions. For brevity only the data from the CL and the pie inserts will be considered.

9.2.4 Analysis

Figures 9.1 to 9.8 show the images obtained from the low noise data for the various combinations of collimator and ROR. For each set of parameters the images have been shown after reconstruction with a range of Butterworth filters and, where useful, the ramp. The cut off frequencies of the filters were chosen to produce a range of images which varied from being too noisy to too smooth. The "best" image from each set of reconstructions was used for the comparison of the effects of the collimation. An example of this is given in figure 9.1 where the images of the CL insert after acquisition with the HR collimator and a ROR of 16cm are shown. The smallest cold rod, 6mm in diameter, can be seen on all the images although if its location was not known it could be missed on the ramp filtered data. For the CL insert the "best" image was taken to be that which was obtained from the Butterworth filter with the highest cut off frequency in which the smallest cold rod could be clearly differentiated from the noise. In figure 9.1 this was taken to be the image from the cut off frequency equal to 0.71cm^{-1} .

An analysis of the NPS of the sinogram for this section showed that the transition frequency, Section 8.5, occurred at 0.53cm^{-1} . As the "best" image was from a cut off frequency of 0.71cm^{-1} this would suggest that a filter shift factor of around 1.3 would be required to produce optimal data. Similar findings were obtained from the other studies. This is consistent with what would be expected from the results of Section 8.5 where a lower value for the filter shift factor, viz. 1.1, was selected to increase the specificity of the

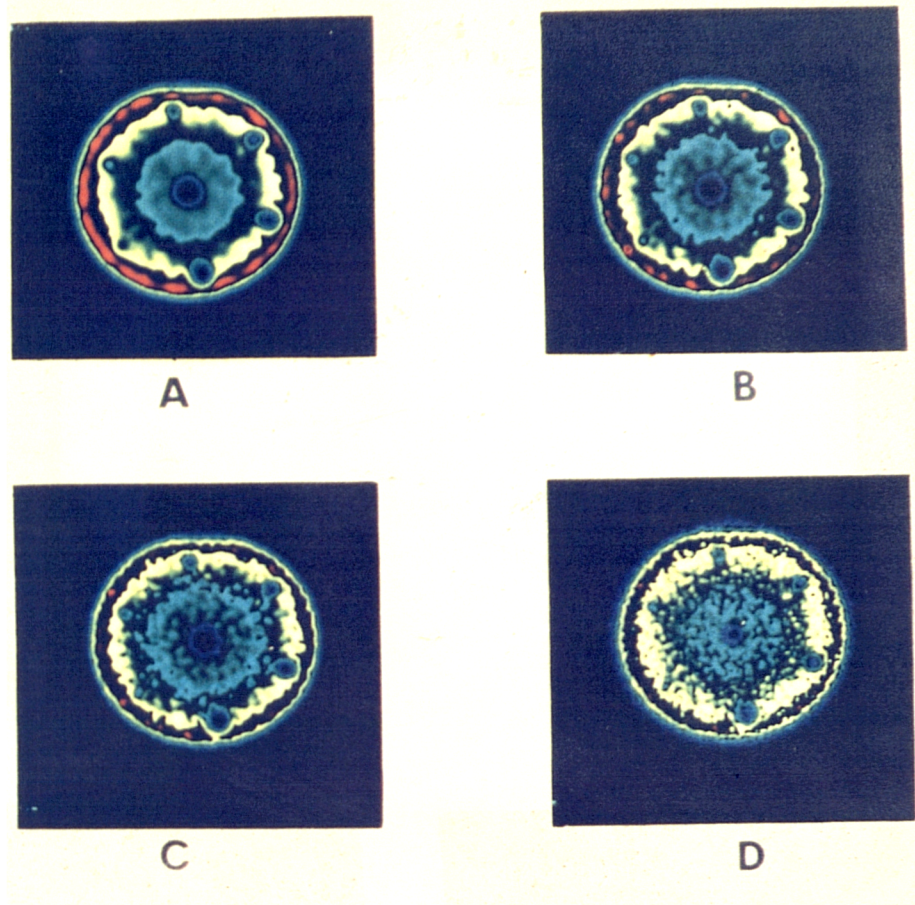


Figure 9.1 Section through the CL insert of thickness 2.8cm. The HR collimator, a ROR of 16cm and an acquisition time of 300 seconds per projection angle were used. The images in A, B and C were obtained from Butterworth filters with cut off values of 0.54cm^{-1} , 0.71cm^{-1} and 0.89cm^{-1} , respectively. The ramp filter was used for image D. The image in B was judged to be the "best".

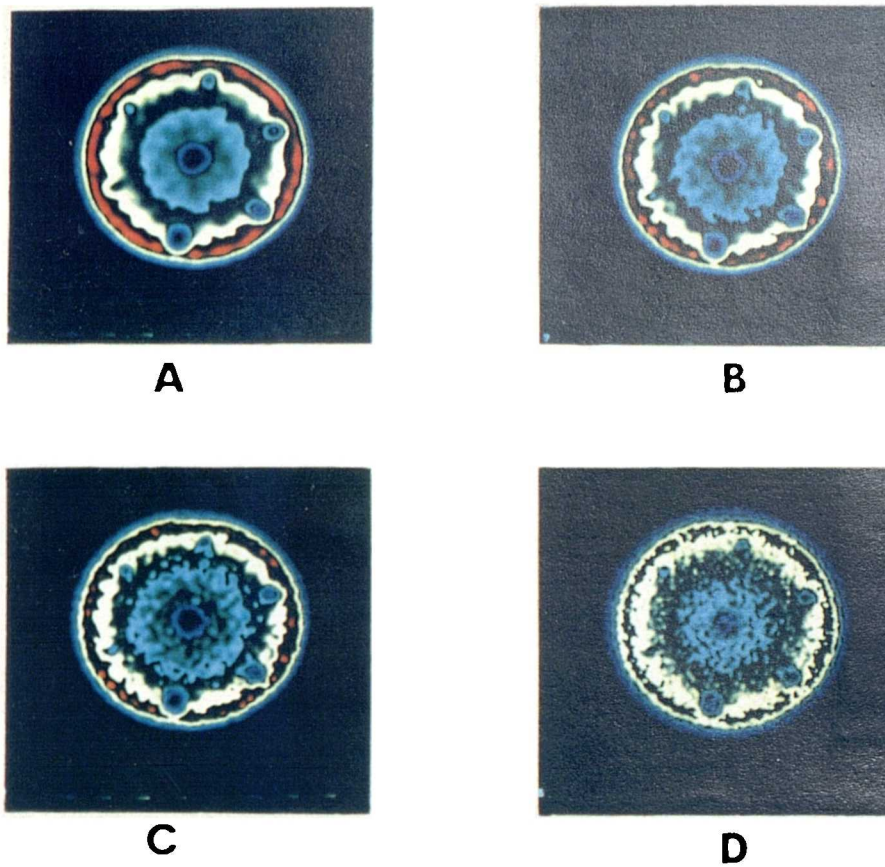


Figure 9.2 Section through the CL insert of thickness 2.8cm. The LEAP collimator, a ROR of 16cm and an acquisition time of 300 seconds per projection angle were used. The images in A, B and C were obtained from Butterworth filters with cut off values of 0.54cm^{-1} , 0.71cm^{-1} and 0.89cm^{-1} , respectively. The ramp filter was used for image D. The image in B was judged to be the "best".

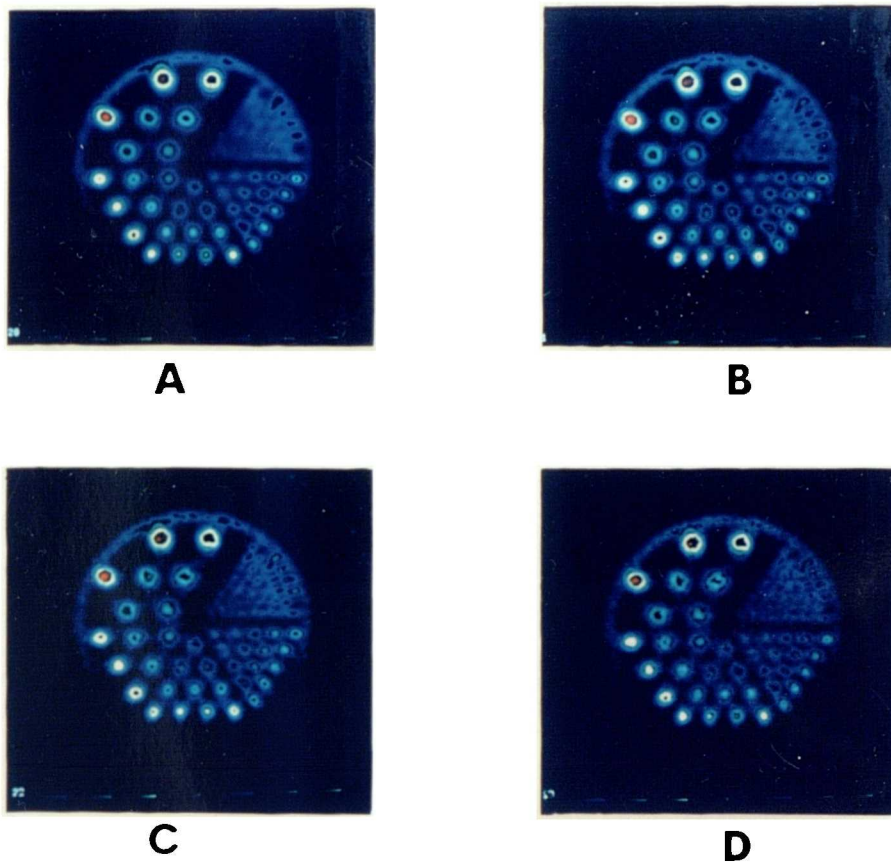


Figure 9.3 Section through the pie insert of thickness 2.8cm. The HR collimator, a ROR of 16cm and an acquisition time of 300 seconds per projection angle were used. The images in A, B and C were obtained from Butterworth filters with cut off values of 0.71cm^{-1} , 0.89cm^{-1} and 1.07cm^{-1} , respectively. The ramp filter was used for image D. The image in B was judged to be the "best".

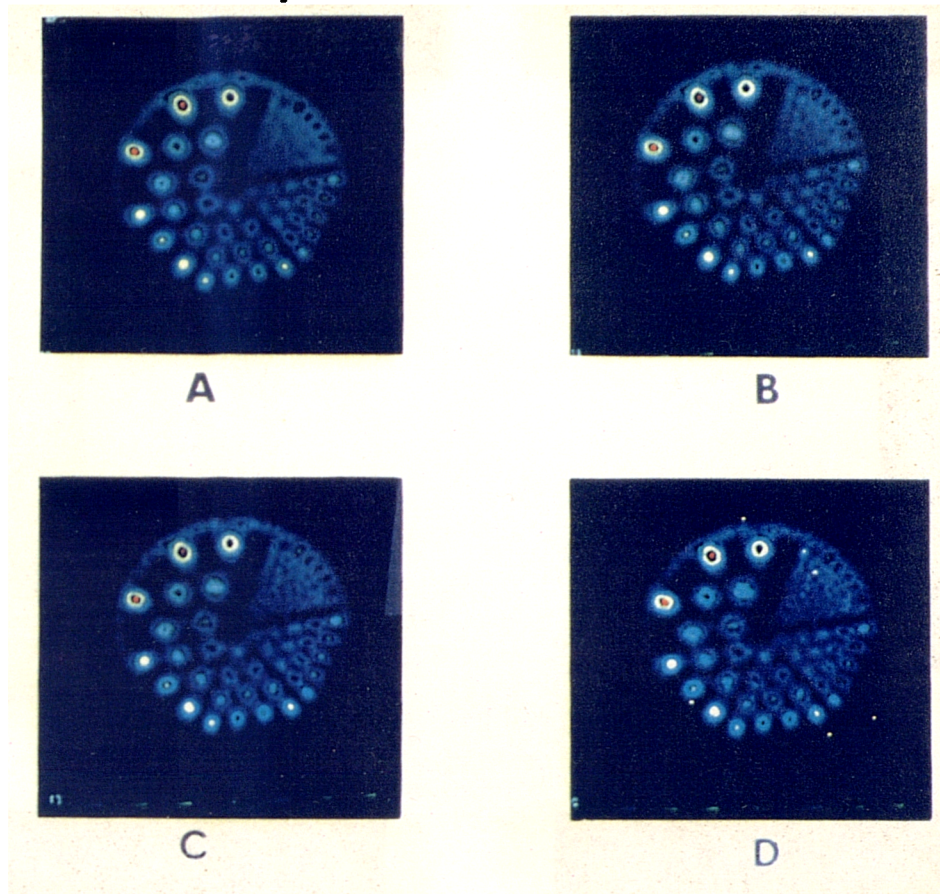


Figure 9.4 Section through the pie insert of thickness 2.8cm. The LEAP collimator, a ROR of 16cm and an acquisition time of 300 seconds per projection angle were used. The images in A, B and C were obtained from Butterworth filters with cut off values of 0.71cm^{-1} , 0.89cm^{-1} and 1.07cm^{-1} , respectively. The ramp filter was used for image D. The image in B was judged to be the "best".

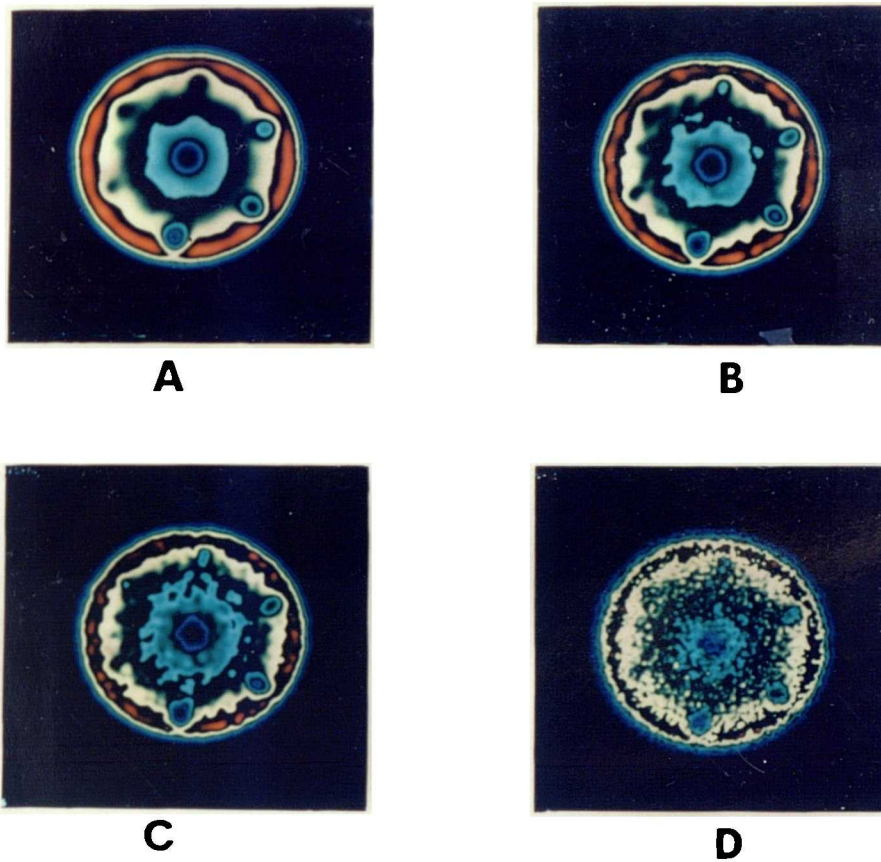


Figure 9.5 Section through the CL insert of thickness 2.8cm. The HR collimator, a ROR of 25cm and an acquisition time of 300 seconds per projection angle were used. The images in A, B and C were obtained from Butterworth filters with cut off values of 0.36cm^{-1} , 0.54cm^{-1} and 0.71cm^{-1} , respectively. The ramp filter was used for image D. The image in B was judged to be the "best".

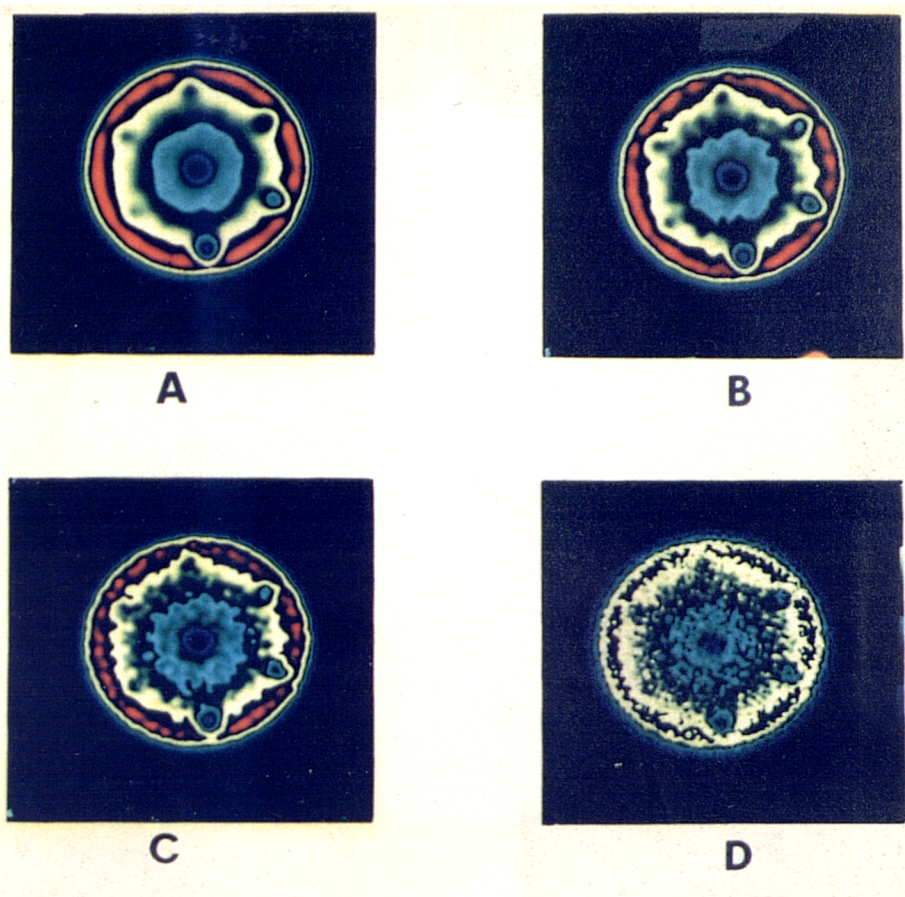


Figure 9.6 Section through the CL insert of thickness 2.8cm. The LEAP collimator, a ROR of 25cm and an acquisition time of 300 seconds per projection angle were used. The images in A, B and C were obtained from Butterworth filters, with cut off values of 0.36cm^{-1} , 0.54cm^{-1} and 0.71cm^{-1} , respectively. The ramp filter was used for image D. The image in B was judged to be the "best".

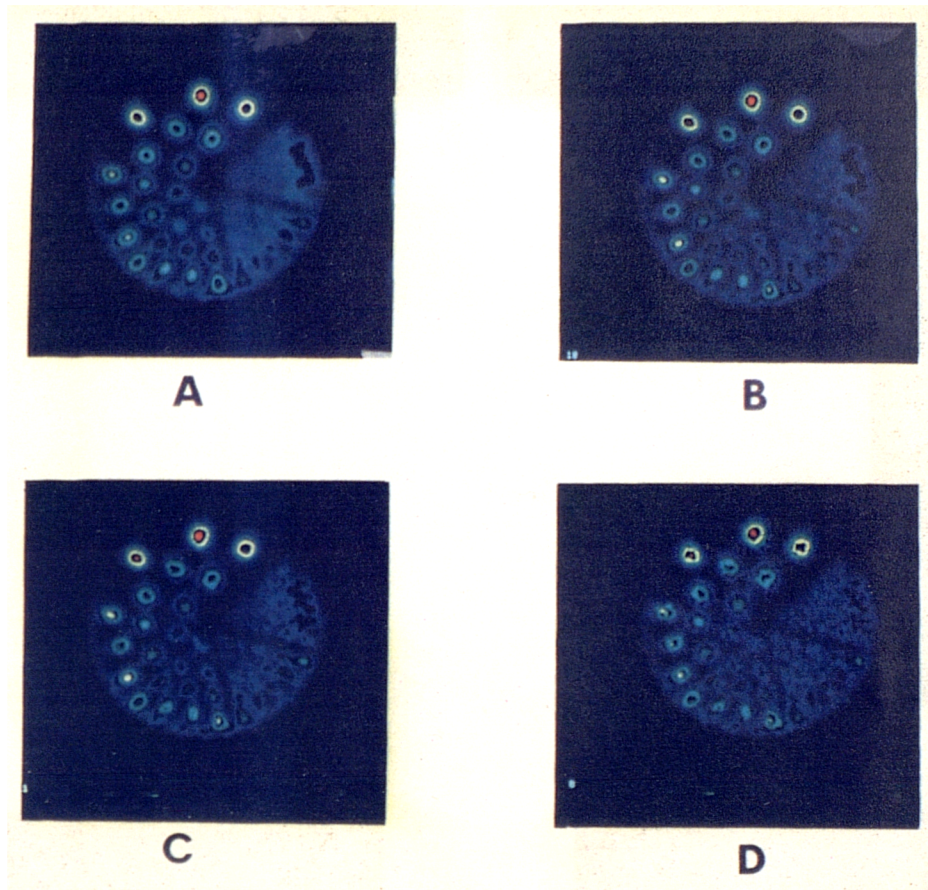


Figure 9.7 Section through the pie insert of thickness 2.8cm. The HR collimator, a ROR of 25cm and an acquisition time of 300 seconds per projection angle were used. The images in A, B and C were obtained from Butterworth filters, with cut off values of 0.36cm^{-1} , 0.54cm^{-1} and 0.71cm^{-1} , respectively. The ramp filter was used for image D. The image in B was judged to be the "best".

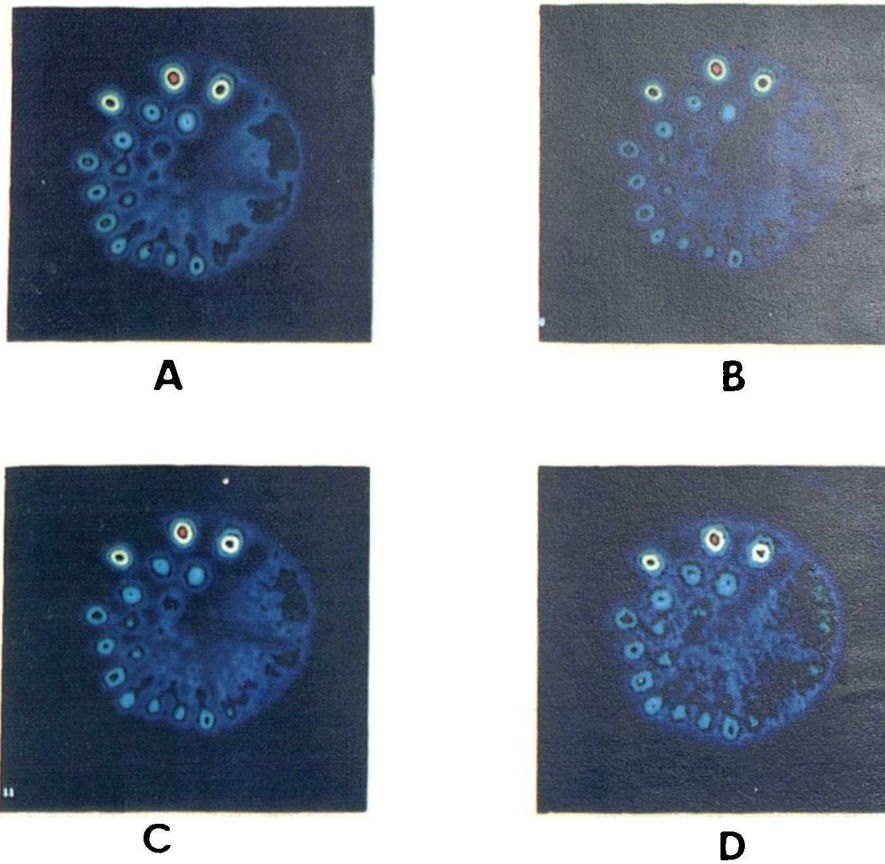


Figure 9.8 Section through the pie insert of thickness 2.8cm. The LEAP collimator, a ROR of 25cm and an acquisition time of 300 seconds per projection angle were used. The images in A, B and C were obtained from Butterworth filters, with cut off values of 0.36cm^{-1} , 0.54cm^{-1} and 0.71cm^{-1} , respectively. The ramp filter was used for image D. The image in B was judged to be the "best".

examination in line with clinical requirements.

For the pie insert, figure 9.3, the "best" image was taken to be that at which the smallest hot rods could be identified. As some features of the 6mm rod segment could be visualised when a cut off value of 0.89cm^{-1} was used this was taken to be the "best" image. The transition frequency for this sinogram was found to be 0.85cm^{-1} . This is close to the cut off frequency of the "best" image suggesting that for the identification of hot lesions a lower filter shift factor may be required than for the identification of cold lesions.

The subjective element in this analysis is recognised but is unavoidable. As the main aim is to compare the effects of the use of different collimators this approach should be accurate enough to allow valid conclusions to be drawn so long as the subjective criteria are applied consistently. The images from a range of cut off frequencies have been included in the figures in addition to the "best" image to demonstrate that the conclusions which are drawn do not depend critically on the choice of filter.

9.2.5.1 Results for low noise studies

A comparison of the images in figure 9.1 with those in figure 9.2 shows that there is very little difference between the HR and the LEAP collimators for the CL insert when a ROR of 16cm is used. The 6mm rod is possibly more accurately defined on the HR collimator images.

A comparison of figures 9.3 and 9.4 shows that there is little difference between the HR and the LEAP images of the pie insert. All of the 9mm rods can be visualised on both images. The second outermost row of the 6mm rods can be seen

with slightly greater clarity on the HR collimator images.

When the ROR is increased to 25cm a comparison of the CL insert data, figures 9.5 and 9.6, shows a clear increase in contrast for the three smallest rods on the HR collimator image. Nevertheless, the smallest rod is still clearly identifiable on the LEAP collimator images.

Figures 9.7 and 9.8 show the pie insert for the HR and LEAP collimators when the ROR was 25cm. The 9mm rods cannot be clearly seen on any of the LEAP collimator images. They can however be identified on the HR collimator images. Thus, there would appear to be a clear advantage to be obtained through the use of the HR collimator at large ROR particularly when identifying hot lesions.

9.2.5.2 Results at clinical noise levels

To assess how these results transfer to the noise levels typically encountered in the clinical situation 1.1cm thick sections through the 30s per projection angle acquisitions were examined. Figures 9.9 and 9.10 show the images obtained from the CL insert when the ROR was 16cm. The three smallest rods can be more clearly identified on the images from the LEAP collimator.

Figures 9.11 and 9.12 show the images obtained from the pie insert when the ROR was 16cm. There is little to choose from between the two sets of images ; the central 9mm rods are possibly more clearly defined on the HR collimator images.

Figures 9.13 and 9.14 show the images obtained from the CL insert when the ROR was 25cm. There is little to choose from between the two sets of images ; the 12mm rod is possibly more clearly defined on the images from the LEAP collimator.

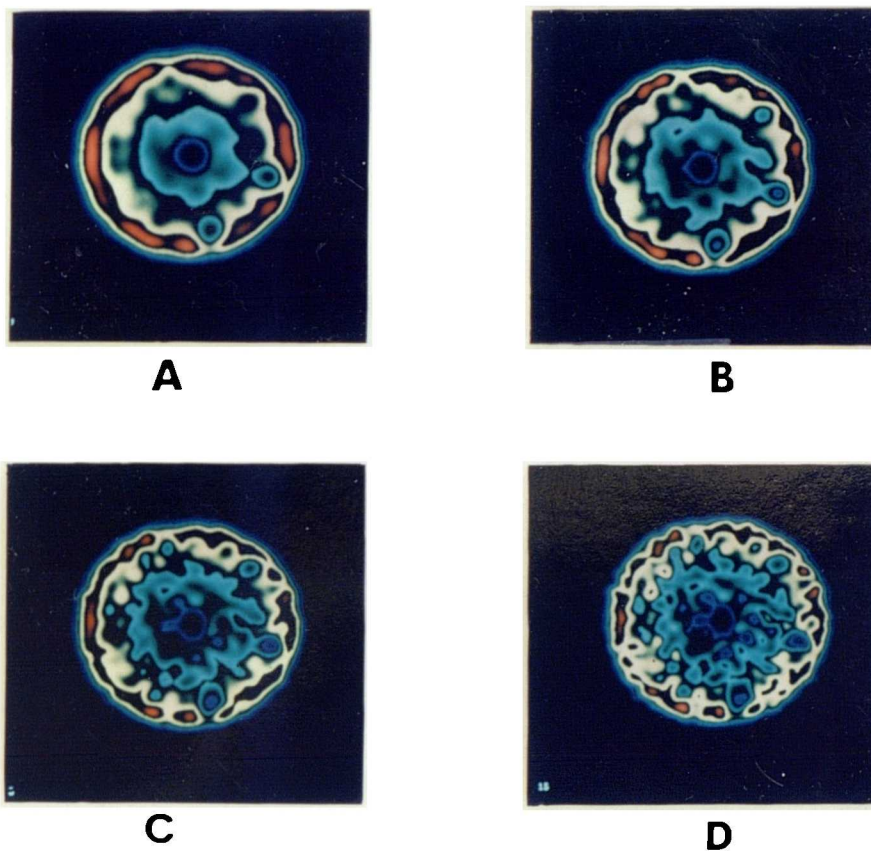


Figure 9.9 Section through the CL insert of thickness 1.1cm. The HR collimator, a ROR of 16cm and an acquisition time of 30 seconds per projection angle were used. The images in A, B, C and D were obtained from Butterworth filters with cut off values of 0.29cm^{-1} , 0.36cm^{-1} , 0.43cm^{-1} and 0.54cm^{-1} , respectively. The image in B was judged to be the "best".

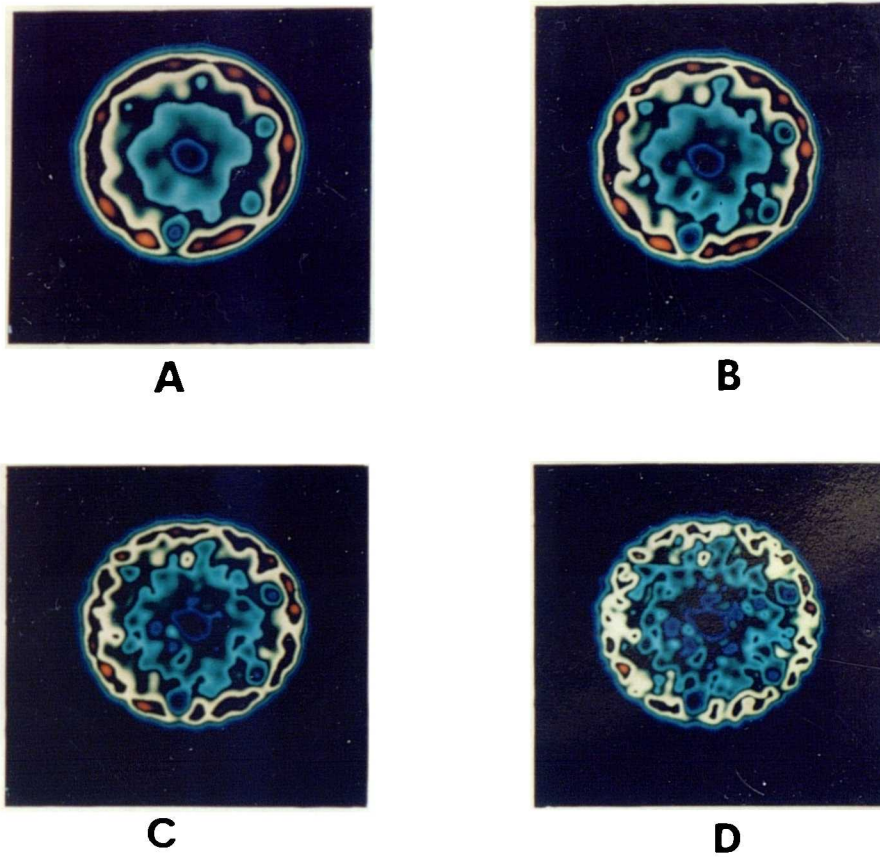


Figure 9.10 Section through the CL insert of thickness 1.1cm. The LEAP collimator, a ROR of 16cm and an acquisition time of 30 seconds per projection angle were used. The images in A, B, C and D were obtained from Butterworth filters with cut off values of 0.29cm^{-1} , 0.36cm^{-1} , 0.43cm^{-1} and 0.54cm^{-1} , respectively. The image in B was judged to be the "best".

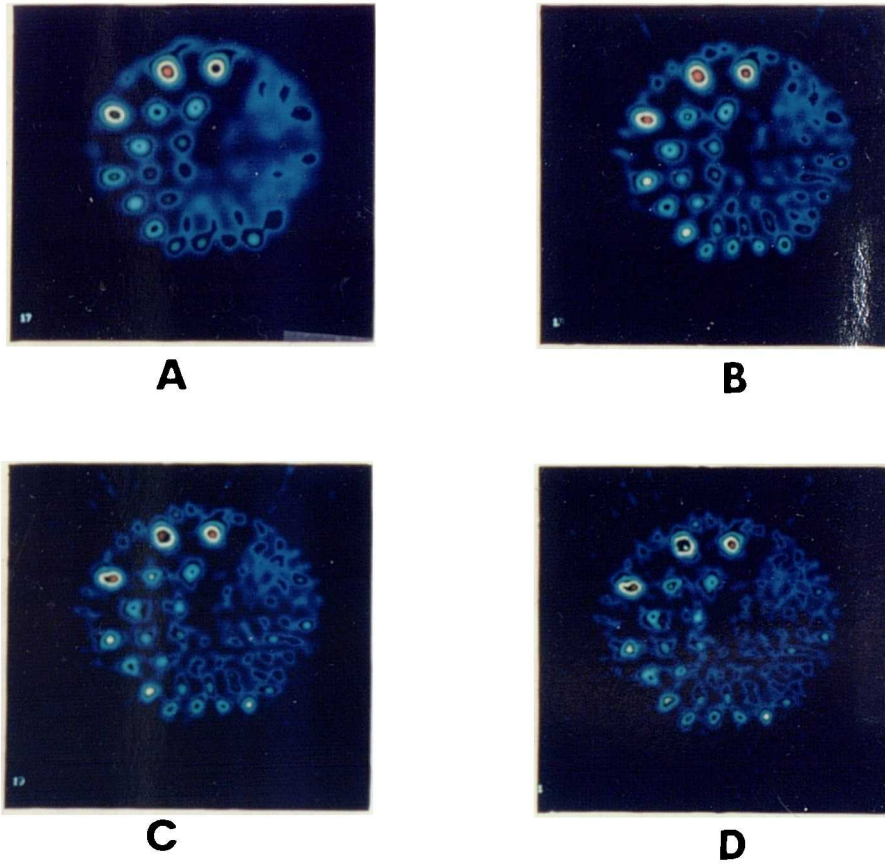


Figure 9.11 Section through the pie insert of thickness 1.1cm. The HR collimator, a ROR of 16cm and an acquisition time of 30 seconds per projection angle were used. The images in A, B, C and D were obtained from Butterworth filters, with cut off values of 0.36cm^{-1} , 0.54cm^{-1} , 0.71cm^{-1} and 0.89cm^{-1} , respectively. The image in B was judged to be the "best".

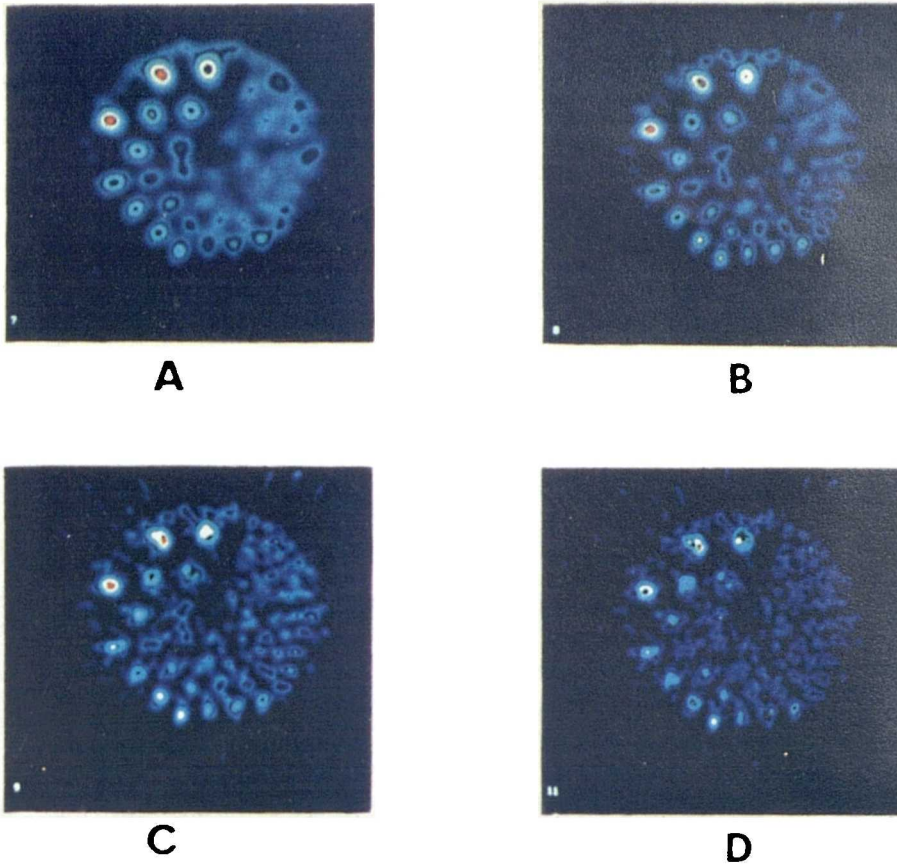


Figure 9.12 Section through the pie insert of thickness 1.1cm. The LEAP collimator, a ROR of 16cm and an acquisition time of 30 seconds per projection angle were used. The images in A, B, C and D were obtained from Butterworth filters with cut off values of 0.36cm^{-1} , 0.54cm^{-1} , 0.71cm^{-1} and 0.89cm^{-1} , respectively. The image in B was judged to be the "best".

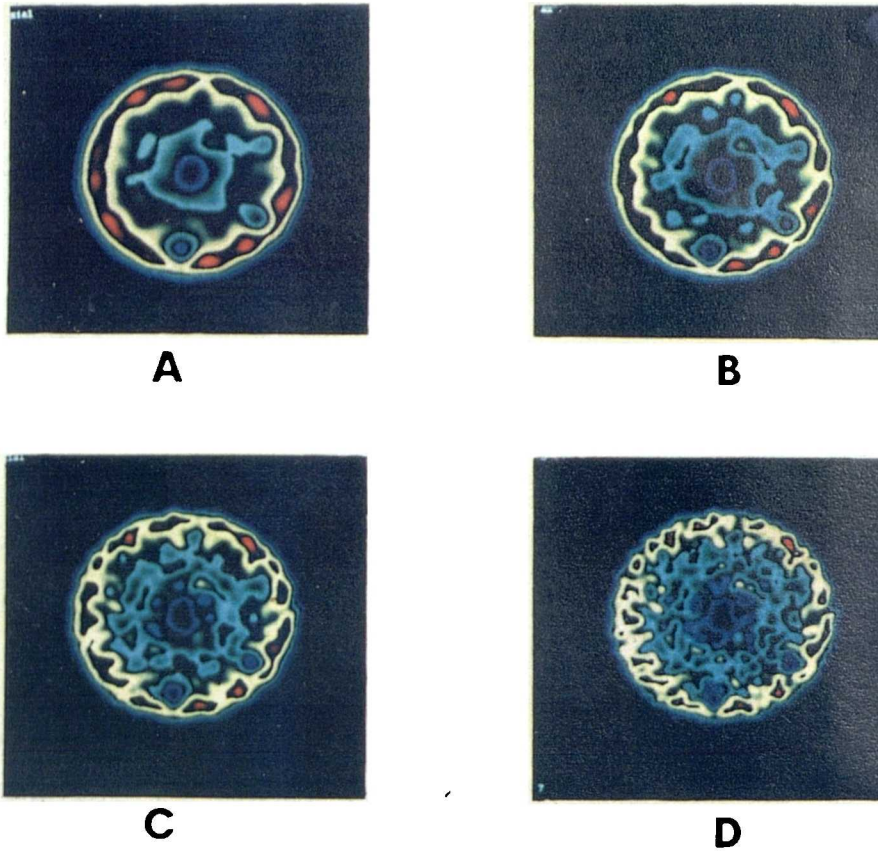


Figure 9.13 Section through the CL insert of thickness 1.1cm. The HR collimator, a ROR of 25cm and an acquisition time of 30 seconds per projection angle were used. The images in A, B, C and D were obtained from Butterworth filters with cut off values of 0.29cm^{-1} , 0.36cm^{-1} , 0.43cm^{-1} and 0.54cm^{-1} , respectively. The image in B was judged to be the "best".

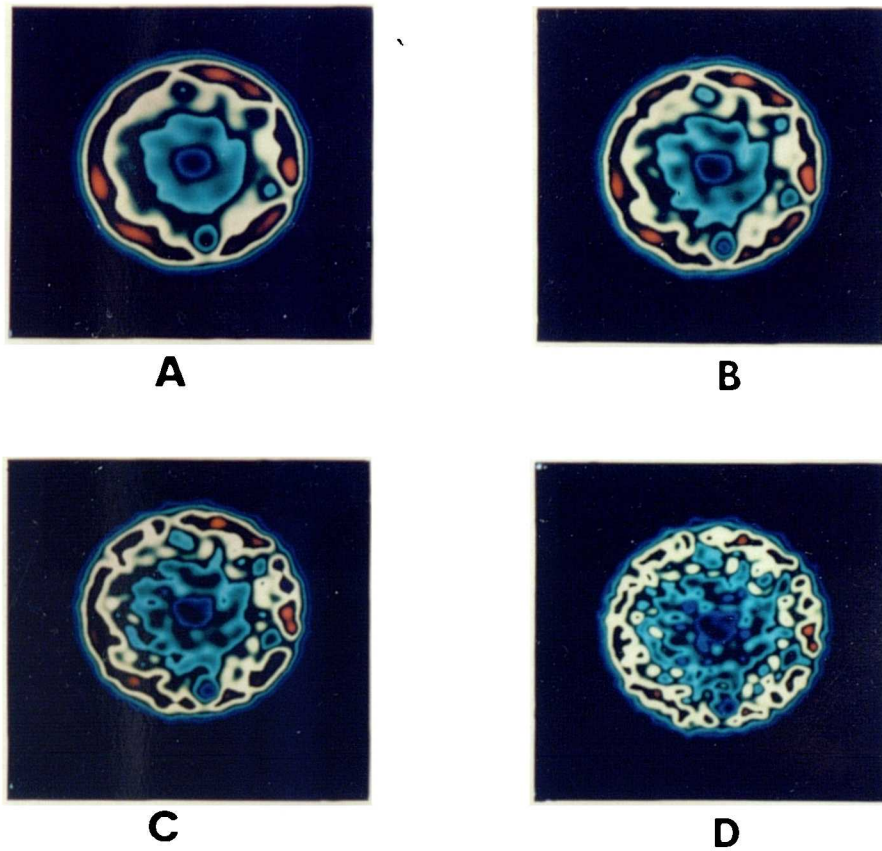


Figure 9.14 Section through the CL insert of thickness 1.1cm. The LEAP collimator, a ROR of 25cm and an acquisition time of 30 seconds per projection angle were used. The images in A, B, C and D were obtained from Butterworth filters with cut off values of 0.29cm^{-1} , 0.36cm^{-1} , 0.43cm^{-1} and 0.54cm^{-1} , respectively. The image in B was judged to be the "best".

Figures 9.15 and 9.16 show the images obtained from the pie insert when the ROR was 25cm. The HR collimator produces higher quality images than the LEAP. The 9mm and 12mm rods are more clearly defined on the HR collimator images.

9.2.6 Conclusions

At small ROR the extra sensitivity of the LEAP collimator more than compensated for its poorer resolution for the detection of the cold rods at clinical count densities.

For the pie insert, however, at small ROR there was little difference in the quality of the images obtained from both collimators.

These results suggest that, at clinical count densities and small ROR, for the detection cold lesions the reduction in the noise level of the surrounding activity distribution, obtained through the use of the LEAP collimator, was more important than the increased resolution obtained with the HR collimator.

As the ROR was increased to 25cm the difference in sensitivity between the two collimators remained unchanged whereas the differences in their resolution characteristics became greater. This meant that for the CL insert there was little to choose from between the collimators. For the pie insert, however, the HR collimator produced images of higher quality allowing smaller hot rods to be identified.

This suggests that, for the detection of hot lesions at clinical count densities and large ROR, the increase in resolution obtained through the use of the HR collimator was more important than the lower noise level obtained with the LEAP collimator.

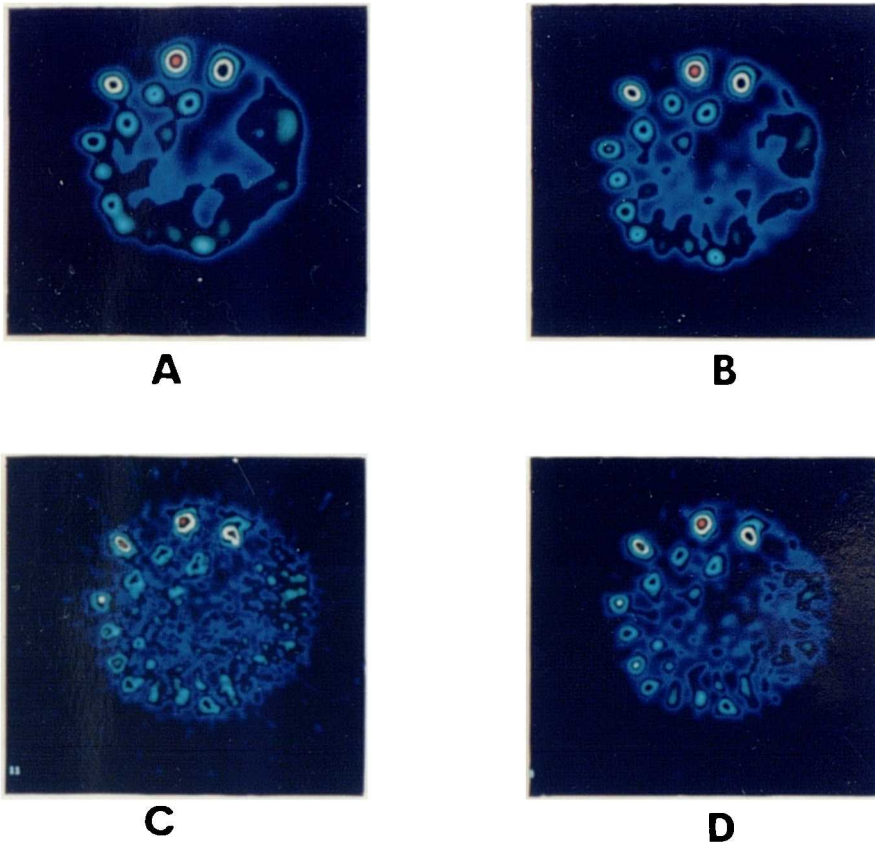


Figure 9.15 Section through the pie insert of thickness 1.1cm. The HR collimator, a ROR of 25cm and an acquisition time of 30 seconds per projection angle were used. The images in A, B, C and D were obtained from Butterworth filters, with cut off values of 0.29cm^{-1} , 0.36cm^{-1} , 0.43cm^{-1} and 0.54cm^{-1} , respectively. The image in C was judged to be the "best".

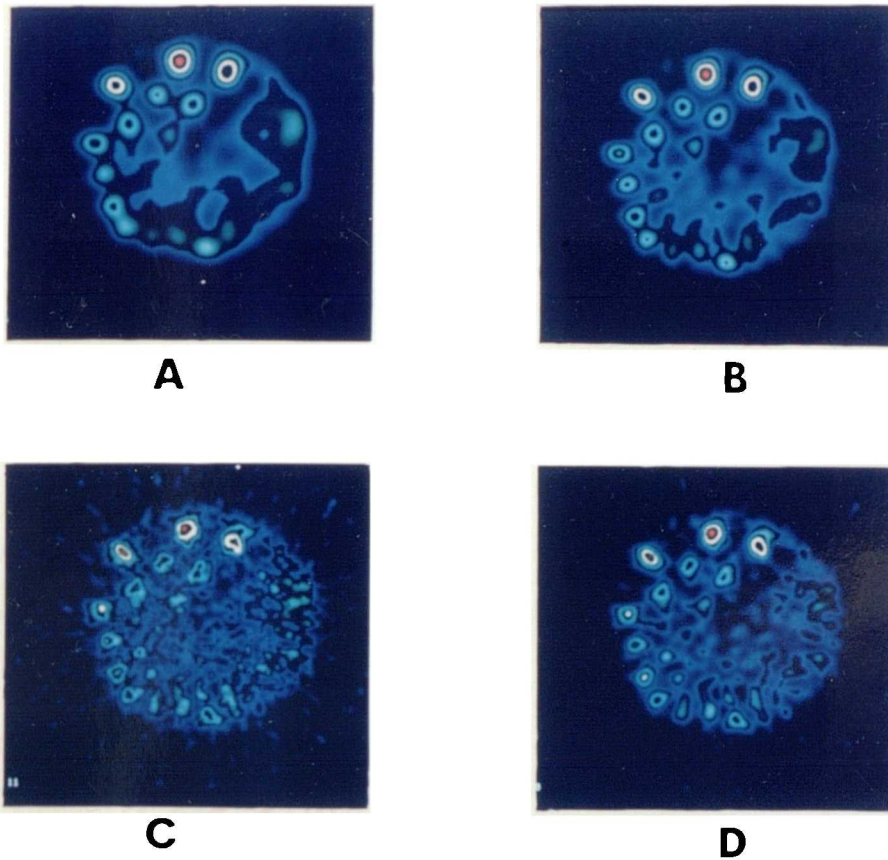


Figure 9.16 Section through the pie insert of thickness 1.1cm. The LEAP collimator, a ROR of 25cm and an acquisition time of 30 seconds per projection angle were used. The images in A, B, C and D were obtained from Butterworth filters with cut off values of 0.29cm^{-1} , 0.36cm^{-1} , 0.43cm^{-1} and 0.54cm^{-1} , respectively. The image in C was judged to be the "best".

Thus, for the collimators studied there are advantages to be gained for the detection of cold lesions at low ROR through the use of the LEAP collimator and for the detection of hot lesions at large ROR through the use of the HR collimator.

A straightforward extension of these results to some practical imaging cases would lead, for example, to the use of the LEAP collimator for HMPAO brain studies where the detection of cold lesions was required. For skeletal studies where a large ROR is required, however, the HR collimator should produce the best results for the detection of hot lesions. For the ^{99m}Tc labelled myocardial imaging agents, where the imaging task is the detection of cold lesions at large ROR, there would appear to be little to choose between the collimators. For Thallium studies, however, the increased sensitivity of the LEAP collimator may be advantageous.

It is recognised that these results have to be applied with care because they are specific to the collimators examined and have been assessed for the simple imaging task of detecting hot and cold rods with contrasts of 100%. For example, it has been suggested by Mueller (1986) that for higher order imaging tasks such as the assessment of the shape, size and uptake of small structures the highest resolution collimator available should be used.

A more general treatment of the problem of optimal collimator selection is extremely complex and to date no general recommendations are available as to which combination of collimator resolution and sensitivity will give the best results for any given imaging situation.

9.3 Attenuation Correction

In Chapter 6 it was demonstrated that the Bellini attenuation correction algorithm produced an accurate quantitative correction for a uniform cylindrical distribution. It was also demonstrated that the correction for the effects of attenuation was intrinsically dependent on a parallel correction for the presence of scattered radiation. However, as no significant improvements in image quality were obtained from the scatter correction methods investigated the application of a quantitatively accurate attenuation correction method is of less importance.

However, a correction for the effects of attenuation can still be useful for the restoration of the contrast in the central structures of an object. Furthermore, by increasing the counts in the centre of a reconstructed section comparisons between central and peripheral structures becomes easier.

Given that no attempt at scatter correction is being made the simplest way to obtain the advantages of attenuation correction alone is to apply the Bellini algorithm with a correction coefficient lower than 0.152cm^{-1} . The actual value of the coefficient which is used will depend on the activity distribution itself, Section 2.6, and so must be determined by trial and error for each separate study.

This procedure was performed for the "best" phantom images obtained from the low noise studies described in Section 9.2. Thus the CL insert image obtained with the HR collimator at a ROR of 16cm after reconstruction with a Butterworth filter with a cut off frequency of 0.71cm^{-1} was used. The Bellini algorithm was applied to these images using a range of

correction coefficients.

Unfortunately, problems with the manufacturer's software meant that the use of 128 projection angle data was not possible. To overcome this every second projection image from the data obtained in Section 9.2 was extracted to form a separate study with 64 projection angles. This results in a slight deterioration in the image quality for high count density studies, Section 7.7.

9.3.1 Results

Figure 9.17 shows the results for the CL insert obtained with the HR collimator at a ROR of 16cm after reconstruction with a Butterworth filter with a cut off frequency of 0.71cm^{-1} . The best value for the attenuation correction coefficient was taken to be that which gave the flattest response over the uniform section of the distribution. For this image this was found to occur at a value of around 0.13cm^{-1} . There was an increase in the noise in the image as a consequence of the attenuation correction procedure, Section 2.6, but despite this there was an increase in the clarity with which the 6mm rod could be seen. This was due to the restoration of counts towards the centre of the distribution which allows the cold areas to be identified against a flat as opposed to a sloping count gradient.

Figure 9.18 shows the results for the pie insert obtained with the HR collimator at ROR of 16cm after reconstruction with a Butterworth filter with a cut off frequency of 0.89cm^{-1} . The application of the attenuation correction algorithm increased the clarity with which the smaller, central rods could be seen. No new detail, however, was observed on the

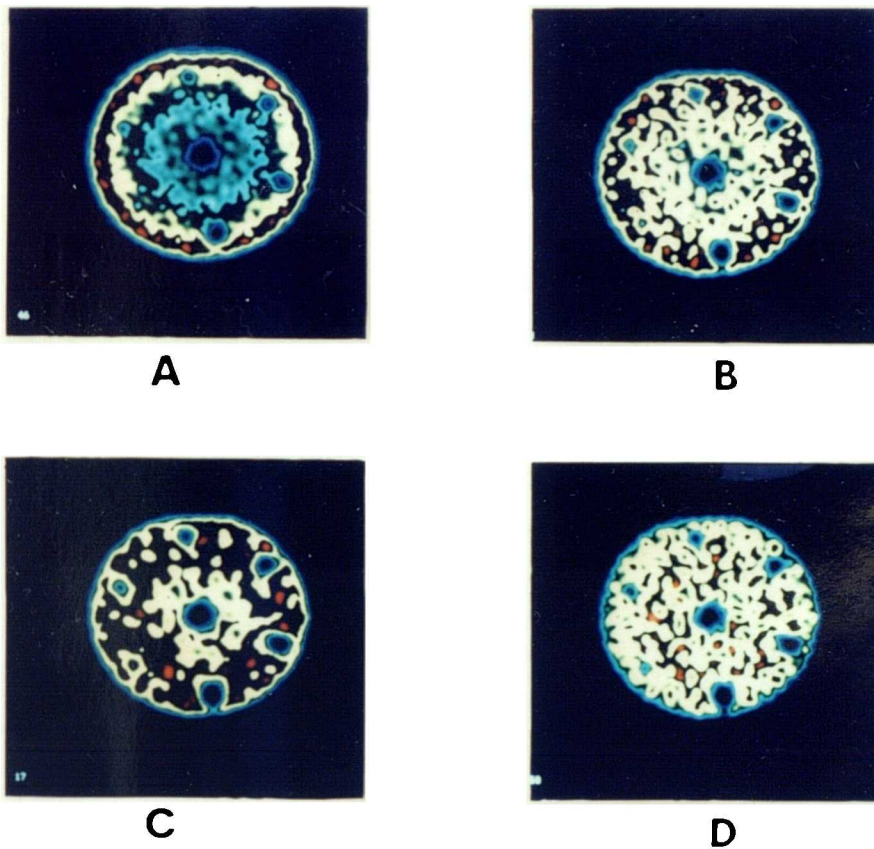


Figure 9.17 Section through the CL insert of thickness 2.8cm. The HR collimator, a ROR of 16cm and an acquisition time of 300 seconds per angle were used. The reconstruction was performed using a Butterworth filter with a cut off frequency of 0.71cm^{-1} . The images in A, B, C and D were obtained after application of the Bellini algorithm with attenuation correction factors of 0cm^{-1} , 0.11cm^{-1} , 0.13cm^{-1} and 0.15cm^{-1} , respectively.

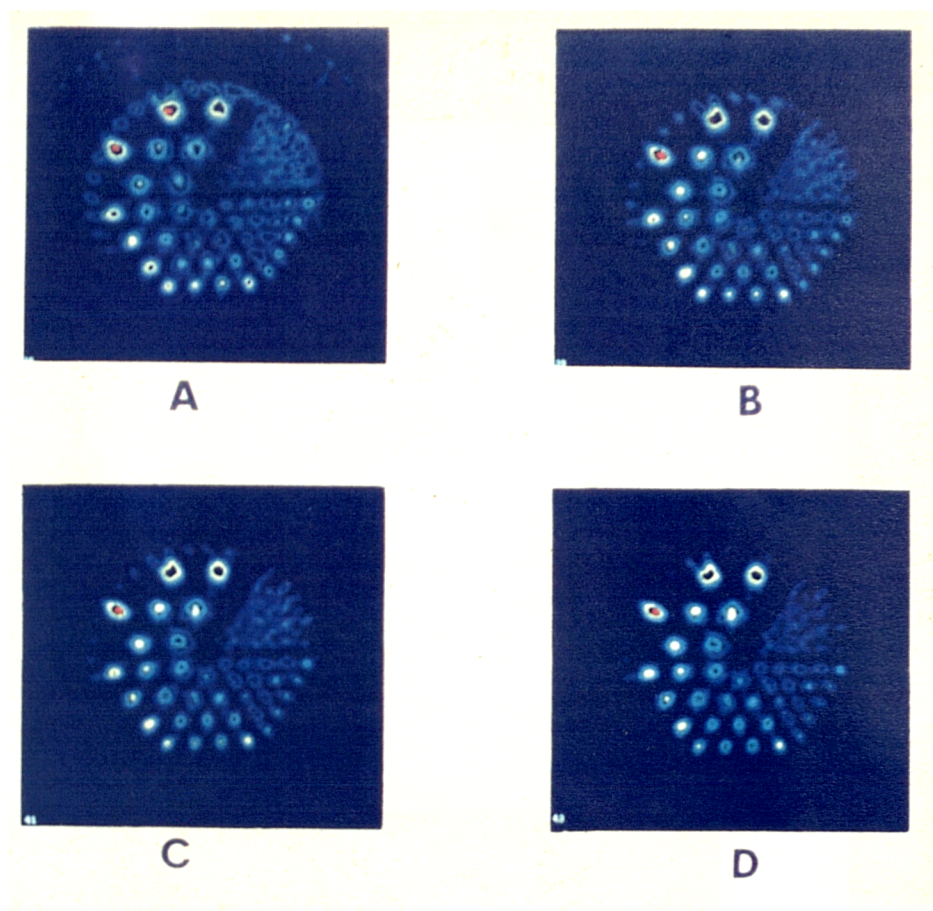


Figure 9.18 Section through the pie insert of thickness 2.8cm. The HR collimator, a ROR of 16cm and an acquisition time of 300 seconds per angle were used. The reconstruction was performed using a Butterworth filter with a cut off frequency of 0.89cm^{-1} . The images in A, B, C and D were obtained after application of the Bellini algorithm with attenuation correction factors of 0cm^{-1} , 0.11cm^{-1} , 0.13cm^{-1} and 0.15cm^{-1} , respectively.

corrected images. Note that even after attenuation correction using a value for the coefficient close to the LAC the count values in the rods closest to the centre of the phantom were not made equal to those at the perimeter. This is because the drop in counts towards the centre of the transaxial section caused by the variation of the amplitude of the planar PSF with distance from the camera is not accounted for. This was discussed in Sections 2.6 and 5.4.

The noise amplification produced by the attenuation correction algorithm did not have as obvious an effect on the pie insert images compared to the CL insert case. This is probably a consequence of the fact that, as described in Section 9.2.6, the influence of noise is less important for the detection of high contrast hot lesions than it is for cold lesions.

9.3.2 Attenuation correction of noisy data

These results were extended to the case of clinical count densities by using the short acquisition time phantom measurements described in Section 9.2.

For the CL insert the best image was obtained using the LEAP collimator with a ROR of 16cm after reconstruction with a Butterworth filter with a cut off frequency of 0.36cm^{-1} , Section 9.2.5. This image was used to assess the effect of attenuation correction. Figure 9.19 shows the effect of attenuation correction on this image with the use of correction coefficient values of 0, 0.11, 0.13 and 0.15cm^{-1} . Again a restoration of the count values in the centre of the distribution has been achieved but the increased noise has led to a deterioration in overall image quality. This conclusion

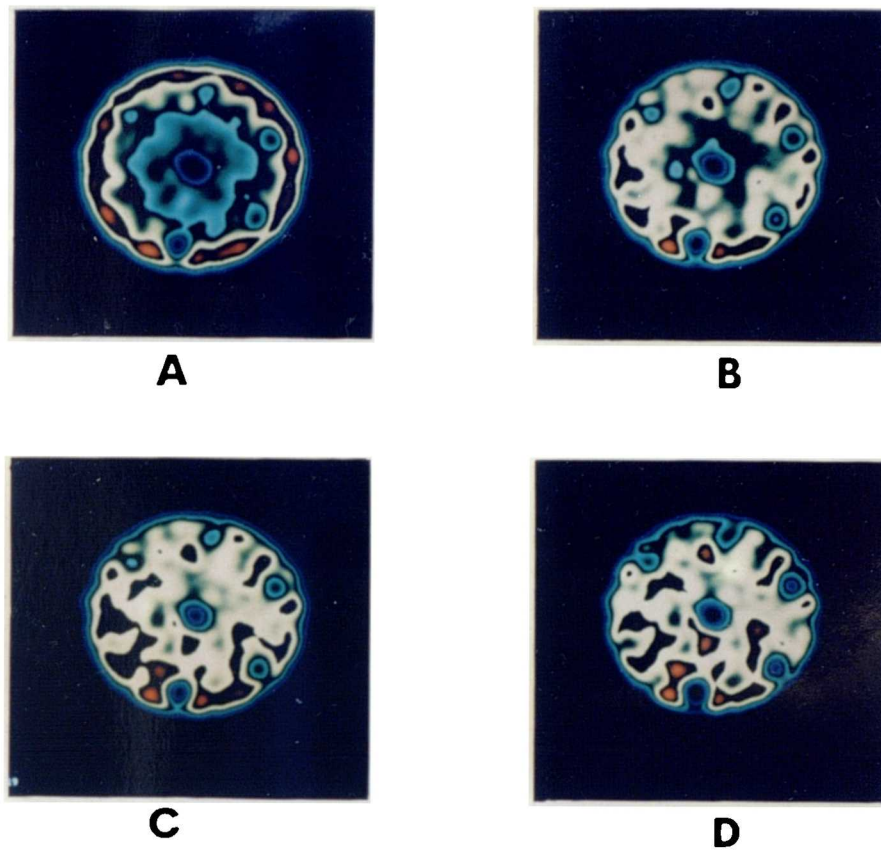


Figure 9.19 Section through the CL insert of thickness 1.1cm. The LEAP collimator, a ROR of 16cm and an acquisition time of 30 seconds per angle were used. The reconstruction was performed using a Butterworth filter with a cut off frequency of 0.32cm^{-1} . The images in A, B, C and D were obtained after application of the Bellini algorithm with attenuation correction factors of 0cm^{-1} , 0.11cm^{-1} , 0.13cm^{-1} and 0.15cm^{-1} , respectively.

has been reached on the basis that the cold areas on the image which correspond to the rods are not demonstrated with greater clarity while the noise mottle has increased the possibility of false positive observations.

For the pie insert, figure 9.20, the image used to assess the effects of attenuation correction was obtained from the LEAP collimator at a ROR of 16cm after reconstruction with a cut off value of 0.54cm^{-1} . Again, there was some restoration of counts in the central structures but, like the high count data, there was no overall improvement in image quality.

9.3.3 Conclusions

For clinical count density data there would appear to be little to be gained from a straightforward application of the attenuation correction algorithm. Although a restoration of counts towards the centre of the distribution is obtained this does not increase the clarity with which any of the structures within the inserts could be identified.

The effects of attenuation can, in practice, be judged reasonably accurately by an experienced observer because the changes which occur are in the form of a smooth function of distance from the centre of the object.

9.4 Uniformity Correction

An initial assessment of the use of a simple multiplicative flood field correction method was made for a low noise, uniform, cylindrical distribution of activity in Chapter 7. It was found that a reduction in the level of circular artefacts in the reconstructed data could be

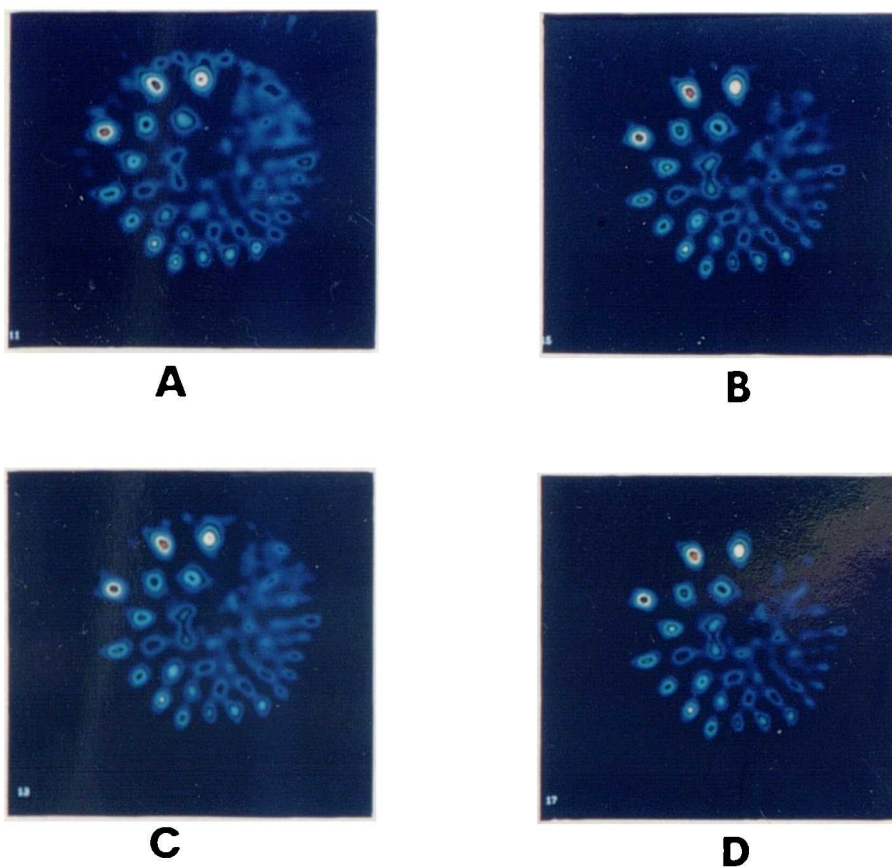


Figure 9.20 Section through the pie insert of thickness 1.1cm. The LEAP collimator, a ROR of 16cm and an acquisition time of 30 seconds per angle were used. The reconstruction was performed using a Butterworth filter with a cut off frequency of 0.32cm^{-1} . The images in A, B, C and D were obtained after application of the Bellini algorithm with attenuation correction factors of 0cm^{-1} , 0.11cm^{-1} , 0.13cm^{-1} and 0.15cm^{-1} , respectively.

obtained.

The extension of these results to the more directly relevant case of the reconstruction of a structured source distribution at count levels similar to those encountered clinically will be made in this section. This can be achieved by analysing the results of the low count phantom studies the acquisitions of which were described in Section 9.2.

9.4.1 Results

From the images shown in figures 9.1 to 9.20 there were no obvious circular artefacts which would be attributable to a non-uniform camera response. This could be a consequence of the smoothing effect of the filter functions which were applied before reconstruction. In Section 7.8 the high count nature of the data meant that the ramp filter could be used in the reconstruction so that no smoothing of non-uniformities occurred.

A further factor could be that, for the images of the CL and pie inserts there was no activity in the centre of the FOV which is the most likely position for artefacts to be observed. To overcome this the images from the linearity insert were investigated. Figure 9.21 shows the reconstruction of 1.1cm thick sections obtained using the LEAP collimator at a ROR of 16cm with sixty four, thirty second projection images. The sections have been reconstructed with Butterworth filters with cut off frequencies of 0.43cm^{-1} and 0.54cm^{-1} . A multiplicative uniformity correction was applied to the projection data using a 120 million count flood field image. The section was then reconstructed using the same filters as previously. The flood field image was also smoothed with the

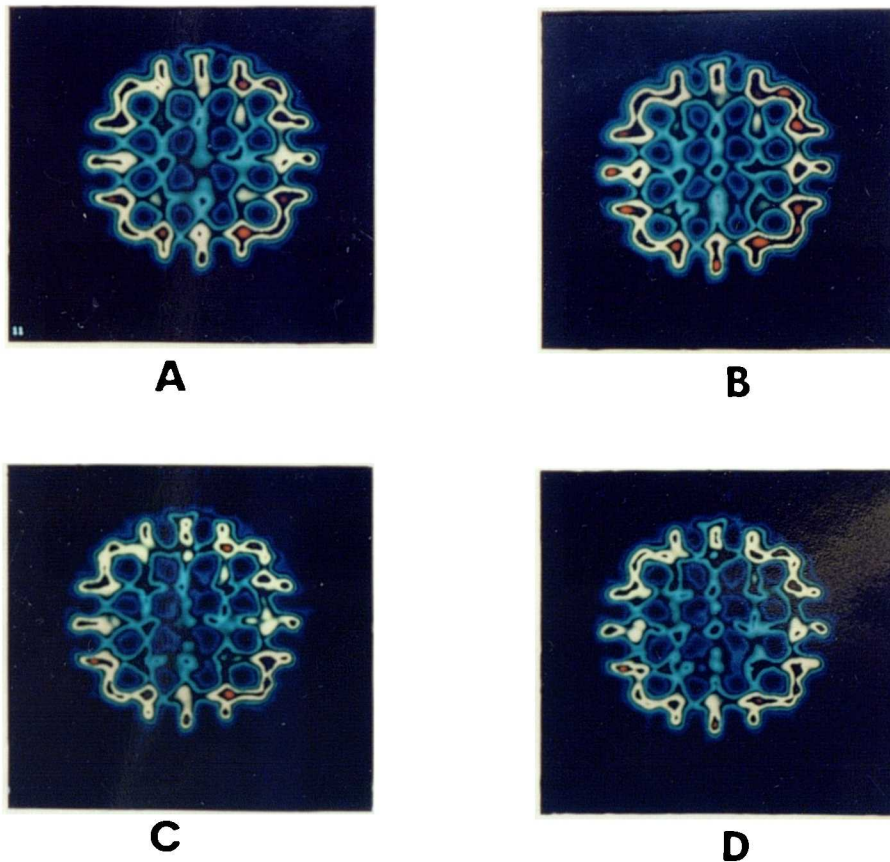


Figure 9.21 Section through the linearity insert of thickness 1.1cm. The LEAP collimator, a ROR of 16cm and an acquisition time of 30 seconds per angle were used. The reconstruction was performed using a Butterworth filter with a cut off frequency of 0.43cm^{-1} for the images in A and B and a frequency of 0.54cm^{-1} for the images in C and D. The images in A and C are before uniformity correction and those in B and D after.

appropriate filter function before the correction was performed.

There would appear to be a small cold area in the centre of the reconstructed sections which is corrected for by the application of the uniformity correction.

9.4.2 Discussion

In practice it would appear that for clinical count densities non-uniformity artefacts do not introduce major artefacts into the data. For the vast majority of phantom studies there was no evidence of the occurrence of circular artefacts.

There may, however, be some count losses over a small area at the centre of the FOV. These losses can be simply corrected for by the application of a multiplicative flood field correction. This suggests that the best strategy for routine clinical imaging would be to acquire high count flood field images on a regular basis, e.g. weekly, but to apply the uniformity correction procedure only to those studies in which there is some doubt about the counts in the image centre.

9.5 General conclusions for Chapter 9

1. When the count density was high and the ROR was small the images from the HR collimator were slightly superior to those obtained from the LEAP. However, at clinical count densities and small ROR the extra sensitivity of the LEAP more than compensated for its poorer resolution for the detection of the cold rods. For the pie insert at clinical count densities and small ROR the difference in quality between the images produced by the LEAP and HR collimators was not significant.
2. At large ROR and high count densities the HR collimator produced superior images of both the CL and the pie inserts. At clinical count densities, however, there was little difference in the quality of the images of the CL insert which were obtained from the LEAP and HR collimators. The superiority of the HR collimator for imaging the hot rods in the pie insert was maintained.
3. Regarding the choice of collimator for routine clinical imaging there are advantages to be gained for the detection of cold lesions at low ROR values through the use of the LEAP collimator and for the detection of hot lesions at large ROR values through the use of the HR collimator.
4. Although there was some increase in the clarity with which cold lesions could be observed after attenuation correction in the high count density studies this effect was not apparent on the clinical count density data. This was due to the increase in the amplitude of the noise in the image.

For the detection of the hot lesions in the pie insert no significant improvement was observed with the correction for attenuation in either the high or the clinical count density studies.

5. The application of a correction for camera non-uniformity removed a small artefact from the centre of the linearity image which was observable even at clinical count density studies.

For routine imaging a correction for camera non-uniformity may be of value if structures located at the centre of the FOV are of clinical importance.

10.1 Introduction

The previous Chapters of this thesis have been concerned with the examination of the physical and technical aspects of a rotating gamma camera SPECT system. Advances in the performance of the constituent parts of the system have been partially responsible for the current extensive increase in interest in SPECT. The other major factor however has been the development of new radiopharmaceutical compounds which has taken place in parallel with the technical improvements.

One of the most important examples of this has been the introduction of a whole new series of lipid soluble compounds which can be used to assess regional cerebral blood flow (RCBF). Of these, the compound at the most advanced stage of development is ^{99m}Tc -HMPAO (hexamethylpropyleneamineoxine). This compound behaves in a similar manner to a chemical microsphere with little redistribution or washout from the brain with time. Its uptake has been shown to be proportional to resting cerebral blood flow in dogs, Costa (1986), although it appears that this correlation breaks down for flow values above 200ml/min.

Clinically, this tracer can demonstrate areas of increased flow (such as in active focal epilepsy) and areas of decreased flow (such as in stroke, dementia, metastases etc.), Ell (1987).

Because of the relatively uniform distribution of ^{99m}Tc -HMPAO within the brain the sensitivity of planar imaging is poor. No serious attempts have been made to assess RCBF using HMPAO without the use of SPECT. The increased contrast

obtained by the tomographic process due to the removal of underlying and overlying structures, Section 1.3, allows the technique to be implemented with clinically useful levels of accuracy, Podreka (1987).

10.2 Methodology

There are a number of practical considerations which have to be addressed which are specific to SPECT imaging of the head. These include the basic positioning of the patient and camera prior to imaging, patient safety and comfort during the acquisition process, the optimisation of the reconstruction procedure (which was discussed in Chapter 8) and finally the display, analysis and interpretation of the resultant images.

10.2.1 Patient positioning - limitation of movement

One of the most difficult practical problems associated with the acquisition of SPECT data using a rotating gamma camera system is the tendency of the subject to move during the acquisition period. As discussed in Section 2.5.3 this makes the projection data inconsistent and introduces artefacts into the reconstructed images.

With the acquisition of 64 projection images and an acquisition time of 30 seconds per image the patient has to remain still for around forty minutes. This can be a difficult task particularly for psychologically disturbed subjects.

The use of mechanical devices (i.e. head supports and restraints) to prevent head movement is limited by the requirement that strongly attenuating material cannot be used. Thus the restraint has to be constructed from materials such as thin perspex, carbon fibre or expanded foam or polystyrene.

The structure of the restraint is also limited by patient comfort. For example a shell which completely surrounds the head has been used, Podreka (1987), but this is likely to cause problems with claustrophobia in a significant fraction of patients. The restraint must also be adaptable to cope with the range of head sizes and shapes which are encountered.

Most manufacturers have chosen a system which consists of a support for the back of the head, usually of thin perspex or carbon fibre, supplemented by velcro strips which are strapped over the patient's chin and/or forehead to supply the element of restraint.

For this investigation the standard head support system supplied by the gamma camera manufacturer was not available. Thus a head support system was developed and fabricated locally. This consisted of an expanded polystyrene base which was shaped to support the back of the head and the nape of the neck. The thickness of polystyrene in the region containing the brain was limited to a maximum of 3cm to prevent unnecessary attenuation and the use of a large ROR.

A vital component in the prevention of head movement is the supervision of the patient during the acquisition period. Any small movements made by the patient can be identified and corrected for by moving the head back to its original position before the magnitude of movement becomes significant. Although close and continuous supervision of the patient is time consuming and labour intensive it is the most effective way to prevent significant head movement.

It is also important to obtain the maximum patient cooperation by clearly explaining what is involved in the imaging procedure.

10.2.2 Assessment of patient movement

Despite intensive efforts to limit head movement, it is extremely difficult to eliminate completely, particularly when imaging severely disturbed patients. The artefacts which are produced usually consist of cold areas which are difficult to distinguish from the appearance of real abnormalities. An example of this is shown in figure 10.1.

Thus, some method of assessing the amount of movement which has occurred during the acquisition of the SPECT study is required.

10.2.2.1 Methods

The simplest and most direct way to assess the degree of patient movement is to examine a cine mode display of the projection images. As the 128*128 images generally have a high level of noise it is useful to bin the images to 64*64. The difference between any two consecutive images should be small. Some forms of patient movement can be detected as unusually large changes between consecutive images in which the head appears to jump from one position to another. A gradual movement of the patient can be detected by comparing the first projection image with the last.

The major disadvantage with the visual assessment of the projection images in cine mode is that it is subjective which makes comparisons between studies difficult. It also makes the creation of, for example, a minimum standard of acceptability a problem.

An attempt can be made to overcome these problems by implementing a subjective scoring system which can function as



A

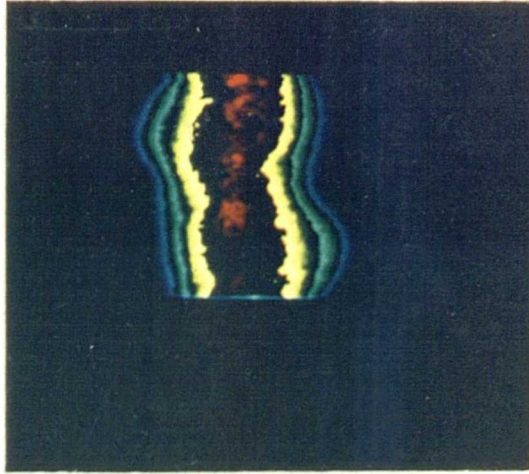
Figure 10.1 An area of apparently decreased uptake is observed in the right temporal lobe. This is an artefact caused by patient movement. It is extremely difficult to distinguish from a real abnormality caused by a reduction in RCBF.

a permanent record of the extent of movement within any particular study. This was performed for the patient group described in Section 10.6. A score of zero to five was assigned to each study with a higher value relating to a greater magnitude of movement.

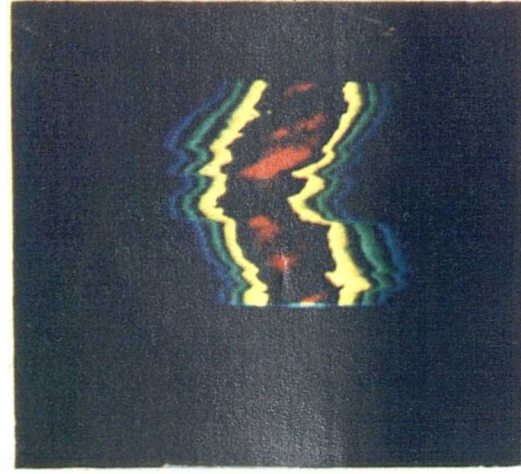
A simple way to produce a summary of the information in the projection data is to display a summed image of all of the sinograms in a study. As described in Section 4.4.3 a point source should appear as a smooth sinusoidal function on the sinogram. For an extended object the sinogram should appear as a superposition of the sinusoidal functions associated with each point in the object. If there is no patient movement the sinogram for the extended object should be a smooth function of projection angle (i.e. the vertical axis on the sinogram). Changes in the position of the patient will appear as discrete changes between adjacent rows of the sinogram. An example of this is given in figure 10.2. The summed sinogram provides a permanent record of the type and magnitude of movement and is useful when comparing different studies.

A further assessment can be made to produce a quantitative description of the magnitude of patient movement. This uses the approximation that the behaviour of the centroid of the projection images is similar to that of a point source of activity. It will be shown that this approximation can be applied, without large errors, to extended objects in which the activity distribution is reasonably uniform and circularly symmetric. $^{99\text{m}}\text{Tc-HMPAO}$ studies of the brain fulfil these criteria.

Using this approximation the methods described in Section 4.4.3 to test the rotational performance of the camera can be



A



B

Figure 10.2 A - Summed sinogram showing good patient cooperation.
B - Summed sinogram from a SPECT study in which patient movement has occurred. This is indicated by the discrete jumps in the sinogram.

applied to quantify the level of patient movement. The x-coordinate of the centroid of the projection images when plotted against the projection angle should be described by a sine function (equation 4.2). An example of this for the study used to produce the image shown in figure 10.4 is shown in figure 10.3. It can be seen that, even as in this case where large defects are present, when there is no patient movement a smooth curve is produced. This can be quantified by assessing the deviation of the mean mean value from opposing images from the centre of the data matrix. It can also be quantified by fitting a sine function to the data, as described in Section 4.4.3, and measuring the deviation of the real data from the ideal function.

Similarly the y coordinates of the centroid should not vary with projection angle. This can be quantified by determining the difference of each point from the mean value.

10.2.2.2 Results

The results of these approaches to the assessment of patient movement are shown in Table 10.1. The values quoted are in terms of pixels which are of size 7mm*7mm. For the x-coordinate values the most useful quantitative parameters, judged from a comparison with the subjective score, were the mean and maximum differences of the centroids from the fitted curves. The fact that most of the studies produced curves in which the differences between the fitted sine functions and the measured data were small justifies the fundamental assumption that the ^{99m}Tc -HMPAO studies can be analysed using the approach designed for point sources.

For the fitted curves using threshold values of 0.3 pixels

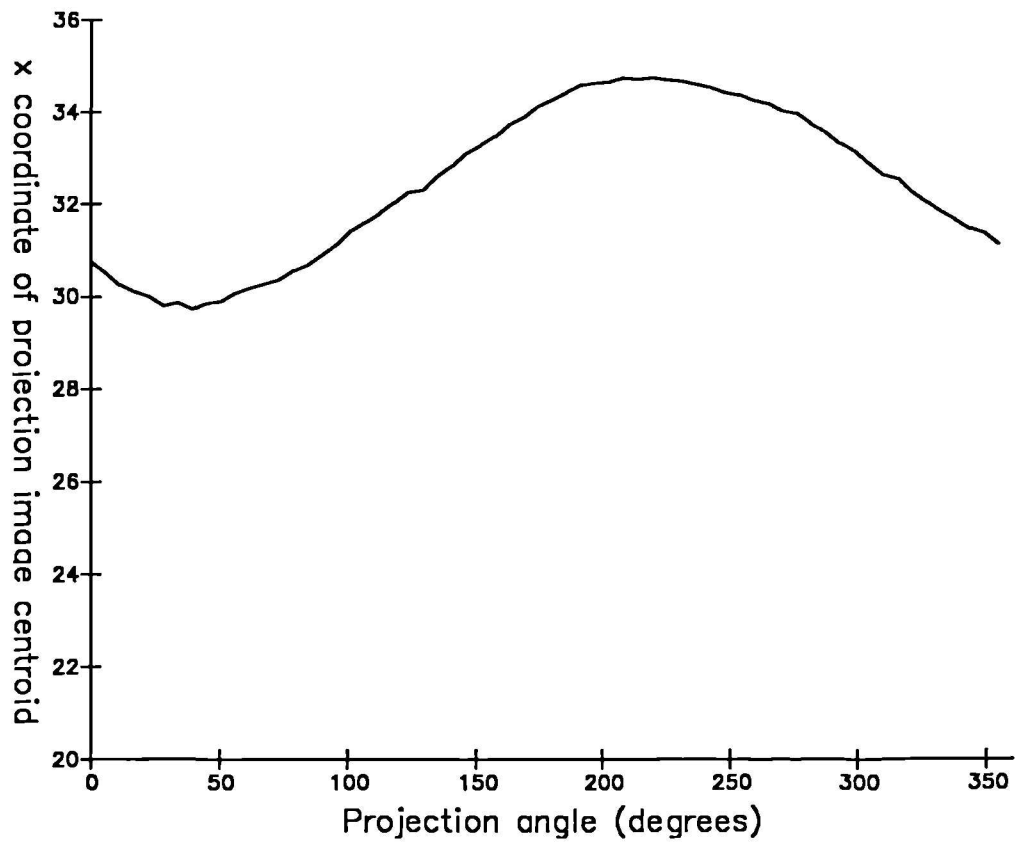


Figure 10.3 The x-coordinate of the centroid of each projection image produces a sinusoidal function when plotted against projection angle.



A

Figure 10.4 Transaxial section reconstructed from the projection data used to produce figure 10.3 ; note the large area of low RCBF in the left occipital lobe.

Patient	DX(max)	DX(mean)	DXF(max)	DXF(mean)	DY(max)	DY(mean)	SC
1	1	.01	1.5	.35	1.2	.32	2.5
2	.65	.11	1.1	.23	.66	.17	1.5
3	1.8	.75	1.3	.63	.63	.26	3
4	.52	.2	.61	.2	.54	.22	0
5	.35	.11	.48	.11	.2	.06	0
6	.27	.05	.34	.11	.47	.13	0
7	.22	.04	.37	.13	.5	.22	0
8	.75	.17	1.1	.29	.42	.15	0
9	.75	.22	.72	.27	.43	.22	1
10	.6	.11	.96	.23	.42	.2	0
11	.31	.06	.57	.2	.56	.2	0
12	.38	.15	.44	.11	.38	.15	0
13	.5	.27	.44	.16	.81	.28	2
14	.35	.01	.61	.18	.84	.11	1
15	.34	.04	.55	.15	.44	.15	1
16	.43	.05	.71	.2	.54	.26	0
17	.25	.08	.33	.1	.54	.26	0
18	.57	.09	.78	.26	.6	.2	0
19	.76	.08	1.1	.32	.3	.09	3
20	.38	.09	.3	.08	.39	.14	0

Table 10.1 Assessment of patient movement

DX(max) is obtained by calculating the difference of the mean value of the x coordinate of the centroids of opposing images from the centre of the data matrix. The maximum difference gives DX(max).

DX(mean) is obtained using the same calculations as DX(max), however, the mean value of the differences is taken.

DXF(max) is obtained by calculating the difference of each x centroid value from the fitted sine curve. The maximum difference gives DXF(max).

DXF(mean) is obtained using the same calculations as DXF(max), however, the mean value of the differences is taken.

DY(max) is obtained by calculating the difference between each individual y coordinate of the centroid and the mean value. The maximum difference gives DY(max).

DY(mean) is obtained using the same calculations as DY(max), however, the mean value of the differences is taken.

Note the values for the above parameters are given in terms of pixels of size 7mm*7mm. SC is the subjective score (from 0 to 5) for patient movement obtained from a visual assessment of the cine display of the projection images.

the possibility that the observed defects are artefacts caused by patient movement.

10.2.3 Correction of patient movement

Having identified the existence and quantified the magnitude of patient movement it would be useful if some attempt could be made to correct for it. This would be a straightforward procedure if the movements involved consisted of translations in the plane parallel to the camera face. However, the most common form of movement, as noted previously, is a rotation of the head. As there is not enough information to correct for this type of movement it was decided not to attempt to apply any kind of correction scheme.

10.3 Choice of acquisition parameters

The selection of the parameters used in the acquisition of the SPECT data such as pixel size, collimator, imaging time and patient set up were made for the particular case of ^{99m}Tc -HMPAO imaging of the brain by utilising the results of the previous Chapters.

10.3.1 Choice of pixel size

An examination of figure 8.11 would suggest that pixels of size 7mm*7mm as opposed to 3.5mm*3.5mm could be used for ^{99m}Tc -HMPAO brain studies without the production of aliasing. The use matrices of dimension 64*64 as opposed to 128*128 which this would permit would have practical advantages in terms of speed of reconstruction and the size of data store required. However, it was decided to use the 128*128 data with pixels of size 3.5mm*3.5mm for the following reasons :

a) The interpolation procedure required prior to back projection is more accurate.

b) The 128*128 data allows a more accurate assessment of the noise level from the power spectrum curves to be made. This is because there are more points at the higher spatial frequencies which are dominated by noise.

c) When the reconstruction is performed, only one quarter of the FOV is required to include the whole of the brain. Thus when the software zoom mode is used only a 64*64 matrix needs to be reconstructed. This takes only 10% longer than the reconstruction of a 64*64 pixel image from 64*64 pixel data.

d) Pixels of edge length 0.35cm were chosen because this is the smallest size which included the brains of all subjects imaged within one quarter of the 128*128 matrix.

10.3.2 Choice of acquisition time

The selection of an appropriate acquisition time is essentially a trade off between patient comfort (and the danger of patient movement) and the statistical noise levels in the reconstructed images. The best compromise was judged to be obtained when an acquisition time of thirty seconds per projection image was used. For a sixty four angle acquisition this gives a total imaging time (including the time between acquisitions, disc writes etc.) of around 40 minutes. For most of the patients encountered this was close to the maximum period of time for which they were able to lie still without distress.

10.3.3 Collimator choice

It was concluded from the work of Chapter 9 that for the detection of cold lesions at clinical count densities when the ROR was small there were advantages to be gained from the use of the LEAP collimator. This was used to perform the acquisitions of the data reported in this section.

10.3.4 ROR

The patient was positioned on the head rest as comfortably as possible. The camera was then positioned to give as small a ROR as achievable. For the twenty patients described in Section 10.6.1 the mean ROR was 14.1cm (range 12.3 to 15.5cm).

10.4 Choice of reconstruction parameters

The selection of the parameters used in the reconstruction of the SPECT data such as reconstruction filter, attenuation correction, uniformity correction and image display were made for the particular case of ^{99m}Tc -HMPAO imaging of the brain by utilising the results of the previous Chapters.

10.4.1 Reconstruction filter

The form of the filter used to reconstruct the data followed the method described in Chapter 8. A two dimensional Butterworth filter was used the cut off value of which was determined for each section from the relationship between the signal and noise in the sinogram.

10.4.2 Attenuation correction

From Chapter 9 it was concluded that for clinical count density data there was little to be gained from a

straightforward application of the attenuation correction algorithm. This was confirmed for the RCBF images used in this Chapter to identify areas of epileptic foci. Figure 10.5 shows the images from a section through a ^{99m}Tc -HMPAO study before and after attenuation correction. There has been an increase in the count levels in the central brain structures relative to the periphery but no obvious increase in image quality. For the particular clinical problem addressed in this Chapter it is uncommon for areas of decreased RCBF to be located in the central brain structures. Thus most attention is given to the consideration of the count levels in the peripheral structures. For this reason the images were not routinely corrected for the effects of attenuation. It was only in special circumstances, where the central brain structures were to be examined, that the correction procedure was applied.

10.4.3 Uniformity correction

It was concluded in Chapter 9 that for clinical count density studies non-uniformity artefacts were only apparent in small regions at the centre of the FOV. Thus, as in the overwhelming majority of cases the centre of the patient's head was positioned at the centre of the FOV, any non-uniformity artefacts which were present would be most likely to affect the count levels of the central brain structures. Again, as these are not considered to be likely sites for epileptic foci, little attention was given to these areas. For this reason the uniformity correction was only applied in a small number of cases where there was some clinical reason for assessing the central brain structures.

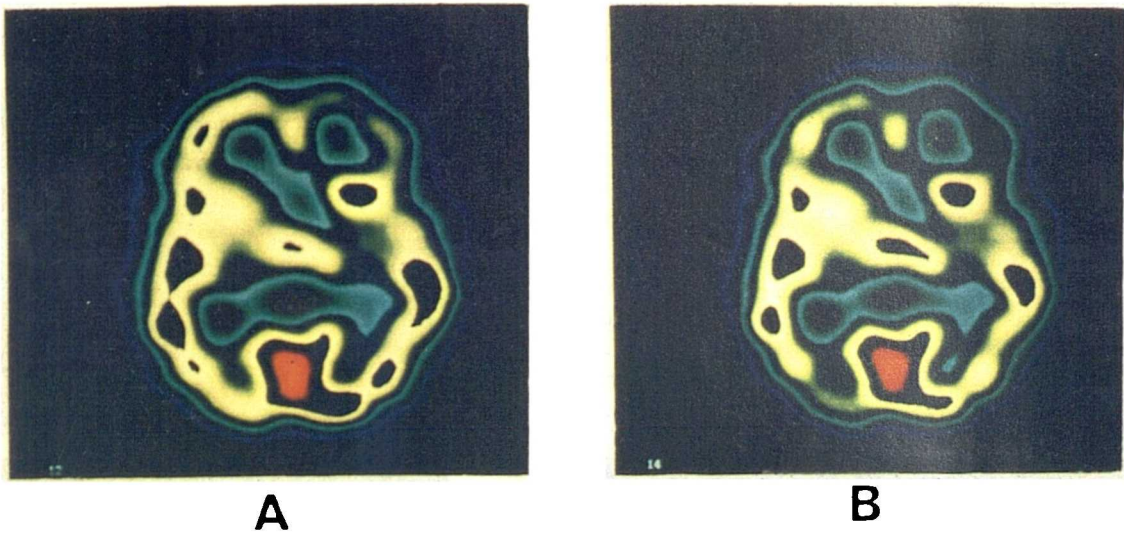


Figure 10.5 Comparison of sections reconstructed before, A, and after, B, attenuation correction. The attenuation correction coefficient used was 0.13cm^{-1} .

An example of the effects of the uniformity correction process on a typical section through a RCBF study is shown in figure 10.6.

10.4.4 Image display

For the clinical group described in Section 10.6.1 the images were assessed in the main by attempting to identify asymmetries in HMPAO uptake between the right and left sides of the brain. For this task it was found that the colour scale described in Section 3.5.1.3 and employed in, for example, figure 10.3 was the most useful.

The main alternatives to the colour mapped type of image use a colour scale in which the pixel values in the image are related to screen brightness (e.g. the "hot metal" scale). It was found to be easier to compare the two sides of the brain when using colour as opposed to brightness.

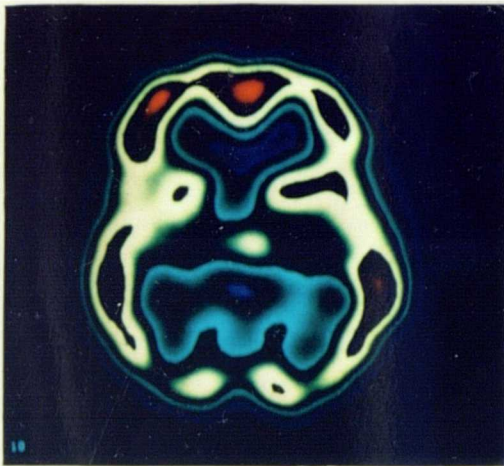
It was also easier to take a hard copy of the colour mapped images using the polaroid camera. The full range of contrast of the screen brightness scales could not be reproduced on the polaroid film.

10.5 Activity administration - Radiation dosimetry

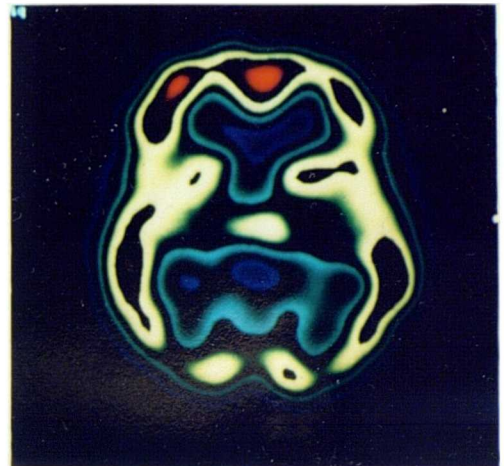
Table 10.2 lists the organ dose estimates for the various body organs of a 70kg adult following i.v. administration of ^{99m}Tc -HMPAO in terms of mGy per 500MBq dose, Soundy (1985).

The human in vivo distribution of HMPAO reflects the findings in rats, Sharp (1986). In man approximately 5% of the injected dose localises in the brain and about 86% of this activity remains 24 hours after injection.

The kidneys excrete 41% of the injected dose over the



A



B

Figure 10.6 Comparison of sections reconstructed without, A, and with, B, uniformity correction of the projection data.

Target organ	Absorbed radiation dose (mGy per 500MBq)
Lachrymal glands	34.7
Gall bladder wall	27.3
Kidney	18.5
Thyroid	15
Liver	8.9
Urinary bladder wall	5.4
Brain	3.8
Ovaries	3.2
Testes	0.6
Whole body	2.1

Table 10.2 Organ dose estimates for a 70kg adult following i.v. administration of ^{99m}Tc -HMPAO.

first 48 hours, and between 8.5% and 13% passes through the liver, enabling the main bile ducts and gall bladder to be visualised.

Lung uptake averages 9% and about 2% was seen in the myocardium of volunteers, Ell (1987).

For this investigation one kit vial of HMPAO was used to study 2 subjects. The HMPAO has to be administered within 30 minutes of reconstitution so both subjects had to be present before activity was added to the vial. The aim was to administer 500MBq to each subject so the kit vial was reconstituted with 1250MBq of ^{99m}Tc in 5ml with 2ml being injected into each subject.

Prior to administration the patient was asked to lie or sit with their eyes closed for five minutes to avoid stimulation of blood flow to the visual cortex.

10.6 Assessment of Intractable Epilepsy

The previously described methodology was used to address a specific clinical question ; the identification of focal abnormalities in the brains of individuals with intractable epilepsy. This has become an important area of investigation because of the recent increase in the use of surgical intervention. Temporal lobectomy can give good results in 70% to 80% of patients with a low morbidity and mortality, Cahán (1986).

Surgical intervention has been restricted by the availability of techniques which can accurately identify lateralising abnormalities. Focal areas of hypometabolism (reduced glucose metabolism) have been identified interictally using PET in patients with partial complex seizures, Engel

(1983). Indeed, greater precision may be obtained if benzodiazapine receptors are used to localise the epileptic foci, Savic (1988). However, the complex and expensive nature of PET imaging means that its use is likely to remain limited to a few major centres.

The main functional diagnostic technique used at present is electrophysiological measurement. Although single surface electroencephalograph (EEG) recordings demonstrate poor localisation sensitivity more involved techniques e.g. depth electrodes can produce reasonable results, Engel (1982). The disadvantages of these methods are that they are complex, time consuming and it is unlikely that, alone, they are sufficiently accurate to be used as an indication for surgery.

The structural imaging modalities, CT and MRI, have also been used to detect lateralising lesions in temporal lobe epilepsy, Theodore (1986). The sensitivity of CT is low with most studies showing that MRI gives an abnormality rate of around 25% in patients with a normal CT, Schorner (1987). However, even MRI is not as sensitive as the RCBF measurements made using PET, Kuhl (1988).

Thus, in conclusion, a readily available technique for the assessment of RCBF, such as SPECT with HMPAO, could play a useful role in the assessment of patients with intractable temporal lobe epilepsy with a view to surgery. The main potential use of SPECT would be as an adjunct to the EEG and either CT or MRI. Concordant results in all tests could be used as a highly specific indication for surgery.

10.6.1 Patient group

The initial patient group consisted of 19 subjects with

intractable epilepsy referred at random from the epilepsy clinic at the Western Infirmary, Glasgow (WIG). A further cohort of 45 patients were studied although the assessment of the results for this group has yet to be completed.

The initial group consisted of 9 males and 10 females, the average age was 31 (range 23 to 47). All subjects were studied interictally. However, there was a wide variation in the time between the SPECT acquisition and the last seizure (2 hours to 6 months).

^{99m}Tc -HMPAO studies were performed on all subjects using the methodology described in Section 10.2 and the reconstruction procedure described in Section 8.7. The data were also reconstructed using the manufacturer's software.

EEG studies were performed on all subjects using surface electrodes.

CT studies were performed on all subjects using a Phillips 350 Tomoscan, producing axial 6mm sections of the whole brain, together with axial 6mm temporal lobe sections angled parallel to the temporal horns, the latter cuts repeated after 50ml (300mg/ml iodine) of intravenous contrast medium.

A subgroup of 8 patients were investigated at the Southern General Hospital, Glasgow where MRI studies were performed. The MRI system was a 0.15 Tesla resistive system manufactured by Picker. Axial 8mm SE 2000/80 T2 weighted images of the whole brain, axial 8mm IR T1 weighted 1660/400/40 images of the temporal lobes, and coronal 5mm balanced SE 700/32 images of the temporal lobes were produced.

SPECT studies were also performed on this group using a Novo 810 dedicated brain SPECT imaging system. Axial sections parallel to the orbito - meatal line 12mm thick were produced.

10.6.2 Assessment of patient studies

The images used to assess the patient studies consisted, in the first instance, of four transaxial sections, 7mm thick, taken parallel to the orbito - meatal line and spaced evenly through the brain. If a suspicious area was identified a coronal section was taken through it for confirmation.

Each transaxial section was analysed quantitatively by comparing the uptake in equivalent regions in the right and left hemispheres using a profile five pixels wide (2.1cm). A side to side difference of 16% or more was taken to be indicative of a significant asymmetry in RCBF. An area of increased RCBF on one side could be differentiated from a decrease on the other by examining the overall pattern of RCBF. Areas of increased RCBF were very uncommon in this study.

10.6.3 Results

The results of these investigations on the group of eight patients (Group A) who were investigated at the SGH and WIG is shown in Table 10.3. A comparison of the results from the SPECT studies performed at the WIG with those of the other imaging modalities is given in Table 10.4. Given that there is no "gold standard" investigation against which the others can be tested, an approximation was made by determining a consensus result from all of the investigations performed on each individual. The results of the WIG and the SGH SPECT studies were then compared against this consensus result.

The best overall agreement was obtained between the "functional" studies i.e. the EEG and the RCBF measurements (as opposed to the "structural" studies of MRI and CT). The

Group A

	MRI	CT	EEG	SGH-SPECT	WIG-SPECT
1	L temporal R temporal	R temporal R 3rd ventricle	Bilateral abnormalities	Reduced perfusion R	L temporal deficit R occipital deficit
2	L temporal	NAD	L focus	Reduced perfusion L	L temporal deficit
3	General atrophy	General atrophy	Bilateral abnormalities	NAD	Patient movement not interpretable
4	NAD	NAD	Bilateral abnormalities	Reduced perfusion L	L frontal deficit
5	R temporal L temporal	NAD	L focus	Reduced perfusion R	NAD
6	L occipital	L occipital	L temporal	Reduced perfusion L	L occipital deficit
7	NAD	NAD	Non-lateralising	NAD	NAD
8	NAD	NAD	L temporal	L temporal	L temporal deficit

Table 10.3 The areas with abnormalities identified by the various investigations performed on the group of subjects studied at the WIG and SGH hospitals.

Group A

	MRI	CT	EEG	SGH	WIG v Consensus	SGH v Consensus
1	A	A	A	A	A	E
2	A	D	A	A	A	A
3	-	-	-	-	-	A
4	D	D	D	A	D	D
5	D	A	D	D	D	E
6	A	A	A	A	A	A
7	A	A	A	A	A	A
8	D	D	A	A	A	A
WIG	4A,3D	4A,3D	5A,2D	6A,1D	5A,2D	-
SGH	4A,2E,2D	4A,1E,3D	6A,1E,1D	-	-	5A,2E,1D

Table 10.4 The elements of the main table show either Agreement, an Equivocal finding or Disagreement between the WIG results and the modality shown at the top of the column. A summary of the results for the WIG and the SGH is given in the bottom two rows.

poorest agreement was between the SPECT studies and the CT which gave normal results with a greater frequency. This is consistent with the low sensitivity previously reported for CT, Schorner (1987). The MRI results gave a slightly better agreement with the SPECT studies although, unlike CT, the differences were evenly divided between positive and negative results.

There was a good agreement between the SGH and WIG SPECT studies. The SGH studies identified more abnormalities and were not affected by patient movement (which invalidated 1/8 studies at the WIG).

Table 10.5 shows the results for the eleven subjects who were investigated only at the WIG (Group B), so no MRI or SPECT results from the SGH are available. A comparison of the results from the SPECT studies performed at the WIG with those from the other modalities is given in Table 10.6. These findings confirm those of Group A. The disagreements between the CT and SPECT studies were all due to negative CT results. There was a reasonable level of agreement between the EEG and the SPECT studies.

10.7 Assessment of the reconstruction method

The method of matching a two dimensional Butterworth filter to the projection data which was used to produce the previous results was compared with the reconstruction method based on a straightforward application of the manufacturer's software.

The best results from the software package were obtained by compressing the projection image data matrix sizes from 128*128 to 64*64. For the 128*128 data the use of the softest

Group B

	CT	EEG	WIG-SPECT
1	R sided contraction	Disorder R hemisphere	Deficit R hemisphere
2	NAD	L temporal	L temporal
3	NAD	Bilateral disturbance more persistent on R	NAD
4	NAD	L temporal	R occipital
5	Mild atrophy L side	L hemisphere	L frontal
6	NAD	R temporal	R temporal L frontal
7	NAD	R temporal	R temporal
8	-	Diffuse disturbance particularly on R	R temporal
9	NAD	L temporal	R temporal
10	R frontal	Bilateral disturbance particularly on R	R occipital deficit L temporal
11	NAD	NAD	Patient movement not interpretable

Table 10.5 The areas with abnormalities identified by the various investigations performed on the group of subjects studied only at the WIG.

Group B

	CT	EEG
1	A	A
2	D	A
3	A	E
4	D	D
5	A	A
6	D	A
7	D	A
8	-	A
9	D	D
10	D	E
11	-	-
Summary	3A,6D	6A,2E,2D

Table 10.6 The elements of the table show either Agreement, an Equivocal finding or Disagreement between the WIG SPECT results and the modality shown at the top of the column.

filter available, the soft Shepp-Logan, still gave images which were dominated by noise (e.g images with noise levels higher than that in figure 10.7A were obtained). The images in figures 10.7A and 10.7B show a typical transaxial section obtained when the Shepp-Logan and the soft Shepp-Logan filters were used to reconstruct the 64*64 projection data. These images can be compared to that of figure 10.6C which was produced using the matched two dimensional Butterworth filter. There is an unequivocal improvement in image quality over that obtained when the "turnkey" approach is used.

The consequences of this improvement in image quality were examined by comparing the results of both methods with the consensus results of Group A and the EEG results of Group B. In Group A there was a better agreement in 3 subjects and a slightly worse agreement in 1. In Group B there was a better agreement in 2, a slightly better agreement in 3, a slightly worse agreement in 1 and a worse agreement in 1. A slightly better agreement was given if the result changed to give an abnormality which was located in the correct hemisphere but the wrong lobe. A slightly worse agreement meant that an abnormality which had previously been located correctly changed to give the same hemisphere but a different lobe.

The total change obtained using the new reconstruction method, as opposed to the "turnkey" approach was that 5 results were better, 3 were slightly better, 1 was slightly worse and one was worse. Thus the improvements in image quality are not simply cosmetic but produce an improvement in the accuracy of the SPECT results as judged from a comparison with other imaging modalities.

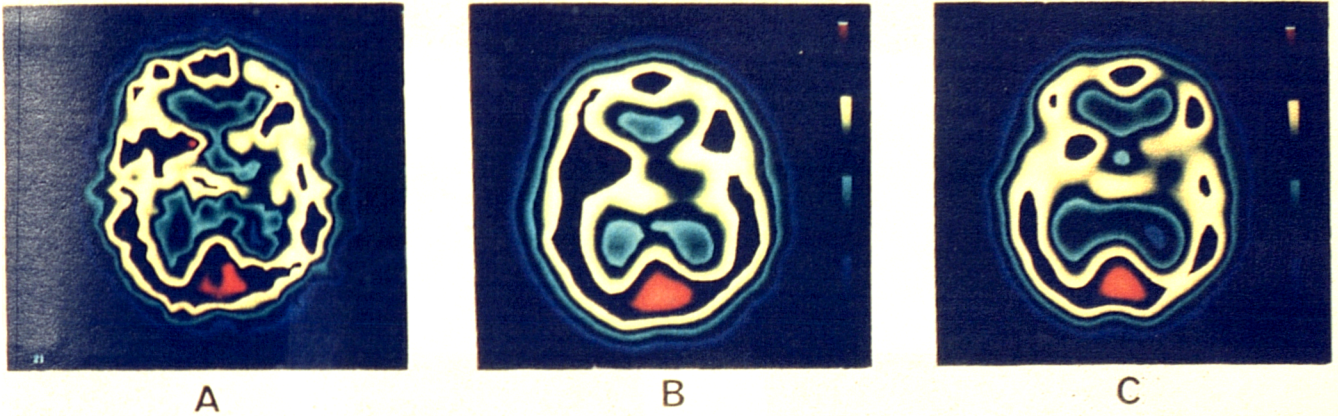


Figure 10.7 Comparison of the "turnkey" approach to reconstruction with that of a matched two-dimensional Butterworth filter. In A and B the projection data have been binned to 64×64 to control the noise. The Shepp-Logan and the soft Shepp-Logan filters have been used to reconstruct the 7mm thick sections shown in A and B. In C a two-dimensional Butterworth filter of power ten and cut off frequency 0.32cm^{-1} has been used.

10.8 General conclusions for Chapter 10

1. A method has been developed for the quantitative assessment of patient movement during the acquisition period of the SPECT study. This allows objective criteria to be set so that unacceptable levels of patient movement can be consistently identified.
2. The parameters used for the acquisition of the ^{99m}Tc -HMPAO data were chosen by utilising the results of the previous Chapters. Thus, the pixel size was $0.35\text{cm} \times 0.35\text{cm}$; the projection matrices were of dimension 128×128 ; 64 projection images were acquired ; the acquisition time per projection image was 30 seconds ; the LEAP collimator was used ; the patient was positioned to minimise the ROR.
3. Similarly the data were reconstructed in a manner which utilised the results of the previous Chapters. A two-dimensional Butterworth filter was used, the cut off value of which was determined for each section from the relationship between the signal and the noise in the sinogram. The attenuation and uniformity correction algorithms were only applied when there was a clinical reason for examining the central brain structures.
4. There was good agreement between the results obtained from the rotating gamma camera at the WIG and the single section SPECT system at the SGH for the detection of sites of reduced RCBF in subjects with intractable epilepsy.

5. There was only moderate agreement between the results of the SPECT studies and those of the structural imaging modalities of CT and MRI, although there was a higher level of concordance with the MRI data.

6. There was a reasonable agreement between the EEG and the SPECT studies. The SPECT studies tended to give a more precisely defined localisation of detected abnormalities.

7. The use of the matched filter approach to the reconstruction of the data, as opposed to a simple application of the manufacturer's software, produced a significant improvement in the SPECT results as judged from a comparison with other imaging modalities.

11.1 Introduction

In a manner analogous to the development of radiopharmaceuticals for the assessment of blood flow to the brain a considerable amount of effort has been expended in the development of a ^{99m}Tc labelled compound for the assessment of myocardial perfusion.

The most commonly used agent to date has been Thallium-201 (^{201}Tl). This is a potassium analogue, acting as a substitute in the sodium-potassium-ATPase system. Areas of ischaemic myocardium appear as areas of reduced uptake on the acquired images. The radiopharmaceutical is injected at maximal exercise, with imaging commencing as soon as possible afterwards. A further set of images is acquired four hours later by which time most ischaemic defects have resolved due to the accumulation into previously underperfused areas ; infarcted areas do not resolve.

There are some significant disadvantages associated with the physical characteristics and physiological behaviour of ^{201}Tl . Compared to ^{99m}Tc the photon yield is reduced because a lower injected dose is determined by the higher absorbed dose to the patient. The energy of the photons principally used to produce the images, 80keV, is lower than the ideal for detection with a NaI crystal which leads to a loss of resolution. They also suffer from higher levels of attenuation and scattering within the body tissue. The reduced signal to noise ratio in the acquired data which is a consequence of these effects is a particular problem for SPECT imaging because of the additional noise amplification which occurs during the reconstruction.

It is assumed when the stress and redistribution images are interpreted that there has been no redistribution into ischaemic areas on the images from the first set of acquisitions and a significant level of redistribution into the second set of images. This makes the timing of the acquisitions important. If there is too long a delay between the completion of the stress test and the start of the image acquisitions then some redistribution may occur. This a particular problem for SPECT imaging where not only is the set up of the patient a more complex and time consuming procedure but the time taken to acquire the SPECT study itself can be significant. Furthermore, a four hour gap may not be sufficient for all ischaemic areas to show a significant level of redistribution.

In response to the disadvantages of ^{201}Tl new families of compounds, labelled with $^{99\text{m}}\text{Tc}$, have been developed which are deposited in the myocardium in relation to blood flow. One of the most promising of these, $^{99\text{m}}\text{Tc}$ -methyl-isobutyl isonitrile (MIBI) will be investigated in this Chapter. The fact that MIBI is labelled with $^{99\text{m}}\text{Tc}$ allows a higher amount of activity to be administered which, in addition to the superior imaging properties of the 141keV photons, should permit the acquisition of images with a higher signal to noise ratio. Furthermore, the redistribution which occurs with MIBI is small, Okada (1988), so that the stress study can take place without stringent time limitations. This does produce a logistical problem, however, because the rest study has, in general, to be performed on a separate day from the stress study. Again, however, this removes the problems with incomplete redistribution encountered with ^{201}Tl .

11.2 Choice of SPECT acquisition parameters

The choice of the parameters used in the acquisition of the SPECT data for the particular case of ^{99m}Tc -MIBI imaging was made by utilising the results from the previous Chapters.

11.2.1 Pixel size

Figure 11.1 shows the LNP(u) curve of the MAPS for a sinogram corresponding to a section through the centre of the left ventricle. The point at which the signal cannot be differentiated from the noise with a confidence level of greater than 90%, i.e. the transition frequency, occurs at 0.31cm^{-1} . As the pixels were of edge length 0.35cm (for $128*128$ data) the Nyquist frequency of 1.43cm^{-1} would appear to be more than sufficient. In fact the use of $64*64$ data with 0.7cm pixels would give a Nyquist frequency of 0.715cm^{-1} which, from figure 11.1, would also appear to be well above the point at which the signal becomes dominated by the noise.

Nevertheless, it was still decided that the $128*128$ data with 0.35cm pixels should be used for reasons very similar to those given for the RCBF imaging in Chapter 10 :

a) The interpolation procedure required prior to back projection is more accurate.

b) The smaller pixel size allows a more accurate assessment of the noise level from the power spectrum curves to be made. This can be seen from figure 11.1 where the data points from 0.715cm^{-1} to 1.43cm^{-1} are available for analysis with the $128*128$ data but not the $64*64$.

c) When the reconstruction is performed, only one quarter of the FOV is required to include the whole of the heart. It was found that a pixel size of 0.35cm was sufficient to

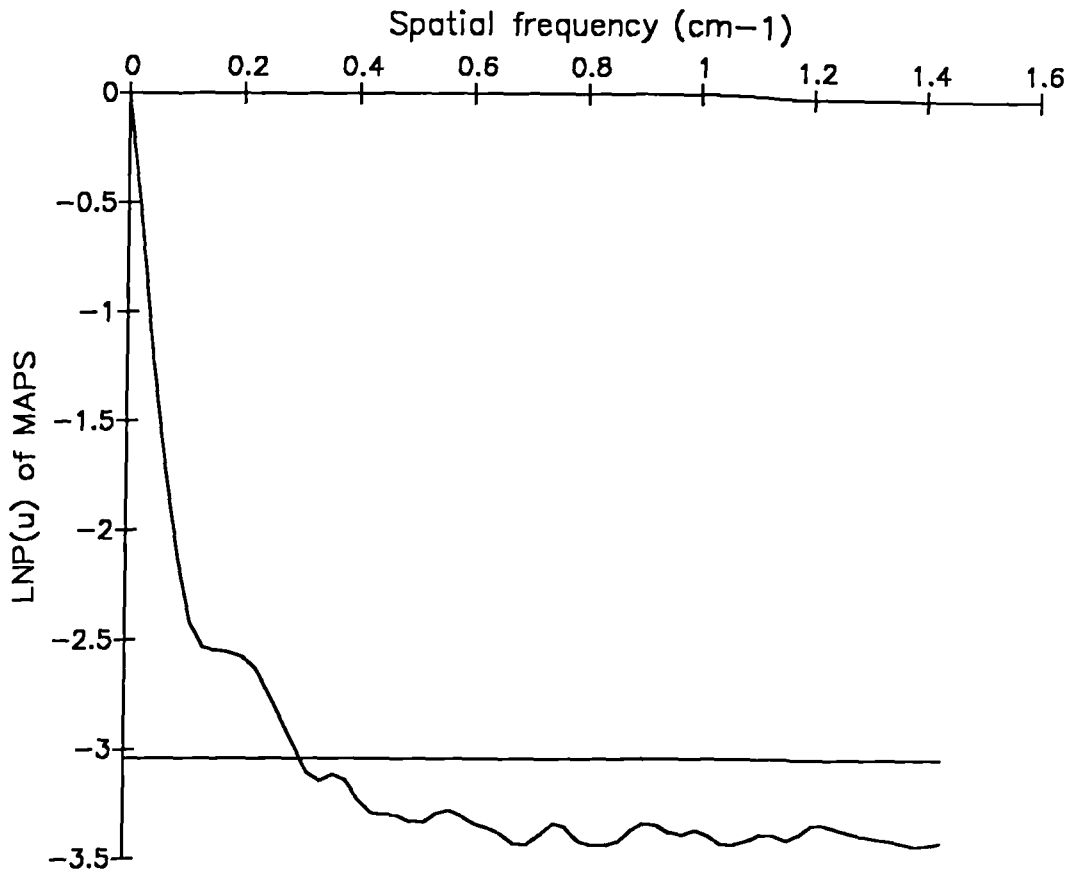


Figure 11.1 LNP(u) curve of the MAPS for a sinogram corresponding to a 7mm thick section through the centre of the left ventricle. Also shown is the 90% confidence limit for the noise. The intersection of the 90% confidence limit with the LNP(u) curve gives the transition frequency.

include all of the hearts imaged within one quarter of the 128*128 matrix. This left the images actually used to interpret the data of a resolution (64*64) which was high enough to avoid the appearance of discrete pixels.

11.2.2 Acquisition Time

The selection of an appropriate acquisition time involves a trade off between patient comfort (and the danger of patient movement) and the statistical noise levels in the reconstructed images. Although patient movement was not found to be as critical a problem for cardiac imaging as for the brains the acquisition time per angle was kept at the same value of 30 seconds. This is because the total acquisition time of 40 minutes which this produces was found to be about the maximum time which most patients were able to lie still, on the SPECT bed, without undue discomfort.

11.2.3 Collimator choice

It was concluded from the work of Chapter 9 that, for the detection of cold lesions at clinical count densities when the ROR was large, there was little difference in the performance of the LEAP and the HR collimators. For continuity it was decided that, as the LEAP collimator was used to perform the majority of investigations, it should also be used to acquire the ^{99m}Tc -MIBI data. This has practical advantages in that extra collimator changes are not required.

11.2.4 ROR selection

The camera was positioned to give as small a ROR as achievable, Chapter 5. The width of the patients thorax was

the factor which limited the minimisation of the ROR. The patients arms were initially placed beneath their heads to remove them from the image volume. However, there was a suspicion that this raised the diaphragm which increased the undesirable attenuation of the inferior wall. Thus, in later studies the patients arms were placed behind their head one at a time as the camera rotated past their right and left sides.

11.2.5 360 degree or 180 degree orbit

It has been suggested by several authors that there are advantages to be gained by acquiring the projection data over 180 as opposed to the conventional 360 degrees, Coleman (1982), Tamaki (1982). This is motivated by the relatively superficial location of the heart within the chest. The projection images acquired at right posterior oblique angles appear to contain little information about the heart because of the large distance between it and the camera. By acquiring projection data over a 180 degree arc, centred on a left anterior oblique angle, more camera time can be spent collecting photons which contain information about the activity in the myocardium. This can produce an increase in the resolution and contrast of the reconstructed images, Tamaki (1982).

The major disadvantage of the 180 degree acquisition is that the variation in the shape of the LSF with source-camera distance can no longer be mediated by the addition of opposing projection images, figure 5.11. This leads to the creation of shape distortions and streak artefacts in the reconstructed images, Knesaurek (1987).

It has been suggested, Eisner (1986), that the advantages

of 180 degree acquisitions outweigh the disadvantages when the imaging agent is ^{201}Tl . However, when $^{99\text{m}}\text{Tc}$ is used the reduction in the level of artefact creation, which results from the 360 degree acquisition, leads to the production of more reliable clinical information, Pettigrew (1983), Eisner (1986), Knesaurek (1987). For this reason, and also because all of the previous work in this thesis is applicable only to 360 degree data, it was decided that the $^{99\text{m}}\text{Tc}$ -MIBI studies should be acquired using 360 degree orbits.

A specific investigation of the advantages and disadvantages of 180 degree image acquisitions for $^{99\text{m}}\text{Tc}$ -MIBI data would be a suitable topic for further investigation.

11.3 Choice of reconstruction parameters

The selection of the parameters used in the reconstruction of the SPECT data such as the filter function, attenuation correction, uniformity correction and image display were made for the particular case of $^{99\text{m}}\text{Tc}$ -MIBI imaging of the myocardium by utilising the results of the previous Chapters.

11.3.1 Filter function

During the course of the analysis of the $^{99\text{m}}\text{Tc}$ -MIBI data it was found that, unlike the RCBF studies, the interpretation of the images was not particularly sensitive to the choice of the Butterworth filter cut off frequency. Values chosen within the range 0.31cm^{-1} to 0.57cm^{-1} produced identical conclusions about the normality or otherwise of the segments of myocardium described in Section 11.4.1. Examples of this are shown in figures 11.2 and 11.3. This is a reflection of the simplicity of the image interpretation task which has to be performed.

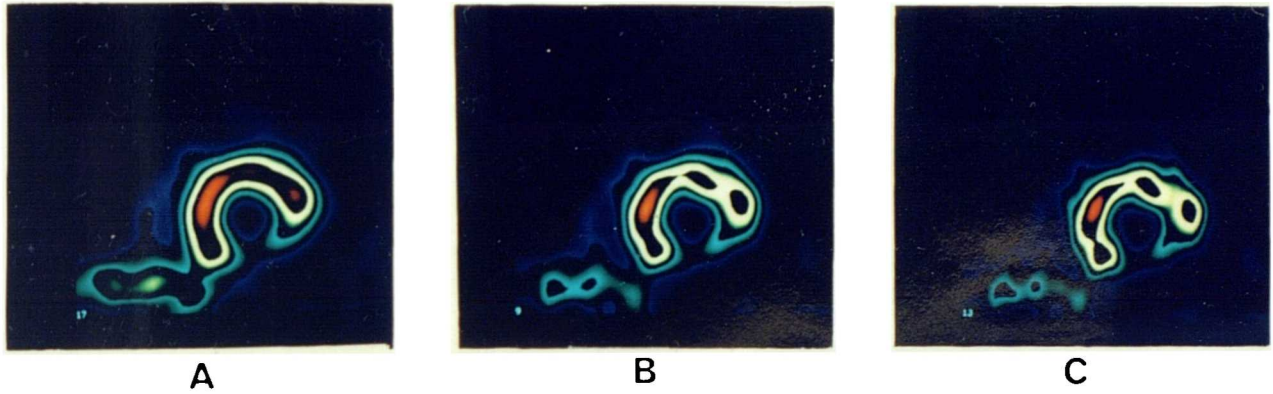


Figure 11.2 Short axis sections through the left ventricle using a two dimensional Butterworth filter with cut off values of 0.31cm^{-1} , 0.43cm^{-1} and 0.57cm^{-1} in A, B and C respectively. The abnormal perfusion of the inferior and infero-lateral walls is evident on all three images.

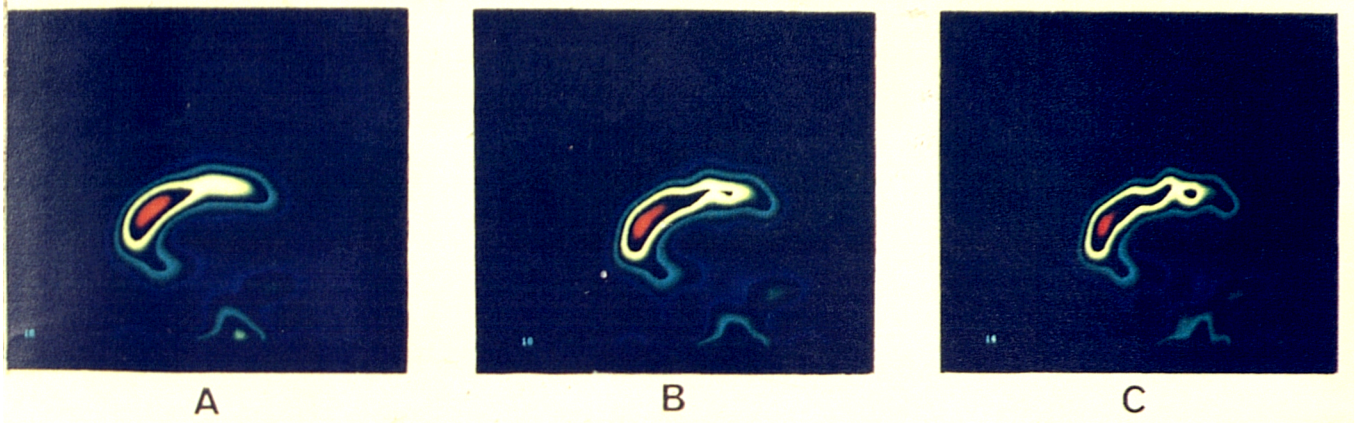


Figure 11.3 Long axis sections through the left ventricle using a two dimensional Butterworth filter with cut off values of 0.31cm^{-1} , 0.43cm^{-1} and 0.57cm^{-1} in A, B and C respectively. The abnormal perfusion of the inferior wall is evident on all three images.

The regions of myocardium defined for analysis are of the order of 3cm-5cm in length by 2cm-3cm wide. The spatial frequencies which these relate to are far lower than the cut-off frequencies of the filters used in the reconstruction. Thus, so long as the cut off frequency of the filter is not high enough to produce images dominated by noise the actual value chosen for use in the reconstruction of the data is not particularly important. This makes the matching procedure described in Section 8.7 unnecessary.

It is conceivable that if the identification of subsegmental abnormalities was found to be clinically relevant then a more precise and controlled optimisation of the filter cut off frequency may be required. However, the experience of this particular investigation was that the level of physiological variability in the territories of myocardium supplied by various coronary arteries and affected by stenoses in those arteries made it difficult to correlate individual lesions with perfusion abnormalities in the large segments chosen for analysis. The association of subsegmental perfusion abnormalities with specific coronary artery stenoses identified by contrast angiography would in the opinion of the author be a task which could not be performed without a high level of error. Possibly the only way in which the territories supplied by individual coronary arteries can be precisely defined is by intracoronary perfusion studies with Xe133 or even Au195m.

11.3.2 Attenuation correction

From Chapter 9 it was concluded that for clinical count density studies there was little to be gained from a

straightforward application of the attenuation correction algorithm. This conclusion was found to be particularly appropriate for the $^{99\text{m}}\text{Tc}$ -MIBI images of the myocardium. As the heart is a relatively small organ which is situated close to the body surface the count gradient across it due to the effects of attenuation was small. Thus a correction for attenuation was found to be unnecessary. An example of the effects of attenuation correction on a section through the left ventricle is shown in figure 11.4.

11.3.3 Uniformity correction

It was concluded in Chapter 9 that for clinical count density studies non-uniformity artefacts were only apparent in small regions at the centre of the FOV. However, as the centre of the patients thorax is generally positioned close to the axis of rotation (so that the ROR can be minimised) the images of the heart are unlikely to be affected by non-uniformity artefacts. For this reason the uniformity correction procedure was not applied to the $^{99\text{m}}\text{Tc}$ -MIBI images.

11.3.4 Image display

It was found that the assessment of the relative levels of uptake in the different walls of the myocardium could be most accurately judged using the colour scale described in Section 3.5.1.3.

The images were always scaled so that the maximum point in the colour scale was associated with a region in the myocardium. There were occasions when activity in the gut was more intense than that of the heart ; in these cases the appropriate scaling allowed the relative myocardial uptake in



A



B

Figure 11.4 Sections through the left ventricle before, A, and after, B, attenuation correction. The attenuation correction coefficient was 0.12cm^{-1} .

different sections to be compared.

11.4 Assessment of coronary artery disease (CAD) with ^{99m}Tc -MIBI

The previously described SPECT methodology was used in the assessment of CAD in ten sequential patients referred for coronary angiography.

11.4.1 Methods

Each patient underwent resting and exercise ^{99m}Tc -MIBI studies and coronary arteriography within a 14 day period. Patients were instructed to cease medication for 24 hours prior to each test, with the exception of sublingual GTN if required.

Both planar and SPECT studies were performed on each patient. For the planar studies anterior, 40 degree and 70 degree left anterior oblique views were acquired into a zoomed 128*128 matrix for 600 seconds each. For the purpose of analysis the views were divided into segments as shown in figure 11.5.

Following the planar imaging, SPECT acquisitions were performed. The data were acquired into matrices of dimension 128*128 with pixels of edge length 0.35cm. 64 projection images were acquired over 360 degrees with an acquisition time per angle of 30s. Care was taken to minimise the ROR by asking the patients to place their hands under their heads ; typical values were about 23cm.

The SPECT studies were reconstructed initially by using the manufacturer's software. For the 128*128 data the Shepp-

Anterior

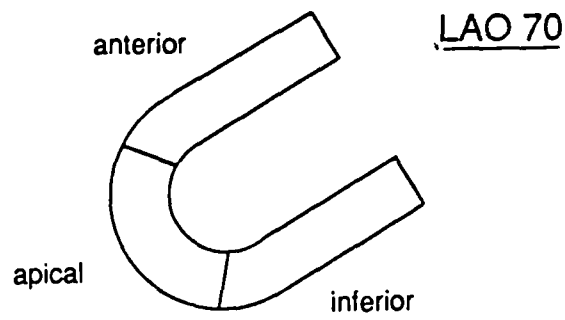
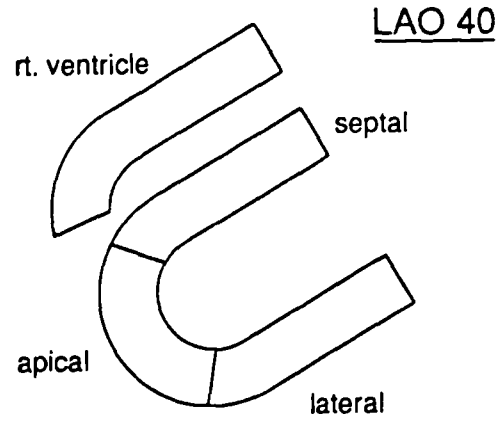
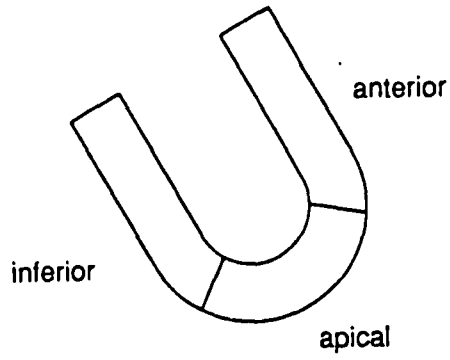


Figure 11.5 The planar studies were divided into the segments shown above for analysis.

Logan filter produced images which were too noisy and the soft Shepp-Logan filter produced images which were too smooth. It was found that the best images were obtained by binning the projection data into 64*64 matrices and applying the Shepp-Logan filter. The reduced Nyquist frequency which resulted from the use of the 7mm pixels gave a cut off frequency for the filter which produced images of reasonable quality.

The SPECT studies were also reconstructed using the method described in detail in Section 11.3.

For purposes of interpretation four sections were used for analysis as shown in figure 11.6. Three short axis sections were selected, one near the apex of the left ventricle, one at the mid point and one near the valve plane. The fourth section was taken vertically through the long axis of the ventricle. The sections were divided into segments as shown for analysis.

Each segment in both the planar and SPECT images was assessed as normal or abnormal. Comparison between rest and exercise studies then permitted each segment to be classified as normal, ischaemic or scarred.

Selective coronary arteriography and left ventriculography were carried out under local anaesthetic and oral sedation using a percutaneous femoral approach. Biplanar images were obtained. For the purposes of analysis, the ventricle was split into five segments, anterior, apical, inferior, lateral and septal. The artery supplying each segment was identified and the appropriate arteriogram was inspected for the presence of lesions, which were judged to be significant if the stenosis was greater than 50% of the luminal diameter. The wall motion of each segment was classified as normal or abnormal from the ventriculogram.

11.4.2 Results

Of the ten patients studied, five had triple vessel disease, two had two vessel disease, one had single vessel disease and two were normal as assessed from the angiography data. The results of the four investigations which were performed is shown in Table 11.1.

11.4.2.1 Simple detection of CAD

For the simple detection of CAD in an individual all subjects were correctly classified by the planar data and also the images from both the SPECT analyses. Thus in this small group of patients the sensitivity and specificity were both 100% for the planar and SPECT data.

11.4.2.2 Identification of abnormal segments

Each of the segments shown in figures 11.5 and 11.6 were classified as normal or abnormal on the basis of the angiography data. The anterior and septal areas were assumed to be supplied by the left anterior descending (LAD) artery, the lateral wall by the circumflex (Cx) and the inferior wall by the right coronary artery (RCA) or the Cx depending on the right or left sided dominance. The inferior wall is supplied by the RCA in 90% of patients, Hurst (1978). The apical segments have a variable vascular supply which is difficult to associate with confidence to any single artery.

The planar scans identified 15/15 normal segments (specificity 100%) and 25/35 abnormal segments (sensitivity 71%).

The SPECT data obtained using the manufacturer's software identified 15/15 normal segments (specificity 100%) and 22/35

patient		segments				
		ant	ap	inf	lat	sep
1	planar	N	N	N	N	N
	SPECT1	N	N	N	N	N
	SPECT2	N	N	N	N	N
	CA	N	N	N	N	N
2	planar	N	N	S	S	N
	SPECT1	N	N	S	S	N
	SPECT2	I	N	S	S	N
	CA	I	I	S	S	I
3	planar	N	S	S	S	N
	SPECT1	N	S	S	S	I
	SPECT2	N	I	S	S	N
	CA	I	I	S	S	I
4	planar	I	I	S	N	S
	SPECT1	I	N	S	N	S
	SPECT2	N	I	I	N	I
	CA	I	I	S	N	I
5	planar	N	I	S	N	N
	SPECT1	N	S	S	N	N
	SPECT2	N	I	S	N	N
	CA	N	I	S	N	N
6	planar	N	I	S	S	N
	SPECT1	N	S	S	S	N
	SPECT2	N	I	S	S	I
	CA	I	S	S	S	I
7	planar	N	N	N	N	N
	SPECT1	N	N	N	N	N
	SPECT2	N	N	N	N	N
	CA	N	N	N	N	N
8	planar	I	S	I	I	I
	SPECT1	I	S	S	I	I
	SPECT2	I	S	S	N	I
	CA	I	S	S	I	I
9	planar	I	S	S	I	I
	SPECT1	N	S	S	S	S
	SPECT2	I	I	S	N	I
	CA	I	S	S	I	I
10	planar	N	I	N	N	N
	SPECT1	N	I	N	N	N
	SPECT2	N	I	I	N	N
	CA	I	I	I	N	I

Table 11.1 Myocardial perfusion results

ant = anterior, ap = apical, inf = inferior, lat = lateral, sep = septal
N = normal, I = ischaemic, S = scar

planar = results from planar images

SPECT1 = results from SPECT data reconstructed using manufacturer's software

SPECT2 = results from SPECT data reconstructed using 2D Butterworth filter

CA = results from contrast angiography data

abnormal segments (sensitivity 63%).

The SPECT data obtained using the technique described in Section 11.3 identified 15/15 normal segments (specificity 100%) and 25/35 abnormal segments (sensitivity 71%).

The small difference in the results of the SPECT data is probably due to the improved image quality which results from the application of the two dimensional Butterworth filter, figures 11.7 and 11.8. However, as was noted in Section 11.3.1 the interpretation of the data was not particularly sensitive to the exact form of the filter function so that a large improvement in the accuracy of the SPECT studies was not expected.

There was no overall change in the accuracy of the results when SPECT as opposed to planar imaging was used. This is not in accordance with the results obtained by a number of authors using ^{201}Tl which showed improvements in sensitivity, Taylor (1989), Walters (1988), Kiat (1988). This may be a consequence of the greater penetration of the $^{99\text{m}}\text{Tc}$ photons which makes the additional contrast obtained by SPECT less important. The greater experience in the interpretation of planar cardiac data may also have been a factor. Alternatively, a larger group of patients with perhaps a larger proportion of patients with an intermediate a priori probability of CAD may be required to clearly demonstrate any differences.

11.4.2.3 Identification of diseased arteries

The planar and SPECT data can also be used to identify abnormalities in individual coronary arteries. The relationship between the segments of myocardium and their vascular supply was taken to be the same as that used in the

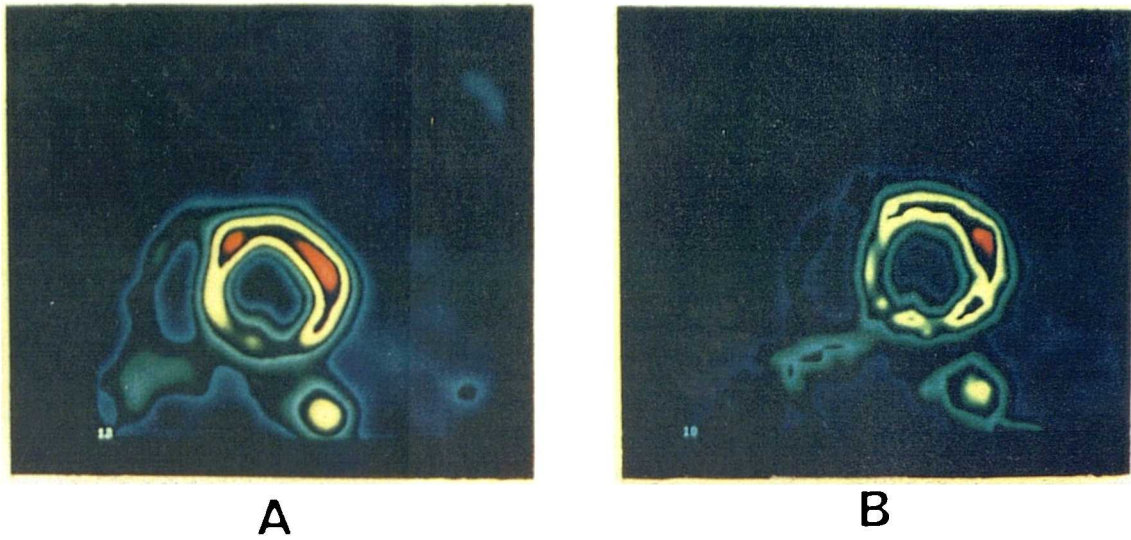


Figure 11.7 Short axis sections after reconstruction with, A, the two dimensional Butterworth filter and, B, the Shepp-Logan filter from the manufacturer's software.

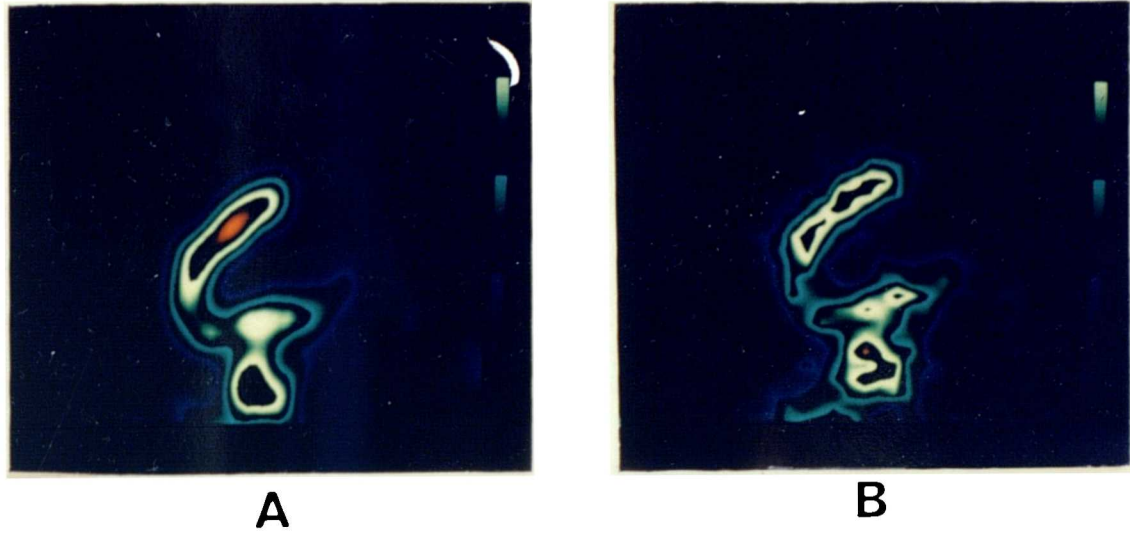


Figure 11.8 Long axis sections after reconstruction with, A, the two dimensional Butterworth filter and, B, the Shepp-Logan filter from the manufacturer's software.

previous section. The results of the angiography examinations were again used to assess the accuracy of the planar and SPECT data.

The planar data correctly identified 10/10 normal coronary arteries (specificity 100%) and 15/20 abnormal arteries (sensitivity 75%).

The SPECT data (using the analytical method described in section 11.3) correctly identified 10/10 normal coronary arteries (specificity 100%) and 16/20 abnormal arteries (sensitivity 80%).

The main source of error occurred in subjects with triple vessel disease. As the assessment of the uptake of isotope in any individual region of the myocardium is made relative to that in other regions there will always be one region in any image which appears "normal". Some form of quantitative analysis may be required to identify all abnormal regions when triple vessel disease is present. Thus, for the planar data three out of the five arteries which were incorrectly assessed as normal were in subjects with triple vessel disease. For the SPECT data three out of the four arteries which were incorrectly assessed were in subjects with triple vessel disease (the fourth was in fact a LAD artery in which the diameter of the stenosis was only slightly above the threshold at which a lesion was considered to be significant).

11.4.2.4 Differentiation between ischaemic and scarred tissue

In the segments which were correctly identified as being abnormal the accuracy with which ischaemia could be differentiated from scarring was assessed. Areas of the left ventricle which displayed normal wall motion on contrast

ventriculography but which were supplied by arteries with significant stenoses were classified as ischaemic. Areas with abnormal wall motion were classified as scarred.

For the planar studies 21/25 (84%) segments were correctly classified. 10/12 (83%) regions were correctly identified as being ischaemic and 11/13 (85%) scarred. Two regions were classified as ischaemic by the isotope studies but were scarred on the contrast studies. Two regions were classified as scarred by the isotopes but were ischaemic on the contrast studies.

For the SPECT data 22/25 (88%) segments were correctly classified. 12/12 (100%) were correctly identified as being ischaemic and 10/13 (77%) scarred. Three regions were classified as ischaemic using SPECT but were scarred on the contrast studies.

These results show a high level of agreement between the isotope and contrast studies. The SPECT data correctly identified all of the ischaemic areas whereas the planar studies classified two as scarred. The planar studies correctly identified 11/13 scarred regions compared to 10/13 for the SPECT. There was a slightly greater likelihood for the SPECT studies to classify a region as ischaemic as opposed to scarred (15/25 regions ischaemic on SPECT compared to 12/25 on the planar images).

11.5 General conclusions for Chapter 11

1. The interpretation of the sections through the heart were found to be relatively insensitive to changes in the cut off frequency of the Butterworth filter. This rendered the application of the filter matching procedure, described in Chapter 8, unnecessary. However, when compared to the manufacturer's software, a straightforward application of the two dimensional Butterworth filter did improve the quality of the images which were produced leading to an increase in clinical accuracy.

2. Utilising the results of the previous Chapters, the SPECT data were acquired over 360 degrees using the LEAP collimator into 64 projection images of dimension 128*128 with pixels of size 3.5mm*3.5mm. The acquisition time was 30s per angle.

The data were reconstructed using the two dimensional Butterworth filter of power 10. The cut off frequency was 0.4cm^{-1} in the majority of cases. Occasionally it was reduced to 0.37cm^{-1} if the noise level was judged to be too high. No corrections for attenuation or uniformity were applied.

3. The use of the $^{99\text{m}}\text{Tc}$ -MIBI produced results with a high level of accuracy when contrast angiography studies were used as the "gold standard". For the detection of CAD in the group of ten patients studied the sensitivity and specificity were 100% for both the planar and SPECT investigations.

4. The $^{99\text{m}}\text{Tc}$ -MIBI images of the myocardium were divided into segments and compared with similar regions on

angiography. The use of the Butterworth filter produced an improvement in the sensitivity with which abnormal segments were identified when compared to the SPECT reconstructions performed with the manufacturer's software.

There was no overall change in the accuracy of the results when SPECT as opposed to planar imaging was used.

5. The ^{99m}Tc -MIBI data were also used to identify abnormalities in individual coronary arteries. This was achieved to a high level of accuracy. All normal coronary arteries were correctly identified. 75% of the abnormal arteries were correctly identified on the planar studies and 80% on the SPECT.

The main source of error occurred in the identification of all of the arteries in a subject with triple vessel disease. Because all assessments of myocardial perfusion were performed relatively there were occasions in which abnormal segments appeared normal when compared to the rest of the myocardium in that section. However, on no occasion was more than one coronary artery incorrectly classified as normal in a patient with triple vessel disease. Thus this problem is unlikely to be clinically significant.

6. The ^{99m}Tc -MIBI studies also showed a high level of accuracy in the differentiation of ischaemic from scarred myocardium. The planar studies correctly classified 84% and the SPECT 88% of the abnormal segments. There was a greater likelihood for the SPECT studies to classify a region as ischaemic as opposed to scarred when compared to the planar data.

7. The overall improvement in the accuracy of the SPECT over the planar data was small. A major factor in this was the constitution of the patient group studied. Only 3/10 patients had one or two vessel disease; the others were normal, 2/10, or had severe disease, 5/10. It is possible that the improved contrast obtained with SPECT data may be of more value in patients with less severe disease and an a priori probability of CAD which is closer to 50%.

Chapter 12 Digital filtering of the bladder in SPECT bone studies of the pelvis.

12.1 Introduction

The work of the previous two Chapters describing clinical applications of SPECT concentrated on the control of the stochastic noise levels. However, there are circumstances in which the main process which limits the quality of the reconstructed data is non-stochastic in nature, Section 2.5. As an example of this the work of this Chapter will address a specific clinical problem in which the feature which limits the clinical applicability of the technique is a non-stochastic noise process.

SPECT studies of the skeleton have been utilised in the investigation of a wide variety of skeletal disorders. One of the most useful applications has been in the diagnosis of avascular necrosis (AVN) of the femoral head. However, SPECT images of the pelvis are often compromised by artefacts which are produced by the presence, within the bladder, of high levels of activity which increase over the acquisition period of the study. In practice, the influence of bladder activity can make 20% of SPECT scans of the pelvis unusable, Collier (1985). In addition to this, the quality of an even larger proportion of scans is reduced.

The most direct method for the removal of the influence of bladder activity from SPECT bone studies of the pelvis is patient catheterisation. However, a significant level of morbidity is associated with catheterisation, which, if employed in all SPECT bone studies of the pelvis would seriously limit the applicability of the test. Thus the removal of the influence of bladder activity through some form

of processing of the acquired data is required, Collier (1987).

12.2 Artefact Production

There are several ways in which the presence of activity within the bladder affects the images in a reconstructed SPECT study. Artefacts, in the form of streaks which can extend across the whole width of a transaxial section, figure 12.1, are produced as a result of the fact that the activity within the bladder increases during the acquisition period of the scan. The streaks have a characteristic fan shaped pattern, Collier (1985), which is a consequence of increased bladder counts in projection images acquired as the camera rotation angle proceeds towards 360 degrees. The most intense streak results from the back projection of bladder counts in the last view collected, when the bladder activity is a maximum, with streak intensity gradually decreasing for views acquired and back projected at smaller angles. This explains why the streak artefacts occur mainly in a NNE to SSW direction when the starting angle for the study corresponds to an anterior view of the patient. As can be seen from figure 12.1 the count densities in the streak artefacts can be greater than those in the femoral heads themselves. In addition there are many cases in which they will overlap one or both femoral heads, substantially reducing the confidence with which structures within the image can be identified.

Perhaps the most pernicious effect, however, that bladder activity can have on SPECT bone studies of the pelvis is the production of photon deficient areas which are most obvious in sections taken in the coronal plane. This is illustrated in

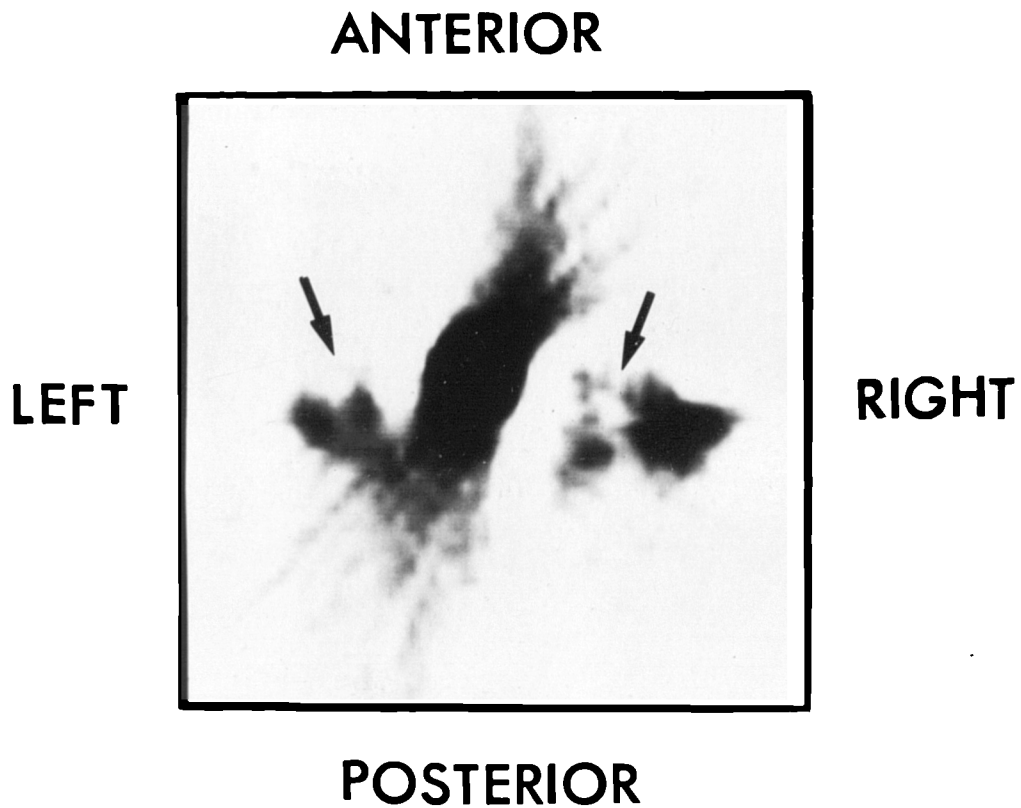


Figure 12.1 Streak artefacts in a transaxial section through the hips produced by changes in the level of activity in the bladder during the acquisition period of the study. In this case there is AVN of both femoral heads; the confidence with which this can be diagnosed is reduced by the presence of the artefacts. This section was obtained from a SPECT acquisition in which projection data were acquired at 64 equally spaced angles over a 360° rotation. The patient was supine and the starting position corresponded to an anterior view.

figure 12.2 where the cold areas in the femoral heads are due to artefacts produced by high levels of activity in the bladder. This is obviously of concern when the scan is being performed to detect AVN of the femoral head where the presence of a cold area is the most important diagnostic feature, Grieff (1980).

The cold areas arise as a result of the fact that the activity in the bladder can be much larger than that in the surrounding structures. In the reconstruction of the data the high bladder count densities produce a reduction in the counts in the neighbouring regions. The loss of counts occurs when the projection data are filtered prior to backprojection. The filter which was used is a ramp function modulated by a Shepp-Logan window: the values of the filter function in the spatial domain are shown in Table 12.1. When the negative values in the filter are multiplied by the counts in the bladder large negative values will be produced. These can be larger than the sum of the positive values obtained for the pixels in regions close to the bladder after the convolution of the projection data with the filter. Typically, the femoral heads are separated from the bladder by around 4 to 10 pixels.

The magnitude of the negative values in the filter can be reduced by choosing a sharper filter function. However, even if an unmodulated ramp function with a discrete cut off at the Nyquist frequency is used there is only a minimal reduction in the level of artefact production.

It is also possible that the count losses could be due to arithmetic overflow during the reconstruction. This was tested by dividing the pixel counts in the planar projection images by a constant value, e.g. 50 before the reconstruction was

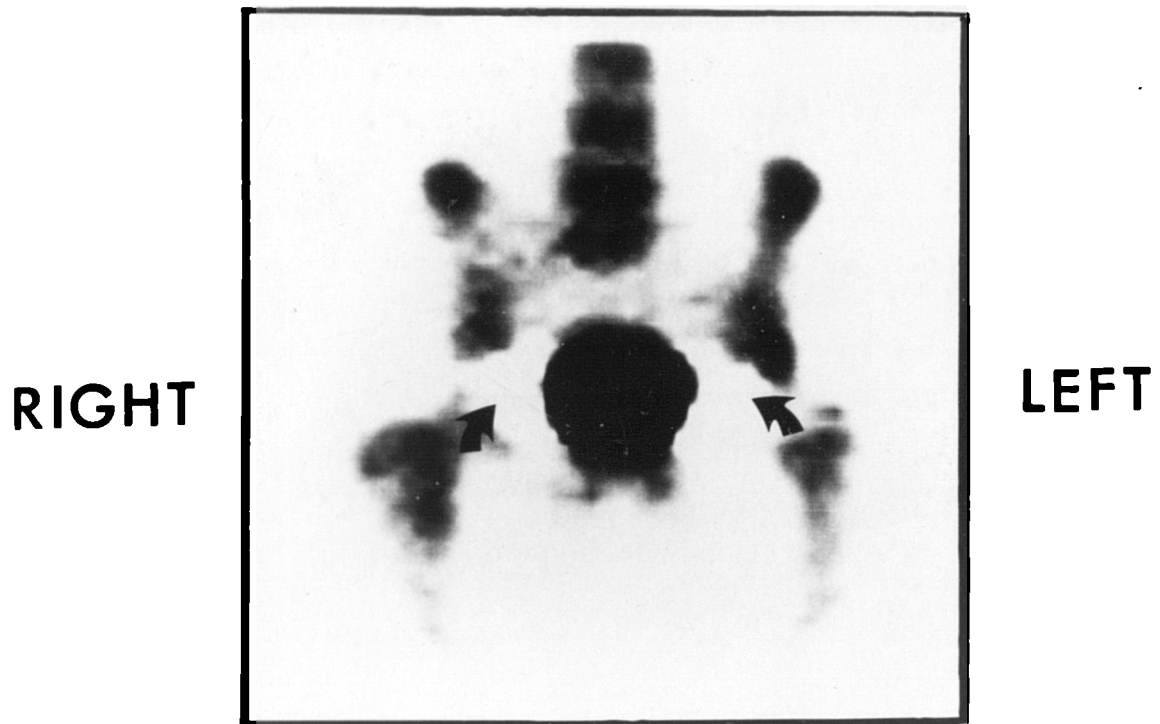


Figure 12.2 Cold area artefacts are present in both femoral heads in this coronal section. They are produced by the high level of activity in the bladder which influences the calculation, in the filtered back projection reconstruction, of the count densities in the lower activity structures.

Point Number	Value
1	13628
2	-4543
3	-909
4	-389
5	-216
6	-138
7	-95
8	-70
9	-53
10	-42
11	-34
12	-28
13	-24
14	-20
15	-17
16	-15
17	-13
18	-12
19	-11
20	-9
21	-9
22	-8
23	-7
24	-6

Table 12.1 The values in the spatial domain are shown for the Shepp-Logan filter. The filter is convolved with projection data 64 pixels in length before back projection. The filter has been truncated to 24 points to reduce computing time.

performed in order to reduce the magnitude of the numbers being handled by the reconstruction algorithm. However, no matter how large the divisor was made the cold area artefacts were still observed; it is the fact that the bladder activity is high relative to the surrounding structures rather than its absolute value which causes the artefacts to be produced.

In general, all practically useful filter functions will produce large negative values when convolved with data which has a large dynamic range. Thus, it is likely that this problem is common to all reconstruction algorithms which utilise the filtered backprojection technique. A fuller examination and characterisation of this problem using some simple phantom studies is given in Appendix 1.

In addition to the production of artefacts, other difficulties can arise because the amount of activity in the bladder can be much larger than that in the femoral heads. This can make the femoral heads difficult to display properly, particularly in the transaxial sections, as demonstrated in figure 12.3. In the coronal plane the problem is less severe because the centre of the bladder is generally anterior to the centre of the femoral heads. Nevertheless, problems still arise in a substantial proportion of cases because the posterior edge of the bladder can extend into the coronal plane of the femoral heads.

12.3 Post-reconstruction processing

There are several methods which can be used to reduce the effects of the bladder activity by processing the SPECT data after reconstruction. For instance, the display problems can be overcome in some cases simply by reducing the upper

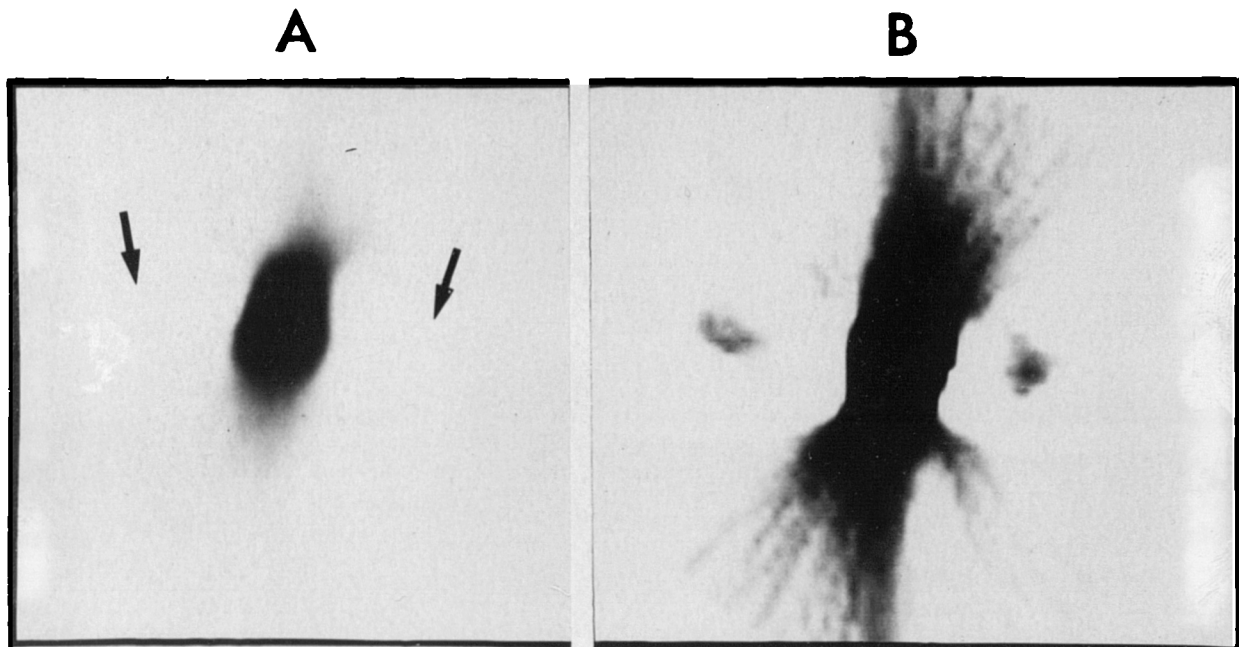


Figure 12.3 The large levels of activity in the bladder can make the femoral heads difficult to visualise as shown in the transaxial section in A. Reducing the upper threshold level of the display window can, in some cases, improve femoral head visibility, B. However, large areas with the same grey scale value are produced and the final contrast within the structures outside the bladder region is often still poor.

threshold level of the display window being used to view the reconstructed images to a point where the femoral heads can be properly visualised. However, this will often mean that large areas of the image will be displayed with the same grey scale value which produces an effect which is visually distracting, figure 12.3B. In addition, unless a nonlinear scale is used, the activities in the femoral heads may only cover a few grey scale levels which will produce an apparent loss of contrast because of the compression of the dynamic range of structures whose activity levels are a small fraction of the maximum, Sharp (1985).

An alternative method is to define a ROI around the bladder for each affected transaxial section and to set the value of each pixel within it to zero. If the ROI is chosen for the section through the bladder centre then it should be large enough to mask the bladder in the other transaxial sections. Thus only a single ROI needs to be defined. Having masked the bladder from the transaxial data, sections in the coronal and sagittal planes will also be free from the effects of high bladder activity.

The problems encountered in the display of the femoral heads due to the large count densities often found in the bladder are resolved using this post-reconstruction masking approach. However, the more serious problem of artefact production is not addressed.

12.4 Pre-reconstruction Processing

The only way in which artefacts can be avoided is to correct for the high and changing levels of activity in the bladder before the reconstruction is performed. This can be

accomplished by manipulating the data in the planar projection images which are acquired at each angle as the camera is rotated around the patient. To do this, however, a method for defining the location of the bladder in each projection view must be employed. A direct approach involving the designation of a ROI around the bladder on each of the projection images, of which there are typically 64 or 128, would be an extremely time consuming and laborious procedure. Thus a method for defining the location of the bladder which involves the definition of only a single ROI has been developed.

12.4.1 Bladder Identification

This method involves the designation of a ROI on a sinogram. An example of a sinogram image corresponding to a transaxial section through the pelvis at the level of the bladder and femoral heads is shown in figure 12.4A. Objects within the transaxial section have a sinusoidal form in the sinogram image. The amplitude and phase of the sinusoid depend on the position of the object within the section. In the sinogram shown in figure 12.4A the bladder is easily identifiable as the most active structure closest to the central vertical axis.

If the sinogram corresponding to the transaxial section through the widest part of the bladder is selected, and a ROI defined to include it, then this is equivalent to identifying the positions of its right and left hand edges in each projection image. The superior and inferior edges of the bladder can be identified by examining the final projection image which is collected when the bladder is at its fullest. Thus the information required to specify a rectangular area

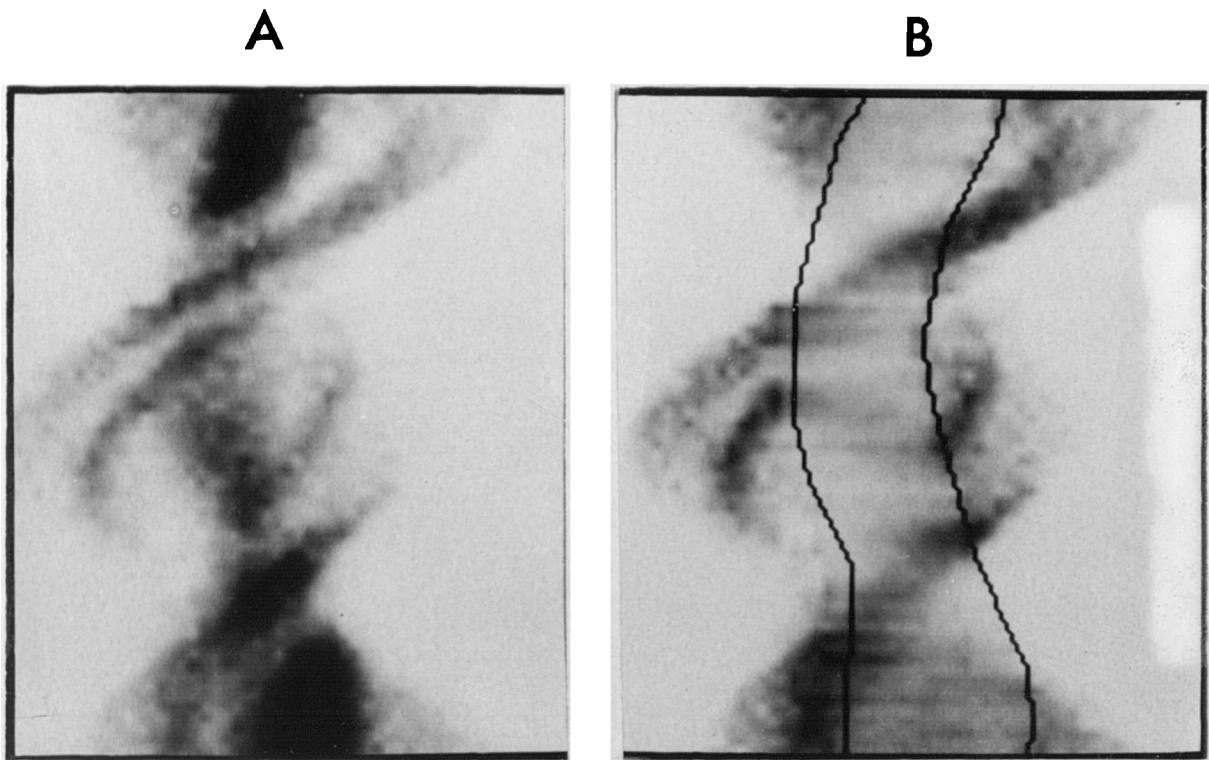


Figure 12.4 Sinogram matrix corresponding to the transaxial section through the centre of the bladder, A. The high and changing count levels in the bladder can be replaced by data which are representative of the activity in surrounding structures by the process of interpolative background replacement, B.

which includes the bladder on all projection images can be determined with very little user input.

Having defined a region to include the bladder on each projection image the simplest way to remove the influence of bladder activity is to set the value of all pixels within the bladder region to zero. The amended images can then be used for the reconstruction calculations. This simple approach will certainly remove the high count levels within the bladder in the reconstructed transaxial sections. However, the backprojection of zero count values and the effect of a discontinuity in the projection profiles would be expected to produce artefacts of their own. In addition to this, counts are removed from the femoral heads themselves when they are included in the region defining the bladder when the two structures overlap, i.e. lateral projections. Thus this approach is only likely to be of value in cases where the artefacts produced by the data manipulation process are less severe than those which were originally created by the varying bladder activity.

12.4.2 Interpolative Background Bladder Replacement

In response to these problems a more sophisticated approach was developed and investigated. The basis of this technique lies in an attempt to replace the counts in the area occupied by the bladder by data which are as representative as possible of the activity in the surrounding regions. Thus, the high and inconsistent count data in the bladder, which produces the problems in the reconstruction of the SPECT studies, are replaced by lower, more consistent count information.

A rectangular ROI is defined for each projection image to include the bladder, making use of the sinogram technique described previously. New values for the counts in the pixels within the defined region are calculated from the counts in the pixels which lie around its perimeter. The way in which the new values are calculated is similar to the process involved in the Goris interpolative background subtraction technique, Goris (1976). However, there is a fundamental difference in that the values calculated from the edge pixels are not subtracted from the counts in the defined region but are actually used to replace them.

For each pixel within the bladder region a new value is calculated using the counts in the four pixels which are situated around the perimeter of the ROI and which lie directly above, below and to the left and right of it. The procedure is illustrated in figure 12.5. A proportion of the counts in each of the four edge pixels is taken and the results added together to produce the new value for the bladder pixel. The proportion of the counts for each edge pixel which is used in the calculation depends on its distance from the bladder pixel in question. The larger the distance the smaller the proportion used. The values for the proportions fall in a linear fashion from unity, when the bladder pixel is adjacent to the edge pixel, to zero when it is adjacent to the opposite edge of the ROI. The values are divided by a factor of two to make the average of the pixel counts within the bladder region equal to the average of the edge pixel values.

The results of this procedure are shown for a sinogram in figure 4B and for planar projection images taken at a

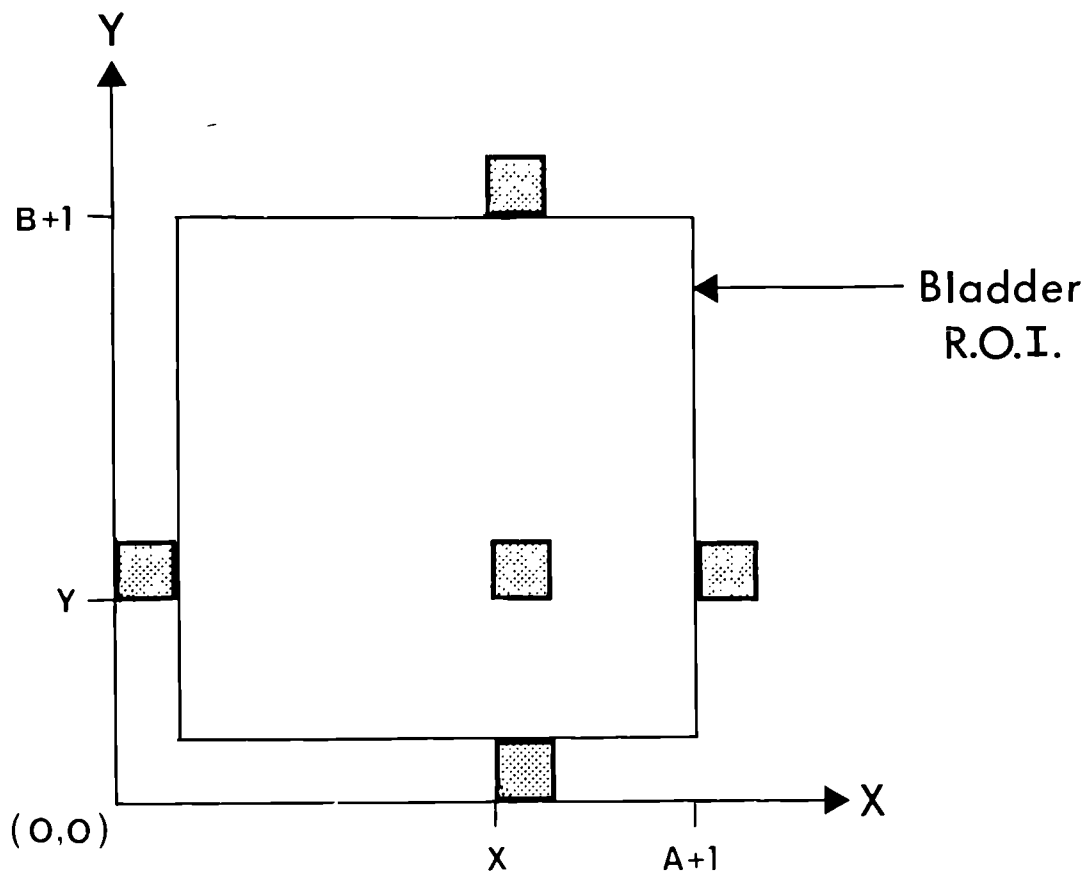


Figure 12.5 To calculate the replacement value of a pixel within the rectangular bladder ROI, the count values of 4 pixels positioned immediately outside it are used. For a rectangular ROI of width A and height B pixels the value of the bladder pixel at position (x,y) is given by:

$$C(x,y) = C(x,0) \cdot \left[\frac{(B-y)}{(2 \cdot (B-1))} \right] + C(0,y) \cdot \left[\frac{(A-x)}{(2 \cdot (A-1))} \right] + C(x,B+1) \cdot \left[\frac{(y-1)}{(2 \cdot (B-1))} \right] + C(A+1,y) \cdot \left[\frac{(x-1)}{(2 \cdot (A-1))} \right]$$

This is performed for $1 < y < B-1$ and $1 < x < A-1$.

selection of camera angles in figure 12.6. As can be seen, reasonable, representative and well behaved images are produced by the replacement of the bladder activity. The largest errors occur when the bladder and femoral heads overlap although, once the backprojection has been performed, the total error in the femoral head counts should be low because the bladder and the femoral heads overlap in a relatively small number of camera angles.

12.5 Assessment of the processing techniques

To assess the relative merits of the processing techniques just described, the SPECT studies of a group of 13 patients referred for the investigation of AVN of the femoral head were analysed.

Each patient received 600MBq ^{99m}Tc - methylene diphosphonate intravenously with SPECT imaging commencing four hours later. The patients were well hydrated and emptied their bladders before the start of the acquisition. Data were collected by the gamma camera using 64 angles over 360 degrees and an acquisition period of 30 seconds per angle. The data matrices were of size 64*64 and each pixel had linear dimensions of 7mm. Reconstruction was performed using the Shepp-Logan filter. As the primary aim of this work was the removal of the effects of the bladder activity no attempt was made to employ the stochastic noise control techniques described in Chapter 8. This would be a suitable topic for further investigation.

Each study was analysed without processing (NP), then with post-reconstruction masking (PRM), and finally with interpolative background replacement (IBR) of the bladder

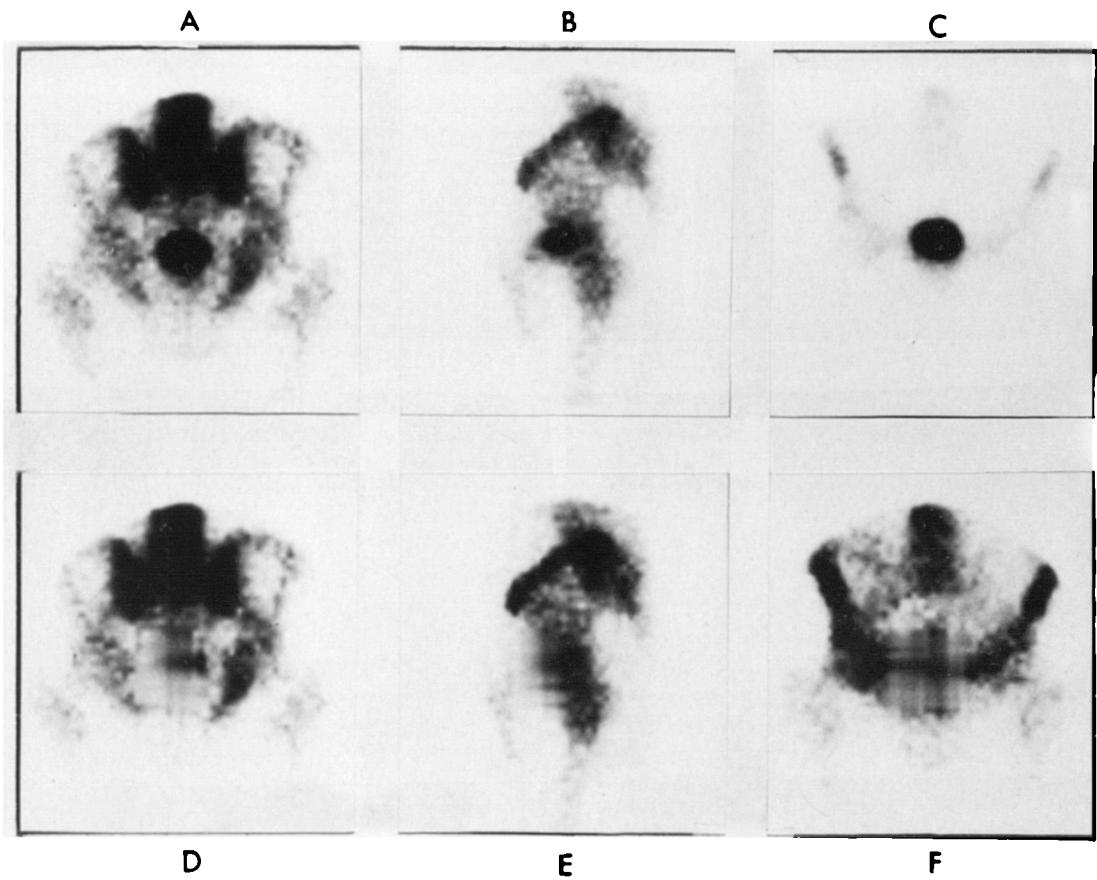


Figure 12.6 The projection views collected when the camera angle was 0, 270 and 360 degrees are shown in the top row (A, B and C). Beneath them are the projection views after interpolative background replacement of the bladder activity (D, E and F respectively). These new views are used to reconstruct the transaxial sections.

employed. The quality of the coronal and transaxial sections taken through the hips was assessed for each method by an experienced nuclear medicine physician (JM). A scoring system was employed whereby a score of one was given to an image which was of poor quality and difficult to interpret, a score of two to an image of intermediate quality which was however, interpretable, and a score of three to an image of good quality in which the anatomical features were clearly defined. In addition, a preference was expressed for the technique which gave the best images even if there was no difference in the scores allocated to them. This was used to detect differences between the techniques which were masked by the relatively crude scoring system.

If the image was interpretable, each hip was assessed for the presence of AVN on the basis of the detection of a cold area within the femoral head. A final diagnosis of the presence of AVN was made separately through an assessment of all of the radiological information in conjunction with a detailed clinical history of the patient, but without reference to the SPECT data. The assessment of the SPECT images was performed blindly in that the assessor had no knowledge of the final diagnosis which was performed independently by JD.

12.6 Results

Table 12.2 shows the relative counts in the bladder and femoral heads for the first and last projection views of the SPECT studies. For this fairly typical group of patients the mean change in counts in the bladder over the period of acquisition of the scan was 54%. More significantly the mean

Patient	B1	B2	FL	FR	B2/B1	B2/FL	B2/FR	(B2-B1)/FL	(B2-B1)/FR
A	219	288	85	102	1.32	3.39	2.82	0.81	0.68
B	478	821	190	100	1.72	4.32	8.21	1.81	3.43
C	1068	1123	328	398	1.05	3.42	2.82	0.17	0.14
D	274	285	281	255	1.04	1.01	1.12	0.04	0.04
E	547	662	75	75	1.21	8.82	8.82	1.53	1.53
F	301	733	119	117	2.44	6.16	6.26	3.63	3.69
G	528	550	55	72	1.04	10	7.63	0.4	0.3
H	337	538		104	1.6		5.17		1.93
I	366	948	170	170	2.6	5.58	5.58	3.42	3.42
J	753	1265	73	100	1.67	17.2	12.56	6.89	5.03
K	273	551	236	110	2.02	2.33	5	1.78	2.53
L	2932	2844	163	177	0.96	17.3	15.6	0.66	0.61
M	422	962	107	112	2.28	9	8.6	5.05	4.82

Table 12.2 The maximum pixel values are shown in the bladder at the start and finish of the SPECT acquisition, B1 and B2, and in the left and right femoral heads, FL and FR. The relative change in the bladder counts during the acquisition, B2/B1, and the ratio of counts in the bladder to that in each of the femoral heads, B2/FL and B2/FR, is calculated. In addition, the change in bladder counts is expressed as fraction of the counts in each femoral head.

In patient H there was a prosthesis in the left hip.

increase in bladder counts was a factor of 2.2 greater than the mean femoral head counts. In addition, the bladder counts were on average 7.2 times the femoral head counts by the end of the acquisition.

Thus it is not surprising that many SPECT studies of the pelvis are difficult to interpret, given the large levels of activity found in the bladder and the magnitude of the changes in bladder counts over the period of acquisition of the scan compared to the count densities found in the femoral heads.

The scores allocated to the different processing methods are shown for each patient in Table 12.3. For the coronal section the image quality was improved after processing in 9/13 patient studies with PRM and in 10/13 studies with IBR. In only two studies was a different score allocated to the PRM and IBR methods with the IBR scoring higher. However, when a preference for the best images was expressed, those obtained using IBR were selected in nine cases, PRM in none, and NP in one.

For the transaxial sections the image quality was improved after processing in 4/13 patient studies using PRM and in 11/13 studies with IBR. Comparing the image quality obtained with PRM and IBR there was an improvement in 8/13 studies using IBR with a deterioration in 1. As to which technique produced the best set of images IBR was selected in eleven studies, PRM in one and NP in one.

The most important finding was the presence of cold area artefacts on the coronal sections of four of the patients, E, G, J, and L, if there was no data processing performed or if PRM was used. These artefacts were removed when IBR was employed. This is illustrated in figure 12.7 where patient J,

Assessment of Processing Methods
Score for image quality of each section

Patient	Coronal Sections			Transaxial Sections			Final Clinical Diagnosis	
	NP	PRM	IBR	NP	PRM	IBR		
A	2 L-R-	2 L-R-	2 L-R-	1 N.I.	1 N.I.	2 L-R-	L-	R-
B	1 L+R-	2 L+R-	2 L+R-	1 N.I.	1 N.I.	2 L+R-	L+	R-
C	2 L+R+	2 L+R+	2 L+R+	1 L+R+	2 L+R+	2 L+R+	L+	R+
D	2 L+R-	2 L+R-	2 L+R-	2 L+R-	2 L+R-	1 L+R-	L+	R-
E	1 N.I.	2 L+R-	2 L-R-	1 N.I.	1 N.I.	1 N.I.	L-	R-
F	2 L-R-	3 L-R-	3 L-R-	1 N.I.	1 L-R-	2 L-R-	L-	R-
G	1 N.I.	3 L+R+	3 L-R-	1 N.I.	1 N.I.	2 L-R-	L-	R-
H	2 L-R+	3 L-R+	3 L-R+	1 L-R+	2 L-R+	3 L-R+	L-	R+
I	2 L+R-	3 L+R+	3 L+R+	1 N.I.	2 L+R+	2 L+R+	L+	R+
J	1 N.I.	2 L+R+	2 L-R-	1 N.I.	1 N.I.	2 L-R-	L-	R-
K	2 L+R-	2 L+R-	3 L+R-	2 L+R-	2 L+R-	3 L+R-	L+	R-
L	1 N.I.	2 L+R+	3 L+R+	1 N.I.	1 N.I.	3 L+R+	L+	R+
M	2 L+R+	3 L+R+	3 L+R+	2 L+R+	3 L+R+	3 L+R+	L+	R+

Table 12.3 The left and right femoral heads are designated by L and R, the presence or absence of AVN by + or -, and if a study was not interpretable it was coded N.I. A score was allocated to each section on the basis of image quality. An image of poor quality in which interpretation was difficult was scored 1; if the image could be interpreted clearly a score of 2 was given; an image in which a confident interpretation could be made and in which the anatomical features were clearly demonstrated was given a score of 3.

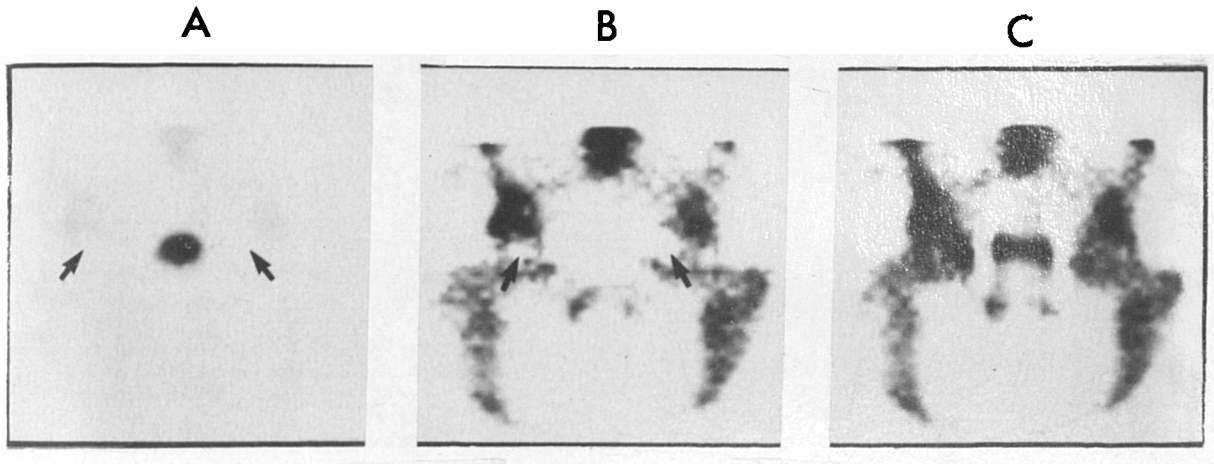


Figure 12.7 A coronal section in a patient with normal hips is shown with no processing (A), post reconstruction masking (B), and interpolative background replacement (C) employed. Cold areas which could be mistaken for AVN are seen in both femoral heads in A and B. However, in C, the femoral heads are correctly shown to be normal.

with normal hips, appeared to have cold regions within the femoral heads which were judged to be indicative of AVN. When IBR was employed it was clear that they were both normal. This was also the case with patients E and G. The fourth patient in which cold artefacts were produced did in fact have bilateral AVN; however, the extent of the disease was grossly exaggerated, figure 12.8. The cold area artefacts were observed in the four patients who had a combination of high bladder activity and a large bladder to femoral head uptake ratio (Table 12.1).

For the sections in the coronal plane, apart from the removal of the cold area artefacts, the application of IBR did introduce an improvement in general image quality, figure 12.9. In the image assessment the images produced using the IBR method were judged to show the anatomical structures most clearly in the majority of cases.

For the sections in the axial plane there was a clear improvement in the quality of the images produced using the IBR method. This is illustrated in figure 12.10 where the bilateral AVN of the femoral heads in patient M can be identified with greater confidence after the removal of the streak artefacts. The improvement in image quality with IBR shown in this case was typical of that seen in the majority of subjects investigated. Without some form of processing, the transaxial sections were of no value in 7/12 of the patients studied as the assessor felt unable to attempt to judge the presence or absence of AVN. This was due to a combination of the presence of streak artefacts and the effects of the high bladder activity levels. After IBR only one patient had transaxial sections which could not be interpreted.

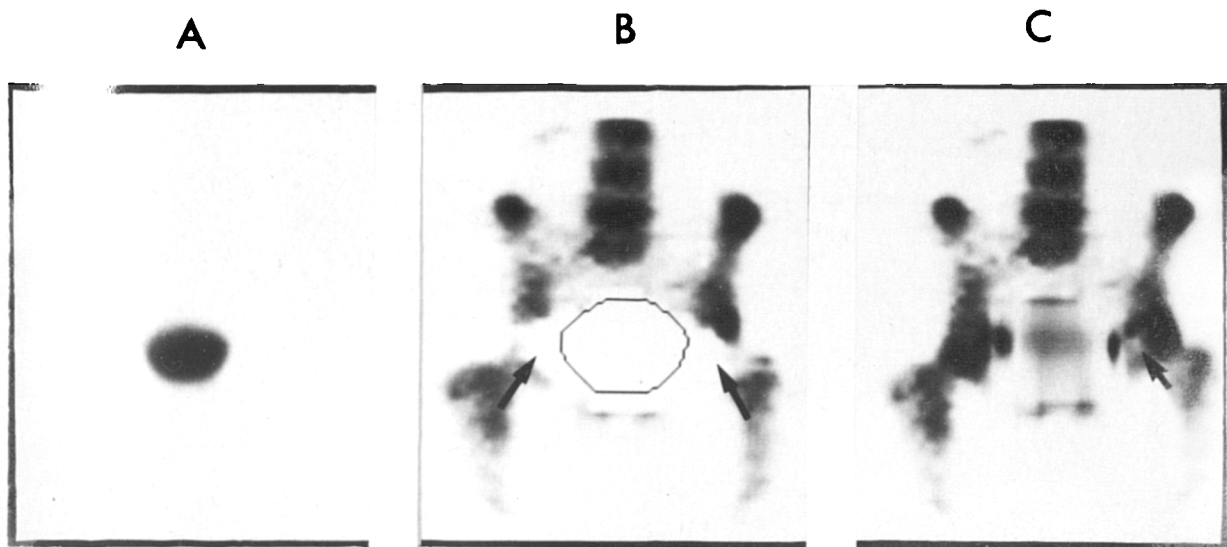


Figure 12.8 Coronal section through the hips of patient L with no processing (A), post reconstruction masking (B), and interpolative background replacement (C) employed. This patient was shown to have bilateral AVN but the severity was grossly exaggerated in A and B. In C, small photon deficient areas are present in both femoral heads which was consistent with the rest of the clinical and radiological data.

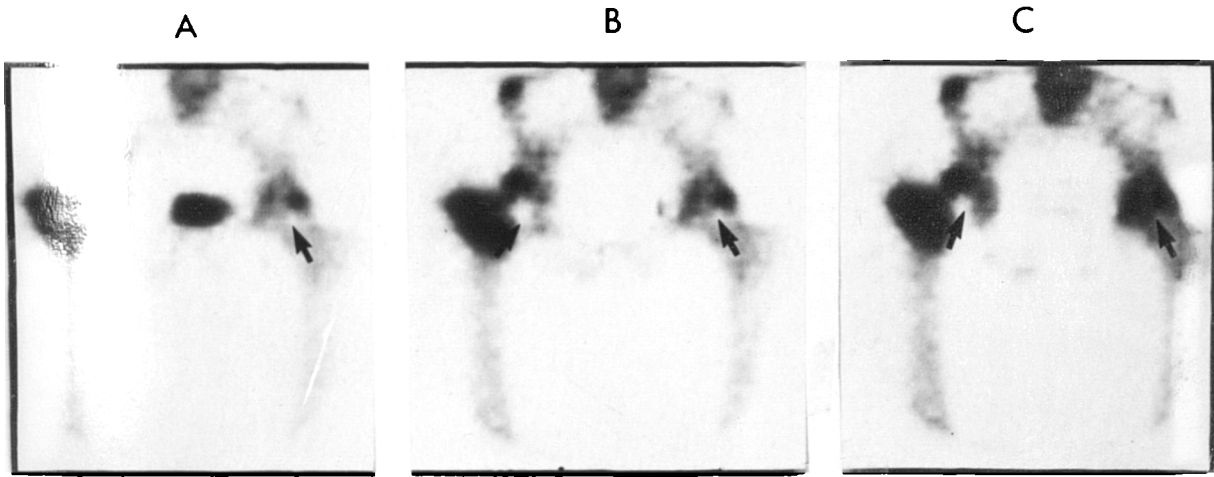


Figure 12.9 Coronal section through the hips of a patient with bilateral AVN of the femoral heads with no processing (A), post reconstruction masking (B), and interpolative background replacement (C) employed. In the assessment of the images all were assigned the same score, 3. However, it was felt there was a slight increase in the clarity with which anatomical features present in image C could be identified (e.g. the acetabulum of the right hip).

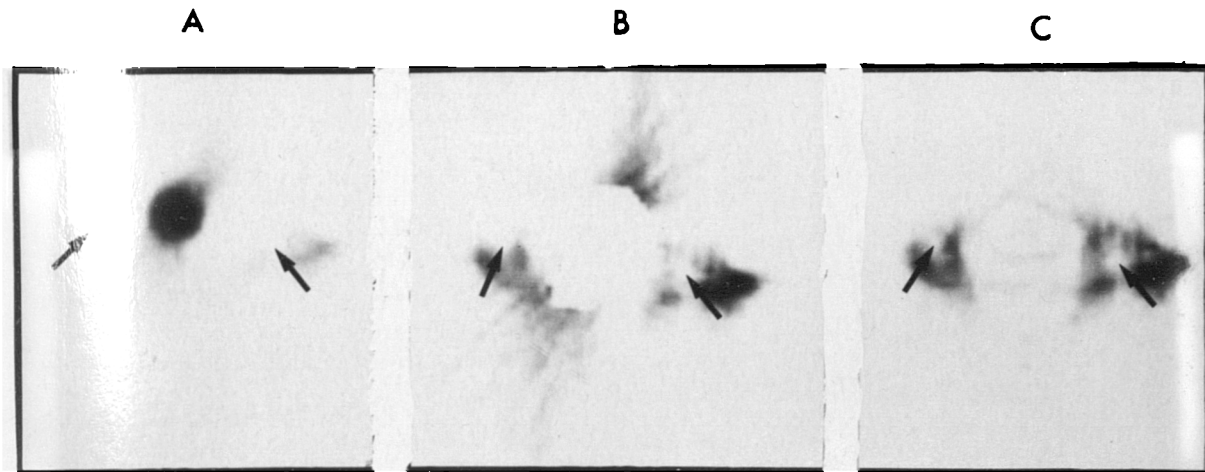


Figure 12.10 Transaxial sections through the hips of a patient with bilateral AVN. The sections are shown with no processing (A), post reconstruction masking (B), and interpolative background replacement (C) employed. The photon deficient areas in both femoral heads can be identified with greater confidence after the removal of the streak artefacts (C).

An examination of the projection images after IBR shows that although the high and changing count values in the bladder region can be successfully removed, they have been replaced by data which are essentially estimates of the values which would have been obtained if the bladder had not been present. The accuracy of this estimate will determine the value of the technique. As discussed previously the largest errors will occur in the projection images where the bladder and femoral heads overlap. However, this only constitutes a small proportion of the total projection data and it is our experience from the clinical studies that serious artefacts are not observed. The major effect of the IBR method is to introduce a slight smoothing of the the processed sections because the interpolated data are correlated and less noisy than the surrounding data.

It should be noted that there are a few cases where the influence of the bladder is insignificant and no processing whatsoever is required. This is illustrated in figure 12.11, for patient D, in which the bladder counts were low and did not increase greatly during the acquisition period of the study. However, this was found to be the case in only one of the thirteen patients who were investigated.

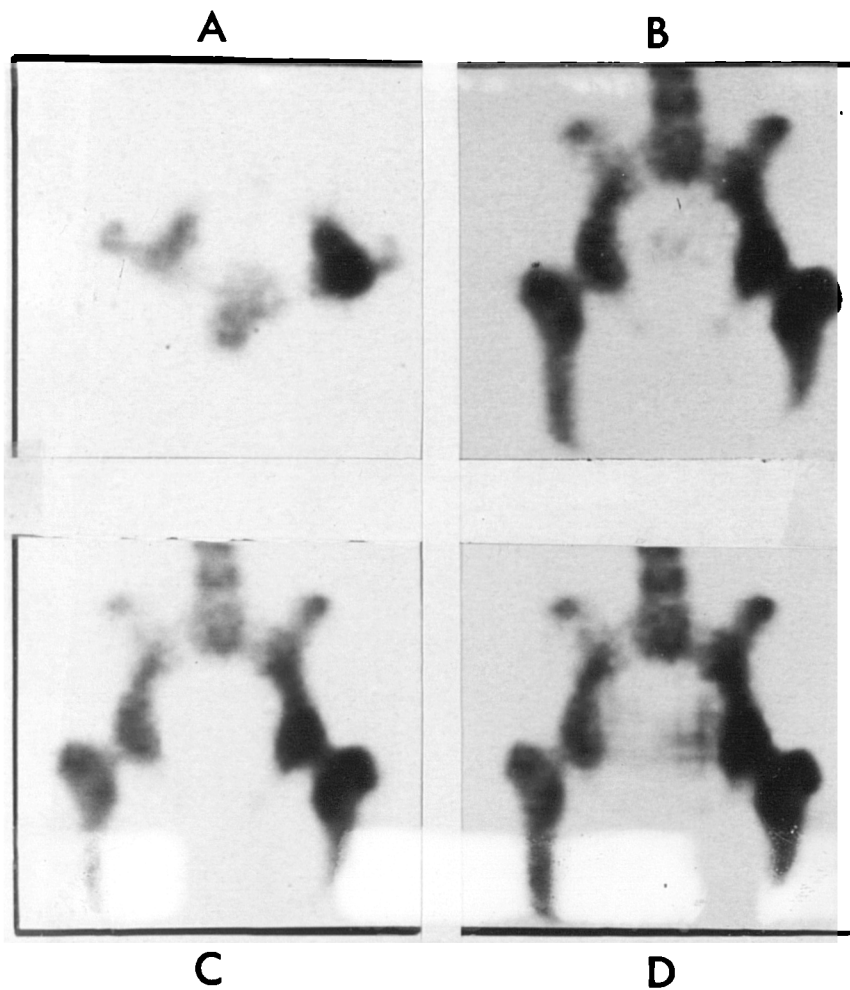


Figure 12.11 Sections through the hips of a patient with low and relatively unchanging bladder activity. The image quality of the transaxial data (A) was such that no processing was required. Similarly the coronal section without processing (B) was not improved significantly after post reconstruction masking (C) or interpolative background replacement of the bladder (D).

12.7 General conclusions for Chapter 12

The aim of this study was to develop a practical method for reducing the influence of bladder activity, especially artefact production, in SPECT bone studies of the pelvis. The experience of Collier (1985) was confirmed in that 20% of the studies were completely uninterpretable without some form of image processing.

Post-reconstruction masking of the bladder is a simple approach, equivalent to reducing the upper threshold level of the display window to a point where the dynamic range covers the count densities found in the femoral heads. It has the advantage over display window threshold adjustment in that visually disturbing areas of intense activity are avoided. The major disadvantage is that the problem of artefact production is not addressed.

For this reason the technique of interpolative background replacement of the bladder was developed and investigated. By replacing large and inconsistent bladder counts by data which are representative of the activity in the regions surrounding the bladder at each camera angle the level of artefact production was dramatically reduced.

Choosing the site of the bladder from the sinogram files reduces the level of user interaction to the definition of a single ROI. The time taken to perform the bladder replacement is less than that required to reconstruct the data. In total, time is saved using this procedure because the images can be interpreted without constant adjustments having to be made to the display window threshold levels. Thus, this is a practical solution to the bladder problem which is suitable for routine

application in nuclear medicine departments possessing standard computing facilities.

It should also be noted that this method is not limited to SPECT. It is applicable to any reconstruction process, for example x-ray computed tomography, where one or more objects in the plane to be reconstructed have values which change or are significantly higher than the rest of the objects in the plane.

It can be concluded that the method of interpolative background replacement of bladder activity significantly increases the image quality and clinical usefulness of SPECT bone studies of the pelvis.

Chapter 13. General conclusions

It was found that the fundamental performance of the SPECT system used for this work was significantly better than that of the previous generation of gamma camera systems. Indeed the results obtained compared favourably with those from most systems of the same generation (i.e. installed in the mid 1980s). The main aspects of this which were relevant to SPECT imaging were good energy resolution, uniformity and mechanical and electrical stability.

Most of the credit for these features can be ascribed to the microprocessor controlled correction circuitry in the camera head, Chapter 3. In particular the DIGITRAC facility produced a significant improvement in the stability of the uniformity over extended time periods (e.g. between six monthly camera services).

It is important to note, however, that there were several elements of the SPECT system which were shown to be operating at an unacceptable level by the rigorous performance assessment which was performed. The collimators were shown to exhibit a non-isotropic PSF as a result of design and manufacturing defects. These were replaced by the manufacturer. The ADCs which were originally present on the computing system were shown to exhibit an unacceptable level of differential non-linearity by a novel measurement method developed by the author. These were also replaced by the manufacturer. Problems were also encountered in setting the tilt of the camera head so that the camera face was parallel to the axis of rotation. The manufacturer was unable to set up the digital readout of the head tilt to the required level of

accuracy so that corrections calculated from a method developed by the author had to be applied. The SPECT bed itself was also found to have problems associated with it. The presence of a metallic strip placed around the edge of the bed and beneath the plastic coating was identified. This produced an unacceptable level of attenuation and so the SPECT bed was replaced.

These factors demonstrated the dangers inherent in operating rotating gamma camera SPECT systems in a "turnkey " manner. There are many aspects of the system which can be faulty. Given that SPECT imaging is an order of magnitude more sensitive than conventional imaging to errors in the data, even major manufacturers have difficulty in ensuring that each individual SPECT system installed is able to perform SPECT in a satisfactory manner. A rigorous and ongoing performance assessment and quality control program is required to ensure that the constituent elements of the SPECT system perform to an acceptable standard during the period of operation of the camera.

Having eliminated the deficiencies in the SPECT system and ensured that all aspects were operating in an acceptable manner the performance of the SPECT system as a whole was optimised. This was achieved by examining the fundamental aspects of the SPECT imaging process and by optimising the selection of the parameters chosen for the acquisition and reconstruction of the data. The main findings of the parameter optimisation process for the acquisition of the projection data were as follows.

It was found that the collection of images at 64 angles was sufficient to avoid angular undersampling artefacts for

clinical count density data. Despite the theoretical prediction that a much higher angular sampling rate would be required, this was not found to hold in practice. When the SLSFs were examined no significant differences were observed between the 64 and 128 angle data. For high count density phantom studies a marginal improvement in image quality was obtained through the use of the 128 angle data. However, when the count density was reduced to that obtained during clinical studies the differences between the 128 and 64 projection angle data were very difficult to discern.

One of the fundamental choices which has to be made concerning the acquisition of the projection data is the particular combination of the resolution and sensitivity characteristics of the collimator.

No attempt was made to produce a general solution to this problem. The main reason for this was that in practice there were only two collimators to choose between, the HR and the LEAP. Thus, for all practical purposes, the problem reduced to a comparison of the effects which the use of the HR and LEAP collimators had on the projection data. A study of planar PSFs and LSFs showed that, as would be expected, the HR collimator transferred all spatial frequencies with a higher gain than the LEAP and that the difference increased with increasing source to collimator distance. However, the difference was significantly reduced at low spatial frequencies when the measurements were made in a scattering medium as opposed to air.

When the SPSFs and SLSFs were measured some features which were common to both collimators were found. The resolution within a SPECT image varies with the direction in which it is

measured and with distance from the COR. The resolution measured in a direction tangential to the surface of the image volume improved with distance from the COR. However, the resolution measured along a radial axis was relatively independent of source position. Thus, the SPSF is circular in shape at the centre of the image plane but becomes elliptical as it is displaced radially.

Similarly, for both collimators the FWHM of the SPSF also increased as the ROR was increased. The rate of increase of the FWHM with the ROR was roughly independent of the source position and the direction in which it was measured. Thus, for the LEAP collimator, an increase of 5cm in the ROR increased the FWHM of the SPSF throughout the image volume by approximately 2.5mm.

Also, when the source was positioned at the COR the FWHM values of the SLSFs for both collimators were very similar to those obtained for the planar LSFs at source to camera distances equal to the ROR. This indicates that when the SPECT system is properly adjusted the resolution in the reconstructed images should be approximately equal to that obtained in planar images at equivalent source to camera distances.

When the SLSF was measured in a scattering medium the variation with position in the image volume was similar to that obtained in air. In fact, again for both collimators, the differences between the individual SLSFs when measured in air and scatter were small.

From a comparison of the behaviour of the collimators in the presence of scatter it was concluded that the resolution differences were small for low ROR values and object positions

distant from the COR but increased with larger ROR values and object positions close to the COR. Thus it appeared that it could be advantageous to use the HR collimator for clinical situations where a large ROR is required and the organ of interest is centrally located. The question of whether the loss of sensitivity resulting from this is compensated for by the gain in resolution was investigated by studying the results obtained from SPECT studies of extended source distributions which were provided by the SPECT phantom with its inserts.

Thus, while the SPSF and SLSF measurements provided useful fundamental information on the comparative properties of the collimators it was only through an investigation of extended source distributions that guidelines which were applicable to the clinical situation could be made.

It was found that when the count density was high and the ROR was small the images from the HR collimator were slightly superior to those obtained from the LEAP. However, at clinical count densities and small ROR the extra sensitivity of the LEAP more than compensated for its poorer resolution for the detection of the cold rods. For the pie insert at clinical count densities and small ROR the difference in quality between the images produced by the LEAP and HR collimators was not significant.

At large ROR and high count densities the HR collimator produced superior images of both the CL and the pie inserts. At clinical count densities, however, there was little difference in the quality of the images of the CL insert which were obtained from the LEAP and HR collimators. The superiority of the HR collimator for imaging the hot rods in

the pie insert was maintained.

Regarding the choice of collimator for routine clinical imaging there are advantages to be gained for the detection of cold lesions at low ROR values through the use of the LEAP collimator and for the detection of hot lesions at large ROR values through the use of the HR collimator.

The final parameter which is involved with the acquisition of the projection data is the linear sampling rate. This was investigated by examining the spatial frequency content of the projection data. To help in the accomplishment of this a novel mathematical construct, the LNP(u) curve, was introduced which allowed the relationship between the noise and the signal in the projection data to be visualised. Using the information which was obtained from this it was clear, from the sampling theorem, that a pixel size of 6mm to 7mm would have been sufficient to transfer, without aliasing, the portion of the signal in the projection data which was not dominated by the noise at clinical count densities. This would effectively mean that acquisition matrices of dimension 64*64 could be used with the complete gamma camera FOV being covered.

However, the choice of the linear sampling rate was also an important aspect of the choice of the form of the filter function used in the reconstruction process. Thus, considerations other than a strict satisfaction of the sampling theorem suggested that pixel sizes of 2.5 mm to 3.5 mm would be the most useful. For pixels of this size an acquisition matrix of dimension 128*128 was required to cover the camera FOV. This had the disadvantage that extra storage space and computing time was required to handle the data. However, there were also some benefits in practice, for

example, the software zoom facility could be used without the effects of pixellation becoming apparent on the transaxial sections. This was found to be useful for RCBF and cardiac imaging where the projection data were acquired into matrices of dimension 128*128 using pixels of edge length 3.5 mm; this meant that virtually all areas of interest could be reconstructed into a quarter of the FOV.

Having studied the optimisation of the parameters used in the acquisition of the data a similar procedure was employed for the reconstruction.

The major element in the reconstruction process is the choice of the form of the filter function. From a theoretical consideration of the available options it was decided that the Butterworth filter provided the best combination of spatial frequency transfer characteristics and flexibility. No attempt was made to study the group of filters with resolution recovery components because of the arbitrary nature of the resolution recovery process and the concomitant danger of introducing artefacts into the data.

The flexibility of the Butterworth was an important feature because it meant that the form of the actual filter used in the reconstruction of a transaxial section could be chosen with regard to the relationship between the signal and the noise in the data.

The first step in this process was to determine the maximum power of the Butterworth filter which could be used without the production of ringing artefacts (it is desirable to use a Butterworth filter with a high power because it will maximise the transfer of the low spatial frequency data for which the noise power is dominated by the signal). This was

determined by reconstructing simulated projection data for a uniform source distribution. It was found that the amplitude of the ripple artefacts could be kept below below 2% if the power of the Butterworth filter was 10 or less. Given the level of local statistical noise which was obtained from the measurements made on the phantom data in Chapter 8 this was taken to be a suitable cut off value.

Having determined a value for the power factor the form of the Butterworth filter can be completely specified by its cut off frequency. This can be used to match the form of the filter function to the relationship between the signal and the noise in the projection data. The method which was developed to accomplish this used only the projection data in the transaxial section which was to be reconstructed. This was achieved by calculating the MAPS from the set of projection profiles. The filter could then be matched to the projection data by identifying the point in the MAPS at which the signal became dominated by the noise (the transition frequency).

The exact relationship between the transition frequency and the cut off frequency of the filter function must be determined for each particular clinical investigation. By using the data from a preliminary trial in which a small number of patient studies were analysed the value which the Butterworth filter should take at the transition frequency could be determined. The optimal value was taken to be that which produced the images which were most frequently judged to be the best by an experienced observer.

The filter matching procedure was extended to two dimensions in a practical manner by operating on the projection data after it had been filtered in the y-direction.

The differences between the two dimensional y-filter and the rotationally symmetrical filter were found to be small. The LNP(u) curve of the MAPS from the y-filtered data showed that the signal to noise ratio for each transaxial section had been increased. The two dimensional filtering also produced significant improvements in the quality of the coronal and sagittal sections.

Inherent in the filtered back projection reconstruction process is an assumption that the projection data are of an ideal form. However, processes such as the scattering and attenuation of the photons emitted from the source distribution mean that the form of the projection data which is actually acquired deviates from the ideal in a number of ways. As part of the reconstruction process a number of corrections for the deviation of the real data from its assumed form can be made.

An example of this is the correction for the presence of scattered photons in the photopeak window. In fact as a consequence of the good energy resolution of the camera it was found that the presence of scatter was not as important a limiting factor on image quality as had been reported by authors using previous generations of cameras Jaszczak (1985). Nevertheless, two simple scatter correction methods were attempted in this work; the use of an asymmetric energy window, and the subtraction of a scatter image from the photopeak image. Neither produced significant improvements in image quality. This was a consequence of the relatively small initial effect which the scattered photons had on the acquired images which resulted from the good energy resolution of the camera and the use of a 15% energy discrimination window

width. It is possible that more sophisticated scatter correction techniques may be required before significant improvements are observed. Many of these require the use of reconstruction methods other than that of filtered back projection, however, and so were outwith the scope of this work Egbert (1980).

Similarly, a consequence of the good and stable uniformity of the camera was that non-uniformity artefacts did not constitute an important limiting factor on the quality of the reconstructed SPECT images. This meant that the implementation of corrections for camera non-uniformity were only required in exceptional circumstances. The simple multiplicative correction method which was employed (using a specially constructed flood field phantom) was shown to be effective in removing non-uniformity artefacts from high count density phantom studies. However, when clinical count density phantom studies were investigated the non-uniformity artefacts were almost completely dominated by the noise in the data. The application of softer filters to produce better noise control had the additional effect of smoothing away most of the non-uniform artefacts. It was only at the COR that a correction for camera non-uniformity was found to be useful (it is at the COR where the amplification of camera non-uniformity is the greatest).

Thus, in practice it was decided that a high count flood field acquisition should be collected on a weekly basis. This can then be utilised to correct for non-uniformities if RCBF or liver studies are acquired in which features close to the COR are of clinical interest. It was not found to be of use for skeletal or cardiac studies where the features of interest

tend to be distant from the COR.

A correction for the effects of attenuation was also investigated. It was demonstrated using a uniform cylindrical source distribution that the Bellini attenuation correction algorithm produced a quantitatively accurate restoration of the counts which were lost as a result of attenuation.

However, when structured source distributions were examined it was found that although the correction algorithm behaved in a reasonable manner, in that there was a restoration of counts in the structures close to the centre of the object, there was little or no improvement in lesion detection or structure definition.

Having developed the optimised methodology for the acquisition and reconstruction of the SPECT data the results which were obtained were applied in the investigation of some specific clinical problems.

RCBF studies for the assessment of intractable epilepsy were performed using ^{99m}Tc -HMPAO. The aim was to identify focal areas of reduced blood flow with a view to surgical intervention.

During the course of this investigation a method was developed for the quantitative assessment of patient movement during the acquisition period of the SPECT study. This allowed objective criteria to be set so that unacceptable levels of patient movement can be consistently identified.

The use of the matched filter approach to the reconstruction of the data, as opposed to a simple application of the manufacturer's software, produced a significant improvement in the SPECT results as judged from a comparison with consensus of the results from the other imaging

modalities.

The results obtained from the rotating gamma camera showed a good agreement with those obtained from a dedicated single section brain SPECT imaging system. However, only a moderate agreement was found with the results obtained from the structural imaging modalities of CT and MRI. The functional information from the EEG measurements gave a reasonable level of agreement although the concordance was not as high as obtained with the dedicated SPECT system.

The SPECT results from both systems contributed useful additional information to that obtained from the other modalities concerning the presence and localisation of focal areas of reduced RCBF. The absence of a "gold standard" for the identification of focal lesions meant that an accurate comparison of the results from the two SPECT systems was not possible.

An investigation of the use of ^{99m}Tc -MIBI for the assessment of ischaemic heart disease was also performed. A high level of accuracy was found not only for the simple diagnosis of the presence or absence of coronary artery disease but also for the identification of individual diseased arteries and the differentiation of ischaemic from scarred myocardium.

It was found that there was an increase in the accuracy of the SPECT results if the two dimensional Butterworth filter was used instead of the manufacturer's software. However, no clear advantage of SPECT over planar imaging was demonstrated. This could be because of the small number of patients studied and their polarisation into either very low or very high a priori disease probability categories.

Finally, the clinical question of the diagnosis of AVN of the femoral head using SPECT imaging with ^{99m}Tc -MDP was addressed. The critical scientific problem related to this was the destructive effect which the high and changing levels of activity in the bladder had on the reconstruction process. A method was developed which successfully addressed this problem.

By replacing, in the projection images, the large and inconsistent count information in the bladder by data which are representative of the activity in the regions surrounding the bladder the level of artefact production was significantly reduced. Choosing the site of the bladder from the sinogram files reduced the level of user interaction to the definition of a single ROI making the implementation of the method a practical proposition.

Thus, in conclusion a systematic evaluation of all major aspects of the SPECT imaging process has been performed. Practical guidelines have been produced to ensure that the maximum amount of relevant clinical information is included in the reconstructed data. Finally, these results have been applied in the investigation of three separate clinical problems.

Appendix 1 Count losses in SPECT due to high dynamic range data

Introduction

Skeletal imaging using SPECT has been shown to be of use for the investigation of avascular necrosis of the femoral heads, Collier (1985). Unfortunately, it is common for 20% or more investigations to be of no value due to the creation of artefacts by the presence of high and changing levels of activity within the bladder. The most obvious type of artefact takes the form of streaks which can extend across the whole width of a transaxial section. The formation of this type of artefact is well known as is its cause, the inconsistent nature of the projection data due to the changes in bladder activity over the duration of the study acquisition. However, another form of artefact may also be present in many studies. This appears as a reduction in counts in structures in the same axial plane as the bladder and occurs if the activity in bladder is high. When coronal sections are taken through the hips the count losses in the femoral heads can easily be mistaken for the photon deficient areas which are diagnostic of femoral head avascular necrosis.

To investigate and quantify this phenomenon some simple phantom studies were performed.

Methods

To represent the bladder and a femoral head two cylindrical containers 11cm in length and 6cm in diameter were used. The phantoms were aligned with the long axes parallel to and equidistant from the axis of rotation and separated by a

centre to centre distance of 12cm.

The container representing the femoral head was filled to give a concentration of ^{99m}Tc which would give similar count densities to those found in the femoral heads during clinical studies. The bladder phantom was filled with a variety of concentrations of ^{99m}Tc chosen to give activity ratios of from 0 to 50 times that in the femoral head phantom. A separate SPECT acquisition was performed for each femoral head to bladder phantom activity ratio. The total activity in both phantoms was such that the countrate was always below 5,000 counts per second ensuring that countrate losses did not occur.

The SPECT acquisitions were performed with a ROR of 20cm using 64 angles over 360 degrees with pixels of edge length 0.7cm. The SPECT data were reconstructed using a Shepp-Logan filter.

To reduce the effects of statistical noise 10 transaxial sections along the centre of each cylinder were summed. A square region of interest was drawn inside the centre of the bladder and femoral head phantoms and the counts determined in each for the set of bladder to femoral head phantom activity ratios.

The exact values of the bladder to femoral head phantom activity ratios were determined by taking planar images.

Results

The variation of counts in the axial sections through the femoral head phantom as a function of bladder to femoral head phantom ratios is shown in Table 1. The femoral head counts are expressed as a percentage of the counts obtained in the

femoral head phantom in the study where the bladder phantom activity was zero. It was observed that the counts in the axial sections through the femoral head phantom decreased as the activity in the bladder phantom increased.

The variation of counts in the axial sections through the bladder phantom for the various SPECT studies is shown in Table 1. The counts in the axial sections through the bladder phantom are expressed relative to those obtained in the study where the bladder to femoral head phantom activity ratio was unity. The counts in the axial sections through the bladder phantom were consistent with the values expected from the planar measurements. The count losses observed in the sections through the femoral head phantom were not observed in the sections through the bladder phantom.

Discussion

The loss of counts in axial sections through structures in the same axial plane as the bladder is shown in Table 1. The count losses were restricted to structures outside the bladder phantom as is shown in Table 2 where the counts in the axial sections through the bladder were as expected from the measurements made using the planar images.

These results imply that the count losses in the femoral head phantom were not due to some kind of arithmetic overflow during the reconstruction on the data. A further check on this was made by dividing the data in the projection views by a constant before reconstructing the SPECT study. However, no matter how large the constant value was made the count losses in the femoral head phantom were still observed. This leads to the important conclusion that it is the high dynamic range in

the data which causes the count losses rather than high absolute count values in the bladder phantom.

Another important point to note is that the count losses could not have been caused by inconsistent data produced by activity levels which changed during the acquisition period of the study. For these phantom measurements the activity in the bladder phantom was constant over the acquisition period.

To check that the count losses were not due to a fault or error which was specific to the particular computing system or the reconstruction algorithm used the tests were repeated on two separate systems at different sites (a Siemens micro-delta attached to a Siemens Orbiter camera and a Link Systems Maps 2000 attached to an I.G.E. 400AT). Very similar results were obtained on all systems indicating that the count loss phenomenon is probably very common and may in fact be inherent in the process of filtered back projection itself and independent of the particular computing system or algorithm used.

Finally a variety of filter functions, including the ramp filter, were used to reconstruct the data without having a significant effect on the results.

It is thought that the origin of the count losses occurs in the filtering process which takes place before the data is back-projected. An examination, in the spatial domain, of the values in the functions used to filter the data shows the presence of negative values a few points distant from the positive central value. When the central value is used to multiply the count data in the femoral head the negative values in the filter can be positioned so that they will be multiplied by the relatively large values in the bladder. The

large negative values so produced can swamp the data leading to the count losses.

The values in any of the functions used to filter the data in the filtered back projection process are essentially arbitrary in nature. They are obtained by modifying the values from the ramp function which, given noise free data sampled infinitely finely at an infinite number of angles, will remove the $1/r$ blurring inherent in back-projection. The use of the ramp filter for real data is an approximation and the use of a window function to suppress noise increases the approximate nature of the filtering process further. Thus, considering the above it is not surprising that in some circumstances, e.g a high dynamic range, the filtered back projection method of reconstruction can produce data with significant errors.

Conclusions

It has been shown that if there is a high dynamic range in data to be reconstructed by filtered back-projection then significant errors in the reconstructed data can occur. These take the form of an underestimation of the activity in the less active structures in the axial plane.

The count losses are independent of the filter used to reconstruct the data. They have been shown to occur when the activity levels in the objects being studied remain constant during the acquisition period of the study. This indicates that the cold area artefacts observed in clinical studies, i.e bone scans of the pelvis, have nothing to do with the inconsistent nature of the projection data caused by changing levels of activity in the bladder .

Appendix 2 Publications resulting from this thesis

Gillen GJ, Hilditch TE and Elliott AT : Non-isotropic point spread function as a result of collimator design and manufacturing defects. J. Nucl. Med. 29:1096-1100, 1988.

Gillen GJ, McKillop JH, Hilditch TE, Davidson JK and Elliot AT : Digital filtering of the bladder in SPECT bone studies of the pelvis. J. Nucl. Med. 29:1587-1595, 1988.

Gillen GJ, McKillop JH, Hilditch TE, Davidson JK and Elliot AT : Digital filtering of the bladder in SPECT bone studies of the pelvis. European. J. Nucl. Med. 14 :8 p421, 1988.

Gillen GJ, Elliott AT, Hilditch TE : Quality control of analogue to digital converters for artefact free SPECT imaging. European J. Nucl. Med. Vol 15 :8; p668, 1989.

Dobson HJ, Gillen GJ and Campbell C : SPECT of the skeleton. Brit. J. Radiol. 61 p1126 Oct 1988

References

- Anger HO, : Scintillation camera. Rev. Sci. Instrum. 29, 27-33, 1958
- Atkins FB, Beck RN, Hoffer PB, et al :Dependence of optimum baseline setting on scatter fraction and detector response function. In Medical Radionuclide Imaging, Vol 1, Vienna, IAEA,pp 101-108, 1977
- Bauer G., Weber D.A., Ceder L. et al: Dynamics of technetium-99m methylene diphosphonate imaging of the femoral head after hip fracture. Clin. Orthop. 152: 85-92, 1980.
- Beck RN: Theory ofradioisotope scanning systems . Medical radioisotope scanning, Vol 1:35-56, Vienna: IAEA 1964.
- Beck RN, Schuh MW, Cohen TD, Lembares N: Effects of scattered radiation on scintillation detector response. Medical radioisotope scintigraphy, Vol 1:595-616, Vienna: IAEA 1969.
- Beck RN, Zimmer LT, Charleston DB, Hoffer PB, Lembares N: The theoretical advantages of eliminating scatter in imaging sytems. Semiconductor detectors in the future of nuclear medicine, Chapter 7:92-113, New York: Society of Nuclear Medicine, 1971.
- Beck RN, Zimmer LT, Charleston DB, Shipley WW, Brunsten BS : A theory of optimum utilisation of all detected radiation. Proc. Univ of California symposiun on semiconductor detectors in nuclear medicine : 273-275. San Francisco: United States Atomic Energy Commision CONF-730321, 1973.

Bellini G : Compensation of tissue absorption in emission tomography. IEEE Transactions on acoustics, speech, and signal processing Vol 12, No 3, June 1979.

Bloch P, Sanders T: Reduction of the effects of scattered radiation on a sodium iodide imaging system. J Nucl Med 14:67-72, 1973

Bieszka JA and Hawman EG : Evaluation of SPECT angular sampling effects: Continuous versus step-and-shoot rotation. J Nucl Med 28:1308-1314, 1987.

Bok BD, Bice AN, Clausen M, Wong DF, Wagner HN : Artifacts in camera based single photon emission tomography due to time activity variation. European J. Nucl Med 13: 439-442, 1987

Bracewell RN and Riddle AC : Inversion of fan beam scans in radio astronomy. Astrophysical J. 150 pp 427-434, 1967.

Brooks RA, Weiss GH, Talbert AJ : A new approach to interpolation in computed tomography. J Comput Assist Tomog 2:577, 1978.

Budinger TF, Derenzo SE, Gullberg GT et al : Emission computer assisted tomography with single photon and positron annihilation photon emitters. J. Comput. Assist. Tomog. 1 ; 131, 1977.

Budinger TF, Gullberg GT : Transverse section Reconstruction in gamma ray emitting radionuclides in patients. From Reconstruction Tomography in Diagnostic Radiology and Nuclear Medicine. Ed Ter-Pogossian University Park press, Ballimore 1979.

Budinger TF, Derenzo SE, Greenberg WL, Gullberg GT, Huesman RH :
Quantitative potentials of dynamic emission computed tomography . J
Nucl Med 19:309-315, 1978.

Cahan LD, Engel J : Surgery for epilepsy - a review, Acta Neurol Scand,
73, 551-60, 1986.

Cappellini V, Constantinides AG, Emiliani P : Digital filters and
their applications. New York, Academic Press, 221-227, 1978.

Chang LT : A method for attenuation correction in radionuclide
computed tomography IEEE Trans Nucl Science NS-25 638-43, 1978

Chessler DA and Riederer SJ : Ripple suppression during reconstruction
in transverse tomography. Phys. Med Biol. 20, 4, 632-636. 1975.

Coleman RE, Jaszczak RJ, Cobb FR : Comparison of 180° and 360° data
sampling techniques for transaxial SPECT Thallium-201 myocardial
perfusion imaging. J. Nucl. Med 26:695-706, 1985.

Collier B.D., Hellman R.S., Krasnow A.Z.: Bone SPECT. Semin. Nucl.
Med. 17: 247-267, 1987.

Collier B.D., Johnson R.P., Carrera G.F. et al : Painful spondylolysis
or spondylolisthesis studied by radiology and single-photon emission
computed tomography. Radiology 154: 207-211, 1985.

Collier B.D., Carrera G.F., Johnson R.P. et al : Detention of Femoral
Head Avascular Necrosis in Adults by SPECT. J. Nucl. Med. 26: 979-987,
1985.

Collier B.D., Carrerra G.F., Messer A.J. et al : Internal derangement of the temporo-mandibular joint: detection by single photon emission computed tomography. Radiology 149: 557-563, 1986.

Collier BD, Palmer DW, Knowbel J, et al : Gamma camera energy windows for ^{99m}Tc bone scintigraphy: Effect of asymmetry on contrast resolution. Radiol 151:495-497, 1984.

Cormack AM : Reconstruction of densities from their projections, with applications in radiological physics. Phys. Med. Biol. 18 pp 195-207, 1973.

Costa DC, Ell PJ : Temporal lobe epilepsy, role of routine functional brain Imaging In press 1989

Costa DC, Jones BE, Steiner TJ : Relative ^{99m}Tc - HMPAO and ^{113}Sn -microspheres distribution in dog brain. Nuclearmedizin 25 : A53, 1986

Crowther RA, de Rosier DJ, Klug A : Proc. R. Soc. A317 pp 319-340, 1970.

Dainty and Shaw : Image Science Academic Press London ISBN 0 12 200850 1974.

Dobson HJ, Gillen GJ and Campbell C : SPECT of the skeleton. Annual meeting of the British Radiology Society, Glasgow 1988.

Egbert S.D. and May R.S. : An integral transport method for Compton scatter radiation in emission computed tomography. IEEE Trans Nucl

Sci. vol NS-27 , 543-547, 1980

Eisner RL, Nowak DJ, Pettigrew Rand Fajman W : Fundamentals of 180° acquisition and reconstruction in SPECT imaging. J. Nucl.Med. 27:1717-1728, 1986.

Ell PJ, Jarritt PH, Costa DC, Cullum ID, Lui D : Functional Imaging of the Brain, Semin Nuc Med Vol XVII, No3, pp214-229, 1987.

Elliott AT, Short MD, Barnes KJ : The performance assessment of gamma cameras , part I, report STB/86/9. Department of Health and Social Security , London, 1980

Elliott AT, Short MD, Barnes KJ : The performance assessment of gamma cameras , part II , report STB/86/9. Department of Health and Social Security , London, 1982

Elliott AT, Short MD, Barnes KJ : The performance assessment of gamma cameras , part III , report STB/86/9. Department of Health and Social Security , London, 1985

Elliott AT, Short MD, Barnes KJ : The performance assessment of gamma cameras , part IV , report STB/86/9. Department of Health and Social Security , London, 1986

Engel J. Kuhl DE, Phelps ME : Functional Imaging of the epileptic brain with positron computed tomography. In: Rose FC, ed. Research progress in epilepsy. London : Pitman, 1983.

Engel J, Kuhl DE, Phelps ME, Crandall PM : Comparative Localisation of

epileptic foci in partial epilepsy by PET and EEG. Ann Neurol, 12, 529-537, 1982.

Feiglin D., Levine M., Stulberg B, et al: Comparison of planar and SPECT scanning in the diagnosis of avascular necrosis of the femoral head. J.Nucl. Med. 27: 952, 1986.

Gilbert P : Iterative methods for the three-dimensional reconstruction of an object from its projections. J. Theoretical Biology 36 pp105-117 1972.

Gilland D.R., Tsui B.M.W., McCartney W.H, Perry J.R. and Berg J. : Determination of the optimum filter function for SPECT imaging. J Nucl Med 29:643-650. 1988.

Gillen GJ, Hilditch TE and Elliott AT : Non-isotropic point spread function as a result of collimator design and manufacturing defects. J. Nucl. Med. 29:1096-1100, 1988.

Gillen GJ, McKillop JH, Hilditch TE, Davidson JK and Elliot AT : Digital filtering of the bladder in SPECT bone studies of the pelvis. J. Nucl. Med. 29:1587-1595, 1988.

Gillen GJ, Elliott AT, Hilditch TE : Quality control of analogue to digital converters for artefact free SPECT imaging. European J Nuclear Medicine Vol 15 :8; p668, 1989.

Goiten M : Three dimensional density reconstruction from a series of two-dimensional projections. Nucl. Instrum. Methods 101 pp 509-518, 1972.

Goodman JW, Belsher JF : Fundamental limitations in linear invariant restoration of atmospherically degraded images. In SPIE Vol 75 Imaging through the atmosphere, Society of Photo-Optical Instrumentation Engineers pp141-154, 1976.

Goris M.L., Daspit S.G., McLaughlin P. et al: Interpolative background subtraction. J. Nucl. Med. 17: 744-747, 1976.

Gordon R, Bender R, Herman GT : Algebraic reconstruction technique (ART) for three dimensional microscopy and X-ray photography. J. Theoretical Biology 29 pp471-481, 1970.

Graham LS, LaFontaine RL, Stein MA : Effects of asymmetric photopeak windows on flood field uniformity and spatial resolution of scintillation cameras. J. Nucl. Med. 27:706-713, 1986

Greyson N.D., Kassel E.E.: Serial bone scan changes in recurrent bone infarction. J. Nucl. Med. 17: 184-186,1976.

Grief J, Lanng S, Hoiland-Carlson PF et al: Early detection by ^{99m}Tc-sn-pyrophosphate scintigraphy of femoral head necrosis following medical femoral neck fractures. Acta. Orthop. Scan. 51: 119-125, 1980.

Gustafson DE : 3-D Biomedical Imaging Vol III Ed Richard A Robb CRC Press Inc, Florida. 1985.

Hall RC, Etchells AH (1986) :A gamma camera phantom support stand for safer and faster non-uniformity procedures Brit. J. Radiol. 700,59

Holmes RA, Chaplin SB, Royston KG et al : Cerebral uptake and retention of ^{99m}Tc -HMPAO. Nuc. Med. Comms (6) 443-447, 1985

Huesman RH : Analysis of statistical errors for transverse section reconstruction. Internal report Donner Lab Berkely CA LBL-4278. 1975.

Huesman RH : The effects of a finite number of projection angles and finite lateral sampling of projections on the propagation of statistical errors in transverse section reconstruction. Physics Med. Biol. 22,511-521. 1977.

Hurst JW: Right Coronary Artery, in Logue RB, Shlant RC, Wenger NK (eds) The Heart McGraw-Hill, New York, p35. 1978.

Hospital Physicists' Association : The theory, specification and testing of Anger type gamma cameras. Topic group report NO 27, Hospital Physicists Association, London. 1978.

Jacobson H., Larsson, S.A., Vesterskold L. et al: The application of single photon emission computed tomography to the diagnosis of ankylosing spondylitis of the spine. Brit. J. Radio1. 57: 133-140, 1984.

Jaszczak RK, Coleman RE, Whitehead FR : Physical factors affecting quantitative measurements using camera based single photon emission computed tomography (SPECT). IEEE Trans Nucl Science NS-28 pp69-80 February. 1981.

Jaszczak RJ, Floyd CE, Coleman RE : Scatter compensation techniques for SPECT. IEEE Transactions in Nuclear Science, Vol NS-32, No 1,

February. 1985.

Jarritt HJ, Ell PJ : Gamma camera emission tomography quality control and clinical applications. Current medical literature Ltd., ISBN 1 85009 005. 1984.

Jenkins GM, Watts DG : Spectral analysis and its applications. San Francisco Holden-Day, 6-8, 126-208, 1986

Kemp MC, Skilling J : Image reconstruction by maximum entropy. Proc. IEEE Electronic Image Processing 6 pp63-67. 1982.

Keyes J.W. : Perspectives on Tomography. J. Nucl. Med 23:633-640, 1982

Kiat M, Maddahi J, Merz R, Roy L, Rosser K, Kimsey P, Friedman J, Berman D : Comparison of ^{99m}Tc MIBI with Tl-201 imaging by planar and SPECT techniques Proc 35th SNM. J Nucl Med 29 793 1988

Kijewski MF, Judy PF : The noise power spectrum of CT images. Phys. Med. Biol. 32 565. 1987.

King M.A. ,Doherty P.W. and Schwinger R.B. : A Wiener filter for nuclear medicine images. Med Phys 10(6) 876-880. 1983.

King M.A., Schwinger R.B., Doherty P.W., and Penney B.C. : Two-Dimensional filtering of SPECT images using the Metz and Wiener filters. J Nucl Med 25:1234-1240. 1984.

King M.A., Glick S.J., Penney B.C., Schwinger R.B. and Doherty P.W. : Interactive visual optimisation of SPECT prereconstruction filtering.

J Nucl Med 28:1192-1198. 1987.

King M.A., Miller R.T., Doherty P.W. and Schwinger R.B. : Stationary and nonstationary spatial domain Metz filtering. Nuclear Medicine Communications 9,3-10. 1988.

Knesaurek K. : Comparison of 360° and 180° data collection in SPECT imaging. Phys. Med. Biol. Vol 32, No 11, 1445-1456. 1987

Kuhl DE, Fishbein D, Dubinsky R : Patterns of cerebral metabolism in patients with partial seizures. Ann Neurol, 38, 1201-1208. 1988.

LaFontaine R, Stein MA, Graham LS, : Contrast enhancement of cold lesions using asymmetric photopeak windows. Radiology 149P :232. 1983.

Lange RC: A simpler method for optimising the window of the Anger camera for Tc-99m. J Nucl Med 13:342, 1972.

Larson S.A. : Gamma camera emission tomography. Acta Radiologica Supplementum 363 1980.

Lewellen T, Murano R., Weimer K, et al : The use of asymmetric windows. In Proc third world congress of nuclear medicine and biology, Raynaud C, ed Vol 2, Paris, Pergamon Press, pp1236-1239 1982

Lewellen T, Murano R, Weimer K, et al : The use of asymmetric windows. J Nucl Med 23:P30, 1982.

Madsen M.T. and Park C.H. : Enhancement of SPECT images by Fourier filtering the projection image set. J Nucl Med 26:395-402. 1985.

- McClellan JH : A 2-D FIR filter structure derived from the Chebyshev recursion. IEEE Trans Circuits Systems CAS-24;372-378 1977.
- Mecklenbrauker WFG, MersereauRM : McClellan transformations for two dimensional digital filtering.; II-Implementation . IEEE Trans Circuits Syst CAS-23:414-422, 1976.
- Metz CE, Strubler KA and Rossmann K : Choice of linespread function sampling distance for computing MTF of radiographic screen film systems. Phys Med Biol 17,638. 1972.
- Miller TR and Sampathkumaram KS : Digital filtering in nuclear medicine. J Nucl Med 23: 66-72, 1982
- Miller TR and Sampathkumaran KS : Design and application of finite impulse response digital filters. Eur J Nucl Med 7 22-27, 1982
- Miller TR, Sampathkumaran KS and King MA : Rapid digital filtering. J Nucl Med 24 625-628, 1983.
- Moore SC, Kijewski MF, Muller SP and Holman BL : SPECT image noise power: effects of nonstationary projection noise and attenuation compensation. J Nucl Med 29:1707-1709. 1979.
- Okada RD, Glover D, Gaffney T, Williams S : Myocardial kinetics of technitium-99m-hexakis-2-methoxy-2-methylpropyl-isonitrile. Circulation 77, 491-498. 1988.
- Penney BC, King MA, Schwinger RB et al : Constrained least squares

restoration of nuclear medicine images: Selecting the coarseness function. Med Phys 14 (5) 849-857, 1987

Penney BC, King MA, Schwinger RB et al : Modifying constrained least squares restoration for application to single photon emission computed tomography projection images. Med Phys 15 (3) 334-342, 1988

Pettigrew RI, Alwood E, Webb R et al : SPECT compared to planar ^{99m}Tc pyrophosphate infarct avid scintigraphy. J. Nucl. Med. 24:P18 1983.

Phelps ME : Emission computed tomography. Semin Nucl Med 1 337, 1977

Meuhllehner G, Wake RH, Sano R : Standards for performance measurements in gamma cameras. J Nucl Med 21,72-77. 1981.

Podreka I, Suess E, Goldenberg G, Steiner M, Brucke T, Muller Ch; Lang W, Neirinckx RD and Deeke L. : Initial experience with ^{99m}Tc HM-PAO Brain SPECT. J. Nucl. Med. 28: 1657-1666, 1987.

Pullan BR, Rutherford RA, Isherwood I : Computerised transaxial tomography. Proc 7th LH Gray Conference Medical Images Formation, Perception and Measurement pp 20-38. 1976.

Radon J. : Uber die Bestimmung von Functionen durch ihre Integralwerte langs Gewisser Mannigfaltigkeiten. Ber. Vrek. Sachs Akad. 69 ,262. 1917.

Rogers WL , Clinthorne NH, Harkness BA, Koral KF, Keyes JW : Field flood requirements for emission computed tomography with an Anger camera . J Nucl Med 23: 162-168, 1982.

- Rollo FD, Schultz AG : Effects of pulse-height selection on lesion detection performance. J. Nucl. Med. 12 (10): 690-696, 1971.
- Sanders TP, Sanders TD, Kuhl DE : Optimising the window of the Anger camera for Tc-99m. J Nucl Med 12:703-706, 1971.
- Sano RM, : Performance standards. Medical radionuclide imaging, Vol 2, pp142,159. IEAE, Vienna 1980.
- Saw CB : Effects of centre of rotation shift on contrast and spatial resolution of the SPECT system. Nuclear Medicine Communications Vol7 No5 373-379, 1986.
- Savic I, Persson A, Roland P, Pauli S, Sedvakk G, Widen L : In-vivo demonstration of reduced benzodiazapine receptor binding in human epileptic foci. Lancet ; ii : 863-66 1988.
- Schorner W, Meenke HJ, Felix R : Temporal Lobe Epilepsy : comparison of CT and MR imaging Am J Neuroradiol, 8, 773-781, 1987.
- Shannon CE, Weaver W : The mathematical theory of communication. University of Illinois press Urbana. 1949
- Sharp PF, Smith FW, Gemmel HG et al : ^{99m}Tc -HMPAO Stereoisomers as potential agents for imaging regional cerebral blood flow. Human volunteer studies. J. Nucl. Med. 27, pp 171-177, 1986
- Sharp PF, Dendy PP, Keyes WI : Radionuclide Imaging Techniques, London, Academic Press, pp 174-177. 1985.

Shepp LA , Stein JA : Simulated reconstruction artifacts in computerised x-ray tomography . In Reconstruction Tomography in Diagnostic Radiology and Nuclear Medicine, Ter-Pogossian MM, Phelps ME, Brownell GL, et al, eds. Baltimore, University Park Press, pp33-49, 1982.

Snyder DL. Cox JR : An overview of reconstruction tomography and limitations imposed by a finite number of projections. Reconstruction tomography in diagnostic radiology and nuclear medicine, Baltimore :University Park Press, 1977

Soundy RG, Tyrrel DA, Ricket RD : Radiation doses to patients following intravenous injection with ^{99m}Tc - HMPAO. Amersham Report PTN 85/8, Corporate Safety Group Technical Note, (Internal Dose Calculation No 34), 1985.

Soussaline FP, Cao A, Le Coq et al : An analytical approach to single photon emission computed tomography with the attenuation effect. European Journal of Nuclear Medicine 7 487-93, 1982.

SPECT and PET in Epilepsy : Editorial, The Lancet, I, 135. 1989.

Stoub EW : Method and circuit for stabilising conversion gain of radiation detectors of a radiation detection system. United States Patent , number 4,583,187, April 1986.

Surgery for Temporal Lobe Epilepsy Editorial, The Lancet, II, 1115, 1988.

Taylor DN, Choraria SK, Maughan J, Mills J and Pilcher J : Diagnosis of coronary artery disease using thallium imaging: tomographic versus planar imaging. Nuc. Med. Comms. 10, 401-407, 1989.

Tamaki N, Mukai T, Ishii Y et al : Comparative study of thallium emission myocardial tomography with 180° and 360° data collection. J. Nucl. Med. 23:661-666, 1982.

Theodore WH, Dorwart R, Holmes M, Porter RJ, Di Chiro G : Neuroimaging in refractory partial seizures. Comparison of PET, CT and MRI. Neurology 36, 750-759, 1986.

Todd-Pokropek AE, PH Jarrit : The noise characteristics of SPECT systems. Computed Emission Tomography pp361-390 Oxford University Press ISBN 019-261347-2. 1982.

Todd-Pokropek AE : The mathematics and physics of emission computed tomography : current trends. Society of Nuclear Medicine, New York (Ed. Esser P.) 1983.

Todd-Pokropek AE, Zorowski S, Soussaline F : Non-Uniformity and artifact creation in tomography J. Nucl. Med. 21:p38 1980.

Walters GL, Hendrix GH, Gordon L, Wigger B : Application of a standard deviation of a normal population to thallium-201 bullseye SPECT J. Nucl. Med. 29 954 1988.